Geology of the Archean Côté Gold Au(-Cu) Intrusion-Related Deposit, Swayze Greenstone Belt, Ontario

by

Laura Rachel Katz

A thesis submitted in partial fulfillment
of the requirements for the degree of
Doctor of Philosophy (PhD)
in
Mineral Deposit and Precambrian Geology

The Faculty of Graduate Studies
Laurentian University
Sudbury, Ontario, Canada

THESIS DEFENCE COMMITTEE/COMITÉ DE SOUTENANCE DE THÈSE
Laurentian Université/Université Laurentienne
Faculty of Graduate Studies/Faculté des études supérieures

Title of Thesis Titre de la thèse	Geology of the Archean Côté Gold Au(-Cu) Intrusion-Related Deposit, Swayze Greenstone Belt, Ontario
Name of Candidate Nom du candidat	Katz, Laura
Degree Diplôme	Doctor of Philosophy
Department/Program Département/Programme	Mineral Deposits and Precambrian Geology
Date of Defence Date de la soutenance	April 05, 2016

APPROVED/APPROUVÉ

Thesis Examiners/Examinateurs de thèse:

Dr. Daniel Kontak
(Supervisor/Directeur(trice) de thèse)

Dr. Pedro Jugo
(Committee member/Membre du comité)

Dr. John Ayer
(Committee member/Membre du comité)

Dr. Alan Galley
(External Examiner/Examinateur externe)

Dr. Harold Gibson
(Internal Examiner/Examinateur interne)

Approved for the Faculty of Graduate Studies
Approuvé pour la Faculté des études supérieures
Dr. David Lesbarrères
Monsieur David Lesbarrères
Dean, Faculty of Graduate Studies
Doyen, Faculté des études supérieures

ACCESSIBILITY CLAUSE AND PERMISSION TO USE

Abstract

The Côté Gold Au(-Cu) deposit is a low-grade, large-tonnage type deposit with an indicated resource of 269 Mt averaging 0.88 g/t Au (7.61 M oz) and an inferred resource of 44 Mt averaging 0.74 g/t Au (1.04 M oz) at a cut-off grade of 0.3 g/t Au. The deposit is located in the Swayze greenstone belt (SGB), part of the larger and gold-rich Abitibi Subprovince and is the first large gold deposit to be discovered in the SGB.

The deposit is hosted by multi-phase tonalite, diorite and quartz diorite intrusions of the Chester intrusive complex (CIC), a multi-phased, laccolith-shaped synvolcanic intrusion. Crosscutting relationships suggest coeval emplacement of the host rocks and high-precision U-Pb ID-TIMS zircon geochronology results constrain the CIC to ca. 2741 to 2739 Ma. Although a close temporal relationship exists between the tonalite and dioritic phases, they appear to be petrogenetically unrelated. The CIC is demonstrated to be petrologically, texturally and geochemically similar to low-Al tonalite-trondhjemite-diorite composite intrusions known to underlie VMS-type mineralization. The CIC was emplaced into tholeiitic mafic metavolcanic rocks of the Arbutus Formation that are interpreted to have formed in a back-arc environment. The CIC is coeval and cogenetic with the felsic to intermediate rocks of the Yeo Formation. Emplacement of the CIC into a shallow crustal level is inferred based on the incorporation of screens and inclusions of the Yeo Formation, consistent with the presence of textures, such as granophyres, miarolitic cavities and pegmatites, and Al-in hornblende geobarometry results of $\leq 1.3 \pm 0.6$ kbars. The intrusive complex is intruded by several younger and petrogenetically unrelated dike phases, as well as overprinted by regional deformation events.

The deposit has a large ore envelope (1200 m by 300 m) within which several styles of mineralization (breccias, disseminations and veins) that are co-spatial and cogenetic to hydrothermal alteration are recognized. The hydrothermal stages consist of: (1) a rare series of gold-bearing amphibole-rich veins and breccias spatially restricted to the south and central parts of the deposit; (2) an extensive, main-stage biotite alteration that is centred on Au- and Cu-bearing hydrothermal biotite breccia bodies. Outwards from the breccia are veins (stockworks and sheeted arrays) and disseminations; (3) an extensive, Au ± Cu-bearing fracture-controlled and replacement-style muscovite alteration in the centre of the deposit; (4) an unmineralized fracture-controlled and disseminated epidote alteration that is localized to the north of the deposit; (5) a texturally destructive albite alteration occurs in the central part of the deposit; and (6) chlorite alteration that overprints biotite alteration. Drill core observations suggest that all the hydrothermal events, except chloritization, broadly overlap with magmatism and are crudely zoned on the deposit scale; chloritization is considered to be metamorphic in origin.

To constrain the timing of hydrothermal events U-Pb ID-TIMS, SHRIMP and LA ICP-MS dating of four hydrothermal titanites from amphibole and albite alteration assemblages and Re-Os dating of two molybdenite samples were analyzed. The hydrothermal titanite ages are centred on a ca. 2740 Ma and the molybdenite ages are 2736.1 ± 11.4 Ma and 2746.8 ± 11.4 Ma. These ages overlap with magmatism and strongly support a syn-intrusion timing for alteration and gold mineralization. Importantly, this age represents a new metallogenic gold event in the Abitibi Subprovince. In addition, two rutile ages at ca. 2667 Ma were obtained and indicate the deposit was affected by subsequent thermal events, such as regional metamorphism.

Several of the alteration types (i.e., amphibole, biotite, muscovite and epidote) are considered to be genetically related to the dioritic phases of the CIC based on relative timing,

distribution, mineralogy and mineral chemistry and whole-rock geochemistry. The progressive crystallization of the dioritic magma chamber is considered to have resulted in the generation of mineralized magmatic-hydrothermal fluids that are thought to be responsible for generating the Côté Gold deposit. The sequence of alteration types, their zonation in the deposit and their chemistry (i.e., gains and losses, REE patterns, metal associations and isotopes) is consistent with the early hydrothermal stages (i.e., amphibole and biotite) having formed from high temperature magmatic-derived dioritic fluids and the later alteration types (i.e., muscovite and epidote) having formed from cooling magmatic fluids mixed with seawater.

The development of albite alteration is thought to be the result of volatile exsolution of tonalite based on its syn-intrusion timing and the Na-rich nature of the fluids. Although albite alteration may be gold-bearing, the erratic distribution of the mineralization and the leaching capacity of fluids suggest earlier gold was remobilized during this event.

Considering the characteristics of the host rocks, the demonstrated overlap of magmatic and hydrothermal events at ca. 2740 Ma, the nature and distribution of alteration, the style of the associated mineralization and the geochemical characteristics of the hydrothermal fluids the Côté Gold deposit is considered to be intrusion-related in origin and formed in a manner similar to Phanerozoic porphyry-type deposits.

Keywords

Côté Gold deposit; Chester intrusive complex; low-Al composite intrusion; Swayze greenstone belt; magmatic-hydrothermal breccia; intrusion-related gold deposit; Archean porphyry deposit

Co-Authorship Statement

This thesis consists of three manuscripts prepared for publication in peer-reviewed journal articles and an additional paper in the Appendix. As such, Chapters 2 to 4 were co-authored by the candidate and several collaborators. The collaborators provided constructive suggestions and edits, along with figures and tables for geochronological data (U-Pb, Re-Os). The candidate is the first author on all manuscripts, except for a paper included in Appendix A. The contribution to this study of the Côté Gold deposit by the candidate includes: (1) drill core logging of 157 diamond drill holes, representing over 77 000 m of core; (2) the detailed mapping of several key outcrops (n = 5) and their digitization into maps; (3) collection of most the samples used for U-Pb geochronology (zircon, titanite and rutile) and all of the samples for Re-Os dating; (4) collection of the several hundred samples for detailed petrographic study and whole-rock geochemistry; (5) petrographic analyses of several hundred samples; (6) compilation and description of approximately 455 samples used for whole-rock geochemistry and the interpretation of these data; (7) a Terraspec study, which utilized equipment provided by IAMGOLD, which involved the in-situ measurement of 3 356 spectra measured over 12 206 m of drill core, creation of relevant cross sections and binary diagrams and the subsequent interpretation of the results; and (8) creation of the majority of the figures and tables.

Significant contributions to each of the manuscripts are outlined below.

- Chapter 2: The geochemical analyses used in this paper were completed at Activation Laboratories Ltd. through the TGI-4 Lode Gold Project conducted in collaboration with Dr. Benoit Dubé of the Geological Survey of Canada (GSC). Dr. Dubé also contributed intellectually with edits and suggestions. The U-Pb ID-TIMS geochronology was also done as part of the TGI-4 Lode Gold Project as

was provided by Dr. Vicki McNicoll of the GSC; she completed the analytical work, provided the ages, the concordia diagrams, data table, descriptions of the results and contributed to the interpretation of the ages. The electron microprobe analyses were conducted by Mr. Dave Crabtree of the Ontario Geological Survey.

- Chapter 3: Dr. Dubé also contributed intellectually with edits and suggestions. The U-Pb ID-TIMS and SHRIMP geochronology was again done under the TGI-4 Lode Gold Project led by Dr. McNicoll of the GSC who completed the analytical work, provided the concordia diagrams, data table, descriptions of the results and contributed to the interpretation of the ages. The LA ICP-MS U-Pb dating was completed by Dr. Joseph Petrus of Laurentian University who analyzed the samples and provided the ages, concordia diagrams, methods, data table and descriptions of the results. The trace element analyses of biotite was done with LA ICP-MS by Dr. Petrus who also provided the methods and data table. The electron microprobe analyses were again conducted by Mr. Dave Crabtree.
- Chapter 4: The geochemical analyses were completed at Activation Laboratories Ltd. through the TGI-4 Lode Gold Project in collaboration with Dr. Dubé of the GSC. The trace element analyses of chalcopyrite was done with LA ICP-MS by Dr. Petrus who also provided the methods and data table.
- Appendix A.1: Dr. Jamie R. Rogers, formerly of IAMGOLD, and Dr. Daniel Kontak wrote the majority of the paper included as part of the appendix along with contributions from Mr. David Beilhartz, Dr. Benoît Dubé, and Dr. Vicki

McNicoll and the candidate. The candidate contributed to some geological aspects of the paper.

Acknowledgments

This study is the result of support from several individuals and groups for which the candidate is most appreciative. Firstly, I would like to thank my supervisor Dr. D.J. Kontak for all of his help and for making me a better researcher and scientist.

Initial funding through Trelawney Mining and Exploration Inc. was supported by Mr. David Beilhartz and he is thanked for his involvement with the project. Considerable funding was subsequently provided by IAMGOLD Corporation which facilitated the deposit-scale study presented in this thesis. I sincerely acknowledge and thank IAMGOLD for their financing and the input of staff, in particular Dr. Jamie Rogers, who made this project possible. Members of the IAMGOLD Côté Gold Project team are thanked for their help over the past several years. In particular, Brian Tomczuk is thanked for his continual help while on site and Joycelyn Smith is thanked for her help mapping.

I further thank Dr. Benoit Dubé, without whom the considerable funding and support provided through the TGI-4 Lode Gold Project for the lithogeochemical and geochronological components of this study would not have been possible. I would like to thank Drs. Benoît Dubé and Vicki McNicoll for their intellectual contribution, time and expertise. Kathleen Lauzière is thanked for her time compiling the geochemical database.

I would like to thank the lab technicians who helped me during this project. Thanks to Willard Desjardins for making thin sections, Dave Crabtree for help with the microprobe and Joe Petrus for his work on the LA ICP-MS.

Finally, Steve Scott is thanked for his time, patience and support.

Table of Contents

List of Figures

List of Tables

List of Appendices

Chapter 1

1 Introduction to the Thesis

1.1 Research Problem

The low-grade, large-tonnage Archean Côté Gold Au(-Cu) deposit is located in the southeastern limb of the Swayze greenstone belt (SGB), part of the gold-rich Abitibi Subprovince. The deposit was discovered in 2009/2010 and due to its recent discovery a limited amount of research on the deposit preceded this study. The first study by Kontak et al. (2013a) addressed some of the aspects of the deposit (i.e., host rocks, whole-rock geochemistry and timing of mineralization) and interpreted it as intrusion-related in origin with an affinity to porphyry-type deposits.

A spatial association of gold with felsic to intermediate intrusions in the Archean is not uncommon. For example, such deposits in the Abitibi greenstone belt include the traditional and well understood syenite-associated clan (e.g., Holt-McDermott, Douay, Beattie, Young Davidson, Canadian Malartic; Robert, 1997; Robert, 2001) that range from approximately 2680 to 2672 Ma (Robert, 2001; Robert et al., 2005). The Côté Gold deposit differs, however, from the syenite-associated clan as it is hosted by a low-Al tonalite, diorite and quartz diorite intrusive complex. Mineralization associated with low-Al composite intrusions has been previously documented, such as the Flavrian-Powell intrusive complex (Don-Rouyn Cu-Mo(-Au) and St. Jude Cu-Mo breccia occurrence; Galley and van Breemen, 2002; Galley, 2003) and the Mooshla intrusive complex (Doyon Au deposit; Galley and Lafrance, 2014), however, they have not garnered much attention and thus has not populated the literature on gold deposits. Importantly,

intrusion-hosted Au-Cu and Cu-Mo mineralization associated with these low-Al composite intrusion has been suggested to be Archean analogues to Phanerozoic-age porphyry deposits (Trowell, 1974; Goldie, 1979; Poulsen and Franklin, 1981; Kennedy, 1985; Galley and van Breemen, 2002; Galley and Lafrance, 2014).

Although the deposit has been previously interpreted in the context of a porphyry-type deposit, the genetic model for this deposit cannot be properly developed without detailed study of the tectonic setting, the nature of host rocks and the timing and nature of alteration and its related mineralization. Thus, the data obtained from this thesis looks to address the nature and origin of this deposit in the context of current models for intrusion-related gold system and to address if this deposit reflects a rarely preserved style of mineralization in the Archean.

1.2 Thesis Objectives

The objective of this thesis is to provide the first comprehensive description of the Côté Gold deposit in order to determine its nature and origin with the intent of classifying the deposit within the current understanding of global gold deposits. The research will emphasize the following:

1) Identify all rock types present in the intrusive complex and establish a relative chronology for each based on mapping and core logging;
2) Establish the absolute chronology of the magmatic and related hydrothermal events by integrating objective 1 with high-precision U-Pb geochronology (zircon, titanite);
3) Describe the nature of mineralization and alteration types and assess their spatial distribution;

4) Determine the geochemical signature of the mineralization and alteration using both whole-rock and mineral chemistry;
5) Constrain the age of gold mineralization using relative crosscutting relationships, based on field mapping, detailed petrographic study and absolute geochronology by using syngenetic ore (Re-Os molybdenite) and alteration (U-Pb titanite and rutile) phases;
6) Develop a geological model for the deposit and assess its nature and origin in the context of the three main gold deposit clans (Poulsen et al., 2000) and;
7) Provide relevant exploration criteria for assessing the mineral potential of Archean granite-greenstone terranes.

1.3 Previous Work

The first detailed study of the Côté Gold deposit, originally the Côté Lake deposit, was initiated in 2010 following its discovery in late 2009 by Trelawney Mining and Exploration Inc. as part of the Discover Abitibi Initiative (see Ayer et al., 2013). This study, which was conducted by Dr. Kontak and colleagues, provided the first description of the host rocks, alteration types, mineralization styles, whole-rock and alteration geochemistry, stable isotope geochemistry and U-Pb zircon and Re-Os molybdenite geochronology (Kontak et al., 2013a). The study can be found as a Miscellaneous Release Data file (MRD 294) published through the Ontario Geological Survey and this work was also presented in Kontak et al. (2013b). Subsequently, Rogers et al. (2013) presented a summary of the exploration history of the deposit and a summary of its geological features for the NewGenGold Conference in Australia. As this paper may be difficult to obtain and it contains important contextual information about the deposit

discovery, a copy of it is included in Appendix A. In addition, the most recently related publication on the deposit, in which the partial contents of this thesis are summarized, is presented as an Open File Report (OF7852) as part of the GSC TGI-4 Lode Gold Project Summary (Katz et al., 2015).

1.4 Methodology

1.4.1 Field work

Field studies at the deposit site were conducted over four field seasons with Trelawney Mining and Exploration Inc. (May to August 2011 and April to June 2012) and IAMGOLD Corporation (June to August 2012, June to August 2013 and July to September 2014). During this time, field work and related studies included: (1) re-logging of 157 drill holes spaced on 100 m lines through the entire deposit area in order to identify major and minor rock types, alteration types and their distribution, and the nature and style of mineralization. This work provided the basis to establish a paragenesis for the intrusive events, alteration and mineralization types in the deposit; (2) creating cross sections using the software Downhole Explorer; (3) preliminary 3D modeling (completed on site) using results of logging and GEMS software; (4) detailed mapping of selected outcrops to define multiple crosscutting relationships between tonalite and dioritic rocks and to map the distribution and relative timing of alteration types and their association with gold mineralization; (5) collecting and describing 455 samples from drill core samples throughout the deposit and from selected outcrops outside of the deposit for whole-rock geochemistry; (6) collection of the majority of geochronology samples from both outcrop and drill core to constrain the age of intrusive phases and hydrothermal alteration; (7) collection of

two molybdenite samples for Re-Os geochronology; and (8) collection of TerraSpec data from of 26 holes throughout the deposit to determine the secondary mineral species, distribution of secondary minerals and relationship of secondary minerals with mineralization.

1.4.2 Petrography and mineral chemistry

Approximately 500 thin sections and polished thin sections were collected to encompass least-altered rocks, all alteration types, vein types and mineralization styles. A petrographic study was completed on the least-altered host rocks and dike rocks to document their primary mineralogy and textures. Of the total number of sections, over 300 were polished thin sections in order to determine the oxide and sulphide mineralogy of the alteration types and mineralization. Over 100 of the polished thin section samples were used specifically to assess the paragenesis of alteration types.

The EPMA method was completed to determine the mineral chemistry of primary and secondary amphibole and secondary biotite, muscovite, epidote and chlorite. In addition, mineral chemistry from SEM-EDS was obtained in order to document the alteration minerals in the hydrothermal alteration assemblages and the textures produced as a result of alteration.

1.4.3 Whole-rock geochemistry

The whole-rock geochemistry dataset collected in this study was sampled in order to: (1) characterize the least-altered rocks of the CIC; (2) characterize the regional metavolcanic rocks of similar age and setting to the CIC to determine if they are geochemically similar to the rocks of the CIC and deduce their paleo-tectonic setting; (3) characterize the least-altered dike rocks

that crosscut the CIC; and (4) geochemically fingerprint of the alteration and mineralization. The entire geochemical dataset can be found in an Open File Report (Katz et al., 2016).

1.4.4 Geochronology

U-Pb zircon and titanite geochronology was conducted to establish the chronology of magmatic events in the deposit. In addition, U-Pb titanite and rutile geochronology was used to constrain timing of hydrothermal events and Re-Os molybdenite dating was used to help constrain the timing of gold mineralization.

1.4.5 Laser ablation-inductively coupled plasma-mass spectrometry (LA ICP-MS)

The trace element chemistry of both biotite and chalcopyrite, as determined using the LA ICP-MS method, was used to investigate the chemical features of these phases. For hydrothermal biotite, the data were used to assess if its trace element signature could be used to distinguish different coloured biotites or biotite alteration styles and if this related to the evolution of the deposit. The same approach was used for chalcopyrite to determine the elemental signatures of this phase and to compare these results against chalcopyrite from the regional vein system.

1.5 Structure of Thesis

The thesis comprises an introductory chapter (Chapter 1), three self-contained manuscripts (Chapter 2, 3 and 4) that will be submitted for publication in peer-reviewed journals and a concluding chapter which also includes future work and outstanding problem (Chapter 5).

Chapters 2 to 4 are supplemented here by additional data in Appendix A (additional paper), B (additional maps and geochemistry of grab samples), C (a complete list of amphibole and biotite probe data) and D (TerraSpec cross sections and metal versus depth plots). Due to the nature of the manuscript-style chapters in the thesis, there is some overlap in their introductory content.

Chapter 1 (the current chapter) introduces the research problem, thesis objectives, previous work, methodology, structure of thesis and statement of original contributions.

Chapter 2 is written as a manuscript entitled "*The geology, petrology, and geochronology of the Archean Côté Gold large-tonnage, low-grade intrusion-related Au(-Cu) deposit, Swayze greenstone belt, Ontario, Canada*" which has been accepted to the Canadian Journal of Earth Sciences. This chapter introduces the deposit and provides the first comprehensive description of the least-altered rock types (host rocks, regional metavolcanic rocks and dike rocks) and their whole-rock geochemistry. In addition, the relative and absolute timing of host rocks is established and a model for the formation of the CIC is proposed. The co-authors on this publication are D.J. Kontak, B. Dubé and V. McNicoll.

Chapter 3 is written as a manuscript entitled "*Mineral paragenesis, alteration and geochronology (U-Pb, Re-Os) of the Archean porphyry-type Côté Gold Au(-Cu) deposit, Swayze greenstone belt, Ontario*" which is prepared to be submitted as a peer-reviewed journal article. This chapter focuses on the alteration and mineralization of the deposit and includes Re-Os molybdenite and U-Pb titanite and rutile geochronology to constrain the absolute timing of deposit formation. In addition, a detailed paragenesis of mineral assemblages of the alteration types is presented, trace element analyses of biotite and chalcopyrite were completed. This

manuscript contains the first genetic model proposed for the Côté Gold deposit. The co-authors on this publication are D.J. Kontak, B. Dubé, V. McNicoll, R. Creaser and J.A. Petrus.

Chapter 4 is written as a manuscript entitled "*Alteration lithogeochemistry of an Archean low-grade, large-tonnage intrusion-related gold deposit: The Côté Gold Deposit, Swayze greenstone belt, Ontario*" which is prepared to be submitted as a peer-reviewed journal article. This chapter focuses on the alteration lithogeochemistry in order to geochemically fingerprint the alteration types and the nature of the fluids responsible for the generation of the deposit. The co-authors on this publication are D.J. Kontak, B. Dubé and J.A. Petrus.

Chapter 5 presents concluding remarks, as well as suggestions for future research and any outstanding problems of the thesis.

1.6 Statement of Original Contributions

This thesis represents the first detailed description of nature and origin of the Côté Gold deposit and provides a genetic model for how this Archean gold system formed. The following list summarizes some of the main contributions of this thesis:

1. First comprehensive description of the Côté Gold deposit which includes the petrology, geochemistry and geochronology of the host rocks;
2. A description of the petrology and whole-rock geochemistry of the regional metavolcanic rocks in the context of the tectonic setting and relationship with the CIC;
3. Documentation of the petrology, relative timing and whole-rock geochemistry of the dike rocks in the deposit;

4. First geological maps for the deposit which document the crosscutting relationships of intrusive phases and relative timing. First study to document the absolute age of all phases of the CIC using U-Pb zircon and titanite geochronology;
5. First alteration maps produced to determine the crosscutting relationships between alteration types. First documentation of the alteration types, their alteration mineralogy and their distribution in the deposit;
6. First documentation of the relative timing of gold mineralization, sulphide paragenesis and the relationships of mineralization with alteration;
7. First study to provide the absolute age of alteration using U-Pb titanite and rutile geochronology;
8. A substantial dataset (455 samples) of lithogeochemistry to fingerprint the hydrothermal fluids responsible for the formation of the Côté Gold deposit; and
9. First comprehensive genetic model and classification of the Côté Gold deposit.

Chapter 2

2 The Geology, Petrology and Geochronology of the Archean Côté Gold Large-Tonnage, Low-Grade Intrusion-Related Au(-Cu) Deposit, Swayze Greenstone Belt, Ontario, Canada

2.1 Abstract

The Archean Côté Gold Au(-Cu) deposit, located in the Swayze greenstone belt, northern Ontario, Canada, is a low-grade, large-tonnage deposit with an indicated resource of 269 Mt averaging 0.88 g/t Au (7.61 M oz) and an inferred resource of 44 Mt averaging 0.74 g/t Au (1.04 M oz) at a cut-off grade of 0.3 g/t Au. The deposit is the first large gold deposit to be discovered in the Swayze greenstone belt, a part of the gold-rich Abitibi Subprovince.

The Côté Gold deposit is hosted by the Chester intrusive complex, a laccolith-shaped synvolcanic intrusion that was formed by multiple intrusions of low-Al tonalite, diorite and quartz diorite, plus magmatic and hydrothermal breccia bodies. Age dating using high-precision ID-TIMS U-Pb zircon geochronology constrains the emplacement of this intrusive complex from 2741 to 2739 ± 1 Ma. Although these phases are co-temporal and co-spatial they appear to be petrogenetically unrelated. Several geochemically unrelated dikes and deformation events crosscut and postdate the CIC.

The CIC was emplaced into tholeiitic mafic metavolcanic rocks of the Arbutus Formation whose geochemistry reflects an extensional back-arc environment. The CIC is coeval and cogenetic with the felsic to intermediate metavolcanic rocks of the Yeo Formation. Emplacement

of the CIC into a shallow crustal level is inferred based on the incorporation of screens and inclusions of the Yeo Formation, consistent with the presence of textures, such as granophyres, miarolitic cavities and pegmatites, and Al-in-hornblende geobarometry results of $\leq 1.3 \pm 0.6$ kbars.

The CIC is petrologically similar to other subvolcanic, low-Al tonalite-trondhjemite-diorite intrusions that underlie VMS-type deposits and which themselves may contain syn-intrusion mineralization. The hydrothermal biotite event is demonstrated to be genetically related to the dioritic phases, and therefore, dioritic magmatism is thought to be responsible for generating the Côté Gold deposit.

2.2 Introduction

The Côté Gold Au(-Cu) deposit, located in the Swayze greenstone belt (SGB) of the Archean Abitibi Subprovince, is a low-grade (<1 g/t Au), large-tonnage deposit (indicated: 296 Mt @ 0.88 g/t Au (7.61 M oz) and inferred: 44 Mt @ 0.74 g/t Au (1.04 M oz); IAMGOLD Corporation, 2013). The deposit is hosted by a ca. 2741 to 2739 Ma subvolcanic, low-Al tonalite and dioritic intrusive complex, known as the Chester intrusive complex (CIC). Tonalite-trondhjemite plutonic suites, which may also contain granodiorite and diorite rocks, are voluminous in the Archean and for this reason have attracted much research attention (Barker and Arth, 1976; Barker, 1979; Condie, 2005; Martin et al., 2005; Bédard, 2006). These suites are subdivided into high-Al (>15 wt. %) and low-Al (<15 wt. %) types based on their Al_2O_3 content at 70% SiO_2, in addition to other geochemical criteria (Barker, 1979). Most of these Archean plutonic rocks belong to the high-Al tonalite-trondhjemite-granodiorite (TTG) suite, whereas

low-Al tonalite-trondhjemite-diorite (TTD) suites are subordinate. Low-Al TTD suites have been documented to form small, composite synvolcanic intrusions in rift environments that underlie and are the inferred heat and/or metal source for spatially related VMS-style mineralization (Campbell et al., 1981; Cathles, 1981; Franklin, 1996; Barrie et al., 1999; Galley et al., 2000; Galley, 2003; Yergeau et al., 2015). The low-Al composite intrusions are compositionally equivalent to FII- or FIII-type rhyolites, and as such, are prospective for base metal mineralization (Lesher et al., 1986). Some of these intrusions have been documented to host Cu-Mo(-Au) mineralization with a porphyry-type affinity (Friske, 1974; Trowell, 1974; Goldie et al., 1979; Poulsen and Franklin, 1981; Kennedy, 1985; Galley and van Breemen, 2002; Galley, 2003; Galley and Lafrance, 2014).

The Côté Gold deposit represents a significant new discovery (2009/2010; Rogers et al., 2013) for several reasons: (1) it is the first large gold deposit (i.e., >1 M oz Au) of any type discovered in the SGB, compared to the gold-rich Abitibi greenstone belt (AGB); (2) the deposit defines a new gold environment in that the mineralization is hosted by a 2741 to 2739 Ma, high-level, subvolcanic tonalite-diorite-quartz diorite intrusive complex, which is unusual in the Abitibi (Robert et al., 2005; Dubé and Gosselin, 2007); and (3) based on Re-Os dating of molybdenite that is cogenetic with gold mineralization, the deposit defines a new gold metallogenic event at ca. 2740 Ma (Kontak et al., 2013a, b). Based on the overlap of magmatic and hydrothermal events, the nature of mineralization (e.g., disseminations, veins and breccias) and associated alteration styles (e.g., amphibole, biotite, muscovite, albite), previous studies have suggested an intrusion-related origin for the deposit with an affinity to Phanerozoic porphyry-type deposits (Kontak et al., 2013a; Katz et al., 2015).

This article constitutes the first detailed description of the geology of the Côté Gold deposit and defines: (1) the relative timing of the intrusive phases through crosscutting relationships; (2) the absolute ages of intrusive units using high-precision ID-TIMS U-Pb zircon geochronology; (3) the lithogeochemistry of the igneous rocks and the tectonic setting of the CIC; and (4) a model for the origin of the CIC. This work builds on the preliminary findings of the nature of the deposit presented by Kontak et al. (2013a) and Rogers et al. (2013). Details of the alteration and mineralization types, geochronological constraints of the timing of mineralization based on U-Pb (zircon, titanite, rutile) and Re-Os (molybdenite) dating, geochemical fingerprinting of the alteration and mineralization and discussion of a proposed model and deposit classification is presented in Chapters 2 and 3.

2.3 Regional Geological Setting

The Côté Gold deposit is located in the southeastern part of the SGB, which is part of the larger, Abitibi Subprovince (Fig. 2.1). The volcano-sedimentary rocks in the SGB are inferred to be contiguous with the southern extension of the AGB. The SGB was once considered to be separate from the AGB, but based on lithological and geochronological data the SGB is now considered to contain many of the equivalent stratigraphic assemblages and structural features typical of the southern AGB (Fig. 2.2; Ayer et al., 2002; van Breemen et al., 2006). The various volcanic and intrusive rock types in the SGB are diverse, ranging from ultramafic to felsic in composition, as well both chemical and clastic sedimentary rock types that range in age from 2750-2675 Ma (Ayer et al., 2002). In the SGB, six supracrustal groups are recognized, which from oldest to youngest are the Chester, Marion, Biscotasing, Trailbreaker, Swayze and Ridout

(Fig. 2.2; Heather, 2001; van Breemen et al., 2006). The correlative assemblages within the southern AGB are respectively named the Pacaud, Deloro, Kidd-Munro, Tisdale, Blake River and Timiskaming (Ayer et al., 2002; van Breemen et al., 2006).

The SGB has a complex structural history which includes polyphase folding with the development of multiple foliations, ductile high-strain zones and late brittle faulting (Heather, 2001). The preserved map pattern within the SGB mainly reflects D_2 deformation, an orogen-wide shortening event (van Breemen et al., 2006). Several, regionally extensive, east-west trending D_2 high-strain and/or fault zones transect the SGB.

The Ridout deformation zone (RDZ), which represents one such D_2 high-strain zone, is up to 2 km wide and transects the length of the southern SGB (Heather, 2001; van Breemen et al., 2006). The RDZ, which occurs approximately 3 km north of the deposit, has a complex history of ductile shearing with later brittle faulting (Heather, 2001; van Breemen et al., 2006; Berger, 2011). Previous studies suggested that the RDZ is the western extension of the gold-rich Larder Lake-Cadillac deformation zone (Heather, 2001; van Breemen et al., 2006). It has been argued, however, that it is unlikely that these two deformation zones are correlative based on different kinematic histories and their location along different parts of the regional stratigraphy (Berger, 2011).

Metamorphic grade within the southern AGB ranges from sub-greenschist to greenschist grade, but locally higher amphibolite grade conditions were attained next to large synvolcanic and syntectonic intrusions (Heather, 2001; van Breemen et al., 2006). The peak of metamorphism in the southern AGB is estimated to have occurred from 2677 to 2643 Ma (Powell et al., 1995).

2.4 Local Geological Setting

The following description, particularly of the volcanic rocks, is largely taken from Heather (2001). The Arbutus Formation is traceable throughout much of the southern SGB and it forms the lowest unit in the Chester Group and consequently in the SGB (Fig. 2.3). This unit contains pillow basalts, mafic flows and massive, medium-grained amphibolite interpreted to be either coarse-grained flows or intrusive sills (Heather, 2001). The Arbutus formation has not been dated directly but the Chester Group is inferred to be ca. 2750 to 2735 Ma. The Arbutus formation is disrupted by the CIC and is overlain conformably by the Yeo Formation (Heather, 2001).

The Yeo Formation, which forms the upper formation in the Chester Group, consists of intercalated felsic and intermediate volcanic rocks, clastic sedimentary and volcaniclastic rocks, iron formation and Fe-rich sedimentary rocks (Heather, 2001). Two U-Pb zircon ages for the felsic lapilli tuffs constrain the age of the formation to 2739 ± 1 Ma (van Breemen et al., 2006) and 2734 ± 2 (Heather and Shore, 1999a, b; see locations in Fig. 2.3). As discussed in more detailed below, the younger age is noted to be closer to the contact with the CIC based on the current map pattern (Fig. 2.3).

The Côté Gold deposit is hosted by the CIC, which is a multi-phase, subvolcanic intrusive complex located along the southern margin of the Ridout syncline in the southeastern extension of the SGB (Figs. 2.1 and 2.3). The CIC has an overall laccolithic shape with dimensions of approximately 35 km (east-west) by 10 km (north-south). Based on the current understanding of the study area, the CIC has been tilted moderately to steeply north from its

original orientation. The CIC contains numerous rafts, screens and inclusions of the Arbutus Formation (Heather, 2001) and Yeo Formation (Berger, 2012; Fig. 2.3).

The CIC can be subdivided into a northern leucocratic tonalite-dominated zone and a southern melanocratic diorite-dominated zone (Heather, 2001; Fig, 2.3). Regionally, the tonalite phase consists of biotite ± amphibole tonalite to a leucocratic quartz-rich tonalite. The diorite phase consists of diorite, quartz diorite and hornblende-plagioclase pegmatite; hornblende is the dominant, and in most cases, the only mafic mineral, but rare primary biotite has been documented (Heather, 2001).

Complex crosscutting relationships and textures occur between the tonalite and diorite phases of the CIC. These relationships are considered to reflect coeval emplacement and possible magma co-mingling between the tonalitic and dioritic magmas (Heather, 1993; Heather and Shore, 1999a; Heather, 2001; Berger, 2011). Evidence supporting this interpretation includes: (1) abundant diorite, quartz diorite and tonalite inclusions of variable size (<1 cm - 10s m) and texture (i.e. fine- to coarse-grained) within the tonalite; (2) fragments of tonalite and rarely diorite within a dioritic matrix and tonalite bodies intruding diorite; (3) rounded, sub-rounded and angular fragments with sharp to diffuse margins; (4) cuspate or lobate contacts between tonalite and diorite (Heather and Shore, 1999a); and (5) a frothy or pitted net-texture in some mafic inclusions (Heather and Shore, 1999a).

Previous U-Pb zircon studies have constrained the age of the tonalite phase of the CIC to 2740 ± 2 Ma (Heather and van Breemen, 1994) and more recently to 2741.1 ± 0.9 and 2738.7 ± 0.8 Ma (Kontak et al., 2013a; see Fig. 2.3 for sample locations). The older age for the Yeo

Formation is coeval with the CIC and a previous study suggested that it may be the eruptive equivalent of the tonalite of the CIC (Berger, 2012).

2.5 Geology of the Côté Gold Deposit

The deposit, located in the northwestern part of the CIC (Fig. 2.3), is of elliptical shape with dimensions of approximately 1.7 km (northeast-southwest) by 1.4 km (northwest-southeast). A surface map showing the geology of the deposit area is shown in Figure 2.4 and a cross section through the deposit is presented in Figure 2.5. The deposit geology, as described below, is based on the detailed logging of 157 diamond drill holes and detailed mapping of a few select, but critical outcrops (Figs. 2.6 and 2.7).

In general, the deposit area is dominated by tonalite with lesser amounts of diorite bodies and various magmatic and hydrothermal breccia bodies. The distribution of the intrusive phases is shown in the plan map (Fig. 2.4) and cross section (Fig. 2.5). It is important to note that on surface there is little manifestation of the extent of the breccia bodies. In contrast, the cross section clearly shows the extent of the magmatic breccias at depth.

Several styles of gold mineralization (e.g., disseminations, veins, breccias) occur and are co-spatial with alteration (e.g., amphibole, biotite, muscovite, albite, chlorite; Katz et al., 2015). The gold mineralization is centred on breccia bodies of magmatic and hydrothermal origin, but also occur as veins (sheeted veins and stockworks) and disseminations in tonalite and dioritic rocks (Fig. 2.5). The best estimate of the age of mineralization is based on two Re-Os molybdenite ages at 2737 ± 11 Ma and 2741 ± 11 Ma (Kontak et al., 2013a). These data

constrain the mineralizing event to 2739 ± 7 Ma, which suggests a syn-intrusion timing for the formation of the deposit.

Several deformation events are recognized in the deposit area (Smith et al., 2014). Small (<3 m wide), east-west trending deformation zones thought to be related to the RDZ overprint the major rock types, alteration and mineralization in the deposit (Smith et al., 2014). A west-striking, moderately to steeply dipping brittle fault zone cuts through the deposit (Fig. 2.4). The last movement on this fault is late with respect to deposit formation and is inferred to have an apparent dextral offset of approximately 100 to 200 m based on results from preliminary 3D modeling of the breccia body, alteration types and correlation of diabase dikes (Fig. 2.4).

2.5.1 Intrusive phases of the Chester intrusive complex

The deposit is hosted by several tonalite (Fig. 2.8) and dioritic (Fig. 2.9) phases that are intruded by breccia bodies of both magmatic and hydrothermal type. The principal characteristics of each phase are summarized in Table 2.1 and are distinguished by their crosscutting relationships, textural features and chemistry. Detailed outcrop mapping was done to help define the relative ages of the host rocks with two of these, the North Breccia Outcrop (Fig. 2.6; 1:300 scale) and Skidder Outcrop (Fig. 2.7; 1:500 scale), presented here as it summarizes the critical features relevant to our interpretation of the CIC. Additional outcrops can be found in Appendix B.

Tonalite: Tonalite occurs as the earliest phase in the deposit into which dioritic phases intrude, but also as a later more voluminous phase that intrudes dioritic phases (Figs. 2.6A, B and 2.7). Tonalite is a light grey, massive, fine- to medium-grained, equigranular leucocratic rock

composed of plagioclase and quartz (Fig. 2.8A), with rare phenocrysts of both phases. Texturally, the tonalite contains granophyric-like texture (Fig. 2.8B) and the plagioclase has polysynthetic twinning and is both zoned and unzoned (Fig. 2.8C). The plagioclase composition ranges from An_{15-40}, and therefore, the leucocratic phases of the intrusive complex comprise both tonalite and trondhjemite based on the normative An-Ab-Or diagram (O'Connor 1965; Barker 1979; see geochemistry section below) but are referred to here as tonalite for simplicity. Small miarolitic cavities (≤1 cm) with spherical shapes are present and are lined by plagioclase and filled with quartz ± carbonate (Fig. 2.8D). In addition, tonalite is characterized by 5 cm- to m-sized, elliptical to angular cavities resembling miaroles that are lined by plagioclase and filled with quartz (Fig. 2.8E), as well as elliptical to rounded quartz-sulphide cavities (<15 cm; Fig. 2.7).

Tonalite breccia: This unit is a magmatic breccia and formed as a result of brecciating diorite (Fig. 2.7) and rarely tonalite along its intrusive margins. Mineralogically and texturally this unit is the same as the tonalite described above, therefore, the presence of diorite fragments distinguishes later tonalite from early tonalite. Two types of contacts are observed: (1) angular to rounded diorite fragments with sharp to diffuse contacts against tonalite (Fig. 2.8F; see Figure B.1. in Appendix B); and (2) rare lobate contacts between the tonalite and diorite (Fig. 2.8G, H). Textures along the lobate contacts include granophyres and rare miarolitic cavities in the tonalite matrix (Fig. 2.8G) and a reduction of grain-size in the fragments (i.e., quenching). In addition, titanite and/or amphibole are present along the interface between the two phases (Fig. 2.8I).

Diorite: The diorite intrudes the early tonalite and commonly exhibits chilled or brecciated margins. Both melanocratic amphibole-rich diorite (Fig. 2.9A) and leucocratic plagioclase-rich diorite are present and both can coarsen internally to pegmatitic segregations.

The more leucocratic diorite typically intrudes the more melanocratic diorite. The melanocratic diorite is dark-green, whereas the leucocratic diorite is light-pink; both are massive to rarely foliated, equigranular to inequigranular, medium- to coarse-grained and contain variable amounts of plagioclase (An_{10-50}), amphibole, titanite, ilmenite and magnetite (Fig. 2.9B). In thin section, both the melanocratic and leucocratic diorite may have a granophyric-like texture and plagioclase shows primary oscillatory zoning, polysynthetic twinning and sieve textures.

Quartz diorite: This unit intrudes diorite and tonalite with sharp or diffuse contacts or with brecciated margins. Quartz diorite is dark- to light-green, medium- to coarse-grained and is massive. The unit consists of plagioclase, amphibole, quartz, titanite, ilmenite and magnetite and locally contains quartz and/or plagioclase phenocrysts (Fig. 2.9C). In thin section, granophyric texture is present and the plagioclase is seen to have primary oscillatory zoning and polysynthetic twinning. Diorite and quartz diorite phases are co-temporal and typically more melanocratic dioritic phases are intruded by leucocratic dioritic phases (Fig. 2.9D), however, the reverse is also observed.

Hornblende-plagioclase± quartz pegmatite: This unit intrudes diorite, quartz diorite and more rarely tonalite with sharp to diffuse contacts (Fig. 2.6C). These dike rocks are dark- to light-green, massive, inequigranular, coarse-grained (<2.5 cm; Fig. 2.9E) and consist of plagioclase, hornblende, quartz, titanite, magnetite, ilmenite and apatite. Rare acicular amphibole grains (<1 cm) occur (Fig. 2.9E). In thin section granophyric-like texture is observed and plagioclase is characterized by both oscillatory zoning and polysynthetic twinning.

Diorite breccia: The second type of magmatic breccia, termed a diorite breccia, is present and it is the result of high-energy injections of dioritic magma brecciating tonalite and dioritic

rocks. The breccia bodies occur as several injections in the southern and central parts of the deposit; these bodies dip moderately to steeply to the north (Fig. 2.5). This breccia contains several different crystalline dioritic matrices based on mineralogy and texture (Table 2.1; Fig. 2.9F, G): (1) a medium- to coarse-grained melanocratic diorite; (2) a fine- to medium-grained melanocratic quartz ± plagioclase-phyric quartz diorite; and (3) a rare fine-grained leucocratic quartz diorite. The breccia is heterolithic and tonalite fragments of variable size and shape dominate the breccia, whereas dioritic fragments are subordinate (Fig. 2.9F). Diorite fragments in the breccia unit are generally more melanocratic than the matrix, but rarely the reverse occurs. The fragments rarely exhibit exfoliation textures (Fig. 2.9H), which are a feature suggestive of collapse or decompression (Sillitoe, 1985). This texture, along with the heterolithic nature of the breccia, suggests transport and some movement of the fragments. Rarely in-situ brecciation occurs and is characterized by tabular tonalite fragments; this texture is more common along the margins of the breccia. This unit is often overprinted by alteration (e.g., biotite, chlorite; Fig. 2.9G) and gold mineralization is erratic.

Hydrothermal amphibole breccia: This breccia is the least abundant of the breccia types and appears to be restricted to the southern and central parts of the deposit area. This unit contains tonalite fragments and rare dioritic fragments in a fine-grained, black amphibole-quartz ± biotite ± carbonate ± pyrite ± chalcopyrite matrix (Fig. 2.10A-C). Amphibole-bearing veins, which are associated with the amphibole breccia, occur and overprint the diorite breccia (Fig. 2.10D). Thus, the hydrothermal amphibole event postdates at least some of the magmatic activity. This unit is gold-bearing, but it does not contain significant sulphide mineralization.

Hydrothermal biotite breccia: The hydrothermal biotite breccia (Fig. 2.11A) occurs predominantly in the central and northern parts of the deposit. The breccia matrix is black, brown

or dark-green and several biotite-rich matrices occur: (1) a fine-grained biotite-quartz ± epidote ± calcite ± pyrite ± chalcopyrite ± magnetite ± allanite ± titanite ± fluorite matrix (Fig. 2.11B, C); (2) a fine- to coarse-grained biotite-magnetite-quartz-ankerite-chalcopyrite-pyrite ± sphalerite ± allanite ± bastnaesite ± apatite ± titanite with up to 40 vol. % magnetite in the matrix (Fig. 2.11D, E); or (3) biotite-ankerite/calcite-quartz-pyrite ± allanite ± apatite ± magnetite ± chalcopyrite ± pyrrhotite with coarse-grained biotite set in finer-grained quartz and carbonate matrix (Fig. 2.11F, G). The breccia is monolithic and contains tonalite fragments which may have chlorite rims (Fig. 2.11F). This breccia type has textures indicative of in-situ brecciation (i.e., mosaic; Fig. 2.11H) which suggests formation by hydro-fracturing (Ross et al., 2002). This unit is consistently mineralized and has the highest average grades of Au (avg. 0.67 g/t) and Cu (avg. 1000 g/t), along with an association of elevated Mo and Ag.

2.5.2 Post-Chester intrusive complex dikes

Several dikes, all of which are barren, are recognized in drill core and observed in outcrop exposures. These dikes and diklets all have sharp contacts with units of the CIC and are distinguished on macroscopic, petrographic and geochemical bases. The dikes include: (1) feldspar ± quartz porphyry of dacitic to andesitic composition; (2) lamprophyre; (3) diorite; (4) gabbro; and (5) diabase. In addition, a non-mineralized tectonic breccia and heterolithic quartz ± carbonate breccia are associated with the west-striking brittle fault that cuts the CIC. The mineralogy, texture and relative crosscutting relationships of these dikes are presented in Table 2.2.

2.6 Analytical methods

2.6.1 Electron microprobe analyses

Amphibole grains from diorite, quartz diorite, an amphibole-titanite-apatite vein and two hydrothermal amphibole breccias were analyzed by electron microprobe analysis (EMPA) to assess their mineral chemistry. The amphiboles were analyzed by wavelength dispersive spectrometry using a Cameca SX 100 electron probe microanalyser at the Ontario Geological Survey Geoscience Laboratories (Geo Labs) in Sudbury, Ontario. The accelerating potential was 20 kV, the beam current was 20 nA and the beam size was 15 µm. Standards used for calibration include diopAST and pyrxBRN. Iron, Mn and V were analyzed using a LLiF crystal; Ti and Cr were analyzed with a PET crystal; K, Cl and Ca were analyzed with a LPET crystal; Si, Al and Mg were analyzed with a TAP crystal; and Na and F were analyzed with a LTAP crystal.

2.6.2 Whole-rock geochemistry

A total of 455 samples were taken from the deposit area as part of this thesis. The samples include all of the main intrusive units, dike rocks, part of the volcanic sequence and all of the alteration types and mineralization styles. In this study only the results for the least-altered samples are reported and include: tonalite, diorite and quartz diorite, hydrothermal biotite breccia matrix, mafic metavolcanic rocks of the Arbutus Formation, felsic to intermediate metavolcanic rocks of the Yeo Formation, feldspar ± quartz porphyries, lamprophyre dikes, dioritic dikes, gabbroic dikes and diabase dikes (total of 57 samples; Table 2.4). The entire geochemical dataset, analytical techniques, sample description and photo of each sample is available as a supplementary Open File Report (Katz et al., 2016).

The whole-rock geochemical data were obtained at Activation Laboratories, Ancaster, Ontario. Major elements were determined by lithium metaborate-tetraborate fusion inductively coupled plasma (ICP) whole-rock method. The FeO was determined by titration and combined with total iron to determine FeO/Fe_2O_3 ratio in all the samples. The trace and rare earth elements (REE) were determined by a combination of fusion ICP, fusion inductively coupled plasma mass spectrometry (ICP-MS) and total digestion ICP-MS. The abundances of the metalloids (e.g., As, Sb, Bi Se and Te) were determined by a combination of aqua regia ICP-MS and nitric peroxide fusion ICP-MS, whereas Au, Pd and Pt were measured by fire assay. All of the anions and volatiles were also determined: (1) Cl by instrumental neutron activation analysis; (2) B by prompt gamma neutron activation analysis; (3) F by ion selective method; and (4) S and CO_2 by infrared analysis. Mercury was determined by the cold vapor flow injection mercury technique.

2.6.3 U-Pb zircon geochronology

Seven samples were selected for U-Pb zircon dating based on their field relationships. The age dating was conducted at the Geochronology laboratories at the Geological Survey of Canada, Ottawa, Ontario. Heavy minerals were concentrated from the samples selected for geochronology using standard crushing and grinding followed by separation on a Wilfley table and by heavy liquid techniques. The mineral separates were sorted by magnetic susceptibility using a Frantz^{TM} isodynamic separator followed by hand-picking using a binocular microscope. Analyses were done on zircon grains that were chemically abraded following the techniques of Mattinson (2005), including annealing for 48 hours at 1000^{o}C prior to leaching with HF at 180^{o}C for varying lengths of time. Details of zircon morphology, quality, and HF leaching times are summarized in Table 2.5. The U-Pb isotope dilution thermal ionization mass spectrometry (ID-

TIMS) techniques utilized in this study are modified after Parrish et al. (1987) with the treatment of analytical errors after Roddick (1987). Procedural blank levels were generally on the order of 0.5-1.0 pg for Pb. U-Pb ID-TIMS analytical results are presented in Table 2.5 and displayed in concordia plots (see below). Age uncertainties are presented at the 2σ level.

2.7 Amphibole Chemistry and Barometry

The results of mineral chemical analyses for diorite, quartz diorite, an amphibole-titanite-apatite vein and two hydrothermal amphibole breccias are presented. See Table C.1 in Appendix C for all amphibole microprobe analyses. Only the results of primary amphibole from quartz diorite are used below to estimate the pressure of emplacement (Table 2.3).

Classification of the different amphibole types follows the scheme of Hawthorne and Oberti (2007). All the amphiboles analyzed are calcic and plot in the tschermakite-actinolite diagram (Fig. 2.12A) and the pargasite-edenite diagram (Fig. 2.12B). The majority of the amphiboles plot in the hornblende to actinolite fields, whereas a few samples plot in the ferrotschermakite and ferropargasite fields. Hornblende and actinolite amphiboles are brown, green or green-blue in plane polarized light in thin section (Fig. 2.13A, C) and correspond to medium- to dark-grey amphiboles in back scattered electron (BSE) images (Fig. 2.13B, D), whereas the ferrotschermakite and ferropargasite amphiboles are often vibrant blue in plane polarized light in thin section and correspond to light-grey areas in BSE images (Fig. 2.13B, D). These noted differences correspond to changes in chemistry with the former containing lower Al contents and the latter containing higher Al contents. Previous studies have indicated that igneous hornblendes have lower Al^{iv} contents than metamorphic hornblendes (Leake, 1971;

Hammarstrom and Zen, 1986). In this study, hornblende and actinolite amphiboles are considered to by chemically and texturally primary, whereas ferrotschermakite and ferropargasite amphiboles are considered to be chemically and texturally secondary. The formation of the latter along rims and cores is likely the result of recrystallization of amphibole during metamorphism.

Due to the calcic nature of the amphiboles in this study, it is possible to use Al-in-hornblende barometry since calcic amphiboles show essential differences in composition (i.e., Al content) and these differences are directly related to the depth of emplacement of the plutons (Hammarstrom and Zen, 1986). Crystallization pressures of the amphiboles from quartz diorite have been calculated using the Al-in-hornblende barometer of Anderson and Smith (1995) and Anderson et al. (2008). The use of this barometer is recommended for samples which contain a quartz-potassium feldspar-plagioclase-hornblende-biotite-iron titanium oxide-titanite mineral assemblage. It is noted that potassium feldspar and biotite are not part of the quartz diorite assemblage, but the absence of the former has been noted not to significantly affect pressure determinations (Anderson and Smith, 1995). The effect of the absence of biotite on the pressure calculations is not known, and therefore, the pressure estimates obtained in this study may not be valid and should be tested against the results of other barometers. The results are presented in Table 2.3 and only samples with the appropriate limiting $Fe^{3+}/(Fe^{3+} + Fe^{2+})$ ratio of ~0.2 (Schmidt, 1992) and $Fe_{tot}/(Fe_{tot} + Mg)$ ratios with a range of 0.4 to 0.6 were used. The calculated pressures range from 0.3 to 1.3 ± 0.6 kbars at 750 ^{O}C and 0.2 to 0.4 ± 0.6 kbars at 800 ^{O}C. The pressure estimates are consistent with a high-level of emplacement, which is implied from the CIC intruding into coeval volcanic rocks (Fig. 2.3).

2.8 Whole-Rock Geochemistry

2.8.1 Sampling

The results reported in this study focus on the least-altered rocks in the deposit area. Least-altered tonalite samples were selected based on visual criteria (i.e., preservation of primary texture, least affected by alteration) and geochemical criteria (i.e., LOI <1.5 wt. %, CO_2 ≤0.61 wt. %, K_2O ≤0.52 wt. %, F ≤0.01 wt. %). The least-altered diorite and quartz diorite samples were selected based on visual criteria (i.e., preservation of primary texture, least affected by alteration) and geochemical criteria (i.e., LOI <2.5 wt. %, CO_2 ≤1 wt. %). Samples from both the Arbutus and Yeo Formations are relatively fresh and only contain minor alteration which is considered insignificant in terms of the overall chemistry. The least-altered dikes were chosen based on visual criteria (i.e., preservation of primary texture, least affected by alteration) and geochemical criteria (i.e., CO_2 <3.5 wt. %). The average compositions for all the rock units are presented in Table 2.4.

2.8.2 Geochemistry of the Chester intrusive complex

Major elements: The intrusive rocks from the CIC are classified on the basis of where they plot in the Zr/TiO_2 vs. Nb/Y (Fig. 2.14A) and normative An-Ab-Or diagram (Fig. 2.14B). Thus, the tonalite suite plots in the tonalite and trondhjemite fields (Fig. 2.14B), however, these rocks are collectively referred to as tonalites for simplicity. In the Zr/TiO_2 vs. Nb/Y diagram, the samples are rhyodacitic in composition (Fig. 2.14A). In terms of the alkalis, the tonalites have between 4.0 and 6.0 wt. % Na_2O with K_2O/Na_2O ratios <0.5 (Fig. 2.14C). The tonalite samples equate to the low-Al type (<15 wt. % Al_2O_3) based on their Al_2O_3 contents at 70 wt. % SiO_2

(Fig. 2.14D; Barker and Arth, 1976; Barker, 1979); this is atypical in the Archean where tonalites are usually of high-Al type (>15 wt. % Al_2O_3). Based on their Zr/Y ratios, all of the tonalites have a calc-alkaline to transitional affinity (Fig. 2.14E) and using Zr/Y ratios and absolute Y contents they equate to the fields for FII- or FIIIa-type rhyolites, but trend towards the FI-type rhyolite field (Fig. 2.14F).

The diorite and quartz diorite phases plot in the basalt to andesite fields in the Zr/TiO_2 vs. Nb/Y diagram (Fig. 2.14A). In terms of their normative mineralogy, the quartz diorite phases rarely extend into the tonalite field as hornblende tonalites. Both phases are tholeiitic to transitional in nature which differs from the calc-alkaline to transitional nature of the tonalitic samples (Fig. 2.14E).

Trace elements: In both the Sr/Y vs. Y (Fig. 2.15A) and La/Yb vs. Yb diagrams (Fig. 2.15B) it is seen that the tonalite and diorite of the CIC plot in the arc-related rock field rather than the fields for TTGs and adakites. These diagrams further emphasize that the tonalite and dioritic phases are atypical in the Archean where high-Al TTG suites are dominant, but not atypical of other recorded TTD subvolcanic suites in the Abitibi VMS camps (Lesher et al., 1986).

In terms of the REE, the least-altered tonalites are characterized by relatively flat REE patterns with La/Yb_N values of 0.48 to 2.36 (Fig. 2.16A). The tonalite samples contain moderate negative Eu anomalies (Eu_N/Eu^*) of 0.30 to 0.81 and Gd/Y ratios of 0.14 to 0.15. These geochemical features, along with other trace element criteria (e.g., Sr and Zr/Y), are most consistent with FII-type rhyolites (Lesher et al., 1986). The primitive mantle-normalized spider diagram for tonalite samples show similar patterns and all display strong negative Ti, and P

anomalies, moderate Nb anomalies and variable Ba, Sr and Eu anomalies, but have positive Zr, Pb, Th and U anomalies (Fig. 2.16B). The negative Eu and Ba anomalies along with the low Sr contents in these rocks are indicative of plagioclase-dominated fractionation. These patterns contrast with the tonalite samples obtained by Berger (2012) to the east of the study area (see inset in Fig. 2.3) where tonalite is characterized by elevated light REE (LREE; Fig. 2.16A, B).

The least-altered diorite and quartz diorite have slightly elevated and concave light LREE profiles with La/Yb_N values of 2.65 to 4.85 and display weak negative Eu anomalies (Eu_N/Eu^* = 0.43 to 0.85; Fig. 2.16C). In addition, the middle REE (MREE) have a slightly sloped pattern (Fig. 2.16C) and Gd/Y ratios of 0.16 to 0.23. Hence, the signatures for these rocks contrast with the REE patterns for the tonalite samples. It is interesting to note that whereas most field evidence suggests fractionation of diorite to quartz diorite over time, the REE data shows that some of the diorite samples are more fractionated than quartz diorite samples (Fig. 2.16C). The primitive mantle-normalized spider diagram patterns for diorite and quartz diorite rocks are very similar, as expected, and confirm they are geochemically related. Diorite and quartz diorite show weak negative Ti Zr, Sr, P and Rb, moderate Ba, Nb, Ta, Sr, P anomalies and weak positive Pb anomalies (Fig. 2.16D). The slightly negative Eu anomalies along with the negative Sr and Ba anomalies in the diorite are consistent with plagioclase fractionation. These patterns are noted to be similar to the diorite samples collected in the eastern part of the CIC by Berger (2012), suggesting a genetic relationship (Fig. 2.16C, D).

The REE and spider diagram patterns of the matrix of the hydrothermal biotite breccia are plotted against the least-altered diorite and quartz diorite samples for comparison (Fig. 2.16E, F). The patterns overlap and suggest a genetic relationship.

2.8.3 Geochemistry of the Arbutus and Yeo Formations

The Arbutus Formation samples are used here to help infer a tectonic setting for the CIC. Three samples of the Arbutus Formation were collected and include one pillow basalt and two massive aphanitic basaltic flows or sills. The samples correspond to low-K tholeiitic basalts (Fig. 2.17A, B) and are characterized by low ∑REEs and flat unfractionated patterns with the absence of a Eu anomaly (Fig. 2.17C). The primitive mantle-normalized spider diagram shows depletions in Th, Nb, Ta, and Cs and enrichments in Ti, K, P and Ba relative to the overall flat profile. The pattern is most similar to those of modern back-arc basin basalts (Fig. 2.17D; e.g., Ewart et al., 1994; Hergt and Farley, 1994).

Seven samples were collected from the Yeo Formation and include feldspar crystal ash-sized tuffs and heterolithic lapilli tuffs; these samples are used for comparative purposes against the tonalite of the CIC. The samples are rhyodacitic in composition (Fig. 2.17A) and have a calc-alkaline affinity (Fig. 2.17B). These samples do not typically plot in the low-Al field and contrast with the chemistry of the tonalites collected in this study (Fig. 2.17E). The samples have Zr/Y vs. Y values which correspond to FII- or FIIIa-type rhyolites (Fig. 2.17F) but are more consistent with FII rhyolites (Lesher et al., 1986). The Yeo Formation samples are enriched in the LREE with a moderately fractionated pattern (La/Yb_N = 5.74 to 7.46) and weak negative Eu anomaly (Eu_N/Eu^* = 0.54 to 0.78; Fig. 2.17G). The primitive mantle-normalized spider diagram shows strongly negative Nb, Ta, Sr, P and Ti anomalies and weak positive Pb and K anomalies (Fig. 2.17H). These features contrast with the chemistry of tonalite from within the study area, but overlap with the regional tonalite collected by Berger (2012; Fig. 2.17G, H).

2.8.4 Geochemistry of dike rocks

The classification of the different dike rock types has been done with the use of a Zr/TiO_2 vs. Nb/Y plot (Fig. 2.18A). All the dike rocks are geochemically distinct from the CIC and contain different fractionation trends, as illustrated by the La/Yb_N vs. Yb_N plot (Fig. 2.18B). The tectonic and heterolithic quartz ± carbonate breccias are not included in this section.

Feldspar ± quartz porphyries are subalkaline and equate to both andesitic to dacitic compositions, with one sample plotting in the trachyandesitic field (Fig. 2.18A). The dacitic dikes have variable silica contents (63 to 72 wt. % SiO_2). This large range in chemistry is also reflected in their variable chondrite-normalized REE patterns (Fig. 2.18C) and some of the more mobile trace elements in the primitive mantle-normalized spider diagram (e.g., Cs, Rb, Ba, K; Fig. 2.18D). The dacitic dikes are enriched in LREE with strongly fractionated patterns (La/Yb_N = 2.78 to 24.58) and weak to moderate negative Eu anomalies (Eu_N/Eu^* = 0.41 to 0.97; Fig. 2.18C). In the primitive mantle-normalized spider diagram the samples reflect an overall variable chemistry, but all contain negative Nb, Ta, P and Ti and positive Pb anomalies (Fig. 2.18D). The andesitic samples contain a flat HREE pattern with slightly elevated, listric-shaped LREE pattern (La/Yb_N = 1.37 to 1.50) with moderate negative Eu anomalies (Eu_N/Eu^* = 0.36 to 0.51; Fig. 2.18C). The andesitic dikes display negative Ba, Nb, Ta, Sr, P, Eu and Ti anomalies and positive Pb and U anomalies (Fig. 2.18D).

The lamprophyre dikes, which include both biotite-phyric and amphibole- and biotite-phyric varieties, are basaltic to andesitic in composition (Fig. 2.18A) and equate to medium-to high-K subalkaline to alkaline suites. These rocks have fractionated patterns (La/Yb_N = 6.55 to 12.52) with little to no Eu anomalies (Eu_N/Eu^* = 0.79 to 0.94; Fig. 2.18E). In the primitive

mantle-normalized spider diagrams, the dikes have well-developed negative Nb, Ta and Ti anomalies and in a few samples also positive Pb anomalies (Fig. 2.18F). These dikes have a very uniform REE, HFSE (e.g., Zr, Nb, Ta), Th and U chemistries. The LILE and (Cs, Rb, Ba) are slightly variable though, which may reflect variable degrees of alteration or the loss of K in some samples due to chloritization of amphibole or biotite.

The dioritic dikes are basaltic to andesitic in composition (Fig. 2.18A), subalkaline to rarely alkaline in nature and have a very uniform chemistry. The dioritic dikes have moderately to strongly fractionated REE patterns (La/Yb_N = 3.83 to 12.83) and lack a significant Eu anomaly (Eu_N/Eu^* = 0.76 to 0.95; Fig. 2.18G). In the primitive mantle-normalized spider diagram there are enrichments in the LILE, Pb, K and Sr and negative Nb, Ta and Ti anomalies (Fig. 2.18H).

The gabbroic dikes are basaltic in composition (Fig. 2.18A), subalkaline in nature and have a uniform chemistry. These gabbroic dikes are distinguished from the other dike rocks by having low ∑REEs, overall flat patterns (La/Yb_N = 0.92 to 2.44) and either a very weak negative Eu anomaly (Eu_N/Eu^* = 0.84 to 1.06) or none (Fig. 2.18I). In the primitive mantle-normalized spider diagram (Fig. 2.18J), these rocks have low overall elemental abundances, as compared to the other dike rocks, and have small negative Nb, Ta and P anomalies, distinctly positive Sr and Pb anomalies in some samples and variability in K and the LILE.

The diabase dikes are basaltic in composition and subalkaline in nature (Fig. 2.18A). These dikes rocks have a slightly fractionated REE pattern (La/Yb_N =2.48 to 2.69) with a weak negative Eu anomaly (Eu_N/Eu^* = 0.78 to 0.85; Fig. 2.18K). In the primitive mantle-normalized

spider diagram the data plot as a tight cluster and show a distinct enrichment in the LILE, positive Pb and K anomalies and negative Sr, P, Nb and Ta anomalies (Fig. 2.18L).

2.9 U-Pb Geochronology

Previously obtained U-Pb zircon ages of tonalite samples from the CIC include a single 2740 ± 2 Ma age by Heather and van Breemen (1994) and two ages at 2741.1 ± 0.9 Ma and 2738.7 ± 0.8 Ma by Kontak et al. (2013a). No diorite samples have been previously dated. U-Pb geochronology was conducted in this study to establish the absolute chronology of tonalite and diorite in the deposit area. Detailed outcrop mapping of the North Breccia Outcrop provided the framework for selecting the host rock samples. In addition, three dike rocks were dated in an attempt to provide a minimum age for the deposit.

Samples selected included five from the North Breccia Outcrop (one diorite, two tonalites, one hornblende-plagioclase pegmatite and one lamprophyre dike) and two feldspar-quartz porphyry samples from drill core; all of the samples are located in the deposit area. The location of the North Breccia Outcrop is shown in Figure 2.4. The location of geochronology samples from the North Breccia Outcrop are shown in Figure 2.6A and their UTM coordinates are included in Table 2.5. In the section below, a brief description is given for each sample, along with an interpretation of the age and a summary of the implications of these new data. The analytical data are presented in Table 2.5, the concordia diagrams are found in Figure 2.19 and a paragenesis is presented in Figure 2.20.

2.9.1 Sample descriptions and U-Pb geochronology results

A) North Breccia diorite (Sample NBxDRLK12; z10896): This sample is a massive, melanocratic, medium-grained, equigranular diorite composed of amphibole, plagioclase and minor titanite. Based on crosscutting relationships, the diorite is interpreted to be the oldest unit in the outcrop.

The zircons from this sample are well faceted, clear, colourless, fractured prismatic crystals and prism tips, ranging in length from ~100 to 250 µm in the longest dimension. Analysis of four single-grain zircon fractions yielded a cluster of concordant and near-concordant data (Fig. 2.19A, Table 2.5). A weighted mean of the $^{207}Pb/^{206}Pb$ ages of all of the analyses is calculated at 2741.5 ± 0.7 Ma (MSWD = 0.53; probability of fit (pof) = 0.66), which is interpreted as the crystallization age of the diorite.

B) North Breccia tonalite (Sample NBxTonaLK12; z10976): The sample is massive, fine-grained, equigranular tonalite composed of plagioclase and quartz. The sample has minor (<3%), fine-grained, secondary disseminated biotite, chlorite alteration after biotite and weak sericite alteration. This tonalite sharply intrudes the diorite (sample A; Fig. 2.6B).

The zircons from this sample are well faceted, euhedral, fractured prismatic zircon grains ranging from ~50 to 125 µm in size. Analysis of two fractions comprised of two grains and five single-grain zircon fractions yielded a cluster of concordant to slightly discordant data (Fig. 2.19B, Table 2.5). The weighted mean of the $^{207}Pb/^{206}Pb$ ages of all of the analyses is calculated to be 2741.4 ± 0.9 Ma (MSWD = 0.40; pof = 0.53), which is interpreted as the crystallization age of the tonalite.

C) North Breccia tonalite (NBxTonbLK12; z10993): The sample is a massive, medium-grained, inequigranular tonalite composed of plagioclase and quartz with <1% coarse-grained plagioclase phenocrysts. Minor alteration occurs as ~5% disseminated fine-grained clusters of biotite, chlorite after biotite and weak fracture-controlled sericite alteration. Based on crosscutting relationship this sample postdates diorite (sample A).

The zircons from this sample are 100 to 250 µm in size, clear, colourless, euhedral prisms with numerous fine fractures and inclusions. Five single-grain zircon fractions yielded a cluster of four overlapping concordant analyses and one slightly discordant analysis (A20-1, 0.7% discordant; Fig. 2.19C, Table 2.5). A weighted mean of the $^{207}Pb/^{206}Pb$ ages of all of the analyses is calculated at 2741.7 ± 0.7 Ma (MSWD = 0.98, pof = 0.42), which is interpreted as the crystallization age of the tonalite.

D) Sample D, North Breccia hornblende-plagioclase pegmatite (NBxPegLK12; z10992): This is a massive, very coarse-grained, inequigranular pegmatite composed of plagioclase, amphibole and minor quartz and titanite. The pegmatite intrudes along the contact of diorite (sample A) and tonalite (sample C; Fig. 2.6C) and, therefore, postdates both phases.

The zircons from this sample are clear, pale brown to colourless, euhedral prisms that contain numerous inclusions and are highly fractured. Analysis of five single-grain zircon fractions yields a cluster of concordant to near-concordant data and two discordant analyses (Fig. 2.19D, Table 2.5). The pegmatite also contains abundant anhedral brown titanite fragments. Analysis of three multigrain titanite fractions results in two near-concordant (TB, TC) analyses and one discordant analysis (TA). The weighted mean of the $^{207}Pb/^{206}Pb$ ages of the most concordant zircon and titanite analyses is calculated to be 2741.0 ± 0.6 Ma (MSWD = 0.89, pof

= 0.47). This date is interpreted to be the age of crystallization of the pegmatite. A crystallization age for the titanite was obtained at 2741.1 + 1.7/-1.4 Ma.

E) *Sample E, North Breccia lamprophyre dike (Nbxlamp02; z11150):* This is a lamprophyre dike from the North Breccia Outcrop. The groundmass is dark-green to black, medium-grained and composed of plagioclase, quartz and chlorite after amphibole, with abundance secondary carbonate. This dike crosscuts a mineralized breccia unit and is deformed with a weakly developed crenulation cleavage defined by chlorite.

Zircon grains from this sample are clear, colourless, euhedral, stubby prismatic to prismatic crystals that ranged from 75 to 250 µm in size and most grains have few, if any, fractures and inclusions. Analyses of four single-grain zircon fractions yielded a cluster of concordant to slightly discordant data (Fig. 2.19E, Table 2.5). A weighted mean of the $^{207}Pb/^{206}Pb$ ages of the analyses is calculated at 2742.2 ± 0.8 Ma (MSWD = 0.27; pof = 0.85), which is interpreted to be the crystallization age of the zircons and by inference the lamprophyre dike, but we note that inheritance may be an issue for this sample.

F) Sample F, Brett Lake feldspar-quartz porphyry dike (E11-119-240m; z10881): This sample was collected from drill core and has 15% phenocrysts of rounded to elongated zoned plagioclase (<6 mm) and rounded quartz (<4 mm) in a medium-grey, fine- to medium-grained groundmass composed of plagioclase, quartz and biotite. The plagioclase phenocrysts are dusted by hematite and epidote alteration. This porphyry dike intrudes biotite altered tonalite.

The zircons from this sample are clear, colourless, euhedral, stubby to elongate prisms that ranged between 100 to 200 µm in size and had few, if any, fractures and inclusions. Analyses of six single-grain zircon fractions yielded a cluster of concordant data (Fig. 2.19F,

Table 2.5). A weighted mean of the $^{207}Pb/^{206}Pb$ ages of the analyses is calculated at 2696.9 ± 0.9 Ma (MSWD = 1.28; pof = 0.27), which is interpreted to be the age of crystallization of the porphyry.

G) Sample G, Brett Lake feldspar-quartz porphyry dike (E12-370-215m; z11113): This is a feldspar-quartz porphyry from drill core that has ~5% quartz phenocrysts that have been elongated due to deformation. The groundmass is medium-grey, fine-grained and composed of plagioclase and quartz. This unit crosscuts a mineralized breccia unit and both the feldspar-quartz porphyry dike and breccia unit show pervasive muscovite alteration. A late-stage sulphide-bearing vein that cuts the porphyry is not gold-bearing (assays results = 0.01 ppm Au).

The zircons from this sample are clear, colourless and prismatic that range in size from 100 to 250 µm and many contain inclusions and some degree of fracturing. Analyses of five single-grain zircon fractions yielded a cluster of concordant to near-concordant data (Fig. 2.19G, Table 2.5). A weighted mean of the $^{207}Pb/^{206}Pb$ ages of these analyses is calculated to be 2697.1 ± 0.8 Ma (MSWD = 0.83, pof = 0.51), which is interpreted as the age of crystallization of this sample.

2.9.2 Summary of U-Pb geochronology data

The new ages from the North Breccia Outcrop include 2741.5 ± 0.7 Ma for the diorite and 2741.4 ± 0.9 Ma and 2741.7 ± 0.7 Ma for the tonalite samples. All of these ages are within analytical error. The age of 2741.0 ± 0.6 Ma for the North Breccia pegmatite is slightly younger, but within analytical error of the other ages obtained. The new ages for the diorite, tonalite and

pegmatite, along with previously obtained tonalite ages, demonstrate that the phases of the CIC are coeval and consistent with the mutually crosscutting relationships presented in this study.

Interestingly, the age obtained from the lamprophyre dike at 2742.2 ± 0.8 Ma is coeval with the intrusive phases of the CIC and is within error. Either the zircons in the lamprophyre dike are xenocrystic or they represent the actual age of this dike. Evidence from crosscutting relationships suggests that this dike postdates the formation of the deposit since unaltered lamprophyre dikes cuts through altered tonalite and diorite. Furthermore, the geochemical data in this study supports a single magmatic pulse of this dike due to its chemical homogeneity, and therefore, several injections of lamprophyre are not supported. In addition, lamprophyre dikes in the Abitibi are documented to be contemporaneous with late to post-tectonic alkaline magmatism (2680 to 2674 Ma; Feng and Kerrich, 1992; Wyman and Kerrich, 1993), and therefore, the zircon likely represents an inherited age, but additional data is needed to definitively determine if this is the case.

Two feldspar-quartz porphyry samples, one of which crosscuts an altered tonalite and one of which crosscuts a mineralized breccia body, were sampled to provide a minimum age for deposit formation. The first sample, an unaltered feldspar-quartz porphyry, yielded an age of 2696.0 ± 0.9 Ma. The second sample, a deformed, muscovite altered feldspar-quartz porphyry yielded a similar age of 2697.1 ± 0.8 Ma. The pervasive muscovite alteration associated with the dike may be related to and accompanied the D_2 related deformation that affects the sample. These results indicate similar ages for magmatism at ca. 2696 Ma and equate to the felsic to intermediate volcanic rocks of the Brett Lake Formation, which is part of the Swayze Group (i.e., Blake River Assemblage in the AGB). In addition, these samples provide an age for some of the

youngest magmatic activity in the SGB and do not constrain well the minimum age for deposit formation.

2.10 Discussion

The study of the CIC highlights its features as a low-Al, subvolcanic, composite intrusion. Such intrusions are characterized by a complex intrusive history, high-level textures, an FII- or FIII-type chemical affinity and coeval and cogenetic volcanic rocks. These intrusions can also host Cu-Au-Mo mineralization, such as the Flavrian-Powell intrusive complex (Goldie et al., 1979; Galley and van Breemen, 2002) and the Mooshla intrusive complex (Galley and Lafrance, 2014). Geochronological evidence comparing the ages of the CIC with the contained gold mineralization indicates that the latter is synchronous with magmatism. It is important, therefore, to understand how the CIC formed in order to put the deposit into a geological context. The following discussion addresses the tectonic setting of the CIC, the relationship between the tonalite and diorite phases and investigates the petrogenetic relationship of the Yeo Formation with the tonalite of the CIC. The nature of the dike rocks is also discussed with regards to their dissimilar geochemistry with the CIC. Finally, the level of emplacement, emplacement history and magmatic evolution of the CIC is discussed.

2.10.1 Tectonic setting of the Chester intrusive complex

Archean TTG/D suites represent the largest portion of preserved Archean continental crust and understanding their origin is important in terms of Archean geodynamic processes, which in turn, is relevant to the formation of Au-Cu deposits such as Côté Gold. Two types of

Archean TTG/D suites can be distinguished geochemically, the voluminous high-Al type (>15 wt. % Al_2O_3) and the rarer low-Al type (<15 wt. % Al_2O_3; Barker, 1979; Martin et al., 2005). The high-Al TTG suite, which chemically equates to FI-type felsic volcanic rocks, are produced by high-pressure melting of hydrated basalt within the garnet stability field (Condie, 2005). In contrast, the low-Al TTD suite, which chemically equates to FII- and FIII-type felsic volcanic rocks, are products of partial melting in a low-pressure source area that lacked garnet and within which plagioclase was stable (Condie, 2005; Martin et al., 2005; Beakhouse, 2011). This is reflected by relatively unfractionated REE distribution patterns, negative Eu anomalies, low Sr values (<300 ppm) and lower Sr/Y ratios. The lower pressure condition of melt generation for the low Al-TTD suites implies that they are generated by a different mechanism than high-Al TTG suites and reflects their formation in a different tectonic setting. This is illustrated by the Sr/Y vs. Y and La/Yb vs. Yb diagrams (Fig. 2.15) in which tonalite and diorite plot in the post-Archean normal arc-related field rather than the Archean adakite and high-Al TTG field.

The low-Al TTD suites are suggested to form in rift-related extensional settings within oceanic-arc environments (Barrie et al., 1993; Galley, 2003; Hart et al., 2004). Settings such as these are consistent with higher geothermal gradients which account for the high degrees of partial melting of the mafic source to generate low-Al TTD magmas.

The tectonic setting of the Arbutus Formation, into which the CIC intrudes, is important to understand. The use of its trace element geochemistry can be used to infer the tectonic setting for the volcanic rocks and by extension, the CIC. Previous studies of the southern AGB have interpreted the volcanic rocks of the Pacaud Assemblage (correlative to the Chester Group in the SGB) to have both ensimatic ocean basin and arc volcanic signatures (van Breemen et al., 2006). The data from this study suggests an undepleted mantle source for the melts based on their flat

REE pattern (Fig. 2.17C). The samples display similar enrichment (Ba, K, P, Ti) and depletion (Th, Nb, Ta) to those of modern back-arc basin basalts and to a lesser extent island-arc tholeiites (Fig. 2.17D). This formation is suggested, therefore, to have formed from an undepleted mantle source in a possible back-arc environment, consistent with the inferred tectonic setting of low-Al composite intrusions.

2.10.2 Petrogenetic relationship between phases of the Chester intrusive complex

In the deposit area, the CIC consists of two geochemically discrete intrusive phases, the first being tonalite and the second being diorite and its related fractionates. Drill core logging and outcrop mapping suggests that the diorite differentiates to quartz diorite, but not the more voluminous tonalite. Observations from this study reveal mutually crosscutting relationships between tonalitic and dioritic phases that suggest they are coeval and this paper confirms their temporal relationship. Of relevance here is the petrogenetic relationship among these phases and whether they are cogenetic.

The geochemical data presented in this study demonstrate all tonalite samples are geochemically related, based on their low-Al nature, transitional to calc-alkaline affinity, chemical signature equating to FII-type rhyolites, unfractionated REE patterns, weak to moderate negative Eu anomalies and similar primitive mantle-normalized profiles (Figs. 2.14D-F and 2.16A, B). Any difference noted in their texture (i.e., presence of diorite fragments) is therefore solely a reflection of the relative timing of emplacement. It is noted that outside the deposit area the tonalite appears to differ geochemically based on REE patterns (Fig. 2.16A, B; Berger, 2012)

and further work is required to address the apparent complexities of the leucocratic phases in the CIC.

The geochemical data presented in this study suggest tonalite and dioritic phases of the CIC are not genetically related. The flatter, less fractionated patterns for tonalite (La/Yb_N = 0.48 to 2.36) are inconsistent with these units being an evolved fractionate of the diorite which is characterized by more fractionated patterns REE patterns (La/Yb_N = 2.65 to 4.85). The difference in Gd/Y ratios between tonalite (Gd/Y = 0.14 to 0.15) and dioritic (Gd/Y = 0.16 to 0.23) rocks, along with the slight differences in the MREE slope between the two suites (Fig. 2.16A, C), suggests they were derived from different source areas; the former from a plagioclase stable source and the latter from a source area where plagioclase and amphibole were stable. The dioritic phases are tholeiitic to transitional in nature, whereas the tonalitic phases have a calc-alkaline to transitional affinity based on their respective Zr/Y ratios (Fig. 2.15E). This variable chemical affinity, and hence, petrogenetic associations has been previously documented in TTD suites and inferred to indicate that the suites are a composite of differentiated lithospheric mantle and lower-crust partial melts (Galley and Lafrance, 2014).

Previous studies have documented mingling textures between tonalite and dioritic phases (Heather, 1993; Heather and Shore, 1999a; Heather, 2001; Berger, 2011) and these textures must be addressed to better understand tonalite and diorite petrogenesis. Magma mingling is a term used to describe magmas that are mixed physically, but heterogeneities exist, such as banding or enclaves due to a lack of chemical exchange (Vernon, 1984; Sparks and Marshall, 1986; Wilcox, 1999; Kuşcu and Floyd, 2001), whereas magma mixing refers to a homogeneous product or composition (Sparks and Marshall, 1986; Neves and Vauchez, 1995; Kuşcu and Floyd, 2001). In magma mixing or mingling, certain textures are often observed, such as mafic ‘pillows’ enclosed

in felsic rocks (Snyder et al., 1997; Wilcox, 1999), irregular shaped mafic enclaves (Vernon, 1984; Vernon et al., 1988), rapakivi feldspars (Baxter and Feely, 2002), acicular grains, ocelli (Baxter and Feely, 2002), normal and reverse zoning in crystals from the same sample (Luhr and Carmichael, 1980; Kuşcu and Floyd, 2001) and disequilibrium textures (i.e., sieve texture, occurrence of normal and sieved plagioclase in the same sample, rounded and embayed crystals, reaction rims on minerals; Stimac and Pearce, 1992; Kuşcu and Floyd, 2001).

The lack of mingling textures and no documented intermediate composition between tonalite and diorite suggest magma mingling did not occur in the deposit area. Instead, the rare lobate contacts observed in the tonalite breccia suggest quenching of diorite fragments (Vernon, 1984). Lobate contacts are typical of the boundaries between two liquids that have different viscosities (Sklyarov and Fedorovskii, 2006) and its presence suggests diorite was still hot when tonalite intruded (Vernon, 1984). The presence of chilled diorite fragments against tonalite (Fig. 2.8G-I), as well as acicular amphibole and miarolitic cavities in tonalite near the matrix/fragment contact (Fig. 2.8G), suggests quenching and undercooling of the fragments.

2.10.3 Petrogenetic relationship between the Yeo Formation and the Chester intrusive complex

The petrogenetic relationship of subvolcanic intrusions and their temporally-related volcanic rocks has been demonstrated in several low-Al composite intrusions (Davis et al., 1985; Bailes and Galley, 1996; Barrett and MacLean, 1999; Galley, 2003). The results presented here show that some geochemical similarities exist between the tonalite in the study area and the Yeo Formation, such as their calc-alkaline nature and affinity with FII-type rhyolites. Some

geochemical differences are noted, however, such as the REE and spider diagram patterns. In contrast, previous studies have shown the Yeo Formation to be geochemically similar to the tonalite of the CIC (Heather et al., 1996; Berger, 2012). The REE patterns of the Yeo Formation samples collected in this study overlap with the tonalite samples collected regionally by Berger (2012; Fig. 2.17G, H). Although the relationship between the tonalite in the study area and the Yeo Formation appears to be more complex than currently understood, the results demonstrate that the Yeo Formation represents the eruptive equivalent of the tonalite in the CIC in the regional context.

2.10.4 Nature of the geochemistry of the dike rocks

The dike rocks in the deposit area postdate the formation of the CIC based on their crosscutting relationships and it is expected, therefore, that the dike rocks have no petrological or geochemical relationship with the tonalitic or the dioritic phases of the CIC. Such geochemical differences are noted above and illustrated in the La/Yb_N vs. Yb_N diagram (Fig. 2.18B).

The feldspar ± quartz porphyries are not petrogenetically related to the CIC based on geochemical evidence. These dikes have steep, more fractionated REE patterns than the tonalite or diorite and chemically resemble FI-type volcanic rocks (Fig. 2.18C; Lesher et al., 1986). The steep REE patterns and low HREE contents suggest a garnet-bearing source area for the melts. The geochemistry of these dikes resembles metavolcanic rocks in younger formations of the SGB, as shown by Heather et al. (1996). The feldspar porphyry dikes are interpreted to be feeder dikes to younger metavolcanic formations in the SGB, which range in age from 2740 to 2696

Ma, and explains their variable chemistry. Geochronology results from this study support this interpretation with two porphyry samples dated at ca. 2696 Ma.

Although mineralogically and texturally different, both the lamprophyre and dioritic dikes have strongly fractionated REE patterns and weakly negative to no Eu anomalies. Thus, a deep, garnet-bearing source area is inferred for these melts based on their depleted HREE profiles (Fig. 2.18E, G). Their similar La/Yb_N values (Fig. 2.18B), Eu anomalies and profiles in primitive mantle-normalized spider plots suggest they were derived from a similar source.

The gabbroic dikes have flat REE patterns with no Eu anomalies, both of which are similar to the Arbutus Formation. The flat pattern reflects the fact that they have undergone little fractionation. These rocks are not known to be temporally-related, but we note that there is no absolute age for the dike rock, and thus, they may have been sourced from the same undepleted primitive mantle source material as the mafic volcanic rocks of the Arbutus Formation.

The diabase dikes, which are the youngest event in the study area, have relatively flat REE patterns with slightly elevated LREE (La/Yb_N = 2.48 to 2.69). The diabase dikes are probably equivalent to the ca. 2450 Ma Matachewan dikes (Heaman, 1997) in the AGB.

The geochemistry of the different dike rocks are highly variable and provide insight into the nature of magmatism and the source areas where the melts were generated. Based on the geochemistry and comparison to the petrology of the units of the CIC the following generalizations can be made: (1) the variation in the ΣREE and their degree of fractionation and Eu anomalies combined with the primitive mantle-normalized spider diagram indicate different source regions were evolved; (2) the degree of REE fractionation indicates different depths where partial melting occurred in these source regions (i.e., garnet stable or not); and (3) that

none of the dike rocks equate geochemically to the units of the CIC. This latter point is significant given the suggested magmatic origin for the mineralization (Kontak et al., 2013a; Katz et al., 2015). It also reveals that the CIC magmatism is geochemically unique to this part of the SGB.

2.10.5 Formation of the Côté Gold deposit

The following discussion addresses the setting of this deposit but not its genesis per se, this being addressed in companion papers. Instead, this section discusses aspects of the CIC in the context of its emplacement history, level of emplacement and magmatic evolution that pertains to the origin of the deposit. A paragenesis is presented in Figure 2.20 and a schematic model for the formation of the CIC and deposit is shown in Figure 2.21.

The CIC was emplaced at ca. 2741 to 2739 Ma as a series of bodies into the volcanic-sedimentary packages of Arbutus and Yeo Formations based on the incorporation of screens and inclusions of these volcanic rocks (Fig. 2.21A; Heather, 2001; Berger, 2012). Although the CIC contains screens and inclusions of the Yeo Formation (Berger, 2012), which suggests the CIC intruded into its own volcanic pile, the ages of 2739 ± 1 Ma (van Breemen et al., 2006) and 2734 ± 2 Ma (Heather and Shore, 1999a) obtained from the Yeo Formation suggests volcanism also occurred syn- to post-magmatism (Fig. 2.20). The current map pattern suggests there is an as of yet undefined structural complexity that may be responsible for the younger 2734 ± 2 Ma age being closer to the contact with the CIC rather than the 2739 ± 1 Ma age (see Fig. 2.3 for the location of the ages).

Several lines of evidence suggest the CIC was emplaced into a high crustal level. The incorporation of screens and inclusions of the coeval and cogenetic Yeo Formation indicates that the CIC intruded into its own volcanic pile. Both tonalite and dioritic phases contain miarolitic cavities, which can form as a result of first boiling or second boiling (Burnham, 1979). In this case, the miarolitic cavities are inferred to have formed from the former process based on the accompaniment of other textures (e.g., granophyres and acicular crystals). As a magma ascends to shallower levels it has the potential be undercooled, which occurs when the melt is cooled below the true crystallization temperature of a mineral within the system, and can result in a variety of textures, such as granophyres, dendritic crystals, acicular crystals, skeletal crystals, aplites, miarolitic cavities and pegmatites (Candela, 1997). In addition, the Al-in-hornblende geobarometry results of $\leq 1.3 \pm 0.6$ kbars are consistent with the above information.

The emplacement history of the CIC is complex and in the deposit area can be broadly simplified into five stages (Fig. 2.21): (1) emplacement at ca. 2741 Ma of multi-phase tonalite and diorite of variable thickness probably along primary stratigraphic contacts. Given our current understanding of the study area, tonalite and diorite likely intruded as sill-like bodies; (2) the diorite evolved at depth to more leucocratic phases; this process may have repeated several times during the history of the intrusive complex. The forceful emplacement of diorite and quartz diorite resulted in brecciation of tonalite and earlier dioritic phases; (3) emplacement of coeval, small hornblende-plagioclase ± quartz pegmatite units within dioritic phases indicates the diorite approached volatile saturation during its fractionation; (4) the continued or renewed injection of tonalite and hence, its contemporaneity with the emplacement of dioritic phases, as evidenced from the lobate contacts between these units; and (5) emplacement of several hydrothermal

stages accompanied by Au-Cu mineralization which are constrained to 2739 ± 7 Ma (Kontak et al., 2013a).

Figure 2.16C shows that the melanocratic diorite can display more fractionated chondrite-normalized REE patterns compared to leucocratic quartz diorite which suggests the addition of mafic melt into the evolving magma chamber. If this was the case, it may have important implications since the injection of hot mafic melt into the colder parent chamber can result in heating of the earlier melt and expansion of the volatiles in addition to increasing the amount of sulphur and metal, which are important aspects of modern models for porphyry systems (Sillitoe, 2000; Hattori and Keith, 2001). In addition, such a process can trigger vigorous convection leading to explosive venting in subvolcanic plutons (Sparks et al., 1977; Huppert et al., 1982) which may result in brecciation and mineralization of the surrounding rocks (Hattori and Keith, 2001). A genetic relationship between biotite alteration and diorite is proposed due to the similar REE and spider diagram patterns (Fig. 2.16E, F). Importantly, the REE pattern of the hydrothermal biotite breccia matrix is relatively less fractionated (Fig. 2.16E), even though it postdates the majority, if not all, dioritic intrusions, which supports the above model.

2.11 Conclusions

The complex intrusive history of the CIC is the result of multi-phase, high-level tonalite and diorite injections which were emplaced into a submarine succession of volcanic and sedimentary rocks of the Arbutus and Yeo Formations in a back-arc setting. The CIC has been constrained at ca. 2741 to 2739 Ma based on high-precision U-Pb ID-TIMS geochronology and is both coeval and cogenetic with the felsic to intermediate rocks of the Yeo Formation.

Although tonalite and dioritic rocks are co-temporal and co-spatial they appear to be petrogenetically unrelated with one representing a mantle differentiate and the other a lower-crust partial melt. The complex history of diorite and its fractionates may have played an important role in the formation of the deposit. The deposit was intruded by several late-stage, geochemically unrelated dike rocks.

The results from this study indicate that the CIC is similar to other low-Al, subvolcanic intrusions that underlie VMS-type mineralization and have been noted to contain porphyry-style Cu-Mo-Au mineralization. Given the FII-type affinity of the Yeo Formation and its broadly coeval timing with the CIC, this formation is considered prospective for VMS-type mineralization.

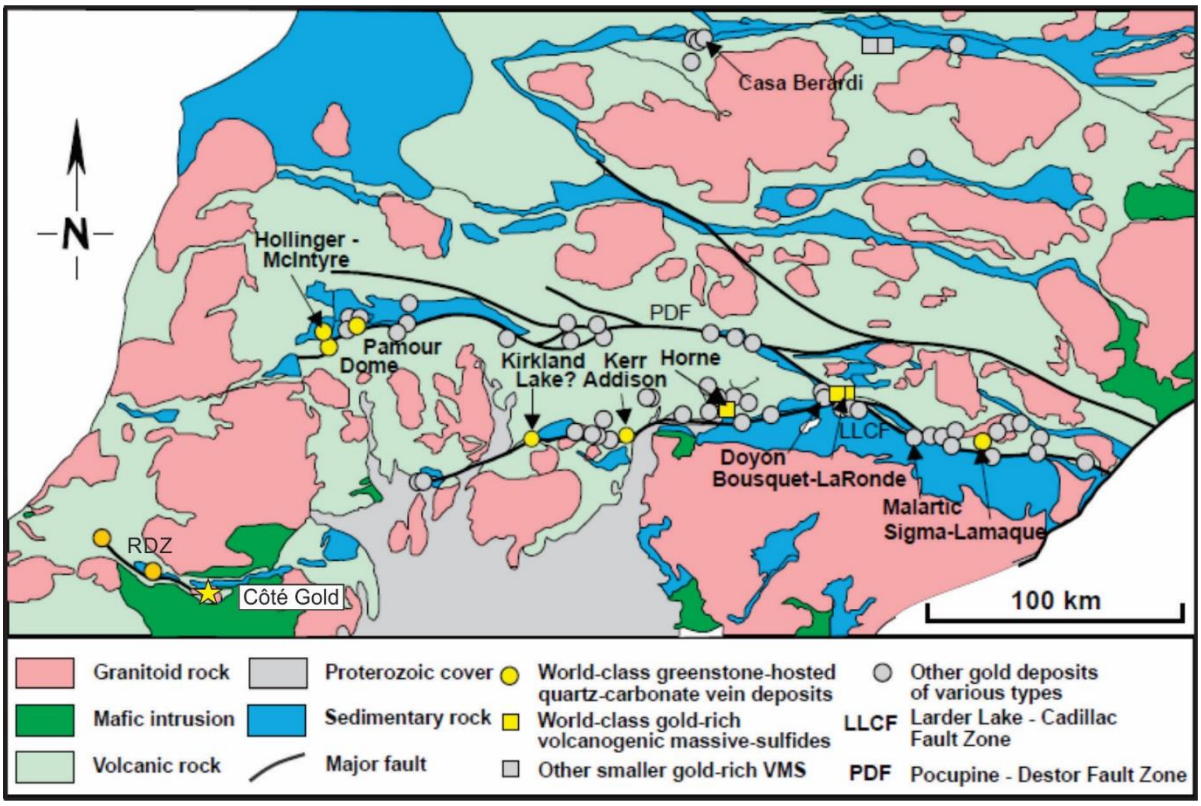

Figure. 2.1. Regional geological map of the Abitibi Subprovince showing the distribution of major gold deposits and also main structural features, in particular the Porcupine-Destor and Larder Lake-Cadiallac faults zones, modified after Dubé and Gosselin (2007). The yellow star shows the location of the Côté Gold deposit, which is located near the Ridout deformation zone (RDZ).

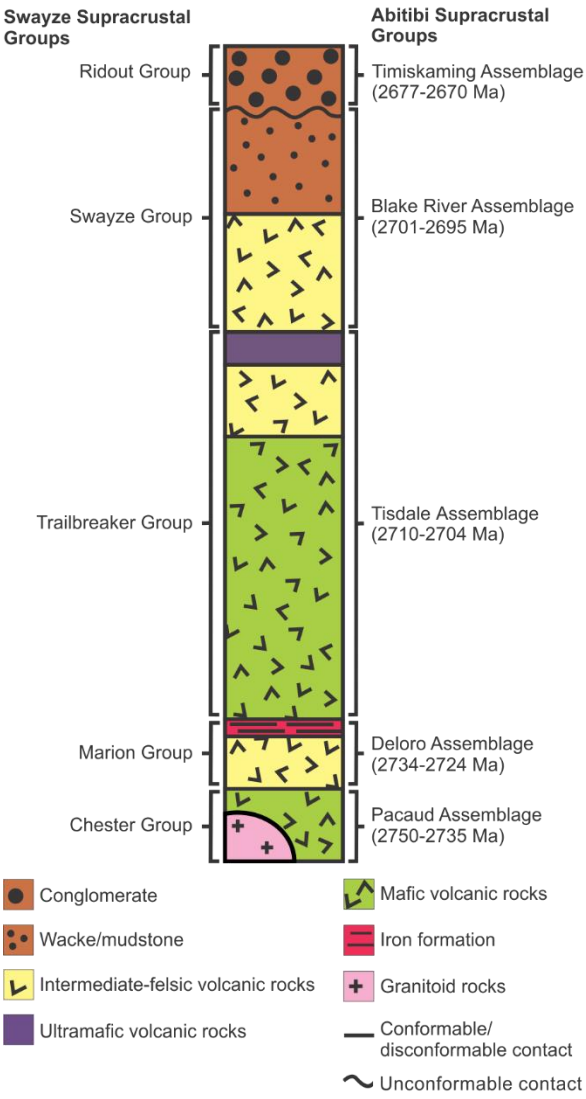

Figure 2.2. Schematic stratigraphic type section from the central Swayze greenstone belt (SGB) modified after Ayer et al. (2002) which correlates the supracrustal groups of the SGB with the Abitibi greenstone belt (AGB). The ages in the AGB from Thurston et al. (2008) apply to the SGB.

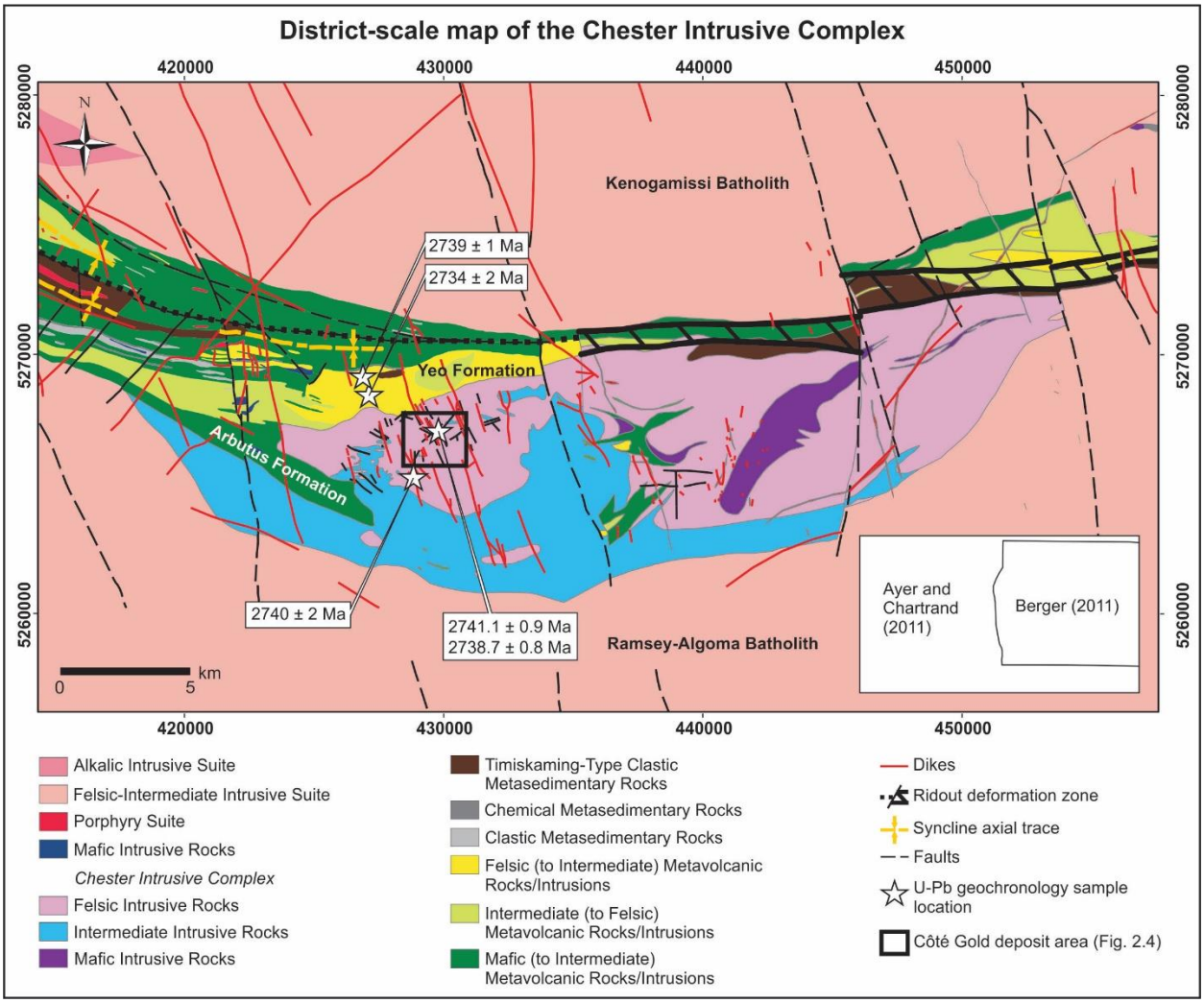

Figure 2.3. Simplified district-scale geological map of the Chester intrusive complex (CIC) and the southeastern arm of the Swayze greenstone belt, compiled from Ayer and Chartrand (2011) and Berger (2011). The inset shows the mapped area by both groups. Note the Ridout deformation zone extends west through the map area past Berger's (2011) more detailed map area. The geological context below the CIC has been lost due to the intrusion of the Ramsey-Algoma Batholith (2715 to 1636 Ma; Berger 2011). The locations of previous geochronology ages from the CIC and Yeo Formation are shown by white stars and are discussed in the text.

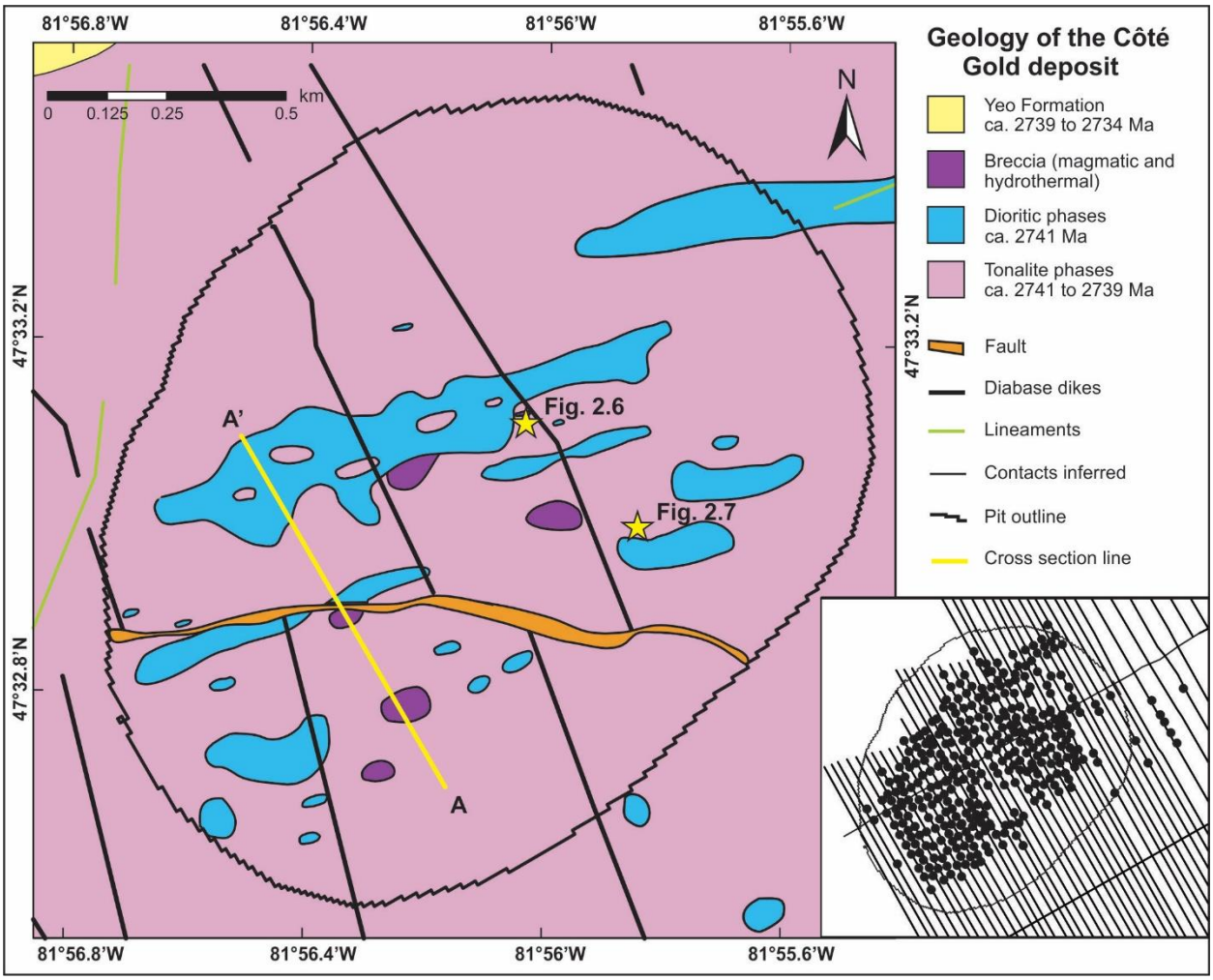

Figure 2.4. Simplified geological map of the Côté Gold deposit area that shows the distribution of major rock types. The deposit outline corresponds to the open pit shell outline as of October 2012 and the geology from within this shell was created by using the first bedrock collared in 373 diamond drill holes along with mapping of several outcrops. The inset shows the distribution of drill holes used to construct the map. The geology from outside the deposit shell is taken from Ayer and Chartrand (2011). The vertical cross section (A-A') is found in Figure 2.5 and the yellow stars show the location of outcrop maps.

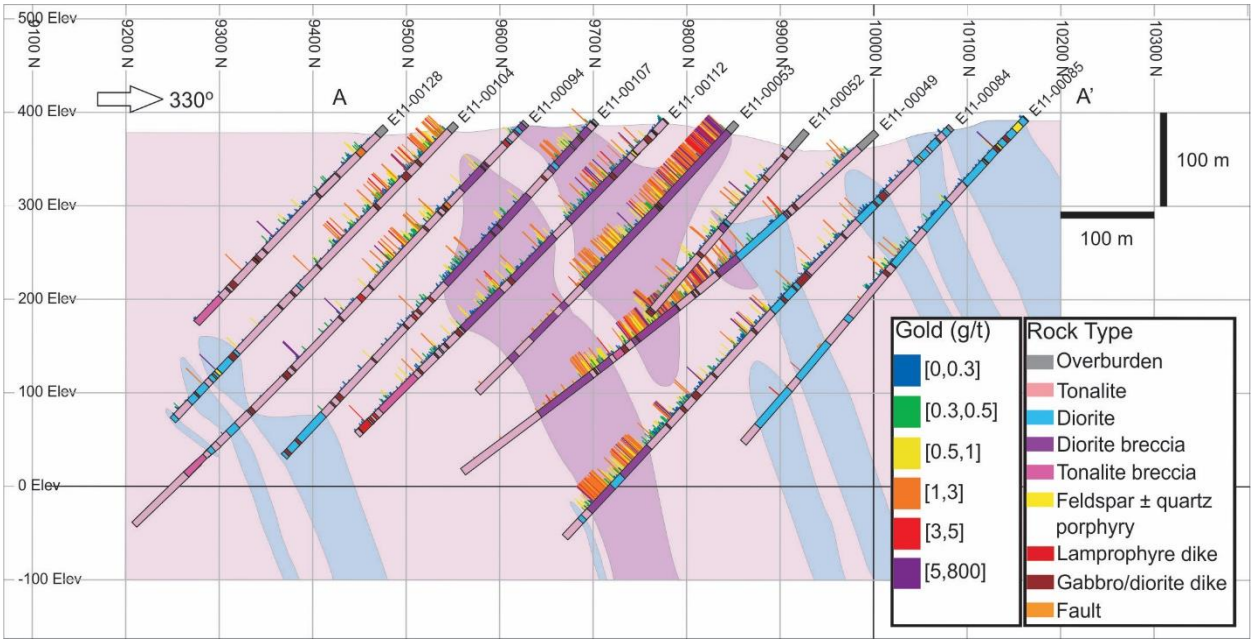

Figure 2.5. Vertical geological cross section of grid line 87+00 (A-A') from the Côté Gold deposit that shows the distribution of major and minor rock types and their associated gold grades. The shaded areas show the interpreted distribution of the host rocks.

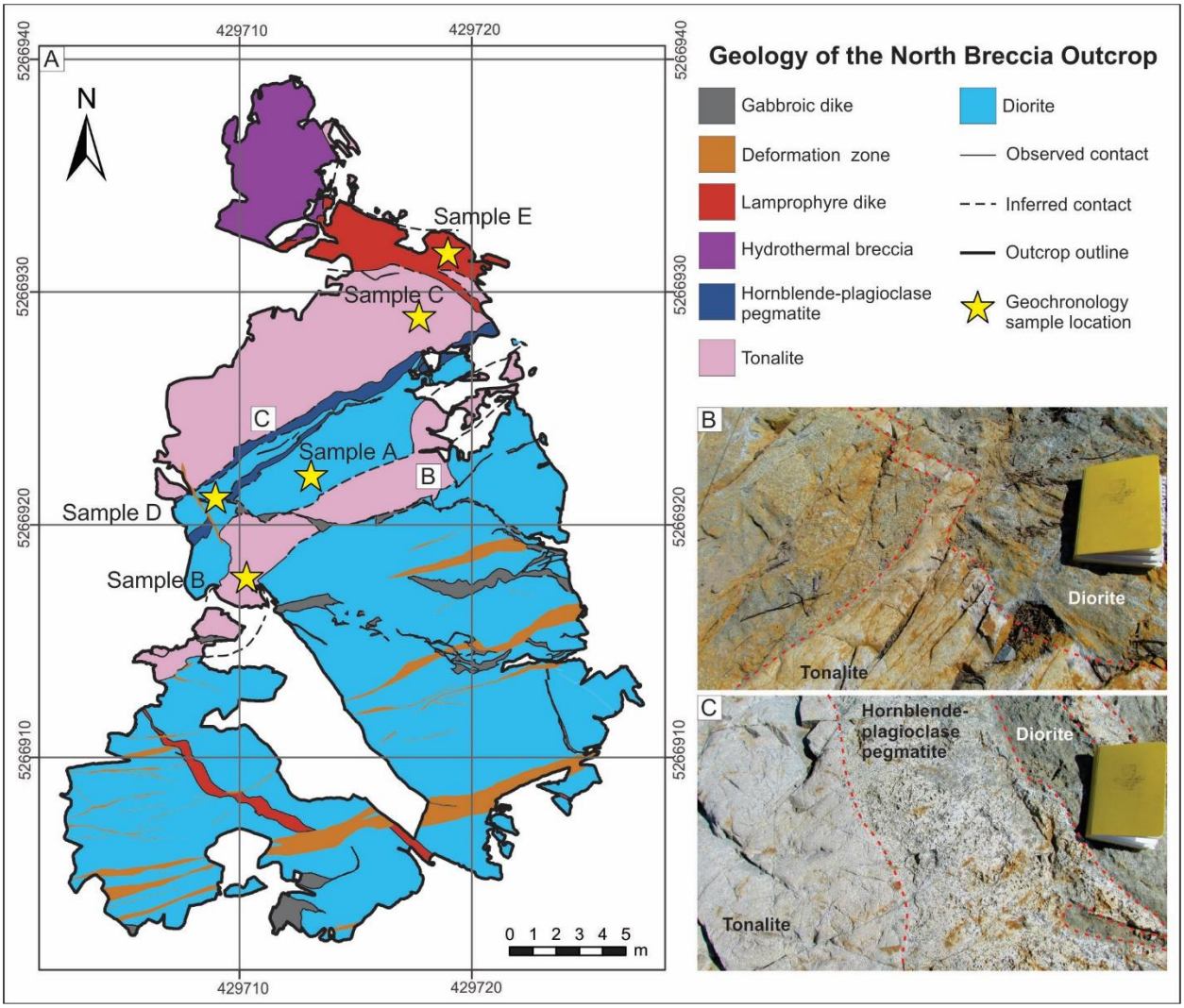

Figure 2.6. A) Geological map of the North Breccia Outcrop which contains important crosscutting relationships as illustrated in B and C. The yellow stars show the locations of U-Pb geochronology samples (A-E). Ages are found in Figure 2.19. B) A tonalite body that sharply intrudes into a diorite. The yellow book for scale is 19 x 12 cm. C) A hornblende-plagioclase pegmatite dike that intrudes sharply along the margin of tonalite and diorite.

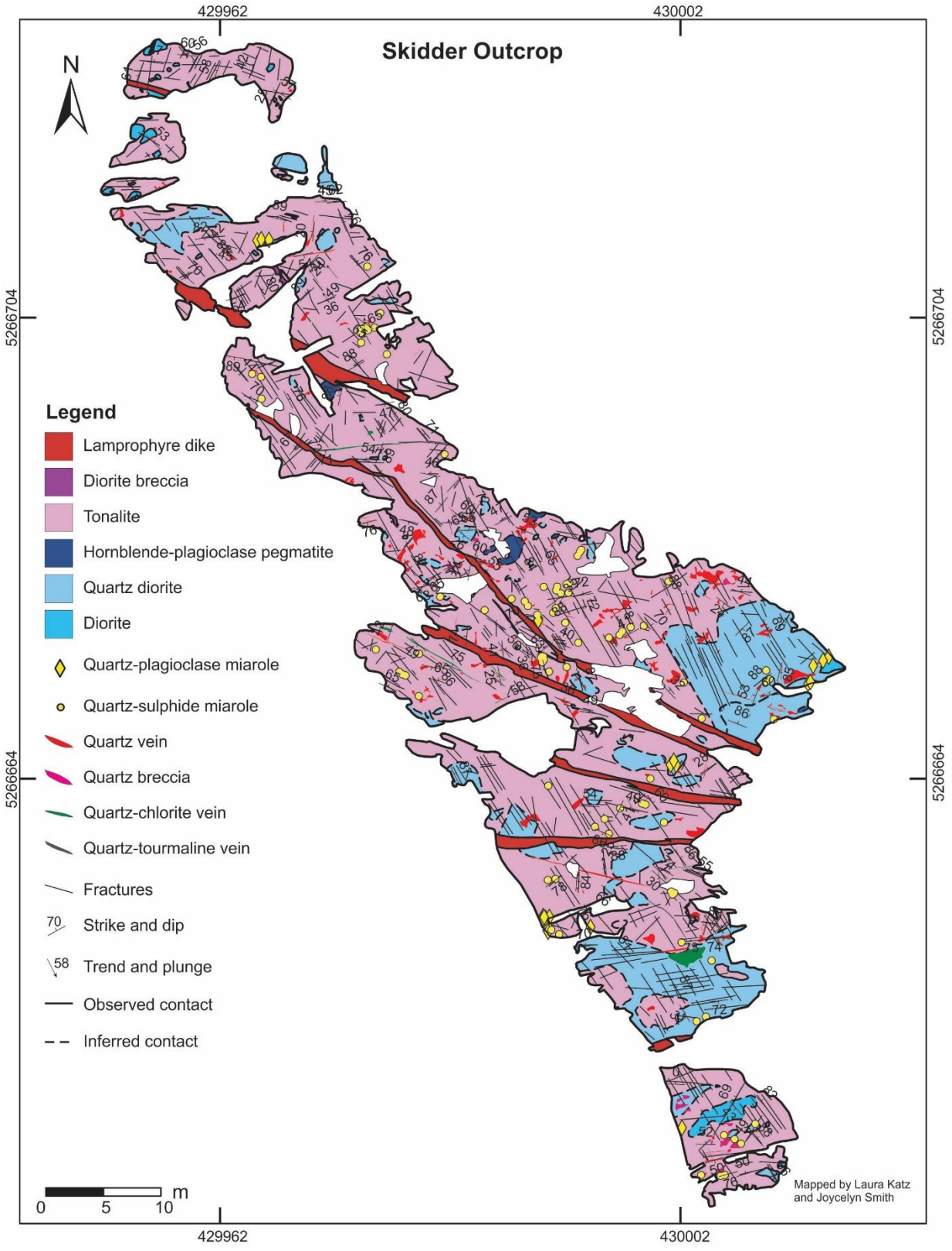

Figure 2.7. Geological map of the Skidder Outcrop which shows tonalite brecciating several dioritic phases and the distribution of quartz-plagioclase and quartz-sulphide miarolitic-like cavities.

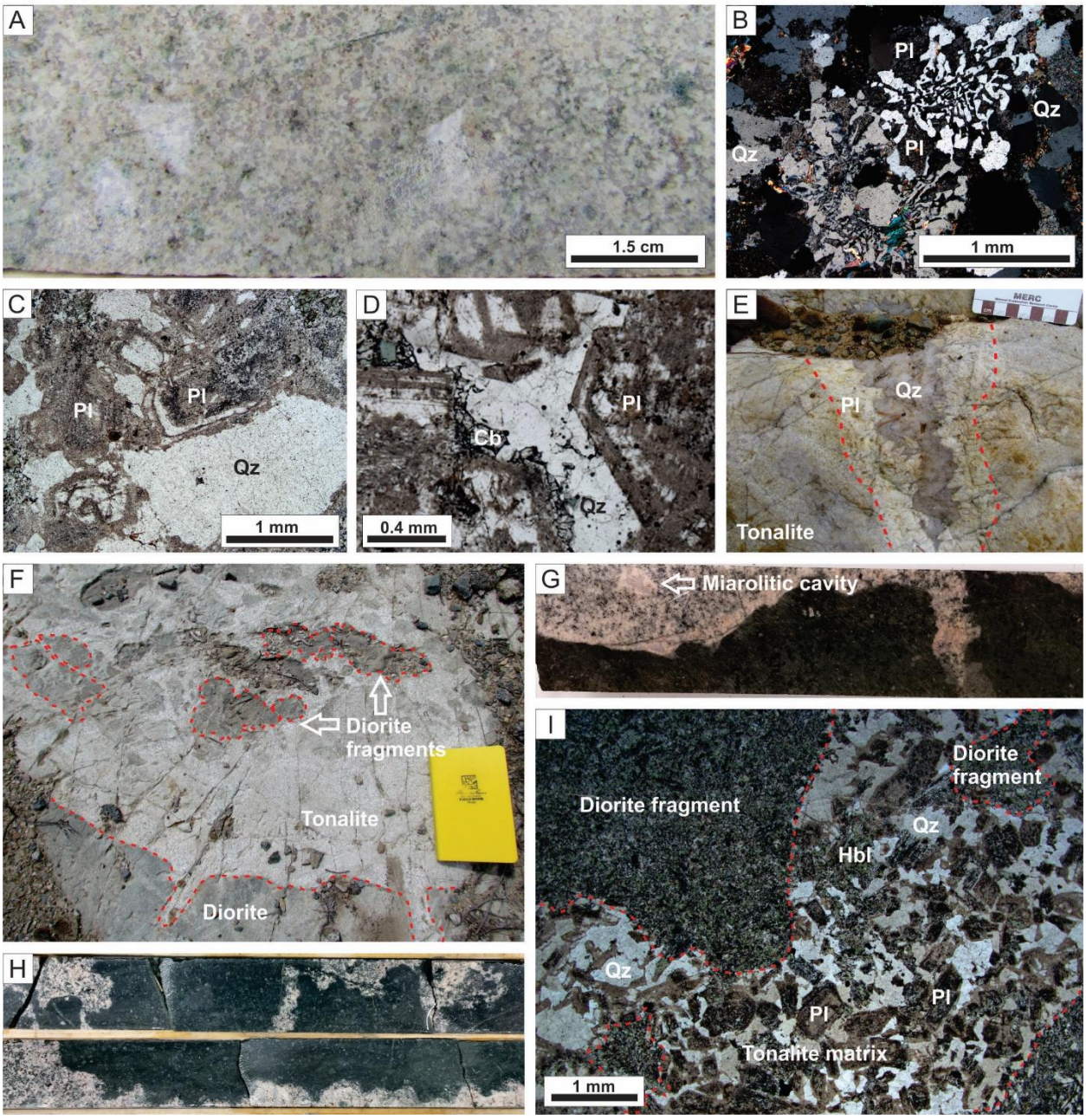

Figure 2.8. Outcrop, drill core (4.5 cm in width) and thin section photographs of tonalite rocks from the Côté Gold deposit. A) Photo of least-altered leucocratic tonalite. B) Thin section photo in crossed polarized light of granophyric-like texture between quartz and plagioclase in tonalite. C) Thin section photo in crossed polarized light of zoned plagioclase in tonalite. D) Thin section photo in plane polarized light of miarolitic cavity in tonalite with inward pointing, euhedral, zoned plagioclase crystals which is filled with secondary carbonate and quartz. E) Outcrop photo of a quartz-plagioclase miarolitic-like cavity outlined by the red dashed lines. F) Tonalite intruding medium-grained diorite with characteristic brecciated contact; diorite fragments are outlined in red dashed lines. G) Photo of lobate contacts between tonalite and diorite with a miarolitic cavity near the contact. H) Lobate contacts between tonalite and diorite. I) Thin section photo in plane polarized light of diorite fragments in tonalite; diorite fragments are outlined in red dashed lines. Note that hornblende from the diorite occurs in small amounts in the tonalite. Abbreviations: Carbonate = Cb, Hornblende = Hbl, Plagioclase = Pl, Quartz = Qz.

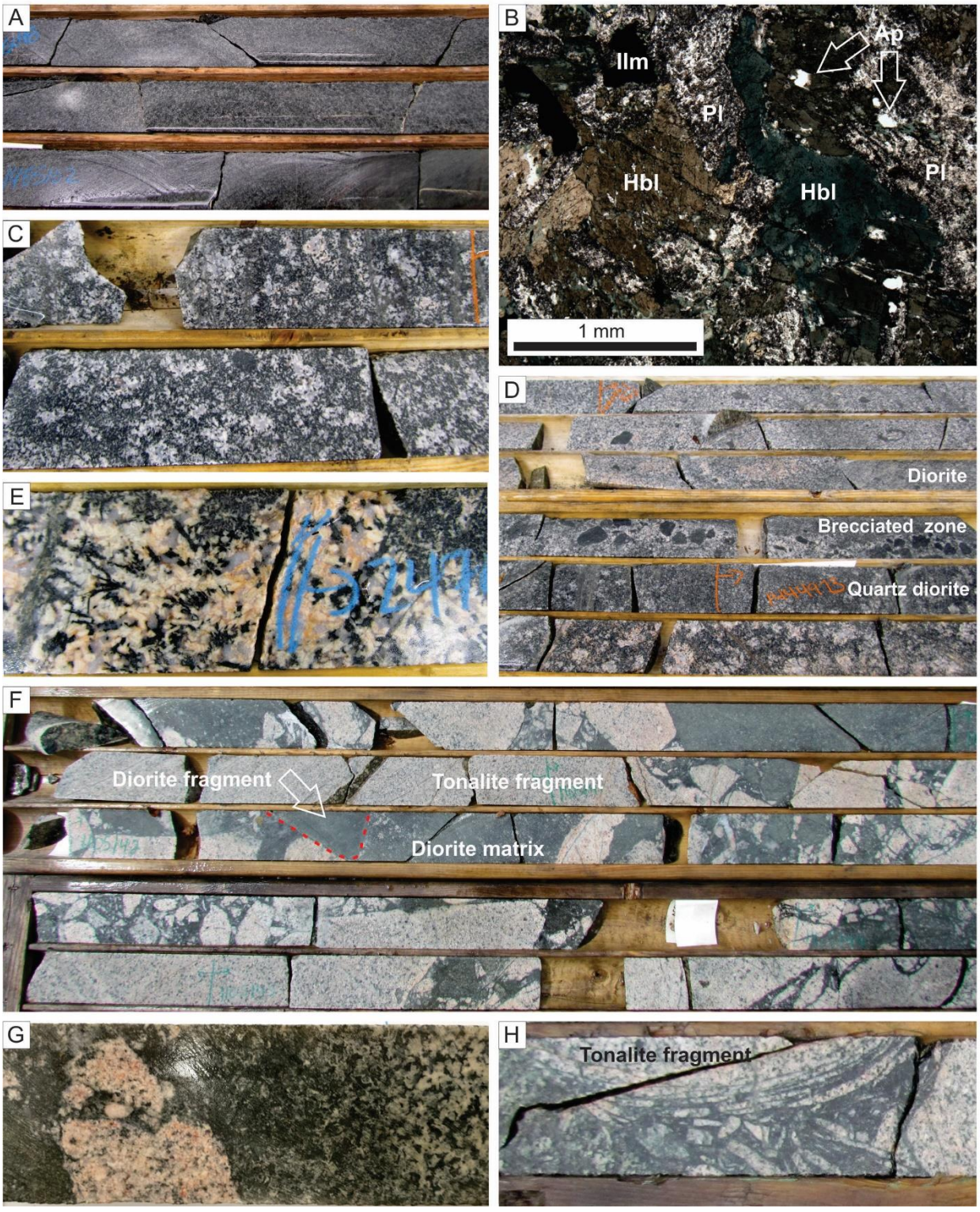

Figure 2.9. Drill core (4.5 cm in width) and thin section photographs of least-altered dioritic rocks and diorite breccias. A) An example of an equigranular, melanocratic diorite. B) Thin section photo in plane polarized light of diorite containing amphibole, epidote altered plagioclase, ilmenite and apatite. C) A melanocratic quartz diorite with quartz phenocrysts. D) An example of a brecciated contact between melanocratic quartz diorite and leucocratic

diorite. Note along the contact the diorite fragments are quenched. E) An example of a hornblende-plagioclase-quartz pegmatite with acicular amphibole. F) An example of the diorite breccia with a melanocratic diorite matrix surrounding variably sized angular to sub-rounded tonalite and subordinate diorite fragments. G) Close-up photo of diorite breccia showing diorite texture in the matrix. Note the finer-grained nature of the diorite matrix closer to the tonalite fragment is due to disseminated fine-grained biotite alteration that alters primary amphibole and plagioclase. H) An example of exfoliation texture of a tonalite fragment. Abbreviations: Apatite = Ap, Hornblende = Hbl, Ilmenite = Ilm, Plagioclase = Pl.

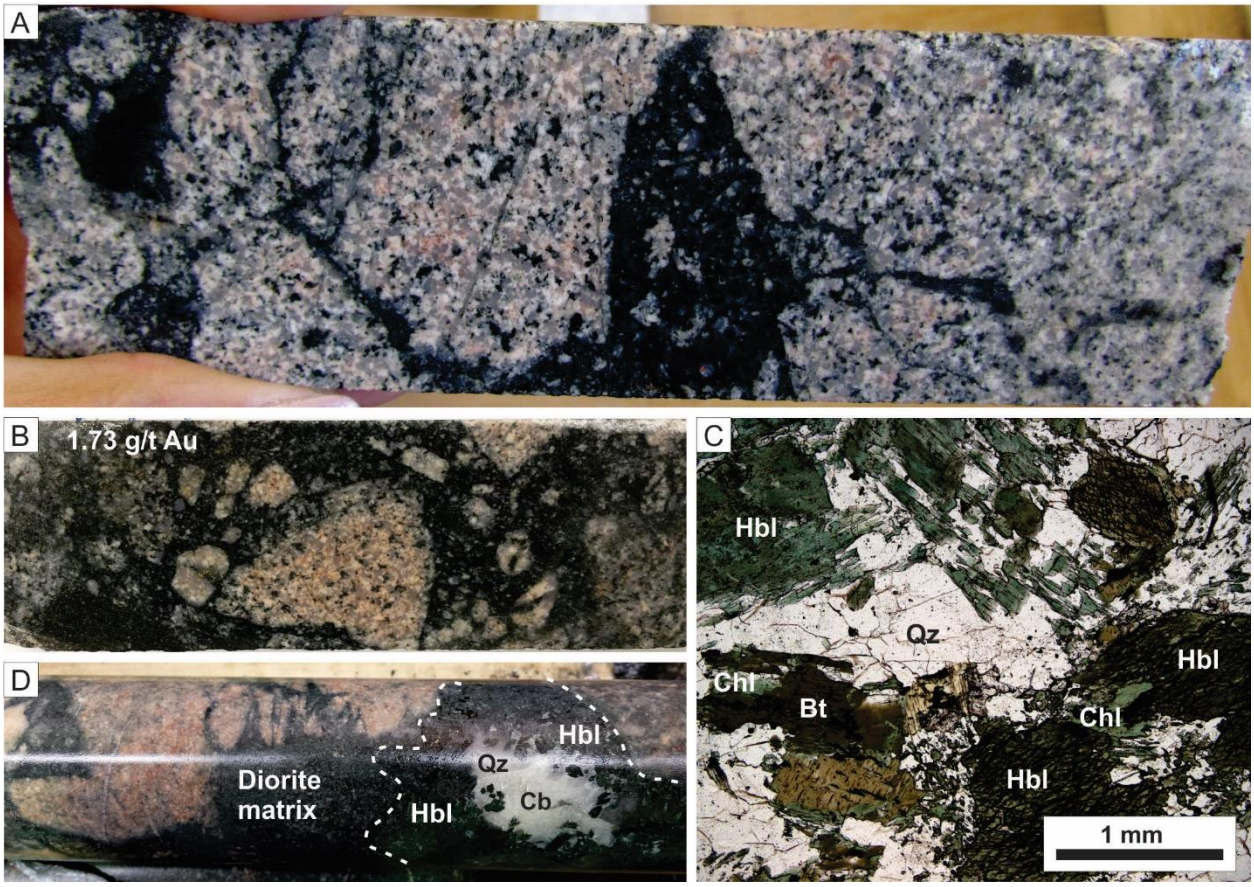

Figure 2.10. Drill core (4.5 cm in width) and thin section photographs of hydrothermal amphibole breccias and vein. A) Hydrothermal amphibole breccia with fine-grained, black amphibole-rich matrix. Fine-grained disseminated black mineral in the tonalite groundmass is secondary amphibole. B) A gold-bearing hydrothermal amphibole breccia with tonalite and diorite fragments set in a fine-grained amphibole-rich matrix. C) Coarse-grained, medium- to dark-green amphibole with quartz and biotite in an amphibole-rich breccia matrix. Note minor chlorite alteration of amphibole and biotite. D) A hydrothermal hornblende-quartz-carbonate vein cutting a diorite breccia with a diorite matrix and tonalite fragments. Abbreviations: Biotite = Bt, Carbonate = Cb, Chlorite = Chl Hornblende = Hbl, Quartz = Qz.

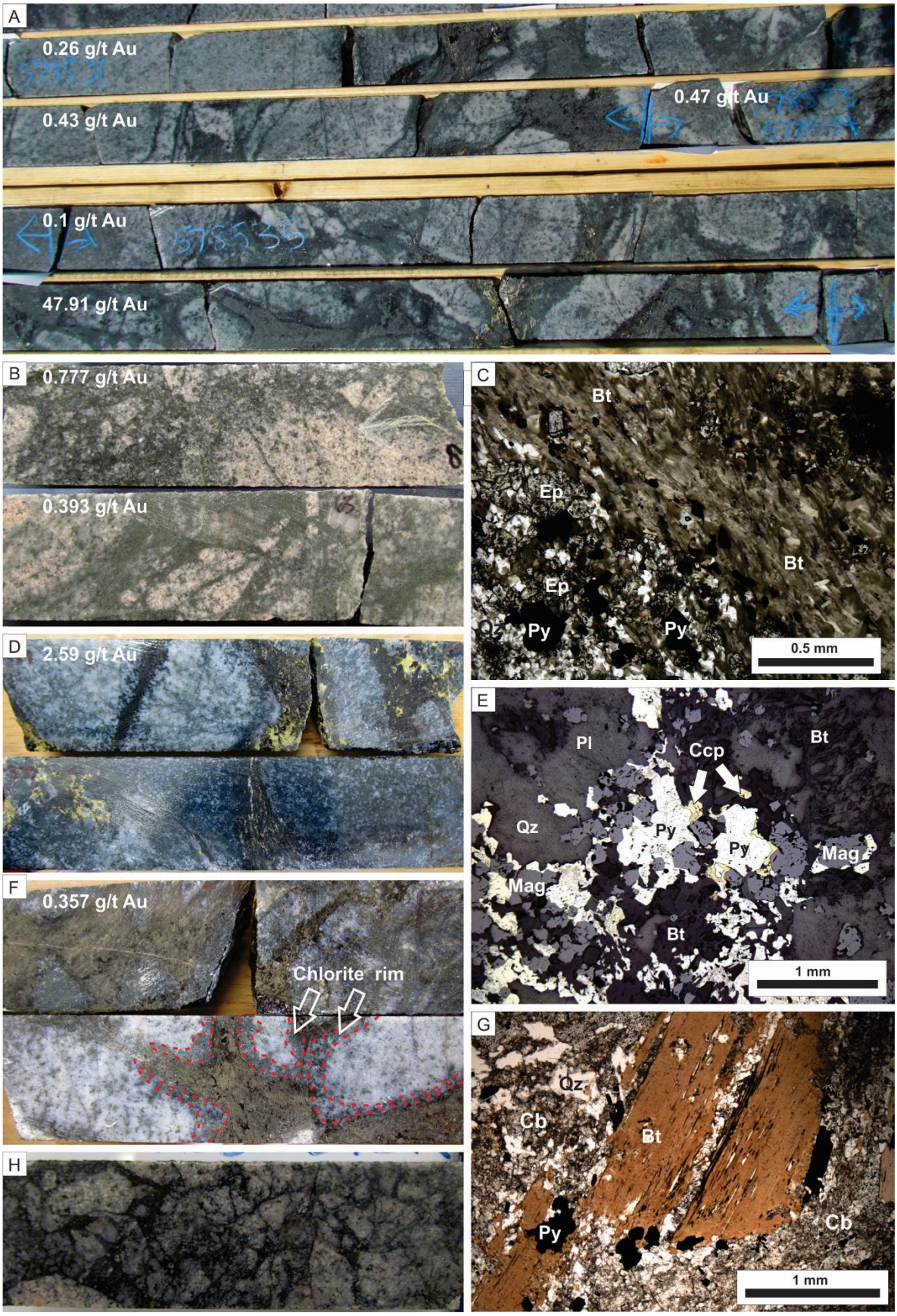
A
0.26 g/t Au
0.43 g/t Au
0.47 g/t Au
0.1 g/t Au
47.91 g/t Au
B
0.777 g/t Au
0.393 g/t Au
C
Bt
Ep
Ep
Bt
Py
Py
0.5 mm
D
2.59 g/t Au
E
Pl
Ccp
Bt
Qz
Py
Py
Mag
Mag
Bt
1 mm
F
0.357 g/t Au
Chlorite rim
G
Qz
Cb
Bt
Py
Cb
1 mm
H

Figure 2.11. Drill core (4.5 cm in width) and thin section photographs of the hydrothermal biotite breccia. A) Hydrothermal biotite breccia with gold mineralization disseminated in the matrix. B) An example of mineralized hydrothermal biotite breccia assemblage 1 with a biotite-quartz-carbonate-epidote-pyrite matrix. Note the green colour of the matrix is due to partial chloritization of the biotite. C) Thin section photo in plane polarized light of assemblage 1 with a biotite-quartz-epidote-pyrite assemblage. D) Mineralized breccia which is characterized by coarse-grained, black biotite and contains a biotite-quartz-magnetite-chalcopyrite-pyrite matrix (assemblage 2). E) Thin section photo in reflected light of assemblage 2 showing abundant magnetite, pyrite and chalcopyrite in the matrix. F) Mineralized breccia which is characterized by coarse-grained brown biotite and contains a biotite-quartz-carbonate-pyrite assemblage (assemblage 3). G) Thin section photo in plane polarized light of a biotite-quartz-carbonate-pyrite breccia matrix (assemblage 3) with coarse-grained orange-brown biotite set in finer-grained quartz, carbonate and sulphides. H) An example of in-situ brecciation in the hydrothermal biotite breccia. Abbreviations: Biotite = Bt, Carbonate = Cb, Chalcopyrite = Ccp, Epidote, = Ep, Magnetite = Mag, Plagioclase = Pl, Pyrite = Py, Quartz = Qz.

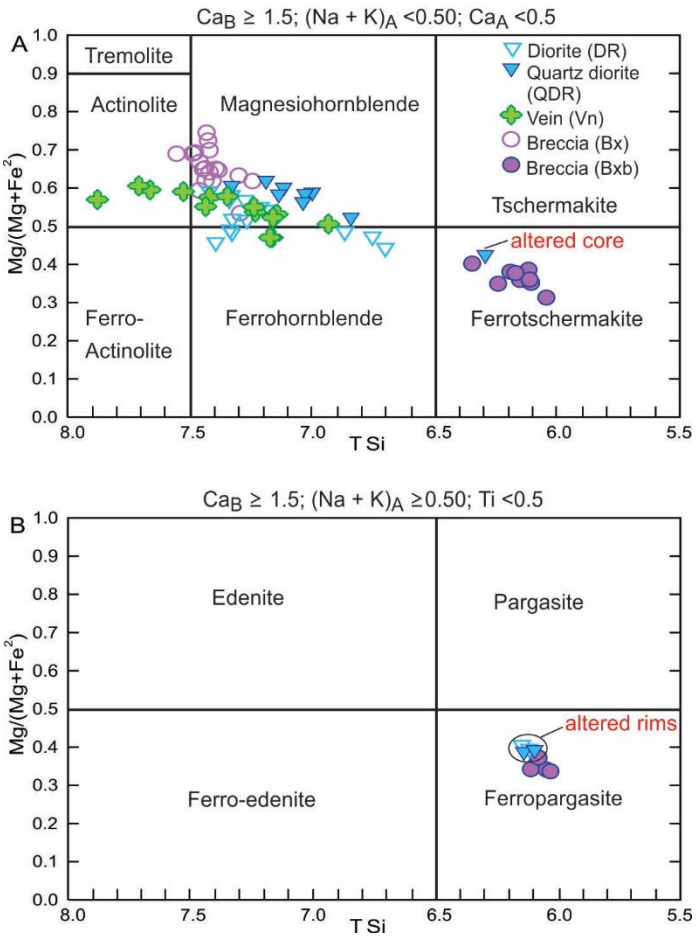

Figure 2.12. Amphibole classification diagrams for calcic amphiboles. Classification of amphiboles is after Hawthorne and Oberti (2007).

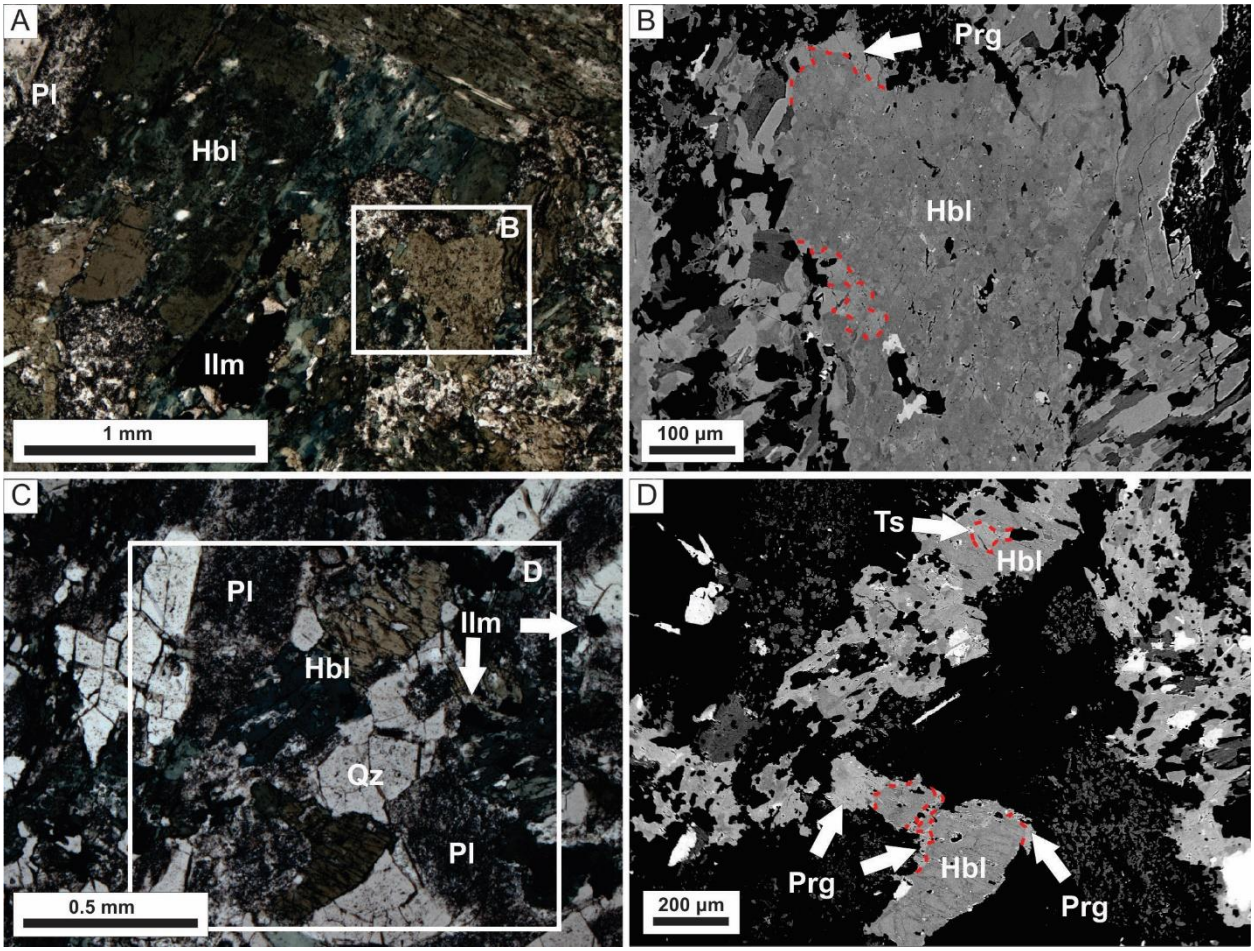

Figure 2.13. Thin section photographs and backscatter electron (BSE) images of amphiboles used for mineral chemistry. A) A brown to green-blue amphibole in diorite. B) A BSE image of amphibole in A with a mottled texture. The red dashed line indicates a secondary overgrowth of pargasite over hornblende. C) A light-tan to green-blue amphibole in quartz diorite. D) A BSE image of amphibole in C that has a mottled texture. The red dashed line shows that medium-grey coloured hornblende is overprinted by light-grey coloured pargasite and tschermakite along rims and in cores. Abbreviations: Hornblende = Hbl, Ilmenite = Ilm, Pargasite = Prg, Plagioclase = Pl, Quartz = Qz, Tschermakite = Ts.

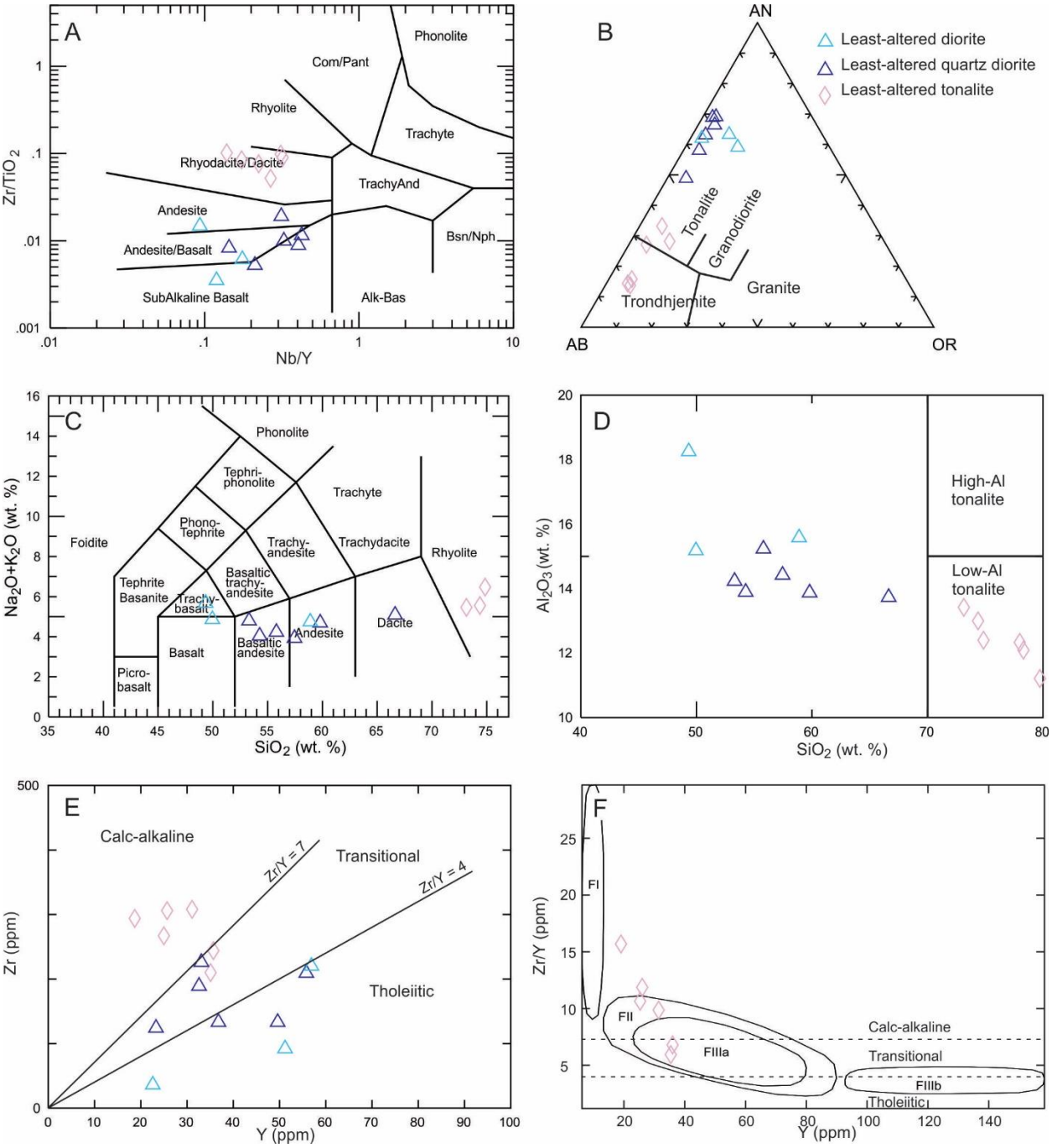

Figure 2.14. Whole-rock geochemistry of least-altered tonalite (n = 6) and dioritic phases (n = 9) of the Chester intrusive complex. A) A Zr/TiO_2 vs. Nb/Y plot (Winchester and Floyd, 1977) of least-altered samples. B) Normative feldspar differentiation diagram plotting tonalite and dioritic phases from Barker (1979) modified after O'Connor (1965). C) Total alkalis vs. silica diagram (Le Bas et al., 1986) of tonalite and dioritic rocks. D) An Al_2O_3 vs. SiO_2 plot showing tonalite is low-Al based on Barker (1979). E) Samples of tonalite and diorite plotted in the Zr vs. Y diagram; the fields for different magma associations from Galley and Lafrance (2014). F) A Zr/Y vs.Y plot which shows the FII or FIIa affinity of tonalite from Lentz (1998) modified after Lesher et al. (1986).

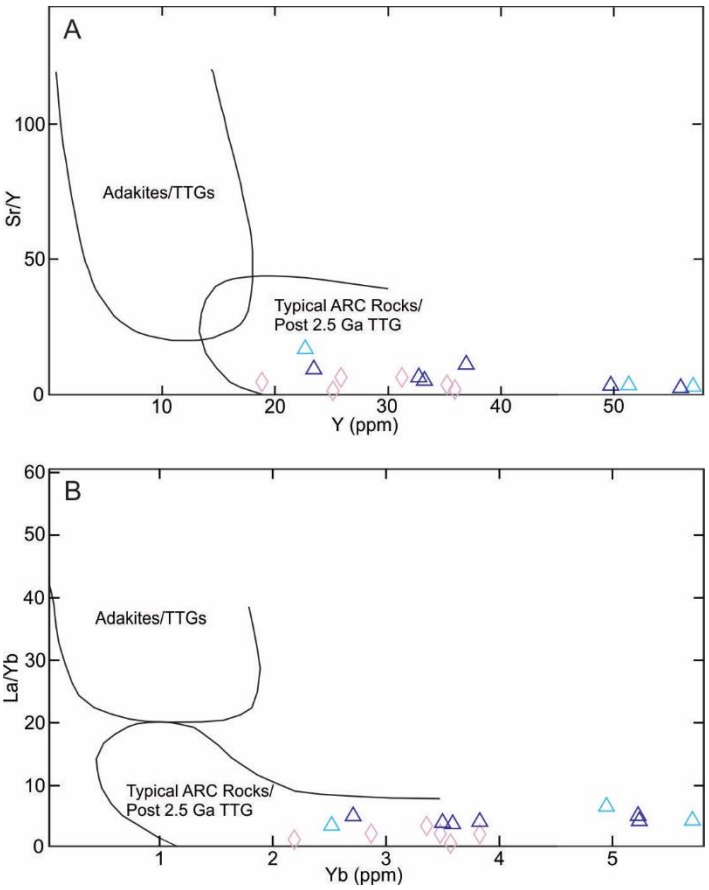

Figure 2.15. Discrimination diagrams between arc-like rocks and adakites/TTG rocks. A) A Sr/Y vs. Y diagram which shows the distribution of least-altered tonalite and diorite phases in comparison to the fields for adakites/high-Al TTGs and normal island-arc andesite-dacite-rhyolite suites from Defant and Drummond (1993) and Richards and Kerrich (2007). B) A La/Yb vs. Yb diagram which show the distribution of least-altered tonalite and diorite phases in comparison with adakites/high-Al TTGs fields and typical arc rocks from Castillo et al. (1999) and Richards and Kerrich (2007). The same legend is used from Figure 2.14.

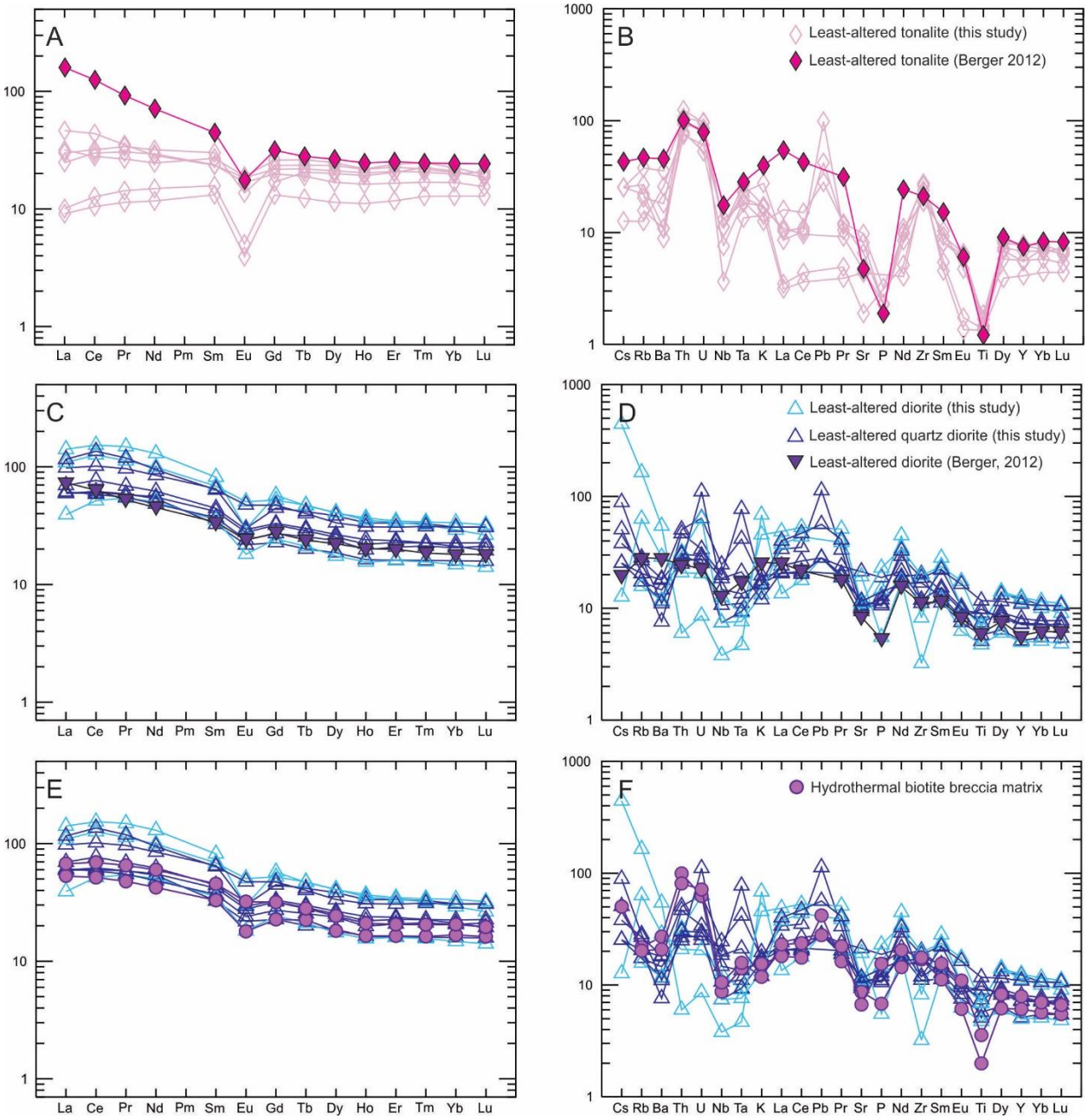

Figure 2.16. Comparison of REE and spider diagrams of least-altered tonalite and dioritic samples from this study against average tonalite (n = 10) and diorite (n = 3) samples from Berger (2012) and the hydrothermal biotite breccia matrix. A) A Chondrite-normalized REE diagram of least-altered tonalite. B) Primitive mantle-normalized spider diagram of least-altered tonalite. C) Chondrite-normalized REE diagram of least-altered diorite and quartz diorite. D) Primitive mantle-normalized spider diagram of least-altered diorite and quartz diorite. E) A chondrite-normalized REE diagram of the hydrothermal biotite breccia matrix plotted against least-altered dioritic phases for comparison. F) Primitive mantle-normalized spider diagram of the hydrothermal biotite breccia matrix plotted against least-altered dioritic phases for comparison. The chondrite normalizing and primitive mantle values are from Sun and McDonough (1989).

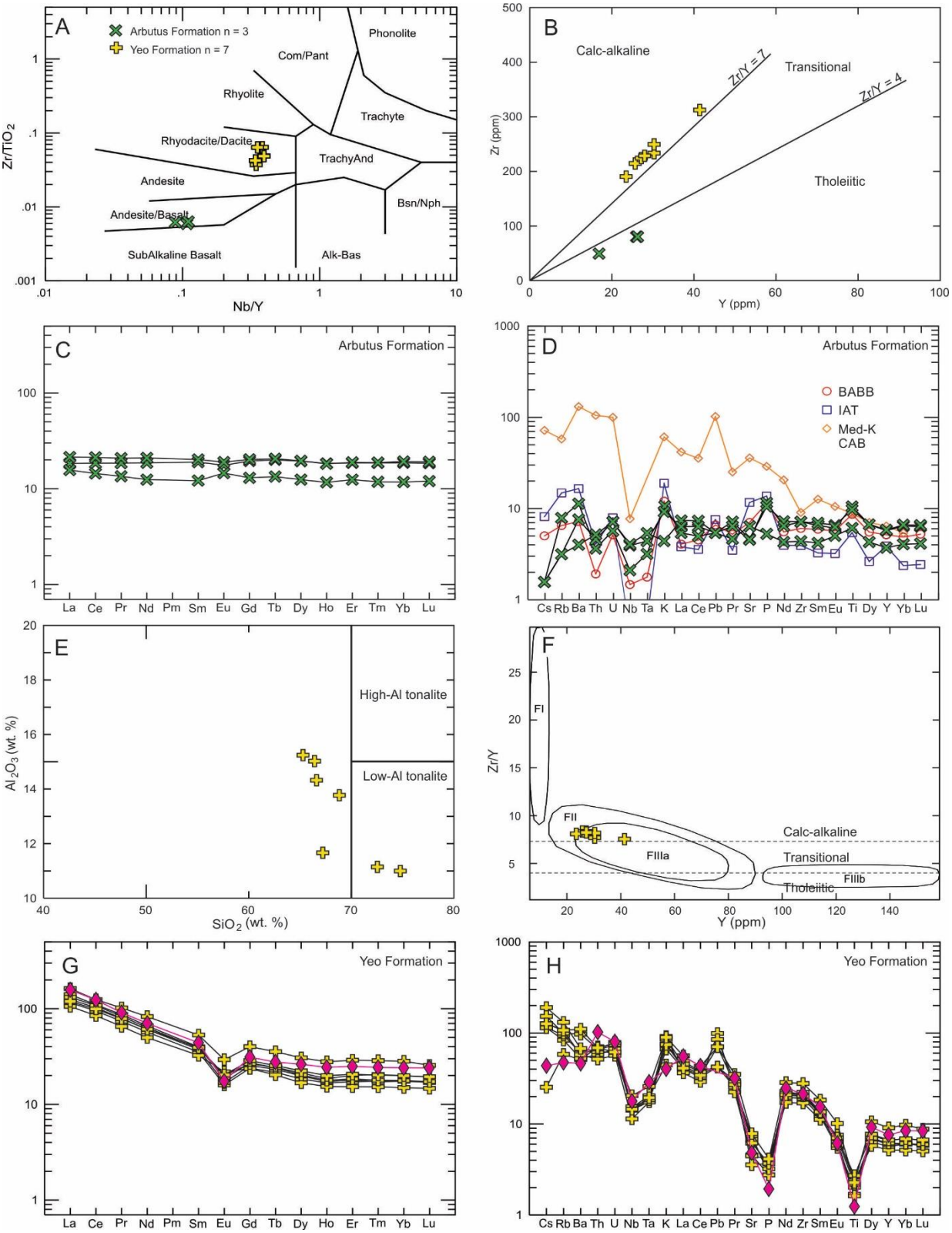

Figure 2.17. Whole-rock geochemistry of metavolcanic rocks of the Arbutus and Yeo Formations. A) A Zr/TiO_2 vs. Nb/Y diagram of Arbutus and Yeo Formation samples. B) A Zr vs. Y diagram of Arbutus and Yeo Formation samples. C) A chondrite-normalized REE diagram of the Arbutus Formation. D) A primitive mantle-normalized

spider diagram of the Arbutus Formation plotted against modern arc basalts for comparison: BABB = back-arc basin basalt (average of sites 834B to 839B in the Lau-Tonga arc and back-arc system (Ewart et al., 1994)); IAT = island-arc tholeiite (average of samples 482-8-11, 482-8-12, 482-8-1, 482-8-8 and 482-8-3 from the Tonga arc (Turner et al., 1997)); and Med-K CAB = medium-K calc-alkaline basalt (average of samples 67150, 67154, B2 and B5 from Flores in the Sunda arc (Stolz et al., 1990)). E) An Al_2O_3 vs. SiO_2 diagram that shows the Yeo Formation samples are not typically low-Al (Barker, 1979). F) A Zr/Y vs. Y diagram that shows an FII or FIIa affinity of Yeo Formation samples from Lentz (1998) modified after Lesher et al. (1986). G) A chondrite-normalized REE diagram of Yeo Formation samples. The average tonalite from Berger (2012) is plotted in pink diamonds in G and H for comparison. H) A primitive mantle-normalized spider diagram of Yeo Formation samples. The CI chondrite and primitive mantle normalizing values are from Sun and McDonough (1989).

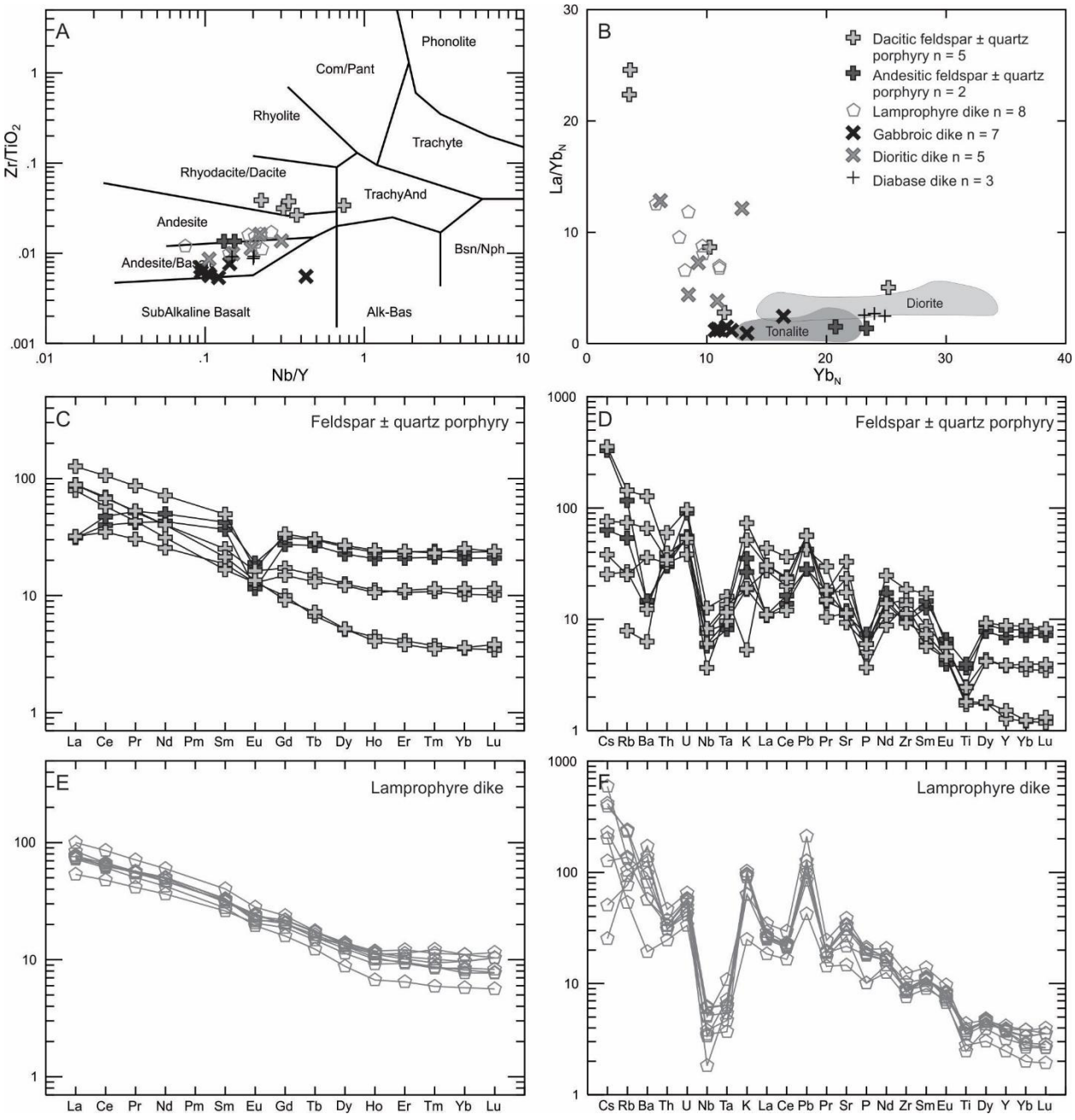
A
Phonolite
Com/Pant
Rhyolite
Trachyte
Rhyodacite/Dacite
TrachyAnd
Andesite
Bsn/Nph
Andesite/Bas
SubAlkaline Basalt
Alk-Bas
Zr/TiO2
Nb/Y
B
Dacitic feldspar ± quartz porphyry n = 5
Andesitic feldspar ± quartz porphyry n = 2
Lamprophyre dike n = 8
Gabbroic dike n = 7
Dioritic dike n = 5
Diabase dike n = 3
Diorite
Tonalite
La/YbN
YbN
C
Feldspar ± quartz porphyry
La Ce Pr Nd Pm Sm Eu Gd Tb Dy Ho Er Tm Yb Lu
D
Feldspar ± quartz porphyry
Cs Rb Ba Th U Nb Ta K La Ce Pb Pr Sr P Nd Zr Sm Eu Ti Dy Y Yb Lu
E
Lamprophyre dike
La Ce Pr Nd Pm Sm Eu Gd Tb Dy Ho Er Tm Yb Lu
F
Lamprophyre dike
Cs Rb Ba Th U Nb Ta K La Ce Pb Pr Sr P Nd Zr Sm Eu Ti Dy Y Yb Lu

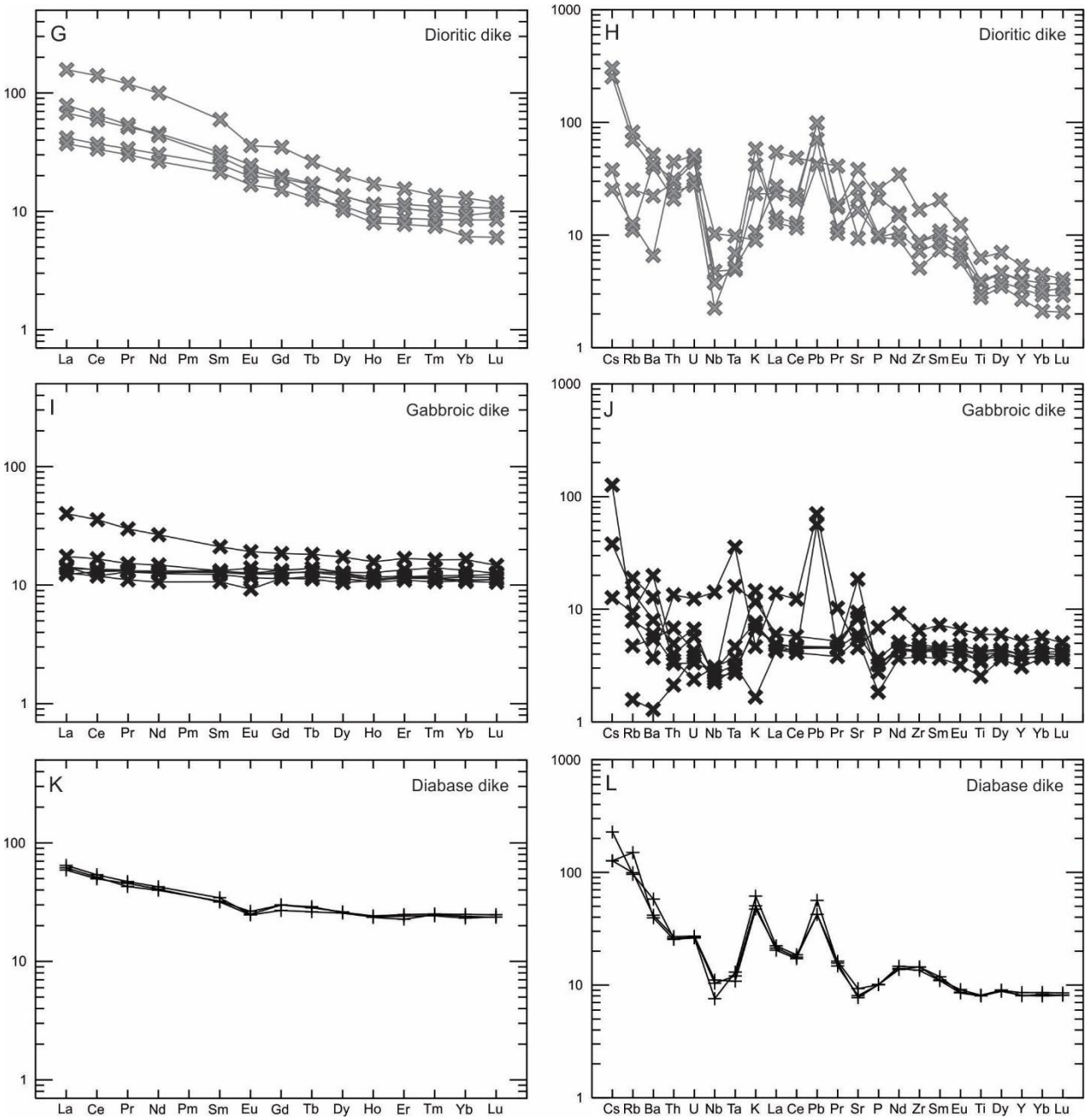

Figure 2.18. Whole-rock geochemistry of least-altered dike rocks types. A) A SiO_2 vs. Nb/Y diagram plotting all of the dike rocks. B) A La/Yb_N vs. Yb_N plot that shows the dike rocks contain a different fractionation trend compared to tonalite and diorite samples of the Chester intrusive complex. C) A chondrite-normalized REE diagram of the feldspar ± quartz porphyries. D) A Primitive mantle-normalized spider diagram of the feldspar ± quartz porphyries. E) A chondrite-normalized REE plot of the lamprophyre dike. F) A primitive mantle-normalized spider diagram of the lamprophyre dike. G) A chondrite-normalized REE diagram of the dioritic dike. H) A primitive mantle-normalized spider diagram of the dioritic dike. I) A chondrite-normalized REE diagram of the gabbroic dike. J) A primitive mantle-normalized spider diagram of the gabbroic dike. K) A chondrite-normalized REE diagram of the diabase dike. L) A primitive mantle-normalized spider diagram of the diabase dike. The chondrite normalizing and primitive mantle values from Sun and McDonough (1989).

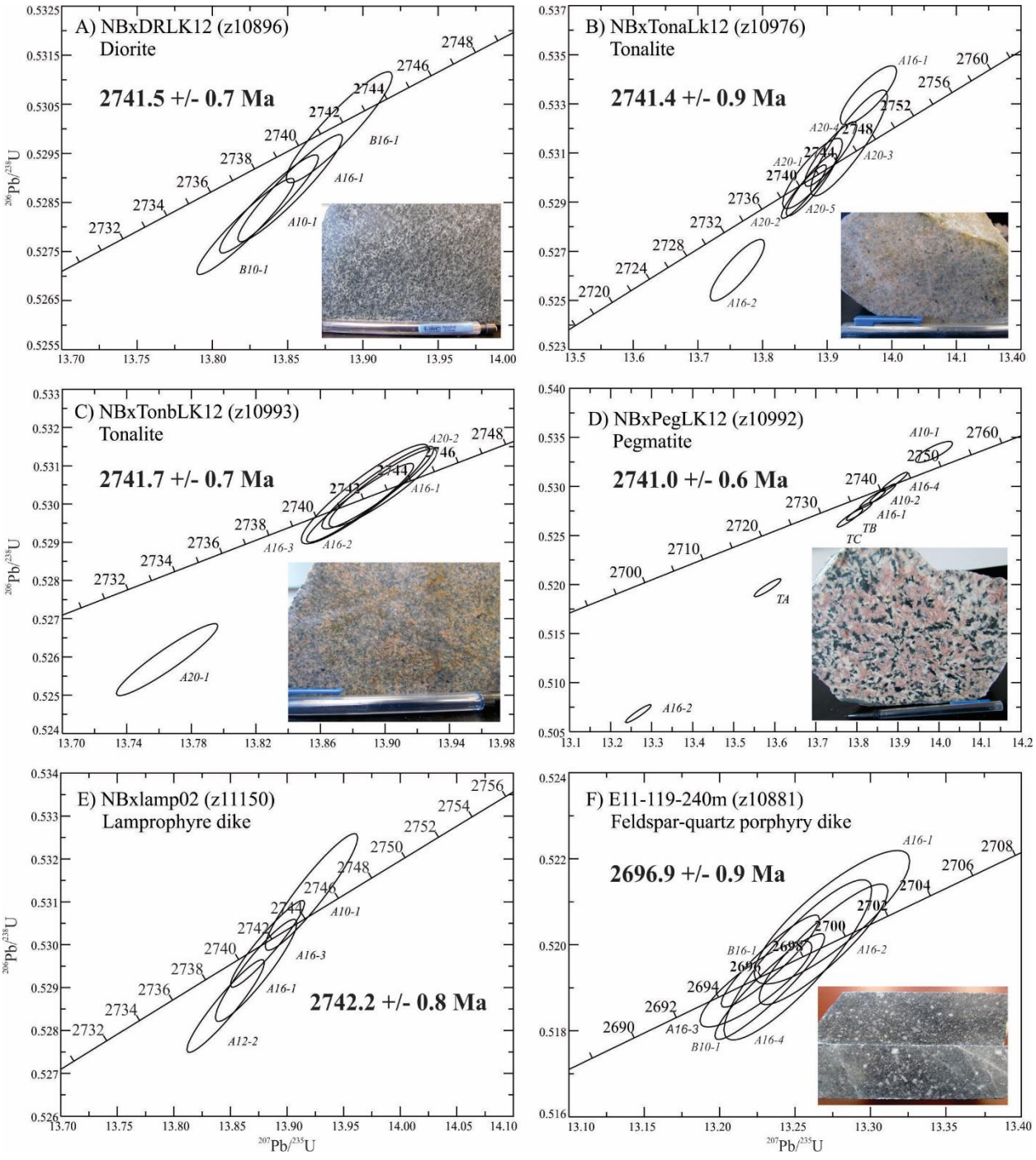
A) NBxDRLK12 (z10896)
Diorite
2741.5 +/- 0.7 Ma
B) NBxTonaLk12 (z10976)
Tonalite
2741.4 +/- 0.9 Ma
C) NBxTonbLK12 (z10993)
Tonalite
2741.7 +/- 0.7 Ma
D) NBxPegLK12 (z10992)
Pegmatite
2741.0 +/- 0.6 Ma
E) NBxlamp02 (z11150)
Lamprophyre dike
2742.2 +/- 0.8 Ma
F) E11-119-240m (z10881)
Feldspar-quartz porphyry dike
2696.9 +/- 0.9 Ma
206Pb/238U
207Pb/235U

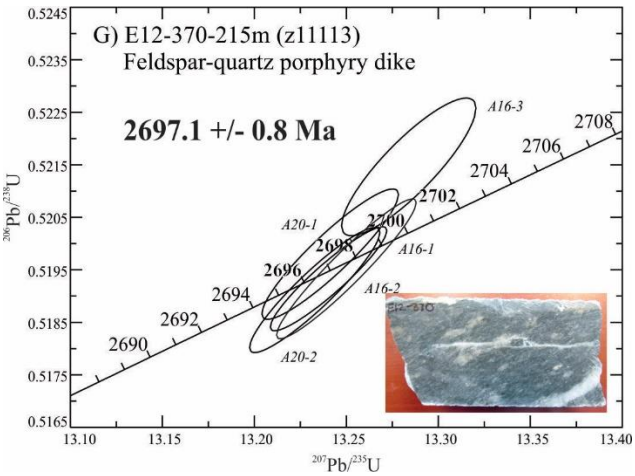

Figure 2.19. Concordia diagrams of U-Pb geochronology samples.

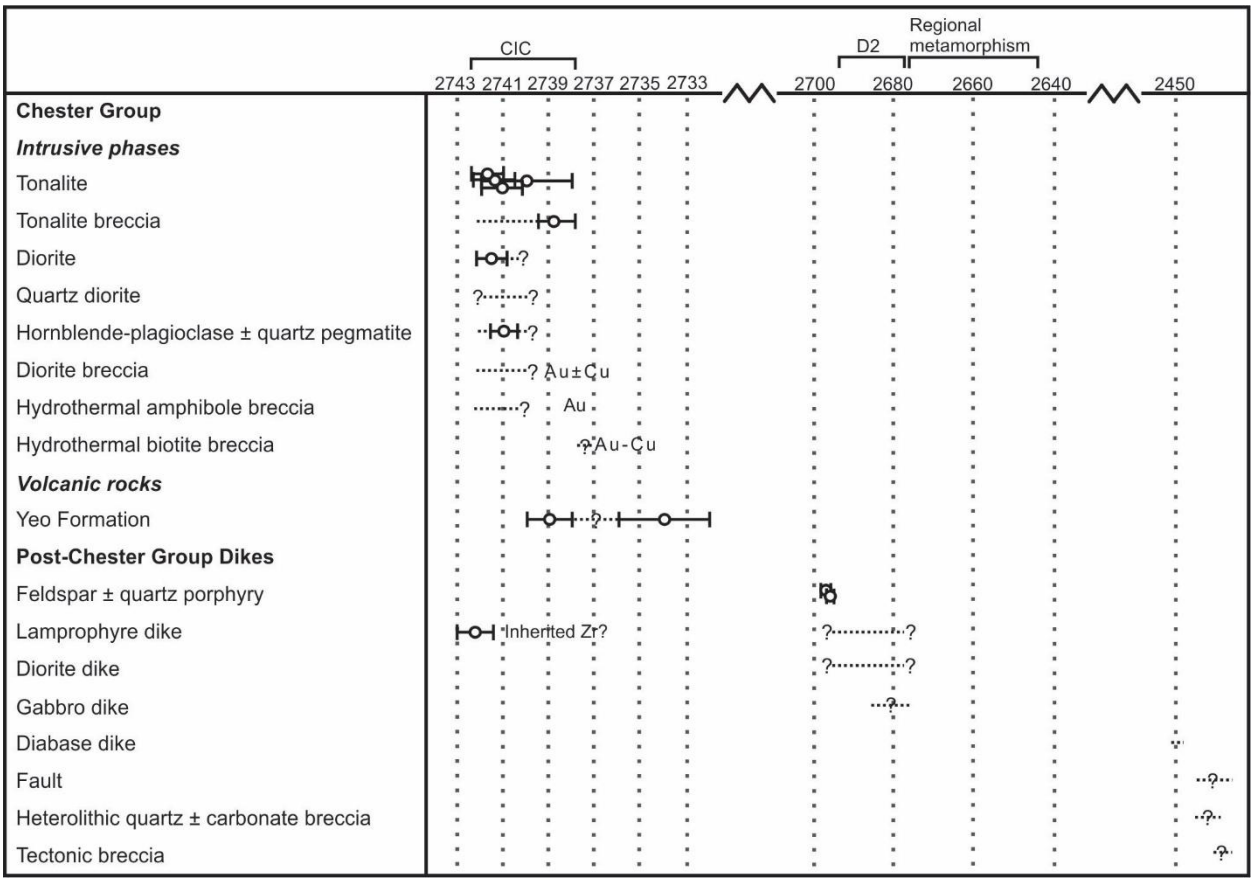

Figure 2.20. Paragenesis of the host rocks of the Chester intrusive complex (CIC), Yeo Formation and post-CIC dikes.

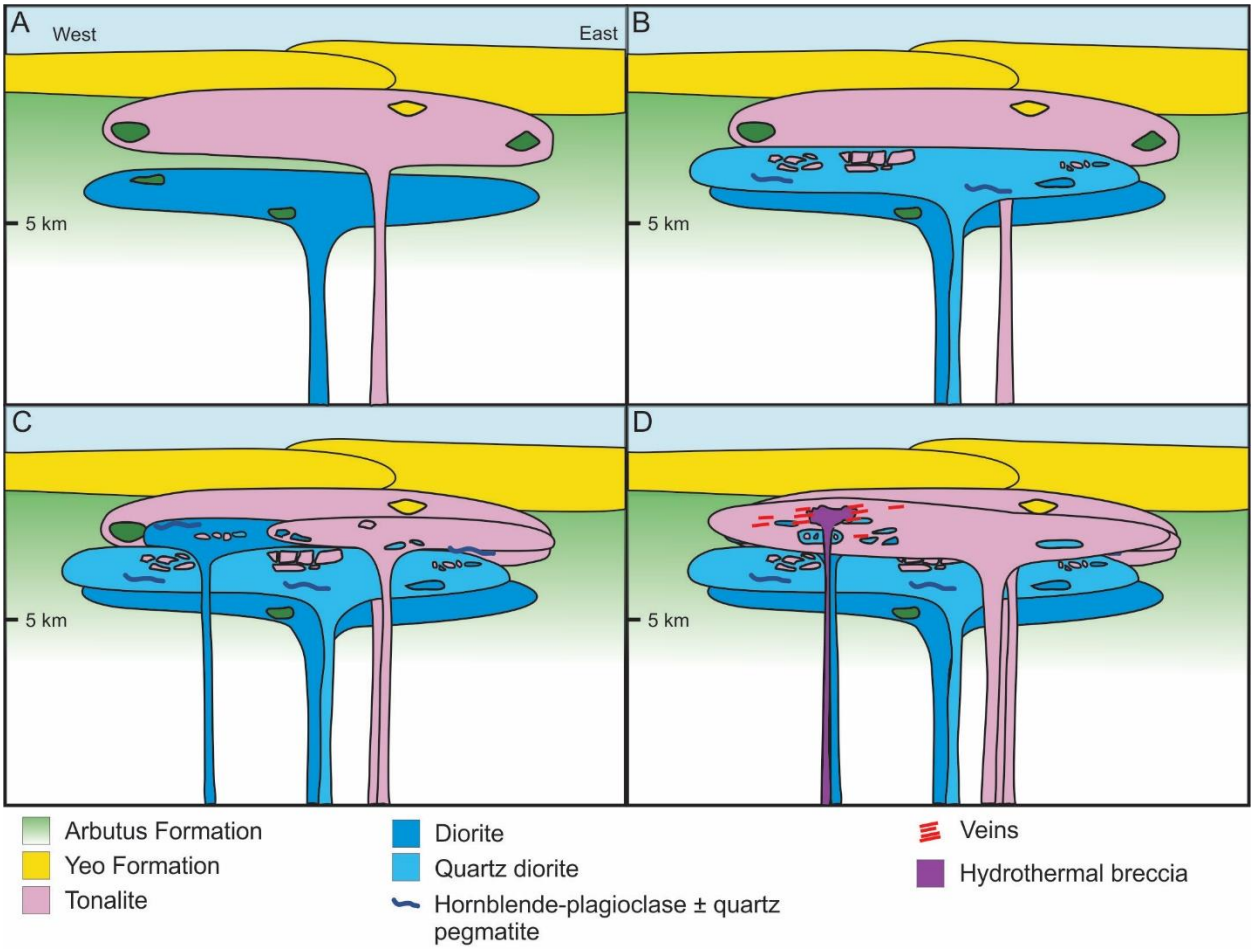

Figure 2.21. Schematic model of the Chester intrusive complex. Each intrusion depicted in the diagram represents multi-phase intrusions.

Table 2.1. Petrographic characteristics, crosscutting relationships and U-Pb geochronology of major rock types at the Côté Gold deposit

Rock Type	Texture	Mineralogy	Crosscutting relationships	Age
Tonalite phases	Few cm to >100 m in apparent width intrusions; fine- to medium-grained, massive, equigranular, with rare quartz and plagioclase phenocrysts; granophyric texture and mariolitic cavities (≤1 cm, spherical-shaped, lined by Pl and filled by Qz ± Cb); majority of tonalite postdates diorite	Pl (50-60%) and Qz (40-50%) with accessory titanite, zircon, apatite, rutile, ilmenite, tourmaline, monazite and xenotime	Early tonalite intruded by all dioritic phases; later tonalite intrudes diorite, quartz diorite and rarely tonalite	2740 ± 2 (Heather and van Breemen, 1994) and 2741.1 ± 0.9 Ma (Kontak et al., 2013); 2741.7 ± 0.7 Ma and 2741.4 ± 0.9 Ma (this study)
Tonalite breccia	Typically restricted to intrusive margins; two types of cm- to m-sized fragments occur: (1) angular to rounded fragments of medium-grained, homogeneous diorite with sharp to diffuse contacts; or (2) rare medium-grained or chilled diorite fragments with lobate contacts; rare angular cm-sized tonalite fragments occur	Fine- to medium-grained, rare quartz and/or plagioclase porphyritic tonalite matrix; mineralogically same as tonalite described above	Brecciates diorite and quartz diorite; rarely brecciates tonalite	2738.7 ± 0.8 Ma (Kontak et al., 2013)
Diorite	Few m to <150 m in apparent width intrusions; appears to dominate in the south of the deposit; medium- to coarse-grained, massive to rarely foliated, equigranular to inequigranular; rare layering, rare granophyric texture	Pl (35-70%), Hbl (35-60%), Qz (0-5%), Ttn (<4%), Ilm and Mag (<2%) with accessory apatite, zircon and rare tourmaline	Co-temporal to quartz diorite and cut by pegmatite; chilled margins against tonalite	2741.5 ± 0.7 Ma (this study)
Quartz diorite	Few m to <150 m in apparent width intrusions; appears to dominate in the north part of the deposit; medium- to coarse-grained, massive, equigranular to inequigranular and often contains quartz and/or plagioclase phenocrysts; granophyric texture	Pl (55-60%), Hbl (30-35%), Qz (5-15%), Ttn (<3%), Ilm and Mag (<2%) with accessory apatite, zircon and rare tourmaline	Co-temporal with diorite and cut by pegmatite	No dates
Hornblende-plagioclase ± quartz pegmatite	Typically <1 m dikes; very coarse-grained, (>2 mm to ≤2.5 cm); spatially associated with diorite and quartz diorite phases; massive, inequigranular; granophyric texture, rare acicular hornblende	Pl(60-65%), Hbl (20-30%), Qz (0-10%), Ttn (<5%), Ilm and Mag (<2%) with accesorry apatite and zircon	Cuts tonalite, diorite and quartz diorite	2741.0 ± 0.6 Ma (this study)
Diorite breccia (Au ± Cu)	Few cm to >100 m in apparent width intrusions; occurs in the southern and central parts of the deposit; rounded to angular tonalite fragments (<1 mm to rarely > 1 m) and diorite, quartz diorite and pegmatite fragments (<50 cm) with sharp contacts; rare exfoliation textures and tabular tonalite fragments	Diorite, quartz diorite; same as the dioritic phases above in terms of mineralogy	Brecciates tonalite, tonalite breccia and all dioritic phases	No dates
Hydrothermal amphibole breccia (Au)	Spatially restricted to southern and central parts of the deposit; fine- to coarse-grained matrix; rounded to angular tonalite and rare diorite fragments (cm-sized); primary zoned amphibole; mariolitic cavities	Hbl (55-95%), Qz (5-45%), Bt (0-7%), Cb (0-3%), Py (<1%) and Ccp (<1%)	Brecciates tonalite and rarely diorite; overprints magmatic breccia	No dates
Hydrothermal biotite breccia (Au ± Cu)	Few cm sized to <200 m in apparent width; occurs in central and northern parts of the deposit; fine- to coarse-grained matrix; angular to sub-rounded tonalite fragments (cm-sized); chlorite rims, in situ, (i.e., mosaic) textures, rare miarolitic cavities (<5 cm)	*Assemblage 1:* Bt-Qz ± Ep ± Cal ± Py ± Ccp ± Mag ± Aln ± Ttn ± Fl *Assemblage 2:* Bt-Mag-Qz-Ank-Ccp-Py ± Sp ± Aln ± Bst ± Ap ± Ttn *Assemblage 3:* Bt-Ank-Cal-Qz-Py ± Aln ± Ap ± Mag ± Ccp ± Po	Brecciates tonalite; *assemblage 3* rarely contains fragments of *assemblage 2*	No dates

Note: Mineral content is estimated from the least-altered samples

Abbreviations: Aln = allanite, Ank = Ankerite, Ap = Apatite, Bst = Bastnaesite, Bt = biotite, Calcite = Cal, Cb = carbonate, Ccp = chalcopyrite, Ep = epidote, Fl = Fluorite, Hbl = hornblende, Ilm = ilmenite, Mag = magnetite, Pl = plagioclase, Po = Pyrrhotite, Py = pyrite, Qz = quartz, Sp = Sphalerite, Ttn = titanite

Table 2.2. Petrographic characteristics and crosscutting relationships of dike rocks at the Côté Gold deposit

Rock type	Subtype	Textures, deformation, relative timing and comments	Mineralogy
Feldspar ± quartz porphyries	Andesitic to dacitic	Fine- to medium-grained, light-grey to dark-grey, foliated and 10 cm to <30 m in apparent width; moderately to strongly epidote, hematite altered and rarely muscovite altered; cut by lamprophyre dikes and represent feeder dikes to the overlying volcanic rocks of the SGB	*Phenocrysts:* < 1 cm Pl (5-20%), <3 mm Qz (1%) *Groundmass:* Variable proportions of Pl, Qz, Ttn, Mag, Py
Lamprophyre dike (or kersantite; Le Maitre et al., 2002)	Biotite-phyric	Fine- to medium-grained black, glomeroporphyritic, dark green or dark-red, foliated and <1 to rarely >50 m in apparent width; N-NW striking; unaltered dike intrudes altered phases of the CIC; the unit can be silicified and/or muscovite altered and cut by epidote veins; typically unmineralized, however, one sample contained VG	*Phenocrysts:* Bt (≤7%) *Groundmass:* Pl (40-70%), Bt (30-40%), Cal (0-10%), Ep (0-5%), Mag (<1%), Py (0-3%)
	Amphibole ± biotite phyric	Fine to medium-grained black, dark-green or dark-red, foliated and <1 m in apparent width; strikes N-NW; unit is characterized by coarse-grained (<2 cm) phenocysts and contains rare myrmekitic texture; the dike can be silicified and/or muscovite altered	*Phenocrysts:* Amp (15%), Bt (0-5%) *Groundmass:* Pl (40-60%), Amp (30-35%), Bt (1-30%), Cal (0-5%), Ep (0-3%), Mag (<1%), Py (<1%)
Dioritic dike		Fine- to medium-grained, typically plagioclase porphyritic, black to dark-grey, massive, and 0.1 to rarely 100 m in apparent width; saussuritization of plagioclase is common; this unit contains chill margins against diorite of CIC	Pl (45-60%), Amp (40-45%), Qz (0-3%), Mag (<1%), Py (<1%)
Gabbroic dike		Fine- to medium-grained, black to dark-green/grey, massive and 0.1 to rarely 100 m in apparent width; saussuritization of plagioclase is common; the unit contains chill margins against the diorite of CIC	Amp (60-90%), Pl (5-40%), Qz (0-3%), Mag (<1%), Py (<1%)
Diabase dike		Aphanitic, often plagioclase glomeroporphyritic (<2 cm) fine-grained or medium-grained, black, massive and magnetic; <0.1 m to 100 m in apparent width; N-NW striking and is offset by the brittle fault; rarely epidote altered and localized brecciation by epidote-quartz veins	*Phenocrysts:* Plagioclase (0-5%) *Groundmass:* Pl (60-70%), Cpx (30-40%), Mag (5%), Ilm (<1%), Py (<1%)
Tectonic breccia		Fine-grained with an incoherent, black to dark-brown matrix and angular to sub-rounded fragments (<10 cm); typically <10 m in apparent width; spatially associated with the west striking brittle fault; the unit postdates muscovite alteration	*Matrix:* rock flour (chloritized and unmineralized) *Fragments:* altered tonalite, altered diorite, veins, xenoliths
Heterolithic quartz ± carbonate breccia		Fine-grained with a light-green to grey matrix and angular to sub-rounded fragments (<1 mm to <5 cm); typically <15 m in apparent width; the unit is characterized by quartz-carbonate flooding that contains Ccp; spatially associated with brittle fault; the unit postdates gold mineralization as VG was found in a quartz vein fragment	*Matrix:* Cal and Qz with up to 4% Ccp *Fragments:* altered tonalite, veins, mafic dikes

Note: Mineral content is estimated from the least-altered samples. Thickness of dike rocks are apparent thickness

Abbreviations: Amp = amphibole, Bt = biotite, Cal = calcite, Ccp = chalcopyrite, Chl = chlorite, Cpx = clinopyroxene, Ep = epidote, Ilm = ilmenite, Mag = magnetite, Pl = plagioclase, Py = pyrite, Qz = quartz, Ttn = titanite

Table 2.3. Microprobe analyses of calcic amphiboles

Sample number	QDR1-3	QDR2-2	QDR3-1
SiO_2	48.59	46.83	47.01
TiO_2	0.97	1.48	1.46
Al_2O_3	4.86	6.19	6.04
FeO	18.97	19.36	19.70
Cr_2O_3	0.02	0.00	0.01
MnO	0.34	0.35	0.34
MgO	11.88	10.92	10.80
CaO	10.48	10.41	10.20
Na_2O	0.75	0.94	0.91
K_2O	0.56	0.40	0.37
F	0.32	0.17	0.17
Cl	0.37	0.23	0.25
Subtotal	98.10	97.29	97.24
O = Cl, F	0.22	0.13	0.13
Total	97.88	97.16	97.11
Cations calculated on the basis of 23 (O, F, Cl) p.f.u. and the average ferric iron constraint (values obtained from the average 15eNK and 13 eCNK)			
Si p.f.u.	7.19	7.00	7.03
Al	0.78	1.00	0.96
Fe^{3+}	0.03	0	0.01
Ti	0	0	0
T sites	8	8	8
Al	0.07	0.09	0.10
Cr	0.00	0	0.00
Fe^{3+}	0.56	0.58	0.59
Ti	0.11	0.17	0.16
Mg	2.62	2.43	2.41
Fe^{2+}	1.62	1.71	1.71
Mn	0.02	0.02	0.02
Ca	0	0	0
C sites	5	5	5
Mg	0	0	0
Fe^{2+}	0.14	0.13	0.15
Mn	0.02	0.02	0.02
Ca	1.66	1.67	1.63
Na	0.11	0.14	0.13
B sites	1.93	1.96	1.94
Ca	0	0	0
Na	0.11	0.14	0.13
K	0.11	0.08	0.07
A sites	0.22	0.22	0.20
cations	15.14	15.17	15.14
Cl	0.09	0.06	0.06
F	0.15	0.08	0.08
Cl/(Cl + F)	0.38	0.42	0.44
Fe^{3+}/Fe^{2+}	0.35	0.34	0.35
Pressure (750 ^oC)	0.28	1.32	1.2
Pressure (800 ^oC)	-	0.36	0.2

Pressures in kbars with an error of ± 0.6 kbars

Table 2.4. Average compositions of least-altered major rocks from the Côté Gold deposit, regional metavolcanics rocks and dike rocks

	Tonalite			Diorite			Hydrothermal breccia matrix			Yeo Formation			Arbutus Formation		
	Avg.	STD	No.	Avg.	STD	No.	Avg.	STD	No.	Avg.	STD	No.	Avg.	STD	No.
SiO_2	76.40	2.39	6	56.16	5.04	9	58.47	4.72	2	68.82	3.28	7	50.41	1.41	3
Al_2O_3	12.41	0.70	6	14.93	1.33	9	12.175	0.825	2	13.17	1.71	7	14.42	0.94	3
FeO	1.1	0.9	6	6.5	1.8	9	5.1	1.7	2	2.8	0.7	7	9.6	0.3	3
FeO_T	1.53	0.95	6	9.42	2.28	9	5.48	1.68	2	4.64	0.88	7	14.05	0.80	3
MnO	0.02	0.01	6	0.14	0.04	9	0.092	0.014	2	0.09	0.98	7	0.21	0.04	3
MgO	0.40	0.25	6	3.69	1.24	9	5.275	2.175	2	1.55	0.59	7	5.37	0.82	3
CaO	1.69	0.65	6	7.75	1.22	9	6.35	0.81	2	2.16	0.70	7	8.47	1.20	3
Na_2O	5.36	0.50	6	3.91	0.40	9	3.35	0.65	2	2.28	0.74	7	2.79	0.55	3
K_2O	0.53	0.14	6	0.75	0.54	9	0.415	0.055	2	2.27	0.46	7	0.20	0.07	3
TiO_2	0.331	0.040	6	1.623	0.473	9	0.612	0.174	2	0.460	0.077	7	1.141	0.249	3
P_2O_5	0.06	0.01	4	0.30	0.11	8	0.245	0.095	2	0.08	0.01	7	0.09	0.03	3
LOI	1.01	0.16	6	1.69	0.37	9	6.98	0.23	2	4.44	1.21	7	3.55	2.59	3
Total	99.7	0.5	6	100.3	0.3	9	100.1	0.9	2	99.9	0.7	7	100.7	0.4	3
Total S	0.09	0.06	6	0.10	0.12	8	0.41	0.17	2	0.07	0.09	4	0.16	0.03	3
CO_2	0.39	0.22	6	0.42	0.21	9	4.00	0.74	2	2.52	1.20	7	1.79	2.25	3
Cs	0.2	0.0	4	0.8	1.1	7	0.4	0	2	1.0	0.4	7	< 0.1	0	3
Rb	14	5	6	26	29	9	14	1	2	62	13	7	3	1	3
Ba	128	67	6	137	95	9	169	22	2	494	151	7	53	21	3
Th	8.11	1.44	6	2.53	1.06	9	7.72	0.79	2	5.37	0.52	7	0.38	0.05	3
U	1.65	0.35	6	0.89	0.62	9	1.42	0.10	2	1.42	0.17	7	0.14	0.01	3
Nb	6.9	2.3	6	9.5	4.5	9	7.0	0.7	2	10.8	1.8	7	2.4	0.6	3
Ta	0.82	0.17	6	0.88	0.90	9	0.615	0.035	2	0.80	0.11	7	0.18	0.04	3
Pb	4	2	3	3	2	6	3	1	2	5	1	7	<2	0	3
Sr	124	55	6	271	86	9	164	21	2	123	32	7	110	18	3
Zr	272	36	6	151	61	9	196	4	2	236	35	7	70	15	3
Y	28.6	6.0	6	40.2	12.7	9	32.3	4.2	2	29.5	5.4	7	23.1	4.4	3
La	6.00	3.06	6	19.82	7.50	9	14.30	1.70	2	30.45	4.08	7	4.37	0.55	3
Ce	15.98	7.01	6	56.18	22.24	9	36.95	5.45	2	63.22	7.12	7	11.04	1.7	3
Pr	2.41	0.88	6	8.15	3.09	9	5.37	0.83	2	7.72	1.00	7	1.67	0.29	3
Nd	10.97	3.53	6	35.20	12.45	9	23.90	4.10	2	29.38	4.37	7	8.1	1.68	3
Sm	3.40	0.91	6	7.99	2.55	9	6.00	0.96	2	6.03	0.92	7	2.61	0.54	3
Eu	0.74	0.36	6	1.80	0.60	9	1.45	0.41	2	1.18	0.23	7	0.98	0.1	3
Gd	4.15	0.87	6	7.78	2.47	9	5.60	0.94	2	5.73	1.07	7	3.61	0.66	3
Tb	0.77	0.16	6	1.25	0.38	9	0.95	0.11	2	0.93	0.17	7	0.67	0.12	3
Dy	4.98	1.13	6	7.48	2.19	9	5.39	0.78	2	5.43	1.05	7	4.35	0.84	3
Ho	1.04	0.21	6	1.47	0.44	9	1.06	0.13	2	1.08	0.21	7	0.91	0.17	3
Er	3.20	0.68	6	4.25	1.17	9	3.06	0.34	2	3.28	0.67	7	2.75	0.49	3
Tm	0.51	0.10	6	0.65	0.17	9	0.47	0.05	2	0.5	0.1	7	0.41	0.08	3
Yb	3.21	0.54	6	4.13	1.11	9	3.17	0.33	2	3.29	0.67	7	2.81	0.57	3
Lu	0.449	0.069	6	0.601	0.160	9	0.455	0.043	2	0.473	0.082	7	0.42	0.082	3

Table 2.4. Continued

	Dacitic Porphyry			Andesitic Porphyry			Lamprophyre Dike			Dioritic Dike			Gabbroic Dike			Diabase Dike		
	Avg.	STD	No.	Avg.	STD	No.	Avg.	STD	No.	Avg.	STD	No.	Avg.	STD	No.	Avg.	STD	No.
SiO_2	67.11	2.3	5	55.94	1.35	2	53.53	2.36	8	52.11	2.92	5	48.37	1.87	7	49.62	0.95	3
Al_2O_3	15.26	0.76	5	15.18	0.29	2	11.98	1.54	8	12.84	2.15	5	13.99	1.27	7	12.88	0.25	3
FeO	2.9	1.0	5	5.50	0.7	2	5.8	0.9	8	6.26	1.08	5	8.2	1.0	7	10.5	0.4	3
Fe_2O_3	4.14	1.25	5	8.15	0.16	2	8.77	1.32	8	9.45	1.15	5	12.63	0.96	7	16.78	0.12	3
MnO	0.04	0.008	5	0.09	0.008	2	0.15	0.02	8	0.14	0.05	5	0.17	0.03	7	0.26	0.03	3
MgO	1.61	0.5	5	4.61	0.18	2	7.99	1.48	8	7.98	1.76	5	8.35	2.28	7	4.89	0.12	3
CaO	4.33	0.93	5	8.28	0.99	2	8.65	1.09	8	8.15	3.27	5	8.46	2.42	7	7.39	0.18	3
Na_2O	4.65	0.78	5	2.77	0.08	2	2.76	0.44	8	3.35	1.14	5	1.82	1.14	7	2.52	0.15	3
K_2O	1	0.75	5	0.93	0.13	2	2.37	0.74	8	0.86	0.57	5	0.23	0.12	7	1.60	0.18	3
TiO_2	0.446	0.071	5	0.823	0.033	2	0.760	0.124	8	0.859	0.269	5	0.861	0.215	7	1.752	0.014	3
P_2O_5	0.11	0.01	5	0.14	0.014	2	0.37	0.09	8	0.33	0.15	5	0.08	0.03	7	0.22	0.00	3
LOI	1.54	0.61	5	3.78	1.8	2	3.10	1.68	8	3.92	1.38	5	5.06	1.88	7	2.18	0.11	3
Total	100.3	0.49	5	100.8	0.25	2	100.4	0.73	8	100.0	0.57	5	100.0	0.67	7	100.1	0.7	3
Total S	0.09	0.12	4	0.02	0	2	0.10	0.05	8	0.14	0.14	5	0.10	0.04	6	0.16	0.01	3
CO_2	0.5	0.39	5	1.39	1.32	2	1.39	1.29	8	1.50	1.19	5	1.45	1.13	7	0.99	0.07	3
Cs	1.0	1.1	4	1.6	1.1	2	2.0	1.5	8	1.2	1.0	4	0.5	0.4	3	1.3	0.4	3
Rb	35	31	5	54	20	2	85	41	8	25	19	5	6	3	7	73	16	3
Ba	345	308	5	101	1	2	656	329	8	227	113	5	57	41	7	324	57	3
Th	3.47	0.85	5	2.58	0.03	2	2.84	0.51	8	2.55	0.70	5	0.46	0.30	7	2.22	0.05	3
U	1.22	0.42	5	1.53	0.37	2	1.06	0.20	8	0.85	0.20	5	0.12	0.07	7	0.56	0.01	3
Nb	5.4	2.1	5	4.9	0.8	2	3.1	1.0	8	3.5	2.0	5	3.0	2.9	7	6.9	1.1	3
Ta	0.51	0.09	5	0.35	0.02	2	0.26	0.08	8	0.26	0.08	5	0.40	0.46	7	0.49	0.04	3
Pb	4	0	5	2	0	2	8	3	8	6	2	4	5	1	2	3	0	3
Sr	397	180	5	242	11	2	607	150	8	472	205	5	182	91	7	176	14	3
Zr	151	36	5	112	5	2	103	15	8	104	44	5	52	9	7	158	5.0	3
Y	17.5	12.3	5	33.9	2.7	2	16.4	2.3	8	17.4	4.0	5	17.9	2.6	7	37.5	1.1	3
La	19.63	7.17	5	7.48	0.09	2	18.16	2.87	8	18.10	10.23	5	4.22	2.18	7	14.63	0.53	3
Ce	41.04	14.03	5	26.70	2.30	2	39.65	5.93	8	41.02	23.57	5	10.16	4.84	7	31.57	1.03	3
Pr	5.02	1.76	5	4.48	0.49	2	5.26	0.73	8	5.47	3.05	5	1.47	0.56	7	4.29	0.17	3
Nd	19.48	7.43	5	21.65	1.65	2	22.34	2.97	8	22.90	12.29	5	6.90	2.31	7	19.17	0.54	3
Sm	4.01	1.83	5	6.04	0.43	2	4.87	0.60	8	5.08	2.08	5	2.10	0.47	7	5.02	0.17	3
Eu	0.84	0.10	5	0.88	0.22	2	1.33	0.15	8	1.37	0.38	5	0.76	0.16	7	1.47	0.04	3
Gd	3.48	1.81	5	6.03	0.43	2	4.20	0.45	8	4.43	1.40	5	2.73	0.46	7	5.94	0.29	3
Tb	0.54	0.32	5	1.06	0.06	2	0.59	0.06	8	0.65	0.18	5	0.51	0.08	7	1.04	0.04	3
Dy	3.14	2.01	5	6.16	0.42	2	3.17	0.40	8	3.48	0.91	5	3.23	0.51	7	6.58	0.07	3
Ho	0.62	0.42	5	1.25	0.08	2	0.58	0.09	8	0.64	0.18	5	0.68	0.09	7	1.35	0.02	3
Er	1.77	1.21	5	3.68	0.23	2	1.63	0.26	8	1.79	0.44	5	2.09	0.31	7	3.95	0.15	3
Tm	0.27	0.18	5	0.58	0.03	2	0.24	0.05	8	0.26	0.05	5	0.32	0.05	7	0.63	0.01	3
Yb	1.84	1.34	5	3.75	0.22	2	1.52	0.28	8	1.62	0.39	5	2.09	0.32	7	4.08	0.12	3
Lu	0.268	0.188	5	0.568	0.037	2	0.229	0.047	8	0.238	0.051	5	0.305	0.032	7	0.610	0.013	3

Note: Major elements, S and CO_2 in wt. % and trace elements in ppm

Table 2.5. U-Pb zircon ID-TIMS analytical data

Fraction[1]	Description[2]	Wt.	U	Pb[3]	$^{206}Pb/^{204}Pb$[4]	Pb[5]	Isotopic Ratios[6]									Ages (Ma)[8]						
							$^{208}Pb/^{206}Pb$	$^{207}Pb/^{235}U$	±1SE Abs	$^{206}Pb/^{238}U$	±1SE Abs	Corr.[7] Coeff.	$^{207}Pb/^{206}Pb$	±1SE Abs	$^{206}Pb/^{238}U$	±2SE	$^{207}Pb/^{235}U$	±2SE	$^{207}Pb/^{206}Pb$	±2SE	% Disc
		ug	ppm	ppm		pg																
(A) North Breccia diorite - NBxDRLK12 (Z10896): UTM NAD83, zone 17, 429713E-5266923N																						
A10-1 (1;Z)	Co,Clr,Tip,Fr,CA10	3.4	56	37	6086	1.0	0.25	13.8376	0.0164	0.5285	0.0005	0.939	0.1899	0.0001	2735.0	4.2	2738.7	2.2	2741.4	1.4	0.3
A16-1 (1;Z)	Co,Clr,Tip,rIn,rFr,CA10	1.7	73	46	4648	0.9	0.19	13.8517	0.0174	0.5288	0.0006	0.944	0.1900	0.0001	2736.3	4.6	2739.6	2.4	2742.0	1.5	0.3
B10-1 (1;Z)	Co,Clr,Eu,St,Fr,CA10	5.0	166	108	8718	3.0	0.24	13.8220	0.0162	0.5280	0.0005	0.946	0.1899	0.0001	2733.1	4.1	2737.6	2.2	2740.9	1.4	0.4
B16-1 (1;Z)	Co,Clr,Eu,Pr,Fr,CA10	1.1	94	62	3702	0.9	0.26	13.8843	0.0176	0.5300	0.0006	0.923	0.1900	0.0001	2741.6	4.7	2741.8	2.4	2742.0	1.6	0.0
(B) North Breccia tonalite - NBxTonaLK12 (Z10976): UTM NAD83, zone 17, 429711E-5269917N																						
A16-1 (2;Z)	Co,Clr,Eu,Pr,Fr,rIn,CA16	1.3	68	42	781	3.8	0.16	13.9639	0.0219	0.5334	0.0006	0.819	0.1899	0.0002	2755.6	5.1	2747.3	3.0	2741.2	3.0	-0.7
A16-2 (1;Z)	Co,Clr,Eu,Pr,Fr,CA16	0.7	106	69	862	2.9	0.26	13.7611	0.0211	0.5262	0.0006	0.848	0.1897	0.0002	2725.6	5.3	2733.4	2.9	2739.2	2.7	0.6
A20-1 (1;Z)	Co,Clr,Eu,Pr,Fr,CA20	1.2	70	44	863	3.3	0.19	13.8773	0.0232	0.5302	0.0007	0.855	0.1898	0.0002	2742.2	6.0	2741.4	3.2	2740.8	2.8	-0.1
A20-2 (2;Z)	Co,Clr,Eu,Pr,Fr,CA20	1.8	122	76	2858	2.5	0.18	13.8639	0.0175	0.5294	0.0005	0.925	0.1899	0.0001	2739.0	4.6	2740.5	2.4	2741.5	1.7	0.1
A20-3 (1;Z)	Co,Clr,Eu,Pr,rFr,In,CA20	1.1	76	48	584	4.8	0.19	13.9339	0.0298	0.5314	0.0011	0.881	0.1902	0.0002	2747.4	9.0	2745.2	4.0	2743.6	3.3	-0.2
A20-4 (1;Z)	Co,Clr,Eu,Pr,Fr,In,CA20	1.0	93	59	1241	2.0	0.20	13.9056	0.0203	0.5310	0.0007	0.885	0.1900	0.0001	2745.5	5.5	2743.3	2.8	2741.7	2.2	-0.2
A20-5 (1;Z)	Co,Clr,Eu,Pr,Fr,In,CA20	1.0	78	49	1514	1.7	0.19	13.8758	0.0196	0.5297	0.0006	0.911	0.1900	0.0001	2740.2	5.4	2741.3	2.7	2742.0	1.9	0.1
(C) North Breccia tonalite - NBxTonbLK12 (Z10993): NAD83, zone 17, 429717E-5266928N																						
A16-1 (1;Z)	Co,Clr,Eu,Pr,Fr,In,CA16	2.7	77	48	2766	2.5	0.18	13.8987	0.0168	0.5304	0.0005	0.913	0.1900	0.0001	2743.2	4.3	2742.8	2.3	2742.5	1.7	0.0
A16-2 (1;Z)	Co,Clr,Eu,Pr,Fr,In,CA16	3.1	91	57	7814	1.2	0.17	13.8846	0.0166	0.5300	0.0005	0.943	0.1900	0.0001	2741.6	4.3	2741.9	2.3	2742.1	1.4	0.0
A16-3 (1;Z)	Co,Clr,Eu,Pr,Fr,In,CA16	1.0	75	45	1635	1.5	0.14	13.8875	0.0197	0.5303	0.0007	0.914	0.1900	0.0001	2742.6	5.5	2742.1	2.7	2741.7	1.9	0.0
A20-1 (1;Z)	Co,Clr,Eu,Pr,Fr,In,CA20	3.9	123	77	6586	2.4	0.18	13.7650	0.0157	0.5259	0.0005	0.936	0.1898	0.0001	2724.3	4.0	2733.7	2.2	2740.6	1.4	0.7
A20-2 (1;Z)	Co,Clr,Eu,St,Fr,CA20	2.0	78	49	2800	1.9	0.18	13.8955	0.0174	0.5304	0.0005	0.927	0.1900	0.0001	2743.3	4.5	2742.6	2.4	2742.1	1.6	-0.1
(D) North Breccia hornblende-plagioclase pegmatite - NBxPegLK12 (Z10992): NAD83, zone 17, 429709E-5266922N																						
A10-1 (1;Z)	pBr,Clr,Eu,Pr,Fr,In,CA10	3.0	115	84	778.2	16.0	0.4	13.9879	0.0227	0.5335	0.0005	0.810	0.1902	0.0002	2756.3	4.5	2748.9	3.1	2743.5	3.3	-0.6
A10-2 (1;Z)	pBr,Clr,Eu,Pr,Fr,In,CA10	5.3	160	118	7323	3.8	0.43	13.8634	0.0160	0.5293	0.0005	0.941	0.1900	0.0001	2738.6	4.0	2740.4	2.2	2741.8	1.4	0.2
A16-1 (1;Z)	pBr,Clr,Eu,Pr,Fr,CA16	4.1	231	170	4307	7.2	0.43	13.8381	0.0160	0.5287	0.0005	0.937	0.1898	0.0001	2736.0	4.0	2738.7	2.2	2740.7	1.5	0.2
A16-2 (1;Z)	pBr,Clr,Eu,Pr,Fr,CA16	3.3	190	134	3231	6.1	0.42	13.2675	0.0158	0.5068	0.0005	0.933	0.1899	0.0001	2643.1	3.9	2698.9	2.2	2740.9	1.6	4.3
A16-4 (1;Z)	Co,Clr,Eu,Pr,Fr,In,CA16	2.0	204	147	8545	1.6	0.38	13.8916	0.0161	0.5305	0.0005	0.940	0.1899	0.0001	2743.5	4.1	2742.3	2.2	2741.5	1.4	-0.1
TA (25;T)	Br,Clr,An,Frag	100.0	103	80	2368	142.0	0.54	13.5825	0.0164	0.5197	0.0005	0.916	0.1896	0.0001	2697.8	3.9	2721.0	2.3	2738.3	1.7	1.8
TB (20;T)	pBr,Clr,An,Frag	60.0	38	29	4123	18.0	0.51	13.8060	0.0159	0.5275	0.0005	0.936	0.1898	0.0001	2730.8	3.9	2736.5	2.2	2740.7	1.5	0.4
TC (20;T)	Br,Clr,An,Frag	60.0	99	82	6184	32.0	0.64	13.7830	0.0158	0.5268	0.0005	0.937	0.1898	0.0001	2727.9	4.0	2734.9	2.2	2740.1	1.5	0.5
E) North Breccia Lamprophyre dike - NBxlamp02 (Z11150): NAD83, zone 17, 429719E-5266932N																						
A10-1 (1;Z)	Co,Clr,Eu,St,fIn,rFr,CA10	1.1	82	52	1903	1.6	0.19	13.9215	0.0204	0.5312	0.0007	0.932	0.1901	0.0001	2746.6	5.7	2744.4	2.8	2742.7	1.8	-0.2
A12-2 (1;Z)	Co,Clr,Eu,Pr,fFr,CA12	1.8	127	77	7556	1.0	0.13	13.8457	0.0171	0.5286	0.0005	0.938	0.1900	0.0001	2735.4	4.6	2739.2	2.3	2742.0	1.5	0.3
A16-1 (1;Z)	Co,Clr,Eu,Pr,CA16	1.2	43	27	6362	0.5	0.16	13.8727	0.0180	0.5294	0.0006	0.925	0.1901	0.0001	2738.9	5.0	2741.1	2.5	2742.6	1.6	0.2
A16-3 (1;Z)	Co,Clr,Eu,Pr,fIn,CA16	4.3	78	50	12355	0.9	0.23	13.8828	0.0164	0.5300	0.0005	0.941	0.1900	0.0001	2741.5	4.3	2741.7	2.2	2741.9	1.4	0.0

Table 2.5. Continued

Fraction[1]	Description[2]	Wt. ug	U ppm	Pb[3] ppm	$^{206}Pb/^{204}Pb$[4]	Pb[5] pg	Isotopic Ratios[6] $^{208}Pb/^{206}Pb$	$^{207}Pb/^{235}U$	±1SE Abs	$^{206}Pb/^{238}U$	±1SE Abs	Corr.[7] Coeff.	$^{207}Pb/^{206}Pb$	±1SE Abs	Ages (Ma)[8] $^{206}Pb/^{238}U$	±2SE	$^{207}Pb/^{235}U$	±2SE	$^{207}Pb/^{206}Pb$	±2SE	% Disc
(F) Brett Lake feldspar-quartz porphyry dike - E11-119-240m (Z10881)																					
A16-1 (1;Z)	Co,Clr,Eu,Pr,Fr,rIn,CA16	1.3	89	53	613	2.3	0.15	13.2745	0.0258	0.5206	0.0008	0.841	0.1849	0.0002	2701.9	6.6	2699.4	3.7	2697.5	3.5	-0.2
A16-2 (1;Z)	Co,Clr,Eu,Pr,Fr,CA16	2.1	54	34	992	13.1	0.23	13.2689	0.0214	0.5200	0.0007	0.893	0.1851	0.0001	2699.2	5.9	2699.0	3.0	2698.8	2.4	0.0
A16-3 (1;Z)	Co,Clr,Eu,Pr,Fr,In,CA16	1.4	221	146	1160	7.6	0.30	13.2241	0.0186	0.5191	0.0005	0.858	0.1848	0.0001	2695.3	4.2	2695.8	2.6	2696.1	2.5	0.0
A16-4 (1;Z)	Co,Clr,Eu,Pr,Fr,CA16	0.6	122	75	750	1.2	0.20	13.2519	0.0245	0.5197	0.0009	0.875	0.1850	0.0002	2697.7	7.9	2697.8	3.5	2697.8	3.0	0.0
B10-1 (1;Z)	Co,Clr,Eu,Pr,rFr,In,CA10	2.0	147	92	2421	0.9	0.22	13.2332	0.0182	0.5190	0.0006	0.932	0.1849	0.0001	2695.1	5.2	2696.4	2.6	2697.4	1.7	0.1
B16-1 (1;Z)	Co,Clr,Eu,Pr,Fr,CA16	0.7	83	51	5396	0.3	0.18	13.2335	0.0163	0.5196	0.0005	0.925	0.1847	0.0001	2697.6	4.5	2696.5	2.3	2695.6	1.6	-0.1
(G) Brett Lake feldspar-quartz porphyry dike - E12-370-215m (Z11113)																					
A16-1 (1;Z)	Co,Clr,Eu,Pr,Fr,In,CA16	0.8	76	44	3069	0.6	0.10	13.2499	0.0190	0.5195	0.0007	0.948	0.1850	0.0001	2697.2	5.6	2697.6	2.7	2697.9	1.5	0.0
A16-2 (1;Z)	Co,Clr,Eu,Pr,In,Fr,CA16	2.1	142	86	3621	2.7	0.18	13.2404	0.0158	0.5193	0.0005	0.929	0.1849	0.0001	2696.4	4.2	2696.9	2.3	2697.4	1.6	0.1
A16-3 (1;Z)	Co,Clr,Eu,Pr,Fr,In,CA16	2.1	63	38	2241	1.9	0.17	13.2839	0.0183	0.5215	0.0007	0.854	0.1848	0.0001	2705.4	5.6	2700.0	2.6	2696.1	2.4	-0.4
A20-1 (1;Z)	Co,Clr,Eu,Pr,Fr,In,CA20	1.6	68	41	1918	1.8	0.16	13.2412	0.0186	0.5198	0.0006	0.916	0.1848	0.0001	2698.3	5.3	2697.0	2.6	2696.0	1.9	-0.1
A20-2 (1;Z)	Co,Clr,Eu Pr,In,Fr,CA20	0.9	91	54	3266	0.8	0.13	13.2325	0.0177	0.5191	0.0006	0.920	0.1849	0.0001	2695.4	5.0	2696.4	2.5	2697.1	1.7	0.1

Notes:

[1]Number in bracket refers to the number of grains in the analysis. Z = zircon; T = titanite; CA = chemically abraded

[2]Fraction descriptions: Co = Colourless, pBr = pale brown, Br = brown, Clr = Clear, Eu = Euhedral, An = Anhedral, Pr = Prismatic, St= Stubby Prism, El = Elongate, Tip = Tip, Frag = Fragment, rFr = Rare Fractures, fFr = Few Fractures, Fr = Fractures, rIn = Rare Inclusions, fIn = Few Inclusions, In = Inclusions, CA10 = Chemically Abraded for 10 hours

[3]Radiogenic Pb

[4]Measured ratio, corrected for spike and fractionation

[5]Total common Pb in analysis corrected for fractionation and spike

[6]Corrected for blank Pb and U and common Pb, errors quoted are 1 sigma absolute; procedural blank values for this study ranged from <0.1- 0.1 pg for U and 0.5-2 pg for Pb; Pb blank isotopic composition is based on the analysis of procedural blanks; corrections for common Pb were made using Stacey and Kramers (1975) compositions

[7]Correlation Coefficient

[8]Corrected for blank and common Pb, errors quoted are 2 sigma in Ma

Chapter 3

3 Mineral Paragenesis, Alteration and Geochronology (U-Pb, Re-Os) of the Archean Porphyry-Type Côté Gold Au(-Cu) Deposit, Swayze Greenstone Belt, Ontario

3.1 Abstract

For the first time a detailed study of the alteration, mineralization and absolute timing constraints that relate to the genesis of the low-grade (~1 g/t), high-tonnage (+8 M oz), intrusion-related Archean Côté Gold Au(-Cu) deposit, located in the Swayze greenstone belt, Ontario, Canada, is presented. Mineralization is centred on magmatic and magmatic-hydrothermal breccia bodies that intrude into the ca. 2741 to 2739 Ma low-Al tonalite and dioritic rocks of the Chester intrusive complex.

The current extent of the mineralization is at least 1200 m with a width of up to 300 m and a depth of greater than 500 m. Within this ore envelope several hydrothermal stages are recognized: (1) a series of rare Au-bearing amphibole-rich veins and breccias that are spatially restricted to the bottom and centre of the deposit; (2) an extensive main-stage biotite alteration that is centred on Au-Cu-bearing hydrothermal biotite breccia bodies with erratically mineralized veins and typically unmineralized disseminations occurring throughout the deposit. Higher gold grades, along with an increased abundance of magnetite (≤40%), during the hydrothermal biotite breccia event is attributed to its formation under higher fO_2 conditions in comparison to the surrounding biotite stockworks and disseminations; (3) biotite alteration is partially overprinted

by extensive fracture-controlled and replacement-style Au ± Cu-bearing muscovite alteration in the core of the deposit; (4) an unmineralized fracture-controlled and disseminated epidote alteration is localized to the north of the deposit; (5) a texturally destructive albite alteration occurs in the central part of the deposit and is responsible for remobilizing earlier gold mineralization; and (6) gold-bearing chlorite zones that are mainly developed in the biotite-rich domains.

Several of the alteration assemblages are considered to be genetically related to magmatism. Amphibole and biotite alteration are considered the result of volatile exsolution of diorite. The mineralogy, relative timing and distribution of muscovite alteration is analogous to phyllic alteration in porphyry systems, whereas epidote alteration represents a lower temperature upflow zone. Albite alteration is considered to be derived from the tonalite. In contrast, chloritization is considered a replacement of the biotite given that relict biotite is generally observed in chloritized areas, chlorite has similar Fe/Mg ratios to the biotite it replaced and chlorite inherits the biotite sulphide assemblage. Chloritization is currently attributed to later regional metamorphism.

U-Pb ID-TIMS and LA ICP-MS dating of four samples containing hydrothermal titanite from amphibole and albite alteration assemblages constrain the timing of hydrothermal alteration to ca. 2740 Ma and two Re-Os molybdenite samples provide ages of 2746.8 ± 11.4 and 2736.1 ± 11.4 Ma. Notably, all the ages presented in this study overlap with the timing of magmatism and strongly support a syn-intrusion timing for alteration and gold mineralization. Two rutile ages at ca. 2667 Ma indicate, however, that the deposit was affected by regional metamorphism.

Considering the overlap of magmatic and hydrothermal events and the nature of alteration and mineralization, the Côté Gold deposit is interpreted to have formed in a manner similar to Phanerozoic porphyry-type deposits. This deposit is significant because in addition to being the first large Au deposit to be discovered in the Swayze greenstone belt, it also represents a new gold metallogenic event in the Abitibi Subprovince for which its regional importance remains to be defined.

3.2 Introduction

Porphyry deposits constitute an important ore deposit type due to their contained metals (i.e., Cu, Au, Mo) and large tonnages which make them preferred exploration targets globally (Seedorff et al., 2005; Sinclair, 2007; Sillitoe, 2010). Archean and Proterozoic porphyry deposits are, however, not well-represented in the geologic record compared to Phanerozoic deposits, in part due to the lack of preservation of these high level systems (Kesler and Wilkinson, 2006; Sillitoe, 2010). For the most part, classification of Archean porphyry deposits is contentious (Sinclair, 2007) and is further complicated by overprinting of deformation and metamorphism. As such, few convincing examples of Archean porphyry-type deposits have been documented, the rare exceptions being Lac Troilus (Fraser, 1993) and Setting Net Lake (Ayres et al., 1982; Nunes and Ayres, 1982) in Canada.

Porphyry deposits, in particular the Cu-Au types, occur in modern-day intra-oceanic and continental type convergent arc settings. These settings also host a wide range of base and precious metal mineralization in a variety of epithermal settings (Sillitoe, 2010). This metallogenic association, however, is less recognized in the much older Archean volcano-

plutonic terranes. Archean low-Al composite intrusions are, however, known to underlie VMS-type mineralization that forms in arc-type environments (Campbell et al., 1981; Cathles, 1981; Franklin, 1996; Galley et al., 2000; Galley, 2003) and have been documented to host porphyry-type Cu-Mo(-Au) mineralization. Examples of these includes the Flavrian-Powell (Goldie 1979; Kennedy, 1985), the Beidelman Bay (Friske, 1974; Trowell, 1974; Poulsen and Franklin; 1981) and Mooshla intrusive complexes (Galley and Lafrance, 2014) in Ontario and Quebec, Canada. This relationship, therefore, may represent the submarine equivalent of the porphyry-epithermal continuum, as advocated by Sillitoe et al. (1996) and Hannington et al. (1997).

The Côté Gold deposit, located in the Swayze greenstone belt (SGB) of northern Ontario, Canada, is a low-grade and high-tonnage (NI 43-101 indicated: 296 Mt @ 0.88 g/t Au (7.61 M oz) and inferred: 44 Mt @ 0.74 g/t Au (1.04 M oz); IAMGOLD, 2013) deposit that is hypothesized to represent a potential Archean porphyry-type deposit based on the spatial and temporal overlap of magmatism and mineralization based on U-Pb and Re-Os geochronology (Kontak et al., 2013a; Katz et al., 2015). Not only is this deposit one of the better documented examples of an Archean porphyry-type system in the Canadian Superior Province, but based on its ca. 2740 Ma age it also represents a previously unknown gold metallogenic event that predates the well-known timing of orogenic gold events in the Abitibi greenstone belt (Robert, 2001). It is important, therefore, to understand the nature, origin and genetic model of this deposit in order to assess its significance in the context of gold metallogeny, evolution of greenstone belts and parameters for exploring for other similar deposit types in the area around Côté Gold specifically, but also elsewhere in the SGB and in other Archean terranes both within the Superior Province and globally.

This paper provides the first comprehensive documentation of the formation of the Côté Gold deposit and: (1) describes the nature of alteration and mineralization types and their distribution; (2) constrains the relative and absolute timing relationships of the hydrothermal events; and (3) develops a geological model for the deposit and classifies the deposit in the context of gold deposit types.

3.3 Regional Geologic Setting

The Côté Gold deposit is located in the southern limb of the SGB, part of the larger, gold-rich (historical production and reserves of ~4827.5 tonnes Au; Dubé and Gosselin, 2007) Abitibi Subprovince (Fig. 3.1). The SGB contains many of the stratigraphic assemblages and structures typical of the southern Abitibi greenstone belt (AGB) based on lithological and geochronological criteria (Ayer et al., 2002; van Breemen et al., 2006). The volcanic and plutonic rocks in the SGB are diverse and range from ultramafic to felsic in composition in addition to both chemical and clastic sedimentary rock types (Ayer et al., 2002); these rocks range in age from 2750-2670 Ma (Thurston et al., 2008). In the SGB, six supracrustal groups are recognized. From oldest to youngest, these groups are the Chester, Marion, Biscotasing, Trailbreaker, Swayze and Ridout Groups (Heather, 2001).

The SGB has a complex structural history which includes polyphase folding and development of associated fabrics, ductile high-strain zones, and late brittle faulting (Heather, 2001; van Breemen et al., 2006). The major D_2 structure in the southern part of the SGB is the east-west trending Ridout deformation zone (RDZ), which is a high-strain zone (up to 2 km

wide; Figs. 3.1, 3.2A) where a complex history of ductile shearing with later brittle faulting is recorded (Heather, 2001; van Breemen et al., 2006; Berger, 2011).

Previous studies have inferred the RDZ to be the western extension of the fertile Larder Lake-Cadillac deformation zone (Heather, 2001; van Breemen et al., 2006). It has also been argued that although of similar age, these two deformation zones are unlikely to be related given that they are localized to different parts of the regional stratigraphy and record different kinematic histories (Berger, 2011). Regardless of the possible structural connection between these two deformation zones, the D_2 event in the SGB, like in the AGB, has been inferred to be synchronous with the generation of orogenic-type gold mineralization (Heather, 2001; van Breemen et al., 2006) and consequently, has been the preferred exploration target in the SGB (see summary in Rogers et al., 2013).

Metamorphic grade within the southern Abitibi greenstone belt ranges from sub-greenschist to greenschist grade. Higher amphibolite grade conditions were locally attained next to large synvolcanic and syntectonic intrusions. Peak metamorphism is estimated to have occurred from 2677 to 2643 Ma (Powell et al., 1995).

3.4 Exploration History

The Chester township, in which the Côté Gold deposit is located, has been prospected and explored intermittently for over a century and as a result a number of gold discoveries, all of which are associated with a structurally controlled quartz ± carbonate ± sulphide vein system, were found (Rogers et al., 2013). Very minor production of the more significant occurrences

occurred, including the Chester 1 (i.e., Chester-1 zone or Chester Mine), Chester 2 (i.e., C-zone) and Chester 3 (i.e., Jack Rabbit or Texas Gulf zone) showings (Rogers et al., 2013; see Fig. 3.2B). Surface and underground exploration during the 1980's in the Chester-1 zone resulted in a non-compliant resource estimate of 144 500 tonnes grading 14.7 g/t Au for 68 000 oz (McBride, 2002). In 2009, Trelawney Mining and Exploration Inc. was initially in the Chester township area to further explore the potential of the Chester-1 zone and several high-grade intervals were reported through an eight-hole diamond drilling campaign (Roscoe and Cook, 2011). In late 2009 the results of three other drill holes, located >2 km west of the Chester-1 zone, generated a new prospect (Rogers et al., 2013). This is now known as Côté Gold deposit and its discovery eclipsed the Chester-1 zone and became the primary focus of exploration efforts.

These veins have been documented over 1 km east, west and north of the deposit area (Fig. 3.2B) and are structurally-controlled, parallel vein sets that represent a conjugate vein system (J. Smith, pers. commun., 2016). The veins are moderately to steeply dipping, approximately east-west trending quartz ± carbonate ± sulphide (i.e., pyrite, pyrrhotite, chalcopyrite) veins that are typically developed in the tonalite rocks of the intrusive complex. The veins are typically narrow (5 to 50 cm) and can be traced along strike for 10s of m to >100 m (Roscoe and Cook, 2011) and are characterized by cm- to m-wide muscovite alteration haloes, but chlorite is also common. Deformation is often localized along these veins due to the muscovite alteration and as a result they often resemble orogenic-type veins. These veins are interpreted, however, to predate regional deformation in the SGB and likely formed due to local stresses during magmatic activity (Smith et al., 2014; Smith, pers. commun., 2016)

3.5 Local Geological Setting

The Côté Gold deposit is hosted by the ca. 2741 to 2739 Ma Chester intrusive complex (CIC), a multi-phase, laccolith-shaped, subvolcanic, tonalite-diorite-quartz diorite intrusion located along the southern margin of the Ridout syncline in the southeastern extension of the SGB (Fig. 3.1). The CIC intrudes into the Chester Group (2750 to 2735 Ma), which consists of low-K tholeiitic mafic metavolcanic rocks of the Arbutus Formation and felsic to intermediate metavolcanic rocks of the Yeo Formation, based on the presence of screens and rafts of the volcanics in the intrusive complex (Heather, 2001; Berger, 2012; Fig. 3.2A, B). Two U-Pb zircon ages at 2739 ± 1 Ma (van Breemen et al., 2006) and 2734 ± 2 Ma (Heather and Shore, 1999a, b; see locations on Fig. 3.2A) were obtained for the Yeo Formation. The broadly similar ages between the CIC and Yeo Formation, along with the incorporation of the volcanic rocks in the intrusive complex, indicates they are coeval.

In terms of the broader setting for the deposition of the Chester Group, it has been inferred that the chemistry of the volcanic rocks are consistent with an ensimatic ocean basin or arc setting (Heather, 2001; Ayer et al., 2002; van Breemen et al., 2006). More recent work has suggested the Arbutus Formation of this package formed in a possible oceanic back-arc basin setting (see Chapter 2).

3.6 Geology of the Côté Gold Deposit

The deposit, located in the northwestern part of the CIC (Fig. 3.2A), is hosted by multi-phase tonalite, diorite and quartz diorite rocks that are intruded by breccia bodies of both

magmatic and magmatic-hydrothermal origin (Fig. 3.3). A brief description of these host rocks is provided below. A more detailed analysis of their petrology, geochemistry, petrogenesis and relative and absolute timing is provided by Katz et al. (2015) and presented in Chapter 2.

The tonalitic and dioritic phases exhibit complex relationships (Heather, 1993; Heather and Shore, 1999a; Heather 2001; see Chapter 2) and suggest their contemporaneous emplacement based on: (1) variable sized tonalite bodies and dikes which intrude and brecciate diorite; (2) fragments of tonalite and diorite within a dioritic matrix; (3) sharp to diffuse contacts for the diorite fragments in tonalite, occasionally with lobate boundaries; and (4) a frothy or pitted net-texture in many fragments. High-precision U-Pb ID-TIMS geochronology supports the inferred contemporaneous injection, with tonalite constrained at ca. 2741 to 2739 Ma (Heather and van Breemen, 1994; Kontak et al., 2013a; Chapter 2) and diorite at ca. 2741 Ma (Chapter 2).

The host rocks to the deposit display many features consistent with a high crustal level of emplacement. For example, the CIC is associated with coeval volcanic rocks (cf. Sillitoe, 2000) and the host rocks contain textures that are consistent with a high-level setting (e.g., granophyres, miarolitic cavities and breccias). In addition, Al-in-hornblende geobarometry of magmatic amphiboles from quartz diorite yielded pressures of $\leq 1.3 \pm 0.6$ kbars (Chapter 2).

3.6.1 Intrusive phases of the Chester intrusive complex

Tonalite: The deposit is partly hosted by several calc-alkaline to transitional, low-Al (Barker, 1979) tonalite phases that form < 1 m to >100 m bodies. The tonalitic units are fine- to medium-grained, leucocratic rocks with subequal amounts of plagioclase (An_{15-40}) and quartz (Fig. 3.4A); rare quartz and/or plagioclase phenocrysts occur.

A magmatic breccia occurs, termed a tonalite breccia, and is the result of tonalite brecciating along its intrusive margins. This breccia contains cm- to m-sized angular to rounded dioritic fragments with sharp to diffuse boundaries (Fig. 3.4B; Table 3.1); rare tonalite fragments occur.

Diorite: The deposit is also hosted by several tholeiitic to transitional phases of melanocratic to leucocratic diorite (Fig. 3.4C) and quartz diorite (Fig. 3.4D) that form m-sized to >100 m-sized intrusions. The diorite is fine- to coarse-grained with rare plagioclase phenocrysts. Diorite is dominated by subequal amounts of hornblende and plagioclase (typically An_{10-50}) with minor titanite, ilmenite and magnetite. The quartz diorite is also fine- to coarse-grained and is often quartz and/or plagioclase porphyritic. Quartz diorite is dominated by plagioclase, amphibole and quartz with the same minor and phases as the diorite. Locally minor hornblende-plagioclase ± quartz pegmatite occur as small <1 m dikes with sharp to diffuse contacts against diorite and quartz diorite.

A second type of magmatic breccia, termed a diorite breccia, occurs and is the result of dioritic injections brecciating earlier tonalite and dioritic rocks. The breccia bodies occur as several injections that range from 10 cm to >100 m in apparent width and dip moderately to steeply to the north (Figs. 3.5A and 3.6A-C) that occur in the south and central parts of the deposit. This breccia contains a dioritic matrix and angular to rounded fragments that range from cm to m-sized and have sharp contacts (Fig. 3.4E; Table 3.1).

Magmatic-hydrothermal breccias: Tonalite and diorite are crosscut by magmatic-hydrothermal breccia bodies, as defined by Sillitoe (1985). The breccia bodies are poorly exposed on surface (Fig. 3.3), thus much of its extent and features are based on drill core. In

detail, however, the size and geometry of these breccia bodies remain poorly defined. The hydrothermal breccias consist of two types: (1) a hydrothermal amphibole breccia with a fine- to medium-grained amphibole-quartz ± biotite ± carbonate ± sulphide matrix (Fig. 3.4F, G; Table 3.1) that forms rare m-sized breccia bodies in the south and centre of the deposit; and (2) a hydrothermal biotite breccia consisting of biotite-rich matrices (Fig. 3.4H; Table 3.1) that forms several bodies up to 200 m in apparent width at depth in the central and northern parts of the deposit. This breccia can be subdivided into three types based on its matrix mineralogy and texture (Table 3.1): (i) a biotite-rich matrix (Fig. 3.4I); (ii) a sulphide- and/or magnetite-rich matrix (Fig. 3.4J); and (iii) a carbonate-rich matrix (Fig. 3.4K).

3.6.2 Dikes

Several later stage magmatic events affect the CIC area are represented by a variety of dike rocks which are, however, minor in abundance. Information regarding the types of dike rocks, their mineralogy, textures, crosscutting relationships and geochemical attributes are summarized in Chapter 2. These dike rocks include: (1) feldspar ± quartz porphyries of dacitic to andesitic composition; (2) lamprophyres; (3) a dioritic dike; (4) a gabbroic dike; (5) diabase; (6) a tectonic breccia; and (7) a heterolithic quartz ± carbonate breccia.

3.6.3 Deformation

Several small (<3 m wide), late-stage, east-west trending deformation zones associated with the RDZ, which occurs approximately 3 km north of the Côté Gold deposit, overprint the major rock units, alteration types and some dike rocks. Deformation zones develop preferentially

in the more ductile diorite, rather than tonalite, but strain can be localized in areas where the tonalite is altered by fine-grained muscovite.

In addition, a west-striking, moderately to steeply north dipping brittle fault extends through the centre of the deposit (Figs. 3.3 and 3.6). This fault zone is characterized by clay minerals (e.g., illite, montmorillonite), quartz-carbonate flooding and a tectonic breccias. Although kinematic indicators are lacking, preliminary work of correlating rock types (i.e., tonalite, diorite, breccia, dike rocks) and alteration domains (i.e., albite) suggest an apparent post-mineralization dextral displacement of around 100 to 200 m.

3.7 Analytical Methods

3.7.1 Petrography

Approximately 500 thin sections and polished thin sections were prepared that encompass least-altered rocks, all alteration types, vein types and mineralization styles. More than 300 were polished thin sections and used to determine the oxide and sulphide mineralogy of the alteration types and mineralization. Over 100 polished thin sections were used specifically to assess the nature and paragenesis of alteration types.

3.7.2 Electron microprobe and scanning electron microprobe analyses

Electron microprobe analysis (EMPA) of secondary biotite, epidote, muscovite and chlorite (Tables 3.3 and 3.4) for a total of 15 samples was done with wavelength dispersive spectrometry (WDS) using a Cameca SX 100 electron probe microanalyzer at the Ontario

Geological Survey Geoscience Laboratories (Geo Labs) in Sudbury, Ontario. The accelerating potential used was 20 kV with a beam current of 20 nA; a 15 µm beam size was used for epidote, titanite and chlorite, whereas it ranged from 5 to 15 µm for biotite and muscovite. The range of beam size for biotite samples was due to changes in grain size. Muscovite is susceptible to decomposition under the operating conditions and to mitigate this problem a beam raster of at least 10 µm was used; where grain size permits, a 15 µm beam was used. Standards used for calibration include diopAST and pyrxBRN. Iron, Mn and V were analyzed using a LLiF crystal; Ti and Cr were analyzed with a PET crystal; K, Cl and Ca were analyed with a LPET crystal; Si, Al and Mg were analyzed with a TAP crystal; and Na and F were analyzed with a LTAP crystal.

In addition to the EMPA work, semi-quantitative scanning electron microprobe - energy dispersive spectrometer (SEM-EDS) analyses were obtained in the Central Analytical Facilities (CAF) at Laurentian University, along with the collection of qualitative elemental X-ray maps. These data were collected using a JEOL6400 SEM instrument with an attached solid-state detector using an accelerating voltage of 20 kV, beam current of ~ 1 nA and collection time of 5 seconds for spot analysis. The data were processed with INCA software package. A total of 31 polished thin sections from all alteration types and mineralization styles were selected in order to identify all the alteration minerals present, their mineral chemistry and textural relationships between alteration phases.

3.7.3 TerraSpec

The TerraSpec is a mineral analyzer that uses wavelength absorption and reflectance to analyze different minerals of interest. The method is rapid and non-destructive and of particular

use in identifying alteration minerals. The intent of this particular study was to determine if a specific alteration mineral(s) or transition zone between alteration minerals coincided with gold mineralization. The spectrometer used measured from the visible near infrared (NIR; 380 to 1300 nm) to the short-wave infrared (SWIR; 1300 to 2500 nm) range. Minerals analyzed that were relevant for this study include muscovite, illitic muscovite, phengite, paragonite, chlorite, biotite, phologopite, epidote, hornblende, illite and montmorillonite. A total of twenty-six holes on four lines in the deposit were analyzed with a total of 3 356 spectra measured over 12 206 m of core. The data collected was processed and its spatial distribution plotted using spectral analysis software called The Spectral Geologist. The dominant mineral (Mineral1), as detected by the TerraSpec software, is included in this study and each spectral measurement was checked and verified. Assay results in all cross sections and x-y plots are from the IAMGOLD database.

3.7.4 Laser ablation-inductively coupled plasma-mass spectrometry (LA ICP-MS)

Biotite trace elements: Biotite trace element concentrations were determined in-situ by LA ICP-MS of each mineral in eight thin sections and results are found in Table 3.5. The measurements were performed in the Chemical Fingerprinting laboratory of Laurentian University, Sudbury, Canada using a 20 ns pulse duration, 193 nm wavelength ArF excimer laser (Resonetics RESOlution M-50) employing a two-volume Laurin Technic sample cell (Müller et al., 2009) coupled to a Ar plasma quadrupole ICP-MS (Thermo X Series II). Ablation took place in He (650 ml/min) which was combined with Ar (800 ml/min) and N_2 for enhanced sensitivity (6 ml/min) prior to the plasma. Biotite data were obtained from spot analyses using a beam diameter of 48 µm, laser repetition rate of 5 Hz and fluence of 7 J/cm^2. The biotite spot analyses typically consisted of 30 s of background followed by 30 s of ablation or longer (for traverses).

The ICP-MS was operated with a forward power of 1450 W and an oxide production rate of < 0.4% as determined by measuring ThO^+/Th^+ while ablating NIST SRM 612. Dwell times were set at 10 ms per analyte for all measurements. Data reduction was done with the Iolite software package (v. 2.5; Paton et al., 2011) using NIST SRM 610 (bracketing and between every 7 or fewer analyses) as an external reference and K (9.0%) as internal references for biotite.

U-Pb geochronology: In-situ U-Pb dating of primary and secondary titanite was conducted using a Resonetics RESOlution M-50 ArF excimer (193 nm) laser ablation system coupled to a Thermo X-Series II quadrupole ICP-MS at Laurentian University. Titanite were selected in standard polished thin sections to be analyzed with spot sizes between 48 to 66 μm, a laser pulse rate of 6 Hz and a fluence of 6 J/cm^2. Mesoproterozoic titanite from a Grenville skarn (Kennedy et al., 2010) was used as the primary reference material and in some cases the BLR1 titanite (ca. 1047 Ma; Aleinikoff et al., 2007) and fish canyon tuff (ca. 28.4 Ma; Schmitz and Bowring, 2001) standards were also analyzed for quality control/assurance purposes. The Iolite (Paton et al., 2010, 2011) software package was used for data reduction in conjunction with VizualAge (Petrus and Kamber, 2012). Importantly, since the primary reference titanite contains a small and variable amount of common Pb, the results were calculated using the modified VizualAge data reduction scheme of Chew et al. (2014).

3.7.5 U-Pb ID-TIMS and SHRIMP geochronology analytical techniques

U-Pb isotope dilution thermal ionization mass spectrometry (ID-TIMS) and Sensitive High Resolution Ion MicroProbe (SHRIMP II) analyses on accessory minerals including hydrothermal titanite and rutile were conducted in the Geochronology laboratories at the

Geological Survey of Canada (GSC), Ottawa, Ontario. Heavy minerals were concentrated from the samples selected for geochronology using standard crushing, grinding, and separation on a Wilfley table and by heavy liquid techniques. Final separation of titanite and rutile grains was completed by magnetic susceptibility using a Frantz™ isodynamic separator and hand-picking using a binocular microscope. Details of grain morphology and quality are summarized in Table 3.6.

U-Pb ID-TIMS techniques utilized in this study are modified after Davis et al. (1997) and Parrish et al. (1987), with the treatment of analytical errors after Roddick (1987). The U-Pb ID-TIMS analytical results are presented in Table 3.6 and displayed in concordia plots (Fig. 3.22) with age uncertainties presented at the 2σ level.

SHRIMP II analytical procedures are described by Stern (1997), with standards and U-Pb calibration methods following Stern and Amelin (2003). Titanite and rutile grains from the samples and fragments of the GSC laboratory standard were cast in an epoxy grain mount (GSC mount IP730), polished with diamond compound to reveal the grain centres, and photographed in transmitted light. Internal features of the grains (such as zoning, structures, alteration, etc.) were characterized in back-scattered electron (BSE) mode utilizing a Zeiss Evo 50 scanning electron microscope (SEM). Mount surfaces were evaporatively coated with 10 nm of high purity Au. Analyses were conducted using an O^- primary beam, projected onto the grains with an elliptical spot 13μm x 16μm in size. The count rates of eleven masses including background were sequentially measured over 6 scans with a single electron multiplier and a pulse counting system with deadtime of 23 ns. Off-line data processing was accomplished using customized in-house software. The SHRIMP analytical data is presented in Table 3.7, where the 1σ external errors of $^{206}Pb/^{238}U$ ratios reported in the data table incorporate a 1.6% error in calibrating the standard

titanite. The data are plotted in a concordia diagram with errors at the 2σ level (Fig. 3.22), using Isoplot v. 3.0 (Ludwig, 2003) to generate the plot.

3.7.6 Re-Os geochronology analytical techniques

The samples were processed at the University of Alberta. A molybdenite mineral separate was made for both samples by metal-free crushing followed by gravity and magnetic concentration methods described in detail by Selby and Creaser (2004). For both samples the ^{187}Re and 1^{87}Os concentrations in molybdenite were determined by isotope dilution mass spectrometry using Carius-tube, solvent extraction, anion chromatography and negative thermal ionization mass spectrometry techniques. A mixed double spike containing known amounts of isotopically enriched ^{185}Re, ^{190}Os, and ^{188}Os analysis was used (Markey et al., 2007). Isotopic analysis used a ThermoScientific Triton mass spectrometer by Faraday collector. Total blanks for Re and Os are less than 3 picograms and 2 picograms, respectively, which are insignificant for the Re and Os concentrations in molybdenite. The molybdenite powder HLP-5 (Markey et al., 1998) is analyzed as a standard and over a period of one year and an average Re-Os date of 220.66 ± 0.21 Ma (1σ uncertainty, n = 5) is obtained. This Re-Os age date is identical to that reported by Markey et al. (1998) of 221.0 ± 1.0 Ma.

3.8 Alteration, Breccia Cement, Mineralization and Vein Types

The mineralogy and paragenesis of the alteration assemblages and the associated mineralization for the Côté Gold deposit is presented here for the first time and is summarized in

Table 3.2 and Figure 3.7. In this study, five alteration types are defined which, from oldest to youngest, are characterized by amphibole-rich, biotite-rich, muscovite-rich, epidote-rich and albite-rich assemblages and are interpreted to be syn-magmatic in timing. Chloritization of earlier biotite occurs and does not appear to form a distinct alteration assemblage. Mineralization is spatially associated with amphibole, biotite, muscovite, albite and chlorite alteration. We note, however, that the distribution of the alteration envelope is larger than the mineralized zone and extends outside the deposit.

Several cross sections are presented and demonstrate the spatial distribution of gold mineralization with rock type, in particular, the breccia bodies on which the delineated ore zone is centred (Figs. 3.5A, and 3.6A-C). In addition, detailed mapping of the 53 and North Breccia Outcrops (see Figure 3.3 for locations), illustrate a relationship among rock type, alteration and vein types with mineralization. The results of channel sampling of the 53 Outcrop (Fig. 3.8; see Table B.5 in Appendix B for Au assays) indicate that Au mineralization is controlled by rock type, vein type and alteration type, as discussed below. The North Breccia Outcrop illustrates the timing of Au mineralization with respect to rock type and deformation (Fig. 3.9; see 3.10 Re-Os geochronology section below).

Several vein types occur in the deposit (see Table 3.2), some of which host both gold and molybdenite. Although veins may host mineralization, there is an overall low-density of quartz veining in the deposit. In addition, there are several types of miarolitic-like cavities which include quartz, quartz-sulphide and quartz-plagioclase types; these miarolitic-like cavities are often mineralized.

3.8.1 Amphibole veins and breccias

Mineralogy and distribution: This is the earliest hydrothermal event in the deposit, occurring as a variety of amphibole-rich veins (Figs. 3.9B and 3.10A-D) and breccia cements (Fig. 3.10E). It is relatively rare and based on current data appears to be restricted to the southern and central parts of the deposit. The assemblage consists of hornblende ± apatite ± titanite ± magnetite ± quartz ± albite ± biotite ± pyrite ± chalcopyrite and is analogous to calcic alteration (e.g., Seedorff et al., 2005; Sillitoe, 2010). The hornblende-bearing veins and breccias crosscut the intrusive phases (e.g. tonalite, diorite, diorite breccia; Figs. 3.9A, B and 3.10A, C), thus they postdate some magmatism of the CIC.

A variety of amphibole-rich vein types occur (see Table 3.2) and are characterized by coarse-grained hornblende (Fig. 3.10D). Veins are typically cm-sized, but rarely exceed 1 m in apparent width. Vein amphibole can be partially altered to biotite (Fig. 3.10D). Sulphides are rare, but gold mineralization often coincides with amphibole-bearing veins and breccias (Fig. 3.10A, E).

Mineral chemistry: Mineral chemistry conducted on vein and breccia amphiboles is described in Chapter 2 and the microprobe data is found in Table C.1 in Appendix C. The amphiboles are calcic and conform to the tschermakite-actinolite series based on the amphibole classification scheme of Hawthorne and Oberti (2007) and plot in the hornblende and actinolite fields. Notably, zoned hydrothermal amphibole grains occur in the breccia and exhibit reverse fractionation with Mg# (Mg/Mg + Fe) increasing from the core outwards (Fig. 3.10F, G), however, the rims may be more Fe-rich. The breccia-hosted amphiboles can have a higher Mg# compared to vein amphibole and magmatic amphiboles (Fig. 3.11A).

3.8.2 Biotite alteration

Mineralogy and distribution: All major intrusive phases contain hydrothermal biotite with a varied association of biotite ± quartz ± magnetite ± epidote ± allanite ± calcite ± ankerite ± pyrite ± chalcopyrite ± pyrrhotite ± apatite ± titanite ± bastnaesite ± fluorite ± sphalerite ± galena. The biotite is found disseminated in diorite and tonalite, in the matrix of the breccia and also as a veins (Fig. 3.12). The biotite can be subdivided based on colour under the microscope in plane polarized light: (1) pale to dark brown; (2) pale green-brown to dark brown-green; and (3) pale brown to orange-brown. The spatial distribution of these three biotite types is, however, currently undefined. An important observation based on an extensive petrographic study is that biotite is partially to wholly replaced by chlorite and, therefore, chlorite is not considered to be part of this hydrothermal event.

Disseminated biotite occurs throughout the deposit and outside the ore envelope. Biotite replaces igneous minerals (i.e., plagioclase and amphibole), as well as hydrothermal amphibole, and forms anhedral to subhedral, fine-grained (<1% to > 50%) spots or clusters (Fig. 3.12A, B). A biotite-epidote ± magnetite ± calcite ± quartz ± apatite ± titanite ± allanite ± bastnaesite ± pyrite ± chalcopyrite alteration assemblage is most common in tonalite rocks, whereas a biotite-calcite-quartz ± allanite alteration assemblage is most common in diorite rocks. Where disseminated biotite alters tonalite and diorite gold mineralization is typically rare and inconsistent. In contrast, when affected by biotite alteration, the diorite breccia can host more consistent Au ± Cu grades reflecting a preferential permeability that is likely responsible for ore grade. Where present petrographic observations indicate that gold and molybdenite can form with chalcopyrite in association with disseminated biotite or chlorite after biotite.

The mineralogy of the hydrothermal biotite breccia is described above and summarized in Table 3.1. This breccia contains the most consistent Au grades (avg. ~0.7 g/t) and is often spatially coincident with Au and Cu mineralization (Figs. 3.12C, 3.13A, B) and less consistently with anomalous Mo (Fig. 3.13C) and Ag (Fig. 3.13D). Pyrite, chalcopyrite, magnetite (Fig. 3.12D), pyrrhotite and rarely visible gold, electrum and molybdenite are disseminated in the breccia matrix and are associated with biotite and/or chlorite after biotite. In addition, a rare bismuth telluride mineral with trace Se and F (i.e., tellurobismuthite or kawazulite) was identified on the SEM-EDS.

A variety of biotite-bearing vein assemblages are documented (see Table 3.2). Vein and fracture morphology is variable and includes sheeted vein sets (Fig. 3.12E), discrete veins or stockwork-like zones (Fig. 3.12A). The sheeted veins are moderately to steeply dipping, east-west trending, planar, subparallel and closely (<10 cm apart) to widely (several m apart) spaced. The vein sets are typically less than 5 m in apparent width, but in rare cases are up to 55 m. These veins occur throughout the deposit but are also found outside the deposit within the CIC (Fig. 3.2B). These veins may contain a biotite assemblage, but this early event is commonly obscured and overprinted by muscovite (Fig. 3.12E) or is chloritized. Mineralization in these veins is erratic, but they can have a Au ± Cu ± Mo ± Ag association, similar to the breccia (Fig. 3.13A-D). In the biotite-rich veins, gold is found within quartz or intergrown with biotite or sulphides, such as pyrrhotite.

The biotite alteration event is associated with some unusual minerals, such as allanite and bastnaesite (Fig. 3.12F). Allanite is a light rare earth-bearing (LREE; Ce-, Nd-, and La-bearing) epidote whereas bastnaesite is a LREE-bearing (Ce-, La-, Nd-, Gd-, Sm-, Pr-, and Y-bearing)

fluoro-carbonate; both these minerals are generally found in REE mineralized alkaline systems (e.g., Chakhmouradian and Zaitsev, 2012).

In the deposit, there is little apparent evidence for the overlap between intermineral magma injection and hydrothermal alteration, a key aspect of many porphyry deposits in general (e.g., Kirkham, 1971; Sinclair, 2007). However, Figure 3.12G shows the rare occurrence of biotite alteration being both crosscut by and crosscutting tonalite, which demonstrates a temporal overlap in magmatic-hydrothermal events. The deposit on the whole, however, lacks evidence of these crosscutting relationships.

Mineral chemistry: The chemistry of biotite is of particular interest since it is a monitor of the chemistry of the hydrothermal fluid implicated in the potassic alteration. A total of 29 samples (12 EMPA and 17 SEM-EDS) were analyzed from disseminated, vein and breccia types. See Table 3.3 and Table C.2 in Appendix C for the biotite probe analyses.

The chemical data from both EMPA and SEM-EDS analyses indicate that different coloured biotite corresponds to changes in Fe and Mg concentrations. Orange-brown and brown coloured biotite grains are more Mg-rich (Fig. 3.11B) with a range of 6.78 to 14.01 wt. % MgO and 17.00 to 30.54 wt. % FeO compared to green-brown biotite which has a range of 4.74 to 8.71 wt. % MgO and 24.29 to 32.58 wt. % FeO. Figure 3.11B also illustrates that biotite from breccia samples typically have a higher Mg# than from disseminated and vein samples, given its respective colour. Given this information, the Mg# shows an overall increase in the breccia, indicating a chemical zonation of biotite in the deposit. Some orange-brown biotite from vein and disseminated samples can also have a higher Mg# similar to the biotite in the breccia. In addition, the EMPA analyses indicate that the breccia samples have, on average, higher F and V

contents and lower Mn than vein and disseminated samples. Trace amounts of CaO (≤0.78 wt. %), Na_2O (≤0.61 wt. %), MnO (≤0.25 wt. %), V_2O_3 (≤0.10 wt. %), Cr_2O_3 (≤0.11 wt. %) were also detected. As for the volatile contents of the biotite, F varied between 0.12 to 1.40 wt. % and Cl from 0.06 to 0.37 wt. %.

LA ICP-MS analysis of trace elements in biotite: A total of 97 analyses for trace element abundances (Li, Mg, Sc, Ti, V, Cr, Mn, Fe, Co, Ni, Cu, Zn, Rb, Sr, Nb, In, Sn, Cs, Ba, Ta, W and the REE) from eight biotite-bearing samples, including three disseminated, two vein and three breccia types, were obtained. The trace element abundances are presented in Table 3.5.

The results indicate that different abundances of some trace elements can distinguish biotite in the breccia from disseminated and vein samples, regardless of biotite colour. Breccia samples typically contain the lowest Ba concentrations (22 to 1119 ppm), whereas vein and disseminated samples contain higher Ba concentrations, (818 to 3600 ppm and 677 to 1536 ppm, respectively; Fig. 3.14A). Similarly, breccia samples contain the lowest Co concentrations (2.1 to 17.8 ppm) compared to vein (46.5 to 62.9 ppm) and disseminated (27.6 to 83.7 ppm; Fig. 3.14A) samples. Conversely, breccia samples contain higher Rb and Cs concentrations (706 to 1409 ppm and 20.5 to 69.4, respectively) compared to vein (358 to 498 ppm and 8.1 to 19.7 ppm, respectively) and disseminated (250 to 710 ppm and 6.5 to 12.3 ppm, respectively; Fig. 3.14B) samples. Higher abundances of V on average in the breccia is consistent with the microprobe analyses.

Regardless of biotite colour or alteration style, all biotites contains similar or overlapping abundances of Mn (244 to 1691 ppm), Ti, (5880 to 22400 ppm), Li (58.7 to 134.3 ppm), Cu (≤10.7 ppm), Ni (13.6 to 231 ppm), Sr (0.3 to 10.6, with anomalous values up to 96.7), Sc (2.8 to

53.7 ppm), Nb (0.9 to 92 ppm), Ta (<4.7 ppm) and W (<3.31 ppm) trace element contents. The REE concentrations are typically low (Table 3.5), except for a few anomalous values which are interpreted to be fine-grained REE-bearing minerals included in biotite.

3.8.3 Muscovite alteration

Mineralogy and distribution: This alteration, occurring as vein-controlled and replacement types, consists of muscovite ± quartz ± calcite ± pyrite ± chalcopyrite ± chlorite ± rutile and is analogous to phyllic alteration in porphyry deposits (e.g., Seedorff et al., 2005; Sillitoe, 2010). Muscovite alteration commonly occurs as haloes around biotite-bearing stockwork zones (Fig. 3.15A) and east-west trending sheeted quartz veins (Figs. 3.12E and 3.15B). Light-grey to dark-grey, and rarely green-grey (solely in diorite), fine-grained, elongate to stubby (<1 mm-sized) muscovite grains occur and replace plagioclase and mafic minerals (e.g., amphibole and biotite; Fig. 3.15C, D). The alteration commonly overprints both the fragment and matrix components of the diorite breccia and hydrothermal biotite breccia (Fig. 3.15E); in extreme cases, the nature of the protolith is obscured.

The extent and shape of the muscovite alteration zone is poorly constrained, as it is based on drill core logging and Terraspec data, however, it appears to be most intense in the core area of the deposit as a relatively continuous fracture-controlled to pervasive alteration zone of approximately 900 m by 200 to 300 m in apparent width trending northeast-southwest by east-west, respectively; rarely this zone may be up to 400 m in apparent width. The alteration front dips shallowly to steeply northwest and decreases in intensity with distance from the ore zone.

Pervasive muscovite alteration can be associated with gold and copper mineralization, but it is not always consistent. An example of this relationship is developed at the 53 Outcrop, as shown from channel sampling assay results (Fig. 3.8B). This relationship is also shown in drill hole E11-161 (Fig. 3.13A, E) where up to 3.53 g/t Au occurs in pervasively muscovite altered rocks. Sheeted quartz veins with muscovite alteration haloes (Fig. 3.15B) are often mineralized, but these veins have an original biotite alteration assemblage and, hence, the mineralization may be earlier. In addition, channel sample assay results from the 53 Outcrop show that muscovite alteration haloes bordering sheeted veins are unmineralized.

Mineral chemistry: Fine-grained white mica alteration was identified using the TerraSpec and these results indicate that several white mica types occur, including muscovite, phengite and paragonite, but muscovite is the dominant one. Selected EMPA analyses are provided in Table 3.4. The low totals (<95 wt. %) for some of the analyses are due to low K and is attributed to a mixed analysis, which is the result of chlorite, as evidenced by significant amounts of FeO (1.40 to 4.10 wt. %) and MgO (0.85 to 2.49 wt. %) in the analyses. Muscovite also contains trace amounts of Na_2O (0.32 to 0.83 wt. %), TiO_2 (0.07 to 0.67 wt. %), CaO (≤0.04 wt. %) and MnO (≤0.32 wt. %), F (≤0.17 wt. %) and Cl (≤0.02 wt. %).

3.8.4 Epidote alteration

Mineralogy and distribution: A zone of intense epidote alteration occurs towards the north end of the deposit which is ~300 m wide by 400 m long and is interpreted to be syn-intrusion. The alteration assemblage consists of epidote ± quartz ± calcite ± chlorite and occurs as disseminated and vein-controlled types (Fig. 3.16A; Table 3.2) and is rarely strongly

pervasive (Fig. 3.16B, C). The veins occur either as discrete or stockwork types. This alteration does not typically contain gold mineralization, but one epidote-quartz vein in drill core is noted to contain visible gold. In addition, the sulphide content is low and consists of pyrite and chalcopyrite.

Not to be confused with this alteration is the presence of weakly developed, patchy disseminated epidote that occurs throughout the deposit and extends outside the deposit. It is noted that the extent of this epidote outside the deposit is unconstrained. Also included in this is the development of saussuritization as fine-grained anhedral to euhedral epidote replacing plagioclase in tonalite (Figs. 3.16D and 3.17G; see below) and diorite.

Mineral chemistry: The EMPA analyses of the intense vein-controlled and disseminated epidote (Table 3.4) indicates a range of Al_2O_3 (22.98 to 28.15 wt. %) and FeO_T (7.47 to 13.41 wt. %) content and minor TiO_2 (≤0.38 wt. %), MgO (≤0.20 wt. %), MnO (≤0.46 wt. %), V_2O_3 (≤0.07 wt. %) and Cr_2O_3 (≤0.64 wt. %). These epidotes trend towards the Al-rich epidote (clinozoisite) field, with one sample plotting in the clinozoisite field. Notably, epidote grains that form as part of the biotite alteration assemblage have on average higher and more consistent FeO_T (12.81 to 13.76 wt. %), higher TiO_2 (0.03 to 0.30 wt. %) and lower Al_2O_3 (20.72 to 23.51 wt. %) than the epidote above. This results in higher Fe/Fe + Al ratios (avg. = 0.3) in epidote from biotite alteration and lower Fe/Fe + Al ratios (avg. = 0.2) in epidote from epidote alteration.

3.8.5 Albite alteration

Mineralogy and distribution: This alteration type was previously referred to as silica-sodic alteration (Katz et al., 2015), but is referred to as albite alteration herein. This alteration

affects tonalite, diorite and earlier alteration assemblages. On surface, albite alteration occurs discontinuously in the central and southern parts of the deposit, whereas a large, continuous fracture-controlled and pervasive zone of albite alteration occurs in the southeast part of the deposit. At depth, albite alteration appears to be most intense towards the centre of the deposit and is fracture-controlled along its margins. This alteration can exceed 200 m in width and dips approximately 50 to 60° north to northwest. The distribution and intensity of the albite alteration at depth is shown for a single cross section in Figure 3.5B.

The alteration assemblage, consisting of albite (Ab_{100}) ± quartz ± calcite ± titanite ± ilmenite ± chlorite ± pyrite (rare), occurs as vein-controlled (Table 3.2) and replacement-style alteration. Albite alteration overprints and texturally destroys earlier amphibole, biotite (Fig. 3.17A) and muscovite (Figs. 3.8B, 3.17B) alteration assemblages, as evident at the outcrop, drill core and thin section scales. In drill core, the alteration is characterized by bleaching, destruction of primary textures, including grain boundaries, and replacement of mafic minerals (Fig. 3.17C, D). In thin section, primary plagioclase and quartz is replaced by albite and rare calcite, which results in a reduction of grain size (Fig. 3.17E, F). Similarly, when examined in backscattered electron imaging, the least-altered samples (Fig. 3.17G) lose their primary texture and mineralogy due to dissolution-precipitation processes (Fig. 3.17H), resulting in a reduction in grain size. This destruction of primary texture and replacement process in albite altered samples is documented in dozens of samples examined in thin section.

A zone of intense vuggy albite alteration having 10 to 11 wt. % Na_2O (i.e., pure albite) rarely occurs within the deposit and its distribution is not well-constrained. Porosity is developed in this zone due to complete replacement of plagioclase by albite and dissolution of quartz (Fig. 3.17I, J). These porous zones, up to multi-m thickness, are also characterized by their pale pink

to brown-red colour due to the presence of disseminated hematite. In thin section, the unit consists of <2 mm-sized, elongated to stubby albite with minor calcite. A later generation of clear albite lines the pore space with trace titanite, hematite, rutile, apatite, zircon and chlorite (Fig. 3.17K). In addition, the new albite is characterized by the presence of abundant, low-density, two-phase liquid-vapor fluid inclusions. The features observed here indicate extensive dissolution-precipitation in the rock and are similar to rocks described as episyenites whereby the rocks record quartz dissolution typically accompanied by albitization, as first defined by Lacroix (1920). The vuggy texture has also been noted in sodic alteration in porphyry deposits and is produced if silica is leached (Seedorff et al., 2008).

Albite altered rocks can contain gold mineralization as demonstrated at the 53 Outcrop (Fig. 3.8B), but overall the presence of gold is inconsistent. Assay results from both the 53 Outcrop (Fig. 3.8B) and Skidder Outcrop (Figs. B.3 and B.4 in Appendix B) indicate that albite altered areas contain higher gold values on average compared to the muscovite altered areas that it overprints (see Table B.5 in Appendix B for Au assay results). In contrast, gold values in albite altered breccias are typically lower than where breccias are free of this alteration, which suggests possible mobilization of gold. The porous, episyenite unit is typically barren of gold mineralization. Sulphide minerals and gold are rare in albite-bearing veins and sulphides are typically absent in albite alteration assemblage.

3.8.6 Chlorite alteration

Mineralogy: Chlorite occurs as disseminated and replacement (i.e., igneous plagioclase and amphibole, hydrothermal amphibole and biotite) types. Chlorite forms rims around tonalite

fragments in the hydrothermal biotite breccia (Fig. 3.18A) and partially to wholly alters biotite (Fig. 3.18B, C), indicating it postdates the biotite alteration. As a result of replacing biotite, Ti-bearing phases, such as ilmenite and rutile form (Fig. 3.18C) and inherits the biotite alteration assemblage. Gold mineralization is commonly spatially coincident with chlorite alteration which is likely due to it replacing biotite.

Mineral chemistry: Selected samples with chlorite were analyzed on the EMPA (Table 3.4) and indicate Mg and Fe contents are quite variable depending on the sample. A larger data set of 101 analyses from a total of 13 samples using the SEM-EDS was completed to compare the Mg# of chlorite formed after biotite. These data indicate that the Mg# of chlorite grains overlap with the Mg# of biotite it replaced (Fig. 3.19), suggesting the Fe/Mg ratios in chlorite are inherited from the biotite. In addition to the major components, minor to trace elements of other element were noted: TiO_2 (≤0.04 wt. %), CaO (≤ 0.04 wt. %) MnO (0.20 to 0.32 wt. %), Cr_2O_3 (≤0.78 wt. %), F (≤0.16 wt. %) and Cl (≤0.04 wt. %).

3.8.7 Syn-D_2 alteration

The study and description of hydrothermal alteration at the Côté Gold deposit is complicated by alteration associated with regional D_2 deformation zones, including chlorite, muscovite, silica, Fe- and Ca-carbonate, sulphidation and tourmaline (Heather, 2001). Within the deformation zones developed in the deposit, there are locally areas of pervasive muscovite and silica alteration with traces of green micas which overprint earlier syn-intrusion biotite, muscovite or albite alteration. Typically these deformation zones are small (<3 m wide) and lack mineralization (Fig. 3.13A-D). The deformation zones can, however, be mineralized where they

cut previous mineralization, such as a breccia or veins. The latter is seen, for example, at the North Breccia Outcrop (Fig. 3.9; see 3.10 Re-Os geochronology section below) and elsewhere in and outside the deposit (Smith et al., 2014).

3.8.8 Relationship of alteration assemblages with gold mineralization

The purpose of the TerraSpec study was to determine if a relationship exists between gold mineralization and a specific alteration mineral or transition zone between alteration assemblages. The cross sections show gold mineralization is not spatially associated with alteration assemblages, however, it is principally associated with magmatic and hydrothermal breccia bodies in the northern and southern parts of the deposit (Figs. 3.6A-C, 3.13A). In contrast, towards the centre of the deposit, where muscovite and albite alteration are strongest and overprint the breccias, the spatial association of gold with breccia bodies is less consistent (Fig. 3.6D-F). These results suggest gold mineralization originally associated with the breccia bodies were redistributed during late stage hydrothermal events. See Appendix D for additional cross sections and depth versus metal plots that emphasize this relationship.

3.8.9 Relationship and timing of gold mineralization with sulphides

A detailed mineral paragenesis for the different alteration and vein types is shown in Figure 3.7. The main sulphide minerals are pyrite and chalcopyrite with minor pyrrhotite, sphalerite, galena and molybdenite, whereas the main oxide mineral is hydrothermal magnetite with minor ilmenite. A general zonal pattern occurs with a pyrite ± chalcopyrite ± magnetite ±

pyrrhotite-bearing hydrothermal biotite breccia and pyrite ± chalcopyrite ± pyrrhotite-bearing veins and disseminations outward from the breccia unit.

In the biotite alteration assemblage the sulphide paragenesis is complex, but importantly it is consistent through all alteration styles (i.e., disseminations, veins, breccias). Three generations of pyrite can be distinguished petrographically and are summarized as follows: (1) fine-grained, euhedral to subhedral, inclusion-bearing pyrite which may contain chalcopyrite, magnetite and/or pyrrhotite inclusions (pyrite 1; Fig. 3.20A-C); (2) fine- to coarse-grained, anhedral to subhedral, inclusion-rich pyrite that may contain sphalerite and/or galena inclusions (pyrite 2; Fig. 3.20A, D); and (3) fine-grained, euhedral, inclusion-free pyrite (pyrite 3; Fig. 3.20A,C, D). Rarely, vein pyrite has a skeletal texture. Two stages of chalcopyrite have been documented based its on relative timing with pyrite: (1) early chalcopyrite, which may be intergrown with magnetite, that is documented as pre- to syn-pyrite 1 (Fig. 3.20C); and (2) late chalcopyrite, which may be associated with pyrrhotite, that postdates pyrite (Fig. 3.20E). The sulphide paragenesis demonstrates that gold is closely associated with both the early chalcopyrite ± magnetite stage (Fig. 3.20B) and the later chalcopyrite ± pyrrhotite stage (Fig. 3.20F, G). Gold has not been documented to be associated with pyrite. In addition, gold is syn- to post-molybdenite, as it occurs along cleavage planes in the molybdenite (Fig. 3.20G).

The paragenesis described above is also found in chlorite and often in muscovite altered samples, which suggests the sulphides were predominantly deposited during biotite alteration. Muscovite and chlorite alteration may, therefore, inherit the sulphide mineralization of the earlier biotite alteration. In addition, the sulphide paragenesis in the deposit area is documented to be the same as with regional east-west trending, sheeted veins outside the deposit.

With regards to gold occurrence, both ore microscopy and SEM studies of gold-rich samples from breccia-, vein- or disseminated-type samples rarely provided visible gold or electrum. Thus, the presence of sub-microscopic gold is suggested, either in sulphides or as disseminations. This conclusion is commensurate with the results of laser ablation elemental mapping of similar samples by Gao et al. (2015) that indicated the presence of disseminated, submicron size gold that correlates with biotite and chlorite zones. Importantly this study also revealed that for the samples analyzed, the pyrite was not enriched in gold.

3.9 U-Pb Geochronology

Seven carefully selected samples were used for U-Pb dating to constrain the time of magmatic and hydrothermal events. Three samples (A-C) were analyzed with the high-precision ID-TIMS (Table 3.6) and SHRIMP (Table 3.7) method and a further four samples (D-G) with the LA ICP-MS method (Table 3.8). Photos of the samples used in this study are presented in Figure 3.21 and the concordia diagrams are found in Figures 3.22 and 3.23. A paragenesis with the new ages showing the timing of hydrothermal events with respect to magmatic events is presented in Figure 3.24.

A) Albite altered diorite (Sample E12-360-LK13-117.8; z11115): This sample is an intensely albite altered diorite cut by a vein of quartz-carbonate-titanite. Titanite occurs as fine- to medium grained disseminated crystals and as fine- to very coarse-grained, subhedral to euhedral vein titanite that are partially pseudomorphed and replaced by yellowish rutile (Fig. 3.21A), both of which were analyzed in this study. The disseminated titanite occurs in the margin of the vein and is interpreted to be secondary in origin. The sample contains abundant light

brown to brown, anhedral titanite grains with minor fractures and inclusions (Fig. 3.22D). Four multigrain titanite fractions were analyzed using ID-TIMS techniques (Fig. 3.22A, Table 3.6). A linear regression of all four titanite analyses has an upper intercept of 2737.5 +2.2/-1.8 Ma (MSWD = 0.19, probability of fit (pof) = 0.82), which is interpreted to be the age of the titanite in the highly altered diorite.

In-situ SHRIMP analysis of titanite from this sample were also undertaken (Fig. 3.22B, Table 3.7). A weighted average of the $^{207}Pb/^{206}Pb$ ages is calculated to be 2747.4 ± 8.9 Ma (MSWD = 0.76, pof = 0.71, n = 15) using only the analyses that are <5% discordance. This date is in agreement with the more precise results from the ID-TIMS analyses described above.

B) Albite altered diorite (Sample E11-107-4.5; z11004): This sample represents pervasively albite altered diorite which contains abundant secondary yellow-brown rutile crystals that replaced igneous ilmenite (Fig. 3.21B). The rutile grains range from altered opaque to clear, orange-brown anhedral grains with some fractures and inclusions (Fig. 3.22D). The highest quality rutile grains were selected for in-situ SHRIMP and ID-TIMS analysis, but high amounts of common Pb and did not produce reliable SHRIMP results. A number of multigrain rutile fractions were analyzed with ID-TIMS, however, the majority of these analyses are not reliable data as a result of very low uranium contents and high amounts of common Pb incorporated in the grains upon their formation. One multigrain rutile analysis (fraction R1) did, however, yield a reliable age of ca. 2667 Ma (Fig. 3.22C, Table 3.6).

C) Albite and muscovite altered diorite (Sample 205716; z11125): This sample is a pervasively albite altered diorite containing bright-green fuchsitic mica and abundant secondary rutile crystals after primary titanite. The sample contained slightly cloudy, orange-brown

anhedral rutile fragments with some fractures and inclusions (Fig. 3.22D). In-situ U-Pb SHRIMP analyses of the rutile indicate high amounts of common Pb, hence reproducible results were not obtained. Two ID-TIMS analyses of multigrain fractions of rutile did, however, yield an age of ca. 2667 (fraction RA) and a very imprecise age of ca. 2741 Ma (fraction RB) (Fig. 3.22C, Table 3.6).

D) Quartz diorite (Sample E11-95-254B): This is a light- to dark-green, coarse- to very-coarse-grained, inequigranular quartz diorite with minor apatite and fine- to coarse-grained, euhedral titanite, interpreted to be primary in origin (Fig. 3.21C). A total of nineteen titanite grains from the sample yielded a cluster of concordant to discordant analyses. The weighted mean of the $^{207}Pb/^{206}Pb$ ages analyses after doing a ^{207}Pb-based correction for common Pb is calculated to be 2744 ± 18 Ma (MSWD = 0.62, pof = 0.89; Fig. 3.23A, Table 3.8). The common Pb composition used for the correction was determined from the Pb evolution model of Kramers and Tolstikhin (1997) at 2744 Ma. This date is interpreted to be the crystallization age of the diorite.

E) Amphibole-titanite-apatite-magnetite vein (Sample E11-116-LK13-172.7): This cm-sized vein rich in amphibole with minor apatite and magnetite contains fine- to medium-grained, subhedral to euhedral titanite that appears to be part of the primary assemblage (Fig. 3.21D, E). Twenty-six of twenty-eight titanite grains yield a cluster of concordant to discordant analyses. The observed discordance is apparently due to sub-recent weathering, as the data are pulled from the concordia back towards the origin of a standard concordia diagram. The weighted mean of the $^{207}Pb/^{206}Pb$ ages with 2σ outlier rejection (N = 24 of 26) is calculated to be 2745 ± 3 Ma (MSWD = 0.72, pof = 0.85; Fig. 3.23B, Table 3.8), which is interpreted to be the crystallization age of titanite in the vein.

F) Titanite vein (Sample E10-19-154): This sample contains a <1 mm wide titanite stringer vein that cuts a sheeted quartz-carbonate-pyrite vein in tonalite with a muscovite alteration halo (Fig. 3.21F). Twenty-five of thirty titanite grains yield a good cluster but with very slightly discordant analyses. A concordia age (Ludwig, 1998) for the cluster was calculated as 2736 ± 7 Ma (MSWD = 0.98, pof = 0.32; Fig. 3.23C, Table 3.8), which is interpreted as the age of the titanite vein.

G) Quartz-carbonate-ilmenite-sulphide vein (Sample E12-178-LK13-340.8): This quartz-carbonate-ilmenite-titanite-rutile-pyrite-chalcopyrite vein, which has a cm-sized albite alteration halo, contains coarse- to very coarse-grained, anhedral to euhedral titanite that partially replaces ilmenite (Fig. 3.21G, H). The titanite is in turn partially replaced by rutile. A total of fourteen titanite grains yield a cluster of concordant analyses with a calculated concordia age of 2745 ± 9 Ma (MSWD = 0.54, pof = 0.46; Fig. 3.23D, Table 3.8) which is interpreted to be the age of titanite crystallization and vein formation.

3.10 Re-Os Geochronology

Two Re-Os molybdenite samples were collected by Kontak et al. (2013), one of which contained high-grade Au. The two samples constrain the timing of the mineralizing event to 2737 ± 11 Ma and 2741 ± 11 Ma and provide the same age within error. To complement the previous Re-Os study two new molybdenite samples, one from well-constrained outcrop (NBxMolyLK13) mapping and one from drill core (E14-479-89.2), were chosen. These age data are found in Table 3.9 and are used to further constrain the timing of the gold mineralizing event.

North Breccia molybdenite (Sample NBxMolyLK13): This sample contains molybdenite in a quartz-molybdenite-gold ± tourmaline vein from the North Breccia Outcrop (Fig. 3.9A). Important crosscutting relationships observed include the presence of numerous cm-sized, east-west trending, quartz-carbonate ± tourmaline veins that are cut by a northwest-southeast trending lamprophyre dike (Fig. 3.9C). The lamprophyre dike is deformed by an east-west trending deformation zone (Fig. 3.9D) related to the regional RDZ (J. Smith, pers. commun., 2016). One of these deformation zones contains an east-west trending quartz-molybdenite-gold ± tourmaline vein (Fig. 3.9E). Given the relative crosscutting relationships, the east-west trending veins must predate lamprophyre dike emplacement and the D_2 deformation event. A separate of this molybdenite yielded a date of 2746.8 ± 11.4 Ma.

Molybdenite-gold vein (Sample E14-47-89.2): This sample contains coarse-grained, radiating grains of molybdenite in a quartz-carbonate-chlorite-molybdenite-gold-chalcopyrite-pyrrhotite vein with a muscovite-chlorite alteration halo. Petrographic observations indicate the gold appears to form with pyrrhotite and molybdenite, but in some areas the gold occurs along cleavage in the molybdenite, hence it is interpreted as syn- to post-molybdenite (Fig. 3.20G). A separate of this molybdenite yielded a date of 2736.1 ± 11.4 Ma.

3.11 Discussion

The examination of the nature and distribution of alteration, its associated mineralization and relative timing relationships provides the basis for examining the temporal and possible genetic relationship of this hydrothermal system with the CIC. The implications and significance of the new age data provide the basis for not only addressing the absolute timing of this system,

but also its importance of the timing of gold mineralization in the broader context of the Abitibi Subprovince. Since the Côté Gold deposit shares characteristics with the intrusion-related gold (IRG) deposit clan (Poulsen et al., 2000), in the following discussion the features of the deposit will be compared to those of IRG deposits. Given the age of the deposit and the presence of overprinting deformation, an orogenic origin is also addressed. In addition, understanding the origin and formation of the deposit is critical in the context of future exploration for similar deposits both in Archean granitoid complexes in the Abitibi Subprovince and elsewhere. Thus, the nature and origin of the hydrothermal system is discussed, along with the timing of gold introduction and the possibility of gold remobilization. Other low-Al diorite-tonalite-trondhjemite intrusions with similar features to Côté Gold are discussed for comparative purposes. Finally, the first comprehensive model for the generation of the Côté Gold deposit is proposed based on all the above data.

3.11.1 Implications of U-Pb and Re-Os geochronology

Titanite is a common accessory mineral and occurs as a primary phase in magmatic rocks, in metamorphic rocks (Frost et al., 2000) and as a hydrothermal phase in a wide variety of ore deposits (Kennedy et al., 2010). Due to its high closure temperature (650-700 ^{0}C; Frost et al., 2000), titanite can be a useful geochronometer in all the aforementioned environments. The CIC has been constrained to ca. 2741 to 2739 Ma based on high-precision U-Pb ID-TIMS zircon geochronology from several samples (Heather and van Breemen, 1994; Kontak et al., 2013; Chapter 2), as well as one magmatic titanite age at 2741.1 +1.7/-1.4 Ma (Chapter 2) which is indistinguishable from the zircon ages. To address if the LA ICP-MS method was suitable for dating titanite in this system, magmatic titanite was analyzed from a least-altered quartz diorite

(sample E11-95-254B) and an age of 2744 ± 18 Ma was obtained. Analyses by both methods indicate the titanite age was not reset by a subsequent event (i.e., hydrothermal or metamorphic) and is demonstrated to be a reliable geochronometer. Titanite can, therefore, be used to determine the age of mineralization and alteration, as has been done in previous studies of ore systems (Li et al., 2010; Chelle-Michou et al., 2015; Deng et al., 2015a, b).

For the Côté Gold deposit, both the U-Pb titanite and Re-Os molybdenite data overlap with the ca. 2741 to 2739 Ma age of magmatic activity. This study has provided four new hydrothermal titanite ages (2737.5 +2.2/-1.8 Ma, 2745 ± 3 Ma, 2736 ± 7 Ma and 2745 ± 9 Ma), interpreted to represent a ca. 2740 Ma hydrothermal event. A weighted average of the two new molybdenite ages and the two previously obtained ages, is calculated to be of 2740.2 ± 5.6 Ma (MSWD = 0.73, pof = 0.53, n = 4). These results, along with an abundance of supporting observational data, provide unequivocal evidence of syn-intrusion timing for the alteration and mineralization (Fig. 3.24).

The presently identified gold-rich metallogenic events or epochs in the AGB occur in three distinct deposit types that are well-defined in terms of their ages: VMS (~2700 Ma), syenite-associated (~2680-2672 Ma) and orogenic (~2664-2656 Ma; Robert, 2001; Robert et al., 2005). The ca. 2740 Ma age for the Côté Gold deposit represents, therefore, an older period of gold mineralization that is not well-defined in the Abitibi Subprovince. In contrast, the ca. 2667 Ma date obtained from both rutile samples suggests that rutile either grew or was reset during a later thermal event. This age coincides with the previously defined age for greenschist facies metamorphism in the southern AGB from 2677 to 2643 Ma (Powell et al., 1995). Thus, these ages for rutile indicate that the deposit was affected to some extent by later metamorphic processes.

3.11.2 Classification of the Côté Gold deposit

The evidence presented above indicates both a spatial and temporal overlap of magmatism and hydrothermal activity, hence, a syn-intrusion origin for the Au-Cu mineralization is inferred. The following discussion focuses, therefore, on how this deposit may be classified in the current IRG classification scheme.

The term IRG refers to base and precious metal deposits that are spatially and genetically associated with felsic to intermediate, water-rich intrusions. The current IRG classification scheme consists of two broad types, oxidized and reduced (Sillitoe, 1991; Sillitoe and Thompson, 1998; Thompson and Newberry, 2000; Lang and Baker, 2001; Hart, 2007; Sillitoe, 2010). The oxidized and reduced deposits differ in part based on their mineralogy, with the former having magnetite and the latter having ilmenite. In general, the oxidized type equates to large, subduction zone related, Phanerozoic age porphyry-type deposits, whereas the reduced type equate to smaller intrusive centres that form in extensional back-arc setting behind a thickened continental margin (e.g., Yukon-Alaska gold belt; Lang and Baker, 2001; Hart, 2007). Also of importance is the presence in the AGB of a further type of IRG deposit style, whereby several gold deposits (e.g., Holt-McDermott; Robert, 1997, Douay; Robert, 1997, Beattie; Davidson and Banfield, 1944 and Canadian Malartic; Helt et al., 2014; De Souza et al., 2015) are related to high-level, oxidized, syenite to quartz monzonite intrusions that are spatially associated with major fault structures (e.g., PDF and LLCF in Fig. 3.1) that bound sequences of clastic sedimentary rocks and alkaline volcanics, such as the Timiskaming sequence (Robert, 2001). These various types of IRG deposits have diverse mineralized styles, such as veins, stockworks, skarns and disseminations and differ in terms of tectonic setting, oxidation state, alteration,

alteration zoning and metal associations. For purposes of discussion, these general features of the three deposit types are provided in Table 3.10.

Given the intrusion-related nature of Côté Gold, it should be best represented by one of the three aforementioned IRG deposit types. The nature of the host rocks and alteration assemblages preclude a syenite-association, whereas the oxidized nature of the mineralization precludes a reduced classification. Thus, this leaves for consideration the porphyry-type deposit. Also to be considered for the sake of completeness is that the deposit is not intrusion-related, but instead represents an orogenic-type deposit and this is discussed below.

A comprehensive model for porphyry copper deposits was first developed by Lowell and Guilbert (1970), but it has become clear that deposit features can vary significantly in terms of host rock petrology, alteration types and metal and ore mineral associations (e.g., Gustafson, 1978; Seedorff et al., 2005; Sillitoe, 2010). Nevertheless, all porphyry deposits show the same fundamental characteristics: (1) a spatial and genetic association with a high-level, typically porphyritic, hydrous felsic to intermediate intrusion; (2) multi-stage igneous intrusions that overlap temporally with the hydrothermal activity; (3) alteration characterized by a potassic(-phyllic) core and an extensive peripheral propylitic zone; (4) disseminated and vein-controlled mineralization spatially and genetically associated with potassic and/or phyllic alteration; and (5) low-grade, high-tonnage type mineralization (Sinclair, 2007; Sillitoe, 2010).

The gold-rich porphyry copper deposits, defined as having gold contents of ≥0.4 g/metric ton (Sillitoe, 1979, 1993, 2000), have characteristic features (Table 3.11), which include: (1) high gold values that are commonly co-spatial with potassic alteration; (2) close association of gold with chalcopyrite (± bornite), particularly in the potassic alteration zone; (3) gold partly

present in its native state and in quantities proportional to copper grade; (4) no direct relationship between gold and pyrite; (5) phyllic alteration overprints the potassic zone and carries lower gold values; and (6) an unusual abundance of magnetite in the potassic alteration zone (3 to 10 vol. %). Also of note is the common presence of subparallel vein arrays and breccias in these deposits (Sillitoe, 1993, 2000). Thus, the features of the Côté Gold deposit (Table 3.11) are consistent with the features of porphyry deposits, in particular, gold-rich porphyry copper deposits.

There are, however, some differences to be noted between this deposit and porphyry deposits in general (see Tables 3.10 and 3.11): (1) poor development of propylitic alteration and a notable absence of advanced argillic alteration; and (2) the Archean age contrasts with most porphyry systems (Sillitoe, 2000, 2010) but rare exceptions are noted, such as Lac Troilus (Fraser, 1993) and Setting Net Lake (Ayres et al., 1982; Nunes and Ayres, 1982). In terms of the latter, the overall lack of porphyry deposits in the Archean is likely due to preservation. Porphyry deposits have been generated since the Archean, but Mesozoic and Cenozoic porphyry systems are the most abundantly preserved (Sillitoe, 2010). Since porphyry deposits form in high-level settings older examples are less likely to be preserved due to erosion (Kesler and Wilkinson, 2006).

Exploration in the SGB, including the CIC, has historically focused on orogenic-style gold mineralization (~2664-2656 Ma age; Robert et al., 2005). Thus, given the proximity of the RDZ to the deposit, an alternative to an intrusion-related origin must be addressed. The characteristic features of orogenic deposits, such as close spatial association with fluvio-alluvial conglomerates (e.g., Timiskaming sediments), formation at intermediate depth (5-10 km), a Au-Ag-As-W-B-Sb-Te-Mo elemental budget and Fe-carbonatization, sericitization, sulphidation alteration types (Poulsen et al., 2000; Groves et al., 2003; Dubé and Gosselin, 2007), are not

present at Côté Gold deposit. With respect to the style of mineralization, the laminated fault-fill veins in brittle-ductile shear zones and faults characteristic of orogenic-type deposits (Dubé and Gosselin, 2007) are also lacking in the deposit. It is noted, however, that stockworks and hydrothermal breccias may occur in orogenic systems when developed in competent units, such as granitoids (Dubé and Gosselin, 2007). The deformation present in the deposit, however, is manifested in the form of small (typically <3 m wide), discontinuous deformation zones that overprint syn-intrusion mineralization (Smith et al., 2014). The deposit is not likely the result of orogenic processes given the lack of features that are characteristic of orogenic-type gold deposits and that the absolute ages of hydrothermal events and mineralization presented in this study predate the timing of regional deformation and metamorphism in the region, as well as the known timing for orogenic-type mineralization in the AGB (Robert et al., 2005; Dubé and Gosselin, 2007).

In summary, the current understanding of the Côté Gold deposit suggests it best equates to an oxidized intrusion-related type, more specifically a porphyry-type. This being said, the U-Pb rutile ages of ca. 2667 Ma for samples from the deposit do indicate later thermal activity occurred in the area and given its age and proximity to the RDZ it is possible that the deposit could have experienced either subsequent remobilization of some gold or a later mineralizing event, but further work outside the scope of this study is required to verify this.

3.11.3 Nature and origin of the magmatic-hydrothermal system

The amphibole hydrothermal event at Côté Gold is analogous to calcic-sodic alteration where it forms as the earliest alteration type and is found in the deepest parts of the system

(Arancibia and Clark, 1996; Sillitoe, 2000, 2010). The alteration mineralogy is also consistent with calcic-sodic alteration in porphyry systems (i.e., amphibole, magnetite, albite and sulphide-deficient; Sillitoe, 2000).

Calcic-sodic alteration in porphyry systems can have variable fluid sources and chemistry, having either a magmatic-derived fluid (John, 1989) or a saline non-magmatic brine (Dilles and Einaudi, 1992; Seedorff et al., 2008). In the context of a magmatic or basinal brine origin, the amphibole alteration at Côté Gold is assigned to the former. Similar mineralogy between diorite and amphibole-bearing breccias and veins (e.g., amphibole, apatite, titanite, quartz, magnetite) supports a magmatic derivation. In addition, a magmatic source is favoured where this alteration is metal-bearing (Sillitoe, 2010) and the generation of calcic alteration is common in diorite and quartz diorite systems because of the greater availability of calcium (Sillitoe, 1993). Notably, calcic-sodic alteration is more typical in gold-rich alkaline porphyry systems (Sillitoe, 2000; Poulsen et al., 2000) as a result of the silica-deficient nature of the causative fluids (Sillitoe, 1993), which is consistent with the lack of quartz in some of the amphibole-bearing veins at Côté Gold and the low-density of quartz veining in general.

Biotite alteration is considered to have formed as a result of volatile exsolution during the late-stage evolution of an evolved dioritic magma, which is consistent with the origin of potassic alteration from magmatic-sourced hydrothermal fluids (Seedorff et al., 2005). This genetic relationship is inferred, in part, based on similar chondrite-normalized REE patterns of the hydrothermal biotite breccia matrix and diorite (Chapter 2). In addition, epidote has been noted to be an important component of the biotite alteration assemblage in calcic systems derived from diorite (Sillitoe, 1993, 2000), as is the case at Côté Gold. The K-Fe-Mg-Ca – bearing fluids

responsible for biotite alteration are consistent with a magmatically derived fluid originating from the diorite.

The muscovite alteration in this deposit is analogous to phyllic alteration commonly present in porphyry deposits. The origin of this alteration is attributed to the mixing of acidic, magmatic fluids with a lower temperature, external fluid of more neutral chemistry (Seedorff et al., 2005; Sillitoe, 2010). This is consistent with an oxygen isotope study by Kontak et al. (2013a), where in addition to a magmatic source a second lighter fluid is required. Given the subaqueous setting for this deposit, this second fluid source is seawater. Based on crosscutting relationships, the generation of muscovite alteration, and consequently subsequent alteration types, appears to postdate magmatic activity.

During potassic alteration, the system heats external water to generate the widespread propylitic alteration ubiquitous in porphyry systems (Seedorff et al., 2005; Sillitoe, 2010). Distinguishing propylitic alteration associated with porphyry deposits from that associated with widespread greenschist grade metamorphism, however, can be difficult (Djouka-Fonkwé et al., 2012). This study focused on the area within the ore deposit shell and as a result the extent of the fine-grained epidote that replaces plagioclase along the margins of the deposit is not constrained. Its presence may be the result of heated external water by lower temperature hydration reactions, similar to a porphyry system, or related to regional metamorphism. If the former is the case, the lack of abundant chlorite as part of the epidote alteration is due to the nature of the tonalite host rock, which is Fe- and Mg-poor. Large-scale mapping of the area surrounding the deposit, along with mineralogical and textural criteria (e.g., Djouka-Fonkwé et al., 2012), may be able to discriminate between the two possibilities.

The small zone of fracture-controlled and replacement-style epidote alteration in the north (or top) of the deposit may be analogous to epidosite alteration. Epidosite alteration is depicted to occur immediately above subvolcanic intrusions as a hydrothermal reaction zone due to the convective circulation of seawater (Galley et al., 2007). This is supported by epidote mineral chemistry (i.e., Fe/Fe + Al), which is a reflection of the conditions during their formation. Epidote in proximity to upflow zones (i.e., epidosite) has been documented to form under more reduced conditions and epidote is noted to be Fe-poor, whereas more Fe-rich epidotes form under relatively more oxidized conditions (Hannington et al., 2003). The difference in epidote mineral chemistry noted above is consistent with spatial distribution of this alteration above the high-temperature, more oxidized hydrothermal biotite breccia bodies. Thus, this alteration is interpreted as syn-magmatic and developed during the cooling of the hydrothermal system. We stress that epidote alteration is weakly developed and the fracture-controlled nature of epidote alteration may not represent a true epidosite alteration.

Some porphyry deposits develop sodic alteration without a calcic component (Dilles and Einaudi, 1992; Sillitoe, 2000; Seedorff et al., 2008), such as observed at Côté Gold. As previously stated, two possible mechanisms of formation are invoked for calcic-sodic alteration in porphyry systems, namely a magmatic-derived fluid and a saline non-magmatic brine. The change from early Fe-Mg-Ca-K metasomatism (amphibole, biotite, muscovite) derived from a dioritic source to the later Na-rich metasomatism responsible for albite alteration is reasonably explained as being the result of volatile exsolution of a ferromagnesian- and potassium-poor and sodium-rich tonalitic magma. A magmatic origin for albite alteration is supported by age dating. In Chapter 2, high-precision ID-TIMS dating obtained a titanite crystallization age (2741.1+1.7/-1.4 Ma) from an unaltered hornblende-plagioclase-quartz pegmatite sample, which is within

error of the zircon crystallization age (2741.0 ± 0.6 Ma) for the sample, both of which were interpreted to be magmatic in origin. In contrast, the hydrothermal titanite crystallization age (Sample A; 2737.5 +2.2/-1.8 Ma) in this chapter, obtained by the same method, is just slightly younger than the pegmatite. This age suggests this alteration is too young to be derived from the ca. 2741 Ma diorite, whereas the protracted tonalite intrusion that is known to extend to 2738.7 ± 0.8 Ma (Kontak et al., 2013a) overlaps with albite alteration. At present, the isotopic data needed to constrain the fluid source of albite alteration is lacking.

Results from this study indicate chlorite replaces earlier biotite, has similar Fe/Mg ratios as the biotite it replaces and inherits sulphides from the biotite alteration assemblage. Chlorite is essentially a replacement of biotite rather than a distinct alteration event and as such is similar to that documented in some porphyry deposits (Gustafson, 1978). In this study, we are unable to discriminate between chlorite being a retrograde of the system or a result of regional greenschist facies metamorphism. At this time, the latter is the preferred mechanism of formation for chlorite.

The evolution of a porphyry system, as shown in a temperature versus pH diagram (Fig. 3.25), follows a typical path from an early, high-temperature potassic to phyllic (sericitic) through to low-temperature advanced argillic alteration with the fluid becoming increasingly more acidic (Seedorff et al., 2005). The hydrothermal alteration in this deposit follows a similar fluid evolution with an early, high-temperature biotite alteration that gives way to a lower-temperature and more acidic muscovite alteration. The lack of an argillic alteration zone in this deposit is a departure from the usual porphyry model. The absence of argillic alteration in the deposit area may be explained by either high fluid/rock ratios due to the ingress of seawater that neutralized the fluids before argillic alteration could form or due to the lack of erosion and

collapse of the system, as evident from the preserved CIC and Yeo Formation relationship (Fig. 3.2A).

The paragenesis and distribution of the hydrothermal alteration stages and are schematically shown in Figure 3.26. The spatial distribution of alteration types at the Côté Gold deposit reveals a crude zoning that mimics porphyry deposits: (1) an apparent restriction of amphibole alteration to the south (or bottom) and centre of the deposit (Fig. 3.26A); (2) a potassic-rich core, represented by the hydrothermal biotite breccia (Fig. 3.26A, B), as is documented in porphyry deposits; and (3) an overprinting muscovite alteration zone preferentially towards the centre of the deposit (Fig. 3.26C). Albite alteration has been noted to be proximal and cutting through the orebody and can extend into higher levels in some systems (e.g., Seedorff et al., 2008; Fig. 3.26D). A notable difference, however, is the small epidote alteration zone which contrasts with the widespread zone of propylitic alteration ubiquitous in porphyry deposits.

3.11.4 Timing and distribution of gold mineralization

In terms of the early hydrothermal events (i.e., amphibole and biotite) a syn-magmatic timing for gold is supported by crosscutting relationships and age dates. Gold-bearing hydrothermal amphibole breccias and veins, constrained to ca. 2740 Ma, are demonstrated to crosscut barren host rocks, hence primary gold mineralization accompanied this hydrothermal event. In terms of the hydrothermal biotite breccia, the gold mineralization is restricted to the breccia matrix and no fragment-restricted veins or mineralized fragments have been documented to occur, suggesting that the breccia formed relatively early in the paragenesis. When

hydrothermal breccias are generated early in gold-rich porphyry deposits they are co-temporal with potassic alteration (i.e., biotite-, magnetite- and chalcopyrite-bearing matrices; Sillitoe, 1993, 2010) and can carry higher gold and copper than the surrounding stockwork and disseminated zones (e.g., Panguna; Clark, 1990 and Endeavour 27 at Goonumbla; Jones, 1985). In gold-rich porphyry copper deposits, both gold and copper are introduced together in close spatial association with the potassic alteration zone (Sillitoe, 2000; Ulrich and Heinrich, 2001; Idrus et al., 2009) with gold typically occurring as inclusions within or at the edge of the Cu-Fe sulphide grains (Kesler et al., 2002), as documented at Côté Gold.

The contrast between the gold contents in the hydrothermal biotite breccia compared to the biotite disseminations and stockwork veins is significant and suggests its formation under different conditions. A significant difference between the biotite alteration styles is the higher Mg# in the hydrothermal biotite breccia compared to biotite disseminations and veins. This is of interest because biotite in potassic alteration zones in porphyry deposits is typically Mg-rich (Beane, 1974; Sillitoe, 1993, 2000), which is taken to be an indication of a higher oxidation state (Wones and Eugster, 1965; Beane, 1974). The Fe/Mg ratios in ferromagnesian silicate minerals (i.e., biotite, amphibole and pyroxene) can be used as an indicator of oxidation state (Wones and Euster, 1965; Rowins et al., 1991; Lalonde and Bernard, 1993; Borodina et al., 1999; Shabani et al., 2003). Wones and Euster (1965) recognized an oxidizing trend where biotite becomes increasingly Mg-rich with falling temperature (or progressive crystallization). An increase in Mg# is a reflection of the oxidized conditions in the magma (Rowins et al., 1991) and under these conditions, Fe^{2+} is oxidized to Fe^{3+}. The Fe^{3+} preferentially partitions into Fe^{3+} – bearing minerals, such as magnetite, leading to a deficiency in Fe^{2+} for the crystallization of ferromagnesian minerals (Rowins et al., 1991; Lalonde and Bernard, 1993). As a consequence,

Mg^{2+} will substitute for Fe^{2+} resulting, which results in higher Mg#. This process has been previously described in porphyry systems where the intrusions hosting porphyry deposits crystallized from oxidized magmas that became progressively more oxidized during crystallization, as evidence from increasing Mg# in amphibole and biotite (Mason, 1978; Chivas, 1981).

In this deposit, the Fe/Mg ratios of amphibole and biotite can be similarly used to infer if the magma was becoming progressively oxidized. The increase in Mg# documented in the hydrothermal zoned amphibole (Fig. 3.10G) indicates progressively higher fO_2 and the dioritic magma was becoming progressively more oxidized. The more Fe-rich rims (Fig. 3.10G), however, do indicate that conditions fluctuated.

The biotite in the hydrothermal biotite breccia is characterized by generally higher Mg# than biotite from disseminations and veins, suggesting that the breccia formed under more oxidized conditions in comparison to disseminations and veins. This is consistent with the marked difference in the abundance of hydrothermal magnetite (≤40%) in the breccia compared to disseminated and vein-controlled biotite assemblages (≤1%). The general increase of Mg# from typically barren disseminated biotite to the ore-bearing hydrothermal biotite breccia is consistent with other porphyry deposits where this ratio has been noted to increase towards the orebody, such as Panguna (Ford, 1978) and Bingham (Moore and Czamanske, 1973; Parry et al., 1978). Thus, the change in both the mineralogy and mineral chemistry noted for the hydrothermal biotite breccia is considered relevant, as the physiochemical conditions favourable for the deposition of abundant magnetite (i.e., high fO_2) during potassic alteration also favours the precipitation of gold (Sillitoe, 1979). In addition, the differences noted in the biotite trace

element data further emphasize that the fluids responsible for the formation of the breccia differed from those responsible for the majority of veins and disseminations.

Although a genetic relationship between gold and early alteration events has been established, a genetic relationship with the later alteration events is less certain. In some porphyry systems, gold exsolved as native grains within or adjacent to its host sulphide in the early potassic alteration may be removed or redistributed by cooling or subsequent alteration, such as lower temperature phyllic overprinting (Gammons and Williams-Jones, 1997; Sillitoe, 2000; Kesler et al., 2002). Since muscovite and chlorite alteration can partially to wholly reconstitute earlier potassic assemblages in porphyry deposits, it is often difficult to determine if metals are inherited from the former alteration assemblage (Sillitoe, 2010). In the case here, detailed petrography indicates that chlorite overprints the biotite alteration assemblage inheriting its sulphide assemblage and possibly metal values.

Albite alteration is commonly spatially coincident with gold mineralization, however, it is likely gold was locally redistributed from earlier alteration assemblages. Hydrothermal fluids responsible for sodic-calcic alteration in porphyry deposits are capable of leaching and transporting components in the fresh rock (Seedorff et al., 2008) or that were added in earlier potassic alteration (e.g., K, Fe, Cu, S), as documented in the Ann-Mason porphyry deposit (Dilles and Einaudi, 1992). At Côté Gold, where albite alteration is strongest in the centre of the deposit, gold distribution is less consistently breccia-controlled and becomes erratic. The presence of barren or lower or higher gold grades in albite alteration compared to earlier biotite and muscovite alteration, along with the gold-only signature suggests the fluids responsible for albite alteration leached gold, along with other components (e.g., Fe, Mg, Ca, K, Cu, S).

3.11.5 Comparison with other low-Al composite intrusions

Low-Al diorite-tonalite-trondhjemite intrusions are interpreted to form in extensional settings in oceanic-arc environments (Galley and van Breemen, 2002; Galley, 2003) that underlie temporally and genetically related felsic to intermediate volcanic rocks and are considered the heat and possibly metal source for spatially related VMS-style mineralization (Campbell et al., 1981; Cathles, 1981; Franklin, 1996; Barrie et al., 1999; Galley et al., 2000; Galley, 2003). Some of these low-Al intrusive complexes have been documented to contain porphyry-type Cu-Mo-Au mineralization, such as the Flavrian-Powell (Goldie, 1979; Kennedy, 1985) and Mooshla intrusive complexes (Galley and Lafrance, 2014), hence the discussion of their features are relevant to the present study.

Mineralization styles in these intrusive complexes include breccias, stockworks and veins, which are spatially associated with magmatic-hydrothermal and hydrothermal alteration types that are analogous to porphyry-type alteration (e.g., biotite, actinolite-magnetite-apatite-sulphides, sericite, epidote-quartz; Galley, 2003). For example, at the Don-Rouyn Cu-Mo deposit, which is hosted by the Powell intrusive complex, there is a halo of ferroactinolite-biotite-apatite-sulphide veins (Goldie et al., 1979), which is analogous to calcic-potassic alteration, surrounding a trondhjemite stock. The veins in this system have been suggested to be the product of volatile exsolution from the late-stage, evolved part of a trondhjemitic magma (Galley and van Breemen, 2002; Galley, 2003). The Flavrian pluton is host to the 600 m diameter St. Jude intrusive breccia pipe occurrence that has a biotite-rich Mo-Cu-Au-bearing core and sericite-rich margins with peripheral Zn-Pb-Cu-Ag-Au veins (Kennedy, 1985; Galley and van Breemen, 2002). Both of these aforementioned examples provide analogues for the Côté

Gold deposit and indicate that other high-level, magmatic-hydrothermal systems with porphyry-type mineralization are present in the Archean.

3.11.6 Deposit model

The formation of the CIC is the result of numerous high-level intrusions in a manner characteristic of some other high-level, low-Al subvolcanic intrusive complexes associated with arc-hosted VMS districts. The intrusion-hosted Cu-Mo and Au-Cu mineralization hosted within these intrusive systems have been considered as part of the submarine equivalents of the porphyry-epithermal continuum, as advocated by Sillitoe et al. (1996) and Hannington et al. (1997).

The Côté Gold deposit appears to represent an Archean analogue to porphyry-type deposits in which a magmatic-hydrothermal system developed from a dioritic magma, resulting in vein, disseminated and breccia-hosted mineralization coincident with the formation of distinct hydrothermal alteration types (amphibole, biotite, muscovite). In contrast, volatile exsolution from the tonalite resulted in a barren albite alteration that overprinted the other alteration assemblages and appears to have remobilized some of the earlier gold.

The smaller size of the system relative to many Phanerozoic porphyry deposits (i.e., >billion tonnes) is considered to be the result of a one-off system which contrasts with the well-demonstrated overlap of multiple magmatic and hydrothermal events in most porphyry systems (Seedorff et al., 2005; Sillitoe 2010), with some lasting several million years (e.g., Sillitoe and Mortensen, 2010). This latter observation may be attributed to the tectonics of the Archean and model for the generation of low-Al diorite-tonalite-trondhjemite intrusions. Although a back-arc

setting is inferred for the deposit, not all modern porphyry systems are part of subduction settings with a few systems having formed in collisional, post-collisional and extensional settings that develop after subduction has ceased (Richards, 2009), for example, Cripple Creek (Kelley et al., 1998; Kelley and Ludington, 2002) and the Climax-type Mo deposits (Ludington and Plumlee, 2009). Thus, a direct link to subduction zone processes is not a necessity for all porphyry deposits.

This study highlights the many similarities between the general features of the Côté Gold deposit with Phanerozoic porphyry deposits. As such, this deposit should be considered an Archean analogue for porphyry-type deposits.

3.12 Conclusions

The Côté Gold deposit is a low-grade, large-tonnage Au(-Cu) deposit with many of its characteristics similar to Phanerozoic gold-rich porphyry copper systems. The evidence of an overlap between magmatic and hydrothermal events at ca. 2740 Ma, supported by robust U-Pb and Re-Os geochronology, and the genetic association of early alteration types, in particular, amphibole and biotite, with a diorite complex suggests the deposit is intrusion-related in origin. Although some differences exist, such as the apparent lack of widespread propylitic alteration, the deposit is broadly similar with porphyry-type deposits in terms of the nature of host rocks, the alteration assemblages (e.g., amphibole, biotite, muscovite, albite) and the mineralization styles (e.g., disseminations, sheeted vein arrays, stockworks and breccias). The characteristics of the deposit, such as the Au- and Cu-bearing potassic core (i.e., the hydrothermal biotite breccia) and its association with abundant hydrothermal magnetite, suggests it is analogous to the gold-

rich porphyry copper deposits. At this time, the potential for remobilization of gold by later alteration stages (i.e., albite) and possible overprinting effects due to later, regional deformation events on the deposit remain poorly constrained but the latter is not considered to be significant.

Importantly, the deposit defines a new gold metallogenic event at 2740 Ma in the prolific Abitibi Subprovince. Lastly, it is suggested that based on this study porphyry-type systems may be more common in the Archean than is presently recognized and that low-Al composite tonalite-trondhjemite-diorite intrusive complexes, which appear to form as part of a submarine porphyry-epithermal continuum, warrant more thorough exploration.

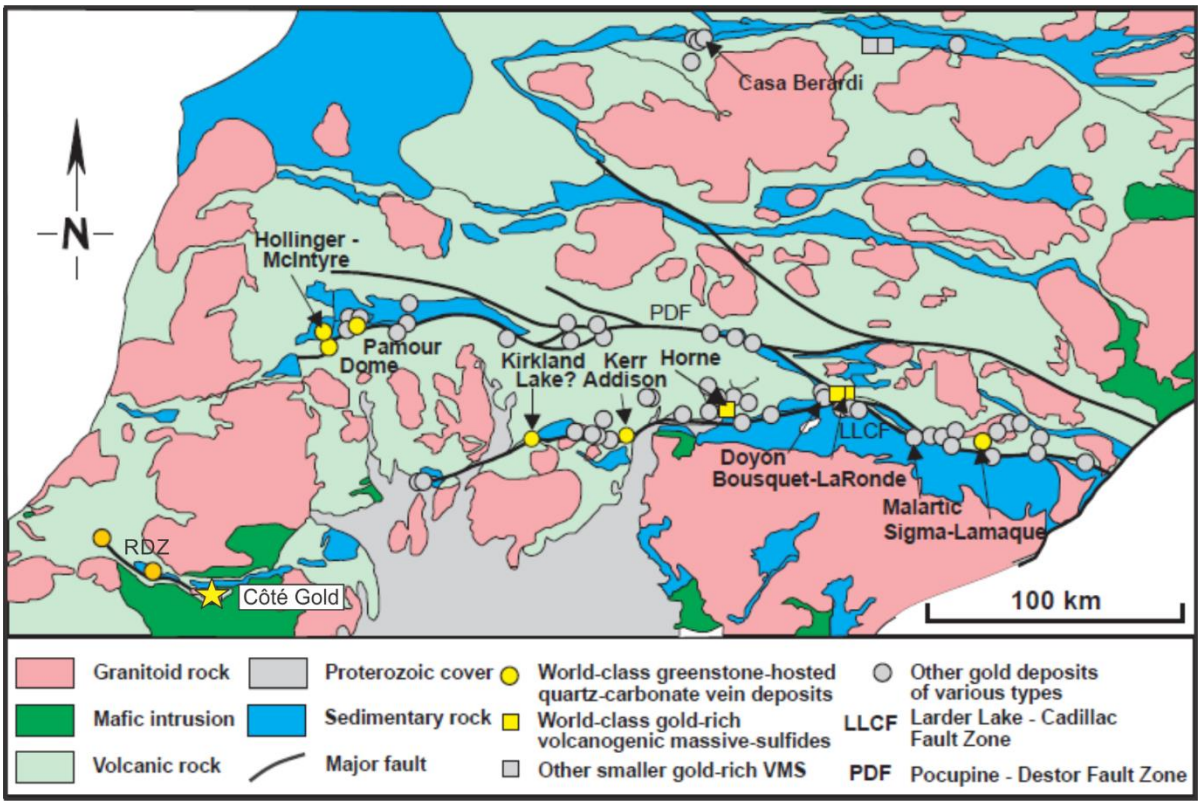

Figure. 3.1. Regional geological map of the Abitibi Subprovince showing the distribution of major gold deposits and also main structural features, in particular the Porcupine-Destor and Larder Lake-Cadiallac faults zones (modified after Dubé and Gosselin, 2007). The yellow star shows the location of the Côté Gold deposit and the Ridout deformation zone (RDZ) is labelled towards the bottom left of the map.

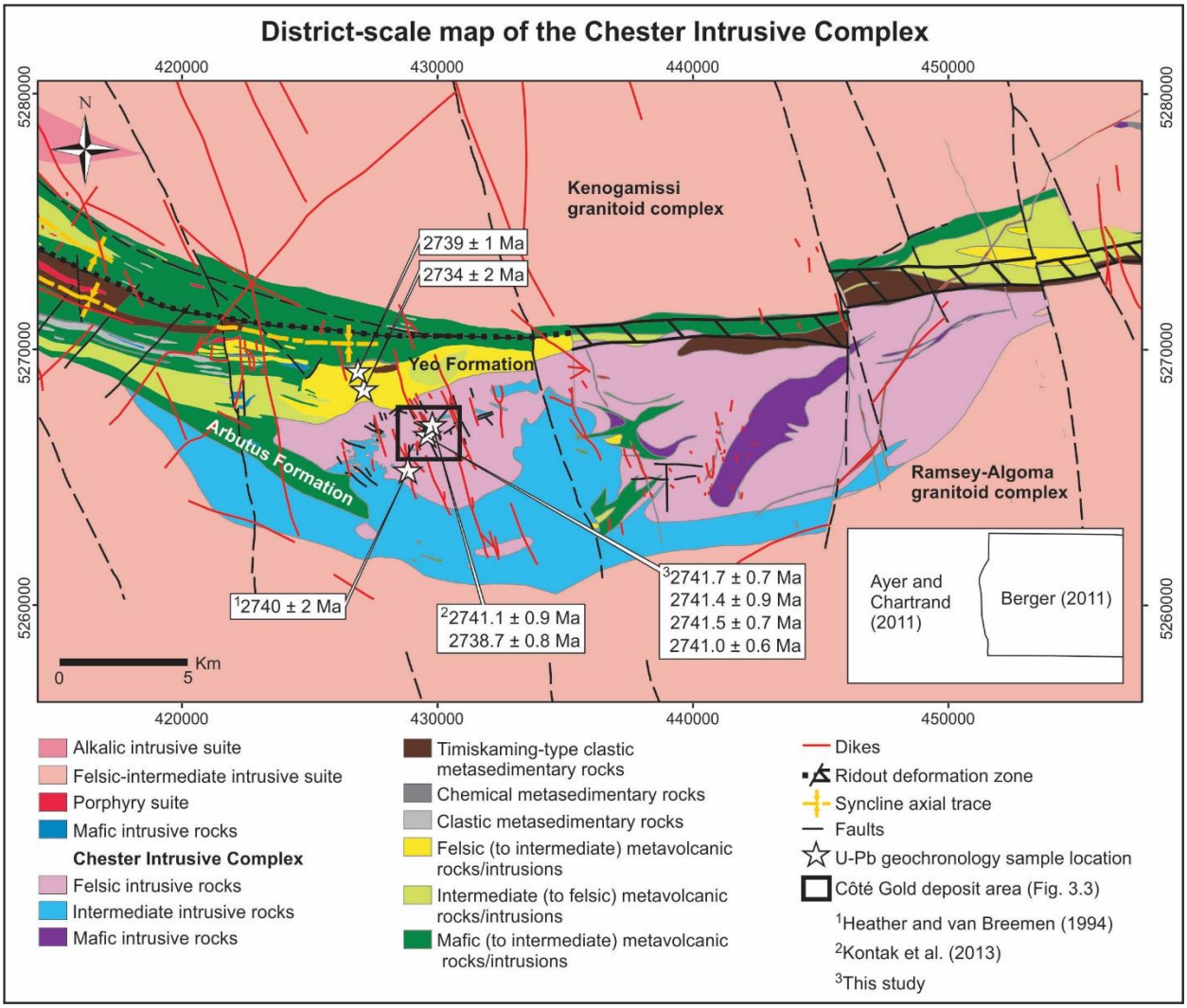

Figure 3.2A. Simplified district-scale geological map of the Chester intrusive complex and the southeastern arm of the Swayze greenstone belt, as compiled from Ayer and Chartrand (2011) and Berger (2011); the inset map shows the area mapped by both groups. Note the Ridout deformation zone extends further west through the map area past where the detailed mapping of Berger (2011) terminates. The Côté Gold deposit area is shown by the black outline. Previous U-Pb geochronology results are discussed in the text.

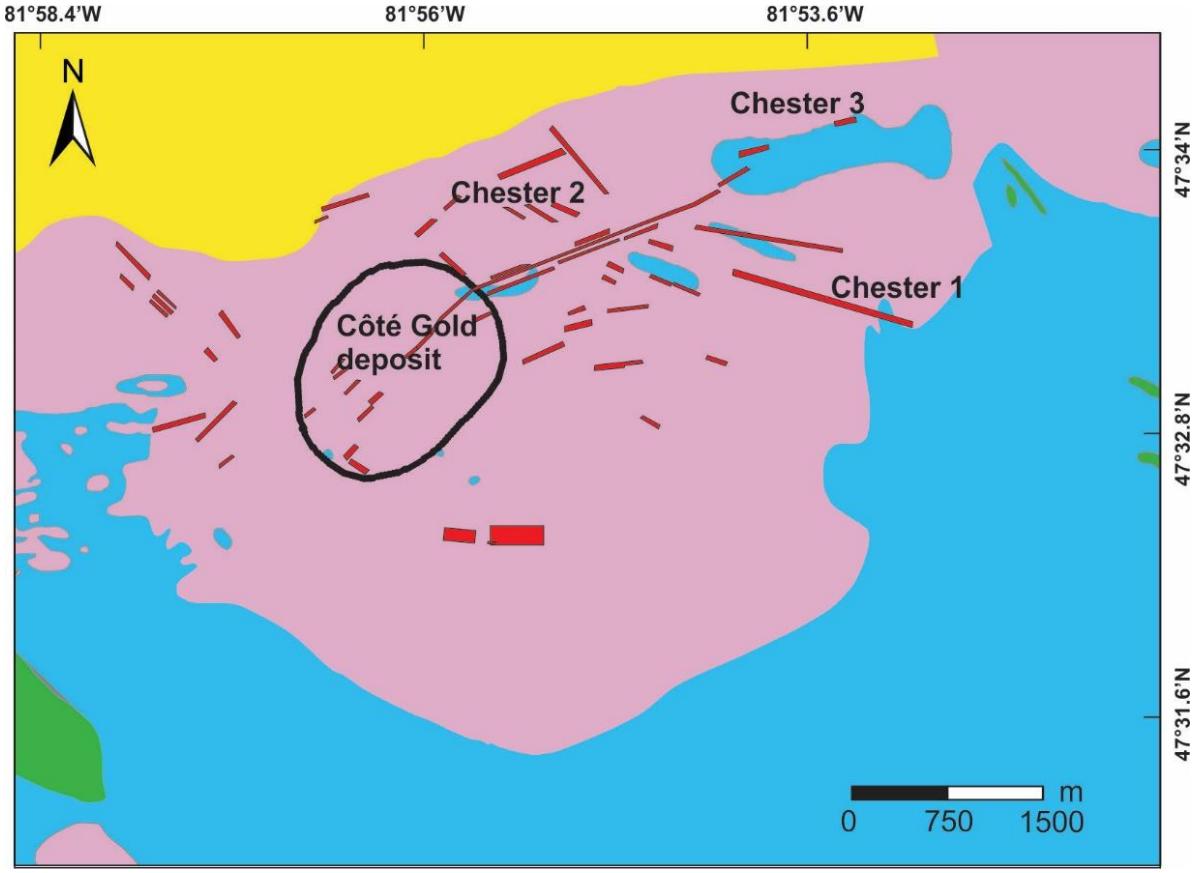

Figure 3.2B. Enlargement of Figure 3.2A showing the Côté Gold deposit and surrounding area; note the geology of the Yeo Formation has been simplified. The legend from Figure 3.2A applies here. The red lines show the location of mineralized zones with the more important occurrences labelled. Note the Chester 1 is also known as the Chester-1 zone.

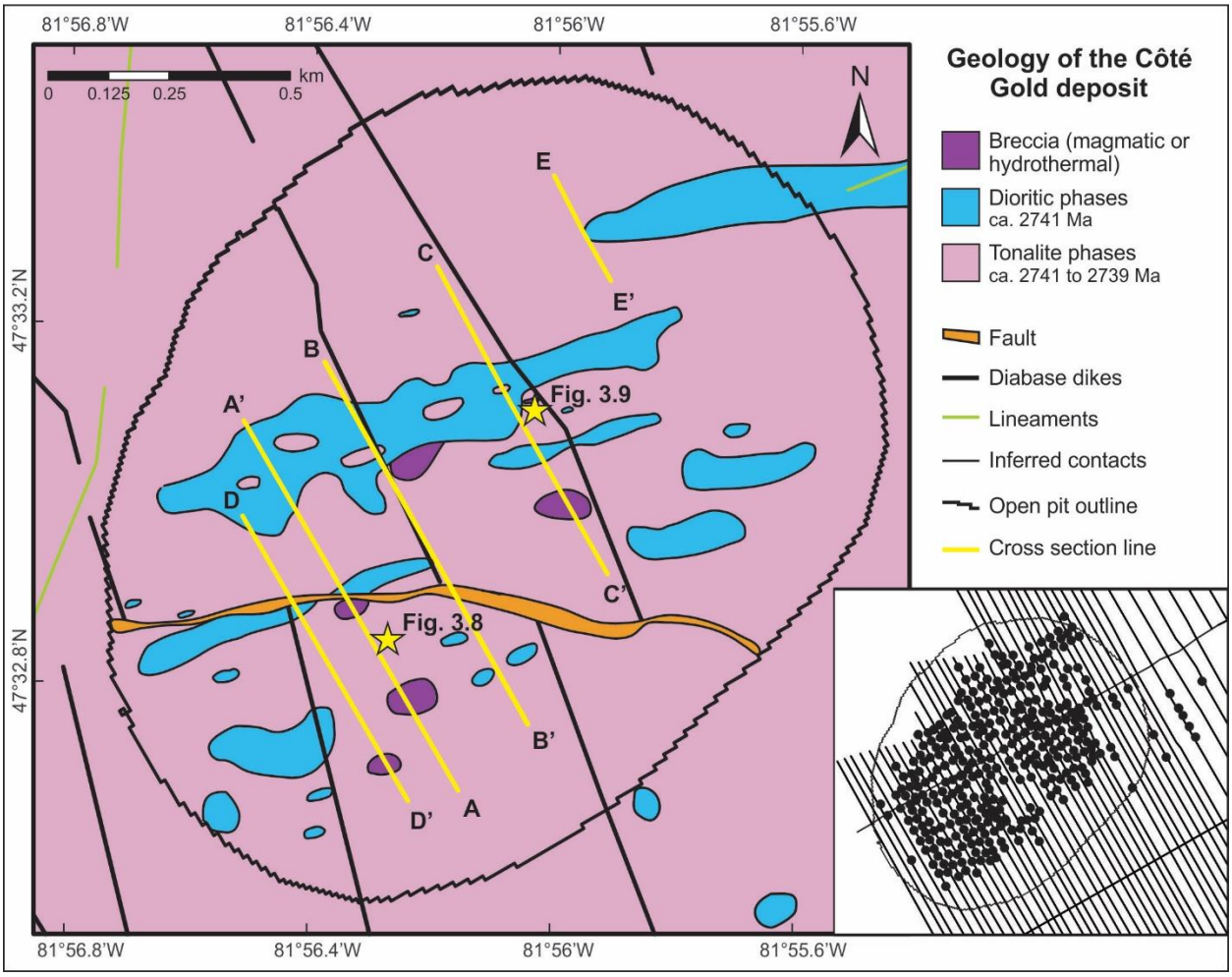

Figure 3.3. Simplified geological map of the open pit shell of the Côté Gold deposit which was created by using the first bedrock collared in the 373 diamond drill holes available and several outcrops in the deposit area. The inset map shows the distribution of the drill holes used to construct the map. The vertical cross sections are denoted by the lines A-A' (Fig. 3.5), B-B' and C-C' (Fig. 3.6), D-D' (Fig. D.1) and E-E' (Fig. D.2); the latter two sections can be found in Appendix D. The yellow stars show the locations of Figures 3.8 and 3.9.

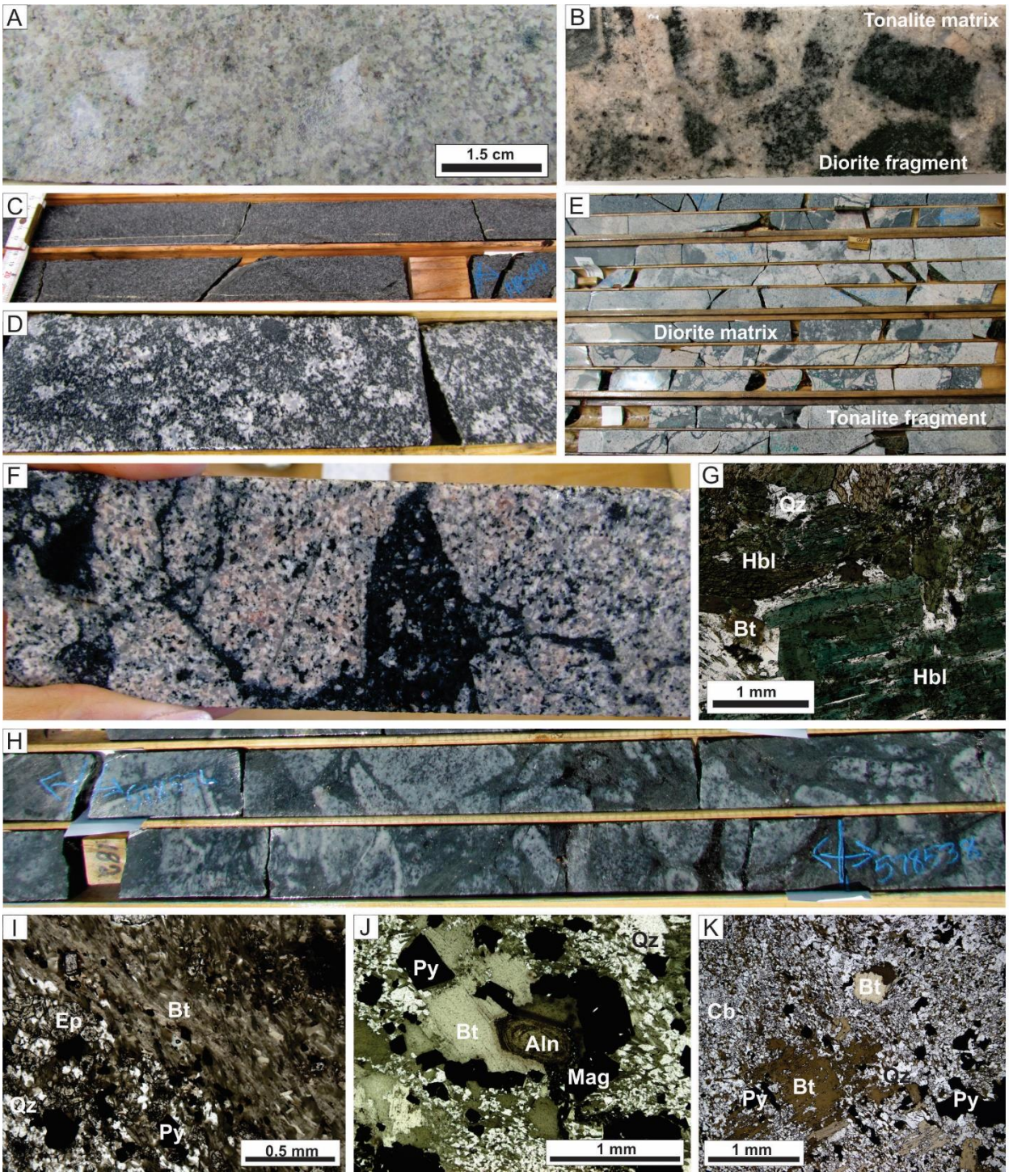

Figure 3.4. Drill core (4.5 cm in width) and thin section photographs in plane polarized light of the major rock types at the Côté Gold deposit. A) The least-altered tonalite with an equigranular texture. B) An example of a tonalite breccia with diorite fragments. C) An example of a medium-grained, melanocratic diorite. D) A medium-grained, melanocratic quartz diorite with quartz phenocrysts. E) A magmatic breccia with tonalite fragments in a medium-grained diorite matrix. F) A hydrothermal amphibole breccia with amphibole altered tonalite fragments in a fine-grained, black amphibole-rich matrix. G) Thin section photo of the hydrothermal amphibole breccia matrix composed of amphibole, quartz and biotite. H) A hydrothermal biotite breccia with fragments of biotite altered

tonalite. I) Thin section photo of the hydrothermal biotite breccia matrix assemblage i. J) Thin section photo of hydrothermal biotite breccia matrix assemblage ii. K) Thin sections of the hydrothermal biotite breccia matrix assemblage iii; note the different mineral assemblages, referred to as i, ii and iii, are found in Table 3.1. Abbreviations: Aln = allanite, Bt = biotite, Cb = carbonate, Ep = epidote, Hbl = hornblende, Mag = magnetite, Py = pyrite, Qz = quartz.

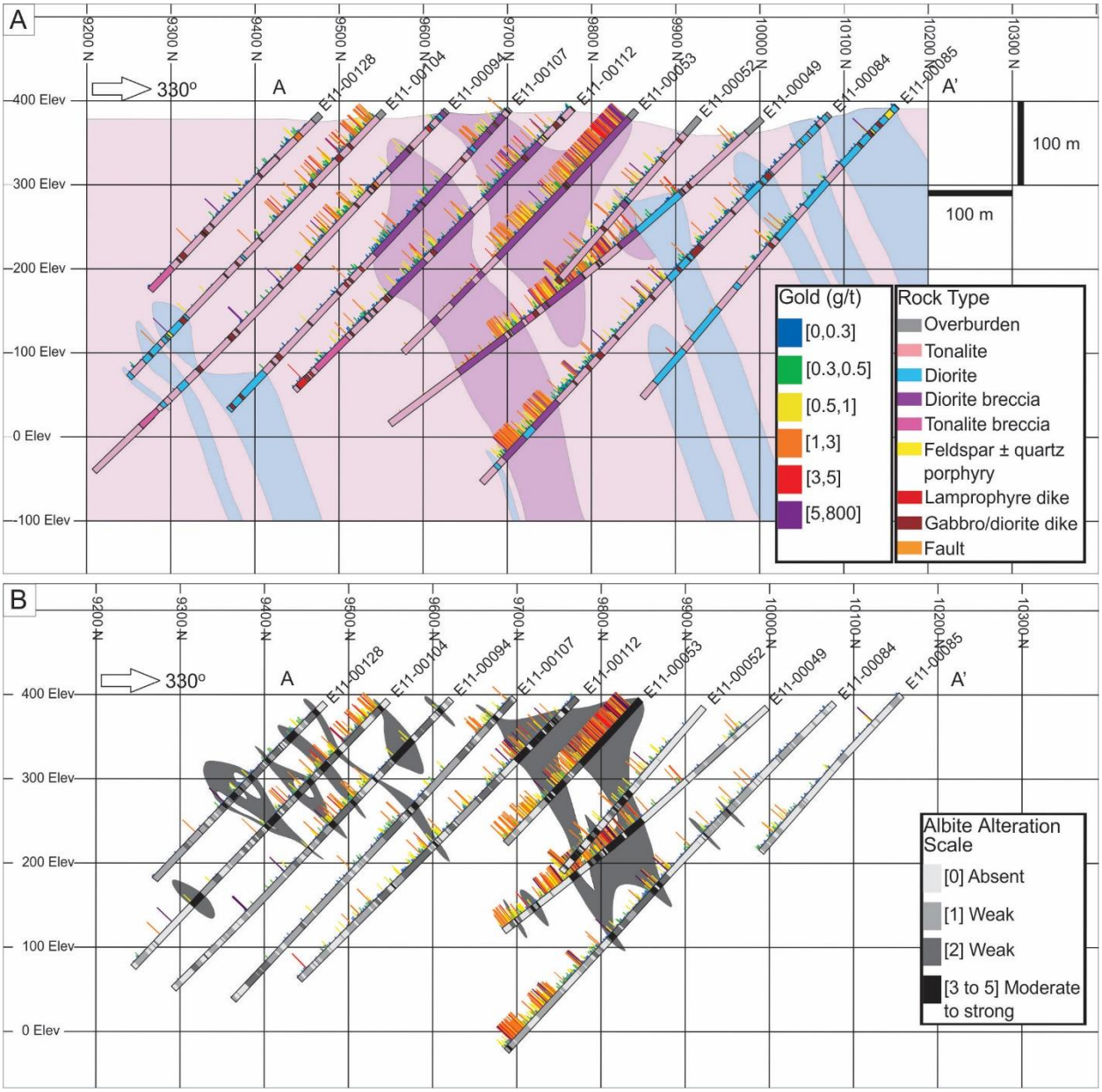

Figure 3.5. Vertical cross sections of grid line 87+00 (A-A'; see Fig. 3.3 for location) from the Côté Gold deposit. A) Geological cross section showing major and minor rock types. Note that the gold mineralization is co-spatial with the breccia body, but mineralization also occurs outside the breccia body in the tonalite shouldering the breccia body. B) Cross section showing both the intensity (scale of 1 to 5; 1 = weak and 5 = strong) and distribution of albite alteration. Areas of more intense albite alteration are shaded in grey.

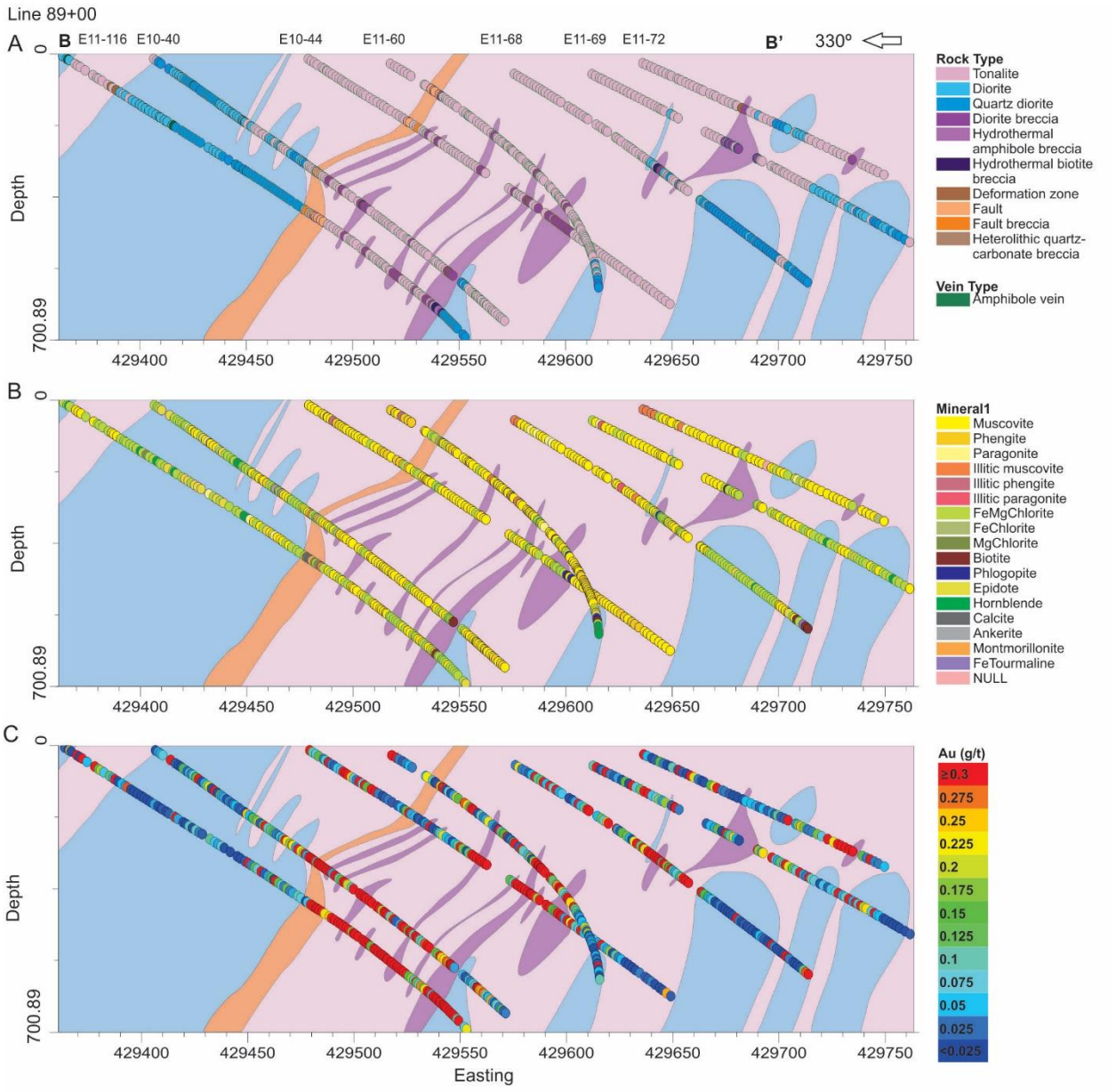
Line 89+00
A
B
E11-116
E10-40
E10-44
E11-60
E11-68
E11-69
E11-72
B'
330°
Depth
0
700.89
429400
429450
429500
429550
429600
429650
429700
429750
Rock Type
Tonalite
Diorite
Quartz diorite
Diorite breccia
Hydrothermal amphibole breccia
Hydrothermal biotite breccia
Deformation zone
Fault
Fault breccia
Heterolithic quartz-carbonate breccia
Vein Type
Amphibole vein
B
Mineral1
Muscovite
Phengite
Paragonite
Illitic muscovite
Illitic phengite
Illitic paragonite
FeMgChlorite
FeChlorite
MgChlorite
Biotite
Phlogopite
Epidote
Hornblende
Calcite
Ankerite
Montmorillonite
FeTourmaline
NULL
C
Au (g/t)
≥0.3
0.275
0.25
0.225
0.2
0.175
0.15
0.125
0.1
0.075
0.05
0.025
<0.025
Easting

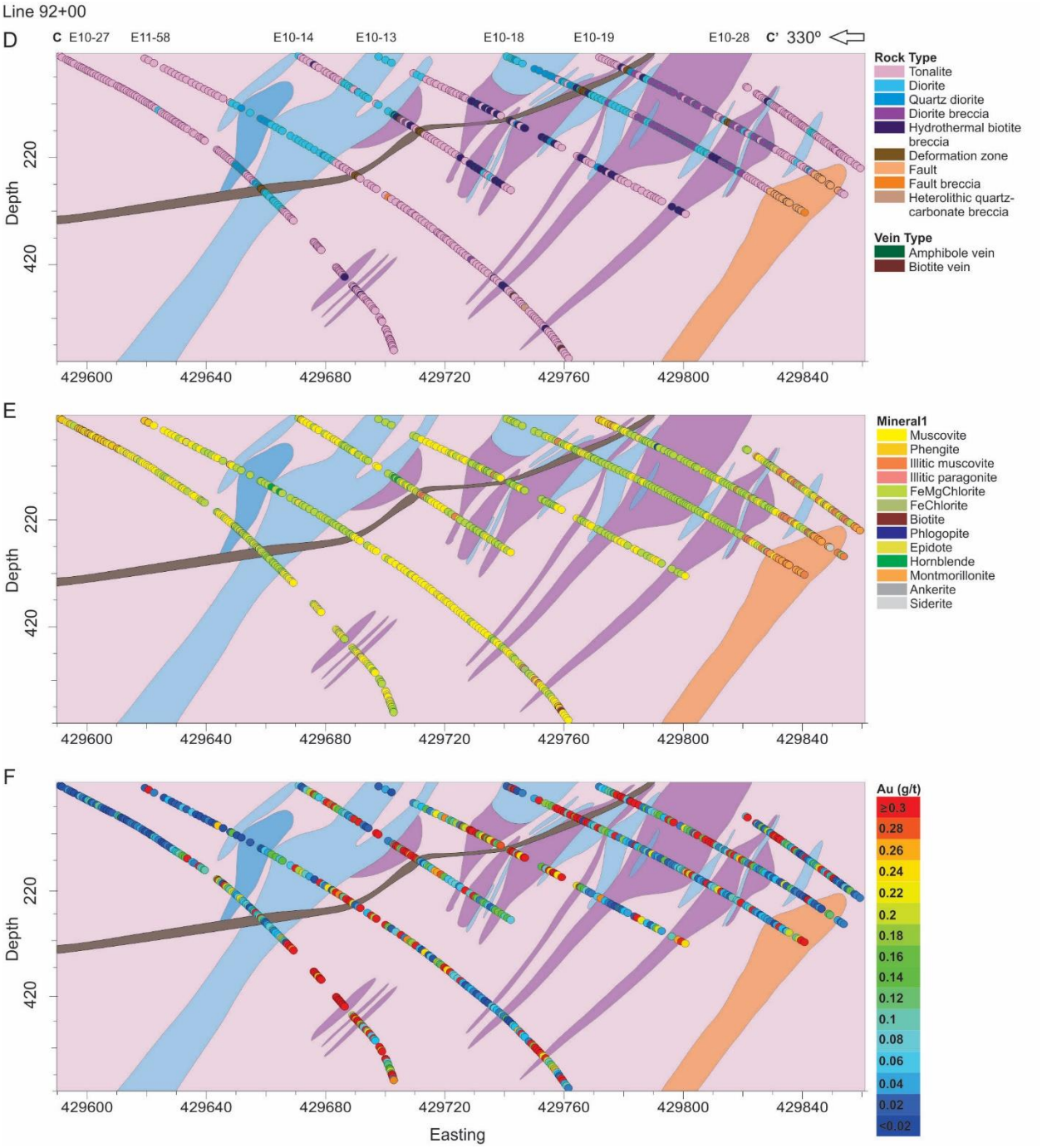

Figure 3.6. Vertical cross sections of grid lines 89+00 (A-C) and 92+00 (E-F) from the Côté Gold deposit based on TerraSpec results. The locations of these sections are found in Figure 3.3. A) A geological interpretation of grid line 89+00 showing major rock types. B) The dominant mineral in the sample (Mineral1), as inferred from TerraSpec measurements, is displayed. C) The distribution of Au is displayed and shown to be spatially coincident with the breccia bodies. D) A geological interpretation of grid line 92+00 showing major rock types. E) The primary alteration mineral present (Mineral1), as inferred from TerraSpec measurements, is displayed. F) The distribution of Au is displayed and shown be erratic. Gold mineralization is not consistently associated with breccia bodies.

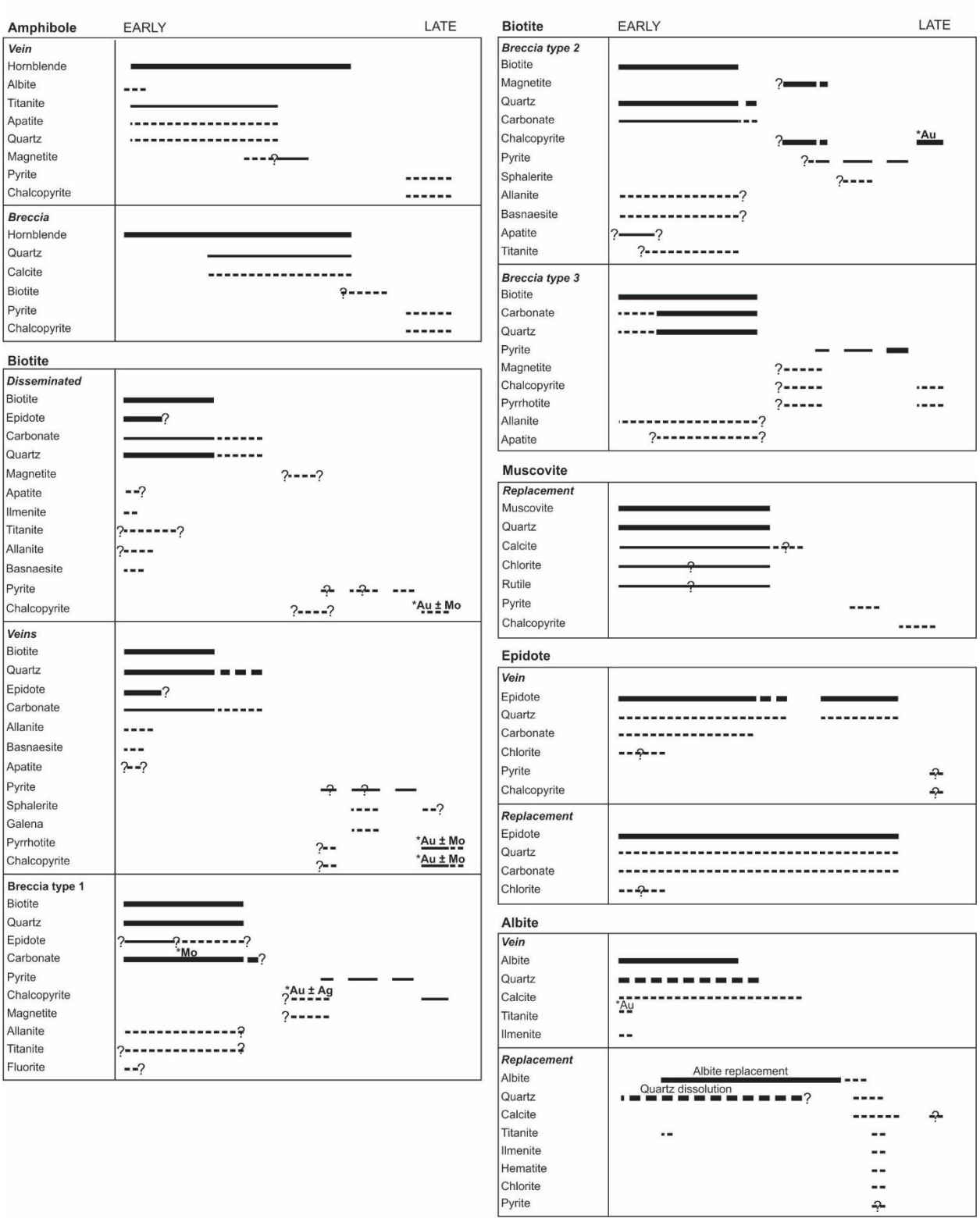

Figure 3.7. Mineral paragenesis for each of the different hydrothermal stages at the Côté Gold deposit.

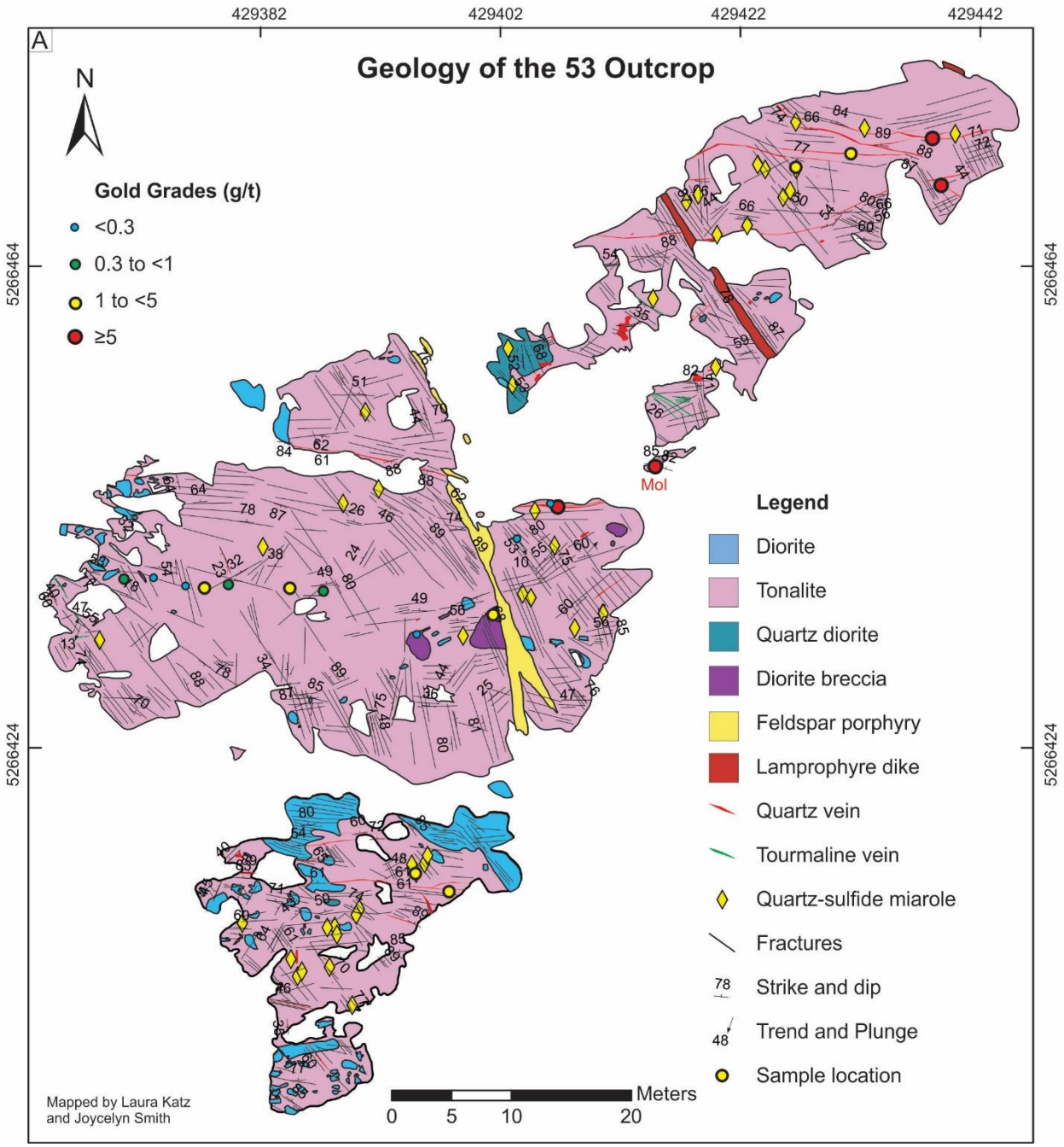
A
Geology of the 53 Outcrop
N
429382
429402
429422
429442
5266464
5266424
Gold Grades (g/t)
<0.3
0.3 to <1
1 to <5
≥5
Mol
Legend
Diorite
Tonalite
Quartz diorite
Diorite breccia
Feldspar porphyry
Lamprophyre dike
Quartz vein
Tourmaline vein
Quartz-sulfide miarole
Fractures
Strike and dip
Trend and Plunge
Sample location
Meters
0 5 10 20
Mapped by Laura Katz
and Joycelyn Smith

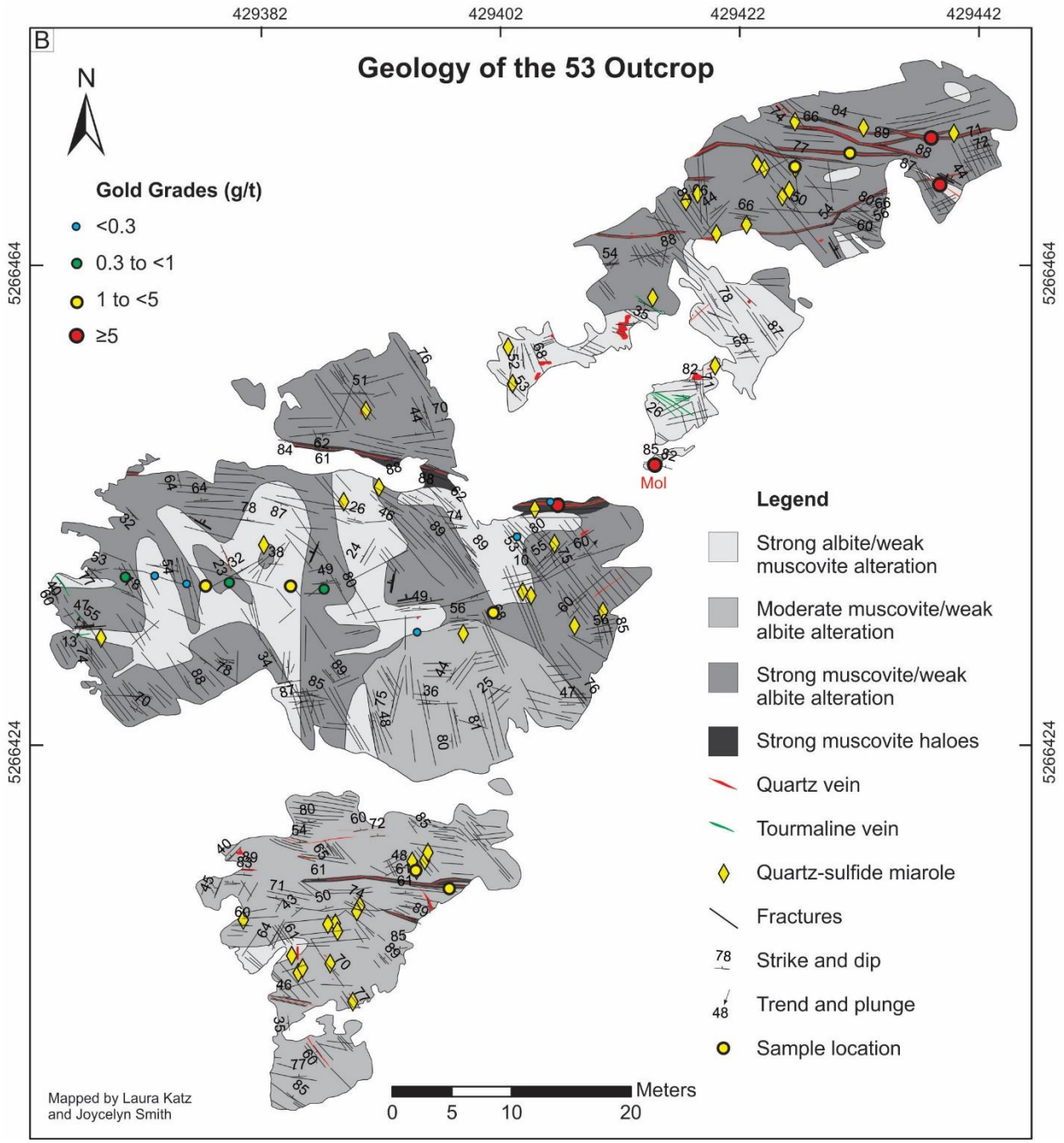

Figure 3.8. A) Geological map of the 53 Outcrop showing the different rock types and their relative timing relationships, distribution and intensity of fractures and the different vein types. B) Alteration map of the 53 Outcrop that shows the relative intensity and distribution of muscovite and albite alteration.

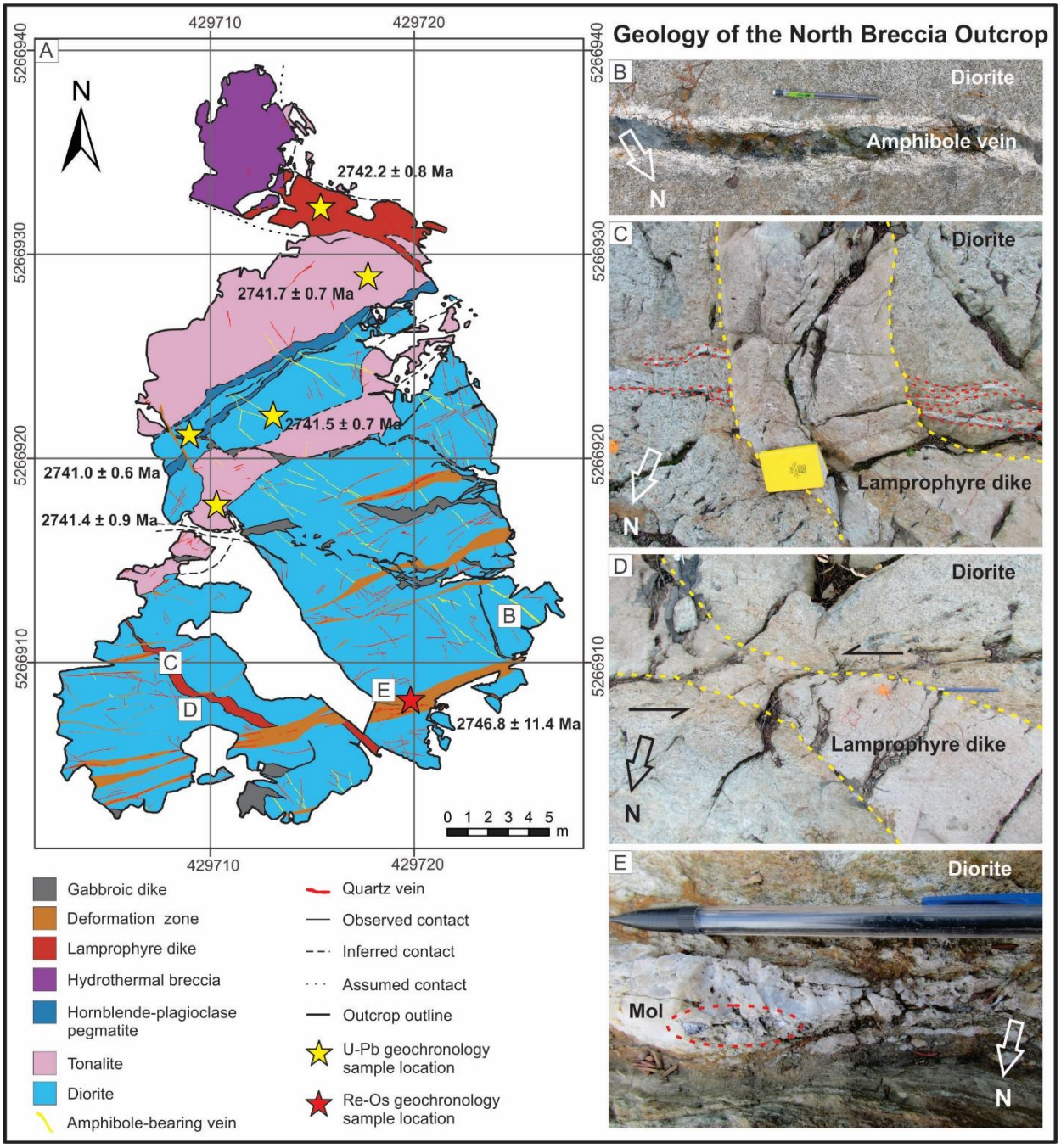

Figure 3.9. A) Geological map of the North Breccia Outcrop which shows the important crosscutting relationships and the location of the Re-Os molybdenite sample (NBxMolyLK13) dated in this study. The locations of U-Pb zircon samples with their ages (Chapter 2) are also shown. Representative amphibole-bearing veins and quartz veins are included. B) An amphibole-bearing vein with an albite selvage cutting diorite. C) East-west trending quartz veins that are cut by a lamprophyre dike. The yellow book for scale is 19 x 12 cm. D) A lamprophyre dike with a sinistral offset that cuts through diorite. The blue pencil for scale is 18 cm long. E) A photo of an east-west trending quartz-molybdenite-gold ± tourmaline vein that is overprinted by the same deformation zone which offsets the lamprophyre dike in C; Mol = molybdenite. Pencil for scale is 15 cm long.

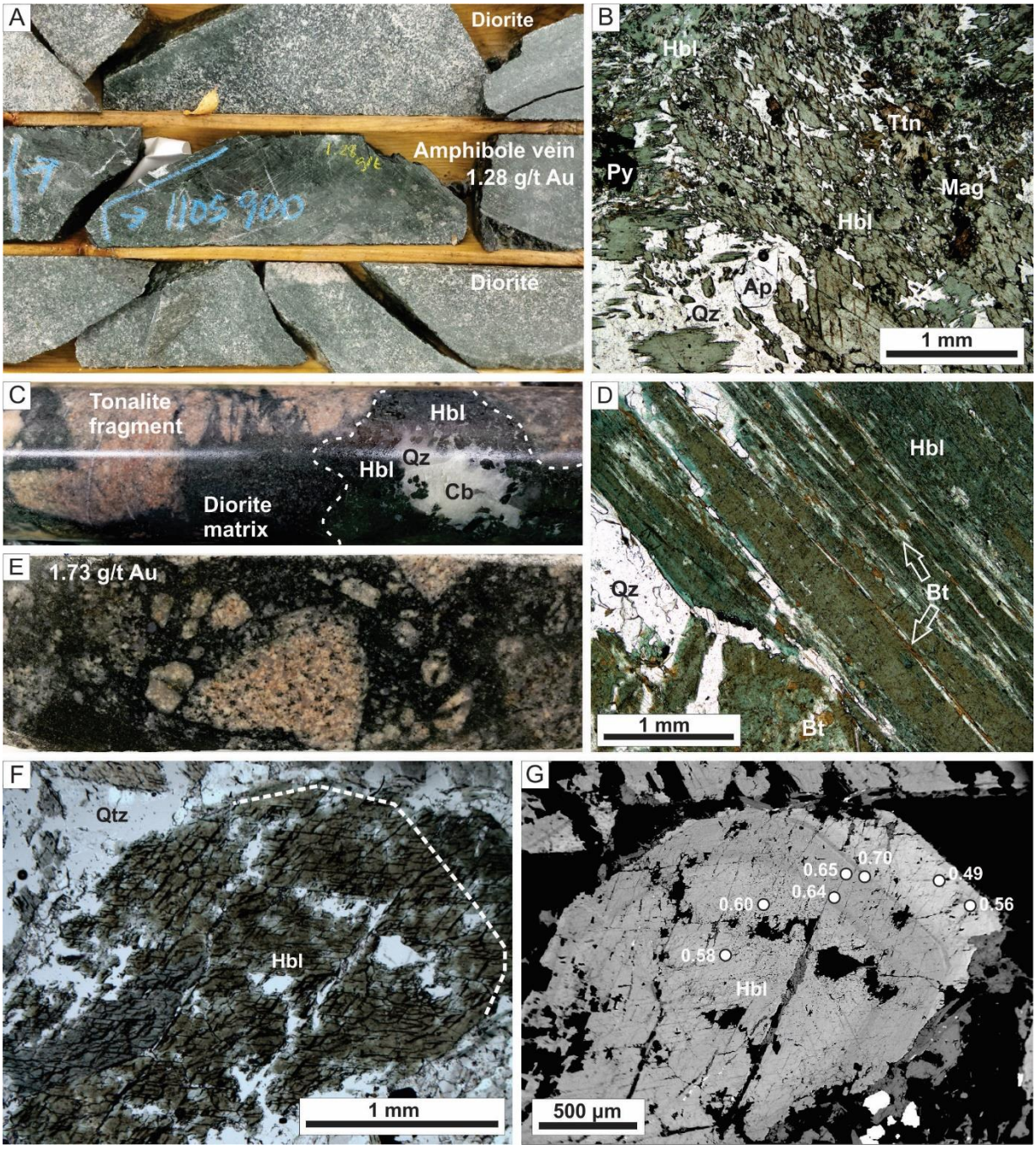

Figure 3.10. Drill core photographs (4.5 cm in width), thin section photographs in plane polarized light and backscatter electron (BSE) images of the hydrothermal amphibole event. A) A gold-bearing hornblende vein (1.28 g/t Au over a 1 m sample) cutting barren diorite. B) Thin section photo of a hornblende-quartz-titanite-magnetite-apatite-pyrite vein. C) A hornblende-quartz-carbonate vein cutting a diorite breccia with tonalite fragments. D) Thin section photo of coarse-grained hornblende in a vein that is partially replaced by biotite along cleavage planes. E) A mineralized (1.73 g/t Au over a 1 m sample) hydrothermal amphibole breccia with tonalite and diorite fragments. F) Thin section photo of a zoned hydrothermal amphibole in G from a breccia. G) A BSE image of zoned amphibole with microprobe analysis location shown in white dots with the associated Mg#. Abbreviations: Ap = apatite, Bt = biotite, Cb = carbonate, Hbl = hornblende, Mag = magnetite, Py = pyrite, Qz = quartz, Ttn = titanite.

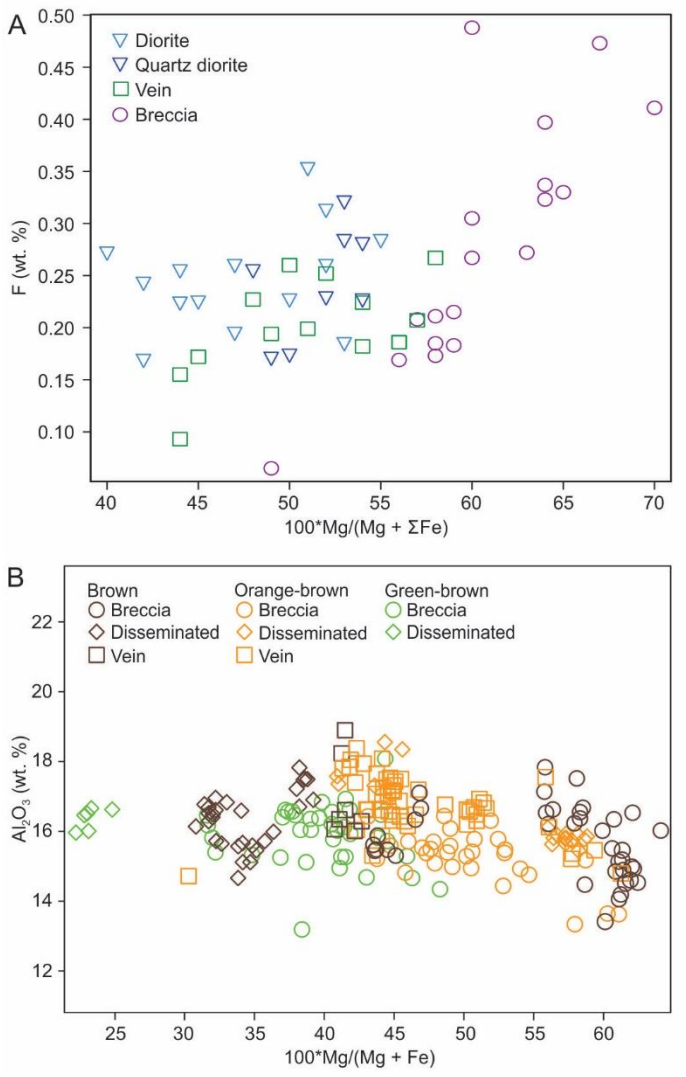

Figure 3.11. A) A bivariate plot of F (wt. %) vs. Mg# (100*Mg/(Mg + ΣFe)) of magmatic and hydrothermal amphiboles from microprobe analyses from samples DR, QDR, Bx and Vn (See Table C.1 in Appendix C for microprobe analyses). B) A bivariate plot of Al_2O_3 (wt. %) vs. Mg# (100*Mg/(Mg + Fe)) for different coloured hydrothermal biotites from microprobe and SEM-EDS analyses (See Table C.2 in Appendix C for microprobe analyses).

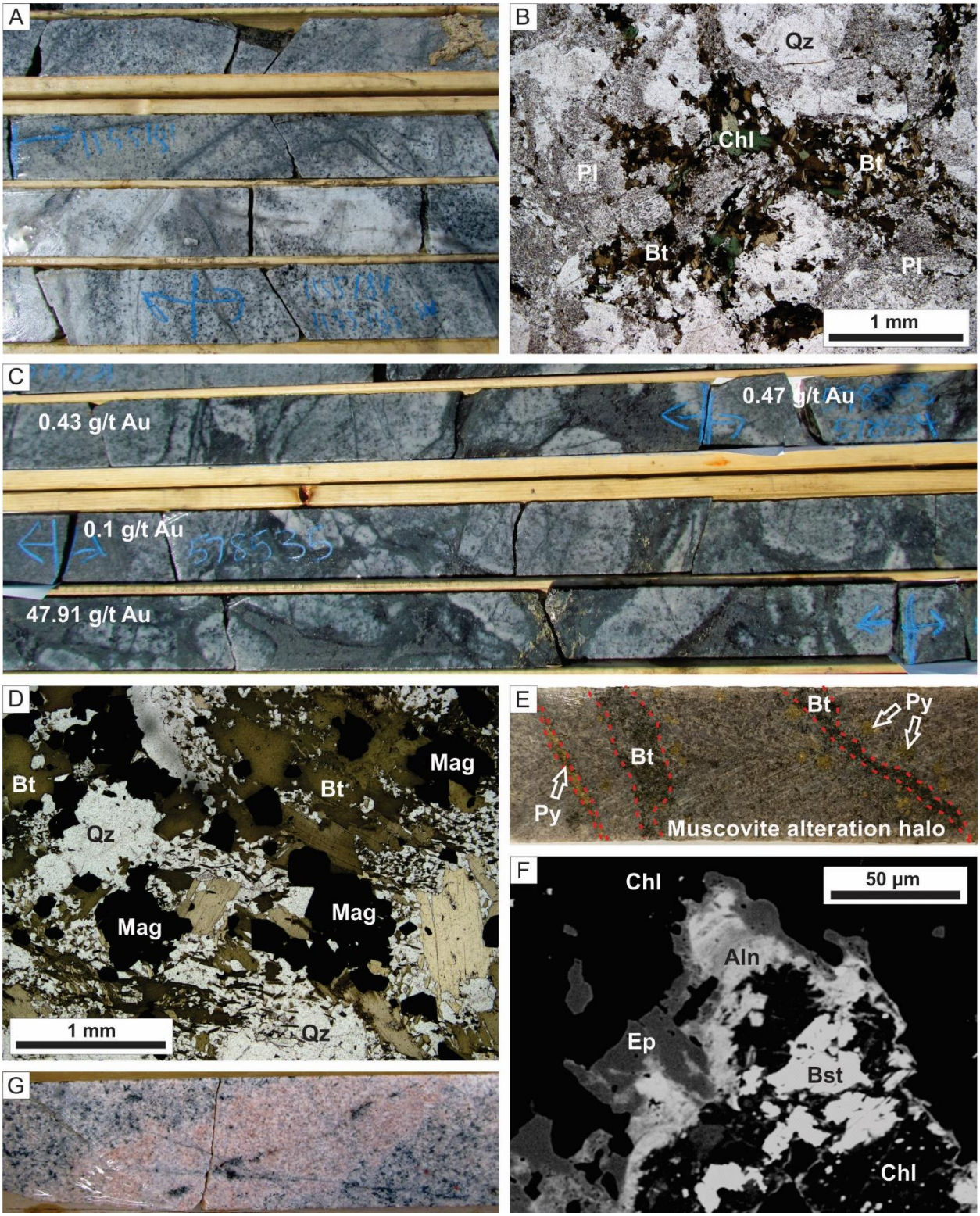

Figure 3.12. Drill core (4.5 cm in width) and thin section photographs, along with a backscatter electron (BSE) image, of biotite alteration. A) Biotite alteration occurring as both disseminated, fine-grained, black to dark-brown material and also coating fractures in the host tonalite. B) Thin section photo in plane polarized light showing secondary, fine-grained, light-brown to dark-brown, anhedral biotite replacing primary plagioclase in tonalite. Note

that chlorite partially replaces biotite. C) Mineralized (Au grades over a 1 m sample) hydrothermal biotite breccia with fragments of biotite altered tonalite. D) Thin section photo in plane polarized light of a hydrothermal biotite breccia matrix with a biotite-quartz-magnetite assemblage. E) Example of subparallel, E-W trending sheeted quartz-pyrite-biotite veins hosted by tonalite; the veins are outlined by red dashed lines. Note the veins are overprinted by muscovite alteration. F) A BSE image of chlorite (after biotite) with bastnaesite which is surrounded by allanite and then epidote in a tonalite sample. G) An unaltered dikelet of tonalite cutting earlier biotite altered tonalite which are both crosscut by biotite-bearing veins. Abbreviations: Aln = allanite, Bst = basnaesite, Bt = biotite, Chl = chlorite, Ep = epidote, Mag = Magnetite, Pl = plagioclase, Py = pyrite, Qz = quartz.

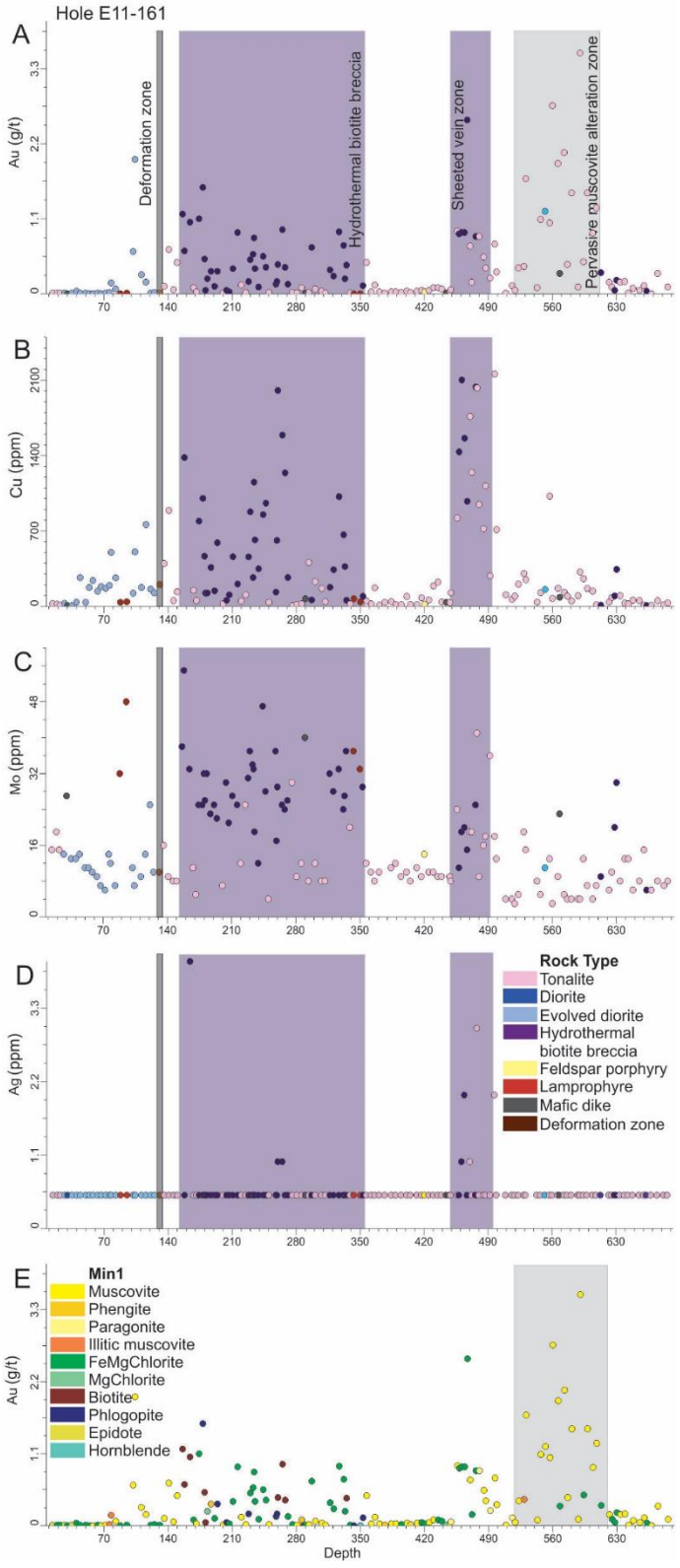

Figure 3.13. Metal vs. depth plot of drill hole E11-161 showing a small deformation zone (130 m), a Au-Cu-Mo ± Ag association in the hydrothermal biotite breccia (150 to 350 m) and sheeted vein zone shouldering a small breccia unit (450 to 500 m) and a Au-only pervasive muscovite alteration zone (520 to 620 m) in tonalite. In these plots high

Au, Cu, Mo and Ag values have been omitted for clarity. This drill hole is found on cross section line E-E'; see Fig. 3.3 for location. A) Gold vs. depth plot. B) Copper vs. depth plot. C) Molybdenum vs. depth plot. D) Silver vs. depth plot. E) Gold vs. depth plot showing the primary alteration mineral (Min1) as determine from TerraSpec analysis. Note that the Au-only zone occurs in a zone of strong, pervasive muscovite alteration where no secondary minerals were detected by the TerraSpec.

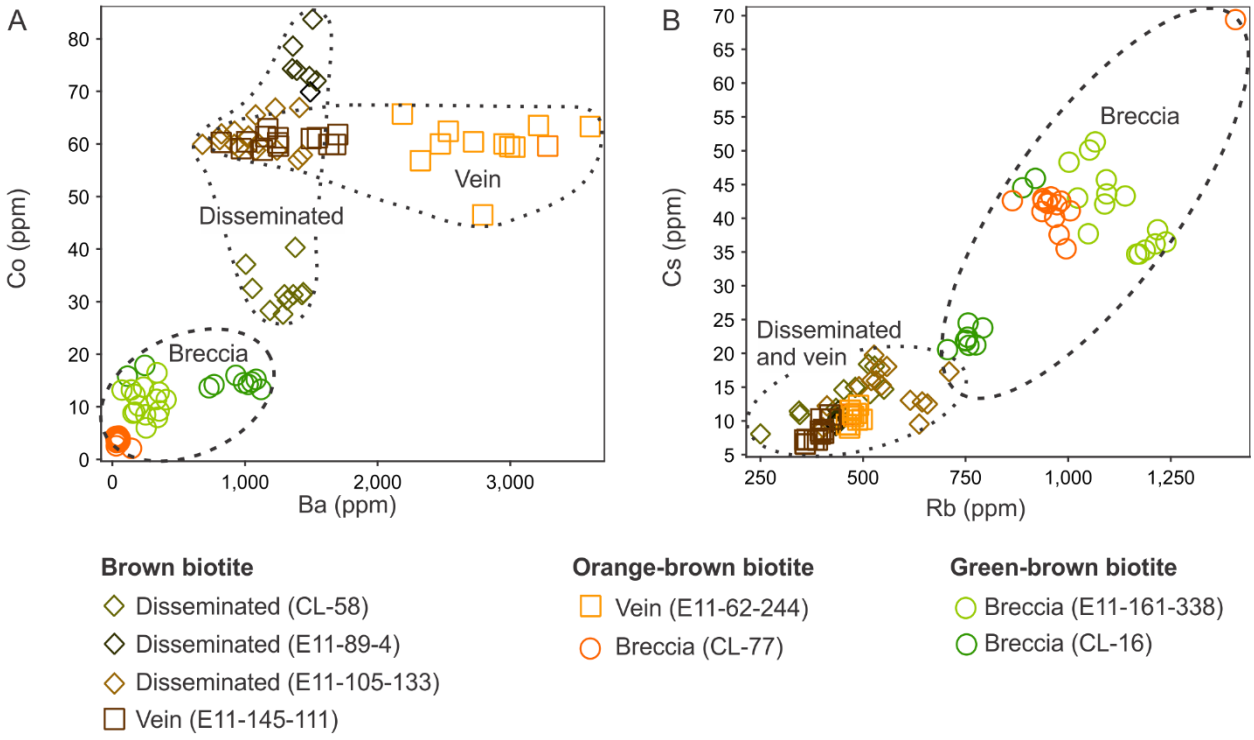

Figure 3.14. Bivariate plots summarizing the trace element chemistry of biotite as determined from LA ICP-MS analysis for disseminated, vein and breccia types. A) Plot of Co vs. Ba. B) Plot Cs vs. Rb.

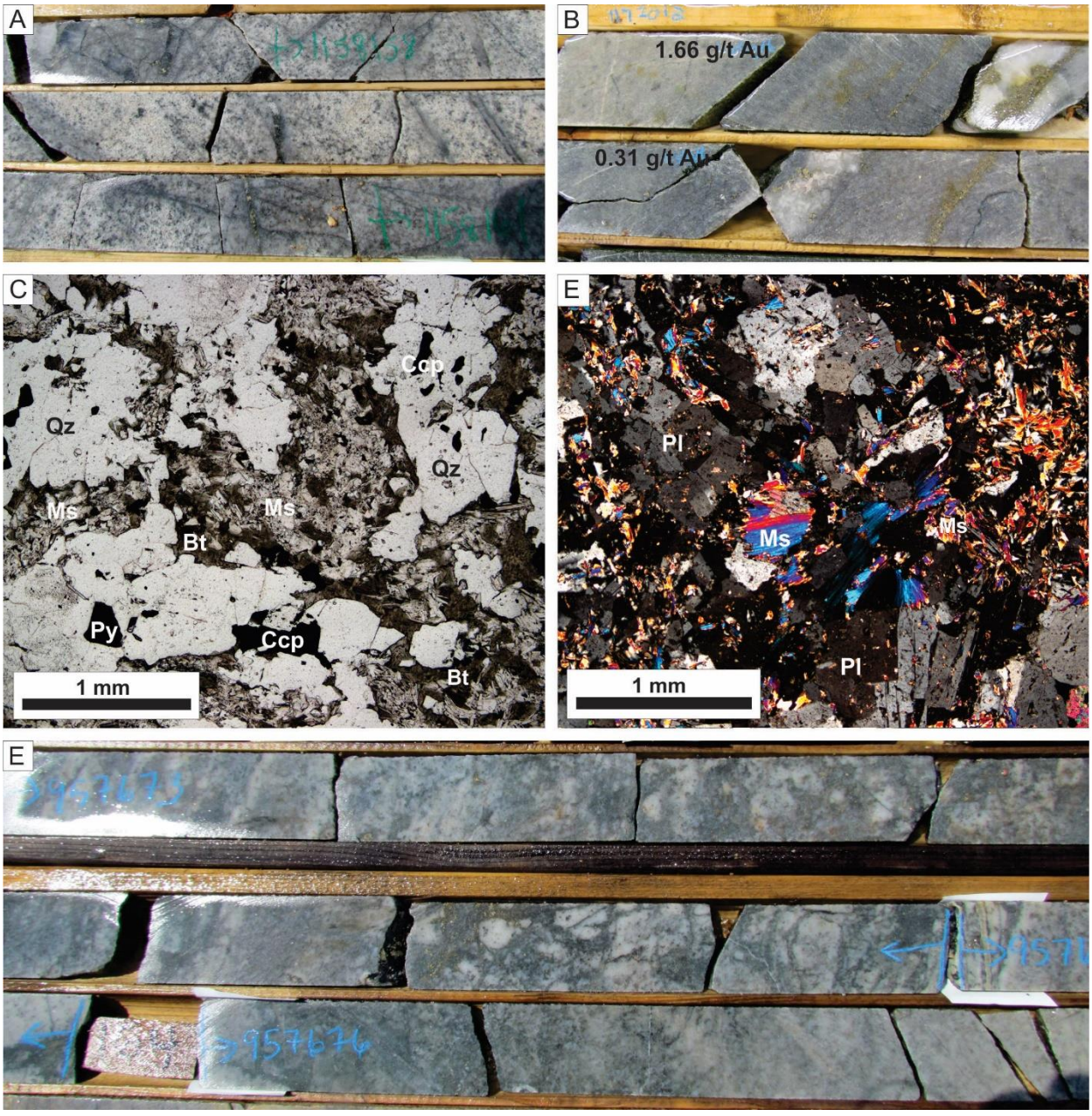

Figure 3.15. Drill core (4.5 cm in width) and thin section photographs of muscovite alteration. A) Quartz-biotite-pyrite stockwork-like veins in tonalite that are overprinted by muscovite alteration haloes (i.e., darker grey areas). B) Sub-parallel, gold-bearing sheeted quartz-pyrite veins with strong muscovite alteration haloes in tonalite; gold grades correspond to 1 m core length samples. C) Thin section photo in plane polarized light of hydrothermal biotite in a sheeted quartz-biotite-pyrite-chalcopyrite vein that is partially replaced by muscovite. D) Thin section photo in cross polarized light of fine-grained muscovite partially replacing primary plagioclase tonalite. E) A breccia unit cutting tonalite with muscovite alteration overprinting both the matrix and fragments. Abbreviations: Bt = biotite, Ccp = chalcopyrite, Ms = muscovite, Pl = plagioclase, Py = pyrite, Qz = quartz.

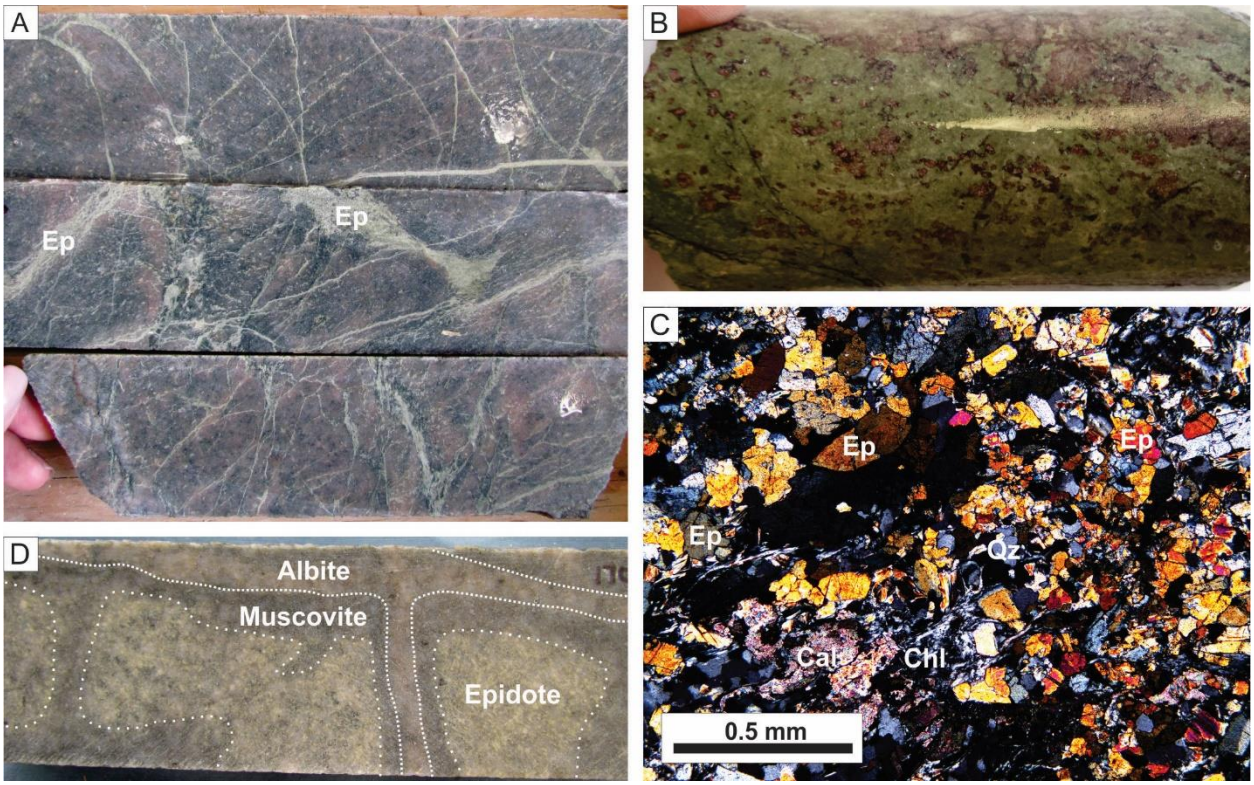

Figure 3.16. Drill core (4.5 cm in width) and thin section photographs of epidote alteration. A) Vein-controlled and disseminated epidote alteration. Note that multiple generations of epidote-bearing veins cut through the muscovite altered tonalite. B) Photo of pervasive epidote alteration. C) Thin section photo in cross polarized light of pervasive epidote alteration as part of an epidote-chlorite-carbonate-quartz assemblage replacing diorite. D) Drill core photo showing disseminated epidote alteration and early fracture-controlled muscovite alteration that is partially overprinted by later fracture-controlled albite alteration. Abbreviations: Cal = calcite, Chl = chlorite, Ep = epidote, Qz = quartz.

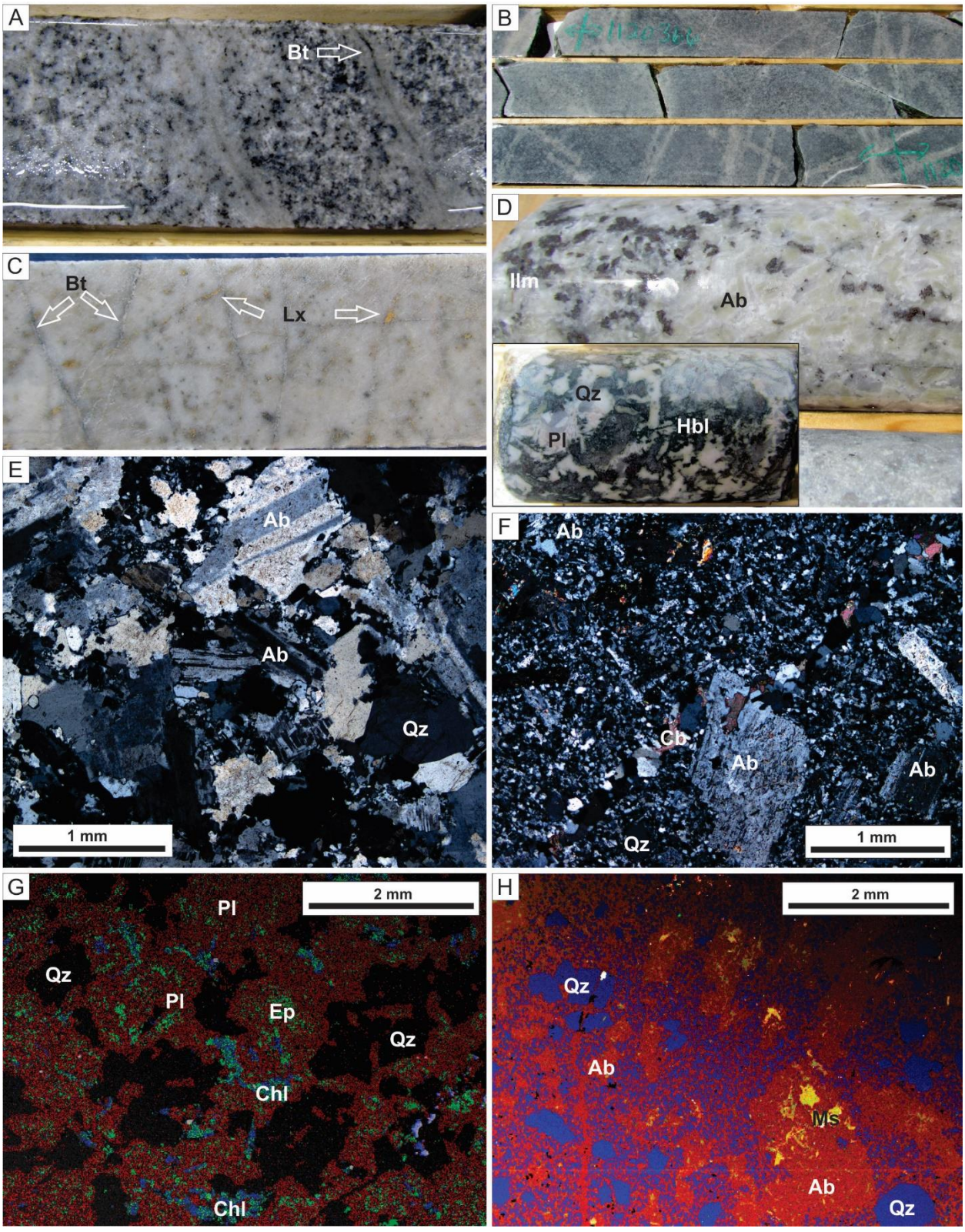
A
Bt
B
C
Bt
Lx
D
Ilm
Ab
Qz
Pl
Hbl
E
Ab
Ab
Qz
1 mm
F
Ab
Cb
Ab
Ab
Qz
1 mm
G
2 mm
Pl
Qz
Pl
Ep
Qz
Chl
Chl
H
2 mm
Qz
Ab
Ms
Ab
Qz

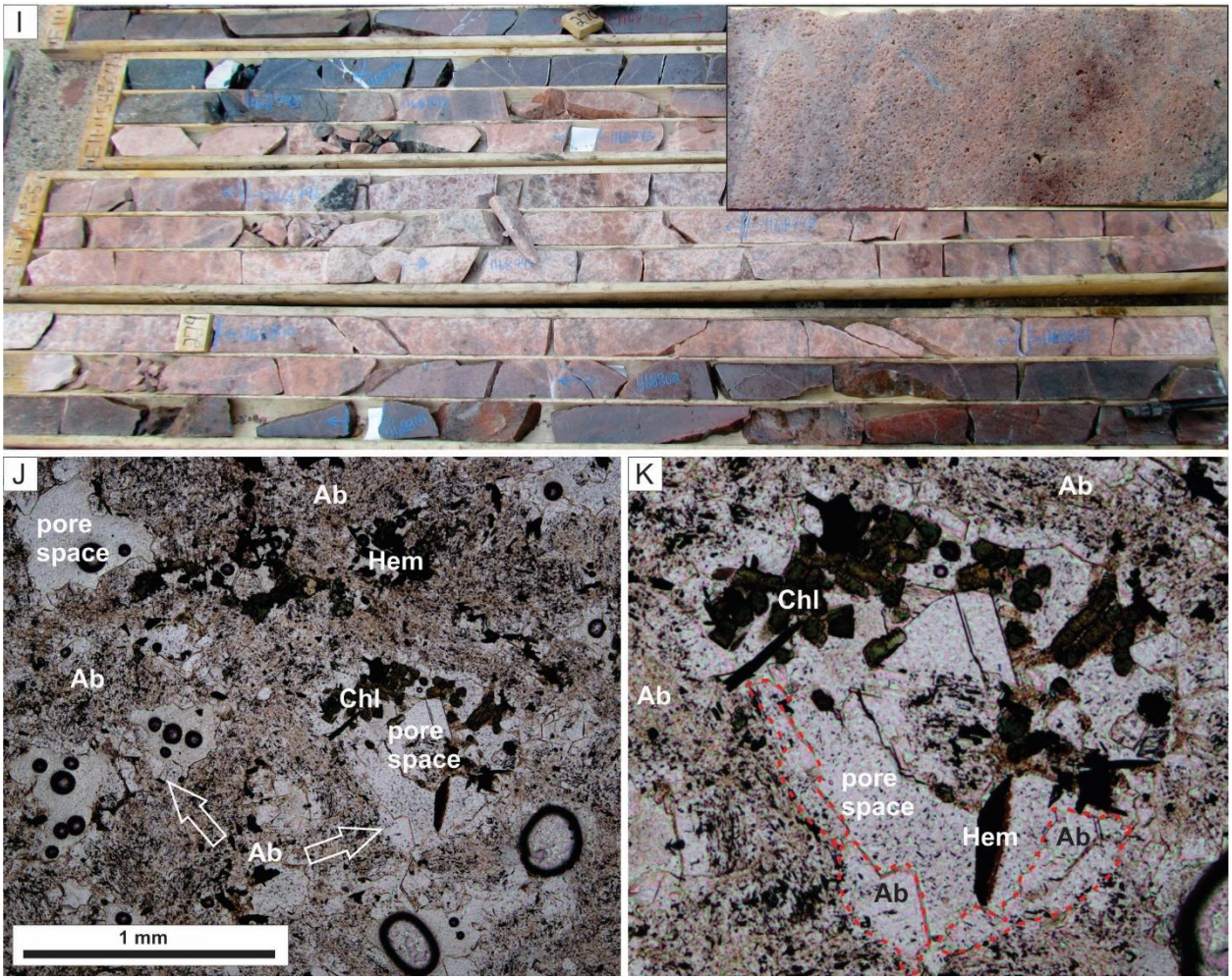

Figure 3.17. Drill core photographs (4.5 cm in width), thin section photographs and X-ray element maps of albite alteration. A) Fracture-controlled albite alteration in biotite altered tonalite that exploited pre-existing biotite-filled fractures. B) Pervasive muscovite altered tonalite that is overprinted by albite alteration along fractures. C) Pervasive, texture-destructive albite alteration with partially healed fracture system in diorite. D) Texture-destructive albite alteration of a hornblende-plagioclase-quartz-ilmenite pegmatite. Primary amphibole, plagioclase and quartz have been replaced by hydrothermal albite. Primary ilmenite remains in the altered rock due to the relative immobility of Ti-bearing minerals. The inset photo shows the primary texture of the unaltered hornblende-plagioclase-quartz-ilmenite pegmatite 12 m downhole. E) Thin section photo in cross polarized light of an albite altered tonalite showing a reduction in grain size in some areas and sutured grain boundaries. F) Thin section photo in cross polarized light showing a reduction of grain size in tonalite and replacement of quartz and plagioclase by albite. G) False colour X-ray map of least-altered tonalite sample showing primary igneous texture (Na (plagioclase) = red, Ca (epidote) = green, Fe (chlorite) = blue, Si (quartz) = grey). H) False colour X-ray map of the sample from F showing the destruction of its primary texture, reduction of grain size and increase in modal albite (Na (albite) = red, K (muscovite) = yellow, Si (quartz) = blue) compared to the X-ray map image in G. I) A sample of light-pink, intensely albite altered tonalite (10-11 wt. % Na_2O); the inset shows the distinctive porous texture that characterizes this alteration type. J) Thin section photo in plane polarized light of intensely albite altered tonalite with abundant pore space. K) Close-up thin section photo in plane polarized light of J that shows a second generation of clear albite lining the pore space. Abbreviations: Ab = albite, Bt = biotite, Cb = carbonate, Chl = chlorite, Ep = epidote, Hbl = hornblende, Hem = hematite, Ilm = ilmenite, Lx = leucoxene, Ms = muscovite, Pl = plagioclase, Qz = quartz.

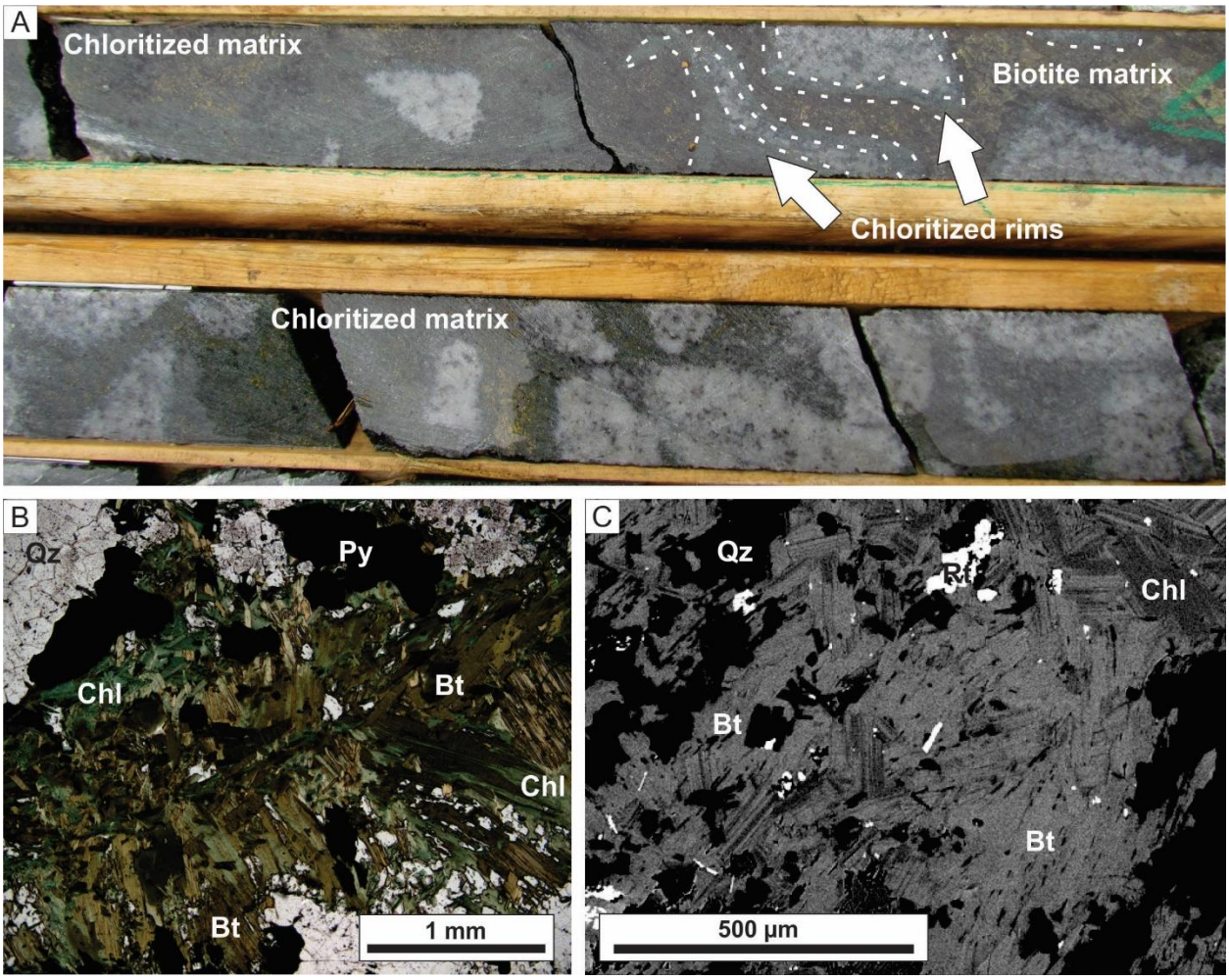

Figure 3.18. Drill core photograph (4.5 cm in width), thin section photograph and a backscatter electron image (BSE) of chlorite alteration. A) A hydrothermal biotite breccia with a brown biotite-rich matrix that is partially replaced by green chlorite along fragment/matrix boundaries, as outlined by white dashed lines. B) Thin section photo in plane polarized light of a hydrothermal biotite breccia matrix with an original biotite-quartz-pyrite assemblage. Chlorite partially replaces biotite along its cleavage planes. C) A BSE image showing chlorite partially replacing biotite with fine-grained rutile due to the alteration reaction. Abbreviations: Bt = biotite, Chl = chlorite, Py = pyrite, Qz = quartz, Rt = rutile.

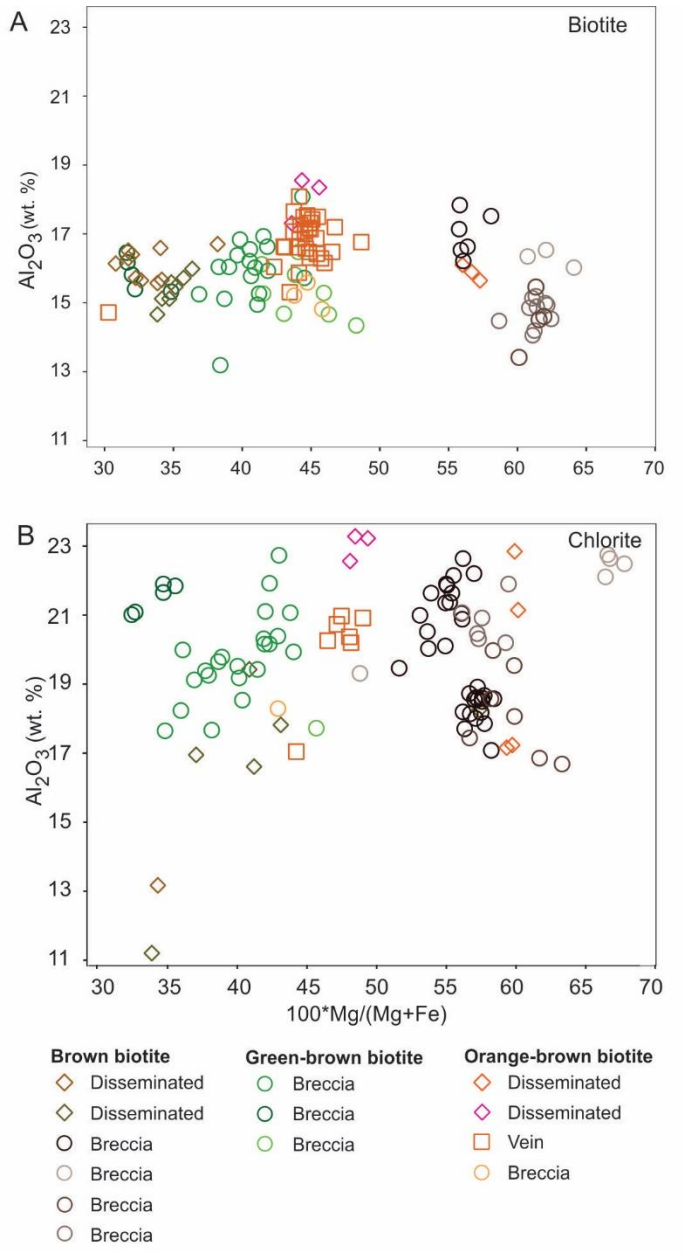

Figure 3.19. A) A bivariate plot of Al_2O_3 (wt. %) vs. Mg# (100*Mg/(Mg + Fe)) for different coloured biotites which represent variable styles of mineralization.. B) A bivariate plot of Al_2O_3 (wt. %) vs. Mg# for chlorite after biotite that shows a similar Mg# for chlorite grains that alter after biotite.

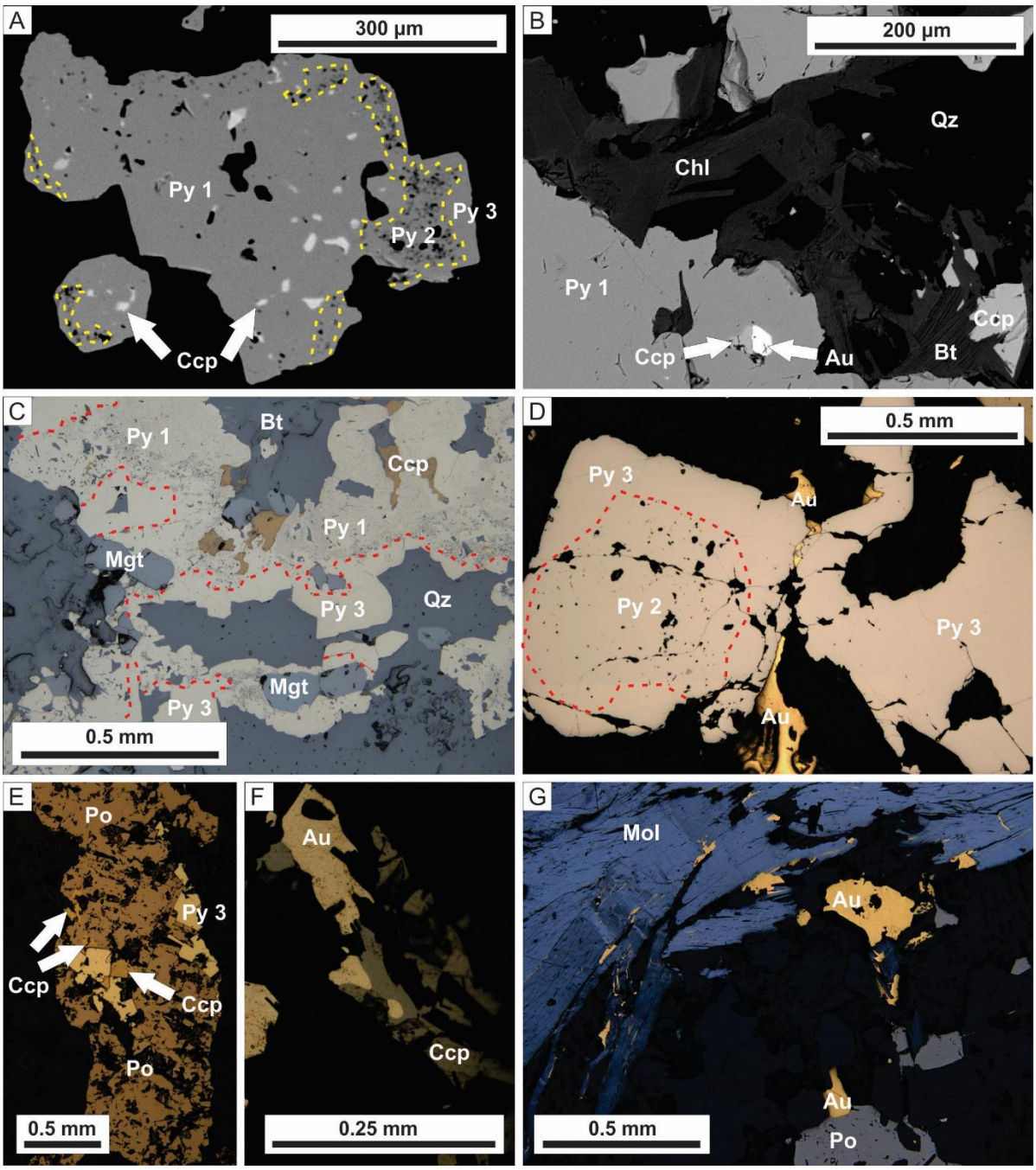

Figure 3.20. Thin section photographs in reflected light and back scattered electron (BSE) images that show the relative timing of gold mineralization with respect to sulphides. A) A BSE image showing three generations of pyrite (Py 1, 2, 3) in a hydrothermal biotite breccia. B) A BSE image of fine-grained chalcopyrite and gold inclusions in Py 1 in a hydrothermal biotite breccia. C) An example of magnetite and chalcopyrite included in Py 1; Py 3 overgrows Py 1. D) Disseminated chlorite (after biotite) altered tonalite sample with pyrite (Py 2, 3) predating gold. E) Chalcopyrite and pyrrhotite postdating Py 3 growth. F) Same sample from D with gold intergrown with chalcopyrite, therefore, both gold and chalcopyrite postdate pyrite. G) Vein sample used for Re-Os dating which shows gold intergrown with pyrrhotite and molybdenite. Abbreviations: Au = gold, Bt = biotite, Ccp = chalcopyrite, Chl = chlorite, Mag = magnetite, Mol = molybdenite, Po = pyrrhotite, Py = pyrite, Qz = quartz.

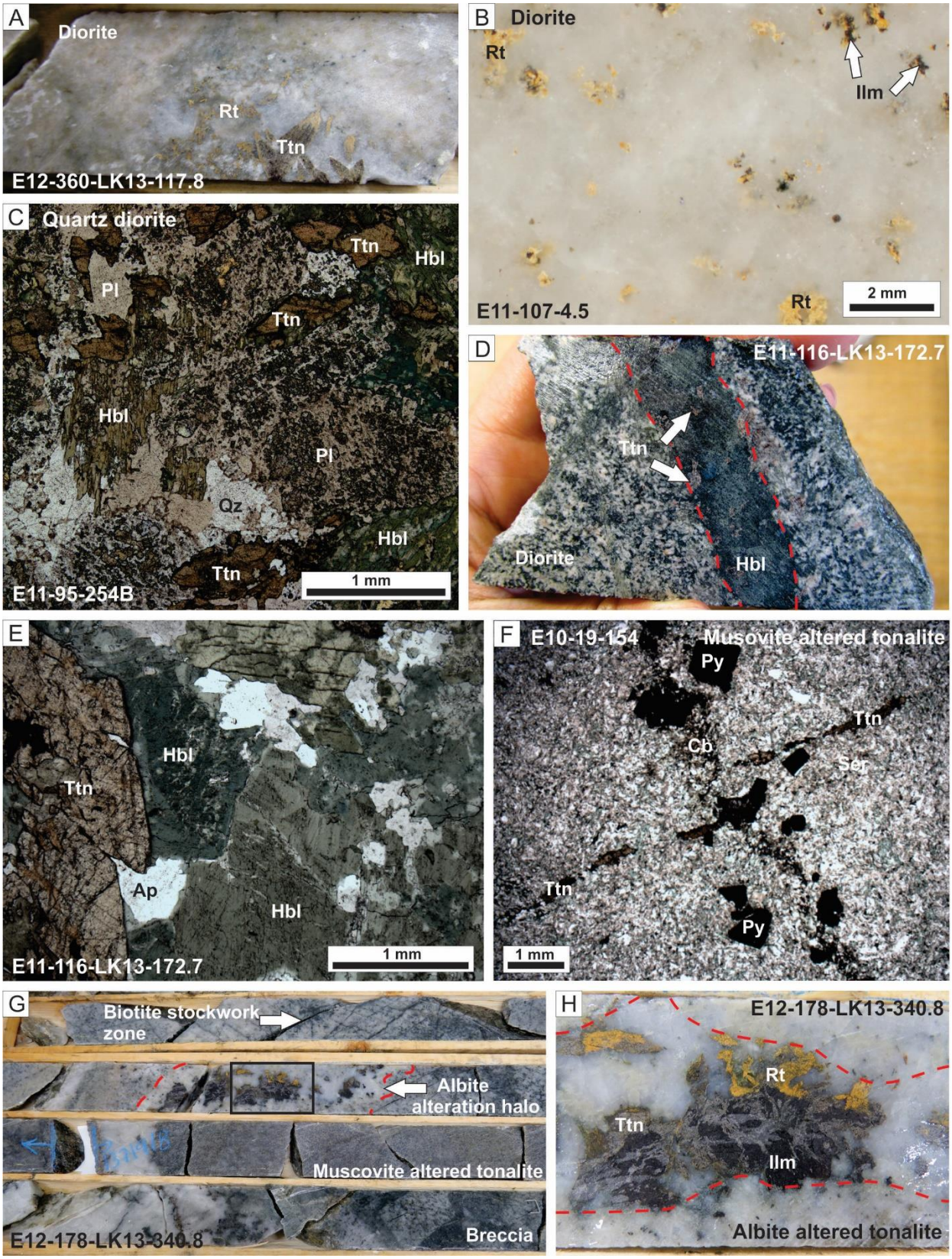
A
Diorite
Rt
Ttn
E12-360-LK13-117.8
B
Diorite
Rt
Ilm
E11-107-4.5
Rt
2 mm
C
Quartz diorite
Ttn
Hbl
Pl
Ttn
Hbl
Pl
Qz
Hbl
Ttn
1 mm
E11-95-254B
D
E11-116-LK13-172.7
Ttn
Diorite
Hbl
E
Hbl
Ttn
Ap
Hbl
1 mm
E11-116-LK13-172.7
F
E10-19-154
Musovite altered tonalite
Py
Ttn
Cb
Ser
Ttn
Py
1 mm
G
Biotite stockwork zone
Albite alteration halo
Muscovite altered tonalite
E12-178-LK13-340.8
Breccia
H
E12-178-LK13-340.8
Rt
Ttn
Ilm
Albite altered tonalite

Figure 3.21. Drill core (4.5 cm in width) and thin section photographs in plane polarized light of samples used for U-Pb geochronology of hydrothermal titanite and rutile. A) An albite altered diorite crosscut by a quartz-carbonate-titanite vein. The brown titanite is partially replaced by yellow-brown rutile. B) Pervasive albite altered diorite containing abundant secondary yellow-brown rutile. C) Thin section photo of quartz diorite with primary brown titanite. D) Drill core photo of an amphibole-titanite-apatite vein intruding diorite. E) Thin section photo of D. F) Thin section photo of a titanite stringer crosscutting an east-west trending quartz-carbonate-pyrite veinlet in a pervasively muscovite altered tonalite. G) A quartz-carbonate-ilmenite-sulphide vein with an albite alteration halo that crosscuts biotite and muscovite altered tonalite. H). A close-up of G (area outlined by black box) showing ilmenite being partially replaced by brown titanite that is in turn partially replaced by yellow-brown rutile. Abbreviations: Ap = apatite, Cb = carbonate, Hbl = hornblende, Ilm = ilmenite, Pl = plagioclase, Py = pyrite, Qz = quartz, Rt = rutile, Ttn = titanite.

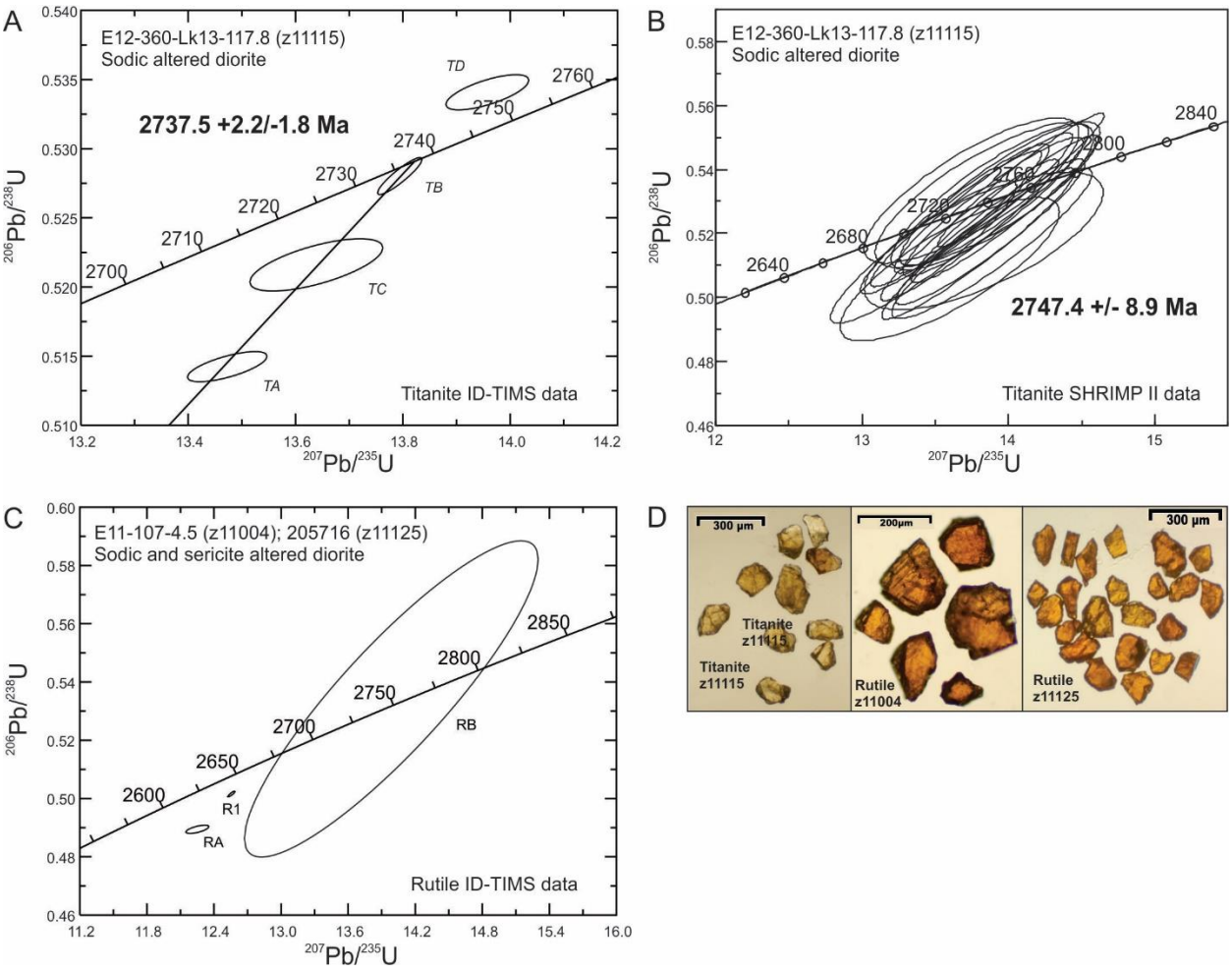

Figure 3.22. Concordia plots of U-Pb ID-TIMS and SHRIMP results of hydrothermal titanite and rutile.

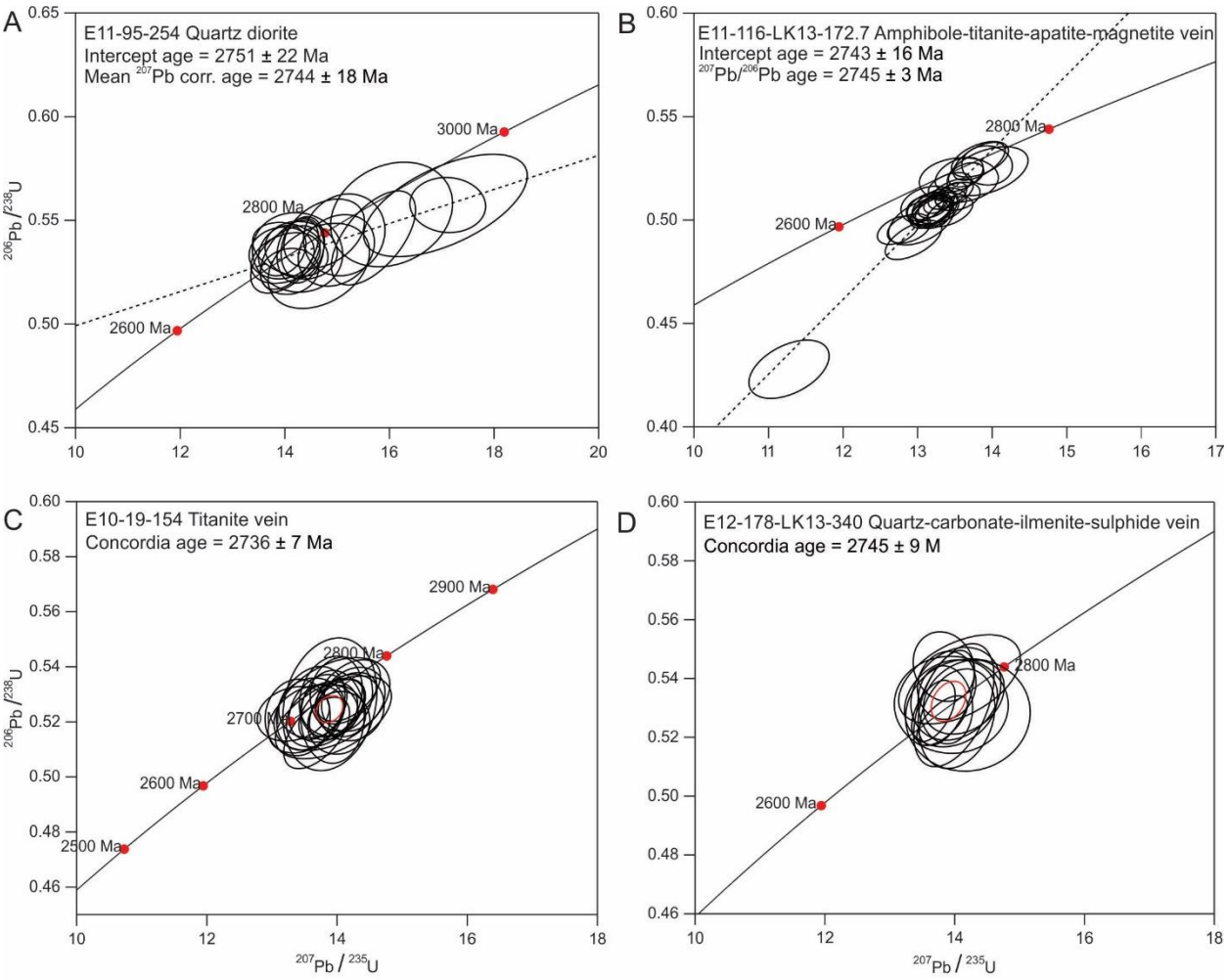

Figure 3.23. Concordia plots of U-Pb LA ICP-MS dating of hydrothermal titanite.

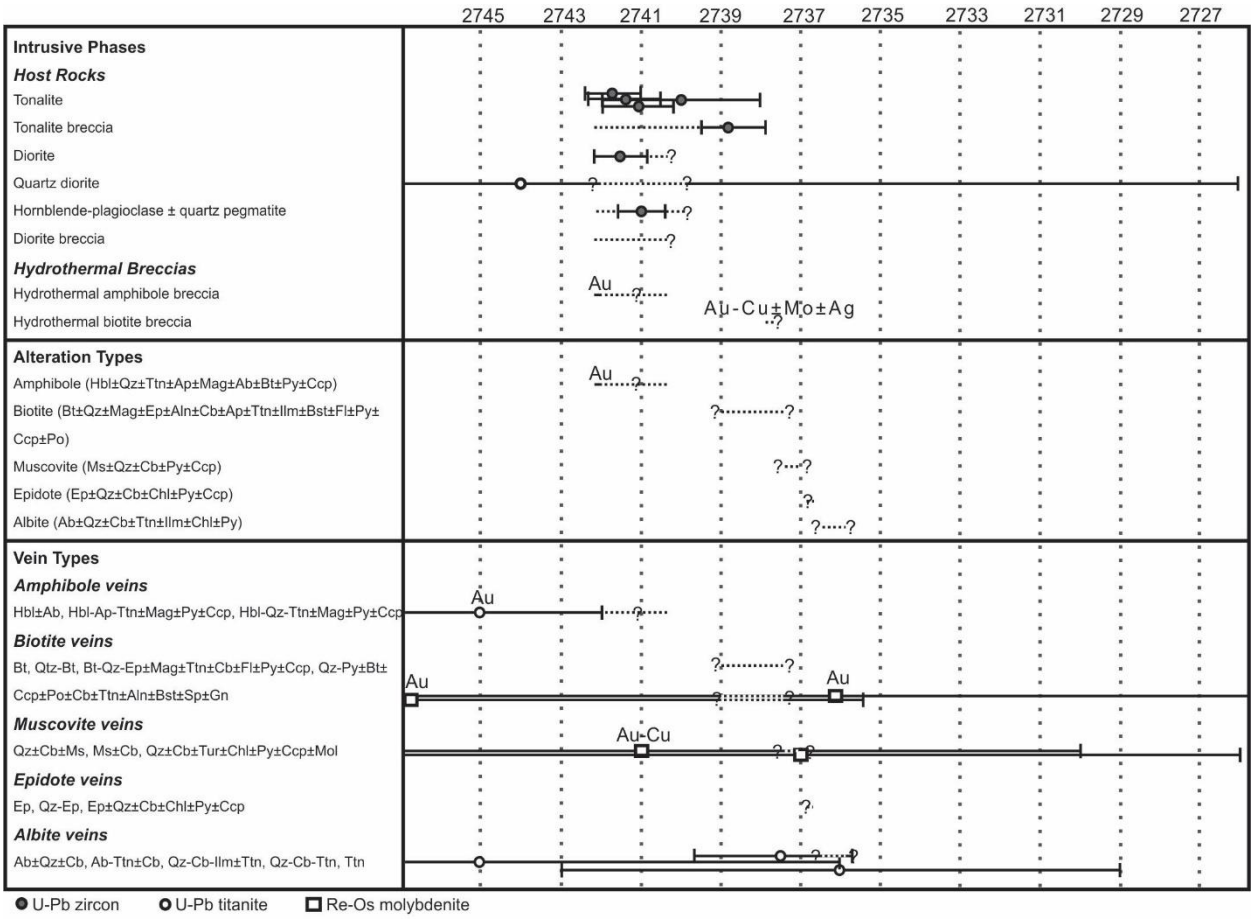

Figure 3.24. A paragenetic diagram which summarizes the different intrusive rock types, alteration types and vein types present, along with the geochronology results from this study and previous studies (Heather and van Breemen, 1994; Kontak et al., 2013a; Chapter 2). See text for discussion of the dates. Ab = albite, Aln = allanite, Ap = apatite, Bst = bastnaesite, Bt = biotite, Cb = carbonate, Ccp = chalcopyrite, Chl = chlorite, Ep = epidote, Fl = fluorite, Gn = galena, Hbl = hornblende = Hbl, Ilm = ilmenite, Mag = magnetite, Ms = muscovite, Py = pyrite, Po = pyrrhotite, Qz = quartz, Sp = sphalerite, Ttn = titanite, Tur = tourmaline.

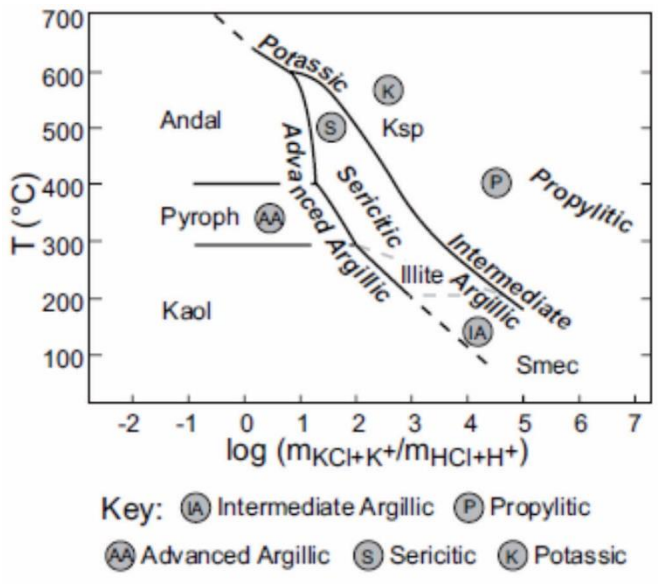

Figure 3.25. A temperature vs. log($m_{KCl + K^+}$ /$m_{HCl + H^+}$) diagram after Seedorff et al. (2005). Abbreviations: Andal = andalusite, Kaol = kaolinite, Ksp = K-feldspar, Pyroph = pyrophyllite, Smec = smectite.

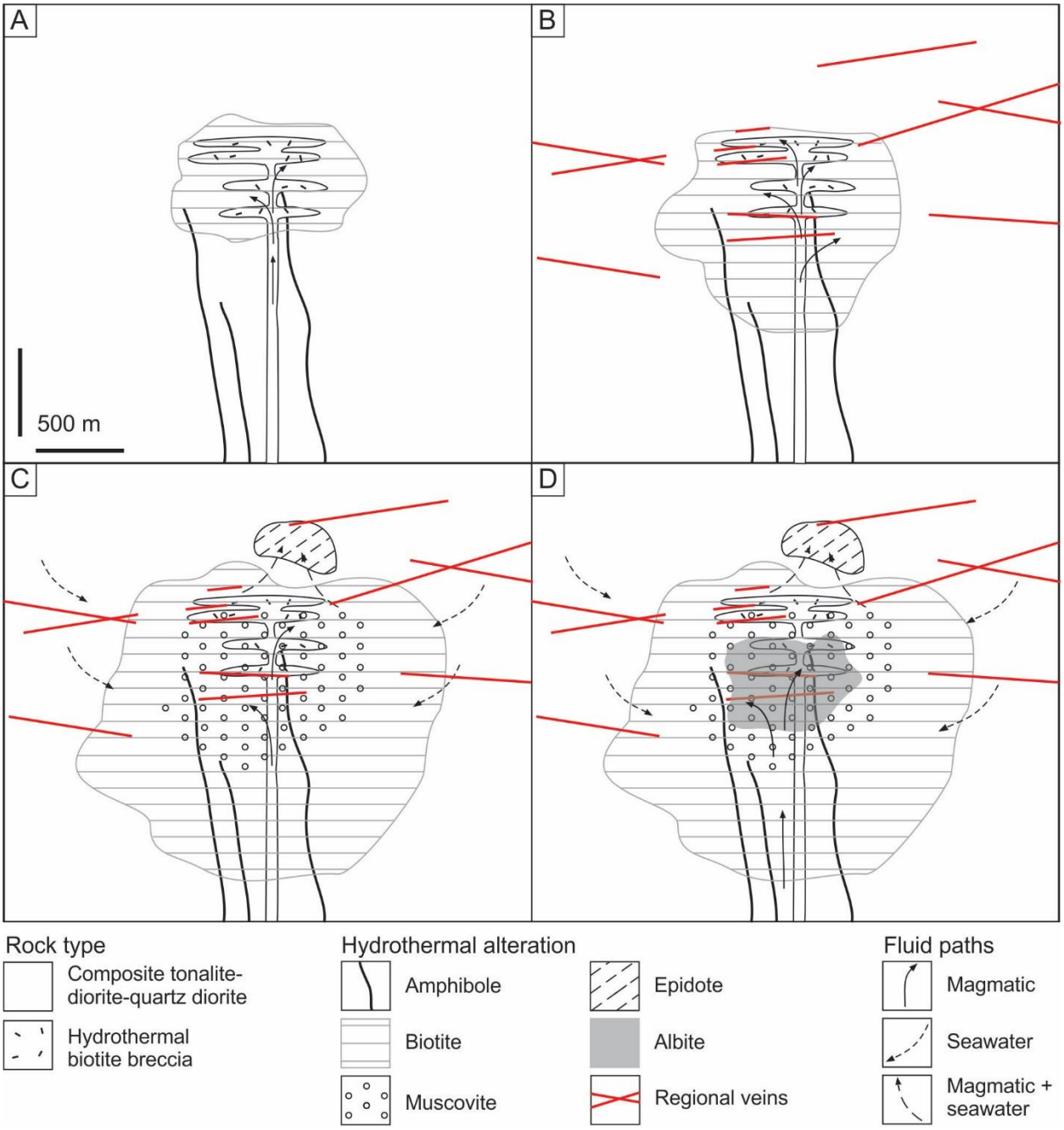

Figure 3.26. Schematic paragenesis and configuration of hydrothermal stages at the Côté Gold deposit. The diagrams are vertical cross sections through the deposit. A) Early gold-bearing amphibole veins and breccias and then gold-bearing hydrothermal biotite breccias, both of which formed from the exsolution of a dioritic magma, intrude into tonalite and dioritic rocks of the CIC; biotite disseminations and stockworks begin to form as the magmatic-derived fluids circulate. B) As the extent of biotite alteration increases it moves into the regional fracture system of sheeted quartz ± carbonate ± sulphide veins. C) Gold-bearing muscovite alteration forms due to the downward circulation of seawater mixing with magmatic fluids and then epidote alteration forms above the hydrothermal biotite breccia as an upflow zone. D) Volatile exsolution of tonalite results in albite alteration in the centre of the deposit that postdates mineralization. Note that the replacement-style, fine-grained epidote is not depicted as its origin is undetermined.

Table 3.1. Summary of the magmatic and magmatic-hydrothermal breccias

Breccia type	Subtype	Fragment type	Matrix mineralogy	Texture	Metals	Spatial distribution
Diorite breccia		Tonalite, diorite, quartz diorite and pegmatite	Diorite or quartz diorite	Rounded to angular and rare tabular fragments; rare exfoliation textures	Au ± Cu	Spatially restricted to south and centre of deposit
Tonalite breccia		Diorite, quartz diorite, rare tonalite	Tonalite	Angular to rounded fragments with sharp to diffuse boundaries; lobate contacts may occur		Occurs along margins of tonalite intrusions
Hydrothermal amphibole breccia		Tonalite, diorite	Hbl-Qz ± Bt ± Cb ± Py ± Ccp	Rounded to angular fragments; rare miarolitic cavities		Least abundant breccia; restricted to south and centre of deposit
Hydrothermal biotite breccia	i) Biotite-rich	Tonalite	Bt-Qz ± Ep ± Cal ± Py ± Ccp ± Mag ± Aln ± Ttn ± Fl	Angular to sub-rounded fragments; in-situ (i.e., mosaic) textures	Au ± Cu	Forms in the central and the northern parts of the deposit
	ii) Magnetite- or sulphide-rich	Tonalite	Bt-Mag-Qz-Ank-Ccp-Py ± Sp ± Aln ± Bst ± Ap ± Ttn	Angular to sub-rounded fragments; in-situ (i.e., mosaic) textures	Au ± Cu ± Mo ± Ag	Up to 50% Magnetite in some samples
	iii) Carbonate-rich	Tonalite; rare assemblage ii fragments	Bt-Ank-Cal-Qz-Py ± Aln ± Ap ± Mag ± Ccp ± Po	Angular to sub-rounded fragments; in-situ (i.e., mosaic) textures	Au ± Cu ± Mo ± Ag	Assemblage ii and iii occur to the most north of the breccia body

Abbreviations: Aln = allanite, Ank = ankerite, Ap = apatite, Bst = bastnaesite, Bt = biotite, Cal = calcite, Ccp = chalcopyrite, Ep = epidote, Fl = fluorite, Hbl = hornblende, Mag = magnetite, Po = pyrrhotite, Py = pyrite, Qz = quartz, Sp = sphalerite, Ttn = titanite

Table 3.2. Characteristics of hydrothermal alteration types and post-emplacement vein types at the Côté Gold deposit

Mineral assemblages	Alteration style and distribution	Vein types	Relative timing and comments
Amphibole Hbl ± Ap ± Ttn ± Mag ± Qz ± Py ± Ccp	Veins and breccias; rare and restricted to the south and centre of the deposit	**Hbl ± Ab**; Hbl-Ap-Ttn ± Mag ± Py ± Ccp; **Hbl-Qz-Ttn ± Mag ± Py ± Ccp**	Sharp to diffuse contacts with wall rock; altered by biotite alteration; veins can be Au-bearing
Biotite Bt ± Qz ± Cal ± Ank ± Ep ± Aln ± Mag ± Py ± Ccp ± Po ± Ap ± Bst ± Ttn ± Ilm ± Fl ± Sp ± Gn	Disseminations, veins (sheeted and stockwork) and breccias; biotite breccia centred on the deposit; disseminations and veins occur throughout the deposit	**Bt**; Qz-Bt, **Qz-Py ± Bt ± Ccp ± Po ± Cb ± Ttn ± Aln ± Bst ± Sp ± Gn ± Mol;** Bt-Qz-Ep ± Mag ± Ttn ± Cb ± Fl ± Py ± Ccp	Variable disseminated and vein assemblage types suggest several generations of biotite alteration; visible Au and Mol is associated with biotite; sharp contacts with wall rock
Muscovite Ms ± Qz ± Cal ± Py ± Ccp ± Chl ± Rt	Veins and replacement; relatively continuous alteration body centred on the deposit	Qz ± Cb ± Ms; Ms ± Cb; **Qz ± Cb ± Tur ± Chl ± Py ± Ccp ± Mol**	Forms alteration haloes around earlier sheeted and stockwork veins; postdates all hydrothermal brecciation
Epidote Ep ± Qz ± Cal ± Chl	Vein and replacement; strong epidote zone spatially restricted to the north of the deposit	Ep, **Qz-Ep**, Ep ± Qz ± Cal ± Chl ± Ccp	Overprints muscovite alteration
Albite Ab ± Qz ± Cal ± Ttn ± Ilm ± Chl ± Py; Ab ± Ttn ± Hem ± Rt ± Ap ± Chl	Veins and replacement; three orientations at approximately 190-205°, 290-330° and 260-275°; strongest towards the centre of the deposit	Ab ± Qz ± Cal; Ab-Ttn ± Cal, Qz-Cal-Ilm ± Ttn; **Qz-Cal-Ttn**; Ttn	Overprints and destroys earlier alteration; sharp contacts with wall rock; predates brittle fault
Chlorite Chl ± Qz ± Cal ± Ilm ± Rt ± Py ± Ccp	Replacement of primary plagioclase and secondary biotite (veins, disseminations and breccias); heterogenously distributed in deposit	Chl ± Qz ± Cal ± Py ± Ccp	Partially to wholly replaces earlier biotite along cleavage planes; inferred to postdate deposit formation

Abbreviations: Ab = albite, Aln = allanite, Ank = ankerite, Ap = apatite, Au = gold, Bst = bastnaesite, Bt = biotite, Cal = calcite, Cb = carbonate, Ccp = chalcopyrite, Chl = chlorite, Ep = epidote, Gn = galena, Fl = fluorite, Hbl = hornblende, Hem = hematite, Ilm = ilmenite, Mag = magnetite, Mol = molybdenite, Ms = muscovite, Po = pyrrhotite, Py = pyrite, Qz = quartz, Rt = rutile, Sp = sphalerite, Ttn = titanite, Tur = tourmaline

Bolded font denotes gold-bearing veins

Table 3.3. Selected microprobe analyses of hydrothermal biotite from disseminations, veins and breccias in the Côté Gold deposit

		Disseminated								Vein		
		E11-95-268 (G)			CL-58 (B)		E11-60-172 (O)			E11-62-244 (O)		
	L.O.D.	1-1	2-1	2-3	1-2	2-3	1-5	1-6	2-1	2-1	3-1	6-1
SiO_2	0.04	34.25	31.38	32.48	35.18	34.07	37.63	37.74	37.73	35.60	35.42	34.97
TiO_2	0.03	2.10	1.54	1.81	2.21	1.93	1.25	1.23	1.22	1.74	1.84	1.82
Al_2O_3	0.03	16.47	16.63	16.02	16.61	16.95	15.82	15.75	15.93	17.93	18.36	17.39
V_2O_3	0.03	b.d.l.	b.d.l.	b.d.l.	b.d.l.	b.d.l.	0.04	0.04	b.d.l.	b.d.l.	b.d.l.	b.d.l.
Cr_2O_3	0.03	b.d.l.	0.00	b.d.l.	0.06	0.00	b.d.l.	0.04	0.04	b.d.l.	b.d.l.	b.d.l.
MgO	0.03	4.74	6.04	5.30	6.87	7.08	13.31	13.41	13.46	8.86	8.90	8.94
CaO	0.03	b.d.l.	0.04	b.d.l.	0.09	b.d.l.	0.04	0.06	b.d.l.	b.d.l.	b.d.l.	0.03
MnO	0.03	0.18	0.25	0.23	0.10	0.09	0.11	0.13	0.12	0.15	0.15	0.15
FeO	0.03	28.63	32.58	31.44	25.81	26.59	17.70	17.52	17.28	21.14	21.64	21.83
Na_2O	0.03	0.00	0.00	0.00	0.06	b.d.l.	0.11	0.10	0.13	0.08	0.05	0.07
K_2O	0.02	9.47	5.80	7.49	9.11	8.59	9.74	9.63	9.53	9.85	9.49	9.46
F	0.10	0.26	0.14	0.12	0.62	0.48	0.90	1.03	0.89	0.32	0.28	0.39
Cl	0.01	0.24	0.15	0.17	0.37	0.29	0.09	0.06	0.07	0.15	0.14	0.12
Total		96.35	94.55	95.09	97.10	96.11	96.75	96.73	96.42	95.84	96.32	95.22
F = O		-0.11	-0.06	-0.05	-0.26	-0.20	-0.38	-0.43	-0.38	-0.14	-0.12	-0.17
Cl = O		-0.05	-0.03	-0.04	-0.08	-0.06	-0.02	-0.01	-0.02	-0.03	-0.03	-0.03
Total		96.19	94.46	94.99	96.76	95.84	96.35	96.28	96.03	95.67	96.17	95.03
Mg/Mg + Fe		0.23	0.25	0.23	0.32	0.32	0.57	0.58	0.58	0.43	0.42	0.42

Table 3.3. Continued

		Vein			Breccia								
		E11-68-536.9 (O)			CL-16 (G)			E12-174-LK13-407 (B)			EL-161-340B (O)		
	L.O.D.	3-1	5-1	7-2	1-2	1-5	1-6	1-2	1-3	1-6	1-3	2-2	3-1
SiO_2	0.04	36.36	36.57	37.00	35.37	35.02	34.94	36.93	37.05	38.43	36.97	36.33	34.95
TiO_2	0.03	1.38	1.54	1.30	1.46	1.40	1.61	1.62	1.53	1.58	1.48	1.51	1.41
Al_2O_3	0.03	16.57	16.63	16.82	16.36	16.47	16.41	16.68	16.38	15.53	15.72	15.73	16.44
V_2O_3	0.03	0.06	0.06	0.06	0.06	0.08	0.07	0.05	0.04	0.06	0.09	0.07	0.10
Cr_2O_3	0.03	0.04	0.06	0.07	b.d.l.	b.d.l.	b.d.l.	b.d.l.	b.d.l.	0.09	b.d.l.	b.d.l.	b.d.l.
MgO	0.03	11.38	11.21	11.47	8.71	8.56	8.25	13.46	13.51	14.01	10.79	10.45	9.99
CaO	0.03	0.36	b.d.l.	b.d.l.	b.d.l.	b.d.l.	b.d.l.	b.d.l.	b.d.l.	0.03	b.d.l.	0.05	0.15
MnO	0.03	0.16	0.16	0.17	0.07	0.07	0.04	0.13	0.10	0.09	0.05	0.04	0.05
FeO	0.03	19.98	19.78	19.36	24.29	25.00	25.07	16.99	17.19	16.21	20.99	21.89	23.50
Na_2O	0.03	0.10	0.10	0.11	0.03	b.d.l.	b.d.l.	0.08	0.05	0.08	0.07	0.03	b.d.l.
K_2O	0.02	8.18	9.60	9.72	9.58	9.52	9.48	9.80	9.60	9.80	9.73	9.33	8.45
F	0.10	0.54	0.59	0.66	0.93	0.77	0.88	0.35	0.49	0.56	1.15	1.22	0.87
Cl	0.01	0.13	0.15	0.12	0.17	0.17	0.17	0.08	0.07	0.06	0.24	0.27	0.20
Total		95.25	96.43	96.86	97.06	97.07	96.94	96.19	96.00	96.52	97.28	96.91	96.10
F = O		-0.23	-0.25	-0.28	-0.39	-0.32	-0.37	-0.15	-0.20	-0.23	-0.49	-0.51	-0.37
Cl = O		-0.03	-0.03	-0.03	-0.04	-0.04	-0.04	-0.02	-0.02	-0.01	-0.05	-0.06	-0.04
Total		94.99	96.15	96.55	96.62	96.71	96.53	96.03	95.78	96.27	96.74	96.34	95.69
Mg/Mg + Fe		0.50	0.50	0.51	0.39	0.38	0.37	0.59	0.58	0.61	0.48	0.46	0.43

Analyses are in wt. %, L.O.D. = average limit of detection and b.d.l. = below detection limit

G = green-brown biotite, B = brown biotite, O = orange-brown biotite

Table 3.4. Selected microprobe analyses of alteration minerals

	Biotite Alteration				Muscovite Alteration							
	Epidote				Muscovite							
	E12-174-2K13-407 (Bx)				E11-161-332 (Diss)				E11-79-403.2B (Vn)			
	1-1	1-3	1-4	1-6	1-1	2-1	2-2	2-3	1-2	1-5	1-6b	1-7b
SiO_2	37.56	37.21	37.29	37.29	46.85	47.74	47.18	47.88	46.67	47.25	45.82	46.51
TiO_2	0.18	0.03	0.17	0.30	0.24	0.10	0.07	0.12	0.33	0.31	0.37	0.67
Al_2O_3	22.70	23.51	22.88	22.93	34.61	32.89	34.52	32.92	33.73	33.88	33.37	30.70
V_2O_3	0.07	0.04	0.08	0.07	b.d.l.	b.d.l.	b.d.l.	b.d.l.	b.d.l.	b.d.l.	b.d.l.	b.d.l.
Cr_2O_3	b.d.l.	b.d.l.	b.d.l.	b.d.l.	b.d.l.	b.d.l.	b.d.l.	b.d.l.	b.d.l.	b.d.l.	b.d.l.	b.d.l.
MgO	0.13	0.09	b.d.l.	0.02	0.97	1.64	1.25	1.72	1.29	1.32	1.19	2.49
CaO	22.84	23.07	23.06	23.07	b.d.l.	b.d.l.	b.d.l.	0.04	b.d.l.	0.03	b.d.l.	b.d.l.
MnO	0.13	0.11	0.08	0.07	b.d.l.	b.d.l.	b.d.l.	b.d.l.	b.d.l.	b.d.l.	b.d.l.	b.d.l.
FeO	13.42	12.81	13.49	13.45	1.83	1.72	1.40	1.60	2.29	2.42	2.32	4.10
Na_2O	b.d.l.	b.d.l.	b.d.l.	b.d.l.	0.78	0.51	0.64	0.39	0.32	0.32	0.37	0.35
K_2O	b.d.l.	0.03	0.02	0.03	10.24	10.61	10.38	10.66	10.94	10.91	11.09	10.84
F	b.d.l.	b.d.l.	b.d.l.	b.d.l.	b.d.l.	0.14	0.17	0.17	b.d.l.	b.d.l.	b.d.l.	0.14
Cl	b.d.l.	b.d.l.	0.00	b.d.l.	b.d.l.	b.d.l.	b.d.l.	b.d.l.	b.d.l.	b.d.l.	b.d.l.	0.02
Total	97.05	96.91	97.07	97.23	95.64	95.34	95.64	95.50	95.63	96.47	94.55	95.84
F = O	0.00	0.00	0.00	0.00	0.00	-0.06	-0.07	-0.07	0.00	0.00	0.00	-0.06
Cl = O	0.00	0.00	0.00	0.00	0.00	0.00	0.00	0.00	0.00	0.00	0.00	0.00
Total	97.05	96.91	97.07	97.23	95.64	95.29	95.57	95.43	95.63	96.47	94.55	95.77

Table 3.4. Continued

	Epidote Alteration					Chlorite Alteration					
	Epidote					Chlorite					
	E11-161-332 (Vn)		E12-338LK13-264 (Diss)			E12-338LK13-264 (Diss)			E11-79-403.2B (Vn)		
	1-2	2-3	1-1	2-2	3-1	1-1	1-2	1-6	1-2	1-3	1-7
SiO_2	38.14	38.31	38.01	38.39	37.35	26.78	27.71	26.60	24.68	24.69	25.17
TiO_2	b.d.l.	0.05	0.19	0.05	0.04	b.d.l.	0.03	b.d.l.	b.d.l.	b.d.l.	b.d.l.
Al_2O_3	26.38	27.21	25.42	27.59	22.98	20.18	20.90	21.80	18.45	18.72	19.10
V_2O_3	0.03	b.d.l.	0.054	0.041	b.d.l.	b.d.l.	b.d.l.	b.d.l.	b.d.l.	b.d.l.	b.d.l.
Cr_2O_3	b.d.l.	b.d.l.	b.d.l.	0.06	b.d.l.	0.73	0.51	0.67	b.d.l.	0.03	b.d.l.
MgO	0.06	b.d.l.	0.036	b.d.l.	b.d.l.	19.03	19.74	18.68	5.17	4.45	5.60
CaO	23.69	23.77	23.50	24.06	22.68	b.d.l.	b.d.l.	b.d.l.	b.d.l.	0.026	0.032
MnO	0.08	b.d.l.	0.05	b.d.l.	0.10	0.20	0.24	0.26	0.32	0.28	0.32
FeO	9.24	8.52	10.77	8.28	13.41	20.11	19.68	20.56	40.28	41.02	39.76
Na_2O	b.d.l.	b.d.l.	b.d.l.	b.d.l.	b.d.l.	b.d.l.	b.d.l.	b.d.l.	b.d.l.	b.d.l.	b.d.l.
K_2O	b.d.l.	b.d.l.	b.d.l.	b.d.l.	b.d.l.	b.d.l.	b.d.l.	b.d.l.	b.d.l.	b.d.l.	b.d.l.
F	b.d.l.	b.d.l.	b.d.l.	b.d.l.	b.d.l.	0.16	0.10	0.14	b.d.l.	b.d.l.	b.d.l.
Cl	b.d.l.	b.d.l.	0.027	b.d.l.	b.d.l.	0.03	0.02	0.02	0.01	b.d.l.	b.d.l.
Total	97.66	97.92	98.07	98.50	96.60	87.30	88.95	88.79	88.99	89.28	90.05
F = O	0.00	0.00	0.00	0.00	0.00	-0.07	-0.04	-0.06	0.00	0.00	0.00
Cl = O	0.00	0.00	-0.01	0.00	0.00	-0.01	0.00	0.00	0.00	0.00	0.00
Total	97.66	97.92	98.06	98.50	96.60	87.22	88.91	88.73	88.98	89.28	90.05

Analyses are in wt. %; Total iron as FeO

Diss = disseminated, Vn = vein and Bx = breccia

Table 3.5. Results of LA ICP-MS measurements from of trace element concentrations in biotite

		Li	Mg	Sc	Ti	V	Cr	Mn	Fe	Co	Ni	Cu	Zn	Rb	Sr	Nb
		m.d.l.	m.d.l.	m.d.l.	m.d.l.	m.d.l.	m.d.l.	m.d.l.	m.d.l.	m.d.l.	m.d.l.	m.d.l.	m.d.l.	m.d.l.	m.d.l.	m.d.l.
Sample number		0.7	1	0.76	3	1	3.3	3	17	0.15	2.1	0.95	1	0.2	0.03	0.03
CL-16 (n = 10)	min.	78.1	50800	15.93	8280	409	n = 2 < b.d.l.	490	172200	13.31	26.7	n = 3 < b.d.l.	192	706	1.05	18.8
Breccia (G)	max.	96.6	75600	18.6	10190	495	11.1	756	249000	17.88	57.8	3.08	322	920	1.99	22.1
	avg.	86	57590	17	8845	434	7	544	195560	14.96	34.9	2.1	231	785	1.5	20.0
E11-161-338 (n = 15)	min.	58.7	40590	18.43	8690	465	n = 4 < b.d.l.	422	184600	5.99	19.6	n = 5 < b.d.l.	258.1	1002	0.294	25
Breccia (G)	max.	95.9	72800	32.9	19130	1072	8.3	1333	412000	16.46	117.7	1.7	648	1238	13.8	69.1
	avg.	76	51521	24.1	11326	683	4	772	266640	10.9	51	0.9	409	1120	2.0	32
CL-77 (n = 14)	min.	79.3	73700	37.8	5880	347	7.14	244.3	104000	2.09	50.4	n = 9 < b.d.l.	140.2	864	0.531	18.6
Breccia (O)	max.	108.7	81800	52.2	9260	500	14	286	111100	4.42	64.7	1.5	152.3	1408	2.07	43.8
	avg.	90.7	77214	45	7447	390	12	272	107550	3.6	61	0.7	147	989	1.0	30
CL-58 (n = 10)	min.	71.8	37400	14.12	10370	52.8	n = 1 < b.d.l.	686	175400	27.6	13.6	1.22	179.2	250	0.534	24.1
Disseminated (B)	max.	97.8	50300	40	13120	68.8	8.4	935	244000	40.3	27.6	10.7	255	551	10.4	38.5
	avg.	80	39929	20	11759	58.2	5.6	787	189960	32.2	20	2.9	200	442	2.2	30.9
E11-105-133 (n = 15)	min.	103.4	41100	2.78	9080	158.9	16.8	1265	157100	57	71	n = 2 < b.d.l.	276	392	0.331	14.8
Disseminated (B)	max.	125.3	49600	9.4	10530	211	79.3	1594	182300	66.9	89.7	1.43	337	710	67	29.8
	avg.	113.9	43999	4	9961	195	42.0	1383	164713	61	81	1	302	546	6	22
E11-89-4 (n = 7)	min.	97.7	61900	5.5	6790	359	122.4	1154	125500	69.9	188	0.94	225	431	0.314	0.9
Disseminated (B)	max.	105.5	75400	10.7	12750	418	534	1547	150900	83.7	223	1.38	281	441	27.4	1.7
	avg.	100.4	67529	7.8	8121	381	341	1331	136100	75	205	1.28	247	437	4.6	1.2
E11-62-244 (n = 12)	min.	74.3	52700	3.43	11580	154.7	8.2	1263	150400	46.5	73.9	n = 2 < b.d.l.	190	459	0.54	34.9
Disseminated and	max.	134.3	75400	53.7	22400	291.7	182.8	1691	272000	65.7	130	7.3	253	498	96.7	92
vein (O)	avg.	117	58108	16	13702	210.5	42	1514	169842	60	98	3.6	219	476	20	46
E11-145-111 (n = 14)	min.	66.3	59800	4.75	6260	248.5	229.1	1287	119900	58.8	206	n = 1 < b.d.l.	214.2	358	0.155	4.05
Vein (B)	max.	85.4	64100	6.69	13800	280.1	351.9	1427	128000	62.9	231	1.44	245	422	30.6	30.9
	avg.	75	61900	6.1	7204	264.3	281	1341	123536	61	220	1	225	389	2.5	7.3

Table 3.5. Continued

		In	Sn	Cs	Ba	La	Ce	Pr	Nd	Sm	Eu	Gd	Tb
		m.d.l.	m.d.l.	m.d.l.	m.d.l.	m.d.l.	m.d.l.	m.d.l.	m.d.l.	m.d.l.	m.d.l.	m.d.l.	m.d.l.
Sample number		0.021	0.2	0.07	0.1	0.01	0.005	0.003	0.01	0.1	0.010	0.04	0.003
CL-16 (n = 10)	min.	0.191	30.7	20.55	111.9	n = < 4 b.d.l.	n = < 2 b.d.l.	n = < 8 b.d.l.	n = < 5 b.d.l.	n = < 14 b.d.l.	n = < 14 b.d.l.	n = < 9 b.d.l.	n = < 9 b.d.l.
Breccia (G)	max.	0.254	37.1	45.9	1119	0.51	0.88	0.11	0.31	-	-	0.31	0.033
	avg.	0.22	33	26.8	803	0.07	0.11	0.02	0.05	-	-	0.16	0.015
E11-161-338 (n = 15)	min.	0.342	52.5	34.68	70.7	n = < 5 b.d.l.	n = < 3 b.d.l.	n = < 4 b.d.l.	n = < 6 b.d.l.	n = < 8 b.d.l.	n = < 6 b.d.l.	n = < 6 b.d.l.	n = < 6 b.d.l.
Breccia (G)	max.	0.99	69.9	51.3	403.5	2.75	3.5	0.83	9.3	15	1.41	28	5
	avg.	0.6	60	41.4	250	0.38	0.7	0.11	0.8	1	0.12	2	0.4
CL-77 (n = 14)	min.	0.114	11.67	35.48	21.6	n = < 12 b.d.l.	n = < 9 b.d.l.	n = < 12 b.d.l.	n = < 14 b.d.l.	n = < 14 b.d.l.	n = < 14 b.d.l.	n = < 14 b.d.l.	n = < 14 b.d.l.
Breccia (O)	max.	0.154	20.61	69.4	143.1	0.0180	0.0097	0.002	-	-	-	-	-
	avg.	0.136	15.6	43.2	48	0.0070	0.0020	0.0003	-	-	-	-	-
CL-58 (n = 10)	min.	0.136	27.8	8.06	1004	n = < 5 b.d.l.	n = < 2 b.d.l.	n = < 6 b.d.l.	n = < 6 b.d.l.	n = < 6 b.d.l.	n = < 4 b.d.l.	n = < 7 b.d.l.	n = < 6 b.d.l.
Disseminated (B)	max.	0.265	31.5	18.38	1437	1.22	7.5	0.75	4.4	3.4	0.63	12.3	3.5
	avg.	0.18	29	14	1274	0.25	1.2	0.1	0.8	0.5	0.10	1.5	0.5
E11-105-133 (n = 15)	min.	n = < 8 b.d.l.	1.61	8.51	677	n = < 7 b.d.l.	n = < 4 b.d.l.	n = 10 < b.d.l.	n = < 12 b.d.l.	n = < 12 b.d.l.	n = < 12 b.d.l.	n = < 13 b.d.l.	n = < 13 b.d.l.
Disseminated (B)	max.	0.047	3.02	19.72	1432	11.4	22.2	2.77	11.9	3.3	0.69	2.97	0.67
	avg.	0.02	2.0	14.16	1071	0.8	1.5	0.19	0.8	0.2	0.05	0.21	0.05
E11-89-4 (n = 7)	min.	n = 5 < b.d.l.	0.66	9.28	1354	n = < 4 b.d.l.	n = < 1 b.d.l.	n = < 3 b.d.l.	n = < 4 b.d.l.	n = < 3 b.d.l.	n = < 3 b.d.l.	n = < 3 b.d.l.	n = < 4 b.d.l.
Disseminated (B)	max.	0.040009	2.7	11.48	1536	0.95	2.12	0.234	1.27	0.23	0.117	0.31	0.053
	avg.	0.024	1.1	10.2	1445	0.22	0.47	0.05	0.30	0.1	0.030	0.104	0.016
E11-62-244 (n = 12)	min.	n = 10 < b.d.l.	2.33	8.93	2184	n = < 2 b.d.l.	n = < 1 b.d.l.	n = < 3 b.d.l.	n = < 5 b.d.l.	n = < 9 b.d.l.	n = < 5 b.d.l.	n = < 7 b.d.l.	n = < 5 b.d.l.
Disseminated and	max.	0.152	6.70	12.3	3600	113	144	16.3	66	15.1	4.6	15.8	2.38
vein (O)	avg.	0.063	4.0	10.6	2840	19	24	2.5	10	2.6	0.7	2.7	0.42
E11-145-111 (n = 14)	min.	n = 10 < b.d.l.	0.66	6.55	818	n = < 6 b.d.l.	n = < 9 b.d.l.	n = < 13 b.d.l.	n = < 12 b.d.l.	n = < 13 b.d.l.	n = < 10 b.d.l.	n = < 13 b.d.l.	n = < 12 b.d.l.
Vein (B)	max.	0.022	3.31	10.88	1698	0.02	0.071	0.024	0.109	0.072111	0.046	0.28	0.118
	avg.	0.014	1.0	8.2	1289	0.01	0.0145	0.004	0.010	0.011	0.006	0.02	0.010

Table 3.5. Continued

		Dy	Ho	Er	Tm	Yb	Lu	Ta	W
		m.d.l.	m.d.l.	m.d.l.	m.d.l.	m.d.l.	m.d.l.	m.d.l.	m.d.l.
Sample number		0.01	0.002	0.01	0.002	0.01	0.002	0.002	0.028
CL-16 (n = 10)	min.	n = < 6 b.d.l.	n = < 6 b.d.l.	n = < 9 b.d.l.	n = < 8 b.d.l.	n = < 7 b.d.l.	n = < 9 b.d.l.	0.9	0.107
Breccia (G)	max.	0.19	0.041	0.07	0.0134	0.13	0.0203	1.36	0.46
	avg.	0.06	0.011	0.04	0.0053	0.04	0.0089	1.0	0.26
E11-161-338 (n = 15)	min.	n = < 4 b.d.l.	n = < 5 b.d.l.	n = < 6 b.d.l.	n = < 7 b.d.l.	n = < 6 b.d.l.	n = < 7 b.d.l.	0.859	0.089
Breccia (G)	max.	20	3.1	6.3	0.6	2.6	0.274	2.86	0.57
	avg.	2	0.3	0.6	0.1	0.4	0.05	1.4	0.23
CL-77 (n = 14)	min.	n = < 14 b.d.l.	n = < 14 b.d.l.	n = < 13 b.d.l.	n = < 14 b.d.l.	n = < 14 b.d.l.	n = < 14 b.d.l.	0.349	n = < 3 b.d.l.
Breccia (O)	max.	-	-	0.007	-	-	-	1.78	0.56
	avg.	-	-	0.001	-	-	-	1.09	0.11
CL-58 (n = 10)	min.	n = < 6 b.d.l.	n = < 6 b.d.l.	n = < 4 b.d.l.	n = < 6 b.d.l.	n = < 3 b.d.l.	n = < 3 b.d.l.	0.742	0.144
Disseminated (B)	max.	46	15.7	77	16.6	165	34	2.81	0.41
	avg.	5	2	8	1.7	17	3	1.67	0.22
E11-105-133 (n = 15)	min.	n = < 12 b.d.l.	n = < 12 b.d.l.	n = < 13 b.d.l.	n = < 13 b.d.l.	n = < 13 b.d.l.	n = < 13 b.d.l.	0.178	0.21
Disseminated (B)	max.	4.09	0.7	1.92	0.268	1.71	0.269	1.68	0.68
	avg.	0.30	0.1	0.1	0.019	0.12	0.018	0.9	0.39
E11-89-4 (n = 7)	min.	n = < 3 b.d.l.	n = < 4 b.d.l.	n = < 3 b.d.l.	n = < 4 b.d.l.	n = < 2 b.d.l.	n = < 3 b.d.l.	0.0026	0.156
Disseminated (B)	max.	0.28	0.055	0.17	0.029	0.129	0.012	0.054	3.31
	avg.	0.10	0.019	0.07	0.007	0.05	0.003	0.024	0.82
E11-62-244 (n = 12)	min.	n = < 4 b.d.l.	n = < 5 b.d.l.	n = < 6 b.d.l.	n = < 6 b.d.l.	n = < 7 b.d.l.	n = < 8 b.d.l.	1.38	0.34
Disseminated and	max.	16.3	3.3	9.8	1.29	8.3	0.92	4.7	1.5
vein (O)	avg.	2.8	0.6	1.76	0.24	2	0.2	2.6	0.6
E11-145-111 (n = 14)	min.	n = < 10 b.d.l.	n = < 12 b.d.l.	n = < 11 b.d.l.	n = < 12 b.d.l.	n = < 11 b.d.l.	n = < 13 b.d.l.	0.083	n = < 2 b.d.l.
Vein (B)	max.	1.32	0.362	1.56	0.337	2.92	0.348	1.95	0.6
	avg.	0.10	0.027	0.12	0.026	0.21	0.025	0.31	0.2

Note: values are in ppm; samples below the detection limit were given the value of the detection limit in the average; b.d.l. = below detection limit and m.d.l. = mean detection limit

G = green-brown biotite, B = brown biotite, O = orange-brown biotite, n = number of samples,

Table 3.6. U-Pb titanite and rutile ID-TIMS analytical data

Fraction[1]	Description[2]	Wt. ug	U ppm	Pb[3] ppm	$^{206}Pb/^{204}Pb$[4]	Pb[5] pg	Isotopic Ratios[6] $^{208}Pb/^{206}Pb$	$^{207}Pb/^{235}U$	±1SE Abs	$^{206}Pb/^{238}U$	±1SE Abs	Corr.[7] Coeff.	$^{207}Pb/^{206}Pb$	±1SE Abs	Ages (Ma)[8] $^{206}Pb/^{238}U$	±2SE	$^{207}Pb/^{235}U$	±2SE	$^{207}Pb/^{206}Pb$	±2SE	% Disc
Titanite																					
Sample E12-360-LK13-117.8 (Z11115)																					
TA (T; 10)	pBr,Clr,Frag,fFr,fIn	20	58	47	340	113	0.64	13.473	0.037	0.514	0.001	0.696	0.190	0.000	2674.7	4.7	2713.4	5.2	2742.3	7.1	3.0
TB (T; 10)	pBr,Clr,Frag,fFr,fIn	20	58	48	1799	21	0.63	13.794	0.021	0.528	0.001	0.908	0.189	0.000	2733.1	5.7	2735.7	2.9	2737.6	2.1	0.2
TC (T; 10)	Br,Clr,Frag,fFr,fIn	30	44	36	196	237	0.61	13.639	0.062	0.522	0.001	0.655	0.190	0.001	2705.9	8.0	2725.0	8.6	2739.1	11.9	1.5
TD (T; 10)	Br,Clr,Frag,fFr,fIn	40	47	40	326	200	0.65	13.958	0.039	0.534	0.001	0.685	0.190	0.000	2758.6	5.4	2746.8	5.3	2738.2	7.0	-0.9
Rutile																					
Sample E11-107-4.5m (Z11004)																					
R1 (R; 6)	Or-Br;Clr,Frag,fFr,fIn	10	30	16	1382	7	0.08	12.557	0.017	0.502	0.001	0.896	0.182	0.000	2620.6	4.3	2647.0	2.5	2667.2	2.1	2.1
Sample 205716 (Z11125)																					
RA (R; 23)	Or-Br;sClr,Frag,fFr,fIn	40	9	5	210	55	0.16	12.251	0.052	0.489	0.001	0.657	0.182	0.001	2568.3	6.2	2623.9	8.0	2667.0	11.4	4.5
RB (R; 25)	Or-Br;sClr,Frag,fFr,fIn	40	13	9	37	851	0.32	13.986	0.657	0.534	0.027	0.883	0.190	0.005	2759.1	228.0	2748.7	89.0	2741.2	76.6	-0.8

[1]Number in bracket refers to the number of grains in the analysis. T = titanite; R = rutile

[2]Fraction descriptions: Br = Brown, pBr = pale brown, Or-Br = orange-brown, Clr = Clear, sCl = slightly cloudy, An = Anhedral, Frag = Fragment, fFr = Few Fractures, Fr = Fractures, fIn = Few Inclusions

[3]Radiogenic Pb

[4]Measured ratio, corrected for spike and fractionation

[5]Total common Pb in analysis corrected for fractionation and spike

[6]Corrected for blank Pb and U and common Pb, errors quoted are 1 sigma absolute; procedural blank values for this study ranged from 5-10 pg for Pb and ~0.1 pg for U; Pb blank isotopic composition is based on the analysis of procedural blanks; corrections for common Pb were made using Stacey and Kramers (1975) compositions

[7]Correlation Coefficient

[8]Corrected for blank and common Pb, errors quoted are 2 sigma in Ma

Table 3.7. SHRIMP U-Pb titanite results

Spot name	U (ppm)	Th (ppm)	Th/U	$^{206}Pb^*$ (ppm)	$^{204}Pb/^{206}Pb$	% ±	$f(206)^{204}$ %	$^{208*}Pb/^{206*}Pb$	% ±	$^{207*}Pb/^{235}U$	% ±	$^{206*}Pb/^{238}U$	% ±	Corr Coeff	$^{207*}Pb/^{206*}Pb$	% ±	Apparent Ages (Ma) $^{206}Pb/^{238}U$	±$^{206}Pb/^{238}U$	$^{207}Pb/^{206}Pb$	±$^{207}Pb/^{206}Pb$	Disc. (%)
Sample E12-360-LK13-117.8: z11115																					
11115-1.1	38	105	2.85	17	1.5E-3	7	1.99	0.58	1.0	13.6	2.8	0.525	2.7	0.950	0.524	1.2	2719	59	2730	15	+1
11115-4.1	28	86	3.24	12	1.1E-3	9	1.50	0.65	1.0	14.0	3.0	0.528	2.9	0.956	0.525	1.3	2731	64	2760	14	+1
11115-3.1	30	95	3.26	13	1.1E-3	9	1.46	0.64	1.0	13.7	2.9	0.521	2.8	0.959	0.517	1.2	2704	62	2752	14	+2
11115-7.1	30	87	2.97	13	1.4E-3	8	1.85	0.57	1.1	13.4	3.1	0.514	2.9	0.919	0.509	1.2	2675	63	2736	20	+3
11115-5.1	28	92	3.35	13	1.5E-3	9	1.96	0.69	1.0	13.9	3.1	0.520	2.9	0.941	0.514	1.3	2701	64	2771	17	+3
11115-6.1	30	88	3.02	14	1.7E-3	15	2.37	0.60	2.3	13.8	3.6	0.532	2.8	0.792	0.534	1.3	2750	63	2730	36	-1
11115-8.1	24	75	3.27	10	1.1E-3	10	1.48	0.67	1.0	13.8	3.2	0.517	3.0	0.955	0.509	1.3	2686	66	2773	15	+4
11115-10.1	43	119	2.84	20	7.8E-4	9	1.05	0.57	0.9	14.1	2.7	0.537	2.6	0.967	0.539	1.2	2770	58	2745	11	-1
11115-9.1	37	108	3.01	17	1.1E-3	10	1.55	0.61	1.0	13.8	2.9	0.530	2.7	0.943	0.530	1.2	2739	61	2737	16	-0
11115-11.1	32	91	2.94	15	1.1E-3	17	1.53	0.59	1.2	13.9	3.1	0.532	2.7	0.896	0.533	1.2	2750	61	2738	22	-1
11115-12.1	28	89	3.32	13	1.5E-3	17	2.01	0.66	1.3	13.9	3.4	0.532	2.9	0.851	0.533	1.3	2749	64	2740	29	-0
11115-14.1	33	91	2.89	15	1.1E-3	8	1.52	0.58	1.0	13.9	2.9	0.528	2.7	0.930	0.527	1.2	2735	61	2748	18	+1
11115-15.1	39	121	3.17	18	1.1E-3	20	1.54	0.63	1.3	13.8	3.9	0.518	2.7	0.707	0.510	1.2	2689	60	2774	45	+4
11115-17.1	30	97	3.33	14	1.5E-3	20	2.04	0.66	1.5	13.7	3.5	0.533	2.8	0.799	0.537	1.3	2756	63	2715	35	-2
11115-18.1	32	89	2.86	14	2.2E-3	7	3.02	0.56	1.4	13.6	3.6	0.509	2.9	0.802	0.498	1.2	2651	63	2775	36	+5
11115-19.1	28	97	3.56	13	1.6E-3	8	2.16	0.69	1.5	13.6	3.1	0.525	2.9	0.945	0.523	1.3	2718	65	2729	17	+0

Grain mount IP730; spot size 13µm x 16µm; # of scans = 6; Error in $^{206}Pb/^{238}U$ calibration = 1.6%

Notes (see Stern, 1997):

Spot name follows the convention x-y.z; where x = sample number, y = grain number and z = spot number. Multiple analyses in an individual spot are labelled as x-y.z.z

Uncertainties reported at 1s (absolute) and are calculated by numerical propagation of all known sources of error

* refers to radiogenic Pb (corrected for common Pb)

Discordance relative to origin = 100 * (($^{207/206}$ age - $^{206/238}$ age)/($^{207Pb/206}$Pb age))

Calibration standard; U = 260 ppm; Age = 1047 Ma; $^{206}Pb/^{238}U$ = 0.176

Table 3.8. U-Pb titanite LA ICP-MS analytical data

Spot name	Compositional data (ppm)				Isotope Ratios										Age Estimates								% Disc.
	U	Th	Pb	U/Th	$\frac{^{207}Pb}{^{235}U}$	2σ	$\frac{^{206}Pb}{^{238}U}$	2σ	ρ	$\frac{^{207}Pb}{^{206}Pb}$	2σ	$\frac{^{238}U}{^{206}Pb}$	2σ	ρ	$\frac{^{206}Pb}{^{238}U}$	2σ	$\frac{^{207}Pb}{^{235}U}$	2σ	$\frac{^{207}Pb}{^{206}Pb}$	2σ	^{207}Pb age	2σ	
Sample E11-95-254B																							
254/1	28	135	43	0.21	14.02	0.66	0.532	0.012	0.33	0.190	0.007	1.880	0.042	0.18	2747	51	2742	44	2760	38	2752	63	5.1
254/2	12	124	41	0.10	14.65	0.97	0.528	0.021	0.39	0.208	0.015	1.894	0.075	0.12	2728	86	2793	69	2873	70	2551	90	12.1
254/3	18	217	74	0.09	14.24	0.86	0.535	0.019	-0.06	0.197	0.014	1.869	0.066	0.53	2759	80	2759	59	2792	41	2780	170	9.2
254/4	13	131	43	0.10	14.31	0.69	0.536	0.014	-0.09	0.197	0.011	1.866	0.049	0.69	2763	58	2762	45	2772	58	2750	100	8.9
254/5	52	443	141	0.12	14.34	0.41	0.537	0.015	0.21	0.198	0.006	1.862	0.052	0.58	2768	62	2769	28	2793	33	2756	98	6.1
254/6	12	117	39	0.11	17.10	1.60	0.557	0.025	0.62	0.224	0.017	1.795	0.081	-0.06	2850	100	2921	90	3006	59	2810	170	8.4
254/7	11	111	39	0.10	16.00	1.20	0.553	0.025	0.21	0.211	0.017	1.808	0.082	0.45	2830	100	2862	72	2899	87	2660	130	11.5
254/8	23	295	96	0.08	14.75	0.77	0.544	0.017	0.35	0.195	0.010	1.838	0.057	0.32	2796	70	2791	46	2800	50	2810	110	7.2
254/9	16	144	50	0.11	15.69	0.80	0.542	0.023	0.59	0.214	0.009	1.845	0.078	0.05	2782	94	2845	50	2953	38	2660	130	12.2
254/10	14	167	56	0.08	15.14	0.78	0.543	0.020	0.12	0.204	0.013	1.842	0.068	0.07	2792	82	2814	48	2930	120	2700	130	11.5
254/1b	35	86	29	0.41	14.30	0.45	0.535	0.016	0.17	0.196	0.005	1.869	0.056	0.82	2762	66	2767	30	2754	61	2770	110	5.7
254/2b	45	56	18	0.81	14.09	0.55	0.533	0.017	-0.29	0.194	0.006	1.876	0.060	0.54	2754	70	2773	53	2803	28	2750	110	5.5
254/3b	61	168	53	0.37	13.94	0.62	0.534	0.012	0.09	0.190	0.008	1.873	0.042	0.27	2758	52	2741	39	2780	69	2760	100	4.8
254/4b	39	92	30	0.43	13.95	0.45	0.535	0.012	0.25	0.191	0.007	1.869	0.042	-0.09	2777	57	2743	30	2745	35	2778	92	6.0
254/5b	33	72	23	0.46	14.10	0.72	0.536	0.013	-0.28	0.199	0.026	1.866	0.045	0.55	2766	54	2792	89	2828	99	2730	130	9.1
254/6b	23	104	32	0.23	14.09	0.55	0.525	0.011	-0.39	0.195	0.009	1.905	0.040	0.52	2721	47	2752	37	2779	42	2695	73	4.8
254/7b	26	168	57	0.15	14.98	0.73	0.536	0.017	0.23	0.205	0.009	1.866	0.059	-0.17	2763	72	2811	46	3100	250	2720	130	5.9
254/8b	16	135	49	0.12	14.01	0.66	0.531	0.016	0.39	0.193	0.008	1.883	0.057	0.31	2745	68	2747	44	2768	23	2750	110	4.7
254/9b	17	69	22	0.25	17.11	0.72	0.557	0.013	-0.02	0.223	0.011	1.795	0.042	0.60	2854	55	2933	40	2974	60	2767	89	8.9
Sample E11-116-LK13-172.7																							
172/1	117	473	171	0.25	13.45	0.21	0.512	0.006	0.49	0.190	0.003	1.952	0.022	0.25	2669	26	2709	15	2744	13			5.1
172/2	40	169	63	0.24	13.93	0.34	0.526	0.010	-0.03	0.191	0.006	1.900	0.034	0.08	2724	39	2739	22	2746	28			8.3
172/3	101	284	104	0.36	13.29	0.21	0.509	0.006	0.51	0.190	0.003	1.965	0.022	0.14	2651	24	2698	15	2740	12			5.0
172/4	100	268	105	0.38	13.65	0.24	0.522	0.006	0.35	0.191	0.003	1.916	0.021	0.28	2706	25	2726	16	2747	14			4.6
172/5	91	165	65	0.56	13.43	0.29	0.517	0.006	0.42	0.190	0.004	1.935	0.023	0.12	2684	26	2710	21	2738	15			4.6
172/6	73	243	96	0.30	13.83	0.35	0.528	0.009	0.57	0.191	0.004	1.893	0.033	0.10	2733	39	2733	24	2752	17			5.1
172/7	33	179	67	0.19	13.29	0.36	0.507	0.009	0.41	0.190	0.005	1.972	0.033	-0.01	2641	37	2693	26	2742	19			7.6
172/8	45	143	54	0.32	13.54	0.30	0.511	0.007	0.31	0.193	0.004	1.955	0.026	0.09	2661	29	2713	21	2763	16			6.6
172/9	86	119	44	0.73	13.26	0.29	0.505	0.008	0.44	0.190	0.004	1.980	0.033	0.28	2640	37	2694	21	2742	17			6.9
172/10	90	154	55	0.58	13.21	0.28	0.504	0.007	0.54	0.191	0.003	1.984	0.028	0.10	2630	30	2691	20	2748	14			5.7
172/11	65	151	52	0.42	13.19	0.28	0.505	0.008	0.50	0.190	0.004	1.981	0.030	0.16	2632	33	2687	21	2742	13			7.3
172/12	31	115	42	0.27	13.94	0.54	0.524	0.012	0.44	0.194	0.006	1.908	0.044	-0.12	2712	50	2738	35	2781	42			6.8
172/13	89	272	86	0.32	12.94	0.38	0.490	0.009	0.60	0.191	0.005	2.039	0.039	0.02	2571	41	2678	25	2746	18			7.1
172/14	39	164	57	0.24	13.55	0.53	0.519	0.011	0.00	0.191	0.008	1.927	0.041	0.47	2695	45	2714	37	2759	36			6.4
172/15	97	280	96	0.34	13.44	0.30	0.513	0.007	0.56	0.191	0.003	1.951	0.028	0.18	2666	32	2707	21	2745	15			4.7
172/16	41	148	51	0.28	13.15	0.38	0.507	0.009	0.22	0.189	0.006	1.972	0.036	0.21	2642	39	2686	26	2739	29			7.5
172/17	71	168	57	0.42	13.56	0.32	0.522	0.008	0.40	0.191	0.004	1.916	0.030	0.26	2706	35	2716	22	2749	23			5.2

Table 3.8. Continued

Spot name	Compositional data (ppm)				Isotope Ratios										Age Estimates								% Disc.
	U	Th	Pb	U/Th	$\frac{^{207}Pb}{^{235}U}$	2σ	$\frac{^{206}Pb}{^{238}U}$	2σ	ρ	$\frac{^{207}Pb}{^{206}Pb}$	2σ	$\frac{^{238}U}{^{206}Pb}$	2σ	ρ	$\frac{^{206}Pb}{^{238}U}$	2σ	$\frac{^{207}Pb}{^{235}U}$	2σ	$\frac{^{207}Pb}{^{206}Pb}$	2σ	^{207}Pb age	2σ	
Sample E11-116-LK13-172.7																							
172/18	76	99	32	0.76	13.16	0.23	0.507	0.007	0.51	0.190	0.003	1.973	0.026	0.19	2642	29	2690	17	2745	12			6.3
172/19	82	260	88	0.31	13.11	0.25	0.506	0.007	0.45	0.190	0.003	1.975	0.027	0.11	2640	29	2684	18	2744	13			5.7
172/20	63	113	35	0.55	12.88	0.29	0.496	0.007	0.38	0.190	0.004	2.016	0.029	0.23	2595	31	2665	21	2743	15			7.5
172/21	38	110	34	0.34	13.14	0.29	0.504	0.008	0.00	0.190	0.005	1.985	0.030	0.22	2628	33	2685	21	2730	25			7.1
172/22	36	280	88	0.13	13.18	0.28	0.504	0.008	0.50	0.192	0.004	1.985	0.030	0.23	2628	33	2687	20	2753	18			6.5
172/23	30	189	59	0.16	12.74	0.28	0.495	0.007	0.43	0.188	0.004	2.020	0.028	0.16	2591	30	2655	21	2727	18			6.5
172/24	50	412	126	0.12	13.05	0.44	0.499	0.011	0.49	0.189	0.006	2.004	0.044	0.13	2609	48	2678	32	2734	24			6.8
172/25	45	179	59	0.25	13.44	0.30	0.504	0.007	0.50	0.195	0.004	1.984	0.029	0.07	2630	31	2705	22	2785	20			6.6
172/26	78	214	72	0.37	13.22	0.21	0.507	0.006	0.47	0.191	0.003	1.974	0.021	0.16	2641	23	2694	16	2751	12			5.2
172/27	75	266	95	0.29	13.84	0.38	0.529	0.009	0.52	0.192	0.005	1.889	0.031	0.10	2738	36	2735	26	2761	23			3.9
172/28	53	360	113	0.15	11.27	0.54	0.428	0.014	0.48	0.192	0.008	2.336	0.076	0.19	2295	64	2541	44	2753	33			14.5
Sample E10-19-154																							
154/1	23	46	17	0.51	13.92	0.89	0.526	0.017	0.42	0.195	0.011	1.901	0.061	0.06	2723	71	2729	61	2783	52			8.5
154/2	43	81	31	0.53	14.03	0.48	0.520	0.011	0.08	0.199	0.007	1.923	0.041	0.02	2693	48	2737	32	2809	29			11.1
154/3	69	130	50	0.54	14.17	0.49	0.531	0.011	0.46	0.197	0.006	1.883	0.039	0.12	2745	47	2753	33	2803	23			6.9
154/4	62	115	44	0.54	13.88	0.44	0.524	0.010	-0.03	0.194	0.006	1.907	0.035	0.09	2715	40	2733	30	2773	23			7.1
154/5	59	107	42	0.56	14.25	0.49	0.528	0.012	0.28	0.198	0.007	1.894	0.043	0.35	2732	49	2762	32	2804	36			6.2
154/6	77	125	51	0.61	14.05	0.39	0.524	0.009	-0.13	0.215	0.037	1.908	0.034	0.18	2714	39	2746	26	2803	20			8.4
154/7	63	105	40	0.60	14.14	0.46	0.529	0.009	0.41	0.196	0.006	1.892	0.033	0.12	2733	40	2751	31	2786	23			6.8
154/8	72	121	44	0.60	13.38	0.38	0.499	0.009	0.49	0.197	0.005	2.006	0.038	0.19	2605	40	2701	27	2798	20			8.4
154/9	70	111	42	0.64	13.91	0.50	0.524	0.011	0.42	0.194	0.006	1.908	0.040	0.20	2714	48	2736	34	2774	27			6.8
154/10	56	103	38	0.54	14.12	0.84	0.523	0.015	0.03	0.193	0.012	1.912	0.055	0.16	2706	60	2723	33	2796	69			12.1
154/11	69	125	46	0.56	14.00	0.43	0.524	0.011	0.47	0.197	0.006	1.908	0.040	0.20	2715	47	2748	31	2798	23			7.1
154/12	63	111	41	0.57	13.61	0.51	0.525	0.011	0.08	0.188	0.008	1.905	0.040	0.43	2718	46	2715	36	2718	38			7.3
154/13	58	94	34	0.61	13.89	0.72	0.526	0.024	0.19	0.185	0.008	1.901	0.087	0.27	2719	94	2732	42	2720	55			9.9
154/14	57	113	43	0.51	13.77	0.55	0.523	0.012	0.34	0.190	0.008	1.912	0.044	0.23	2709	50	2728	40	2745	30			5.4
154/15	68	120	48	0.58	14.07	0.48	0.530	0.013	0.07	0.195	0.006	1.887	0.046	0.07	2748	54	2745	32	2785	24			8.4
154/16	54	101	37	0.54	13.93	0.49	0.522	0.017	0.01	0.192	0.007	1.916	0.062	0.04	2699	67	2734	32	2770	27			10.9
154/17	75	112	38	0.68	12.90	0.31	0.493	0.007	0.55	0.192	0.004	2.030	0.030	0.10	2580	31	2665	23	2752	17			7.8
154/18	68	117	44	0.59	13.90	0.48	0.529	0.015	0.20	0.188	0.008	1.890	0.054	0.30	2734	61	2735	33	2741	38			8.9
154/19	62	111	41	0.57	13.52	0.58	0.521	0.012	0.67	0.185	0.007	1.919	0.044	-0.31	2701	52	2707	41	2737	44			7.3
154/20	66	116	44	0.57	13.71	0.44	0.525	0.012	0.33	0.189	0.006	1.905	0.044	0.31	2719	50	2723	31	2729	23			8.3
154/21	64	122	44	0.53	13.39	0.50	0.522	0.014	0.10	0.185	0.008	1.916	0.051	0.50	2704	59	2702	34	2695	39			8.2
154/22	77	117	41	0.66	13.28	0.55	0.519	0.012	0.50	0.186	0.006	1.927	0.045	-0.09	2691	53	2690	40	2724	24			6.7
154/23	73	119	42	0.62	13.33	0.55	0.523	0.010	0.22	0.180	0.005	1.912	0.036	0.01	2709	42	2694	34	2677	50			7.7
154/24	78	123	43	0.64	12.84	0.33	0.504	0.009	0.57	0.185	0.004	1.985	0.034	0.04	2632	35	2660	25	2694	15			6.6
154/25	50	99	34	0.51	13.69	0.51	0.516	0.013	0.55	0.190	0.006	1.938	0.049	0.12	2679	55	2721	36	2742	23			7.1

Table 3.8. Continued

Spot name	Compositional data (ppm)				Isotope Ratios										Age Estimates								% Disc.
	U	Th	Pb	U/Th	$\frac{^{207}Pb}{^{235}U}$	2σ	$\frac{^{206}Pb}{^{238}U}$	2σ	ρ	$\frac{^{207}Pb}{^{206}Pb}$	2σ	$\frac{^{238}U}{^{206}Pb}$	2σ	ρ	$\frac{^{206}Pb}{^{238}U}$	2σ	$\frac{^{207}Pb}{^{235}U}$	2σ	$\frac{^{207}Pb}{^{206}Pb}$	2σ	^{207}Pb age	2σ	
Sample E10-19-154																							
154/26	65	117	41	0.56	13.30	0.45	0.507	0.010	0.38	0.189	0.006	1.972	0.039	0.03	2642	44	2695	31	2718	21			7.7
154/27	41	70	26	0.58	12.78	0.55	0.493	0.012	0.35	0.190	0.007	2.028	0.049	0.07	2579	52	2649	39	2736	32			10.2
154/28	70	114	42	0.62	13.60	0.53	0.525	0.015	0.31	0.187	0.007	1.905	0.054	0.26	2716	64	2721	40	2717	30			9.2
154/29	76	110	38	0.69	12.81	0.45	0.498	0.011	0.50	0.185	0.006	2.008	0.044	0.00	2601	46	2652	31	2713	28			9.6
154/30	28	58	21	0.47	13.94	0.89	0.522	0.015	0.51	0.194	0.010	1.916	0.055	-0.15	2700	63	2718	52	2771	55			9.8
Sample E12-178-LK13-340.8																							
340/1	41	114	35	0.34	14.14	0.62	0.534	0.013	0.26	0.194	0.009	1.873	0.046	0.16	2755	53	2752	41	2797	47			7.2
340/2	30	21	9	1.32	13.99	0.62	0.531	0.021	0.01	0.193	0.008	1.883	0.074	0.57	2740	88	2741	41	2802	42			10.5
340/3	98	104	32	0.83	13.95	0.88	0.531	0.016	-0.01	0.192	0.011	1.883	0.057	0.22	2744	69	2738	54	2850	110			6.4
340/4	25	20	6	1.10	14.02	0.69	0.535	0.016	0.24	0.191	0.010	1.869	0.056	0.22	2759	66	2753	51	2778	51			9.7
340/5	81	160	50	0.47	13.83	0.47	0.544	0.012	-0.11	0.186	0.005	1.838	0.041	0.22	2798	49	2732	31	2692	20			6.6
340/6	60	163	49	0.40	13.87	0.43	0.533	0.016	0.93	0.200	0.014	1.876	0.056	-0.95	2751	70	2756	50	2748	29			7.2
340/7	86	223	70	0.44	14.04	0.58	0.526	0.017	0.25	0.195	0.005	1.901	0.061	0.72	2725	72	2749	39	2763	56			3.7
340/8	102	288	92	0.42	13.85	0.42	0.531	0.013	-0.08	0.198	0.014	1.883	0.046	0.25	2743	55	2735	28	2801	63			9.4
340/9	61	154	48	0.48	13.94	0.72	0.532	0.015	0.17	0.192	0.008	1.880	0.053	0.17	2744	61	2734	43	2798	58			8.2
340/10	68	197	60	0.43	13.67	0.34	0.529	0.010	0.51	0.191	0.004	1.890	0.036	0.33	2735	44	2724	23	2751	11			6.3
340/11	55	156	50	0.45	13.88	0.45	0.538	0.012	0.09	0.188	0.005	1.859	0.041	0.17	2782	53	2735	28	2725	21			7.8
340/12	47	126	40	0.49	14.20	0.96	0.528	0.019	0.05	0.198	0.015	1.894	0.068	0.04	2746	88	2741	52	2775	72			13.2
340/13	44	131	43	0.44	14.07	0.94	0.540	0.015	0.51	0.191	0.011	1.852	0.051	0.01	2782	63	2751	63	2760	47			4.3
340/14	37	91	30	0.53	13.80	0.39	0.526	0.009	0.63	0.193	0.004	1.902	0.031	-0.44	2722	35	2731	26	2756	18			4.5

Note: The ^{207}Pb ages used a ^{207}Pb based common Pb correction assuming a common Pb composition following Kramers and Tolstikhin 1997 at 2.65 Ga; this was only calculated for samples displaying an obvious common Pb component.

Table 3.9. Summary of Re-Os analyses for molybdenite samples from the Côté Gold deposit

Sample number	Re (ppm)	± 2σ	^{187}Re (ppm)	± 2σ	^{187}Os (ppm)	± 2σ	Total common Os (pg)	Model age (Ma)	± 2σ with 1 (Ma)
NBxMolyLK13	341.7	0.88	214754	555.5	10055.9	7.36	11.9	2746.8	11.4
E14-479-89.2	334.2	0.86	210068	543.5	9797.2	7.83	3.9	2736.1	11.4

Table 3.10. Comparison of the features of Côté Gold deposit with intrusion-related gold deposit types

	Côté Gold deposit	Porphyry copper deposits[1]	Reduced intrusion[2]	Syenite associated[3]
Tectonic setting	extensionsal back-arc setting	Extensional to transtenional arc or back-arc setting	Extensional back-arc setting behind a thickened continental margin	Compressional setting along a major fault zones
Nature of host rocks	Tonalite and diorite; tholeiitic to calc-alkaline	Diorite to granodiorite to quartz monzonite; calc-alkaline to alkaline	Granodiorite to granite; calc-alkaline	Syenite to monzonite; alkaline
Depth	Shallow	~1 to 5 km	5 to 9 km	Shallow
Oxidation state	Oxidized	Oxidized	Reduced	Oxidized
Alteration types	Calcic (Amp), potassic (Bt), phyllic (Ms), sodic (Ab)	Calcic-sodic, potassic, phyllic,propylitic, argillic	Potassic, sericite, chlorite	Carbonate, albite, potassic, sericite
Alteration zoning	Potassic core (breccias) with phyllic overpint	Potassic → phyllic → propylitic	N/A	N/A
Mineralization styles	Breccias, veins, disseminations	Veins, disseminations, breccias	Vein, disseminations, breccias	Disseminations and veins
Metal associations	Au ± Cu ± Te ± (Mo-Ag)	Cu ± Mo ± Au ± Ag ± (Zn-Pb-Ag)	Au-Bi-Te-W-Mo-As ± (Pb-Zn-Ag)	Au-Cu-As-Te ± (Pb, W, Mo, Zn)

[1]Seedorff et al. (2005) and Sillitoe (2010)

[2]Thompson and Newberry (2000), Lang and Baker (2001), Hart (2007)

[3]Robert (2001)

Table 3.11. Comparison of the features of the Côté Gold deposit to key features of gold-rich porphyry copper deposits

	Côté Gold deposit	Gold-rich porphyry deposits
Tecontic setting	Extensional back-arc setting	Extensional oceanic- or continental-arc setting
Age	Archean; ca. 2740 Ma	Predominantly Tertiary in age
Level of emplacement	Shallow	1-2 km
Host rocks	Low-K tholeiitic diorite and quartz diorite and calc-alkaline tonalite	Low-K calc-alkaline diorite, quartz diorite and tonalite, through high-K calc-alkaine quartz monzonite to alkaline monzonite and syenite
Alteration types	Calcic (Amp), potassic (Bt), phyllic (Ms), epidote, sodic (albite) and chlorite	Calcic-sodic, potassic, propylitic, intermediate argillic, phyllic and advanced argillic
Alteration zoning	Deep calcic, central potassic (hydrothermal biotite breccia) with phyllic overprint	Deep calcic-sodic and central potassic alteration zone overprinted by later alteration types
Hydrothermal magnetite	Estimated ~ 3 vol. % in hydrothermal biotite breccia	Average 3 to 10 vol. % in potassic alteration zone
Mineralization styles	Hydrothermal breccias, stockworks and sheeted veins and disseminations	Stockworks and/or subparallel veins, disseminations and breccias
Metal association and sulphides	Au-Cu correlation in the hydrothermal biotite breccia; pyrite, chalcopyrite	Au-Cu correlation in potassic alteration zone; chalcopyrite (± bornite), pyrite

Note: Characteristic features of gold-rich porphyry copper deposits from Sillitoe (1979, 1993, 2000)

Chapter 4

4 Alteration Lithogeochemistry of an Archean Low-Grade, Large-Tonnage Intrusion-Related Gold Deposit: The Côté Gold Au(-Cu) Deposit, Swayze Greenstone Belt, Ontario

4.1 Abstract

A detailed analysis of the alteration lithogeochemistry and its implications for the genesis of the low-grade, large-tonnage Archean Côté Gold Au(-Cu) deposit, located in the Swayze greenstone belt, is presented. The deposit is hosted by tonalite and diorite of the ca. 2741 to 2739 Ma Chester intrusive complex. Mineralization occurs as disseminations, breccias and veins that are co-spatial with hydrothermal alteration (e.g., amphibole, biotite, muscovite, epidote, albite); all of this is constrained to ca. 2740 Ma.

The hydrothermal alteration and mineralization developed in several stages and are geochemically distinct. The first pulse of hydrothermal alteration resulted in a rare hydrothermal amphibole event, which manifests as veins and breccias. Mineral chemistry of the hydrothermal amphiboles indicates enrichments in MgO, SiO_2, CaO and F and lower TiO_2 and Cl contents in comparison to magmatic amphiboles. Main-stage biotite alteration resulted in several alteration styles with a central ore-bearing hydrothermal biotite breccia with disseminations and veins (i.e., sheeted and stockworks) occurring outwards. Biotite alteration is characterized by gains of FeO, MgO, MnO, CaO K_2O, Li, Rb, Cs, Ba, LREE, Zn, Pb, Te, F and LOI with additional enrichments of Au, Cu, Mo, Ag, Se and Bi documented in the hydrothermal biotite breccia and

sheeted veins. Muscovite occurs as replacement style alteration in the central portion of the deposit and is enriched in K_2O, Rb, Cs, Ba, CO_2, LOI and variably enriched in Au, Cu, Bi, W, S, Te, As, Pb, Sn, Mo and Ag. Epidote alteration occurs in the northern portions of the deposit as vein-controlled and replacement style and is characterized by gains of CaO, FeO_T, Sr and Bi. Albite alteration occurs in the centre of the deposit and is characterized by gains of Na_2O and losses of most elements. As a result of the intense leaching during albite alteration, most metals (i.e., Au, Cu) were remobilized, and in some cases removed, from the system. Chloritization is characterized by gains of P_2O_5, Sn, S, Bi, CO_2, LOI, Au and Cu and losses of K_2O, FeO, CaO, Li, Rb, Cs, Ba, Zn and Te; the losses reflect overprinting and destruction of the biotite alteration assemblage.

Changes in REE concentrations are documented in several hydrothermal stages, which reflects changing conditions during the evolution of the system. Similar REE concentrations between least-altered diorite and biotite altered diorite samples suggest a magmatic derivation for the biotite alteration. Subsequently, the LREE are depleted during muscovite alteration as a result of higher fluid/rock ratios and lower pH conditions during this hydrothermal stage; these fluid conditions support the ingress of seawater, which mixed with magmatic-derived fluids. Albite alteration is also noted to have depleted LREE, likely as the result of the instability of secondary LREE-bearing minerals.

A crude metal zoning in the deposit is noted, with the hydrothermal biotite breccia and sheeted veins are characterized by a Au-Cu-Mo-Ag-Te-Bi-Se association, whereas outwards from this the stockwork and disseminated zones have a Te-Se-Zn-Pb-As association. The magmatic-hydrothermal system responsible for the deposit is demonstrated to extend outside the

deposit (>2 km) into the regional east-west trending fracture system based on similar trace element concentrations in chalcopyrite from samples both inside and outside the deposit.

The lithogeochemical results presented in this study are consistent with a porphyry-type model for the deposit presented in Chapter 3. The data suggests the system developed from an early high-temperature magmatic-hydrothermal system derived from the dioritic melt, resulting in amphibole and biotite alteration, which mixed with lower temperature seawater, resulting in muscovite and epidote alteration.

This magmatic-hydrothermal system is demonstrated to extend outside the deposit and represents a large area for future exploration. This study provides useful exploration criteria to vector towards mineralization in the area surrounding the deposit and for exploration in other similar intrusive complexes in Archean greenstone belts.

4.2 Introduction

Alteration types and their geochemical signatures are used in part to define and distinguish different ore deposit types. The variation in the character and scope of this variation both among and within (e.g., porphyry deposits) different ore deposits are used to constrain the nature and origin of a deposit and also to define exploration vectors for specific deposits. In the case of the former, elemental associations and elemental gains and losses in alteration zones have been used to constrain the nature and source of fluids in many different ore deposit types. For example, these parameters have long been used to differentiate different gold deposit types, in particular, those of metamorphic versus magmatic affinity (e.g., McCuaig and Kerrich, 1994; Goldfarb et al., 2005).

In this paper, we describe the alteration geochemistry of a world class gold deposit that is unusual in many respects. The site of study is the Côté Gold Au(-Cu) deposit, a ca. 2740 Ma low-grade, large-tonnage deposit located in the Swayze greenstone belt (SGB) of northern Ontario, Canada. At the time of writing, total indicated resources were estimated at 296 Mt at 0.88 g/t Au (7.61 M oz) with an additional inferred 44 Mt at 0.74 g/t Au (1.04 M oz; IAMGOLD, 2013). The deposit is hosted by a tonalite-diorite-quartz diorite intrusive complex with the mineralization (e.g. veins, disseminations, breccias) both temporally and spatially related to magmatic-hydrothermal alteration (amphibole, biotite, muscovite, albite) and, as such, has been interpreted as an intrusion-related deposit with a porphyry-type affinity (Kontak et al., 2013a; Katz et al., 2015; Chapter 3). The Côté Gold deposit is the only significant gold deposit discovered thus far in the SGB and, therefore, it not only represents an uncommon deposit type in the Archean, but it also represents a new gold metallogenic event at 2740 Ma in the Abitibi Subprovince. Given the significance of this deposit, the intent of the study is to focus on characterizing the geochemical fingerprint of the alteration in order to constrain its genesis and better define exploration parameters. Some results on the nature of the fluids, as constrained from stable isotopes, can be found in Kontak et al. (2013a).

Previous studies of the deposit have focused on documenting the nature and timing of the host rocks (Kontak et al., 2013a; Katz et al., 2015; Chapter 2), as well as the nature, origin and timing of hydrothermal alteration and its associated mineralization (Kontak et al., 2013a; Chapter 3). Although certain geochemical aspects were reported by Kontak et al. (2013a), a detailed investigation of the alteration geochemistry and elemental mass balance is needed to improve the understanding of the deposit. In order to completely characterize the chemical attributes of the alteration and mineralization 405 samples from the deposit are utilized in this study. These

samples are used to expand on earlier work and provide a comprehensive documentation of the whole-rock geochemistry and mass balance calculations of the hydrothermal alteration assemblages in the Côté Gold deposit.

4.3 Regional Geology

The Côté Gold deposit is located in the southeastern limb of the SGB, which is part of the gold-rich Abitibi Subprovince (Fig. 4.1). The SGB is contiguous with the southern Abitibi greenstone belt (AGB), as it contains many of the same stratigraphic assemblages and structures typical of the southern AGB based on lithological and geochronological criteria (Ayer et al., 2002; van Breemen et al., 2006). Volcanic and plutonic rock types in the SGB are diverse and include ultramafic to felsic types, as well as both chemical and clastic sedimentary rock types. These rock units range in age from 2750 to 2675 Ma (Ayer et al., 2002).

The Chester intrusive complex (CIC), in which the deposit is hosted, was emplaced into the lowest group of the SGB, the Chester Group. The Arbutus Formation forms the oldest formation in the Chester Group and, hence, it comprises the oldest rocks within the SGB. This formation contains pillow basalts, mafic flows and massive, medium-grained amphibolite, interpreted to be either flows or intrusive sills (Heather, 2001). The formation has not been dated directly, but the Chester Group is inferred to be ca. 2750 to 2735 Ma.

The Yeo Formation forms the upper formation in the Chester Group and overlies the CIC based on the current map pattern. The Yeo Formation consists of intercalated felsic and intermediate volcanic rocks, clastic sedimentary and volcaniclastic rocks, iron formation and Fe-rich sedimentary rocks. Two U-Pb zircon ages from felsic lapilli tuffs constrain the formation to

2739 ± 1 (van Breemen et al., 2006) and 2734 ± 2 Ma (Heather and Shore, 1999a, b), indicating that it is a broadly co-temporal with the CIC.

The SGB has a complex structural history of polyphase folding with the development of multiple foliations, ductile high-strain zones and late brittle faulting (van Breemen et al., 2006). The preserved map pattern within the SGB formed during D_2 orogen-wide shortening (2696-2675 Ma; van Breemen et al., 2006) that contains several, regionally extensive, D_2 high-strain zones similar to the high-strain zones in the AGB (i.e., Larder Lake-Cadillac Deformation zone). Importantly, like in the AGB, the D_2 event in the SGB is inferred to have been synchronous with the generation of orogenic-style gold mineralization (Heather, 2001; van Breemen et al., 2006).

In the past, the potential for gold mineralization in the SGB was considered to be favourable based on both its proximity to and similar geology with the AGB (van Breemen et al., 2006), hence, it is not surprising that many prospects and occurrences have been documented (Siragusa, 1993a, b; Fumerton and Houle, 1993). A few of these occurrences were developed into small gold producers, such as Jerome (56, 897 oz Au) and Joburke (50, 150 oz Au; Heather et al., 1995). The Chester-1 zone (or Chester Mine), located approximately 2 km east-northeast of the Côté Gold deposit, was exploited for high-grade, sheeted quartz ± carbonate ± sulphide vein mineralization that was considered orogenic in origin. The Chester-1 zone was eclipsed, however, by the discovery of the Côté Gold deposit in 2009/2010.

Metamorphic grade within the southern AGB ranges from sub-greenschist to greenschist grade. Higher amphibolite grade conditions were locally attained next to large synvolcanic and syntectonic intrusions. Peak metamorphism is estimated to have occurred from 2677 to 2643 Ma (Powell et al., 1995).

4.4 Deposit Geology

4.4.1 Intrusive phases of the Chester intrusive complex

The Côté Gold deposit is hosted by the ca. 2741 to 2739 Ma CIC, a multi-phase, laccolith-shaped, synvolcanic intrusive complex that is 35 km (east-west) by 10 km (north-south; Fig. 4.2). The deposit is situated in the northwestern part of the CIC and is hosted by tonalite, diorite and quartz diorite rocks, plus magmatic and magmatic-hydrothermal breccia bodies (Fig. 4.3). A brief description of the host rocks is provided below. Readers are referred to Chapter 2 for a more comprehensive description of the host rocks.

Tonalite: The deposit is partly hosted by several calc-alkaline to transitional, low-Al (Barker, 1979) tonalite. The tonalite is the most common rock type in the deposit and forms numerous bodies of 10 to >100 m in thickness. The tonalite is a fine- to medium-grained leucocratic rock composed of equigranular quartz and plagioclase and rarely contains quartz or plagioclase phenocrysts.

A magmatic breccia occurs, termed a tonalite breccia, and is the result of tonalite brecciating along its intrusive margins. This breccia contains cm- to m-sized angular to rounded dioritic and rare tonalite fragments with sharp to diffuse boundaries.

Diorite: The deposit is also hosted by several tholeiitic to transitional phases of melanocratic to leucocratic diorite and quartz diorite with minor local hornblende-plagioclase ± quartz pegmatite dikes. Diorite and quartz diorite phases form 5 to <150 m thick intrusions, whereas the hornblende-plagioclase ± quartz pegmatite phase occurs as small <1 m dikes. The diorite is fine- to coarse-grained with rare plagioclase phenocrysts. Diorite is dominated by subequal amounts of hornblende and plagioclase with minor titanite, ilmenite and magnetite. The

quartz diorite is also fine- to coarse-grained and often has quartz and/or plagioclase phenocrysts. Quartz diorite is dominated by plagioclase, amphibole and quartz with the same minor phases as the diorite.

The second type of magmatic breccia occurs, termed a diorite breccia, and is the result of dioritic injections brecciating earlier tonalite and dioritic rocks. The breccia bodies occur as several injections that range from 10 cm to >100 m in apparent width. The bodies dip moderately to steeply to the north and occur in the south and central parts of the deposit. This breccia contains a dioritic matrix and angular to rounded fragments that range from cm to m-sized and have sharp contacts.

Magmatic and magmatic-hydrothermal breccias: Tonalite and diorite are crosscut by two types of magmatic-hydrothermal breccias: (1) amphibole-rich; and (2) biotite-rich. The breccia bodies are poorly exposed on surface, thus, much of its extent and features are based on drill core. In detail, however, the size and geometry of these breccia bodies remain poorly defined.

The hydrothermal amphibole-rich breccia unit is the least abundant of the breccia types and appears to be restricted to the southern and central part of the deposit. The breccia contains a fine- to coarse-grained black matrix that is composed of amphibole-quartz ± biotite ± chlorite ± carbonate ± sulphides with tonalite and rarely diorite fragments.

The hydrothermal biotite breccia occurs in the central and northern part of the deposit. The breccia contains several biotite-rich matrices: (1) a fine-grained biotite-quartz ± epidote ± calcite ± pyrite ± chalcopyrite ± magnetite ± allanite ± titanite ± fluorite; (2) a fine- to coarse-grained biotite-magnetite-quartz-ankerite-chalcopyrite-pyrite ± sphalerite ± allanite ± bastnaesite ± apatite ± titanite with ≤40% magnetite; or (3) biotite-ankerite/calcite-quartz-pyrite ± allanite ±

apatite ± magnetite ± chalcopyrite ± pyrrhotite. The breccia contains sub-rounded to angular monolithic tonalite fragments.

4.4.2 Alteration mineralogy, breccia cement and mineralization

The hydrothermal alteration and mineralization in the deposit developed in several stages with a total of five alteration assemblages identified which, from earliest to oldest, include: amphibole (calcic), biotite (potassic), muscovite (phyllic), epidote and albite (sodic). Chloritization of biotite occurs throughout the deposit but is interpreted to be the result of greenschist facies metamorphism (see Chapter 3). Figure 4.4 shows representative photos of the alteration assemblages and Table 4.1 summarizes the alteration assemblages and related vein types. The relationship between the timing of intrusions, certain alteration assemblages and mineralization is shown schematically in Figure 4.5 and is based on previous U-Pb titanite and Re-Os molybdenite dating (Kontak et al., 2013a; Chapter 3). All of the alteration assemblages are interpreted to be syn-intrusion in origin, except for chloritization. A detailed description of alteration assemblages, their distribution, associated veins, mineralization and a paragenesis is presented in Chapter 3 and what is presented below is a summary of this work.

Amphibole veins and breccias: The earliest hydrothermal event occurs as rare amphibole-bearing veins and breccias. This alteration occurs in the central and southern portions of the deposit. The amphibole hydrothermal event consists of amphibole-bearing breccias and several types of amphibole-bearing veins (Fig. 4.4A, B; Table 4.1). The veins are characterized by coarse-grained (<4 cm) hornblende. An amphibole-titanite-apatite-magnetite vein yielded an age of 2745 ± 3 Ma, constraining the age of this event (Chapter 3).

Amphibole veins and breccias are seen to cut barren diorite and tonalite and are typically gold-bearing (Fig. 4.4A), however, this alteration type is sulphide-poor. The paucity of this hydrothermal event within the deposit and its apparent lack of continuity means it does not make up a significant portion of ore.

Biotite alteration: The term "biotite alteration" is used herein in contrast to the common terms of potassic or K-silicate alteration, which was initially defined by Meyer and Hemley (1967). The biotite alteration assemblage is variable and occurs as a biotite ± quartz ± magnetite ± epidote ± allanite ± calcite ± ankerite ± pyrite ± chalcopyrite ± pyrrhotite ± apatite ± titanite ± bastnaesite ± fluorite ± sphalerite ± galena assemblage. Biotite is the most widespread alteration assemblage and occurs as disseminations (Fig. 4.4C), veins (Fig. 4.4C) and breccias (Fig. 4.4D). Biotite veins and disseminated are observed outward from the breccia and are known to extend outside the presently defined ore envelope.

The biotite alteration assemblage includes unusual LREE-bearing minerals, such as allanite (Fig. 4.4E, F) and bastnaesite (Fig. 4.4F), which occur as fine- to medium-grained, anhedral to euhedral crystals intergrown with biotite, epidote and titanite. These minerals are common in biotite altered samples being present in 10 of 19 biotite altered sections analyzed on the scanning electron microprobe analyses.

In drill core, disseminated biotite alteration occurs as spotted, black or brown biotite that makes up typically 3-12%. Disseminated biotite alteration occurs as fine-grained replacement of primary plagioclase and amphibole and replacement of hydrothermal amphibole. Veins occur as stockwork-like veins (Fig. 4.4C), discrete vein or subparallel sheeted vein sets with a variety of vein assemblages (Table 4.1). Sheeted veins are moderately to steeply dipping, east-west

trending, planar, subparallel, closely (cm to 10's of cm apart) to widely (several m apart) spaced veins that occur both in and outside the deposit. The sheeted veins are typically overprinted by muscovite alteration resulting in muscovite alteration haloes (Fig. 4.4G). Stockwork zones cut through both fragment and matrix in the breccia and therefore, postdate breccia formation.

Gold and copper mineralization are closely associated with the hydrothermal biotite breccia and are restricted to the breccia matrix. Gold mineralization is most consistent in the hydrothermal biotite breccia compared to erratically mineralized veins and typically unmineralized disseminations. The main sulphides are pyrite and chalcopyrite; the only Cu mineral is chalcopyrite and it is intergrown with gold.

Muscovite alteration: This alteration consists of muscovite ± quartz ± calcite ± pyrite ± chalcopyrite ± chlorite ± rutile. Muscovite alteration often occurs as alteration haloes around veins (Fig. 4.4G) and as replacement style alteration (Fig. 4.4H). Muscovite partially to wholly overprints biotite alteration in the central portions of the deposit.

Muscovite alteration is often spatially coincident with gold mineralization but is commonly inconsistent. Muscovite altered samples may have a Au ± Cu association. Sheeted quartz veins with muscovite alteration haloes are often mineralized (Fig. 4.4G), however, as noted in Chapter 3 these veins had an original biotite assemblage, and hence, some of the mineralization may be inherited. This overprinting of metals was documented in Chapter 3, where it was noted that muscovite alteration inherits the biotite sulphide assemblage.

Epidote alteration: Weakly developed patchy epidote alteration occurs throughout the deposit, but a zone of strong fracture-controlled epidote alteration thought to be syn-intrusion in timing occurs towards the north of deposit. The latter occurs in a small area ~300 m wide by 400

m long that contains a relatively continuous alteration zone that occurs north of the hydrothermal biotite breccia. The epidote alteration occurs as disseminated and vein-controlled alteration (Fig. 4.4I) and consists of epidote ± quartz ± calcite ± chlorite. Where veins occur, they often exhibit drusy textures. This alteration zone was interpreted to analogous to epidosite alteration (Chapter 3); epidosite alteration forms as part of a high-temperature reaction zone defining areas of upwelling seawater heated by an underlying intrusive body (Galley et al., 2007).

Epidote alteration is not typically associated with gold mineralization, however, one epidote-quartz vein did contain visible gold. Sulphide content is low in this alteration type and consists of pyrite and chalcopyrite.

Albite alteration: This alteration overprints and destroys earlier amphibole, biotite and muscovite alteration assemblages (Fig. 4.4H). At depth, this alteration appears to be most intense towards the centre of the deposit. The alteration envelope can be greater than 200 m wide and is moderately to steeply dipping to the north or northwest. The alteration assemblage consists of albite ± quartz ± calcite ± titanite ± ilmenite ± chlorite ± pyrite and is characterized by the replacement of primary minerals by albite (Fig. 4.4J), destruction of primary textures and bleaching of the rock (Fig. 4.4K). Albite occurs as both vein-controlled (Fig. 4.4H; Table 4.1) and replacement-style alteration. The timing of this alteration event is constrained based on three U-Pb titanite ages at 2737.5 ± 2.2/-1.8 Ma, 2736 ± 7 Ma and 2745 ± 9 Ma (Chapter 3).

Rarely this alteration becomes very intense (10 to 11 wt. % Na_2O) and occurs as small, light-pink to brown-red porous zones, typically <15 m in apparent width. Albite is the dominant mineral due to the replacement of plagioclase and mafic minerals and dissolution of quartz. The dissolution of quartz results in variable amounts of porosity, which is filled with a second

generation of clear albite that lines the pore space along with trace amounts of titanite, hematite, rutile, apatite, zircon and chlorite. This intense albite alteration type has been termed episyenite.

The albite alteration zone is co-spatial with the gold mineralization, but it is patchy and inconsistent. The inconsistent nature of the mineralization was suggested to be the result of remobilization of earlier mineralization associated with the biotite and muscovite alteration (see Chapter 3). Sulphides are generally not present in samples affected by pervasive albite alteration.

Chlorite alteration: Chlorite is ubiquitous throughout the deposit and occurs as disseminated and replacement-style alteration. Petrographic observations indicate that chlorite partially to wholly replaces primary plagioclase, amphibole and hydrothermal amphibole and biotite. Chlorite commonly replaces the earlier biotite alteration (Fig. 4.4L, M), hence it is associated with titanium-bearing phases, such as ilmenite and rutile.

Gold mineralization is spatially associated with chlorite, but chlorite pseudomorphs earlier, higher-temperature hydrothermal biotite alteration and inherits the biotite sulphide paragenesis (Chapter 3). Thus, a genetic association remains to be established.

4.5 Analytical Methods

4.5.1 Petrography and scanning electron microprobe analyses

Petrographic analysis, in both transmitted and reflected light, of approximately 500 thin and polished thin sections from drill core was done to establish the alteration mineral assemblages. Of the 500 thin section samples, 310 polished thin sections contained corresponding complete whole-rock geochemical analyses. Petrography was an important aspect

of this study because identification of diagnostic minerals in each alteration assemblage can be used to help chemically fingerprint the hydrothermal stages. In addition, the information gathered from the petrographic analysis was used to explain why certain elements were gained or lost in the mass balance section.

In addition to the petrography work, semi-quantitative scanning electron microprobe - energy dispersive spectrometer (SEM-EDS) analyses were obtained in the Central Analytical Facilities (CAF) at Laurentian University. These data were collected using a JEOL6400 SEM instrument with an attached solid-state detector using an accelerating voltage of 20 kV, beam current of ~ 1 nA and collection time of 5 seconds for spot analysis. The data were processed with INCA software package. A total of 31 polished thin section were used in order to identify all the alteration minerals present and textural relationships between alteration phases.

4.5.2 Laser ablation-inductively coupled plasma-mass spectrometry (LA ICP-MS)

Chalcopyrite trace element concentrations were determined in-situ by LA ICP-MS method. The chalcopyrite trace element study was completed in order to: (1) compare the results from samples within the deposit to samples outside the deposit in the Chester-1 zone; and (2) see if there was anything anomalous or unusual in chalcopyrite. The results are found in Table 4.2.

The measurements were performed in the Chemical Fingerprinting laboratory of Laurentian University, Canada, using a 20 ns pulse duration, 193 nm wavelength ArF excimer laser (Resonetics RESOlution M-50) employing a two-volume Laurin Technic sample cell (Müller et al., 2009) coupled to a Ar plasma quadrupole ICP-MS (Thermo X Series II). Ablation took place in He (650 ml/min) which was combined with Ar (800 ml/min) and N_2 for enhanced

sensitivity (6 ml/min) prior to the plasma. For chalcopyrite, traverses were preferred over spots to avoid ablating through the mineral and into the thin section below due its rapid ablation rate. The traverses were carried out with the beam diameter (26 to 90 µm) and speed (10 – 35 µm/s) adjusted according to the grain size to provide adequate sampling time and maximum signal intensities. Only sample CL-10-03 had to be analyzed as spots, where a beam diameter of 66 µm was used. For all chalcopyrite analyses the laser repetition rate and fluence were 6 Hz and 5 J/cm^2, respectively. The chalcopyrite spot and line analyses typically consisted of 30 s of background followed by 30 s of ablation or longer (for traverses). The ICP-MS was operated with a forward power of 1450 W and an oxide production rate of < 0.4% as determined by measuring ThO^+/Th^+ while ablating NIST SRM 612. Dwell times were set at 10 ms per analyte for all measurements. Data reduction was done with the Iolite software package (v. 2.5; Paton et al., 2011) using NIST SRM 610 (bracketing and between every 7 or fewer analyses) as an external reference and Cu (34.6%) as internal references for chalcopyrite. Mass 108 was used to determine Pd concentrations after being corrected for ^{108}Cd by the measured ^{111}Cd and assuming $^{108}Cd/^{111}Cd = 0.06953$. Reference materials BHVO-2g and Po725 (Sylvester et al., 2005) were also analyzed periodically and typically return concentrations within 15% of their accepted values. Segments of the data displaying abnormal behaviour, presumably due to cracks or inclusions, were avoided during data reduction.

4.5.3 Geochemistry

A total of 455 samples were collected as part of the study of the deposit. Of these samples, 405 were collected from 15 drill holes selected from throughout the deposit (see locations in Figure 4.3) in order to chemically characterize the nature of the alteration and

fingerprint the mineralization; with an additional 12 samples collected from either outcrops or specifically selected intersections in drill core. The samples used in this study include tonalite, diorite, quartz diorite, diorite breccia, magmatic-hydrothermal breccia and veins. All of the geochemical data, analytical methods, location of sample (drill collar, depth), a representative photo of the sample and a brief sample description can be found in Katz et al. (2016).

Whole-rock analyses of the samples were done in two batches at Activation Laboratories in Ancaster, Ontario. Major elements were determined by lithium metaborate-tetraborate fusion inductively coupled plasma (ICP) mass spectrometry (MS), whereas trace and rare earth elements were determined by a combination of fusion ICP, fusion inductively coupled plasma mass spectrometry (ICP-MS) and total digestion ICP-MS. For As, Sb, Bi Se and Te, abundances were determined by a combination of aqua regia ICP-MS and nitric peroxide fusion ICP-MS, whereas Au, Pd and Pt were measured by fire assay. The FeO contents were determined by titration. For the anions, Cl was determined by instrumental neutron activation, B by prompt gamma neutron activation and F by ion selective method. Both S and CO_2 were determined by infrared analysis and Hg by cold vapor flow injection mercury technique.

4.5.4 Mass balance

In order to quantify the changes in rock volume and elemental concentrations in the alteration zones, the best-fit isocon method of Grant (1986) was used for mass balance. This procedure was performed on 115 samples collected along 14 drill holes and one outcrop sample in order to calculate the respective gains and losses. For these calculations, the least-altered tonalite and dioritic rocks were first identified on the basis of petrographic and geochemical

criteria, although in some cases the selection of appropriate least-altered samples was difficult due to the common presence of alteration in much of the deposit. However, a group of 5 tonalite, 4 diorite and 6 quartz diorite samples were selected from the several hundred analyses to define the average composition of the least-altered protoliths; these data are given in Tables 4.3 and 4.4.

The calculations were performed using the least-altered tonalite, diorite and quartz diorite samples and representative samples for a specific alteration assemblage, which in this case included biotite, muscovite, epidote, albite and chlorite samples. In order to constrain the overall geochemical trends, as well as their variability, the samples for each alteration type were averaged (Tables 4.3, 4.4). Following this, the data were plotted on isocon diagrams (Grant, 1986) which allowed identification of a reference isocon (i.e., a line of constant concentration for element ratios that remained constant during alteration) for each of the main alteration types. In general, the elements used to define the isocons were Al_2O_3, TiO_2, Zr and SiO_2.

4.6 Alteration Geochemistry and Elemental Mass Balance

This section serves to geochemically fingerprint all alteration assemblages in the deposit. Several down-hole geochemical profiles (Fig. 4.6) are also provided to illustrate the distribution of the alteration and the diagnostic elements used to discriminate the alteration assemblages. In addition, the geochemical profiles easily show which rock and/or alteration type is spatially associated with Au mineralization. Chondrite-normalized REE diagrams and several binary element plots are also used to geochemically fingerprint the different alteration assemblages. Mass balance calculations provide semi-quantitative results of elemental gains and losses and the geochemical signatures of the fluids responsible for the hydrothermal events.

The main hydrothermal events spatially associated with mineralization include biotite, muscovite, albite and chlorite, thus they are the most significant and are the focus of the geochemical study. The amphibole hydrothermal event is spatially coincident with gold mineralization, but given its paucity in the deposit and its hydrothermal alteration style (e.g., veins and breccias) it is not focused on in this study.

4.6.1 Alteration geochemistry

Amphibole alteration: Due to the nature of the amphibole hydrothermal event (i.e., veins and breccias) it is difficult to geochemically characterize this hydrothermal event, however, microprobe analyses of magmatic and hydrothermal amphibole from Chapter 2 (see Table C.1 in Appendix C for microprobe results) allow some degree of characterization. The microprobe results reveal hydrothermal amphiboles typically contain higher SiO_2 and CaO contents than magmatic amphiboles, whereas TiO_2 is the reverse. In particular, the amphiboles from the breccia contain higher Mg and F contents and lower Cl contents than vein or magmatic amphiboles.

Biotite alteration: The mineralogy of this alteration assemblage can be used to geochemically fingerprint it with LREE-bearing minerals (e.g., allanite, bastnaesite) and F-bearing minerals (i.e., biotite, fluorite, apatite, titanite) being particularly useful. In the case of the former, the presence of minor amounts of the LREE-bearing minerals results in an increase in the LREE compared to the least-altered samples. Thus, a La/Yb_N ratio of greater than around 4 identifies biotite altered tonalite samples (Fig. 4.7A). The F enrichment appears to depend on the amount of biotite present in samples as it is the main carrier of F. Thus, the lack of a correlation

between K_2O and F in the biotite altered tonalite samples is attributed to the low percentage of disseminated biotite (typically <12%) which contrasts with the positive trend seen in the hydrothermal biotite breccia (r = 0.93; Fig. 4.7B) where >50% biotite in the assemblage is common, along with higher abundances of other F-bearing phases. The biotite altered tonalite samples also display a strong positive correlation between K_2O and Ba (r = 0.79; Fig. 4.7C) and moderate positive correlation between K_2O and Rb (not shown; r = 0.66). The hydrothermal biotite breccia samples, however, contain a distinctly different trend between K_2O and Ba with only a moderate positive correlation (r = 0.45; Fig. 4.7C). Thus, the data suggest that an increase La/Yb_N ratio and elevated K, Rb and Ba values can serve as a chemical fingerprint for biotite alteration, whereas F is only a useful discriminate for the hydrothermal biotite breccia.

Geochemical profiles of drill holes E10-13, E11-161 and E11-116 (Fig. 4.6A, B, C, respectively) demonstrate the spatial association of Au with the hydrothermal biotite breccia. Not only is there an association of breccia with Au, but the geochemical profiles also highlight a Au-Cu ± Te association in this unit. The Au-Cu ± Te association is particularly evident in hole E11-161 (Fig. 4.6B), which notably is the least-altered of all the geochemical profiles. Hole E11-161 also shows a clear increase in K_2O, FeO_T, and Rb associated with the breccia unit. Furthermore, the Cu vs. Au plot shows a Au-Cu correlation in the hydrothermal biotite breccia (Fig. 4.7D) that is not seen in the disseminated biotite altered tonalite and diorite.

Muscovite alteration: This alteration assemblage is quite simple compared to biotite alteration in terms of its simpler mineralogy and the associated chemical signature of only Rb, Ba and F. The profile for hole E11-116 shows a muscovite altered zone that overprints the hydrothermal biotite breccia and tonalite from 530 to 650 m depth which corresponds to an increase in K_2O and Rb (Fig. 4.6C). This latter feature is illustrated better in Figure 4.8A, a

binary plot of Rb vs. K_2O, in which a strong positive correlation (r = 0.89; Fig. 4.8A). The muscovite alteration shows a moderate positive correlation of K_2O with F (r = 0.47; Fig. 4.8B) and Ba (r = 0.60; Fig. 4.8C).

Although there is no correlation between Au and Cu in the muscovite altered samples, these zones are often coincident with Au ± Cu mineralization. For example, hole E10-13 shows that Au-Cu mineralization continues from the footwall of the hydrothermal biotite breccia body into biotite and muscovite altered tonalite (Fig. 4.6A). Gold-only mineralization has been noted in pervasive muscovite altered rocks (Chapter 3).

Since both muscovite and biotite alterations are types of K-silicate alteration, some geochemical parameters must be used to discriminate between these alteration assemblages. Thus, note that biotite altered tonalite samples show a distinct lack of correlation between K_2O and F, whereas a moderate correlation with muscovite altered tonalite samples exist (Fig. 4.8B). In addition, the Ba vs. K_2O diagram shows that biotite and muscovite altered tonalite samples follow two different trends, therefore, Ba may be useful to differentiate between these two alterations (Fig. 4.8C). Finally, in a plot of Sr vs. Rb (Fig. 4.8D), it is demonstrated that Sr is enriched in biotite altered samples compared to muscovite altered samples.

Albite alteration: Albite alteration, by virtue of its characteristic bleaching and texturally destructive nature, can result in an almost complete replacement of primary minerals (e.g., plagioclase and hornblende) by albite, thereby complicating field identification of protolith rock types. In many cases, the protolith can only be positively identified using geochemistry.

Even during hydrothermal alteration Zr and Ti are considered immobile elements (Petersen, 1983; Petersson and Eliasson, 1997), however, their relative immobility in this system

must be examined. In some albite altered samples Ti and Zr appear to be conserved (Fig. 4.9A), yet in some instances, both titanite and zircon show some evidence of dissolution-precipitation (Fig. 4.9B-E). Leucoxene, an alteration product of Ti-bearing minerals, can be seen to be redistributed along fractures in albite altered rocks (Fig. 4.9B). Similarly, in the episyenite Ti-bearing minerals are re-precipitated in the pore space developed from the dissolution of primary quartz (Fig. 4.9C, D). Zircon shows dissolution-precipitation textures along its margins and these areas contain trace Ca, P, Na, and F (Fig. 4.9E); hydrothermal zircons have been documented to be enriched in Al_2O_3, P_2O_5, Y_2O_3, CaO, REE, HFSE and F (Putnis, 2002; Corfu et al., 2003; Hoskin and Schaltegger, 2003; Schaltegger, 2007; Toscano et al., 2014). Although these textures are suggestive of remobilization, based on petrographic and SEM-EDS analyses it appears that dissolution and re-precipitation occur only on a local scale. Both Zr and Ti are considered, therefore, to be relatively immobile and can be used to effectively distinguish between the host rocks. In particular, a plot of SiO_2 vs. Zr/TiO_2 demonstrates that altered tonalite and diorite can, for the most part, be discriminated (Fig. 4.10A). A Zr/TO_2 ratio of >250 is indicative of tonalite, whereas a ratio of <250 is indicative of dioritic rocks, although outliers do exist (Fig. 4.10B).

The compositional differences in major elements between albite altered samples compared to least-altered samples are significant, as seen in Figure 4.11A where albite altered tonalite are characterized by extreme enrichment in Na_2O (up to ~11 wt. %) and an apparent decrease in SiO_2. In contrast, the dioritic samples show a different trend in Figure 4.11A owing to an increase in both Na_2O and SiO_2. Due to the intense replacement of all minerals by albite, the La/Yb_N ratio vs. Na_2O can also be used to discriminate between biotite altered and albite altered rocks (Fig. 4.11B). Albite altered samples can be spatially associated with gold, but it is erratic. No correlation of Au with Cu exists in albite altered samples.

4.6.2 Behaviour of the rare earth elements

The rare earth elements (REE) are typically found to be immobile in most systems, even when subjected to intense hydrothermal alteration, however, exceptions to this occur (Taylor and Fryer, 1980, 1982, 1983; Palacios et al., 1986; Schneider et al., 1988; Ward et al., 1992; Poitrasson et al., 1995, Petersson and Elisasson, 1997; Fulignati et al., 1999; Parsapoor et al., 2009). Thus, it is relevant to note here that in both the tonalite and diorite the REE concentrations, in particular, the LREE, can change dramatically during hydrothermal alteration (Fig. 4.12). In this system, chondrite-normalized REE patterns can be used to differentiate between some of the alteration assemblages.

Biotite altered samples contain a straight sloped, strongly fractionated LREE pattern due to the presence of LREE-bearing minerals (e.g., allanite, bastnaesite) in this alteration assemblage (Fig. 4.12A, B). This pattern contrasts with the relatively unfractionated, flat REE patterns exhibited by the least-altered tonalite samples. In a similar manner, the biotite altered diorite samples also display a straight sloped LREE pattern compared to the curved LREE pattern exhibited by the least-altered diorite. In this case, however, there appears to be an apparent loss in many of the LREE. Regardless of the LREE concentration, the straight sloped pattern is characteristic of the biotite alteration.

Since the muscovite alteration is superimposed on the earlier biotite alteration zones, the chondrite-normalized REE patterns are compared to biotite altered samples. Weak to moderate muscovite altered samples contain the sloped LREE patterns similar to that in the biotite altered samples (Fig. 4.12C), but in contrast many of the moderate to intensely muscovite altered samples show flatter REE patterns than biotite altered. These contrasting patterns in the same

alteration type suggest the elevated LREE signature was inherited from biotite altered samples and survives in the more weakly muscovite altered samples, whereas LREE-bearing minerals are destroyed in samples where intense muscovite alteration occurs. Muscovite altered samples are also characterized by larger negative Eu anomalies than biotite altered samples which reflects the destruction of plagioclase in these samples. The HREE appear to be relatively unaffected by muscovite alteration, except for a few samples where HREE concentrations increased.

The REE patterns for the albite altered samples also indicates that remobilization of REE occurred (Fig. 4.12D, E). The biotite altered diorite samples have a sloped REE pattern with small to moderate negative Eu anomalies, whereas the albite altered diorite samples contrast markedly with their strong decrease in LREE, moderate to strong negative Eu anomalies and flatter HREE pattern (Fig. 4.12D). Similarly, albite altered tonalite samples typically have lower concentrations of LREE and flatter patterns compared to biotite altered tonalite samples (Fig. 4.12E), which suggests the destruction of the LREE-bearing minerals in the biotite alteration assemblage. The increase in the negative Eu anomalies in albite altered samples is associated with the alteration of the original plagioclase by albite.

Chlorite altered diorite also shows some REE mobility compared to both least-altered and biotite altered diorite (Fig. 4.12F). For the most part, the chlorite altered diorite samples display a similarly curved LREE pattern as the least-altered diorite samples, but some samples do contain the straight sloped pattern characteristic of biotite alteration. Thus, where straight sloped patterns occur it is likely that these chlorite-rich samples inherited the pattern from earlier biotite altered samples. Interestingly, however, is that where chloritization is most intense these samples show depletions in their REE concentrations.

4.6.3 Whole-rock metal associations

Whole-rock data for 401 samples from the Côté Gold deposit have been used to assess the possibility of different metal associations in varied alteration zones. It is noted that data indicate an overall lack of correlations in tonalite and diorite (Fig. 4.13), but some metals are anomalous and display enrichments, consistent with results reported by Kontak et al. (2013a). The metal enrichments are most evident in the hydrothermal biotite breccia and sheeted veins.

Both the hydrothermal biotite breccia and sheeted veins have a Au, Cu, Mo, Ag, Te, Bi, Se association. In Chapter 3, a Au-Cu-Mo-Ag association in the hydrothermal biotite breccia and sheeted veins was noted. The geochemical profiles (Fig. 4.6A, B, C) included in this study show a Au and Cu association in the breccia, along with variable Mo and Te associations. The ternary plot shows that higher Te and Bi values correspond to higher Au grades in the breccia unit and sheeted veins (Fig. 4.14A, B, respectively); no such association exists in tonalite or dioritic rocks (not shown). It is noted that higher Mo contents occur almost exclusively in the hydrothermal biotite breccia and rarely the magmatic diorite breccia (Fig. 4.14C), but higher Mo contents do not equate to higher Au grades.

4.6.4 Trace element chemistry of chalcopyrite

A total of 70 analyses of chalcopyrite in nine samples using the LA ICP-MS method were obtained for a suite of trace elements (Table 4.2). Eight samples representing the three styles of mineralization (i.e., breccia, disseminated and vein) within the deposit and one vein sample outside of the deposit from the Chester-1 zone were used. The data reveals trace but variable amounts of Zn (28 to 1900 ppm), Ag (0.1 to 259.2 ppm), Se (30.4 to 214.8 ppm), Pb (1 to127

ppm), Bi (1.7 to 119 ppm), Sn (0.72 to 114 ppm), In (5.03 to 100.3 ppm), Au (0.004 to 17.2 ppm), Cd (0.45 to 47.9 ppm), Te (below detection limit to 6.8 ppm) and Sb (0.04 to 0.81 ppm). Of these elements, Se, In and Sb are not noted to contain correlations. Abundances of Co, Ni, Pd and Pt were typically close to their detection limits or below (see Table 4.2).

Enrichments in Au in vein samples correspond to enrichments in Bi and Pb, resulting in a strong correlation between Bi and Pb (r = 0.77; Fig. 4.15A). The Au contents in chalcopyrite samples are quite variable within and among samples. Notably, all the gold-bearing (above cut-off grade >0.3 g/t Au) hydrothermal biotite breccia samples analyzed contain the lowest Au values (0.004 to 0.258 ppm), which suggests it forms as microscopic inclusions in chalcopyrite or as free Au in the samples. Likewise, the Te contents are lowest in the breccia samples, which given its previously established association in this unit, indicates that it forms as Te-bearing minerals, as has been documented (Chapter 3). Interestingly, Te and Bi are moderately correlated in vein and breccia samples (r = 0.68 and 0.49, respectively), but no correlation is present in disseminated samples. Silver and Zn have a strong correlation (r = 0.83; Fig. 4.15B) with elevated concentrations in breccia and vein samples (sheeted vein and Chester vein), but not in disseminated chalcopyrite. Similarly, Cd has strong correlations with Ag and Zn.

4.6.5 Mass balance

The geochemical data have been used to semi-quantitatively evaluate the mass balance of the major oxides and trace elements during the different alteration stages following the method described above. In Figure 4.16 it can be seen that some combination of TiO_2, Zr, Al_2O_3 and SiO_2 are constant during alteration and, therefore, can be interpreted as immobile elements. The

particular immobile elements used for each alteration type are indicated on the isocon diagrams (Fig. 4.16) and in Table 4.5, along with the gains and losses for each alteration type. The geochemical changes (i.e., gains and losses) of elements during alteration for each individual sample is summarized as histogram plots in Figure 4.17. For simplicity, the below description of the mass balance results focuses on the average gains and losses and not on the variations in individual samples.

Biotite alteration: Given that biotite alteration is early and widespread, unlike the rare amphibole alteration, the samples are plotted against the least-altered equivalent tonalite and quartz diorite. The biotite altered tonalite samples include disseminated/stockwork style alteration, whereas biotite altered quartz diorite include only disseminated altered samples. For both the tonalite and quartz diorite, it is seen that both mass and volume are essentially conserved with Al_2O_3, SiO_2 and TiO_2 defining the isocon (Fig. 4.16A, B).

The mass balance calculations for the averaged biotite altered tonalite samples indicate that for the major elements there are overall gains of K_2O, FeO, Fe_2O_3, FeO_T, MgO, MnO, CaO, P_2O_5 and LOI and minor losses of Na_2O (Figs. 4.16A, 4.17A). The trace elements show overall gains in Li, Rb, Cs, Sr, Ba, La, Ce, Zn, Te, Se, Pb, As, F and LOI, whereas there are overall losses of Au, Cu, Bi, S, Dy, Yb and CO_2 (Fig. 4.16A; Table 4.5).

Compared to the average least-altered quartz diorite, the average biotite altered quartz diorite shows consistent gains in K_2O and variable, but overall gains in CO_2 and LOI with overall weak losses in FeO, Fe_2O_3, FeO_T, MnO, Na_2O, CaO and P_2O_5; MgO is essentially conserved (Figs. 4.16B, 4.17B). As for the trace elements, there are overall gains in Li, Rb, Cs,

Ba, Zn, Te, Se, Pb, As, CO_2 and LOI, whereas there are overall losses of Sr, La, Ce, Dy, Lu, F, Au, Cu, Bi, and S (Fig. 4.16B; Table 4.5).

As expected, K_2O, Li, Rb, Cs, Ba, and LOI correspond to the gains in biotite altered tonalite and quartz diorite samples. Differences between the overall gains and losses in major oxides (i.e., FeO, MgO, CaO and P_2O_5) between tonalite and quartz diorite samples are attributed to the differences in geochemistry between the rock types. In tonalite samples gains of K_2O are commensurate with increases of FeO, Fe_2O_3, MgO, CaO and P_2O_5 and reflect the presence of secondary biotite, epidote, magnetite and apatite, whereas in quartz diorite samples the calculations indicate no net addition of Fe, Mg, Ca and P was needed to form secondary biotite, epidote, calcite or apatite by alteration of primary silicates (i.e., amphibole, plagioclase, apatite). Similarly, gains of Sr in biotite altered tonalite are commensurate with gains of CaO and Fe_2O_3 and reflect the addition of epidote as part of the biotite alteration assemblage, whereas the weak overall depletion of Sr in quartz diorite samples is consistent with the weak losses of CaO and Fe_2O_3. Locally, rare losses of CaO and Sr in tonalite samples may be the result of epidote not consistently being part of the biotite alteration assemblage and/or the destruction of the calcic component of plagioclase (Fig. 4.17A, B). The strong gains of La and Ce in biotite altered tonalite samples reflect the addition of LREE-bearing minerals, whereas minor losses of LREE occur in quartz diorite samples; this is attributed to higher abundances of LREE in least-altered diorite compared to least-altered tonalite. Gains in Te occur, similar to the hydrothermal biotite breccia, however, not in enough abundance to constitute correlations in tonalitic or dioritic rocks, as was previously shown (Fig. 4.14A). Gains in Zn, Pb, Se and As occur in biotite altered samples, but gains Zn are characteristic of this alteration (Table 4.5). Although individual samples show gains, an overall loss of Au, Cu, Bi and S occurs in disseminated and stockwork

biotite altered samples, however, given the paucity of sulphides and that they do not they do not contain enrichments in the ternary diagrams (Fig. 4.14) or the box and whisker plots (Fig. 4.13), this is not unexpected.

Muscovite alteration: The muscovite altered tonalite is normalized to the biotite altered tonalite, its precursor, as indicated by overprinting relationships. Using these averaged samples indicates that Al_2O_3, SiO_2, TiO_2 and Zr appear immobile and thus define an isocon (Fig. 4.16C). When fracture-controlled and pervasive muscovite altered quartz diorite are plotted against least-altered quartz diorite samples, Al_2O_3, SiO_2 and Zr define an isocon (Fig. 4.16D). Thus, these results indicate that muscovite altered samples conserve their mass and volume.

Mass balance results for the averaged muscovite altered tonalite indicate that K_2O was added, whereas FeO, MnO, CaO, Na_2O and P_2O_5 record losses (Figs. 4.16C, 4.17C); however, FeO and MgO are quite variable and display both gains and losses. Although an overall gain of Fe_2O_3 and FeO_T is noted, it is due to strong gains in one sample and both typically display losses. There are overall gains of Rb, Cs, Ba, Dy, Yb, Au, Cu, Mo, Ag, Te, Bi, As, Pb, W, Sn, S, F, CO_2 and LOI, whereas overall losses are noted for Li, Sr, La, Ce and Zn (Fig. 4.16C; Table 4.5).

Compared to the averaged least-altered quartz diorite, the averaged muscovite altered quartz diorite shows elevated concentrations of K_2O and typically Na_2O, whereas overall losses are noted for FeO, Fe_2O_3, FeO_T, MgO, MnO, CaO and P_2O_5 (Figs. 4.16D, 4.17D). Trace elements that display overall gains are Li, Rb, Cs, Ba, Ce, Dy, Yb, Au, Cu, Mo, Ag, Te, Bi, Se, As, Pb, W, Sn, S, CO_2 and LOI, whereas La, Sr and F display overall losses (Fig. 4.16D; Table 4.5).

As expected K_2O, Rb, Cs, Ba, LOI and CO_2 are strongly to weakly gained in both muscovite altered tonalite and quartz diorite samples, which corresponds to the addition of muscovite and carbonate. Losses in CaO and Sr indicate the replacement of plagioclase by muscovite. Losses of FeO, MgO and P_2O_5 in muscovite altered tonalite samples are the result of destruction of secondary biotite and apatite. Losses of FeO, MgO, CaO, TiO_2, P_2O_5 and F in muscovite altered quartz diorite samples indicates primary minerals (i.e., hornblende, plagioclase, titanite, ilmenite and apatite) were replaced by white mica. An overall strong gain of F in altered tonalite samples contrasts with an overall loss of F in altered quartz diorite samples. The loss of F in the latter is likely due an original higher abundance of F due the presence of primary titanite and apatite. The inconsistency of Li (i.e., gains and losses; Fig. 4.17C) is likely the result of being inherited from early biotite alteration, which is supported by losses of Li concomitant with Mg. The consistent loss of both La and Ce in muscovite altered tonalite samples reflects the destruction of LREE-bearing minerals that were present in biotite altered samples. Conversely, the variability (i.e., gains and losses; Fig. 4.17D) of La and Ce in muscovite altered quartz diorite samples is attributed to some samples having inherited LREE-bearing minerals from earlier biotite alteration and destruction of these minerals in other samples. Overall significant gains in Au and Cu are noted, but gains in Au do not always correspond to gains in Cu (Fig. 4.17C, D). In addition, this alteration is characterized by enrichments Mo, Ag, Te, Se, As, Pb, W and Sn. Gains of Fe may reflect the abundance of pyrite and corresponds to large gains in S in some samples.

Epidote alteration: The results for the averaged fracture-controlled and pervasive epidote altered tonalite samples, when compared to average fracture-controlled muscovite altered tonalite, its precursor, indicate mass and volume are conserved (Fig. 4.16E) with Al_2O_3, SiO_2 and

TiO_2 defining the isocon. The results for averaged epidote altered diorite, when plotted against average least-altered diorite, also indicate mass and volume are conserved with Al_2O_3, SiO_2, TiO_2, and Zr defining the isocon (Fig. 4.16F).

For epidote altered tonalite, changes in the major elements include overall enrichments of FeO, Fe_2O_3, FeO_T, MgO, MnO, CaO, K_2O and P_2O_5, whereas weak to moderate losses of Na_2O occur (Figs. 4.16E, 4.17E). Overall gains in Rb, Cs, Ba, Sr, La, Ce, Bi, As and F occur and overall losses are noted for Li, Dy, Yb, Zn, Te, Se, S, Au, LOI and CO_2 (Fig. 4.16E; Table 4.5).

Compared to the averaged least-altered diorite samples, the averaged epidote altered diorite shows overall gains in MgO, CaO and P_2O_5 and minor to strong losses in FeO, Na_2O and K_2O (Figs. 4.16F, 4.17F). Both Fe_2O_3 and FeO_T are essentially conserved. The calculations indicate overall gains in Li, Rb, Sr, La, Bi, As, F and LOI, whereas Cs, Ba, Ce, Dy, Yb, Au, Cu, Zn, Te, Se, S and CO_2 are overall typically lost (Fig. 4.16F; Table 4.5).

Differences in geochemistry between the rock types result in differences in gains and losses. As expected, both epidote altered tonalite and diorite samples show enrichment CaO, however, the conservation of Fe_2O_3 and FeO_T in diorite altered samples reflects higher original abundances compared to tonalite. Overall gains of FeO and MgO in tonalite samples may reflect the accompaniment of chlorite with epidote. The addition of MgO and loss of K_2O in altered diorite samples reflects the addition of chlorite and the replacement of primary hornblende, respectively. The addition of LOI in altered diorite samples reflect the abundance of epidote. In tonalite and diorite samples the overall gains of Sr is the result of substitution for Ca in epidote and the overall loss of Na_2O reflects the replacement of plagioclase by epidote. The overall loss of CO_2 in tonalite samples does not reflect the presence of calcite that is typical in this alteration

assemblage. This is interpreted as the result of being calculated against its precursor rock, muscovite alteration, which contains comparatively higher abundances of CO_2. Similarly, the overall loss of LOI in tonalite samples is attributed to its precursor, muscovite alteration, being more LOI-rich. The increase in Bi in both tonalite and diorite samples suggests an association of Bi in this alteration assemblage. The overall loss of Au and typical loss of Cu is expected for epidote alteration, which is rarely mineralized.

Albite alteration: The albite altered rocks are normalized to their precursor, pervasive muscovite altered rock, based on crosscutting relationships. Albite altered samples were also normalized to least-altered tonalite samples for comparison. Results using the least-altered tonalite samples indicate gains in K_2O, Rb, Ba, LOI, CO_2 and Bi, which does not correspond with petrographic analyses, and therefore confirms the choice of muscovite altered samples as the precursor. In terms of dioritic samples, it is noted that muscovite altered quartz diorite is plotted as the least-altered precursor even though it is impossible to definitively determine if the altered samples were quartz diorite or diorite. Despite large changes in several constituents, including losses in most of the major oxides and variability, particularly in the dioritic samples, Al_2O_3, SiO_2, TiO_2, and Zr concentrations yield an isocon close to a slope of 1 with a slight mass and/or volume loss in tonalite and mass and/or volume gain in diorite (Fig. 4.16G, H).

In pervasively albite altered tonalite, changes in the major elements include strong enrichment in Na_2O with an overall moderate to strong depletions in the other major oxides (Figs. 4.16G, 4.17G). Notably, all the trace elements are depleted in pervasive albite altered tonalite, except for Sr (Fig. 4.17G; Table 4.5) and therefore, it must reside in albite.

In the albite altered diorite, the changes in the major elements include weak to moderate enrichments of Na_2O and strong losses in FeO, Fe_2O_3, FeO_T, MgO, MnO and P_2O_5 (Figs. 4.16H, 4.17H). Both CaO and K_2O can display gains or losses depending on the sample (Fig. 4.17H). Strong overall losses in trace elements include Li, Cu, Zn, Te, Bi, S, F and LOI, whereas Rb, Cs, Ba, Sr, La, Ce, Dy, Yb, Se, As, Pb, Au and CO_2 show overall gains (Fig. 4.16H; Table 4.5).

As expected, Na_2O is added in albite altered samples, corresponding with the intense replacement of primary minerals and secondary mineral from earlier biotite and muscovite alteration by albite and this is reflected in losses of FeO, Fe_2O_3, FeO_T, MgO, MnO, P_2O_5, Li, Zn, Te, Bi, F, S and LOI. The overall loss of all the REE is consistent with chondrite-normalized REE patterns of albite altered samples presented above. Gains of CaO and CO_2 in albite altered diorite samples may reflect the addition of carbonate. The overall enrichments of K_2O, Rb and Cs in albite altered diorite samples are interpreted to be due to remnant muscovite. In albite altered tonalite samples, CaO, K_2O, Rb, Cs, Ba, La, Ce, Dy, Yb, Au, Cu and CO_2 display consistent losses, whereas in albite altered diorite samples these major oxides and trace elements display both gains and losses. The variability in the gains and losses in the latter compared to the former may be the result of the variability of diorite samples, as noted above, or the result of inheriting these elements from muscovite alteration. A strong decrease in S is consistent with observation that sulphides are not typically associated with albite alteration. The overall loss of Au in tonalite samples and gain in diorite samples reflects the erratic association of Au mineralization in albite altered samples. Losses of metals (i.e., Cu, Zn, Te, Bi, etc.) emphasize the strong leaching capability of the fluids.

Chlorite alteration: Only quartz diorite samples are included for chlorite altered samples and when compared to their precursor biotite altered quartz diorite Al_2O_3, SiO_2 and Zr define an

isocon that indicates slight mass and/or volume loss (Fig. 4.16I). Samples show overall gains of Fe_2O_3, Na_2O and P_2O_5 and losses of FeO, K_2O and CaO (Figs. 4.16I, 4.17I). Overall loses of Li, Rb, Cs, Sr, Ba, Zn, Te, As and Pb occur, whereas La, Ce, Dy, Yb, Au, Cu, Bi, Se, S, F, CO_2 and LOI display overall gains (Fig. 4.17I; Table 4.5).

Overall losses of K_2O, Li, Rb, Cs and Ba are due to the replacement of biotite by chlorite. Interestingly, gains in La and Ce in some samples occur and are probably due to remnant LREE-bearing minerals in chlorite altered samples that formed during biotite alteration. This latter observation demonstrates that LREE-bearing minerals can be robust in chlorite altered samples (Fig. 4.12F). Again, as expected gains in Au are not consistently associated with gains in Cu.

4.7 Discussion

The use of geochemistry in the study of ore deposits has been an important tool, not only for ore genesis and exploration (Harris et al., 1999; Prendergast, 2007; Carranza and Sadeghi, 2012), but for ore deposit classification (McCuaig and Kerrich, 1994; Carranza, 2012). In this particular case, the use of geochemistry can be helpful in discriminating between intrusion-related porphyry versus orogenic deposit types with the former having been previously favoured for this deposit (Kontak et al., 2013a; Katz et al., 2015; Chapter 3).

Porphyry deposits have been shown to have a direct spatial, temporal and genetic link to a contemporaneously evolving felsic or intermediate intrusive centre, as reviewed by Seedorff et al. (2005) and Sillitoe (2010). As a consequence of the latter, zoned alteration assemblages form due to magmatic-derived fluids moving away from their intrusive source, cooling and reacting with the surrounding country rock. This process typically results in the development of a zoned

alteration with a central potassic zone that typically gives way to phyllic zone (Hedenquist and Lowenstern, 1994) and is followed by the formation of a large propylitic alteration halo that exceeds the limit of the orebody. In comparison, orogenic type deposits, considered to have been generated during or immediately after compressive deformation and post-peak regional metamorphism, are characterized by a more focused and restricted alteration footprint that lack a magmatic geochemical signature (McCuaig and Kerrich, 1994; Goldfarb et al., 1998; Groves et al., 1998; Dubé and Gosselin, 2007). In these deposits, the alteration (Fe-carbonatization, sericitization and sulphidation) is focused along the structural conduits (i.e., faults, shear zones) with a lateral and vertical zonation rather than a zonation developed on the deposit scale (McCuaig and Kerrich, 1994; Groves et al., 2003). As a consequence of these different modes of formation, these two deposit types have distinct characteristics, with the intrusion-related being distinguished from orogenic by: (1) an overlap of hydrothermal activity with magmatism; (2) a genetic association of the hydrothermal alteration with the causative intrusion; (3) their metal association and zonation; and (4) their fluid chemistry as reflected by lithogeochemistry, fluid inclusions or isotopic signatures. Even using these four parameters, where a deposit has been overprinted by deformation and metamorphism the correct assignment of a deposit to an ore system can be difficult. For example, this has been particularly challenging in the case of proposed Archean porphyry deposits, such as Lac Troilus (Fraser, 1993; Goodman et al., 2005) and the Canadian Malartic system (Helt et al., 2014; De Souza et al., 2015), as well as Phanerozoic reduced intrusion-related deposits in metamorphic belts (e.g., Ryan Lode; Sillitoe and Thompson, 1998).

The first two criteria noted above were addressed by Kontak et al. (2013a) and in Chapters 2 and 3 of this thesis. These studies demonstrated an overlap between magmatic and

hydrothermal events at ca. 2740 Ma, along with a genetic connection of some of the hydrothermal activity (i.e., amphibole and biotite) with dioritic magmatism. This absolute timing of events is also supported by an independent structural study which demonstrated that regional deformation in the SGB (~2696 to 2670 Ma; Heather et al., 1995) overprints veins and alteration related to the early magmatic-hydrothermal system (Smith et al., 2014; J. Smith, pers. commun., 2016). These results are consistent, therefore, with an intrusion-related model.

Although this study is the first to examine the alteration lithogeochemistry of this deposit, some aspects of the fluid chemistry have been examined previously. Kontak et al. (2013a) first addressed the nature of the fluids using stable isotopic (O, C, S) signatures of minerals from the vein- and disseminated-style mineralization, as well as vein samples from the Chester-1 zone (i.e., Chester 1 vein system; see Fig. 3.2B) approximately 2 km east of the deposit. The results for all samples are consistent with a dominantly magmatic source, but the data, in particular, the calculated $\delta^{18}O_{H2O}$ values, also indicated the input of a relatively light water is required (Kontak et al., 2013a); this could either be meteoric water or seawater. Given the subaqueous setting for the deposit seawater must be the second fluid.

Proper classification of the Côté Gold deposit is critical, as its genesis has important implications for understanding the formation of gold deposits in Archean greenstone belts and exploration for such deposits. The following discussion focuses on the nature of the fluids responsible for the observed hydrothermal alteration in terms of elemental gains and losses, REE mobility, and elemental associations, as well as the implications of the trace element chalcopyrite data. These data are also used to evaluate the intrusion-related model proposed in Chapter 3.

4.7.1 Source of the hydrothermal fluids

Amphibole alteration: Differences between the chemistry of magmatic and hydrothermal amphibole can provide chemical information regarding the nature of the hydrothermal fluid. A fluctuating but general increase in fO_2 (i.e., higher Mg#) from magmatic to hydrothermal conditions has been noted in some porphyry deposits (Ford 1978; Chivas, 1981) and this change in condition is recorded in minerals such as amphibole and biotite. For example, Chivas (1981) noted that the hydrothermal amphiboles have higher Si, Mn, Ca, but lower Fe, Ti, Na, K and Cl relative to less oxidized, magmatic domains. In this deposit, an increase in Mg# was noted in amphibole from the hydrothermal amphibole, suggesting relatively more oxidized conditions compared to the magmatic stage (Chapter 2). In these Mg-rich domains higher Si, Ca and F and lower Ti and Cl contents are noted in comparison to magmatic amphiboles, consistent with the change in fluid chemistry documented by Chivas (1981). Thus, the documented change in mineral chemistry supports a genetic relationship from an early magmatic system which evolved to a hydrothermal-dominated system.

Biotite alteration: The results indicate similar FeO, MgO, MnO, CaO, K_2O, P, Li, Rb, Cs, Ba, LREE, Zn, Pb, Te, F and LOI enrichments in all the biotite altered zones (i.e., disseminations, veins and breccias), therefore, the same fluid can be attributed to formation of these alteration styles. In Chapter 3, the LA ICP-MS study of biotite trace element concentrations also noted appreciable quantities of Li (58 to 134 ppm), Rb (250 to 1408 ppm), Cs (7 to 70 ppm), Ba (22 to 3600 ppm), Mn (244 to 1594 ppm) and Zn (140 to 648 ppm). Thus, the trace element chemistry of biotite is consistent with the calculated gains noted above and confirms that these elements were indeed added during this hydrothermal event.

Both Rb and Cs can substitute for K due to similar geochemical characteristics (Kerrich and Fryer, 1988), whereas Li has been documented to substitute for Mg in igneous rocks (Shannon, 1976; Kerrich and Fryer, 1988; Rieder et al., 1998). In contrast, Ba is more enigmatic in potassic alteration zones in porphyry systems as it is noted to be both lost (e.g., Bajo de la Alumbrera; Ulrich and Heinrich, 2001 and Batu Hijau; Idris et al., 2009) and gained (e.g., Sierrita; Anthony and Titley, 1994). Ba may substitute for K in potassium-bearing minerals (Kerrich and Fryer, 1988; Rieder et al., 1998) and indicates the altering fluids were Ba-bearing.

The addition of Zn noted is attributed not only to its incorporation into biotite, but also to the presence of sphalerite in the alteration assemblage. Enrichments in Zn and Pb in disseminated and stockwork-type alteration outwards from the high-temperature breccia is consistent with base metal zonation in porphyry systems (Sillitoe, 2010; Catchpole et al., 2015). Zinc has been documented to be initially enriched in potassic alteration zones, but then subsequently remobilized outward (e.g., Panguna; Ford, 1978); in this deposit, Zn remains enriched in the biotite alteration.

The geochemical behaviour of Sr during magmatic and hydrothermal processes is controlled by the abundance of Ca (Olade and Fletcher, 1975). As a result, Sr is usually depleted in potassic alteration zones in porphyry systems and this depletion can be even more pronounced due to the replacement of original Ca-bearing minerals (i.e., plagioclase; Olade and Fletcher, 1975; Armbrust et al., 1977). In this system the gain of Sr is attributed to the addition of epidote in the biotite alteration assemblage.

Potassic alteration is ubiquitous in porphyry systems and forms early in their high-temperature cores (Seedorff et al., 2005; Sillitoe, 2010), but can also occur in orogenic gold

deposits hosted by granitoid rocks (McCuaig and Kerrich, 1994). The inferred genetic relationship between the hydrothermal biotite breccia and diorite presented in Chapter 2, along with the Fe-Mg-K-Ca – bearing fluids responsible for biotite alteration, are consistent with a magmatic fluid having exsolved from the co-spatial and contemporaneous diorite complex at ca. 2740 Ma. Importantly, the elemental gains in the biotite alteration zones are similar to elemental gains noted in potassic alteration zones in porphyry deposits, such as Panguna (Ford, 1978), Sierrita (Anthony and Titley, 1994), Bajo de la Alumbrera (Ulrich and Heinrich, 2001) and Batu Hijau (Idrus et al., 2009). The large addition of K to the system during this alteration event suggests that the dioritic magma evolved at depth and became more fractionated. Evidence of an evolved, biotite-rich diorite is not present in the deposit area, but must have been part of the system at depth.

Muscovite alteration: Mass balance data indicate the muscovite alteration is enriched in K_2O along with enrichments in Rb, Cs, Ba, CO_2, and LOI with inconsistent but strong overall enrichments in Au, Cu, Bi, W, and S; moderate to weak enrichments are noted for Te, As, Pb, Sn, Mo and Ag. Rubidium, Cs and Ba substitutes for K, whereas Sr is controlled by Ca (Olade and Fletcher, 1975; Armbrust et al., 1977), resulting in losses of both CaO and Sr due to the replacement of plagioclase by muscovite. No Sn- or W-bearing minerals have been found in the deposit, thus, their gains could be attributed to these elements substituting into the muscovite structure (Ahrens, 1952; Shannon, 1976), which has been documented at Ann-Mason (Cohen, 2011) and more recently in muscovite from ongonites (Dostal et al., 2015).

Muscovite alteration, which partially overprints the biotite alteration in the central part of the deposit, has a Au-Cu-Mo-Ag-Te-Bi-Se-Pb-As-W-Sn association that is similar to the breccia, but notably the Au, Cu, Mo, Ag, Te and Bi concentrations are lower on average in the former

compared to the latter. Elevated Bi and Pb concentrations in chalcopyrite grains from sheeted vein samples also illustrate the overprint of muscovite on earlier biotite altered samples. The overall increase in Au and Cu in muscovite altered samples compared to disseminated/stockwork biotite altered samples, along with additional gains in S, Bi, W and Sn, indicate that some primary mineralization accompanied muscovite alteration.

Muscovite alteration is common in both porphyry deposits, where it is represented by the phyllic zone (Seedorff et al., 2005; Sillitoe, 2010), and orogenic systems (McCuaig and Kerrich, 1994; Dubé and Gosselin, 2007). The gains and losses noted here in muscovite altered rocks are similar to those reported in porphyry systems (e.g., Bajo de la Alumbrera; Ulrich and Heinrich, 2001 and Ann-Mason; Cohen, 2011; Derakhshani and Abdolzadeh, 2009), however, many of the elements associated with muscovite alteration at Côté Gold are not discriminatory against orogenic deposits. In fact, many orogenic deposits are also characterized by enrichments in LILE (K_2O, Rb, Ca, Li, Cs, Tl), As, S and volatiles (H_2O, CO_2; McCuaig and Kerrich, 1994) and as such these elements are not helpful in terms of indicating the fluid source. On the other hand, the association of base metals (i.e., Cu, Mo, Ag, Bi, Te, Sn and W) in this alteration assemblage is less characteristic of orogenic deposits (Ludden et al., 1984; McCuaig and Kerrich, 1994; Dubé and Gosselin, 2007). Thus, this latter aspect of the geochemical signature, along with its widespread distribution in the deposit (i.e., not along shears) and the isotopic data presented in Kontak et al. (2013a), altogether is more indicative of a magmatic origin for these fluids.

Due to the typical addition of Rb and loss of Sr in phyllic alteration in porphyry systems, both these elements have been advocated to be potential pathfinders for porphyry deposits emplaced in volcanic rocks, but inadequate for altered granitic intrusive rocks (Olade and Fletcher, 1975). It is suggested here that Rb and Sr are useful in this system as the loss of Sr in

muscovite alteration demonstrated above (Fig. 4.8D) can be used to distinguish between it and biotite altered rocks. In fact, combining Rb and Sr into a Rb/Sr ratio may be used to vector towards muscovite alteration, which in comparison to disseminated and stockwork biotite altered samples, is more favourable for gold mineralization.

Epidote Alteration: The most prominent geochemical features of epidote alteration is the addition of CaO, which is accompanied by gains of FeO_T, Sr and Bi. Propylitic alteration in porphyry deposits is characterized not only by the appearance of chlorite and epidote, both of which are sinks for Fe, but also of calcite and albite (Djouka-Fonkwé et al., 2012). Although minor chlorite and calcite are seen to accompany the epidote alteration at the deposit, albite is not present as evidenced by loss of Na. The main chemical changes in the propylitic alteration zone in porphyry systems is the addition of volatiles such as CO_2, $H_2O \pm S$ (Meyer and Hemley, 1967; Seedorff et al. 2005, 2008; Djouka-Fonkwé et al., 2012). The lack of CO_2 and S addition at Côté Gold differs from some porphyry systems. Bismuth has been documented to be spatially associated with intrusions and is commonly enriched in reduced intrusion-related deposits (Sillitoe, 1991; Lang and Baker, 2001; Hart, 2007), suggesting that fluids exsolved from the intrusions contributed to the Bi signatures (Prendergast, 2007). Bismuth is the only element common to the biotite, muscovite and epidote alteration zones and may, therefore, be an indication of their formation from a magmatic-sourced fluid.

Albite Alteration: Albite alteration is characterized by gains in Na_2O and strong depletions in all the other major oxides and metals when compared its precursor. In progressing from biotite to muscovite to albite alteration there is a general decrease in CaO, FeO_T, MgO and LREE as a consequence of the replacement of plagioclase, mafic minerals and destruction and remobilization of LREE-bearing minerals.

Albitization is common in greenschist facies metamorphic rocks and orogenic deposits (McCuaig and Kerrich, 1994), but the age dates presented in Chapter 3 constrain the age of the albite hydrothermal event to syn-magmatic at ca. 2740 Ma, which precludes the involvement of a regional metamorphic fluid. The formation of sodic alteration in porphyry systems is attributed to a low-T sodium metasomatism, but its origin can be complex (Seedorff et al., 2005, 2008) and is attributed to variable fluid sources involving either a magmatic reservoir (John, 1989) or ingress of a non-magmatic saline fluid sourced regionally (Dilles and Einaudi, 1992; Seedorff et al., 2008). The geochemical results from this study are consistent with the interpretation in Chapter 3 that the fluids responsible for the albite alteration were derived from the Na-rich and Fe- and Mg-poor tonalite as a consequence of its exsolving a fluid phase. This source is consistent with both the lack of Ca enrichment and the metal deficient nature of the alteration.

Hydrothermal fluids responsible for sodic-calcic alteration in porphyry deposits are capable of leaching and transporting components from the precursor unaltered rock (Seedorff et al., 2008) or mobilizing what was added in earlier potassic alteration, as observed in the case of the depletion of K, Fe, Cu and S in the Ann-Mason porphyry deposit (Dilles and Einaudi, 1992). The latter observations are consistent with the results of this study. Although drill core and outcrop assay results indicate albite altered zones may be Au-bearing, the overall loss of metals compared to the precursor rock, as indicated by mass balance results, suggests the metals were in fact leached. A quantitative analysis of the amount of redistribution or removal of metals during albite alteration requires further work, hence this aspect is not resolved here.

Chlorite alteration: This alteration type has been previously suggested to be an overprinting event based on the observation that the chloritized zones inherit the biotite alteration assemblage, its sulphide assemblage and the Mg# of the precursor biotite (see Chapter 3). The

loss of K_2O, FeO, MgO, CaO, Li, Rb, Cs, Ba, Zn and Te are consistent with chlorite overprinting and destroying the biotite alteration assemblage. In addition, some of the REE patterns for chlorite altered samples closely resemble those of biotite altered samples, which also demonstrates the overprinting nature of this alteration type. Furthermore, this study has shown that the signature of the chloritized zone is marked by gains in P_2O_5, Sn, S, Bi, CO_2, LOI, Au and Cu, and notably, these gains are similar to those in the muscovite altered rocks. The presence of chlorite towards the core of the deposit, specifically in areas where albite alteration has overprinted earlier biotite and muscovite alteration, is also evidence of it replacing early alteration assemblages. Although further work is required on the nature of chloritization it is interpreted here as a result of greenschist facies metamorphism.

4.7.2 Implications of REE enrichments and depletions

The data presented above indicate that the REE concentrations changed during the hydrothermal evolution of the deposit. The mobility of trace elements, such as the REE, during fluid-rock interaction is of interest because, in some cases, they can be used to interpret hydrothermal processes. In this context, several studies have documented alteration related REE mobilization (Ludden and Thompson, 1978; Ward et al., 1992; Poitrasson et al., 1995, Petersson and Elisasson, 1997; Fulignati et al., 1999; Parsapoor et al., 2009) in a variety of deposit types, including porphyry (Taylor and Fryer, 1980, 1982, 1983; Palacios et al., 1986; Schneider et al., 1988; Norman et al., 1989), greenstone-hosted orogenic gold (Kerrich and Fryer, 1979; Luddden et al., 1984) and hydrothermal U-REE deposits (McLennan and Taylor, 1979; Taylor and Fryer, 1982; Metz et al., 1985). The mobility of REE has been reported to be favoured by several factors, such as low pH, a change in temperature, high fluid/rock ratios, stability of REE phases

and the abundance of complexing ions (CO_3^{2-}, F^-, Cl^-, PO_4^{3-}, SO_4^{2-}) in hydrothermal solutions (Taylor and Fryer, 1980; Lottermoser, 1990, 1992; Williams-Jones, 2015).

In alteration assemblages related to an inferred magmatic fluid, such as potassic alteration, the concentration of REE in hydrothermal fluids is related to the composition of the crystallizing magma (Flynn and Burnham, 1978; Lottermoser, 1992). In this deposit, biotite altered tonalite samples have LREE enrichments, but not diorite samples; this discrepancy is due to the lower original abundance of REE in tonalite compared to diorite. The similarity of the REE abundances in the altered versus fresh diorite samples supports a magmatic origin for biotite alteration.

The transition between potassic and phyllic alteration types in porphyry systems is accompanied by decreasing temperatures and pH, whereas fluid/rock ratios increase (Gustafson and Hunt, 1975; Seedorff et al., 2005). Under these conditions, the REE have been documented to be progressively leached (Alderton et al., 1980, Taylor and Fryer, 1980, 1982, 1983; Schneider et al., 1988) or enriched (Palacios et al., 1986; Lottermosser, 1990) with increasing alteration intensity. Depletion of the LREE concomitant with increasing alteration intensity has been documented in phyllic alteration zones in porphyriess (e.g., Bakircay and Ulutas prospects; Taylor and Fryer, 1980 and Murgul; Schneider et al., 1988) which is consistent with them being the most mobile under intense fluid/rock interaction (Kerrich and Wyman, 1996; Williams-Jones et al., 2012) and under low pH conditions (Taylor and Fryer, 1980, 1982, 1983). In this deposit, the depletion of the LREE in muscovite altered samples is attributed to a similar change in fluid conditions as noted above in porphyry systems. Given the requirement of a second non-magmatic fluid source in this system, based on stable isotope results (Kontak et al., 2013a), the

mechanism for the decrease in temperature and pH and increase in fluid/rock ratios could be the result of seawater mixing with the magmatic-derived fluids.

Similar to the muscovite alteration, the strong depletion of LREE in albite alteration is favoured by high fluid/rock ratios. In addition, the leaching nature of the fluid appears to have affected the stability of the secondary LREE-bearing phases (i.e., bastnaesite, allanite). The absence of secondary mineral phases in the albite altered samples that might host the REE appears to have been a factor controlling the REE mobility during albite alteration.

4.7.3 Metal associations and zoning

By virtue of the different processes in which porphyry and orogenic deposit types form, the nature of their fluids, and consequently, their metal associations differ. Porphyry deposits typically have a Cu-Mo-Au-Ag-Pd-Te-Se-Bi-Zn-Pb signature (Sillitoe, 2010) and contain a distinct metal zoning, typically with Cu ± Mo ± Au cores giving way to an outward enrichment in base metals such as Zn ± Pb ± Ag (Jones, 1992; Sillitoe, 2010; Catchpole et al., 2015); although the metals present and their zoning can vary from system to system (Seedorff et al., 2005). Conversely, the geochemical signature of orogenic deposits has Au associated with variable abundances of Ag, As, W, B, Sb, Te, Mo, Bi with relatively low Cu, Zn and Pb contents; in addition, there is a lack of a distinct deposit scale zonation (Ludden et al., 1984; McCuaig and Kerrich, 1994; Groves et al., 2003; Dubé and Gosselin, 2007).

Based on the results from Chapter 3 and the above data, the hydrothermal system responsible for the Côté Gold deposit is interpreted to be the result of magmatic-derived fluids that migrated outwards during progressive cooling of the magmatic centre rather than focusing of

a fluid along a conduit, such as a shear zone. The metal associations from biotite alteration and its zoning support this, displaying a Au-Cu-Mo-Ag-Te-Bi-Se association in the hydrothermal biotite breccia core and a Te-Se-Zn-Pb-As association in biotite disseminations and stockworks outwards from the breccia. The metal associations and their zonation in the deposit are considered to more closely resemble those of porphyry systems rather than orogenic deposits.

4.7.4 Implications of trace element chalcopyrite data

The trace element signature of chalcopyrite can also be used to discriminate amongst ore systems due to predictable enrichments in chalcophile and siderophile elements in certain deposit types (Lazich, 2010; Lazich et al., 2010). The trace element chalcopyrite data in this study (e.g., Se, Sn, In, Ag, Sb, Au, Zn, Cd) are consistent with the trace element chalcopyrite data for porphyry systems from Lazich's (2010) database. A previous sulphur isotope study of vein chalcopyrite from the Chester 1-zone and pyrite, chalcopyrite and molybdenite in vein and disseminated samples from the deposit obtained an average $\delta^{34}S$ near 0‰, which suggests a magmatic source for the sulphur (Kontak et al., 2013a). These results are consistent with the chalcopyrite trace element data and imply an intrusion-related origin for the deposit.

The magmatic-hydrothermal fluids responsible for the formation of the deposit appear to have extended outside the deposit area (>2 km; see Figure 3.2B) and into the regional fracture system east-west trending fracture system that consists of sheeted quartz ± carbonate ± sulphide veins. Not only are these veins interpreted as part of an early fracture system in the intrusive complex based on a structural study (Smith et al., 2014), but are also noted to have the same biotite sulphide paragenesis as samples from within the deposit (see section 3.8.9 in Chapter 3).

Furthermore, the isotope results from Kontak et al. (2013a) suggest similar fluid chemistry from both samples within and outside the deposit (Chester-1 zone). In terms of the trace element chalcopyrite data from this study, both the deposit and Chester-1 zone vein samples have similar trace element abundances and signatures (i.e., Bi-Pb and Ag-Zn associations). Given that Zn enrichment is characteristic of biotite alteration in the deposit, elevated Zn concentrations in chalcopyrite grains from the Chester vein sample supports that this hydrothermal event extends outside the deposit. Altogether, these data imply the development of an extensive magmatic-hydrothermal system.

4.8 Conclusions

The results from this study indicate that different alteration assemblages present in the deposit can be fingerprinted based on geochemical criteria and that associated geochemical changes are consistent with the alteration mineralogy. The chemistry of hydrothermal amphiboles indicate higher MgO, SiO_2, CaO and F and lower Ti and Cl than magmatic amphiboles, which demonstrates a change from magmatic to hydrothermal conditions. Biotite alteration is characterized by gains of FeO, Fe_2O_3, MgO, MnO, CaO, K_2O, P_2O_5, Li, Rb, Cs, Ba, LREE, Zn, Pb, Te, F and LOI, with additional enrichment of Au, Cu, Mo, Ag, Se and Bi noted in a hydrothermal biotite breccia, which is likely due to its more evolved or fertile nature. Muscovite alteration is consistently enriched in K_2O, Rb, Cs, Ba, CO_2, LOI and contains inconsistent, but overall enrichments in Au, Cu, Bi, W, S, Te, As, Pb, Sn, Mo and Ag; these are considered to be primary features of this alteration rather than inherited from earlier altered rocks. Epidote alteration is characterized by gains of CaO, FeO_T, Sr and Bi whereas albite

alteration is fingerprinted by gains in Na and consistent losses in most other elements except for the HREE. Chloritization is characterized by gains of P_2O_5, Sn, S, Bi, CO_2, LOI and Au which relates to it overprinting the earlier biotite and muscovite alteration assemblage. The metal associations and elemental ratios (i.e., La/Yb_N and Rb/Sr), along with the above geochemical criteria, provides vectors towards favourable alteration assemblages that can be used in the exploration for similar intrusion-related deposits in Archean greenstone terranes.

The convincing evidence for REE mobility and its behaviour during different hydrothermal stages in the evolution of the systems is a reflection of the changing fluid regimes from a system dominated by early high-temperature magmatic fluids to one in which lower pH fluids played an increasingly important role. This study shows that the behaviour of REE during different hydrothermal stages can effectively monitor changing fluid conditions and may be a useful tool to help constrain the genesis of hydrothermal ore deposits.

The geochemical data presented in this study suggest that the Côté Gold deposit resulted from magmatic-hydrothermal processes and are consistent with the interpretations from both earlier and ongoing studies (Kontak et al., 2013a; Chapter 3; J. Smith, pers. commun., 2016). The sequence of alteration assemblages, their zonation in the deposit and their chemistry (i.e., gains and losses, changing REE patterns, metal associations and trace element chalcopyrite concentrations) is consistent with the early hydrothermal amphibole and biotite stages having formed from high-temperature magmatic-derived fluids sourced from an evolving dioritic magma and the later hydrothermal muscovite and epidote stages having formed from the mixing of a cooling magmatic fluid with downward infiltrating seawater. Our current level of understanding of this world class gold deposit supports a magmatic origin, specifically with an affinity to porphyry-type systems.

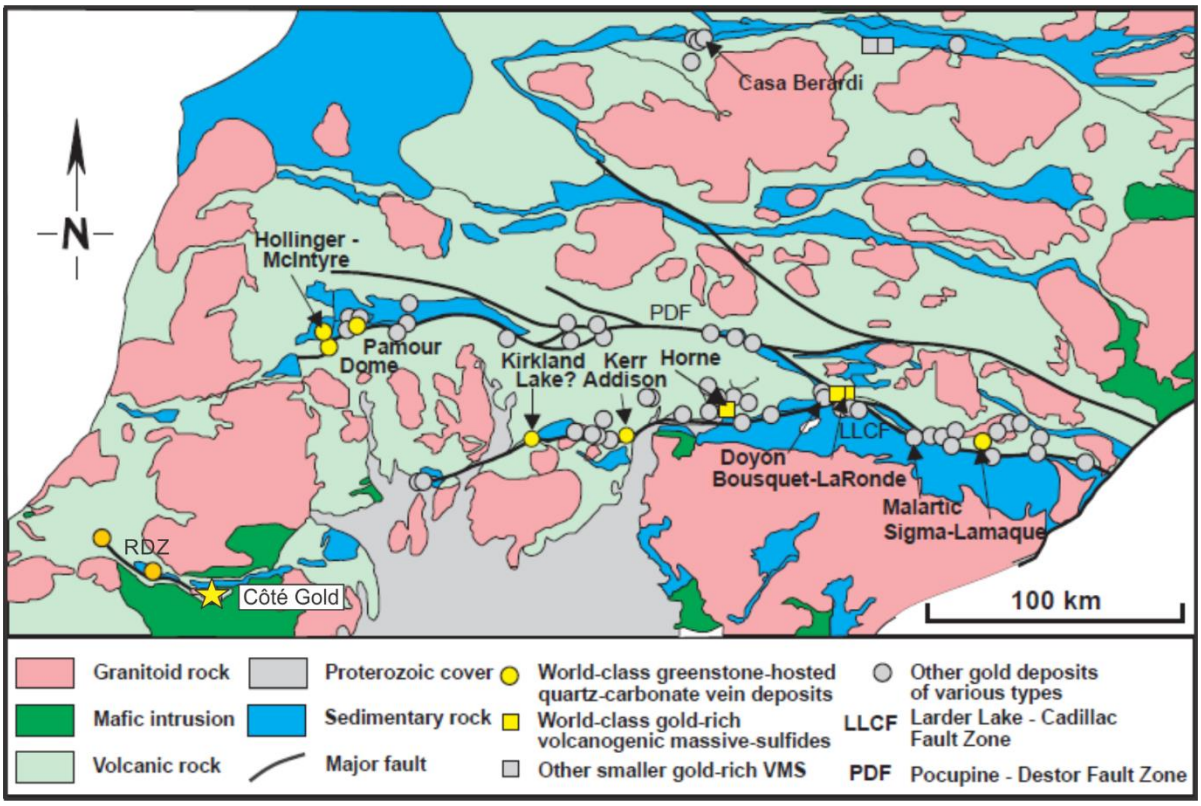

Figure 4.1. Regional geological map of the Abitibi Subprovince showing the distribution of major gold deposits and also main structural features, modified after Dubé and Gosselin (2007). The yellow star shows the location of the Côté Gold deposit and the Ridout deformation zone (RDZ) is labelled towards the bottom left of the map.

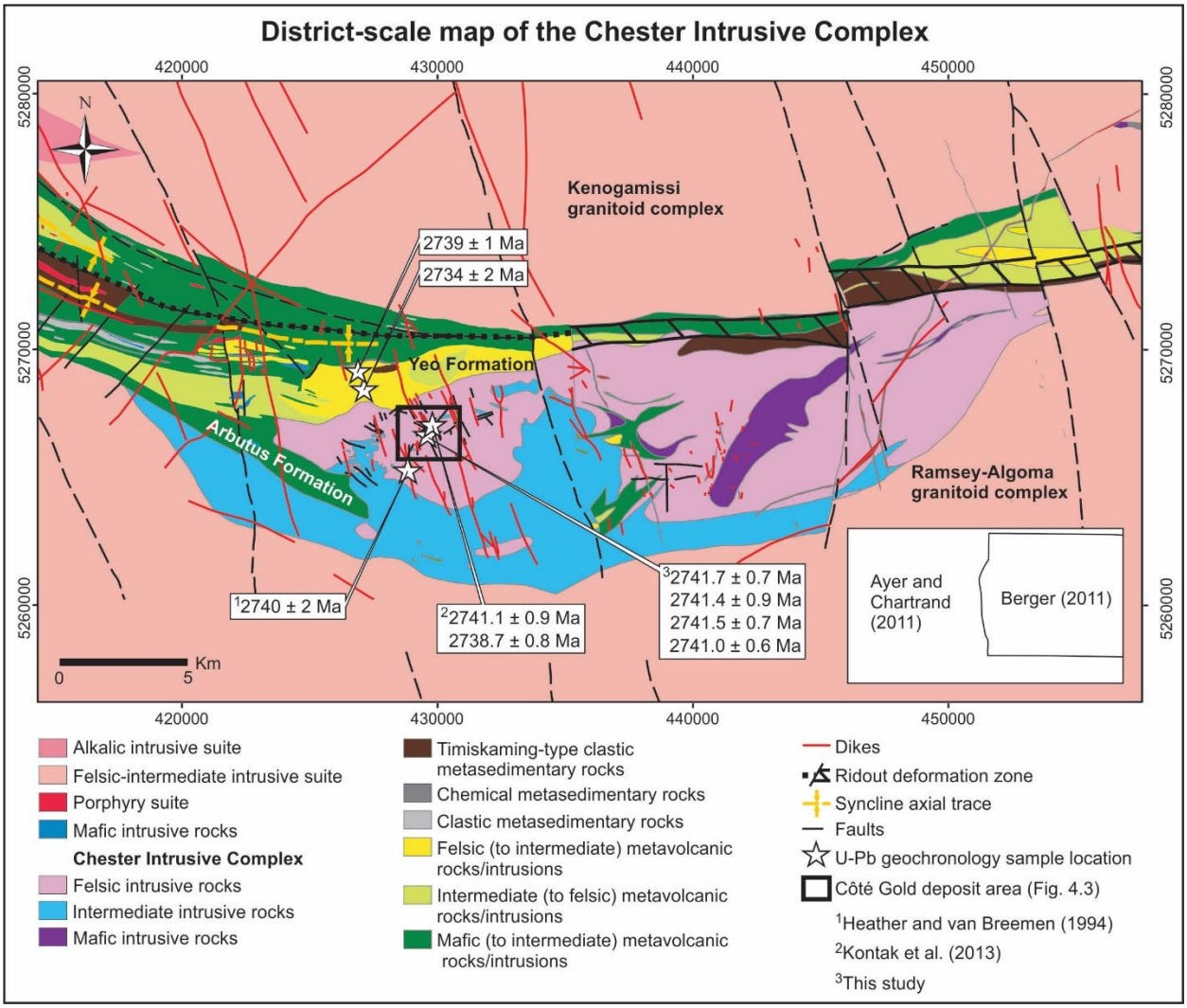

Figure 4.2. Simplified district-scale map of the Chester intrusive complex and the southeastern arm of the Swayze greenstone belt, as compiled from Ayer and Chartrand (2011) and Berger (2011); the inset shows the area mapped by both groups. See Chapter 2 for a discussion of the ages presented in the map.

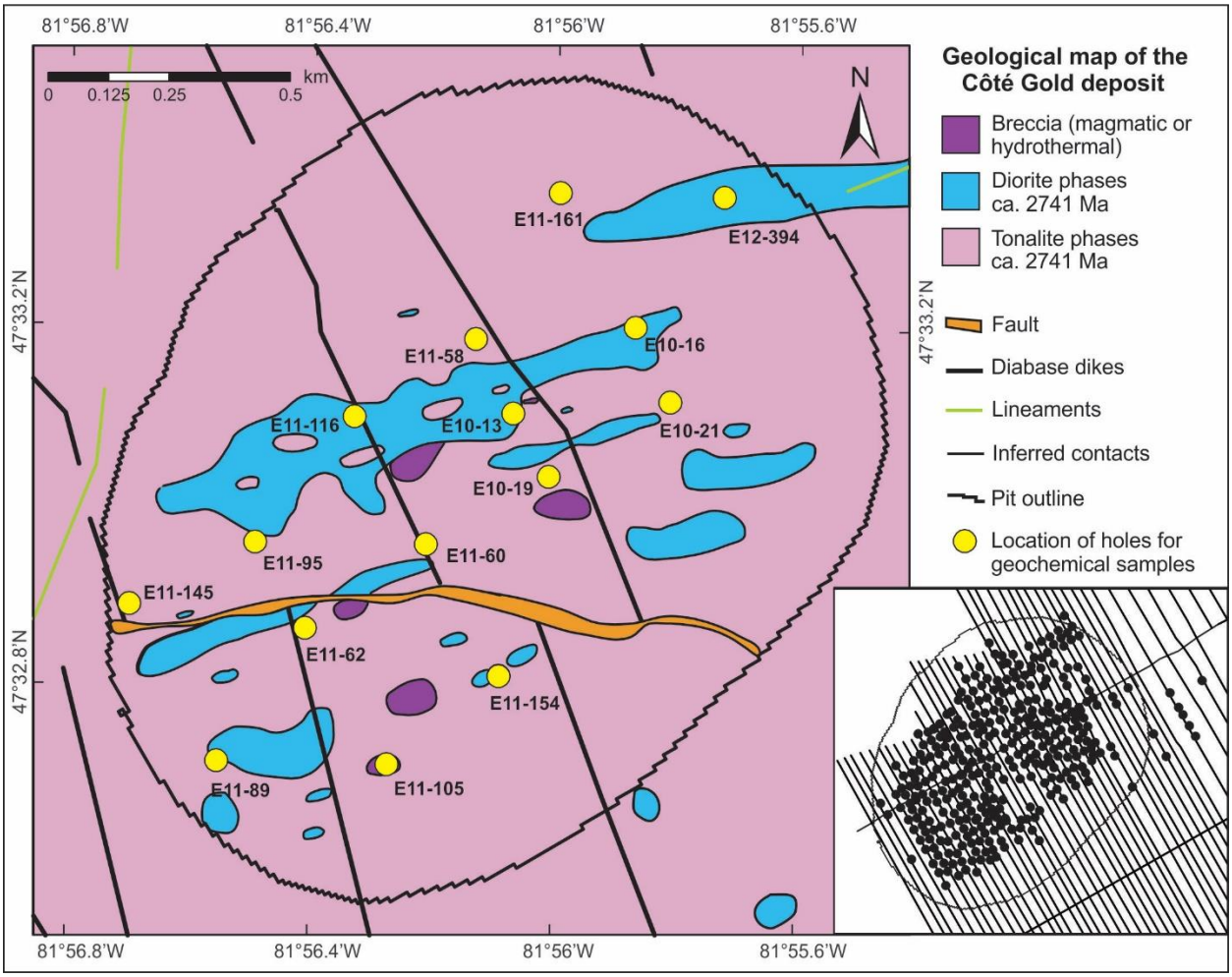

Figure 4.3. Simplified geological map of the Côté Gold deposit area that shows the distribution of major rock types. The deposit outline corresponds to the open pit shell outline as of October 2012 and the geology from within this shell was created by using the first bedrock collared in 373 diamond drill holes along with mapping of several outcrops. The inset shows the distribution of drill holes used to construct the map. The geology from outside the deposit shell is taken from Ayer and Chartrand (2011). The yellow circles show the location of the drill holes selected for geochemical analyses.

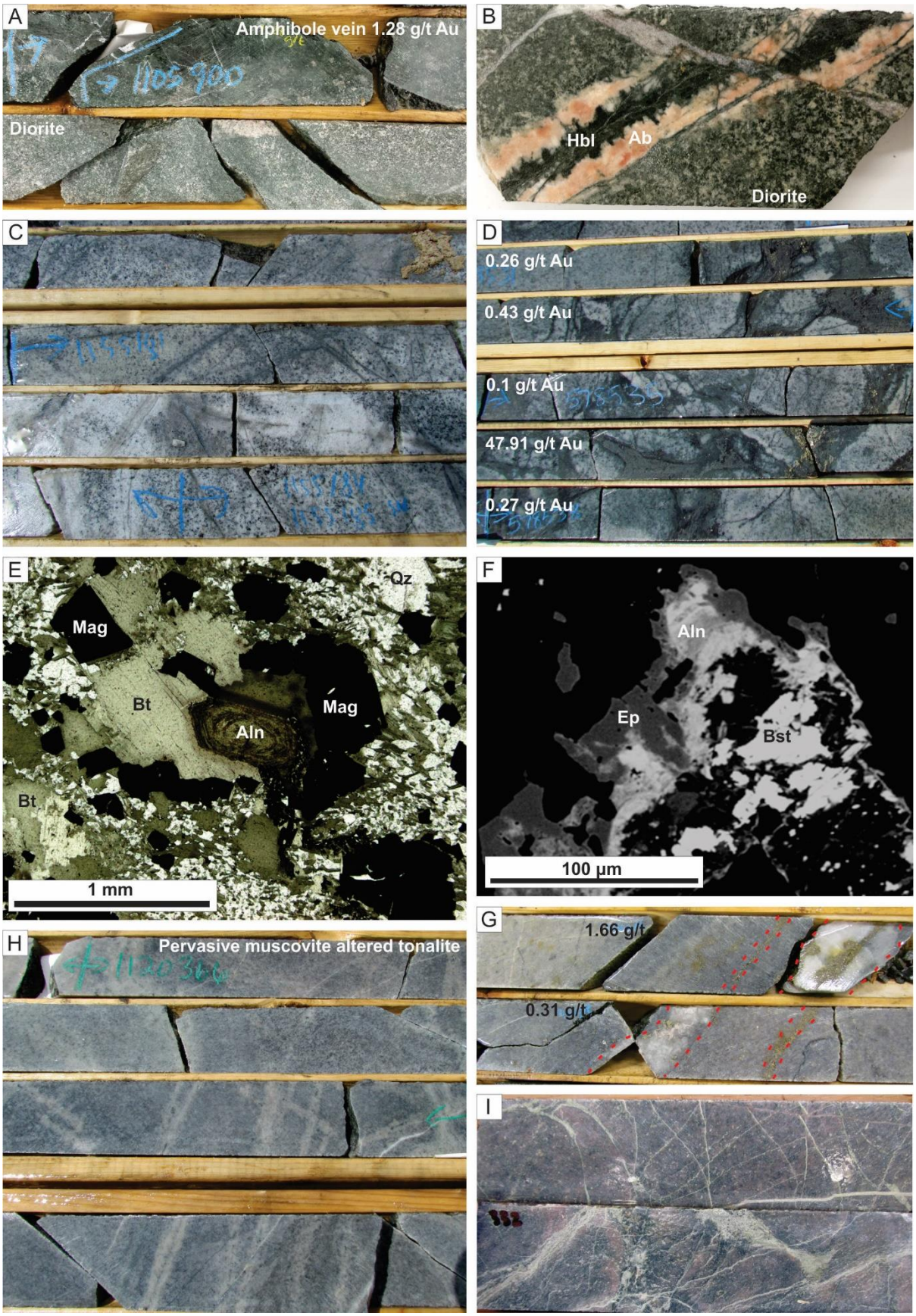
A
Amphibole vein 1.28 g/t Au
Diorite
B
Hbl
Ab
Diorite
C
D
0.26 g/t Au
0.43 g/t Au
0.1 g/t Au
47.91 g/t Au
0.27 g/t Au
E
Qz
Mag
Bt
Mag
Aln
Bt
1 mm
F
Aln
Ep
Bst
100 µm
G
1.66 g/t
0.31 g/t
H
Pervasive muscovite altered tonalite
I

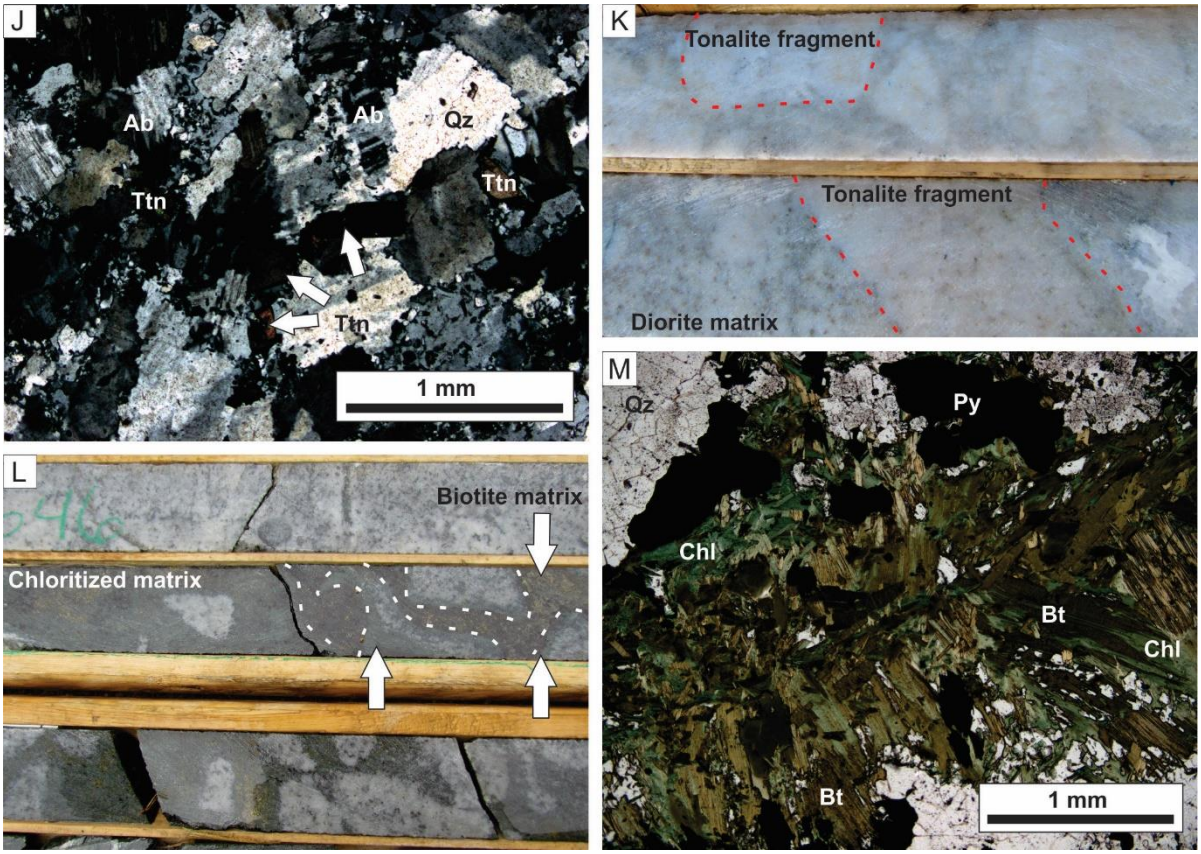

Figure 4.4. Drill core (4.5 cm in width) and thin section photographs, as well as a backscatter electron (BSE) image showing representaive examples of the different alteration assemblages at the Côté Gold deposit. A) Gold mineralized amphibole vein (1.28 g/t Au over 1 m) cutting barren diorite in lower part of the photo. B) Amphibole vein in diorite that is rimmed by orange feldspar. C) Disseminated and vein-controlled biotite alteration in tonalite. D) Gold-bearing hydrothermal biotite breccia that contains biotite and muscovite altered tonalite fragments. E) Thin section photo in plane polarized light of a hydrothermal biotite breccia matrix with a biotite-quartz-magnetite-allanite assemblage. F) A BSE image of epidote, allanite and bastnaesite associated with chlorite (after biotite) in a biotite altered tonalite. G) Muscovite alteration haloes around gold-bearing sheeted quartz-sulphide veins; the veins are outlined by red dashed lines. H) Pervasive muscovite altered tonalite that is overprinted by fracture-controlled albite alteration. I) A zone of vein-controlled epidote alteration in tonalite. J) Thin section photo in crossed polarized light of albite altered sample of albite replacing plagioclase and undulose grain boundaries resulting in destruction of primary texture. K) Pervasive albite altered diorite breccia with the fragment/matrix boundary still visible. Some of the tonalite fragments are outlined by a red dashed line. L) Chloritization of the matrix of a hydrothermal biotite breccia. Note the presence of a chlorite rim around some fragments. M) Thin section photo in plane polarized light of a hydrothermal biotite breccia matrix with chlorite partially replacing biotite. Abbreviations: Ab = albite, Aln = allanite, Bst = bastnaesite, Bt = biotite, Chl = chlorite, Ep = epidote, Hbl = hornblende, Mag = magnetite, Py = pyrite, Qz = quartz, Ttn = titanite.

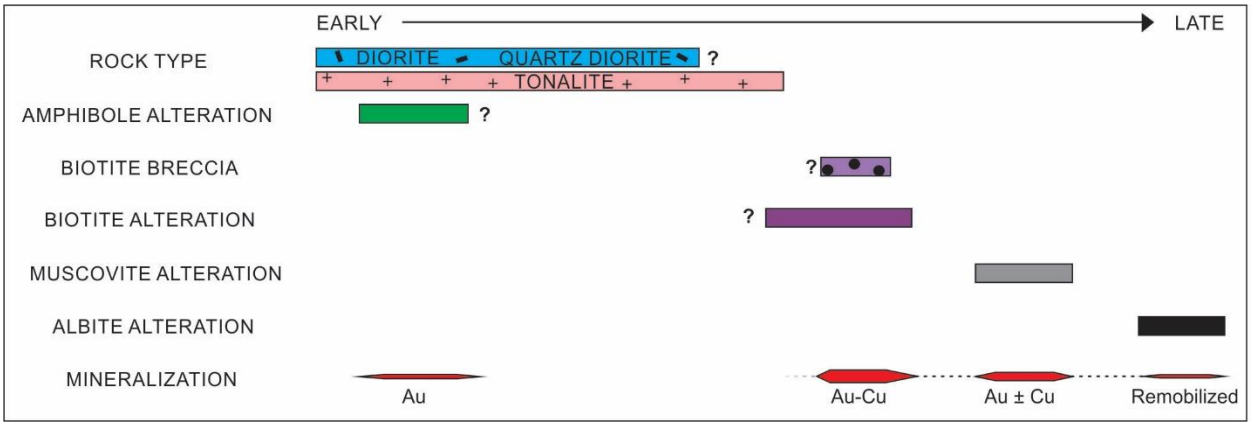

Figure 4.5. Schematic paragenetic diagram that shows that relative timing of hydrothermal alteration and mineralization with respect to magmatism at the Côté Gold deposit.

A Drill hole E10-13

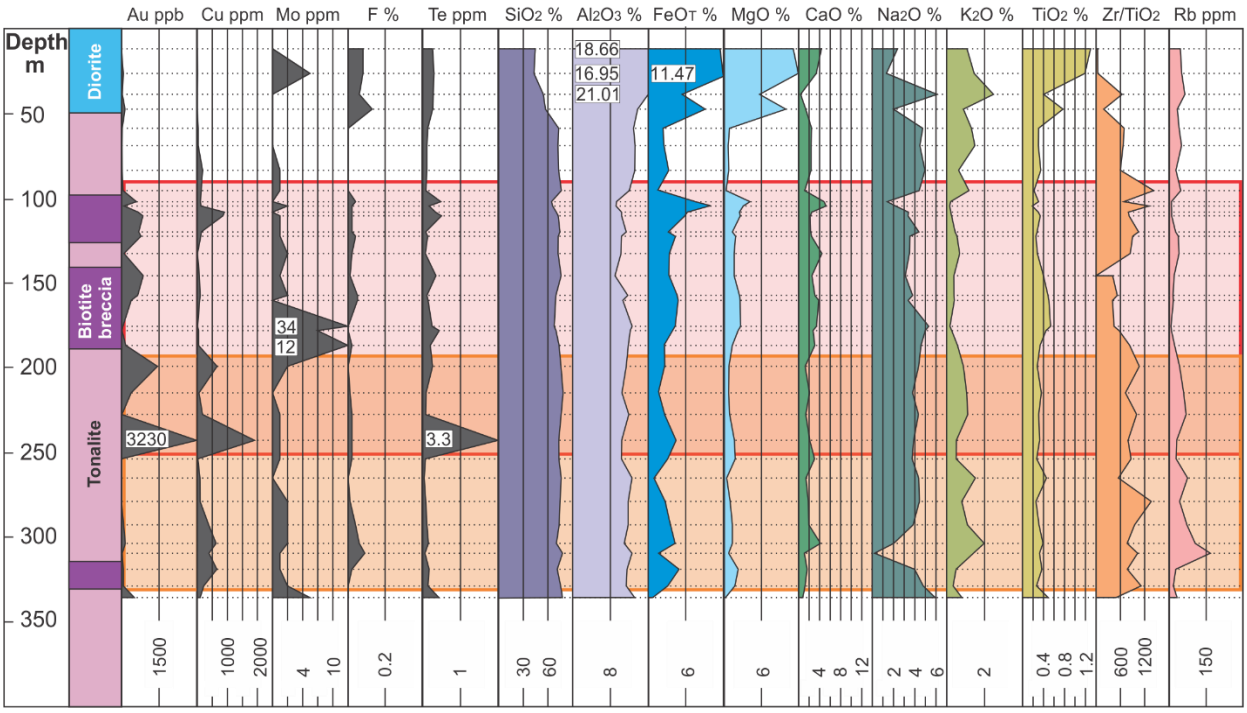

B Drill hole E11-161

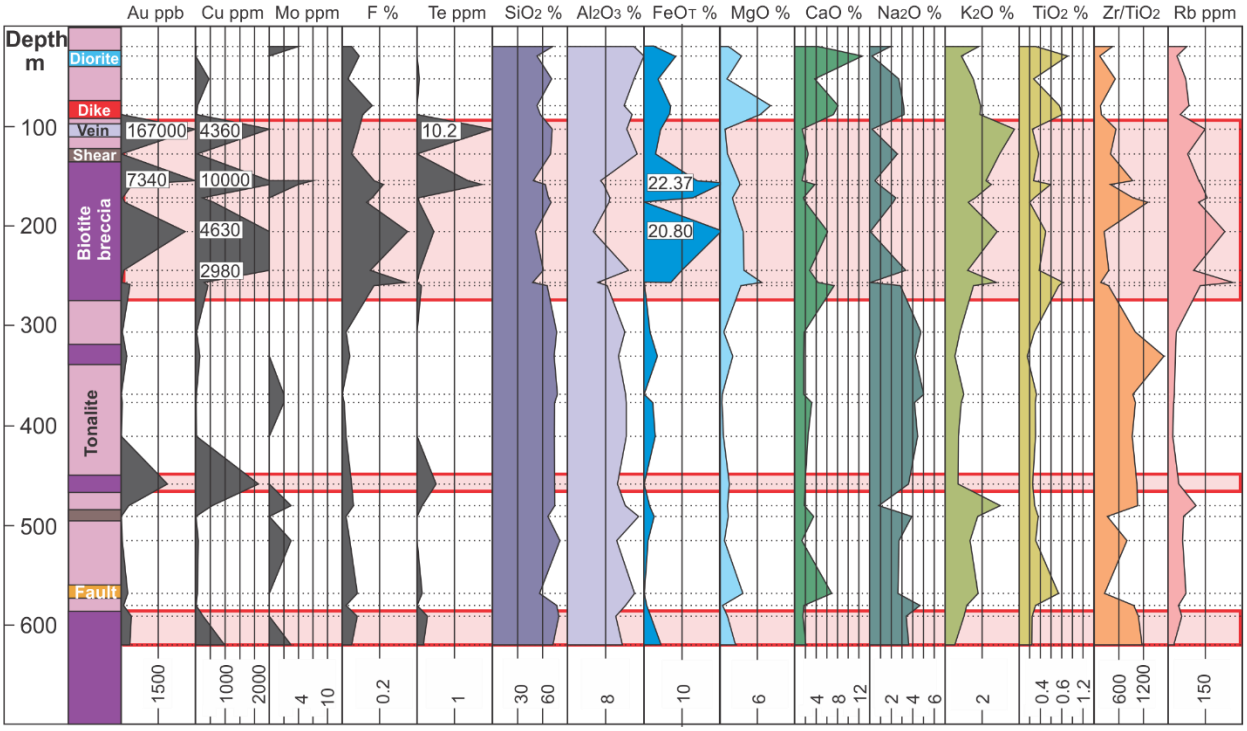

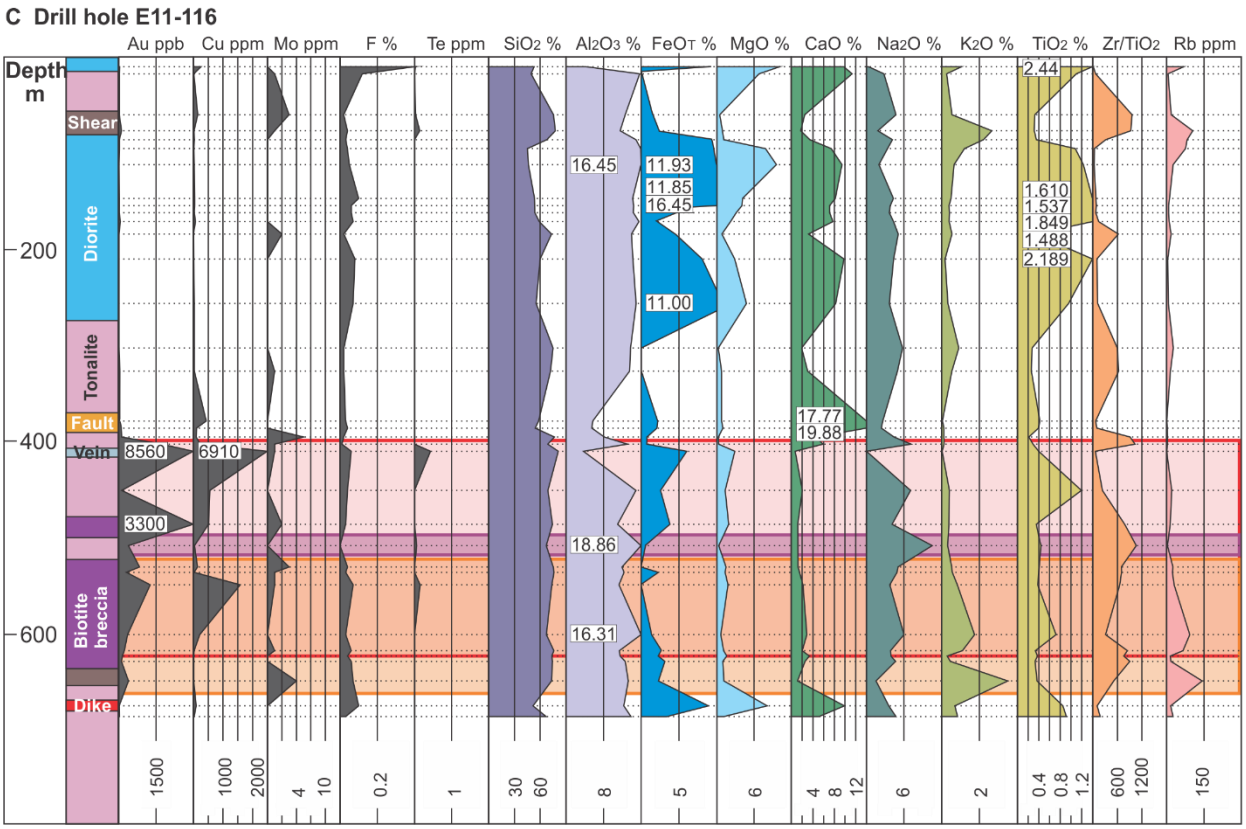

Figure 4.6. Geological logs and geochemical profiles for selected elements from drill holes E10-13, E11-161 and E11-116; see Figure 4.3 for their location in the deposit. For each of the profiles the locations of the analyzed samples are indicated by dashed horizontal lines and the numbers in the profiles indicate out of scale results. Note that the scale for FeO (wt. %) and Na_2O (wt. %) changes between geochemical profiles. The red shaded area delineates the ore zone, whereas the orange and purple shaded areas indicate zones of muscovite and albite alteration, respectively.

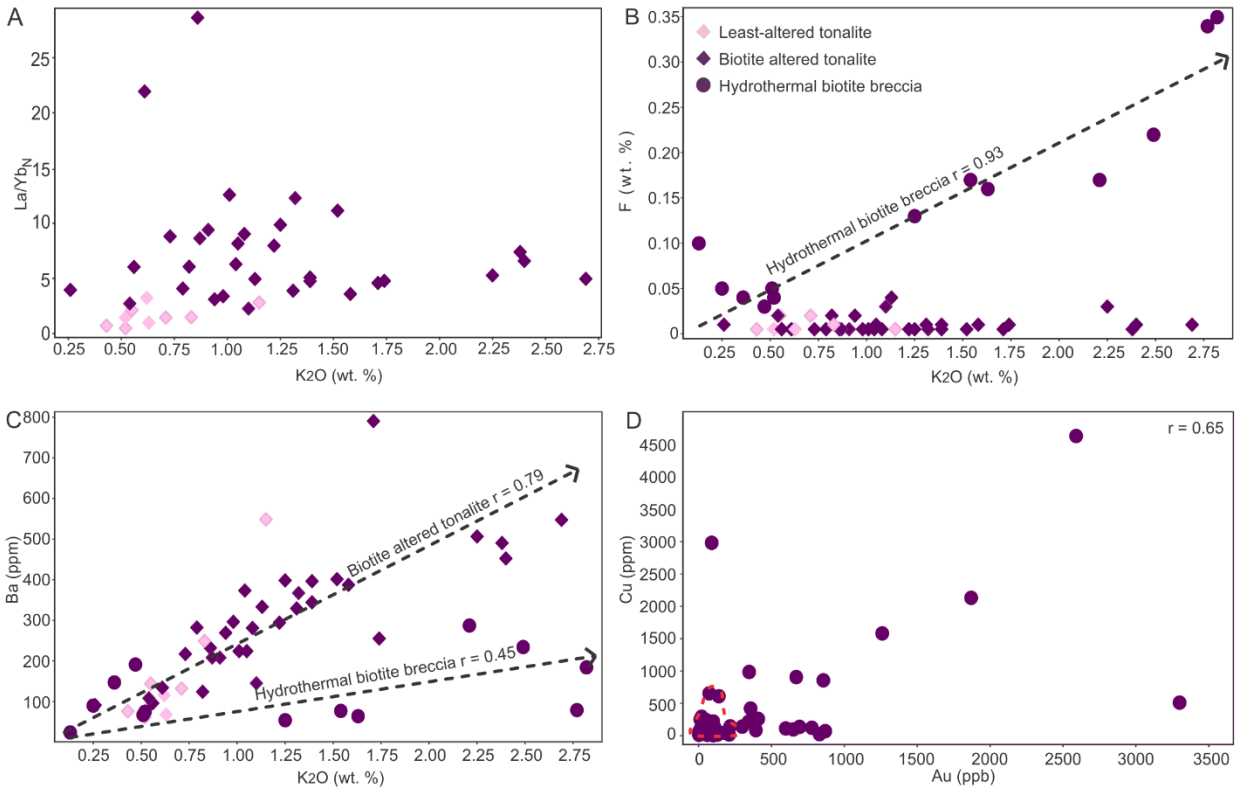

Figure 4.7. Binary element plots illustrating the geochemical characterization of biotite altered tonalite and hydrothermal biotite breccia. A) A plot of La/Yb_N vs. K_2O that shows an increase in La/Yb_N in biotite altered tonalite samples (n = 32) compared to least-altered tonalite samples (n = 9). The chondrite normalizing values are after Sun and McDonough (1989). B) A plot of F vs. K_2O that shows a strong positive correlation in the hydrothermal biotite breccia (n = 13; r = 0.93) and no correlation in both the least-altered tonalite and the biotite altered tonalite samples. C) A plot of Ba vs. K_2O showing a strong positive correlation for the biotite altered tonalite samples (r = 0.79) and a weak positive correlation for the hydrothermal biotite breccia samples (r = 0.45). D) A plot of Cu vs. Au for biotite breccia with different types of alteration. The plot shows a correlation (r = 0.65) between Cu and Au in the hydrothermal biotite breccia samples (n = 41), whereas no correlation in biotite altered tonalite samples, shown by the dashed red line for clarity, exists. Note that the diagram has been scaled down and two samples with high Au and Cu values have been removed.

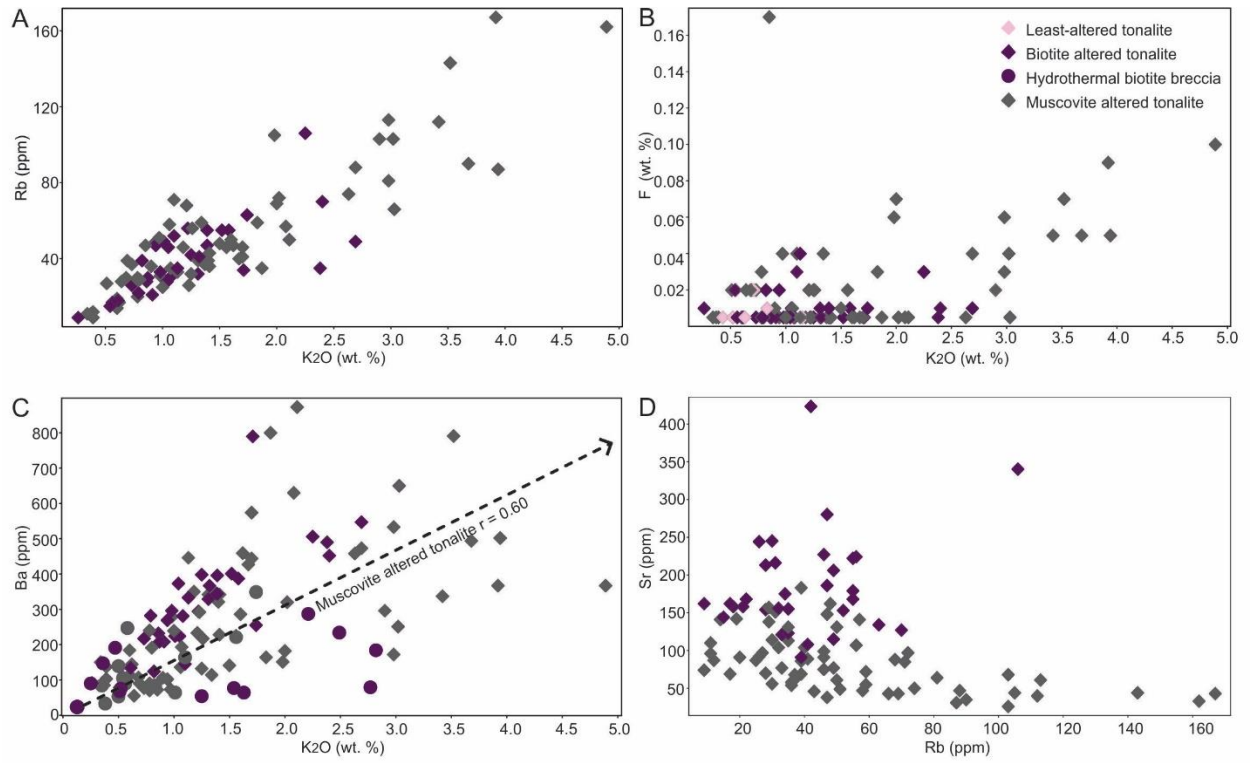

Figure 4.8. Binary element plots showing geochemical characterization of muscovite altered tonalite samples. A) A plot of Rb vs. K_2O which shows a strong correlation in muscovite altered tonalite samples (n = 64) with a correlation coefficient of 0.89 compared to 0.66 for biotite altered tonalite samples (not shown). B) A plot of F vs. K_2O that shows a positive correlation in muscovite altered tonalite samples. Note that the biotite altered tonalite samples are included for comparison. C) A plot of Ba vs. K_2O that shows biotite altered tonalite, hydrothermal biotite breccia and muscovite altered tonalite samples have different trends. D) A plot of Sr vs. Rb that shows biotite and muscovite altered tonalite can, for the most part, be discriminated.

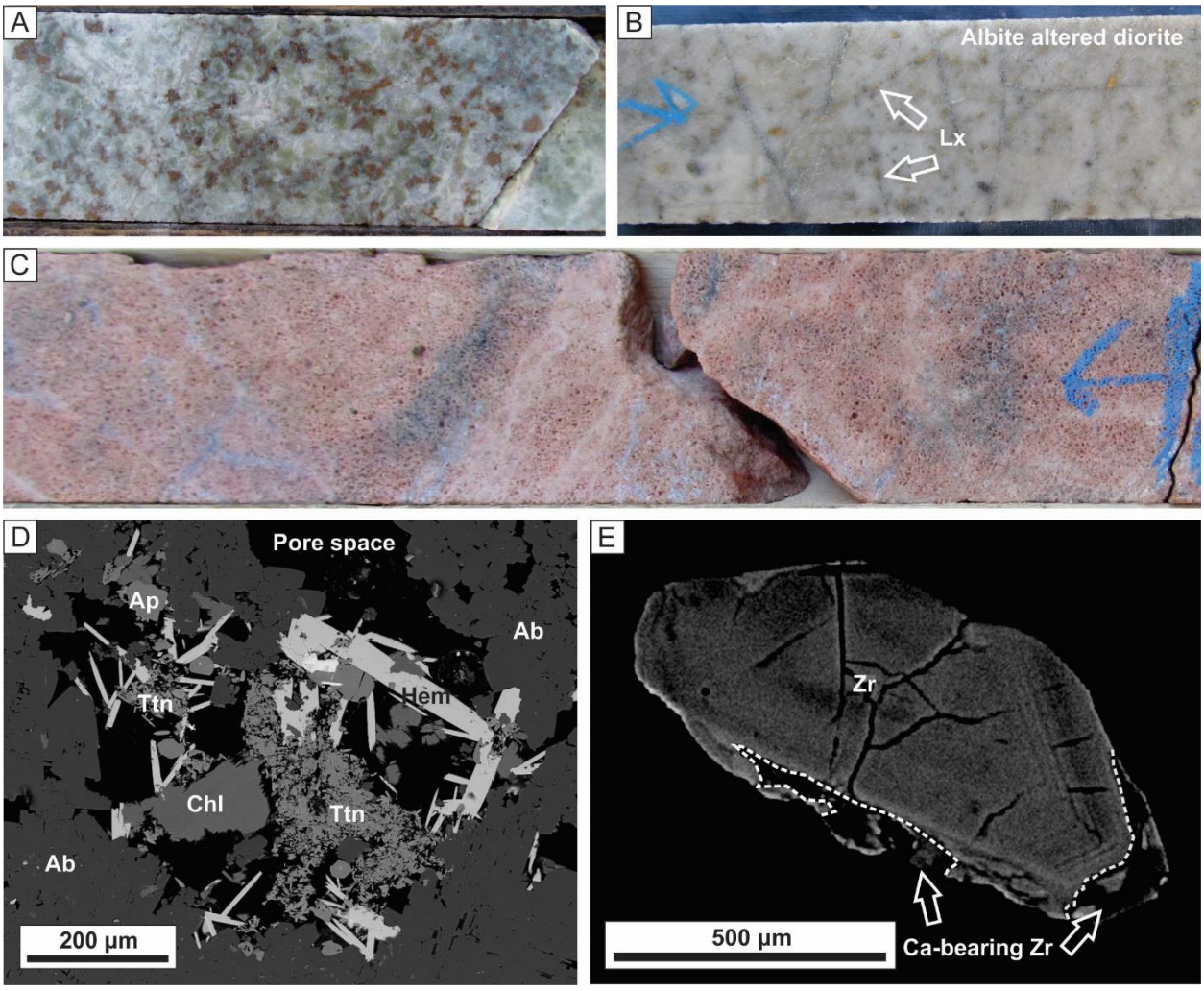

Figure 4.9. Drill core photos (4.5 cm in width) and backscatter electron (BSE) images of Ti and Zr mobility during alteration. A) A pervasive albite altered diorite with primary amphibole and calcic plagioclase replaced by albite and primary titanite or ilmenite pseudomorphed by brown rutile. B) A pervasive albite altered diorite with leuxocene after primary titanite or ilmenite; some of the leucoxene has been mobilized along the fractures. C) An example of an episyenite with pore space created due to dissolution of quartz. D) A BSE image of an episyenite where titanite, apatite, chlorite and hematite have been remobilized into the pore space. E) A BSE image of a zoned zircon in tonalite with dissolution-precipitation along rims, which has trace amounts of Ca. Abbreviations: Ab = albite, Ap = apatite, Chl = chlorite, Hem = hematite, Lx = leucoxene, Ttn = titanite, Zr = zircon.

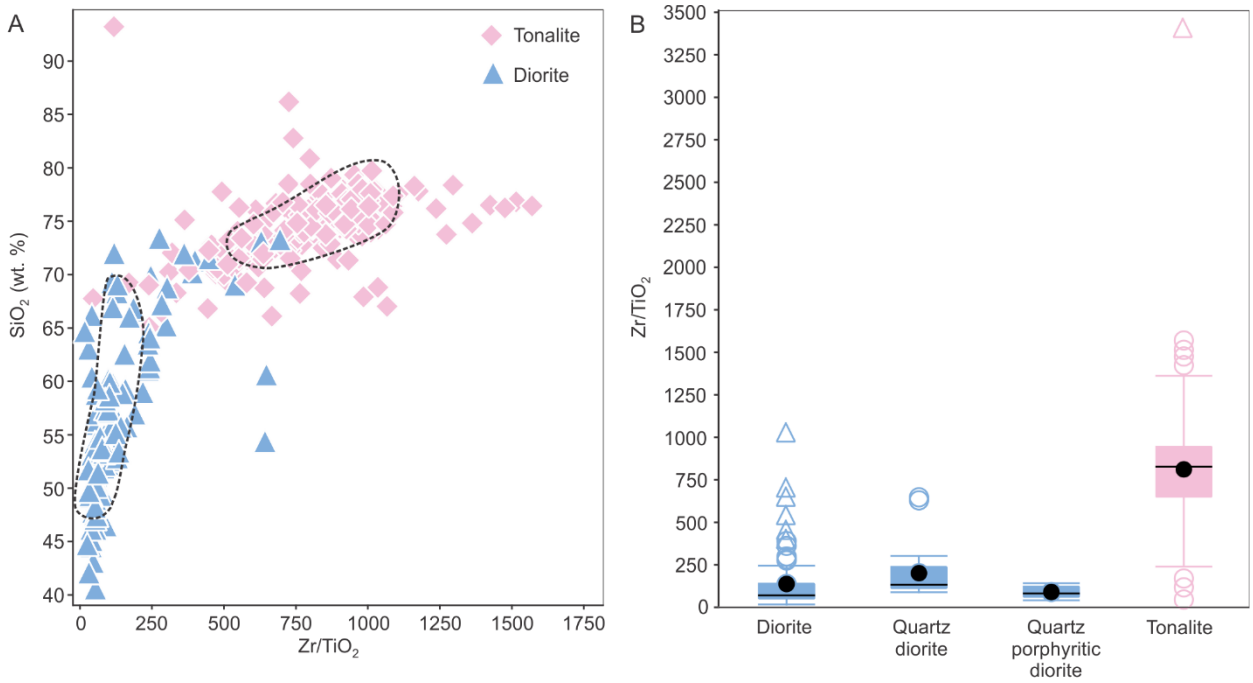

Figure 4.10. A) A SiO_2 vs. Zr/TiO_2 plot that discriminates between altered tonalitic and dioritic rocks. The dashed black outline shows the areas where least-altered tonalite (n = 9) and diorite (n = 16) plot. The data that fall outside the least altered areas reflects scatter is the result of alteration. One far outlier was removed from this diagram. B) A box and whisker plot that shows the different Zr/TiO_2 ratios amongst tonalite (n = 209), diorite (n = 78), quartz diorite (n = 23) and quartz porphyritic diorite (n = 9) samples. The black circle is the mean and the central box is the middle 50% of the data from Q1 to Q3. The circles represent the outliers and the triangles represent far outliers.

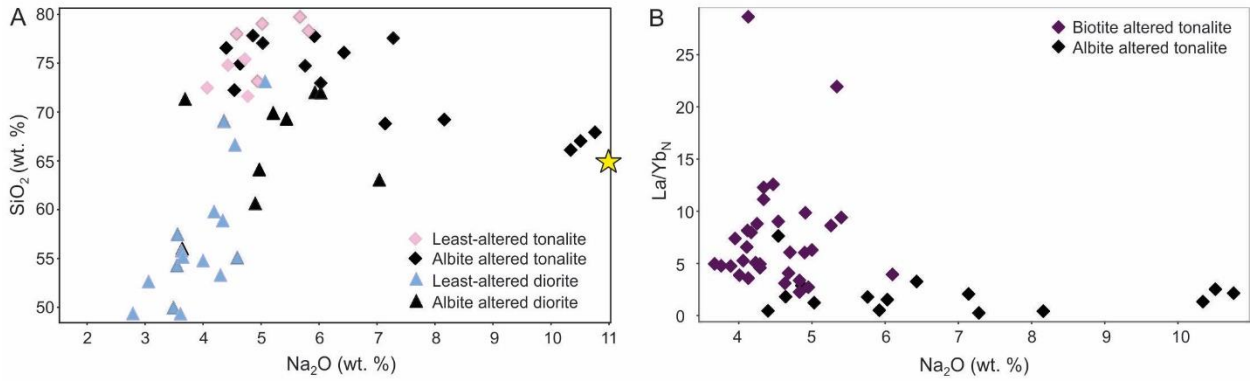

Figure 4.11. Geochemical characterization of the albite altered tonalite and diorite samples. A) A binary plot that shows an increase of Na_2O and loss of SiO_2 in albite altered tonalite (n = 15) compared to an increase of Na_2O and SiO_2 in albite altered diorite (n = 9). Note that tonalitic samples plot towards pure albite, which is shown by the yellow star. B) A plot of La/Yb_N vs. Na_2O that distinguishes albite altered samples from biotite altered samples. The chondrite normalizing values are after Sun and McDonough (1989).

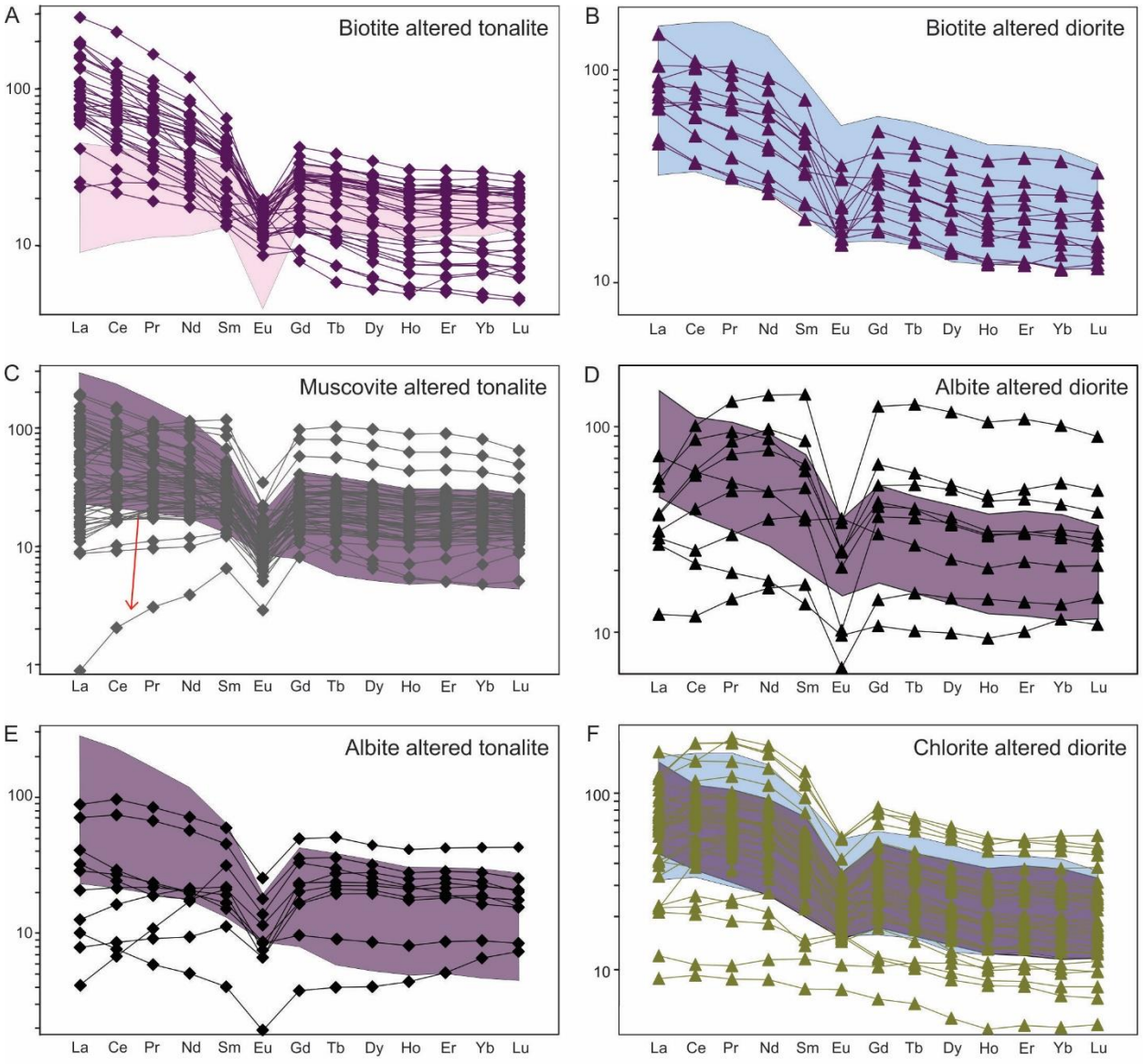

Figure 4.12. A series of chondrite-normalized REE diagrams that are used to characterize the various alteration assemblages within the Côté Gold deposit. A) A comparison of the flat, unfractionated pattern of least-altered tonalite (n = 9) in the shaded pink area with the LREE-enriched profiles for biotite altered tonalite in purple diamonds (n = 32). B) A comparison of biotite altered diorite samples (n = 12) in purple triangles with least-altered diorite (n = 16) in the shaded blue area. C) Muscovite altered tonalite pattern (n = 64) in grey diamonds that exhibits two REE patterns: (1) a LREE-enriched, negative-sloped pattern; and (2) a relatively flat REE pattern. The REE pattern for biotite altered tonalite samples (from A) is shown in the purple shaded area for comparison. D) Albite altered diorite (n = 9) in black triangles that show depletions in the LREE compared to biotite altered diorite in the purple shaded area. E) Selected samples of strongly albite altered tonalite (n = 10) in black diamonds that show depletion in ∑REE, but particularly the LREE, compared to biotite altered tonalite samples shown in the purple shaded area. F) Chlorite altered diorite (n = 36) in green triangles typically have the concave-shaped LREE profile of least-altered diorite, but also shows some depletion of ∑REE. Both least-altered and biotite altered samples are included for comparison. The chondrite normalization values are from Sun and McDonough (1989).

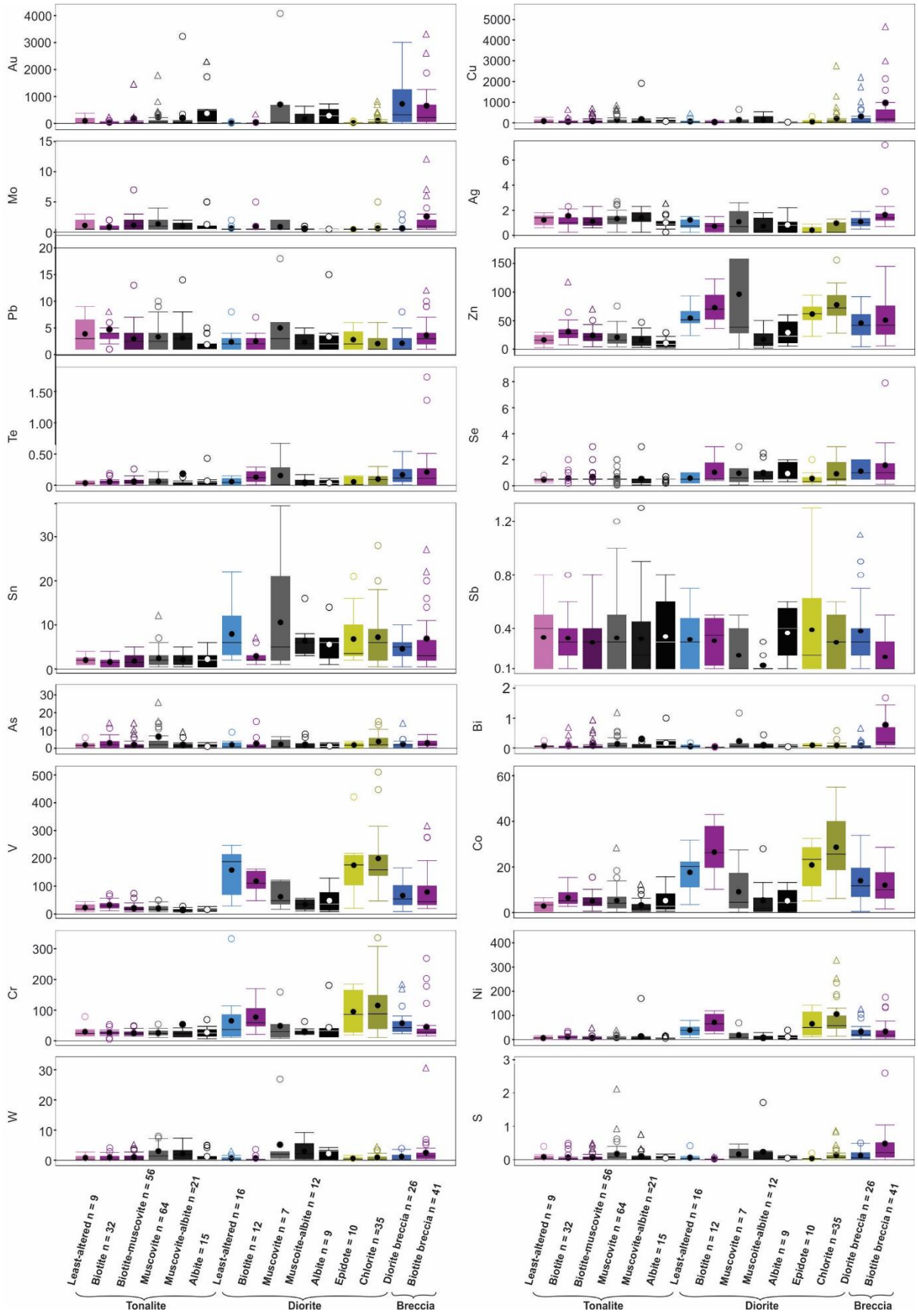
Au
Cu
Mo
Ag
Pb
Zn
Te
Se
Sn
Sb
As
Bi
V
Co
Cr
Ni
W
S
Least-altered n = 9
Biotite n = 32
Biotite-muscovite n = 56
Muscovite n = 64
Muscovite-albite n =21
Albite n = 15
Least-altered n = 16
Biotite n = 12
Muscovite n = 7
Muscoite-albite n = 12
Albite n = 9
Epidote = 10
Chlorite n =35
Diorite breccia n = 26
Biotite breccia n = 41
Tonalite
Diorite
Breccia

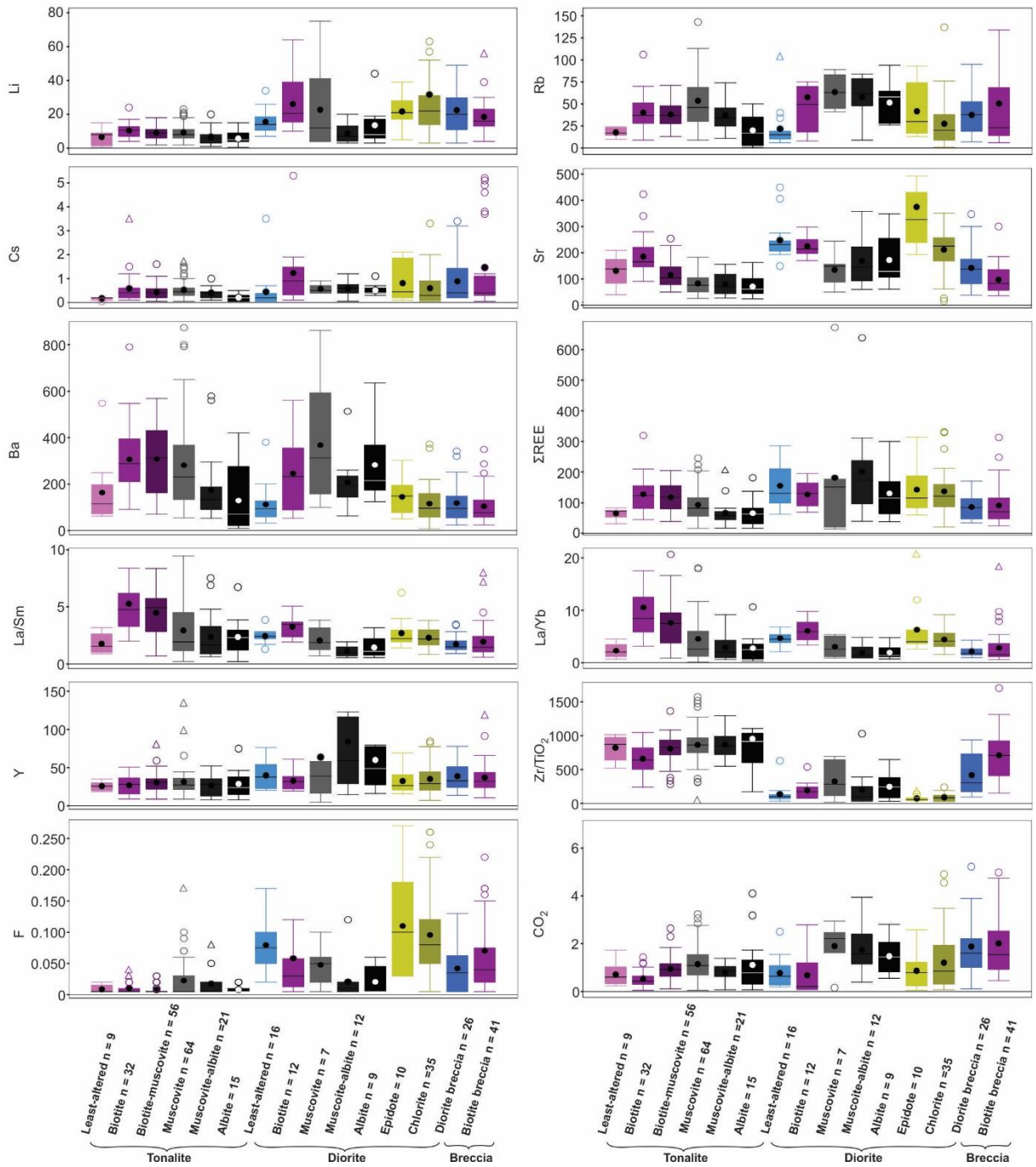

Figure 4.13. Box and whisker plots of the overall abundance of certain elements, oxides and ratios for different alteration assemblages in the Côté Gold deposit. The bottom of the box is Q1, the top of box isQ3 and the whiskers are the extreme values that are not outliers. An outlier (circle) is further than 1.5*(Q3-Q1), whereas a far outlier is further than 3*(Q3-Q1); some outliers were omitted for several plots (Zn, Ag, Se, V, Cr, S, Rb, Sr, La, Lu, Cs, Y, Zr/TiO_2, La/Yb, F, La/Sm) and far outliers were omitted for several plots (Au, Ag, Te, W, Cu, Ni, Pb, CO2, Sn, Bi, Li, La/Yb, F) for clarity.

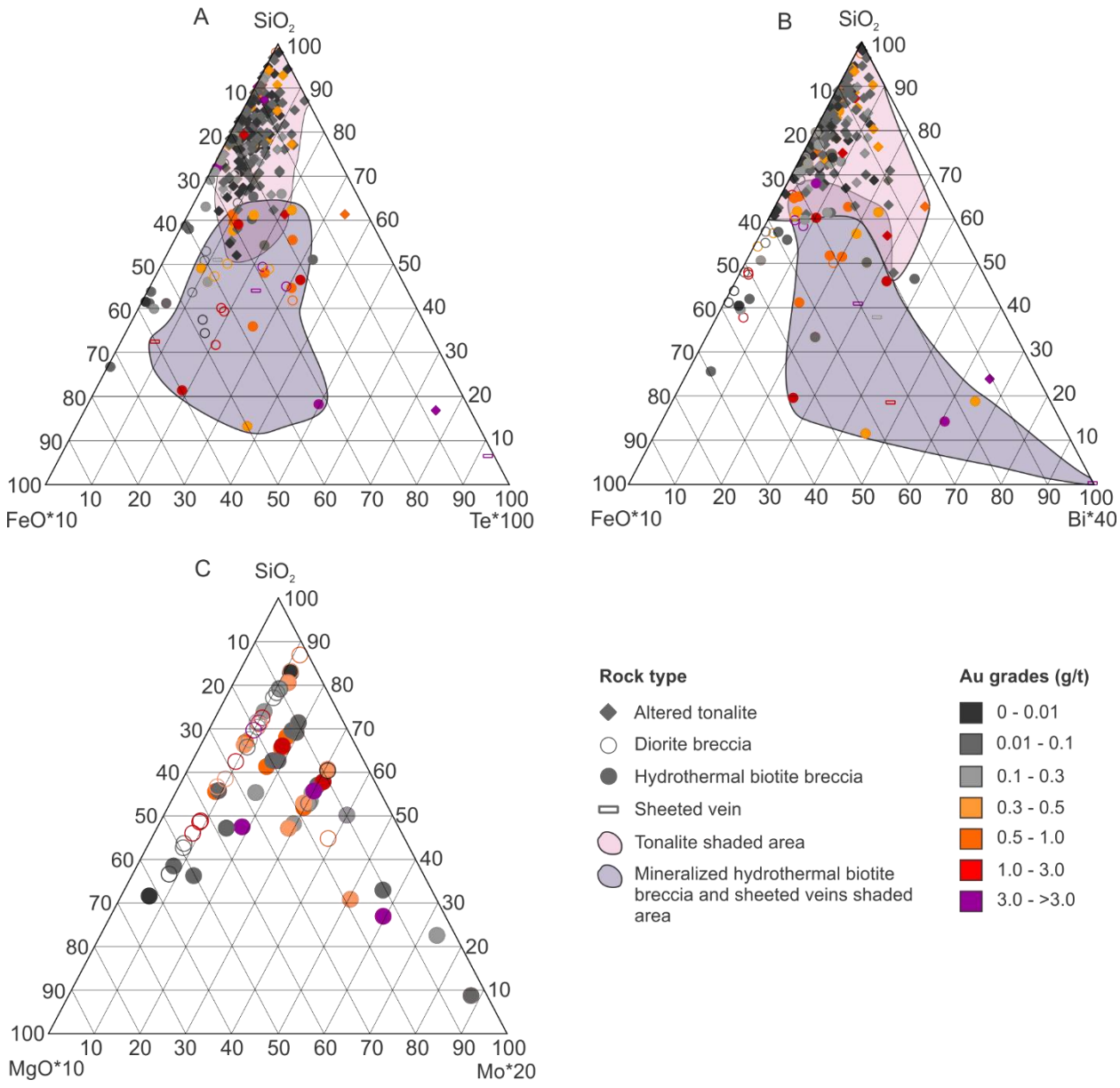

Figure 4.14. Ternary diagrams that show the metal associations in the hydrothermal biotite breccia. A) SiO_2-FeO*10-Te*100 diagram that shows enrichments of Te, as well as FeO, in both the hydrothermal biotite breccias and sheeted veins compared to tonalite samples. Note, diorite samples are not shown for clarity. B) SiO_2-FeO*10-Bi*40 diagram that shows enrichments in Bi in hydrothermal biotite breccias and sheeted veins. Some altered tonalite samples trend towards Bi and these samples are typically muscovite altered. C) SiO_2-MgO*10-Mo*20 diagram that shows, regardless of Au grade, the hydrothermal biotite breccia contains enrichments in Mo, whereas the diorite breccia does not.

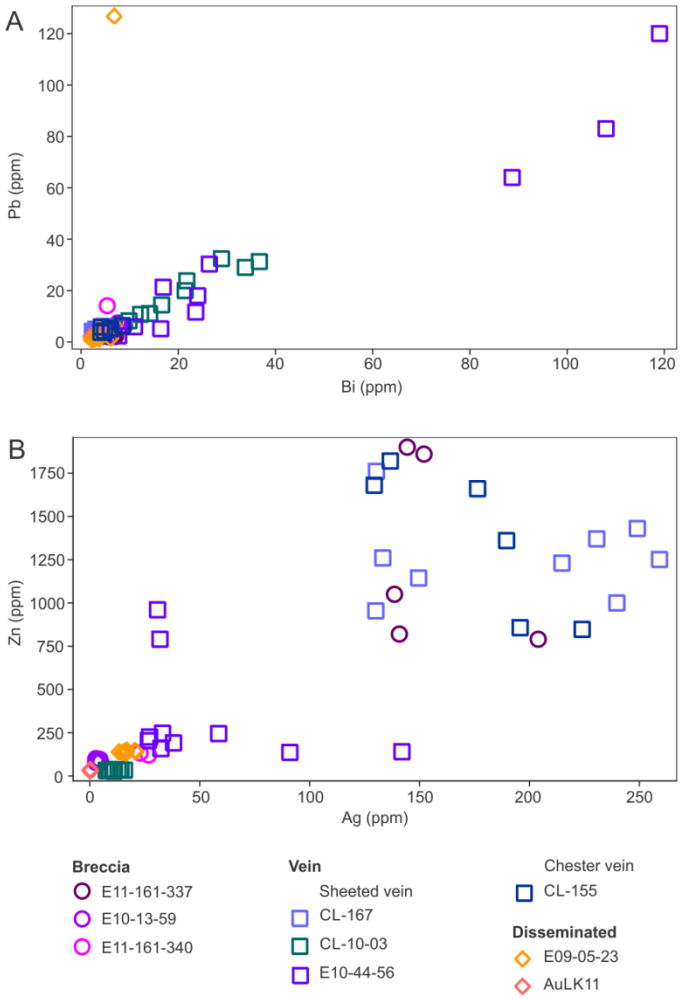

Figure 4.15. Bivariate plots showing the concentrations of selected trace elements in chalcopyrite grains from a variety of settings. A) Plot of Pb vs. Bi showing a positive correlation, particularly in the vein samples (r = 0.98) B) Plot of Zn vs. Ag showing a positive correlation with increases of Zn and Ag in a hydrothermal biotite breccia, sheeted vein and Chester vein samples (r = 0.83).

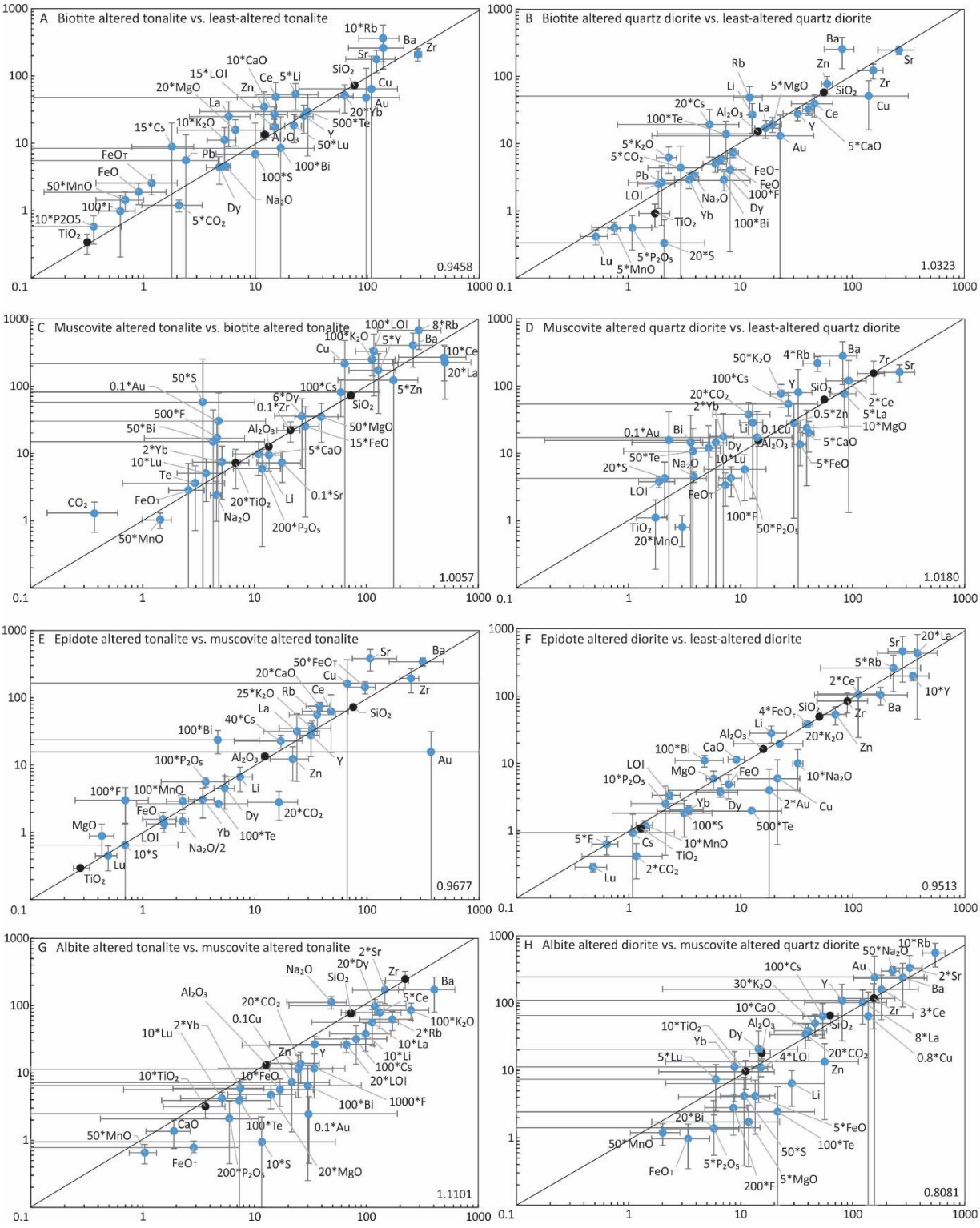
A Biotite altered tonalite vs. least-altered tonalite
0.9458
B Biotite altered quartz diorite vs. least-altered quartz diorite
1.0323
C Muscovite altered tonalite vs. biotite altered tonalite
1.0057
D Muscovite altered quartz diorite vs. least-altered quartz diorite
1.0180
E Epidote altered tonalite vs. muscovite altered tonalite
0.9677
F Epidote altered diorite vs. least-altered diorite
0.9513
G Albite altered tonalite vs. muscovite altered tonalite
1.1101
H Albite altered diorite vs. muscovite altered quartz diorite
0.8081

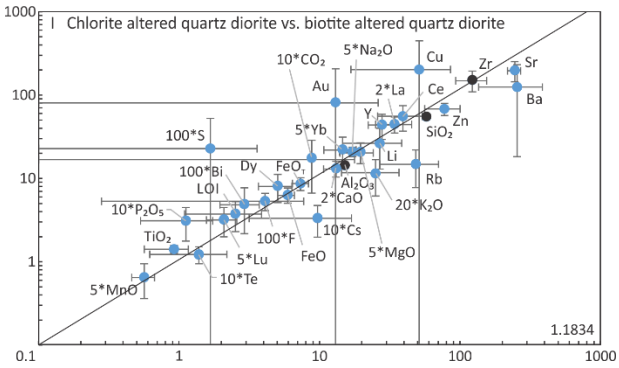

Figure 4.16. Summary of representative isocon diagrams using the most relevant elements for the different alteration assemblages within the Côté Gold deposit. Note that data for various elements have been multiplied or divided to fit a common scale of the diagram. The black isocon lines are defined by the ratios of various immobile elements, denoted by black circles, which were used for calculating the gains and losses (see Fig. 4.17 and Table 4.5). The grey error bar lines represent the standard deviation.

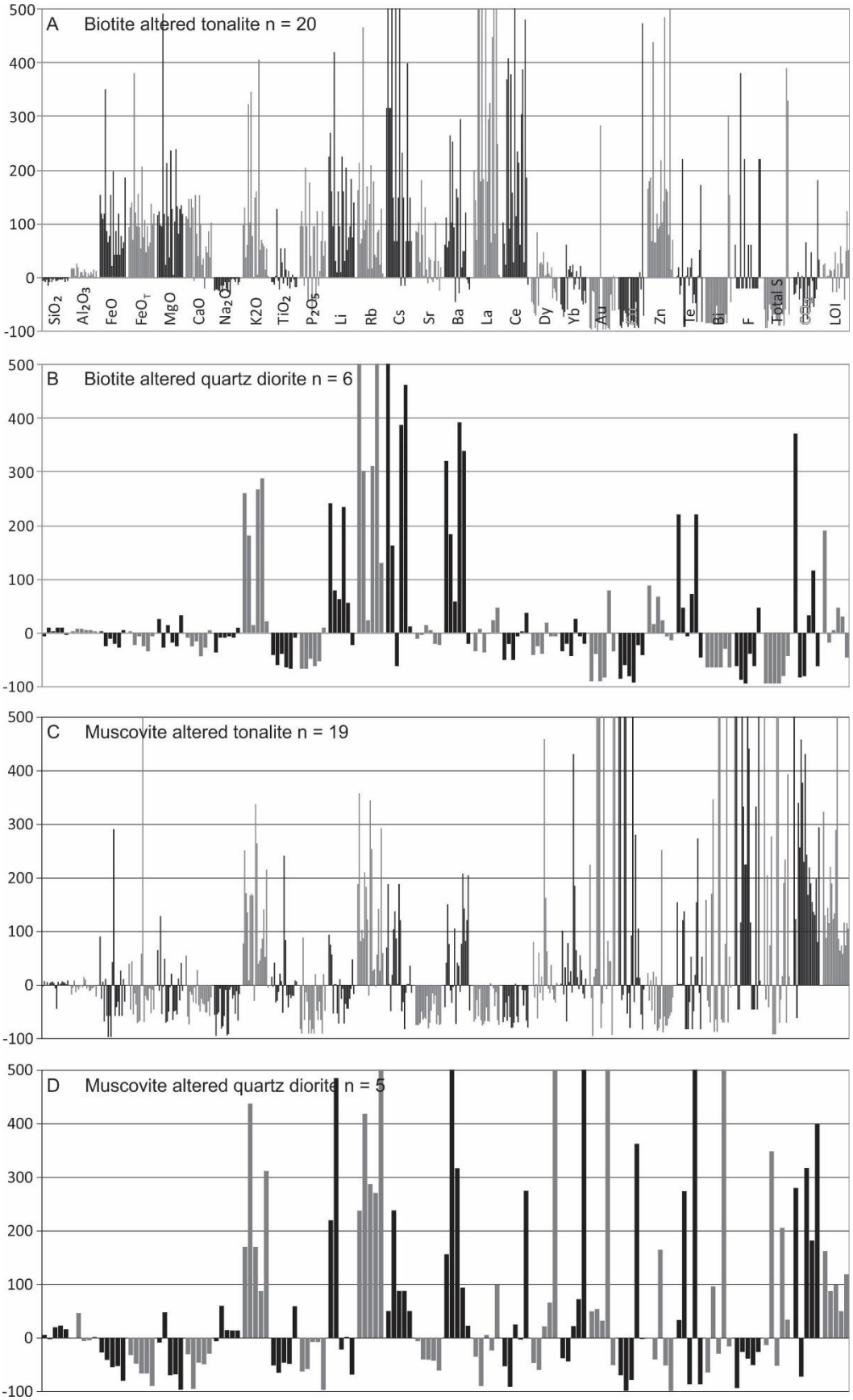
A Biotite altered tonalite n = 20
B Biotite altered quartz diorite n = 6
C Muscovite altered tonalite n = 19
D Muscovite altered quartz diorite n = 5
500
400
300
200
100
0
-100
SiO2
Al2O3
FeO
FeOT
MgO
CaO
Na2O
K2O
TiO2
P2O5
Li
Rb
Cs
Sr
Ba
La
Ce
Dy
Yb
Au
Zn
Te
Bi
F
Total S
LOI

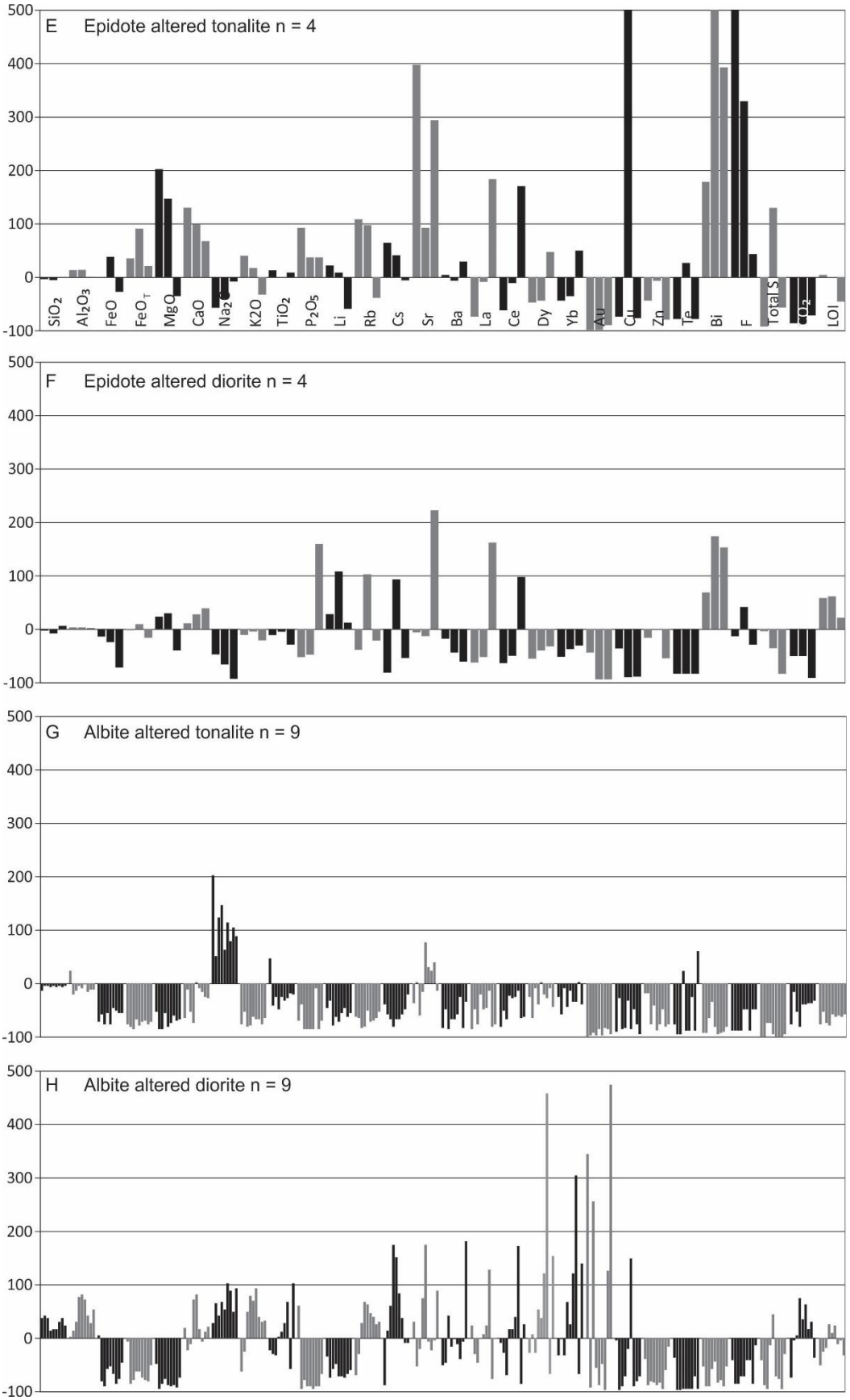
E Epidote altered tonalite n = 4
F Epidote altered diorite n = 4
G Albite altered tonalite n = 9
H Albite altered diorite n = 9
500
400
300
200
100
0
-100
SiO2
Al2O3
FeO
FeOT
MgO
CaO
Na2O
K2O
TiO2
P2O5
Li
Rb
Cs
Sr
Ba
La
Ce
Dy
Yb
Au
Cu
Zn
Te
Bi
F
Total S
CO2
LOI

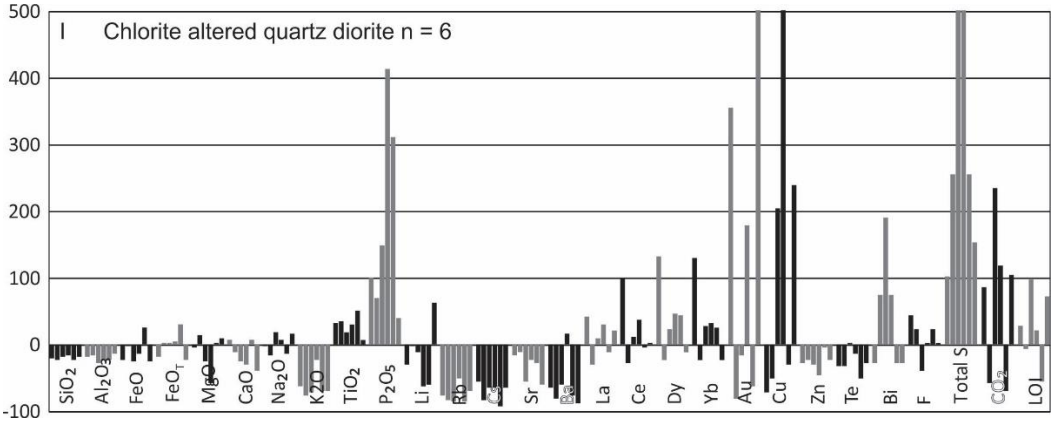

Figure 4.17. Histogram diagrams showing the gains and losses of major and trace elements in the main alteration assemblages at the Côté Gold deposit using the Grant-type isocon method. All gains are cut-off at 500%.

Table 4.1. Summary of alteration assemblages at the Côté Gold deposit

Timing	Early (syn-magmatism)		Transitional to late (post-magmatism)			
Alteration type	Amphibole (*calcic*)	Biotite (*potassic*)	Muscovite (*phyllic*)	Epidote	Albite (*sodic*)	Chlorite
Alteration assemblage	**Hbl** ± Qz ± Ttn ± Ap ± *Mag* ± Ab ± *Bt ± Py ± Ccp*	**Bt** ± **Qz** ± Cal ± Ank ± **Ep** ± *Aln* ± **Mag** ± Py ± Ccp ± *Po* ± *Ap* ± *Bst* ± *Ttn* ± *Fl* ± *Sp* ± *Gn*	**Ms** ± Qz ± Cal ± Py ± Ccp	**Ep** ± **Qz** ± Cal ± Chl ± *Py* ± *Ccp*	**Ab** ± Qz ± Cal ± *Ttn* ± *Ilm* ± *Chl* ± *Py;* **Ab** ± *Ttn* ± *Rt* ± *Hem* ± *Ap* ± *Chl*	**Chl** ± Qz ± Cal ± Ilm ± Rt ± Py ± Ccp
Vein types	**Hbl ± Ab** **Hbl**-**Ap-Ttn** ± Mag ± *Py* ± *Ccp* **Hbl-Qz-Ttn** ± Mag **±** *Py* **±** *Ccp*	**Bt, Bt** ± **Qz,** **Bt**-**Qz**-**Py** ± **Ccp** ± Po ± Cb ± *Aln* ± *Ttn* ± *Bst* ± *Sp* ± Gn **Bt**-**Qz**-**Ep** ± Cb ± *Mag* ± *Ttn* ± *Fl* ± *Py* ± *Ccp*	**Qz** ± **Cal** ± Ms, **Ms** ± Cal, **Qz-Cb** ± Tur ± Chl ± *Py* ± *Ccp*	**Ep, Qz-Ep**, **Ep ± Qz** ± Cal ± Chl ± *Py* ± *Ccp*	**Ab** ± **Qz** ± Cal, **Ab**-Ttn, **Ttn**, **Qz**-**Cb**-**Ilm** ± Ttn, **Qz-Cal**-Ttn	**Chl** ± Qz ± Cal ± Py ± Ccp
Alteration style	Vein-controlled, breccias	Disseminations, vein-controlled, breccias	Vein-controlled, replacement	Disseminations, vein-controlled	Vein-controlled, replacement	Replacement

Note: Bold font indicates high abundance; regular font indiates moderate abundance; italics font indicates minor abundance.
Mineral abbreviations: Ab = Albite, Aln = Allanite, Ank = Ankerite, Ap = Apatite, Au = Gold, Bt = Biotite, Bst = Basnaesite, Cal = Calcite, Cb = Carbonate, Chl = Chlorite, Ccp = Chalcopyrite, Ep = Epidote, Fl = Fluorite, Gn = Galena, Hbl = Hornblende, Hem = Hematite, Ilm = Ilmenite, Mag = Magnetite, Mol = Molybdenite, Ms = Muscovite, Qz = Quartz, Rt = Rutile, Po = Pyrrhotite, Py = Pyrite, Rt = Rutile, Sp = Sphalerite, Ttn = Titanite, Tur = Tourmaline

Table 4.2. Results of LA ICP-MS measurements from of trace element concentrations in chalcopyrite

Sample number		Fe	Co	Ni	Zn	Se	Ag	Pd	Cd	In	Sn	Sb	Te	Pt	Au	Pb	Bi
		m.d.l.	m.d.l.	m.d.l.	m.d.l.	m.d.l.	m.d.l.	m.d.l.	m.d.l.	m.d.l.	m.d.l.	m.d.l.	m.d.l.	m.d.l.	m.d.l.	m.d.l.	m.d.l.
		5	0.04	0.34	0.7	1.8	0.03	0.007	0.12	0.01	0.07	0.05	0.24	0.000	0.003	0.05	0.01
E10-13-59	min.	281800	n = 3 b.d.l.	n = 5 b.d.l.	79.2	167.3	2.67	n = 6 b.d.l.	0.61	14.96	6.72	0.04	n = 1 b.d.l.	b.d.l.	0.041	2.87	3.68
Bx (n = 8)	max.	291500	0.09	0.95	100	190.9	4.85	0.02	0.84	16.23	21.1	0.22	0.51	b.d.l.	0.258	7.4	8.94
	avg.	286200	0.05	0.36	87	179.3	3.49	0.01	0.71	15.58	17	0.11	0.17	b.d.l.	0.142	5.1	6.3
	STD	3791	0.03	0.23	8	8.9	0.86	0.00	0.07	0.43	5	0.06	0.16	b.d.l.	0.066	1.4	1.9
E11-161-	min.	284900	n = 4 b.d.l.	0.32	790	136.2	138.6	n = 4 b.d.l.	21.1	19.55	48.5	0.03	0.24	b.d.l.	0.006	1.98	4.35
337	max.	291600	0.01	0.39	1900	141.3	204	0.006	47.9	20.23	114	0.05	0.41	b.d.l.	0.023	2.36	7.09
Bx (n = 5)	avg.	288220	0.01	0.35	1284	123.6	156	0.003	33.2	19.78	82	0.04	0.34	b.d.l.	0.013	2.11	5.92
	STD	2895	0.00	0.02	495	25.4	24	0.002	11.8	0.25	26	0.01	0.06	b.d.l.	0.006	0.14	0.96
E11-161-	min.	291400	0.14	12.36	121	82.7	22.79	n = 1 b.d.l.	3.71	99.4	13.63	0.37	b.d.l.	b.d.l.	0.004	9.46	1.7
340	max.	295700	0.18	12.89	132.6	84.2	26.7	0.028	5.48	100.3	20.9	0.52	b.d.l.	b.d.l.	0.017	14.1	5.4
Bx (n = 2)	avg.	293550	0.16	12.63	127	83.5	24.7	0.014	4.60	99.9	17.3	0.44	b.d.l.	b.d.l.	0.011	11.8	3.6
	STD	2150	0.02	0.27	6	0.8	2.0	0.014	0.88	0.4	3.6	0.08	b.d.l.	b.d.l.	0.006	2.3	1.9
CL-10-03	min.	272000	n = 8 b.d.l.	b.d.l.	27.81	85.6	7.5	n = 6 b.d.l.	0.45	26.84	5.63	0.04	0.25	n = 9 b.d.l.	0.091	6	6.2
Vn (n = 10)	max.	288900	0.04	b.d.l.	37.1	98.6	15.73	0.014	0.83	29.45	70	0.21	2.27	0.003	0.973	32.4	36.7
	avg.	281610	0.02	b.d.l.	33.3	92	10.8	0.007	0.6	28.0	16	0.13	1.23	0.000	0.484	19	20.2
	STD	5299	0.01	b.d.l.	2.6	4	2.6	0.004	0.1	0.7	20	0.06	0.66	0.001	0.291	9	9.8
CL-167	min.	296100	37	90	954	100.9	130.1	n = 8 b.d.l.	15.19	6.6	18.48	0.21	0.67	n = 5 b.d.l.	0.119	3	2.33
SVn n = 9)	max.	312000	85	230	1760	157.9	259.2	0.011	29.2	8.32	26.54	0.60	1.48	0.005	0.293	6.07	4.72
	avg.	307644	67	135	1267	123	193.0	0.004	20	7.3	21.4	0.32	0.95	0.001	0.2	4	3.10
	STD	5401	16	45	228	22	52.6	0.003	4	0.6	3.0	0.11	0.22	0.002	0.1	1	0.67
AuLk11	min.	270800	n = 9 b.d.l.	n = 3 b.d.l.	29.2	91.6	0.13	n = 8 b.d.l.	0.46	2.94	0.72	0.07	n = 7 b.d.l.	b.d.l.	0.107	2.4	1.91
Diss (n = 10)	max.	282900	0.17	2.77	36.7	178	0.33	0.036	1.17	3.28	1.1	0.36	1.27	b.d.l.	0.71	6.48	6.91
	avg.	276490	0.11	1.43	32	152	0.21	0.018	0.84	3.1	0.9	0.20	0.74	b.d.l.	0.3	4.5	3.82
	STD	3775	0.03	0.79	2	23	0.06	0.007	0.18	0.1	0.1	0.10	0.29	b.d.l.	0.2	1.3	1.30
E10-44-56	min.	275700	n = 3 b.d.l.	n = 3 b.d.l.	136	38.7	26.6	n = 6 b.d.l.	1.48	14.33	10.84	0.13	n = 4 b.d.l.	b.d.l.	0.317	2.32	7.74
SVn (n = 10)	max.	291000	1.4	2.02	960	61.9	142	0.03	8.3	27.47	14.2	0.81	4.1	b.d.l.	17.2	120	119
	avg.	282980	0.4	1.1	330	54	51	0.02	2.9	20.0	12.1	0.41	1.4	b.d.l.	4	36	44
	STD	3989	0.5	0.4	278	7	36	0.01	2.0	4.9	1.0	0.25	1.2	b.d.l.	5	38	41
E09-05-23	min.	280300	0.21	n = 1 b.d.l.	131.5	195.8	13.31	n = 9 b.d.l.	1.65	16.8	28.81	0.05	1	b.d.l.	0.112	1	1.94
Diss (n = 10)	max.	292600	0.35	0.77	148.7	214.8	20.96	0.01	2.25	18.17	52.1	0.66	6.8	b.d.l.	2.05	127	6.69
	avg.	288000	0.26	0.6	140	205	16.7	0.01	2.04	17.7	40.8	0.14	4	b.d.l.	0.44	14	3.4
	STD	3463	0.04	0.1	5	6	2.3	0.00	0.16	0.4	7.8	0.18	2	b.d.l.	0.54	38	1.5
CL-155	min.	297500	3.34	9.76	847	30.4	129.4	n = 4 b.d.l.	12.53	5.025	15.49	0.12	0.77	n = 2 b.d.l.	0.056	3.71	4.07
CVn (n = 6)	max.	317200	5.77	55	1820	32.4	224	0.036	18.0	6.418	19.54	0.27	2.67	0.002	0.121	6.38	8.52
	avg.	309183	4.30	30	1371	31.1	175	0.013	16	5.7	16.89	0.19	1.53	0.001	0.096	5.1	5.62
	STD	6397	0.84	18	391	0.8	33	0.014	2	0.5	1.48	0.05	0.64	0.001	0.021	0.9	1.52

Note: Values are in ppm; m.d.l. = mean detection limit and b.d.l. = below detection limit; samples below the detection limit were given the value of the detection limit in the average

Bx = breccia, Vn = vein, SVn = sheeted vein, CVn = Chester vein and Diss = disseminated

Table 4.3. Average composition of least-altered and altered tonalite samples from the Côté Gold deposit for mass balance calculations

	Tonalite																	
	Least-altered			Disseminated/ stockwork biotite			Fracture-controlled muscovite			Pervasive muscovite			Disseminated/fracture-controlled epidote			Pervasive albite		
	Average	STD	n	Average	STD	n	Average	STD	n	Average	STD	n	Average	STD	n	Average	STD	n
SiO_2	77.052	2.08	5	72.58	2.45	20	75.30	1.94	20	72.77	8.21	19	72.62	1.51	3	76.12	2.65	9
Al_2O_3	12.206	0.58	5	13.38	0.89	20	12.30	0.69	20	12.68	1.17	19	13.41	0.75	3	13.04	1.68	9
FeO	0.91	0.78	5	1.90	0.67	20	1.52	0.49	20	1.69	1.61	19	1.57	0.41	3	0.57	0.25	9
Fe_2O_3	1.32	0.90	5	1.89	0.67	20	0.45	0.38	20	1.31	3.15	19	1.37	0.24	3	0.24	0.20	9
FeO_T	1.19	0.81	5	2.58	0.85	20	1.92	0.57	20	1.17	2.83	19	1.23	0.22	3	0.22	0.18	9
MnO	0.01	0.01	5	0.03	0.01	20	0.02	0.01	20	0.02	0.01	19	0.03	0.01	3	0.01	0.00	9
MgO	0.33	0.23	5	0.79	0.33	20	0.43	0.11	20	0.70	0.41	19	0.89	0.44	3	0.24	0.09	9
CaO	1.48	0.50	5	2.70	0.77	20	1.90	0.49	20	1.90	0.80	19	3.76	0.49	3	1.37	0.62	9
Na_2O	5.44	0.51	5	4.57	0.52	20	4.54	0.53	20	2.44	1.45	19	2.93	0.92	3	5.63	1.18	9
K_2O	0.53	0.16	5	1.12	0.61	20	1.30	0.64	20	2.50	1.08	19	1.40	0.40	3	0.85	0.24	9
TiO_2	0.317	0.026	5	0.339	0.111	20	0.278	0.049	20	0.363	0.213	19	0.296	0.016	3	0.316	0.10299	9
P_2O_5	0.04	0.03	5	0.06	0.03	20	0.04	0.02	20	0.03	0.03	19	0.06	0.01	3	0.01	0.01	9
LOI	0.99	0.16	5	1.16	0.36	20	1.56	0.44	20	3.32	2.61	19	1.34	0.35	3	1.31	0.32	9
Total	99.71	0.56	5	99.57	0.73	20	99.79	0.98	20	99.89	1.03	19	99.90	0.52	3	99.73	0.68	9
Total S	0.10	0.06	5	0.07	0.13	20	0.07	0.14	20	1.17	3.95	19	0.07	0.07	3	0.09	0.13	9
CO_2	0.42	0.23	5	0.37	0.24	20	0.82	0.38	20	1.29	0.62	19	0.14	0.06	3	0.68	0.33193	9
F	0.01	0.00	5	0.01	0.01	20	0.01	0.00	20	0.03	0.03	19	0.03	0.02	3	0.01	0.01	9
Au	98	110	5	48	82	20	371	1519	20	304	492	19	16	16	3	24	20	9
Cu	109.0	89.6	5	64.0	133.3	20	66.7	107.8	20	215.6	261.2	19	162.1	206.4	3	72.8	59.6	9
Mo	0.8	0.6	5	0.7	0.4	20	1.2	0.7	20	1.5	1.0	19	3.0	0.8	3	1.0	0.6	9
Ag	1.2	0.4	5	1.0	0.3	20	1.2	0.4	20	1.2	0.6	19	1.2	0.6	3	1.2	0.5	9
Sb	0.4	0.3	5	0.4	0.2	20	0.3	0.2	20	0.3	0.3	19	0.2	0.1	3	0.3	0.3	9
Te	0.06	0.05	5	0.06	0.05	20	0.05	0.04	20	0.07	0.06	19	0.03	0.02	3	0.04	0.04	9
Bi	0.17	0.17	5	0.09	0.16	20	0.05	0.06	20	0.30	0.59	19	0.24	0.09	3	0.07	0.06	9
Se	0.5	0.0	5	0.7	0.4	20	0.7	0.4	20	0.7	0.6	19	0.3	0.2	3	0.4	0.1	9
As	2.4	2.0	5	3.4	3.5	20	1.6	1.5	20	16.9	38.7	19	2.1	1.8	3	1.4	1.4	9
Pb	2	2	5	6	8	20	3	2	20	7	11	19	3	2	3	2	1	9
W	0.86	1.06	5	0.77	1.07	20	0.61	0.79	20	7.26	15.04	19	0.40	0.21	3	1.64	1.36	9
Zn	12.0	2.4	5	34.7	23.4	20	21.8	8.2	20	24.5	26.2	19	12.3	6.5	3	11.3	7.0	9
Li	5	3	5	11	5	20	7	2	20	10	5	19	7	3	3	4	2	9
Rb	14	6	5	37	20	20	36	16	20	85	41	19	56	24	3	31	10	9
Cs	0.1	0.1	5	0.6	0.7	20	0.4	0.3	20	0.8	0.5	19	0.6	0.1	3	0.3	0.2	9
Sr	121	60	5	176	65	20	107	34	20	73	36	19	385	135	3	86	32	9
Ba	139	69	5	260	133	20	314	164	20	405	213	19	342	47	3	172	93	9
V	14	5	5	32	15	20	17	6	20	22	11	19	31	10	3	13	3	9
Y	27.2	5.8	5	25.4	11.4	20	31.6	7.5	20	34.6	26.7	19	27.8	14.4	3	26.7	7.6	9
Zr	284	25	5	210	44	20	247	50	20	222	74	19	194	76	3	248	73	9
La	5.8	3.3	5	25.1	16.1	20	23.8	12.2	20	11.3	8.1	19	31.7	26.0	3	5.6	3.1	9
Ce	15.3	7.5	5	49.1	30.7	20	47.8	21.6	20	26.4	14.4	19	63.1	47.6	3	15.8	6.7	9
Dy	4.78	1.15	5	4.42	1.94	20	5.39	1.24	20	5.94	4.94	19	4.58	2.36	3	4.88	1.27	9
Yb	3.16	0.58	5	2.56	1.15	20	3.44	0.78	20	3.75	2.70	19	3.08	1.45	3	2.97	0.74	9
Lu	0.443	0.074	5	0.368	0.164	20	0.492	0.104	20	0.510	0.317	19	0.450	0.182	3	0.418	0.096	9

Note: Major elements, total S, CO_2 and F are in wt. %, Au is in ppb and trace elements are in ppm

Table 4.4. Average composition of least-altered and altered dioritic samples from the Côté Gold deposit for mass balance calculations

	Quartz diorite														Diorite					
	Least-altered			Disseminated biotite			Fracture-controlled/ pervasive muscovite			Pervasive albite			Disseminated chlorite			Least-altered			Pervasive epidote		
	Average	STD	n	Average	STD	n	Average	STD	n	Average	STD	n	Average	STD	n	Average	STD	n	Average	STD	n
SiO_2	55.97	2.14	6	57.74	3.90	6	62.76	5.33	5	65.22	5.16	9	55.02	1.39	6	50.33	1.36	4	49.52	2.97	3
Al_2O_3	14.44	0.51	6	15.14	0.30	6	15.46	2.81	5	18.07	3.33	9	14.32	0.96	6	15.91	1.43	4	16.33	0.05	3
FeO	6.80	0.99	6	5.93	0.87	6	2.70	1.39	5	0.83	0.61	9	6.32	1.30	6	7.80	1.04	4	4.93	1.96	3
Fe_2O_3	2.09	0.92	6	1.53	0.48	6	0.77	0.45	5	0.15	0.15	9	2.57	0.84	6	2.31	0.47	4	5.13	1.48	3
FeO_T	1.88	0.83	6	1.37	0.43	6	0.69	0.40	5	0.14	0.14	9	2.31	0.76	6	2.07	0.42	4	9.55	1.01	3
MnO	0.15	0.02	6	0.11	0.02	6	0.04	0.02	5	0.02	0.01	9	0.13	0.06	6	0.14	0.03	4	0.12	0.02	3
MgO	3.90	0.60	6	3.92	0.98	6	2.36	2.03	5	0.34	0.27	9	4.16	1.16	6	5.71	0.74	4	5.94	1.78	3
CaO	8.15	0.80	6	6.55	1.26	6	4.02	1.94	5	3.89	1.09	9	6.58	1.41	6	9.14	1.28	4	11.46	1.04	3
Na_2O	3.81	0.31	6	3.43	0.52	6	4.53	0.83	5	6.06	0.87	9	4.18	0.54	6	3.24	0.33	4	1.00	0.61	3
K_2O	0.46	0.09	6	1.25	0.52	6	1.54	0.57	5	1.67	0.59	9	0.57	0.27	6	1.11	0.67	4	0.98	0.07	3
TiO_2	1.741	0.535	6	0.919	0.348	6	1.111	0.922	5	0.969	0.438	9	1.407	0.151	6	1.285	0.223	4	1.088	0.130	3
P_2O_5	0.22	0.12	6	0.11	0.06	6	0.12	0.08	5	0.03	0.04	9	0.31	0.13	6	0.21	0.11	4	0.25	0.21	3
LOI	1.87	0.63	6	2.51	1.43	6	3.79	0.69	5	2.77	0.75	9	3.76	1.47	6	2.31	0.64	4	3.39	0.42	3
Total	100.34	0.38	6	99.81	0.59	6	99.49	0.32	5	100.06	0.81	9	100.01	0.58	6	100.36	0.43	4	100.70	0.22	3
Total S	0.11	0.14	6	0.02	0.02	6	0.21	0.16	5	0.08	0.08	9	0.23	0.29	6	0.03	0.02	4	0.02	0.01	3
CO_2	0.59	0.31	6	0.88	0.95	6	1.89	0.96	5	1.72	0.68	9	1.76	1.10	6	0.59	0.39	4	0.21	0.11	3
F	0.08	0.02	6	0.04	0.04	6	0.04	0.02	5	0.01	0.01	9	0.05	0.01	6	0.13	0.03	4	0.13	0.04	3
Au	23	21	6	13	14	6	157	258	5	241	260	9	82	125	6	9	8	4	2	2	3
Cu	140.4	148.6	6	51.2	35.2	6	171.7	243.0	5	80.3	102.6	9	202.0	247.6	6	21.3	12.1	4	6.0	5.4	3
Mo	0.6	0.2	6	1.3	1.7	6	1.1	0.7	5	0.5	0.0	9	0.5	0.0	6	0.6	0.2	4	0.5	0	3
Ag	0.7	0.2	6	0.6	0.3	6	1.0	0.6	5	0.6	0.5	9	0.8	0.4	6	2.2	3.2	4	0.4	0.2	3
Sb	0.5	0.2	6	0.4	0.1	6	0.2	0.2	5	0.2	0.2	9	0.4	0.1	6	0.2	0.1	4	0.1	0.0	3
Te	0.08	0.06	6	0.14	0.08	6	0.21	0.25	5	0.02	0.03	9	0.12	0.03	6	0.05	0.02	4	0.01	0.00	3
Bi	0.07	0.05	6	0.03	0.01	6	0.29	0.44	5	0.07	0.04	9	0.05	0.03	6	0.05	0.02	4	0.11	0.02	3
Se	0.6	0.3	6	1.1	0.7	6	1.2	1.0	5	1.1	0.6	9	1.4	0.6	6	0.5	0.3	4	0.2	0.1	3
As	1.8	1.6	6	1.9	1.9	6	2.0	2.3	5	2.6	2.5	9	1.7	1.6	6	0.9	0.5	4	1.6	1.7	3
Pb	2	1	6	3	2	6	3	2	5	4	4	9	2	1	6	1	0	4	2	1	3
W	0.48	0.25	6	0.81	1.25	6	6.92	10.01	5	3.17	1.50	9	0.57	0.45	6	0.25	0	4	0.45	0.15	3
Zn	59.9	8.1	6	77.5	22.6	6	56.4	54.2	5	13.4	11.5	9	68.1	11.3	6	70.1	18.7	4	53.3	16.1	3
Li	13	3	6	27	12	6	29	26	5	6	3	9	26	13	6	19	7	4	28	8	3
Rb	12	3	6	49	22	6	55	13	5	56	22	9	15	7	6	46	36	4	52	29	3
Cs	0.3	0.2	6	1.0	0.6	6	0.5	0.2	5	0.6	0.3	9	0.3	0.1	6	1.1	1.4	4	0.9	0.8	3
Sr	262	85	6	246	35	6	161	46	5	168	88	9	198	54	6	278	74	4	465	304	3
Ba	82	26	6	255	125	6	280	175	5	240	152	9	125	107	6	177	132	4	104	1	3
V	194	19	6	125	33	6	74	38	5	33	17	9	144	46	6	226	20	4	180	20	3
Y	32.8	9.4	6	27.8	5.9	6	80.5	95.5	5	109.3	81.9	9	44.0	14.7	6	34.4	12.8	4	19.9	2.9	3
Zr	154	40	6	122	30	6	155	79	5	118	77	9	152	43	6	90	41	4	84	28	3
La	16.9	4.8	6	17.1	5.0	6	15.4	10.5	5	12.8	6.7	9	22.4	4.9	6	18.8	10.0	4	21.7	19.4	3
Ce	46.2	16.9	6	39.2	14.3	6	60.1	59.4	5	53.0	34.1	9	55.7	18.8	6	56.2	26.5	4	53.2	41.0	3
Dy	6.02	1.53	6	5.03	1.26	6	14.46	17.74	5	20.90	17.55	9	8.11	3.01	6	6.57	2.57	4	3.76	0.61	3
Yb	3.50	0.95	6	2.92	0.76	6	8.83	10.59	5	11.28	7.83	9	4.45	1.78	6	3.44	1.18	4	2.05	0.30	3
Lu	0.517	0.144	6	0.416	0.104	6	1.198	1.383	5	1.475	0.979	9	0.641	0.246	6	0.481	0.154	4	0.287	0.041	3

Note: Major elements, total S, CO_2 and F are in wt. %, Au is in ppb and trace elements are in ppm

Table 4.5. Calculated gains and losses in alteration zones for averaged tonalite and dioritic rocks

	Biotite		Muscovite		Epidote		Albite		Chlorite
	Tonalite	Quartz diorite	Tonalite	Quartz diorite	Tonalite	Diorite	Tonalite	Diorite	Diorite
SiO_2	**-0.4**	**-0.1**	**-0.3**	**10.2**	**-0.3**	**3.4**	**-5.8**	**28.6**	**-19.5**
Al_2O_3	**15.9**	**1.6**	**-5.8**	**5.2**	**12.6**	**8.0**	**-7.4**	**44.6**	**-20.1**
FeO	120.2	-15.5	-11.4	-61.0	6.5	-33.5	-69.8	-61.8	-10.0
FeO_T	129.6	-18.5	10.6	-73.8	54.1	1.6	-75.3	-64.6	-0.2
MnO	120.3	-27.5	-27.9	-73.8	31.7	-9.2	-43.3	-26.5	-3.0
MgO	151.1	-2.6	-11.5	-40.5	111.1	9.5	-69.8	-82.0	-10.3
CaO	92.0	-22.2	-30.0	-51.6	104.9	31.9	-35.2	19.9	-15.2
Na_2O	-11.2	-12.9	-47.0	16.8	-33.3	-67.4	108.3	65.3	2.9
K_2O	122.4	163.9	122.6	228.9	11.4	-7.7	-69.4	34.0	-61.5
TiO_2	**13.1**	**-48.8**	**6.7**	-37.3	**10.2**	**-11.0**	**-21.5**	**8.0**	29.3
P_2O_5	71.8	-48.7	-49.5	-48.1	60.4	25.3	-68.0	-70.1	134.6
LOI	24.6	30.4	184.3	99.3	-11.2	54.1	-64.5	-9.6	26.4
Total S	-27.0	-84.6	1580.4	100.2	-3.7	-38.3	-92.7	-51.8	1057.7
CO_2	-5.2	44.2	244.6	215.0	-82.4	-62.3	-52.6	12.2	69.5
F	56.5	-51.6	267.7	-48.3	342.9	4.4	-69.3	-60.0	10.4
Au	-48.3	-44.8	531.8	573.7	-95.6	-76.6	-92.8	90.8	431.9
Cu	-38.0	-64.7	235.1	20.1	151.1	-70.4	-69.6	-42.2	233.1
Mo	-4.2	107.6	102.1	85.2	169.6	-15.9	-38.9	-43.8	-66.2
Ag	-11.2	-16.3	22.3	38.3	5.1	-81.1	-13.2	-17.5	17.1
Sb	-7.5	-17.5	-14.8	-47.6	-40.6	-53.3	0.1	14.6	-22.8
Te	5.7	78.7	23.3	180.3	-42.0	-93.3	-52.1	-85.9	-25.7
Bi	-25.6	-60.6	249.9	296.1	423.1	143.4	-80.5	-70.7	42.4
Se	47.6	79.9	1.5	105.4	-50.1	-55.7	-45.1	9.3	10.5
As	48.4	2.2	390.5	10.3	41.8	81.8	-92.4	55.7	-26.5
Pb	146.7	29.2	20.6	57.2	-0.2	96.2	-76.4	54.7	-41.9
W	-5.6	64.9	837.6	1331.1	-32.2	89.2	-85.9	-43.3	-40.8
Sn	-40.0	-61.3	105.8	36.2	459.1	-60.6	-44.3	-7.5	101.9
Zn	205.9	25.3	-29.7	-7.5	-41.9	-20.1	-58.4	-70.6	-25.7
Li	149.4	102.5	-9.8	118.9	-6.9	57.0	-65.4	-72.1	-17.1
Rb	179.6	286.2	131.8	340.8	60.7	19.6	-67.1	27.2	-74.2
Cs	419.8	262.5	36.6	98.9	37.0	-9.8	-64.8	46.4	-70.9
Sr	53.7	-9.2	-58.7	-39.7	272.5	76.0	5.4	29.0	-31.8
Ba	98.0	202.3	54.9	236.6	12.4	-37.9	-61.6	6.1	-58.7
V	138.3	-37.6	-33.2	-62.8	96.2	-16.0	-44.4	-45.3	-2.9
Y	-1.3	-17.8	35.3	141.5	-9.1	-39.1	-30.4	68.0	33.8
Zr	-21.9	-20.6	**5.4**	**-1.4**	-18.6	**-1.3**	**0.6**	**-5.2**	**4.6**
La	357.8	-2.1	-55.1	-10.9	37.8	21.4	-55.4	3.1	10.6
Ce	240.1	-17.9	-46.6	27.7	36.3	-0.6	-46.1	9.2	20.1
Dy	-2.3	-19.0	33.6	136.1	-12.2	-39.8	-26.0	78.9	36.2
Yb	-14.2	-19.3	45.5	147.8	-7.3	-37.3	-28.7	58.1	28.9
Lu	-12.2	-22.1	37.8	127.5	-5.5	-37.2	-26.2	52.3	30.2

Note: Values for major elements, S, CO_2 and F are given in %, trace elements in ppm and Au in ppb

Bold font indicates elements used for isocon

Chapter 5

5 Conclusions

5.1 Conclusions

The Côté Gold deposit, located in the Swayze greenstone belt (SGB), Ontario, is a low-grade, high-tonnage deposit with its salient features similar to those of Phanerozoic porphyry systems. The deposit is hosted by ca. 2741 to 2739 Ma tonalitic and dioritic rocks of the Chester intrusive complex (CIC) and was emplaced into a sequence of coeval and cogenetic volcanic and sedimentary rocks of the Yeo Formation in a back-arc setting. The features of the CIC are similar to low-Al tonalite-trondhjemite-diorite intrusions that underlie VMS-type deposits and have been noted to contain porphyry-style Cu-Mo-Au mineralization.

The Côté Gold deposit is similar to porphyry-type deposits, in particular the gold-rich porphyry copper deposits, based on: (1) a spatial and genetic association with a high-level dioritic intrusion; (2) an overlap of magmatic and hydrothermal events at ca. 2740 Ma; (3) a biotite (potassic) core, represented by the hydrothermal biotite breccia, which is overprinted by muscovite (phyllic) alteration; (4) mineralization styles (e.g., breccias, disseminations and veins) that are spatially and genetically associated with biotite and muscovite alteration; (5) a close association of gold with chalcopyrite in the hydrothermal biotite breccia; and (6) abundant magnetite in the hydrothermal biotite breccia. The characteristics of this deposit are consistent with the emplacement of a dioritic intrusion into a high-level setting which underwent volatile exsolution during late-stage fractional crystallization in the magma chamber, resulting in vein, disseminated and breccia-hosted mineralization coincident with the formation of distinct

hydrothermal alteration assemblages. The results from this study demonstrate that this deposit represents one of the better known examples of an Archean porphyry-type deposit and is most appropriately classified as such.

The deposit represents a new gold metallogenic event at ca. 2740 Ma in the Abitibi Subprovince and this new age suggests that older intrusive complexes are prospective for gold mineralization in the Abitibi. The magmatic-hydrothermal system responsible for the formation of the deposit is demonstrated to be widespread and the surrounding regional vein system is considered prospective for gold mineralization. The Yeo Formation is prospective for base metal mineralization given its coeval timing with the CIC and its FII-type affinity.

5.2 Future Work and Outstanding Problems

The goal of this thesis was to provide the first general, but thorough description of the Côté Gold deposit. Due to the nature of this project and this being the first detailed study of the deposit there are many topics of interest for future study and several outstanding problems that should be addressed in order to better understand the nature and origin of the deposit.

Deposit-scale detailed mapping and drill core logging of the host rocks and breccias should be documented in more detail to delineate the complex crosscutting relationships and distribution of phases. In particular, a detailed delineation of the size, shape and distribution of all of the breccia bodies in the deposit is warranted due to their spatial association with gold mineralization.

Given the importance of the hydrothermal biotite breccia, further research is suggested to focus on the mineral chemistry of the biotites. In such a study, the distribution of different coloured biotite, biotite geothermometry to estimate the temperature at which biotite alteration formed and calculating the HF, HCl and H_2O fugacity of the hydrothermal fluids responsible for biotite alteration is of interest. In such a study, the collection of biotite altered samples from outside the deposit regionally within the Chester intrusive complex is recommended in order to compare and contrast ore-bearing samples with barren samples. In addition, an Ar-Ar geochronology study of the biotite in the hydrothermal biotite breccia is recommended to constrain the brecciation event. Such a study would also identify if biotite was reset by subsequent high-temperature hydrothermal event.

An isotope (i.e., O and H) and fluid inclusion study on the seawater that infiltrated the magmatic-dominated system is warranted to complement the drill core observations, mineral chemistry and lithogeochemistry presented in Chapters 3 and 4 of this thesis. Such a study would be beneficial in order to improve the understanding of the nature of the fluids responsible for the alteration types responsible for the formation of the deposit, since O- and H-isotopic compositions of hydrothermal minerals can help trace the origin(s) of the hydrothermal fluid and fluid inclusions can help delineate the type of fluid and its temperature of formation.

The size of the plagioclase-quartz miarole-like cavities is unusual, and therefore, their origin and distribution in the deposit should be studied in detail. Detailed mapping or drill core logging of this texture may shed light on its distribution within the deposit and an isotope study may provide important information about the origin of fluids.

Albite alteration requires further study of its texture and the nature of the fluids. The texture of albite altered rocks are complex and can result in grain size reduction in some samples. In this case, a cathodoluminescence study of least-altered to progressively albite altered samples may be a useful tool to determine how these textures formed. Albite alteration, including the rocks termed as episyenites (10-11 wt. % Na_2O), should be studied in detail by undertaking a fluid inclusion and isotope study to determine the true source of the albite alteration. In addition, the distribution of the episyenite in the deposit should be fully constrained.

A better understanding of the distribution of gold within the deposit is necessary and should be addressed in order to further improve the knowledge of the deposit and for exploration regionally within the intrusive complex. In order to accomplish this, a study of gold distribution at the microscopic and submicron scale is suggested. The remobilization of gold in the deposit is of particular interest as albite alteration may be responsible for the current distribution of gold in the central portions of the deposit where this alteration is strongest and may have remobilized gold outside of the system.

Although chlorite alteration has been demonstrated to replace biotite alteration, its origin and timing has not been well-constrained here. Future work should focus on the distribution of chlorite inside and outside the deposit and its mineral chemistry. In addition, future study should definitely determine if any genetic relationship to gold exists.

References

Ahrens, L.H., 1952, The use of ionization potentials. Part 1. Ionic radii of the elements.: Geochimica et Cosmochimica Acta, v. 2, p. 155-169.

Alderton, D.H.M., Pearce, J.A., and Potts, P.J., 1980, Rare earth element mobility during granite alteration: Evidence from southeast England: Earth and Planetary Science Letters, v. 48, p. 149-165.

Aleinikoff, J. N., Wintsch, R.P., Tollo, R.P., Unruh, D.M., Fanning, C.M., and Schmitz, M.D., 2007, Ages and origins of rocks of the Killingworth dome, south-central Connecticut: Implications for the tectonic evolution of southern New England: American Journal of Science, v. 307, p. 63-118.

Anderson, J.L., and Smith, D.R., 1995, The effects of temperature and f_{O2} on the Al-in-hornblende barometer: American Mineralogist, v. 80, p. 549-559.

Anderson, J.L., Barth, A.P., Wooden, J.L., and Mazdab, F., 2008, Thermometers and thermobarometers in granitic systems: Reviews in Mineralogy and Geochemistry, v. 69, p. 121-142.

Anthony, E.Y., and Titley, S.R., 1994, Patterns of element mobility during hydrothermal alteration of the Sierrita porphyry copper deposit, Arizona: Economic Geology, v. 89, p. 186-192.

Arancibia, O.N., and Clark, A.H., 1996, Early magnetite-amphibole-plagioclase alteration-mineralization in the Island Copper porphyry copper-gold-molybdenum deposit, British Columbia: Economic Geology, v. 91, p. 402-438.

Armbrust, G.A., Oyarzún, J., and Arias, J., 1977, Rubidium as a guide to ore in Chilean porphyry copper deposits: Economic Geology, v. 72, p. 1086-1100.

Ayer, J.A., and Chartrand, J.E., 2011, Geological compilation of the Abitibi greenstone belt: Ontario Geological Survey, Miscellaneous Release Data 282.

Ayer, J., Amelin, Y., Corfu, F., Kamo, S., Ketchum, J., Kwok, K., and Trowell, N., 2002, Evolution of the southern Abitibi greenstone belt based on U-Pb geochronology: Autochthonous volcanic construction followed by plutonism, regional deformation and sedimentation: Precambrian Research, v. 115, p. 63-95.

Ayer, J.A., Kontak, D.J., Linnen, R.L., and Lin, S., 2013, Results from the Shining Tree, Chester Township and Matachewan gold projects and the Northern Cobalt Embayment polymetallic vein project: Ontario Geological Survey, Miscellaneous Release Data 294.

Ayres, L.D., Averill, S.A., and Wolfe, W.J., 1982, An Archean molybdenite occurrence of

possible porphyry type at Setting Net Lake, Northwestern Ontario, Canada: Economic Geology, v. 77, p. 1105-1119.

Bailes, A.H., and Galley, A.G., 1996, Setting of Paleoproterozoic volcanic-hosted massive base metal sulphide deposits, Snow Lake, *in* Bonham-Carter, G.F., Galley, A.G., and Hall, G.E.M., ed., EXTECH 1: A Multidisciplinary Approach to Massive Sulphide Research in the Rusty Lake-Snow Lake Greenstone Belts, Manitoba: Geological Survey of Canada, Bulletin 426, p. 105-138.

Barker, F., 1979, Trondhjemites, dacites and related rocks. New York, Elsevier, 659 p.

Barker, F., and Arth, J.A., 1976, Generation of trondhjemitic-tonalitic liquids and Archean bimodal trondhjemite-basalt suites: Geology, v. 4, p. 596-600.

Barrett, T.J., and MacLean, W.H., 1999, Volcanic sequences, lithogeochemistry, and hydrothermal alteration in some bimodal volcanic-associated massive sulfide systems: Reviews in Economic Geology, v. 8, p. 101-133.

Barrie, C.T., Cathles, L.M., and Erendi, A., 1999, Finite element heat and fluid flow computer simulations of a deep ultramafic sill model for the giant Kidd Creek volcanic-associated massive sulfide deposit, Abitibi Subprovince, Canada: Economic Geology Monograph 10, p. 529-540.

Barrie, C.T., Ludden, J.N., and Green, T.H., 1993, Geochemistry of volcanic rocks associated with Cu-Zn and Ni-Cu deposits in the Abitibi Subprovince: Economic Geology, v. 88:, p. 1341-1358.

Baxter, S., and Feely, M., 2002, Magma mixing and mingling textures in granitoids: examples from the Galway Granite, Connemara, Ireland: Mineralogy and Petrology, v. 76, p. 63-74.

Beakhouse, G.P., 2011, The Abitibi Subprovince plutonic record: Tectonic and metallogenic implications: Ontario Geological Survey, Open File Report 6268, p. 1-161.

Beane, R.E., 1974, Biotite stability in the porphyry copper environment: Economic Geology, v. 69, p. 241-256.

Bédard, J.H., 2006, A catalytic delamination-driven model for coupled genesis of Archean crust and sub-continental lithospheric mantle: Geochimica et Cosmochimica Acta, v. 70, p. 1188-1214.

Berger, B.R., 2011, Geological Investigations South of Gogama, in Summary of Field Work and Other Activities 2011: Ontario Geological Survey, Open File Report 6270, 7 p. 1-7.

Berger, B.R., 2012, Interpretation of Geochemistry in the South of Gogama Area, in Summary of

Field Work and Other Activities 2012: Ontario Geological Survey, Open File Report 6280, p. 1-14.

Borodina, N.S., Fershtater, G.B., and Votyakov, S.L., 1999, The oxidation ratio of iron in coexisting biotite and hornblende from granitic and metamorphic rocks: The role of P, T and $f(O_2)$: The Canadian Mineralogist, v. 37, p. 1423-1429.

Burnham, C.W., 1979, Magmas and hydrothermal fluids, *in* Barnes, H.L., ed., Geochemistry of Hydrothermal Ore Deposits, 3rd ed.: New York, John Wiley & Sons, p. 63-123.

Campbell, I.H., Franklin, J.M., Gorton, M.P., Hart, T.R., and Scott, S.D., 1981, The role of subvolcanic sills in the generation of massive sulfide deposits: Economic Geology, v. 76, p. 2248-2253.

Candela, P. A., 1997, A Review of Shallow, Ore-related Granites: Textures, Volatiles, and Ore Metals: Journal of Petrology, v. 38, p. 1619-1633.

Carranza, E.J.M., 2012, Geochemical characteristics of mineral deposits: Implications for ore genesis: Geochemistry: Exploration, Environment, Analysis, v. 12, p. 89-92.

Carranza, E.J.M., and Sadeghi, M., 2012, Primary geochemical characteristics of mineral deposits – implications for exploration: Ore Geology Reviews, v. 45, p. 1-4.

Castillo, P.R., Janney, P.E., and Solidum, R.U., 1999, Petrology and geochemistry of Camiguin Island, southern Philippines: insights to the source of adakites and other lavas in a complex arc setting: Contributions to Mineralogy and Petrology, v. 134, p. 33-51.

Catchpole, H., Kouzmanov, K., Putlits, B., Seo, J.H., and Fontboté, L., 2015, Zoned base metal mineralization in a porphyry system: origin and evolution of mineralization fluids in the Morococha District, Peru: Economic Geology, v. 110, p. 39-71.

Cathles, L.M., 1981, Fluid flow and the genesis of hydrothermal ore deposits: Economic Geology 75th anniversary volume, p. 442-457.

Chakhmouradian, A.R., and Zaitsev, A.N., 2012, Rare earth mineralization in igneous rocks: Sources and processes: Elements, v. 8, p. 347-353.

Chelle-Michou, C., Chiaradia, M, Selby, D., Ovtcharova, M, and Spikings, R.A., 2015, High-resolution geochronology of the Coroccohuayco porphyry-skarn deposit, Peru: A rapid product of the Incaic Orogeny: Economic Geology, v. 110, p. 423-443.

Chew, D.M., Petrus, J.A. and Kamber, B.S., 2014, U–Pb LA–ICPMS dating using accessory mineral standards with variable common Pb: Chemical Geology, v. 363, p. 185–199.

Chivas, A.R., 1981, Geochemical evidence for magmatic fluids in porphyry copper

mineralization. Part 1. Mafic silicates from the Koloula igneous complex: Contributions to Mineralogy and Petrology, v. 78, p. 389-403.

Clark, G.H., 1990, Panguna copper-gold deposit: Australasian Institute of Mining and Metallurgy Monograph 14, p. 1807-1816.

Cohen, J.F., 2011, Mineralogy and geochemistry of hydrothermal alteration at the Ann-Mason porphyry copper deposit, Nevada: Comparison of large-scale ore exploration techniques to mineral chemistry: Unpublished M.Sc. thesis, Oregon, U.S.A., Oregon State University, 580 p.

Condie, K.C., 2005, TTGs and adakites: are they both slab melts?: Lithos, v. 80, p. 33-44.

Corfu, F., Hanchar, J.M., Hoskin, P.W.O., and Kinny, P, 2003, Atlas of zircon textures: Reviews in Mineralogy and Geochemistry, v. 53, p. 469-500.

Davidson, S., and Banfield, A.F., 1944, Geology of the Beattie gold mine, Duparquet, Quebec: Economic Geology, v. 39, p. 535-556.

Davis, D.W., Krogh, T.E., Hinzer, J., and Nakamura, E., 1985, Zircon Dating of Polycyclic Volcanism at Sturgeon Lake and Implications for Base Metal Mineralization: Economic Geology, v. 80, p. 1942-1952.

Davis, W.J., McNicoll, V.J., Bellerive, D.R., Santowski, K., and Scott, D.J., 1997, Modified chemical procedures for the extraction and purification of uranium from titanite, allanite, and rutile in the Geochronology Laboratory, Geological Survey of Canada, *in* Radiogenic Age and Isotopic Studies: Report 10: Geological Survey of Canada, Current Research 1997-F, p. 33-35.

Defant, M.J., and Drummond, M.S., 1993, Mount St. Helens: Potential example of the partial melting of the subducted lithosphere in a volcanic arc: Geology, v. 21, p. 547-550.

Deng, X.D., Li, J.W., Zhao, X.F., Wang, H.Q., and Qi, L., 2015a, Re-Os and U-Pb geochronology of Laochang Pb-Zn-Ag and concealed porphyry Mo mineralization along the Changning-Menglian suture, SW China: implications for ore genesis and porphyry Cu-Mo exploration: Mineralium Deposita, p. 1-12, (doi:10.1007/s00126-015-0606-z).

Deng, X.D., Li, J.W., Zhou, M.F., Zhao, X.F., and Yan, D.R., 2015b, In-situ LA-ICPMS trace elements and U-Pb analysis of titanite from the Mesozoic Ruanjiawan W-Cu-Mo skarn deposit, Daye district, China: Ore Geology Reviews, v. 65, p. 990-1004.

Derakhshani, R., and Abdolzadeh, M., 2009, Geochemistry, mineralization and alteration zones of Darrehzar porphyry copper deposits, Kerman, Iran: Journal of Applied Sciences, v. 9, p. 1628-1646.

De Souza, S., Dubé, B., MvNicoll, V.J., Dupuis, C., Mercier-Langevin, P. Crease, R.A., and

Kjarsgaard, I.M., 2015, Geology, hydrothermal alteration, and genesis of the world-class Canadian Malartic stockwork-disseminated Archean gold deposit, Abitibi, Quebec, *in* Dubé, B., and Mercier-Langevin, P., ed., Targeted Geoscience Initiative 4: Contributions to the Understanding of Precambrian Lode Gold Deposits and Implications for Exploration: Geological Survey of Canada, Open File 7852, p. 113-126.

Dilles, J.H., and Einaudi, M.T., 1992, Wall-rock alteration and hydrothermal flow paths about the Ann-Mason porphyry copper deposit, Nevada—A 6-km vertical reconstruction: Economic Geology, v. 87, p. 1963-2001.

Djouka-Fonkwé, M., Kyser, K., Clark, A.H., Urqueta, E., Oates, C.J., and Ihlenfeld, C., 2012, Recognizing propylitic alteration associated with porphyry Cu-Mo deposits in lower greenschist facies metamorphic terrain of the Collahuasi District, northern Chile-Implications of petrographic and carbon isotope relationships: Economic Geology, v. 107, p. 1457-1478.

Dostal, J., Kontak, D.J., Gerel, O., Shellnutt, J.G., and Fayek, M., 2015, Cretaceous ongonites (topaz-bearing albite-rich microleucogranites) from Ongon Khairkhan, central Mongolia: Products of extreme magmatic fractionation and preservation metasomatic fluid: rock interaction: Lithos, v. 236-237, p. 173-189.

Dubé, B., and Gosselin, P., 2007, Greenstone-hosted quartz-carbonate vein deposits, *in* Goodfellow, W.D., ed., Mineral Deposits of Canada: A Synthesis of Major Deposit-Types, District Metallogeny, the Evolution of Geological Provinces, and Exploration Methods: Geological Association of Canada, Mineral Deposits Division, Special Publication No. 5, p. 49-73.

Ewart, A., Bryan, W.B., Chappell, B.W., and Rudnick, R.L., 1994, 24. Regional geochemistry of the Lau-Tonga arc and backarc systems: Proceedings of the Ocean Drilling Program, Scientific Results, v. 135, p. 385-425.

Feng, R., and Kerrich, R., 1992, Geochemical evolution of granitoids from the Archean Abitibi Southern Volcanic Zone and the Pontiac Subprovince: Implications for tectonic history and source regions: Chemical Geology, v. 98, p. 23-70.

Flynn, R.T., and Burnham, C.W., 1978, An experimental determination of rare earth partition coefficients between a chloride containing vapor phase and silica melts: Geochimica et Cosmochimica Acta, v. 42, p. 685-701.

Ford, J.H., 1978, A chemical study of alteration at the Panguna porphyry copper deposit, Bougainville, Papua New Guinea: Economic Geology, v. 73, p. 703-720.

Franklin, J.M, 1996, Volcanic-associated massive sulphide base metals, *in* Eckstrand, O.R., Sinclair, W.D., and Thorpe, R.I., ed., Geology of Canadian Mineral Deposit Types: Geological Survey of Canada, Geology of Canada, no. 8, p. 158-183.

Fraser, R.J., 1993, The Lac Troilus gold-copper deposit, northwestern Quebec: A possible Archean porphyry system: Economic Geology, v. 88, p. 1685-1699.

Friske, P., 1974, The Beidelman Bay copper porphyry deposit: Unpublished B.Sc. thesis, Thunder Bay, Canada, Lakehead University, 109 p.

Frost, B.R., Chamberlain, K.R., and Schumacher, J.C., 2000, Sphene (titanite): Phase relations and role as a geochronometer: Chemical Geology, v. 172, p. 131-148.

Fulignati, P., Gioncada, A., and Sbrana, A., 1999, Rare-earth element (REE) behaviour in the alteration facies of the active magmatic-hydrothermal system of Vulcano (Aeolian Islands, Italy): Journal of Volcanology and Geothermal Research, v. 88, p. 325-342.

Fumerton, S., and Houle, K., 1993, Mineral showings, occurrences, deposits and mines of the Swayze greenstone belt, interim report: Ontario Geological Survey, Open File Report 5872, p. 1-112.

Galley A.G., 2003, Composite synvolcanic intrusions associated with Precambrian VMS-related hydrothermal systems: Mineralium Deposita, v. 38, p. 443-473.

Galley, A.G., and Lafrance, B., 2014, Setting and Evolution of the Archean Synvolcanic Mooshla Intrusive Complex, Doyon-Bousquet-LaRonde Mining Camp, Abitibi Greenstone Belt: Emplacement history, petrogenesis, and implications for Au metallogenesis: Economic Geology, v. 109, p. 205-229.

Galley, A.G., and van Breemen, O., 2002, Timing of synvolcanic magmatism in relation to base-metal mineralization, Rouyn-Noranda, Abitibi volcanic belt, Quebec: Geological Survey of Canada, Current Research Paper 2002-F8, p. 1-9.

Galley, A.G., van Breemen O., and Franklin, J.M., 2000, The relationships between intrusion-hosted Cu-Mo mineralization and the VMS deposits of the Archean Sturgeon Lake mining camp, northwestern Ontario: Economic Geology, v. 95, p. 1542-1550.

Galley, A.G., Hannington, M.D., and Jonasson, I.R., 2007, Volcanogenic massive sulphide deposits, *in* Goodfellow, W.D., ed., Mineral Deposits of Canada: A Synthesis of Major Deposit-Types, District Metallogeny, the Evolution of Geological Provinces, and Exploration Methods: Geological Association of Canada, Mineral Deposits Division, Special Publication No. 5, p. 141-161.

Gammons, C.H., and Williams-Jones, A.E., 1997, Chemical mobility of gold in the porphyry-epithermal environment: Economic Geology, v. 94, p. 1193-1211.

Gao, J-F., Jackson, S.E., Dubé, B., Kontak, D.J., and De Souza, S., 2015, Genesis of the Canadian Malartic, Côté Gold and Musselwhite gold deposits: Insights from LA-ICP-MS element mapping of pyrite, *in* Dubé, B., and Mercier-Langevin, P., ed., Targeted Geoscience Initiative 4: Contributions to the Understanding of Precambrian Lode Gold

Deposits and Implications for Exploration: Geological Survey of Canada, Open File 7852, p. 157-175.

Goldfarb, R.J., Phillips, G.N., and Nokleberg, W.J., 1998, Tectonic setting of synorogenic gold deposits of the Pacific Rim: Ore Geology Reviews, v. 13, p. 185-218.

Goldfarb, R.J., Baker, T., Dubé, B., Grover, D., Hart, C.J.R., and Gosselin, P., 2005, Distribution, character, and genesis of gold deposits in metamorphic terranes: Economic Geology 100th anniversary volume, p. 407-450.

Goldie, R., Kotila, B., and Seward, D., 1979, The Don Rouyn Mine: An Archean porphyry copper deposit near Noranda, Quebec: Economic Geology, v. 74, p. 1680-1684.

Goodman, S., Williams-Jones, A.E., and Carles, P., 2005, Structural controls on the Archean Troilus gold-copper deposit, Quebec, Canada: Economic Geology, v. 100, p. 577-582.

Grant, J.A., 1986, The isocon diagram—A simple solution to Gresens' equation for metasomatic alteration: Economic Geology, v. 81, p. 1976-1982.

Groves, D.I., Goldfarb, R.J., Gebre-Mariam, M., Hagemann, S.G., and Robert, F., 1998, Orogenic gold deposits: A proposed classification in the context of their crustal distribution and relationship to other gold deposit types: Ore Geology Reviews, v. 13, p. 7-27.

Groves, D.J., Goldfarb, R.J., Robert, F., and Hart, C.J.R., 2003, Gold deposits in metamorphic belts: Overview of current understanding, outstanding problems, future research, and exploration significance: Economic Geology, v. 98, p. 1-29.

Gustafson, L.B., 1978, Some major factors of porphyry copper genesis: Economic Geology, v. 73, p. 600-607.

Gustafson, L.B., and Hunt, J.P., 1975, The porphyry copper deposits at El Salvador, Chile: Economic Geology, v. 70, p. 857-912.

Hammarstrom, J.M., and Zen, E., 1986, Aluminum in hornblende: An empirical igneous geobarometer: American Mineralogist, v. 71, p. 1297-1313.

Hannington, M.D., Poulsen, K.H., Thompson, J.F.H., and Sillitoe, R.H., 1997, Volcanogenic gold in the massive sulfide environment, *in* Barrie, C.T., and Hannington, M.D., ed., Volcanic-Associated Massive Sulfide Deposits: Processes and Examples in Modern and Ancient Settings: Reviews in Economic Geology, v. 8, p. 325-356.

Hannington, M.D., Santaguida, F., Kjarsgaard, I.M., and Cathles, L.M., 2003, Regional-scale hydrothermal alteration in the Central Blake River Group, western Abitibi Subprovince, Canada: Implications for VMS prospectivity: Mineralium Deposita, v. 38, p. 393-422.

Harris, J.R., Wilkinson, L., Grunsky, E., Heather, K., and Ayer, J., 1999, Techniques for analysis and visualization of lithogeochemical data with applications to the Swayze greenstone belt, Ontario: Journal of Geochemical Exploration, v. 67, p. 301-334.

Hart, C.J.R., 2007, Reduced intrusion-related gold systems, *in* Goodfellow, W.D., ed., Mineral deposits of Canada: A Synthesis of Major Gold Deposit types, District Metallogenic, the Evolution of Geological Provinces, and Exploration Methods: Geological Association of Canada, Mineral Deposits Division, Special Publication No. 5, p. 95-112.

Hart, T.R., Gibson, H.L., and Lesher, C.M., 2004, Trace element geochemistry and petrogenesis of felsic volcanic rocks associated with volcanogenic massive Cu-Zn-Pb sulfide deposits: Economic Geology, v. 99, p. 1003-1013.

Hattori, K.H., and Keith, J.D., 2001, Contribution of mafic melt to porphyry copper mineralization: evidence from Mount Pinatubo, Philippines, and Bingham Canyon, Utah, USA: Mineralium Deposita, v. 36, p. 799-806.

Hawthorne, F.C., and Oberti, R., 2007, Classification of the Amphiboles: Reviews in Mineralogy and Geochemistry, v. 67, p. 55-88.

Heaman, L.M., 1997, Global mafic magmatism at 2.45 Ga: Remnants of an ancient large igneous province?: Geology, v. 25, p. 229-302.

Heather, K.B., 1993, Regional geology, structure, and mineral deposits of the Archean Swayze greenstone belt, southern Superior Province, Ontario: Geological Survey of Canada, Current Research Paper 93-1C, p. 295-305.

Heather, K.B., 2001, The geological evolution of the Archean Swayze greenstone belt, Superior Province, Canada: Unpublished Ph.D. thesis, Keele, England, Keele University, 370 p.

Heather, K.B. and Shore, G.T., 1999a, Geology, Swayze greenstone belt, Ontario: Geological Survey of Canada, Open File 3384a, sheet 2, scale 1:50 000.

Heather, K.B. and Shore, G.T., 1999b, Geology, Gogama, Swayze greenstone belt, Ontario, Geological Survey of Canada, Open File 3384g, scale 1:50 000.

Heather, K.B., and van Breemen, O., 1994, An interim report on geological, structural, and geochronological investigations of granitoid rocks in the vicinity of the Swayze greenstone belt, southern Superior Province, Ontario: Geological Survey of Canada, Current Research Paper 1994-C, p. 259-268.

Heather, K.B., Percival, J.A., Moser, D., and Bleeker, W., 1995, Tectonics and metallogeny of Archean crust in the Abitibi-Kapuskasing-Wawa region: Geological Survey of Canada, Open File 3141, p. 1-148.

Heather, K.B., Shore, G.T., and van Breemen, O., 1996, Geological investigations in the Swayze

greenstone belt, southern Superior Province, Ontario: a final update: Geological Survey of Canada, Current Research 1996-C, p. 125-136

Hedenquist, J.W., and Lowenstern, J.B., 1994, The role of magmas in the formation of hydrothermal ore deposits: Nature, v. 370, p. 519-527.

Helt, K.M., Williams-Jones, A.E., Clark, J.R., Wing, B.A., and Wares, R.P., 2014, Constraints on the genesis of the Archean oxidized intrusion-related Canadian Malartic gold deposit, Quebec, Canada: Economic Geology, v. 100, p. 713-735.

Hergt, J.M., and Farley, K.N., 1994, 26. Major element, trace element and isotope (Pb, Sr, and Nd) variations in site 834 basalts: Implications for the initiation of backarc opening: Proceedings of the Ocean Drilling Program, Scientific Results, v. 135, p. 471-485.

Hoskin, P.W.O., and Schaltegger, U., 2003, The composition of zircon and igneous and metamorphic petrogenesis: Reviews in Mineralogy and Geochemistry, v. 53, p. 27-62.

Huppert, H.E., Sparks, R.S.J., and Turner, J.S., 1982, Effects of volatiles on mixing in calc-alkaline magma systems: Nature, v. 297, p. 554-557.

IAMGOLD Corporation, 2013, IAMGOLD provides mineral resource update for Côté Gold and reports strongest quarter for production in 2012 with confirmed production guidance for 2013: IMG press release. Available from http://www.iamgold.com/English/investors/news-releases/news-releases-details/2013/IAMGOLD-provides-mineral-resource-update-for-Ct-Gold-and-reports-strongest-quarter-for-production-in-2012-with-confirmed-prod/default.aspx [cited 22 Janurary 2013].

Idrus, A., Kolb, J., and Meyer, F.M., 2009, Mineralogy, lithogeochemistry and element mass balance of the hydrothermal alteration associated with the gold-rich Batu Hijau porphyry copper deposit, Sumbawa Island, Indonesia: Resource Geology, v. 59, p. 215-230.

Jacobs, D.C., and Parry, W.T., 1976, A comparison of the geochemistry of biotite from some Basin and Range Stocks: Economic Geology, v. 71, p. 1029-1035.

John, D.A., 1989, Geologic setting, depths of emplacement, and regional distribution of fluid inclusions in intrusions of the central Wasatch Mountains, Utah: Economic Geology, v. 84, p. 386-409.

Jones, B.K., 1992, Application of metal zoning to gold exploration in porphyry copper systems: Journal of Geochemical Exploration, v. 43, p. 127-155.

Jones, G.J., 1985, The Goonumbla porphyry copper deposits, New South Wales: Economic Geology, v. 73, p. 1250-1259.

Katz, L.R., Kontak, D.J., Dubé, B., and McNicoll, V., 2015, The Archean Côté Gold intrusion-

related Au(-Cu) deposit, Ontario: A large-tonnage, low-grade deposit centred on a magmatic-hydrothermal breccia, *in* Dubé, B., and Mercier-Langevin, P., ed., Targeted Geoscience Initiative 4: Contributions to the Understanding of Precambrian Lode Gold Deposits and Implications for Exploration: Geological Survey of Canada, Open File 7852, p. 139-155.

Katz, L., Kontak, D.J., Dubé, B., Mercier-Langevin, P., Bécu, V., Lauzière, K. 2016, Whole-rock lithogeochemistry of the Archean intrusion-related Côté Gold Au(-Cu) deposit, Ontario, Canada. Geological Survey of Canada, Open File 8040, 1 .zip file.

Kelley, K.D., and Ludington, S., 2002, Cripple Creek and other alkaline-related gold deposits in the southern Rocky Mountains, USA: Influence of regional tectonics: Mineralium Deposita, v. 37, p. 38-60.

Kelley, K.D., Romberger, S.B., Beaty, D.W., Pontius, J.A., Snee, L.W., Stein, H.J., and Thompson, T.B., 1998, Geochemical and geochronological constraints on the genesis of the Au-Te Deposits at Cripple Creek, Colorado: Economic Geology, v. 93, p. 981-1012.

Kennedy, A. K., Kamo, S. L., Nasdala, L. and Timms, N. E., 2010, Grenville skarn titanite: Potential reference material for SIMS U-Th-Pb analysis: The Canadian Mineralogist, v. 48, p. 1423-1443.

Kennedy, L.P., 1985, The geology and geochemistry of the Archean Flavrian pluton, Noranda, Quebec: Unpublished Ph.D. thesis, London, Canada, University of Western Ontario, 460 p.

Kerrich, R., and Fryer, B.J., 1979, Archean precious-metal hydrothermal systems, Dome Mine, Abitibi greenstone belt. II. REE and oxygen isotope relations: Canadian Journal of Earth Sciences, v. 16, p. 440-458.

Kerrich, R., and Fryer, B.J., 1988, Lithophile-element systematics of Archean greenstone belt Au-Ag vein deposits: implications for source processes: Canadian Journal of Earth Science, v. 25, p. 945-953.

Kerrich, R., and Wyman, D.A., 1996, The trace element systematics of igneous rocks in mineral exploration: An overview, *in* Wyman, D.A., ed., Trace Element Geochemistry of Volcanic Rocks: Applications for Massive Sulphide Exploration: Geological Association of Canada, Short Course Notes, v. 12, p. 1-50.

Kesler, S.E., and Wilkinson, B.H., 2006, The role of exhumation in the temporal distribution of ore deposits: Economic Geology, v. 101, p. 919-922.

Kesler, S.E., Chryssoulis, S.L., and Simon, G., 2002, Gold in porphyry copper deposits: Its abundance and fate: Ore Geology Reviews, v. 21, p. 103-124.

Kirkham, R.V., 1971, Intermineral intrusions and their bearing on the origin of porphyry copper

and molybdenum deposits: Economic Geology, v. 66, p. 1244-1249.

Kontak, D.J., Creaser, R.A., and Hamilton, M., 2013a, Geological and geochemical studies of the Côté Lake Au(-Cu) deposit Area, Chester Township, Northern Ontario, *in* Ayer, J.A., Kontak, D.J., Linnen R.L., and Lin S., ed., Results from the Shining Tree, Chester Township and Matachewan Gold Projects and the Northern Cobalt Embayment Polymetallic Vein Project: Ontario Geological Survey, Miscellaneous Release Data 294.

Kontak, D.J., Katz, L., Creaser, R.A., and Hamilton, M., 2013b, The Archean Côté Gold Au(-Cu) deposit, northern Ontario, Canada: A large tonnage, low-grade Au deposit centred on a 2740 Ma magmatic-hydrothermal diorite complex [abs.]: Geological Association of Canada-Mineralogical Association of Canada, Annual Meeting, Winnipeg, Manitoba, 2013, Abstracts.

Kramers, J.D. and Tolstikhin, I.N., 1997, Two terrestrial lead isotope paradoxes, forward transport modelling, core formation and the history of the continental crust: Chemical Geology, v. 139, p. 75–110.

Kuşcu, G.G., and Floyd, P.A., 2001, Mineral compositional and textural evidence for magma mingling in the Saraykent volcanics: Lithos, v. 56, p. 207-230.

Lacroix, M.A., 1920, Les roches éruptive du Crétacé pyrénéen et la nomenclature des roches éruptives modifiées: Comptes Rendus de l'Académie des Sciences Paris, v. 170, p. 685-690.

Lalonde, A.E., and Bernard, P., 1993, Composition and color of biotite from granites: Two useful properties in the characterization of plutonic suites from the Hepburn internal zone of Wopmay orogen, Northwest Territories: Canadian Mineralogist, v. 31, p. 203-217.

Lang, J.R., and Baker, T., 2001, Intrusion-related gold systems: The present level of understanding: Mineralium Deposita, v. 36, p. 477- 489.

Lazich, B., 2010, The trace-element chemistry of chalcopyrite and its potential application to discriminate ore deposit types: Application to the Archean, syenite-associated Beaver Cu-Au deposit, Kirkland Lake, Ontario: Unpublished B.Sc. thesis, Sudbury, Canada, Laurentian University, 26 p.

Lazich, B., Kontak, D.J., and Ulrich, T., 2010, Trace-element geochemical characterization of chalcopyrite using LA-ICP-MS – Possible application as an ore deposit discriminator [abs.]: Goldschmidt Meeting, Annual Meeting, Knoville, Tennesee, 2010, Abstracts.

Leake, B.E., 1971, On aluminous and edenitic hornblendes: Mineralogical Magazine, v. 38, p. 389-407.

Le Bas, M.J., Le Maitre, R.W., Streckeisen, A.L., and Zanettin, B., 1986, A chemical

classification of volcanic rocks based on the total alkali-silica diagram: Journal of Petrology, v. 27, 745-750.

Le Maitre, R.W., Streckeisen, A., Zanettin, B., Le Bas, M.J., Bonin, B., Bateman, P., Bellieni, G., Dudek, A., Efremova, S., Keller, J., Lameyre, J., Sabine, P.A., Schmid, R., Sørensen, H., and Woolley, A.R., 2002, Igneous rocks: A Classification and Glossary of Terms, 2nd ed.: Cambridge, Cambridge University Press, 236 p.

Lentz, D.R., 1998, Petrogenetic evolution of felsic volcanic sequences associated with Phanerozoic volcanic-hosted massive sulphide systems: the role of extensional geodynamics: Ore Geology Reviews, v. 12, p. 289-327.

Lesher, C.M., Goodwin, A.M., I.H. Campbell, and Gorton, M.P., 1986, Trace-element geochemistry of ore-associated and barren, felsic metavolcanic rocks in the Superior Province, Canada: Canadian Journal of Earth Sciences, v. 23, p. 222-237.

Li, J.W., Deng, X.D., Zhou, M.F., Liu, Y.S., Zhao, X.F., and Guo, J.L., 2010, Laser ablation ICP-MS titanite U-Th-Pb dating of hydrothermal ore deposit: A case study of the Tonglushan Cu-Fe-Au skarn deposit, SE Hubei Province, China: Chemical Geology, v. 270, p. 56-67.

Lottermoser, B.G., 1990, Rare-earth element and heavy-metal behaviour associated with the epithermal gold deposit on Lihir Island, Papua New Guinea: Journal of Volcanology and Geothermal Research, v. 40, p. 269-289.

Lottermoser, B.G., 1992, Rare earth elements and hydrothermal ore formation processes: Ore Geology Reviews, v. 7, p. 25-41.

Lowell, J.D., and Guilbert, J.M., 1970, Lateral and vertical alteration-mineralization zoning in porphyry ore deposits: Economic Geology, v. 65, p.373-408.

Ludden, J.N., and Thompson, G., 1978, Behaviour of rare earth elements during submarine weathering of tholeiitic basalt: Nature, v. 274, p. 147-149.

Ludden, J.N., Daigneault, R., Robert, F., and Taylor, R.P., 1984, Trace element mobility in alteration zones associated with Archean Au lode deposits: Economic Geology, v. 79, p. 1131-1141.

Ludington, S., and Plumlee, G.S., 2009, Climax-type porphyry molybdenum deposits: U.S. Geological Survey, Open-File Report 2009-1215, p. 1-16.

Ludwig, K.R., 1998, On the treatment of concordant uranium-lead ages: Geochimica et Cosmochimica Acta, v. 62, p. 665–676.

Ludwig, K.R., 2003, User's manual for Isoplot/Ex rev. 3.00: A geochronological toolkit for Microsoft Excel: Special Publication, 4, Berkeley Geochronology Center, Berkeley, 70 p.

Luhr, J.F., and Carmichael, I.S.E., 1980, The Colima volcanic complex, Mexico: I. Post-caldera andesites from volcán Colima: Contributions to Mineralogy and Petrology, v. 71, p. 343-372.

Markey, R., Stein, H., and Morgan, J., 1998, Highly precise Re-Os dating for molybdenite using alkaline fusion and NTIMS: Talanta, v. 45, p. 935-946.

Markey, R., Stein, H.J., Hannah, J.L., Zimmerman, A., Selby, D., and Creaser, R.A., 2007, Standardizing Re-Os geochronology: A new molybdenite reference material (Henderson, USA) and the stoichiometry of Os salts: Chemical Geology, v. 244, p. 74-87.

Martin, H., Smithies, R.H., Rapp, R., Moyen, J.-F., and Champion, D., 2005, An overview of adakite, tonalite-trondhjemite-granodiorite (TTG), and sanukitoid: Relationships and some implications for crustal evolution: Lithos, v. 79, p. 1-24.

Mason, D.R., 1978, Compositional variations in ferromagnesian minerals from porphyry copper-generating and barren intrusions of the western Highlands, Papau New Guinea: Economic Geology, v. 73, p. 878-890.

Mattinson, J.M., 2005, Zircon U-Pb chemical abrasion ("CA-TIMS") method: Combined annealing and multi-step partial dissolution analysis for improved precision and accuracy of zircon ages: Chemical Geology, v. 220, p. 47-66.

McBride, D.E., 2002, Qualifying Report on the Chester Township Property for Northville Gold Corporation. Filed on SEDAR, July 29, 2002 by Condor Gold Corp.

McCuaig, T.C., and Kerrich, R., 1994, P-T-t-deformation-fluid characteristics of lode gold deposits: Evidence from alteration systematics, *in* Lentz, D.R., ed., Alteration and Alteration Processes Associated with Ore-formation Systems: Geological Association of Canada, Short Course Notes, v. 11, p. 339-379.

McLennan, S.M., and Taylor, S.R., 1979, Rare earth element mobility associated with uranium mineralisation: Nature, v. 282, p. 247-250.

Metz, M.C., Brookins, D.G., Rosenberg, P.E. and Zartman, R.E., 1985, Geology and geochemistry of the Snowbird Deposit, Mineral County, Montana: Economic Geology, v. 80, p. 394-409.

Meyer, C., and Hemley, J.J., 1967, Wall rock alteration, *in* Barnes, H.L., ed., Geochemistry of Hydrothermal Ore Deposit: New York, Holt Rinehart and Winston, p. 166-235.

Moore, W.J., and Czamanske, G.K., 1973, Compositions of biotites from unaltered and altered monzonitic rocks in the Bingham mining district, Utah: Economic Geology, v. 68, p. 269-274.

Müller, W., Shelley, M., Miller, P. and Broude, S., 2009, Initial performance metrics of a new custom-designed ArF excimer LA-ICPMS system coupled to a two-volume laser-ablation cell: Journal of Analytical Atomic Spectrometry, v. 24, p. 209-214.

Neves, S.P., and Vauchez, A., 1995, Successive mixing and mingling of magmas in a plutonic complex of Northeast Brazil: Lithos, v. 34, p. 275-299.

Norman, D.I., Kyle, P.R., Baron, C., 1989, Analysis of trace elements including rare earth elements in fluid inclusion liquids: Economic Geology, v. 84, p. 162-166.

Nunes, P.D., and Ayres, L.D., 1982, U-Pb zircon age of the Archean Setting Net Lake porphyry molybdenum occurrence, Northwestern Ontario, Canada: Economic Geology, v. 77, p. 1236-1239.

O'Connor, J.T., 1965, A classification for quartz-rich igneous rocks based on feldspar ratios: U.S. Geological Survey, Professional Paper 525B, p. 79-84.

Olade, M.A., and Fletcher, W.K., 1975, Primary dispersion of rubidium and strontium around porphyry copper deposits, Highland Valley, British Columbia: Economic Geology, v. 70, p. 15-21.

Palacios, C.M., Hein, U.F., and Dulski, P., 1986, Behaviour of rare earth elements during hydrothermal alteration at Buena Esperanza copper-silver deposit, northern Chile: Earth and Planetary Science Letters, v. 80, p. 208-216.

Parrish, R.R., Roddick, J.C., Loveridge, W.D., and Sullivan, R.W., 1987, Uranium-lead analytical techniques at the Geochronology Laboratory, Geological Survey of Canada: Geological Survey of Canada, Paper 87-2, p. 3-7.

Parry, W.T., Ballantyn, G.H., and Wilson, J.C., 1978, Chemisty of biotite and apatite from a vesicular quartz latite porphyry plug at Bingham, Utah: Economic Geology, v. 73, p. 1308-1314.

Parsapoor, A., Khalili, M., and Mackizadeh, M.A., 2009, The behaviour of trace and rare earth elements (REE) during hydrothermal alteration in the Rangan area (Central Iran): Journal of Asian Earth Sciences, v. 34, p. 123-134.

Paton, C., Woodhead, J.D., Hellstrom, J.C., Hergt, J.M., Greig, A., and Maas, R., 2010, Improved laser ablation U-Pb zircon geochronology through robust downhole fractionation correction: Geochemistry, Geophysics, Geosystems, v. 11, p. 1-36.

Paton, C., Hellstrom, J., Paul, B., Woodhead, J. and Hergt, J., 2011, Iolite: Freeware for the visualisation and processing of mass spectrometric data: Journal of Analytical Atomic Spectrometry, v. 26, p. 2508–2518.

Petersen, M.D., 1983, The use of the "immobile" elements Zr and Ti in lithogeochemical

exploration for massive sulphide deposits in the Precambrian Pecos greenstone belt of northern New Mexico: Journal of Geochemical Exploration: v. 19, p. 615-617.

Petersson, J., and Eliasson, T., 1997, Mineral evolution and element mobility during episyenitization (dequartzification) and albitization in the postkinematic Bohus granite, southwest Sweden: Lithos, v. 42, p. 123-146.

Petrus, J. A. and Kamber, B. S., 2012, VizualAge: A novel approach to laser ablation ICP-MS U-Pb geochronology data reduction: Geostandards and Geoanalytical Research, v. 36, p. 247-270.

Poitrasson, F., Pin, C., and Duthou, J.-L., 1995, Hydrothermal remobilization of rare earth elements and its effect on Nd isotopes in rhyolite and granite: Earth and Planetary Science Letters, v. 130, p. 1-11.

Poulsen, K.H. and Franklin, J.M., 1981, Copper and gold mineralization in an Archean trondhjemitic intrusions, Sturgeon Lake, Ontario: Geological Survey of Canada, Paper 81-1a, p. 9-14.

Poulsen, K.H., Robert, F., and Dubé, B., 2000, Geological classification of Canadian gold deposits: Geological Survey of Canada, Bulletin 540, p. 1-106.

Powell, W.G., Carmichael, D.M., and Hodgson, C.J., 1995, Conditions and timing of metamorphism in the southern Abitibi greenstone belt, Québec: Canadian Journal of Earth Sciences, v. 32, p. 787-805.

Prendergast, K., 2007, Application of lithogeochemistry to gold exploration in the St Ives goldfield, Western Australia: Geochemistry: Exploration, Environment, Analysis, v. 7, p. 99-108.

Putnis, A., 2002, Mineral replacement reactions: From macroscopic observations to microscopic mechanisms: Mineralogical Magazine, v. 66, p. 689-708.

Richards, J.P., 2009, Postsubduction porphyry Cu-Au and epithermal Au deposits: Products of remelting of subduction-modified lithosphere: Geology, v. 37, p. 247-250.

Richards, J.P., and Kerrich, R., 2007, Special Paper: Adakite-like rocks: Their diverse origins and questionable role in metallogenesis: Economic Geology, v. 102, p. 537-576.

Rieder, M., Cavazzini, G., D'Yakonov, Y.S., Frank-Kamenetskii, V.A., Gottardi, G., Guggenheim, S., Koval P.V., Müller, G., Neiva, A.M.R., Radoslovich, E.W., Robert, J.L., Sassi, F.P., Takeda, H., Weiss, Z., and Wones, D.R., 1998, Nomenclature of the micas: The Canadian Mineralogist, v. 36, p. 41-48.

Robert, F., 1997, A preliminary geological model for syenite-associated disseminated gold

deposits in the Abitibi belt, Ontario and Quebec: Geological Survey of Canada, Current Research 1997-C, p. 201-210.

Robert, F., 2001, Syenite-associated disseminated gold deposits in the Abitibi greenstone belt, Canada: Mineralium Deposita, v. 36, p. 503-516.

Robert, F., Poulsen, K.H., Cassidy, K.F., and Hodgson, C.J., 2005. Gold metallogeny of the Yilgarn and Superior cratons, *in* Hedenquist, J.W., Thompson, J.F.H., Goldfarb, R.J., and Richards, J.P., ed., Economic Geology 100th anniversary volume, p. 1001-1033.

Roddick, J.C., 1987, Generalized numerical error analysis with applications to geochronology and thermodynamics: Geochimica et Cosmochimica Acta, v. 51, p. 2129-2135.

Rogers, J.R., Beilhartz, D., Kontak, D.J., Katz, L., Dubé, B., and McNicoll, V., 2013, The Côté Gold deposit: discovery of a new generation low-grade, multi-million once gold resource in the Archean Superior Province of Canada [ext. abs.]: NewGenGold Conference, Perth, Australia, 2013, Extended Abstracts, p. 159-174.

Roscoe, W.E., and Cook, R.B., 2011, Technical Report on the Cote Lake Deposit, Chester Property, Ontario, Canada. Filed on Sedar, April 21, 2011 by Trelawney Mining and Exploration Inc.

Ross, P.S., Jebrak, M., and Walker, B.M., 2002, Discharge of hydrothermal fluids from a magma chamber and concomitant formation of a stratified breccia zone at the Questa porphyry molybdenum deposit, New Mexico: Economic Geology, v. 97, p. 1679-1699.

Rowins, S.M., Lalonde, A.E., and Cameron, E.M., 1991, Magmatic oxidation in the syenitic Murdock Creek intrusion, Kirkland Lake, Ontario: Evidence from the ferromagnesian silicates: Journal of Geology, v. 99, p. 395-414.

Schaltegger, U., 2007, Hydrothermal zircon: Elements, v. 3, p. 51.

Schmidt, M.W., 1992, Amphibole composition in tonalite as a function of pressure: An experimental calibration of the Al-in-hornblende barometer: Contributions to Mineralogy and Petrology, v. 110, p. 304-310.

Schmitz, M.D., and Bowring, S.A., 2001, U-Pb zircon and titanite systematics of the Fish Canyon Tuff: An assessment of high- precision U-Pb geochronology and its application to young volcanic rocks: Geochimica et Cosmochimica Atca, v. 65, p. 2571-2587.

Schneider, H.-J., Özgür, N., and Palacios, C.M., 1988, Relationship between alteration, rare earth element distribution, and mineralization of the Murgul Copper deposit, Northeaster Turkey: Economic Geology, v. 83, p. 1238-1246.

Seedorff, E., Dilles, J.H., Proffett, J.M., Jr., Einaudi, M.T., Zurcher, L., Stavast, W.J.A., Johnson,

D.A., and Barton, M.D., 2005, Porphyry deposits: Characteristics and origin of hypogene features: Economic Geology 100th anniversary volume, p. 251-298.

Seedorff, E., Barton, M.D., Stavast, W.J.A., and Maher, D.J., 2008, Root zones of porphyry systems: Extending the porphyry model to depth: Economic Geology, v. 103, p. 939-956.

Selby, D., and Creaser, R.A., 2004, Macroscale NTIMS and microscale LA-MC-ICP-MS Re-Os isotopic analysis of molybdenite: Testing spatial restrictions for reliable Re-Os age determinations, and implications for the decoupling of Re and Os within molybdenite: Geochimica et Cosmochimica Acta, v. 68, p. 3897-3908.

Shabani, A.A.T., Lalonde, A.E., and Whalen, J.B., 2003, Composition of biotite from granitic rocks of the Canadian Appalachian orogen: A potential tectonomagmatic indicator?: The Canadian Mineralogist, v. 41, p. 1381-1396.

Shannon, R.D.J., 1976, Revised effective ionic radii and systematic studies of interatomic distances in halides and chalcogenides: Acta Crystallographica, v. 32, p. 751-767.

Sillitoe, R.H., 1979, Some Thoughts on gold-rich porphyry copper deposits: Mineralium Deposita, v. 14, p. 161-174.

Sillitoe, R.H., 1985, Ore-related breccias in volcanoplutonic arcs: Economic Geology, v. 80, p. 1467-1514.

Sillitoe, R.H., 1991, Intrusion-related gold deposits, *in* Foster, R.P., ed., Gold Metallogeny and Exploration: Glasgow, Blackie, p. 165-209.

Sillitoe, R.H., 1993, Gold-rich porphyry copper deposits: Geological model and exploration implications, *in* Kirkham, R.V., Sinclair, W.D., Thorpe, R.I., and Duke, J.M., ed., Mineral Deposit Modeling: Geological Association of Canada, Special Paper 40, p. 465-478.

Sillitoe, R.H., 2000, Gold-rich porphyry deposits: Descriptive and genetic models and their role in exploration and discovery: Reviews in Economic Geology, v. 13, p. 315-345.

Sillitoe, R.H., 2010, Porphyry Copper Systems: Economic Geology, v. 105, p. 3-41.

Sillitoe, R.H., and Mortensen, J.K., 2010, Longevity of porphyry copper formation at Quellaveco, Peru: Economic Geology, v. 105, p. 1157-1162.

Sillitoe, R.H., and Thompson, J.F.H., 1998, Intrusion-related vein gold deposits: Types, tectono-magmatic settings and difficulties of distinction from orogenic gold deposits: Resource Geology, v. 48, p. 237-250.

Sillitoe, R.H., Hannington, M.D., and Thompson, J.F.H., 1996, High sulfidation deposits in the volcanogenic massive sulfide environment: Economic Geology, v. 91, p. 204-212.

Sinclair, W.D., 2007, Porphyry Deposits, *in* Goodfellow, W.D., ed., Mineral Deposits of Canada: A Synthesis of Major Deposit-Types, District Metallogeny, the Evolution of Geological Provinces, and Exploration Methods: Geological Association of Canada, Mineral deposits Division, Special Publication No. 5, p. 223-243.

Siragusa, G.M., 1993a, Geology, geochemistry and mineralization of the southern margin of the Swayze belt: Ontario Geological Survey Open File Report 5844, p. 1-144.

Siragusa, G.M., 1993b, Lithogeochemistry of three gold settings in the southern Swayze belt: Ontario Geological Survey, Open File Report 5858, p. 1-42.

Sklyarov, E.V., and Fedorovskii, V.S., 2006, Magma mingling: Tectonic and Geodynamic Implications: Geotectonics, v. 40, p. 120-134.

Smith, J, Lafrance, B., and Kontak, D., 2014, A comparative study of the deformation history of auriferous quartz veins in the Archean Côté Gold deposit and the structural evolution of the spatially-related Ridout deformation zone, Swayze greenstone belt, northern Ontario [abs.]: Geological Association of Canada-Mineralogical Association of Canada, Annual Meeting, Fredericton, New Brunswick, 2014, Abstracts.

Snyder, D., Crambes, C., Tait, S., and Wiebe, R.A., 1997, Magma mingling in dikes and sills: The Journal of Geology, v. 105, p. 75-86.

Sparks, R.S.J., and Marshall, L.A., 1986, Thermal and mechanical constrains on mixing between mafic and silicic magmas: Journal of Volcanology and Geothermal Research, v. 29, p. 99-124.

Sparks, S.R.J., Sigurdsson, H., and Wilson, L., 1977, Magma mixing: A mechanism for triggering acid explosive eruptions: Nature, v. 267, p. 315-318.

Stacey, J.S. and Kramers, J.D. 1975. Approximation of terrestrial lead isotope evolution by a two-stage model: Earth and Planetary Science Letters, v. 26, p. 207-221.

Stern, R.A., 1997, The GSC Sensitive High Resolution Ion Microprobe (SHRIMP): Analytical techniques of zircon U-Th-Pb age determinations and performance evaluation, In: Radiogenic Age and Isotopic Studies, Report 10: Geological Survey of Canada, Current Research 1997-F, p. 1-31.

Stern, R.A., and Amelin, Y., 2003, Assessment of errors in SIMS zircon U-Pb geochronology using a natural zircon standard and NIST SRM 610 glass: Chemical Geology, v. 197, p. 111-146.

Stimac, J.A., and Pearce, T.H., 1992, Textural evidence of mafic-felsic magma interaction in dacite lavas, Clear Lake, California: American Mineralogist, v. 77, p. 795-809.

Stolz, A.J., Varne, R., Davies, G.R., Wheller, G.E., and Foden, J.D., 1990, Magma source components in arc-continent collision zone: the Flores-Lembata sector, Sunda arc, Indonesia: Contributions to Mineralogy and Petrology, v. 105, p. 585-601.

Sun, S.S., and McDonough, W.F., 1989, Chemical and isotopic systematics of ocean basalts: implications for mantle composition and process, *in* Saunders, A.D., and Norry, M.J., ed., Magmatism and Ocean Basins: Geological Society of London, p. 313-345.

Sylvester, P.J., Cabri, L.J., Tubrett, M.N., Mcmahon, G., Laflamme, J.H.G., and Peregoedova, A., 2005, Synthesis and evaluation of a fused pyrrhotite standard reference material for platinum group element and gold analysis by laser ablation-ICPMS [ext. abs.], *in* Törmänen, T.O., and Alapieti, T.T., ed., 'Platinum-Group Elements – from Genesis to Beneficiation and Environmental Impact': 10th International Platinum Symposium, Oulu, Finland, August 8-11, 2005, Extended Abstract, p. 16-20.

Taylor, R.P., and Fryer, B.J., 1980, Multiple-stage hydrothermal alteration in porphyry copper systems in northern Turkey: The temporal interplay of potassic, propylitic, and phyllic fluids: Canadian Journal of Earth Sciences, v. 17, p. 901-926.

Taylor, R.P., and Fryer, B.J., 1982, Rare earth element geochemistry as an aid to interpreting hydrothermal ore deposits, *in* Evans, A.M., ed., Mineralization Associated with Acid Magmatism: New York, John Wiley and Sons Ltd., p. 357-365.

Taylor, R.P., and Fryer, B.J., 1983, Rare earth element lithogeochemistry of granitoid mineral deposits: Canadian Institute of Mining Bulletin, v. 76, p. 74-84.

Thompson, J.F.H., and Newberry, R.J., 2000, Gold deposits related to reduced granitic intrusions: Review in Economic Geology, v. 13, p. 377-400.

Thurston, P.C., Ayer, J.A., Goutier, J., and Hamilton, M.A., 2008, Depositional Gaps in the Abitibi Greenstone Belt Stratigraphy: A Key to Exploration for Syngenetic Mineralization: Economic Geology, v. 103, p. 1097-1134.

Toscano, M., Pascual, E., Nesbitt, R.W., Almodóvar, G.R., Sáez, R., and Donaire, T., 2014, Geochemical discrimination of hydrothermal and igneous zircon in the Iberian Pyrite Belt, Spain: Ore Geology Reviews, v. 56, p. 301-311.

Trowell, N.F., 1974, Geology of the Bell Lake-Sturgeon Lake area, districts of Thunder Bay and Kenora: Ontario Geological Survey, Report 113, p. 1-67.

Turner, S., Hawkesworth, C., Rogers, N., Bartlett, J., Worthington, T., Hergt, J., Pearce, J., and Smith, I., 1997, ^{238}U-^{320}Th disequilibria, magma petrogenesis, and flux rates beneath the depleted Tonga-Kermadec island arc: Geochimica et Cosmochimica Acta, v. 61, p. 4855-4884.

Ulrich, T., and Heinrich, C.A., 2001, Geology and alteration geochemistry of the porphyry Cu-

Au deposit at Bajo de la Alumbrera, Argentina: Economic Geology, v. 96, p. 1719-1742.

Van Breemen, O., Heather, K.B., and Ayer, J.A., 2006, U-Pb geochronology of the Neoarchean Swayze sector of the southern Abitibi greenstone belt: Geological Survey of Canada, Current Research Paper 2006-F1, p. 1-32.

Vernon, R.H., 1984, Microgranitoid enclaves in granites- globules of hybrid magma quenched in a plutonic environment: Nature, v. 309, p. 438-439.

Vernon, R.H., Etheridge, M.A., and Wall, V.J., 1988, Shape and microstructure of microgranitoid enclaves: Indicators of magma mingling and flow: Lithos, v. 22, p. 1-11.

Ward, C.D., McArthur, J.M., and Walsh, J.N., 1992, Rare earth element behaviour during evolution and alteration of the Dartmoor granite, SW England: Journal of Petrology, v. 33, p. 785-815.

Wilcox, R.E., 1999, The idea of magma mixing: History of a struggle for acceptance: The Journal of Geology, v. 107, p. 421-432.

Williams-Jones, A.E., 2015, The hydrothermal mobility of the rare earth elements, *in* Simandl, G.J., and Neetz, M., ed., Symposium on Strategic and Critical Materials Proceedings, November 13-14, 2015, British Columbia, British Columbia Ministry of Energy and Mines, British Columbia Geological Survey, Paper 2015-3, p. 119-123.

Williams-Jones, A.E., Migdisov, A.A., and Samson, I.M., 2012, Hydrothermal mobilization of rare earth elements – a tale of "ceria" and "yttria": Elements, v. 8, p. 355-360.

Winchester, J.A., and Floyd, P.A., 1977, Geochemical discrimination of different magma series and their differentiation products using immobile elements: Chemical Geology, v. 20, p. 325-343.

Wones, D.R., and Eugster, H.P., 1965, Stability of biotite; experiment, theory and application: American Mineralogist, v. 50, p. 1228-1272.

Wyman, D.A., and Kerrich, R., 1993, Archean shoshonitic lamprophyres of the Abitibi Subprovince, Canada: Petrogenesis, age, and tectonic setting: Journal of Petrology, v. 34, p. 1067-1109.

Yergeau, D., Mercier-Langevin, P., Dubé, B., Malo, M., McNicoll, V.J., Jackson, S.E., Savoie, A., and La Rochelle, F., 2015, The Archean Westwood Au deposit, southern Abitibi: Telescoped Au-rich VMS and intrusion-related Au systems, *in* Dubé, B., and Mercier-Langevin, P., ed., Targeted Geoscience Initiative 4: Contributions to the Understanding of Precambrian Lode Gold Deposits and Implications for Exploration: Geological Survey of Canada, Open File 7852, p. 177–191.

Appendix A

The Côté Gold deposit: discovery of a new generation low- grade, multi-million ounce gold resource in the Archean Superior Province of Canada.

Jamie R. Rogers *(presenter)*, **David Beilhartz, Daniel J. Kontak, Laura Katz, Benoit Dubé and Vicki McNicoll**

Contact:

IAMGOLD Corporation

401 Bay Street, Suite 3200, Toronto, Ontario, Canada M5H 2Y4

Ph: +1 416 360 4710

Jamie Rogers: jamie_rogers@iamgold.com

The Côté Gold deposit, Ontario, Canada

Abstract

The Côté Gold deposit is located on the southeastern margin of the Archean Swayze greenstone belt in northern Ontario. The deposit is hosted by the multi-phase, syn-volcanic (ca. 2742 Ma) Chester Intrusive Complex, where gold mineralisation is spatially associated with a series of semi-continuous breccia bodies. The main mineralisation zone reaches 600 metres in width and has been delineated in drilling for 1.2 kilometres along strike and to a vertical depth of over one kilometre.

Prospecting and exploration activities have been carried out over the Swayze greenstone belt since the early 1900's. However, no significant gold resource had been delineated prior to the discovery of the Côté Gold deposit by Trelawney Mining and Exploration in December 2009. The belt is host to several small historical gold operations which exploited narrow, high-grade quartz-carbonate vein systems. This mineralization style was maintained as the singular exploration target for the majority of mining and exploration companies to have operated in the district during the twentieth century.

Several key factors contributed to the discovery of the Côté Gold deposit. Consolidation of historical landholdings at the turn of the twenty-first century allowed exploration to be conducted at a more holistic level than had previously been possible. The timing of the discovery during a period of dramatically rising gold prices increased the potential economic viability and hence marketability of the project, enabling exploration to be financed beyond an initial drill phase. But perhaps the most important element was the willingness of the Trelawney team to challenge the local doctrine and investigate a non-traditional exploration target in the Swayze greenstone belt.

In June 2012, IAMGOLD completed the acquisition of Trelawney and its interests in the Côté Gold properties. A prefeasibility study on the project is currently in progress and is based upon an NI 43-101 compliant resource estimate comprising Indicated Resources of 269 Mt averaging 0.88 g/t Au (7.61 Moz) and an Inferred Resource of 44 Mt averaging 0.74 g/t Au (1.04 Moz).

Introduction

The Côté Gold deposit can be assigned to a class of large (+5 Moz), low-grade (<1.5 g/t Au) gold mineralised systems in the Archean Superior Province of Canada that have been delineated over the last decade. This has been made possible by rising gold prices between 2002 and 2012 supporting the potential viability for bulk tonnage mining scenarios. New opportunities have been identified within historical mining camps (e.g. Canadian Malartic, Detour Lake, Magino, Hollinger-McIntyre), stalled exploration projects rejuvenated (e.g. Rainy River, Springpole and Hammond Reef) and genuine grassroots discoveries made (e.g. Borden Lake). The Côté Gold deposit was discovered in late 2009 by Trelawney Mining and Exploration during exploration focussed on the delineation of an orogenic-style gold-bearing quartz vein system. The company supplemented that program with three additional drillholes to offset an intercept of 0.64 g/t Au over 262.9 metres produced by Condor Gold in 2003. The first of these, E09-01, returned 1.16 g/t Au over 136 metres and is the discovery hole. Three years and 293 diamond drillholes (158,047m) later, the project comprises estimated Indicated Resources totalling 7.61 Moz (269 Mt averaging 0.88 g/t Au) and additional Inferred Resources totalling 1.04 Moz (44 Mt averaging 0.74 g/t Au) at a 0.3 g/t Au cut-off grade (IAMGOLD, 2013).

The Côté Gold project is located approximately halfway between the cities of Timmins and Sudbury in the province of Ontario, a six hour drive north of Toronto (Fig. 1). The project landholdings cover an area of 516 km^2 and incorporate ten contiguous properties that were consolidated through a combination of staking and various option agreements. The Côté Gold deposit, the orogenic-style 'No. 3 Vein' system and several other documented gold occurrences are overlain by the Chester property situated in the central part of the project area (Fig. 2).

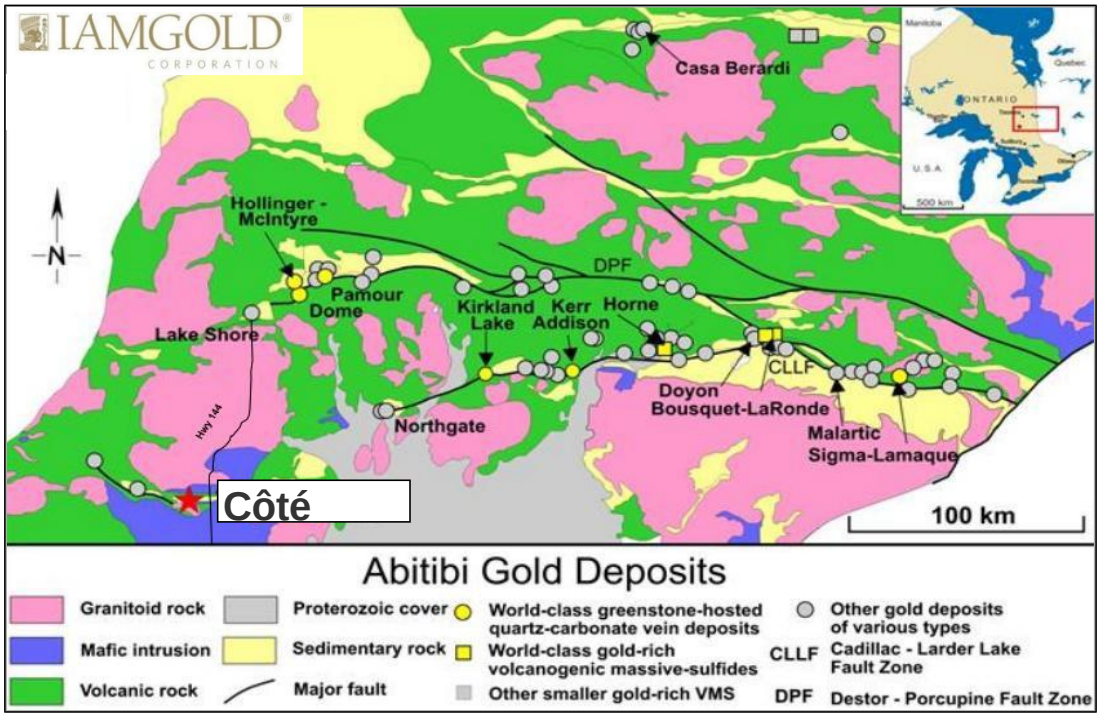

Figure 1: Simplified geological map of the Abitibi Subprovince of the Archean Superior Province of the Canadian Shield, illustrating the location of significant gold deposits and the Côté Gold project. Diagram is modified after Poulsen et al. (2000) and Dubé and Gosselin (2007).

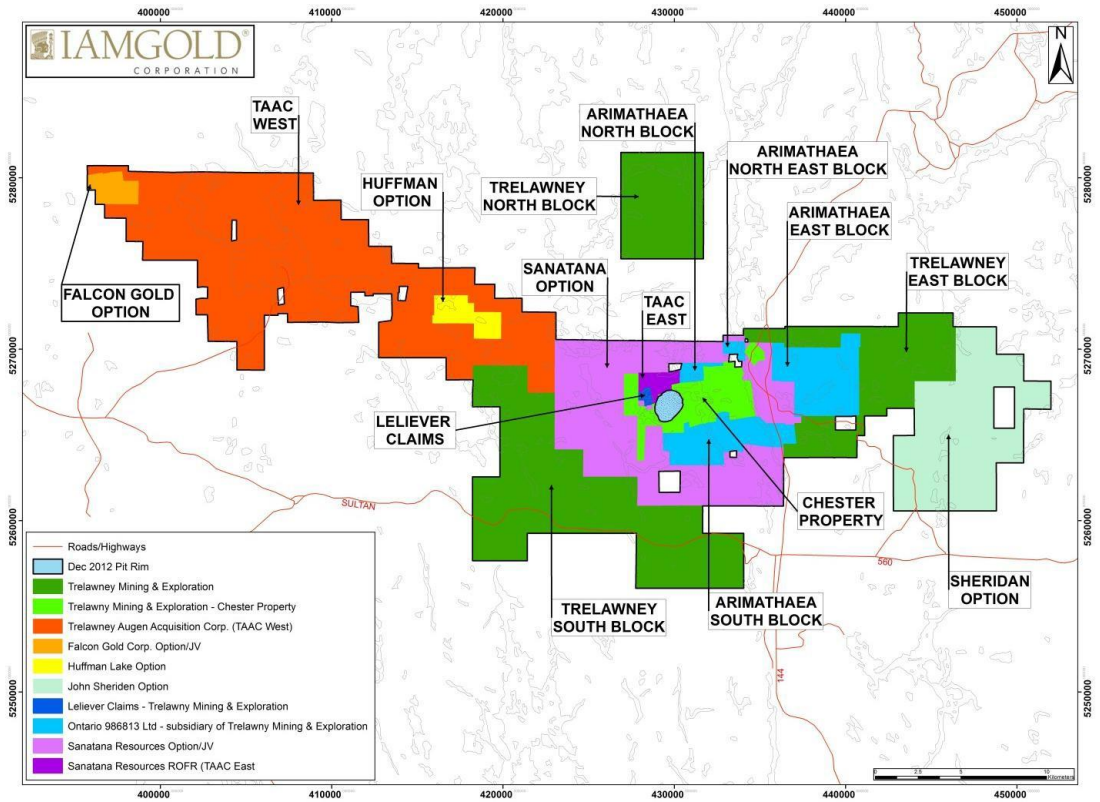

Figure 2: Summary diagram of the contiguous landholdings, covering 516 km^2, that collectively constitute the Côté Gold Project.

Exploration History

Historical Exploration

The Chester property has been prospected and explored intermittently for over a century. In the early 1930's, a minor gold rush was triggered when Alfred Gosselin reported 'a spectacular showing of native gold' in a lenticular quartz vein on the east shore of Three Duck Lakes (Laird, 1932; Fig. 3). A number of gold discoveries followed, all of which are associated with structurally-hosted quartz and/or carbonate vein systems. Very minor production was realised from several of the more significant occurrences, including the 'No. 1 Vein', 'No. 3 Vein' and 'C-Zone' showings (Fig. 3).

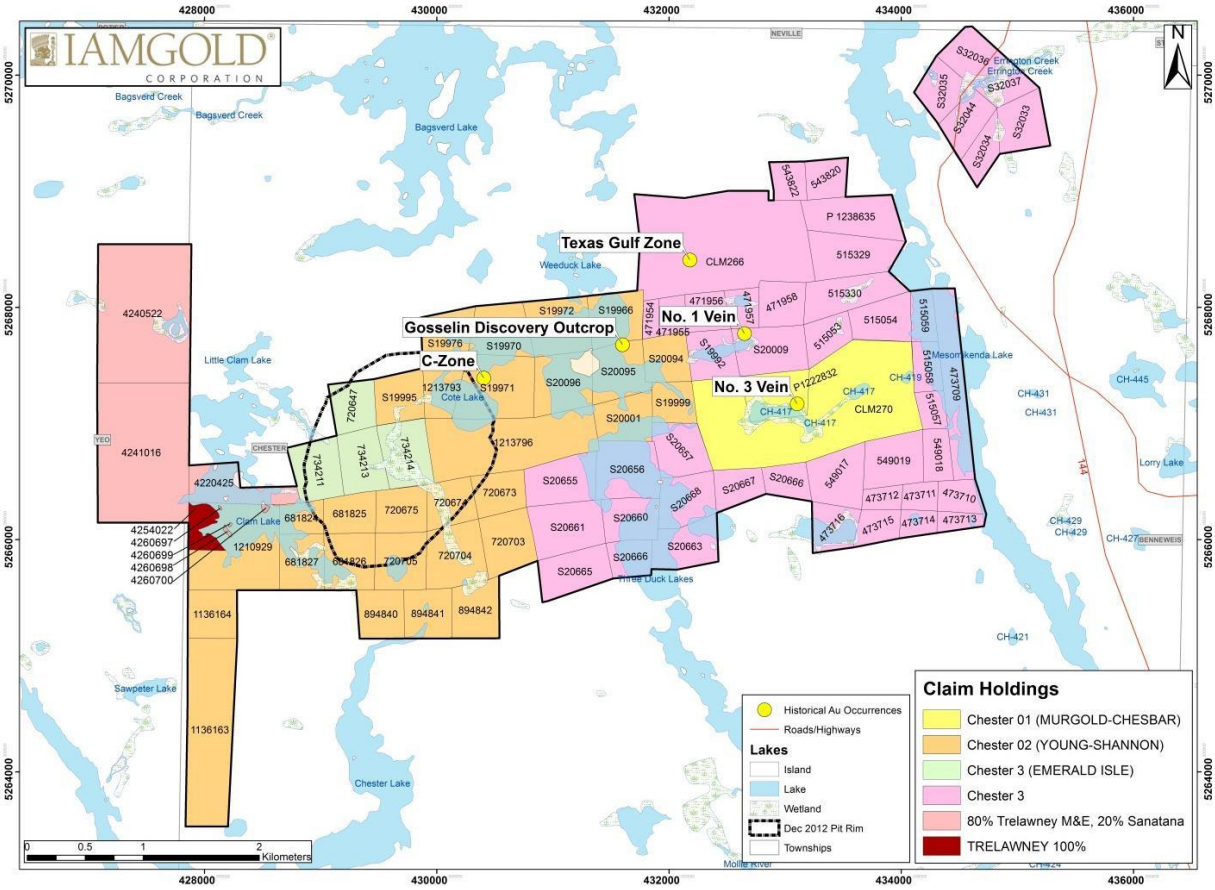

Figure 3: Summary diagram of the historical land packages and significant known gold occurrences surrounding the Côté Gold Project. Note the current pit outline of the Côté Gold deposit, which incorporates the historical Emerald Isle claims where drilling in the early 1990s first intersected gold mineralisation that would later become the Côté Gold deposit, as discussed in the text.

Chester 1 (Murgold-Chesbar) Claims: Gomak Mines explored the Murgold-Chesbar property in the years 1932-1935 and 1937-1938. The 'No. 1 Vein' was exploited to a depth of 75 feet during the earlier period with minor production (Siragusa, 1993). In 1937, Strathy Basin Mines sank an inclined shaft to a depth of 116 feet on the 'No. 3 Vein'. These and other mineralised quartz vein systems on the Murgold-Chesbar property were further explored by Chesgo Mines (1945-1948), Strathmore Mines (1947), Rinaldi Mines (1963), Three Duck Gold Mines (1968-1969), Kingsbridge Mines (1967-1971) and Olympian International Resources (1974-1975; Siragusa, 1993). In 1979, Murgold Resources acquired, through options and staking, a large property package that included both the 'No. 1 Vein' and 'No. 3 Vein' occurrences (McBride, 2002). Over the following decade (from 1986 with Chesbar Resources as partner and operator) Murgold expanded the original development on the 'No. 3 Vein', sank the Bates shaft in the central part of the system, drove a 1.5 km-long decline to a depth of 160m and completed multiple phases of surface and underground exploration. The result of this work was a non-compliant resource estimate of

144,500 tonnes grading 14.7 g/t Au for 68,000 ounces (McBride, 2002). No further development was carried out on the 'No. 3 Vein' until Trelawney commenced rehabilitation and evaluation of the underground workings in 2010.

Chester 2 (Young-Shannon) Claims: Young-Shannon Gold Mines sunk a inclined shaft on the C-Zone to a depth of 200 feet and developed drifts on two levels in 1936-1937 (Siragusa, 1993). A stamp mill was installed but there is no recorded production. Apart from several small surface drilling campaigns in the mid-1940's, no further work was carried out at this locality until Canadian Gold Crest Ltd. leased the property in 1978, constructed a steel headframe and 60 tpd flotation mill, and operated for seven months to produce a gold-copper concentrate (Lavigne and Roscoe, 2012). It should be noted that the enrichment of these veins in chalcopyrite is an unusual feature of these orogenic-type veins in the Chester area. Between 1984 and 2005, Young-Shannon Gold Mines and/or their various joint venture partners completed additional drilling campaigns and internal resource estimates on the C-Zone, but no further development ensued.

Chester 3a (Emerald Isle) Claims: Originally incorporating the TAAC East claims, this property changed ownership multiple times after Shannon Minerals commenced modern exploration activities in 1965. Consequently, exploration programs were never substantially advanced and only limited drilling had been completed prior to Trelawney optioning the property in 2009. Nevertheless, the historical drilling programs of Gogama Minerals (1971), Emerald Isle Resources (1991-1992) and Condor Gold (formerly Northville Gold; 2002-2003) all reported mineralised intersections from what is now recognised as the Côté Gold deposit. The six-hole Emerald Isle program returned best results of 0.46 g/t Au over 14.6 metres (drillhole EI-91-4) and 0.20 g/t Au over 21.7 metres (drillhole EI-91-2; Brown, 1992). Condor Gold followed up these results with drillhole E-03-27, which cut 0.64 g/t Au over 262.9 metres (Condor Gold, 2003).

Chester 3b (Jackrabbit) Claims: The most significant historical gold occurrence on this property is referred to as the 'Texas Gulf Zone' (Fig. 3), where gold-copper mineralisation is associated with discrete zones of sub-parallel, silicified and locally sulphide bearing shear structures in felsic host rocks (Siragusa, 1993). The prospect was first explored by Sulmac Exploration Services (1965) and subsequently by Viewpoint Exploration (1972), Texas Gulf Canada (1977-1979), Chester Resources (1981), Rockwell (1982) and Gold Bar (1989; Roscoe and Cook, 2012). The latter two companies completed modest drilling campaigns targeting two segments of the principal host structure ('No. 1 and No. 3 Zones') over a combined strike length of 600 metres and to a vertical depth of 180 metres. However, no significant mineral resource was delineated.

At face value, the southern Swayze greenstone belt could be viewed as a relatively mature exploration district, given the duration and intensity of prospecting and exploration carried out over the various properties. How then, could a multi-million ounce gold deposit be overlooked, even when intersected in drilling on three separate occasions? An obvious explanation is that the prevailing economic conditions were unfavourable at the time when exploration results were received and/or published. The Emerald Isle drill results were never publicly released, in all likelihood because intercepts averaging less than 0.5 g/t gold would not have been considered material in early 1992, when gold prices were sub-$400 per ounce and on a downward trend. Condor Gold were faced with identical market conditions in early 2003, and although stating that the E-03-27 drillhole intercept could potentially represent an open-pittable, multi-million ounce, low-grade gold resource (Condor Gold, 2003), the market was totally unresponsive and project funding could not be maintained.

An additional contributing factor is that the Chester area properties have had a complex and fragmented ownership history, with the Côté Gold deposit straddling the boundary of the historical Young-Shannon and Emerald Isle/TAAC East claim blocks. It was not until the turn of the twenty-first century that all of the various claim blocks were consolidated into a single contiguous landholding (discussed in more detail below), thereby providing a sole operator with the freedom to compile and acquire geologic data at a more meaningful scale, and generate exploration targets from a more global perspective.

A final consideration is that, with the singular exception of Condor Gold, the accepted exploration target for the Swayze greenstone belt (high-grade gold mineralisation in quartz-carbonate vein systems) and the envisioned exploitation method (narrow-vein underground mining) remained unchanged for one hundred years. As it transpired, the discovery of the Côté Gold deposit was first made in the existing historical data, but only when viewed and subsequently promoted with a fundamentally different exploration philosophy.

Property

In the early 2000's, Condor Gold assembled the historical claim blocks described above into a contiguous property through various option agreements and staking. In early 2003, it completed a senior secured debt financing transaction with Treelawn Investment Corp (Treelawn) for $1.5 million to continue exploration activities on the property. However, Condor Gold became insolvent in early 2005 and the following year transferred all of its assets to Treelawn pursuant to a vesting order and debt settlement agreement. These assets included all of its Chester claims except the Young Shannon property, which reverted back to Young-Shannon Gold Mines.

In 2009, Trelawney entered into separate option agreements with Treelawn on the Chester 1 (Murgold-Chesbar) and Chester 3 (Emerald Isle and Jackrabbit) claims, and executed a third agreement with Young-Shannon Gold Mines to purchase its 92.5% interest in the Chester 2 (Young Shannon) claim block. By the end of 2011, Trelawney had satisfied all earn-in conditions on the Treelawn properties to hold a 70% and 92.5% interest in the Chester 1 and Chester 3 claims respectively. Trelawney had also acquired interests in nine other properties to form the contiguous landholdings as illustrated on Figure 2.

In June 2012, IAMGOLD completed the acquisition of Trelawney and its interests in the Côté Gold properties. The total cost of the transaction was $542.6 million, representing an acquisition cost of $78.98 per ounce of gold.

The Côté Gold project site lies within the traditional land use areas of the Wabun Tribal Council. IAMGOLD has continued to build upon the relationship and has maintained the Exploration Agreement established by Trelawney with the Mattagami and Flying Post First Nations groups.

Recent Exploration (2009-2010)

Trelawney's initial motivation in the Chester area was to further explore the potential of the 'No. 3 Vein' (renamed the Chester-1 Zone). An eight-hole diamond drilling campaign was completed in late 2009, with the first five holes targeting the mineralised structure at depth. Several narrow, high-grade intervals were reported and Trelawney commenced rehabilitation of the underground workings the following year (Roscoe and Cook, 2011). However, the results of the three other drillholes, E09-01 to E09-03, generated a new prospect that would rapidly eclipse the Chester-1 Zone as the primary exploration focus.

Drillholes E09-01 to E09-03 were designed to follow-up on the historical Emerald Isle and Condor intercepts that had been rediscovered in assessment reports filed with the Ontario Geological Survey and in other public documents as part of a regional data compilation and target generation exercise. E09-01 and E09-03 each cut wide intervals of low-grade gold in altered, sulphide-bearing and brecciated felsic host rocks (i.e. leucotonalite), e.g. 136 metres grading 1.16 g/t Au and 0.1% Cu in E09-01 (Trelawney, 2010a).

A second drilling phase commenced in early 2010, initially on a single fence to test the E09-01 and E09-03 mineralised intercepts at depth (Section 9300E; Fig. 4). Encouraging assay results were received and the newly branded 'Côté Lake Zone' was publicised at the PDAC convention in March 2010, significantly raising the project profile and triggering a 125% increase in Trelawney's share price (Fig. 5). Over the next few months, two additional drill fences were completed at 100 metres on either side of line 9300E, with favourable assay results confirming the lateral continuity of gold grades (Table 1). At this point, the

potential for a large-tonnage gold mineralised system was recognised by the geological team even if the market did not react positively to the corresponding public disclosures of April and May, 2010 (Fig. 5).

By year-end 2010, Trelawney had completed a total of 47 holes for 23,500 metres and expanded the Côté Zone for 800 metres along strike to a maximum vertical depth of 500 metres. Selected highlights of the 2010 drilling program are restated in Table 1 from successive Trelawney press releases (but recalculated using a cut-off grade of 0.3 g/t Au, maximum internal dilution of five metres and a global assay cap of 25 g/t Au).

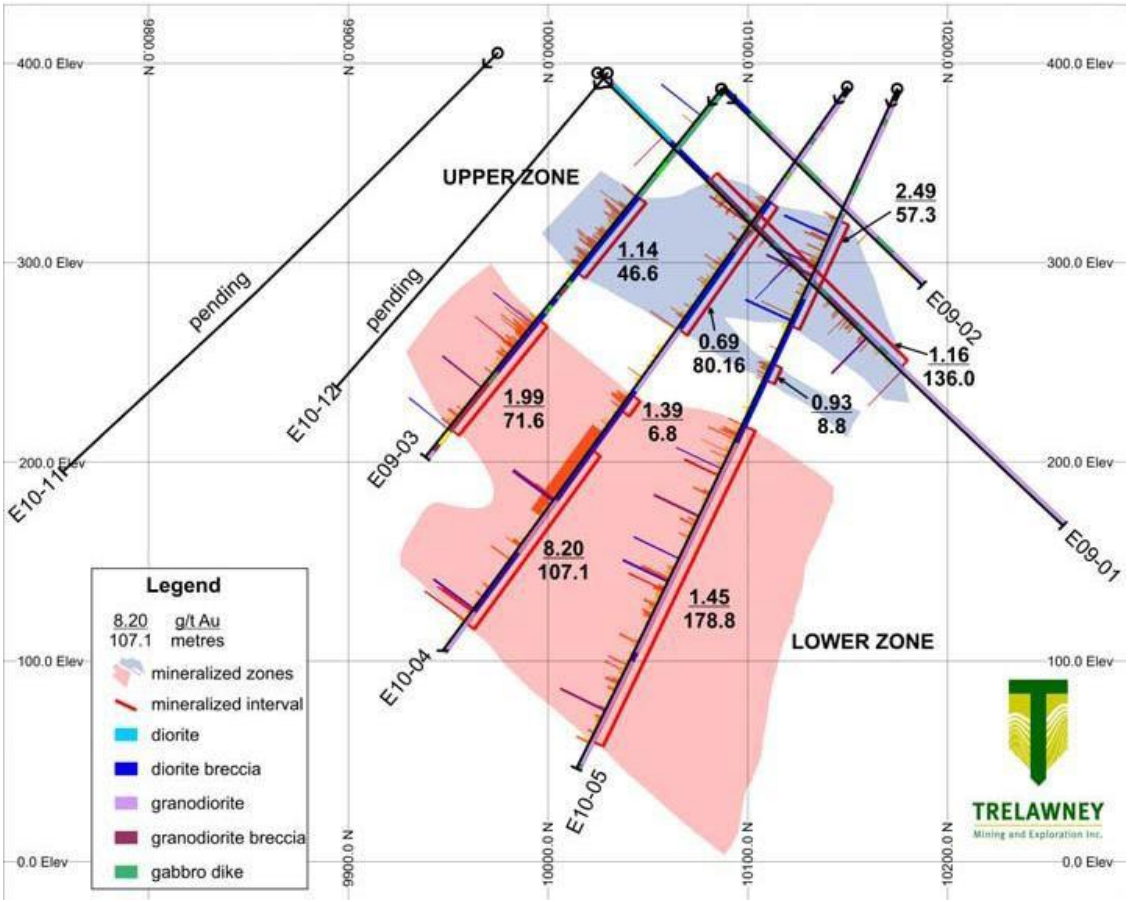

Figure 4: Section 9300E of the Côté Gold deposit as seen in the archived records of Trelawney Mining and Exploration Inc. Note that in the legend the granodiorite units should be tonalite and the diorite breccia can be either magmatic or hydrothermal in origin, as discussed in the text.

Hole	Section	From (m)	To (m)	Length (m)	Au (g/t)	Press Release Date
E10-09	9400E	89.91	285.75	195.84	1.11	22-Apr-10
E10-10	9400E	54.83	84.00	29.17	1.38	
E10-13	9200E	99.01	211.40	112.39	1.57	17-May-10
E10-14	9200E	99.00	122.00	23.00	2.96	
		128.50	166.50	38.00	1.04	
E10-16	9500E	196.00	218.00	22.00	0.91	21-Jun-10

Hole	Section	From (m)	To (m)	Length (m)	Au (g/t)	Press Release Date
		225.00	253.00	28.00	0.74	
		258.51	308.00	49.49	0.87	
		314.00	330.00	16.00	1.99	
E10-27	9200E	335.40	524.40	189.00	2.41	08-Sep-10
		535.90	584.00	48.10	1.11	
E10-29	9100E	448.00	550.00	102.00	1.10	18-Oct-10
E10-31	9000E	484.09	604.00	119.91	0.85	
E10-33	9400^{E}	81.00	135.40	54.40	1.02	16-Nov-10
		185.10	256.32	71.22	1.25	
		470.00	616.63	146.63	0.72	
E10-40	8900E	252.60	342.00	89.40	1.16	05-Jan-11
		348.00	386.60	38.60	1.43	
		392.85	445.50	52.65	1.29	
E10-43	9400E	441.00	490.71	49.71	1.30	25-Jan-11
E10-47	9000E	223.31	346.07	122.76	0.82	08-Feb-11

Table 1: Summary of significant assay results returned from the 2009-2010 Côté Gold drilling campaigns.

In an October 18, 2010 press release, Trelawney declared a conceptual 'Exploration Potential' of between 3.5 and 6.0 Moz Au for the Côté Gold deposit based on an estimated tonnage and an average grade range of 1.0 to 1.4 g/t Au calculated from reported drillhole intercepts (Trelawney, 2010b). This statement, being delivered exactly three weeks after the gold price had first breached the $1,300 per ounce mark, finally drew the attention of the market (Fig. 5).

An NI 43-101 compliant mineral resource estimate based on the initial 47 drillholes was announced on March 7, 2011, approximately fifteen months after drillhole E09-01 was collared. An estimated Inferred Resource of 131 Mt at an average grade of 1.00 g/t Au (4.22 Moz) was reported at a cut-off grade of 0.3 g/t Au and constrained within a preliminary pit optimisation shell using a gold price of $1,200 per ounce and metallurgical recovery of 95% (Roscoe and Cook, 2011).

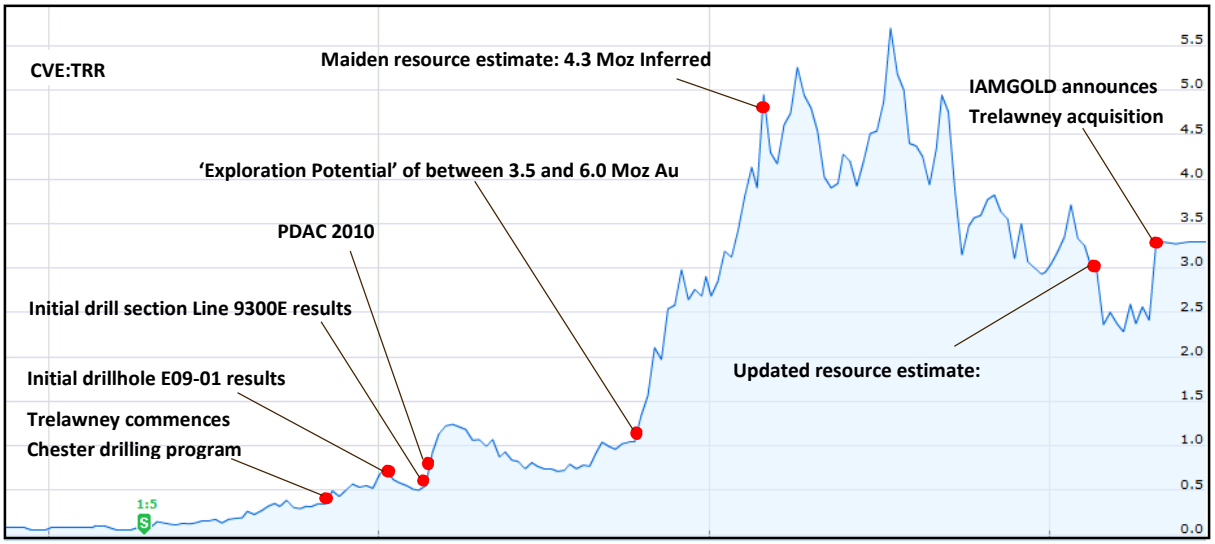

Figure 5: Summary of the running stock price for Trelawney Mining and Exploration Inc. (TRR) on the Toronto Stock Exchange from 2008 to the date of its takeover by IAMGOLD in June 2012. The red dots indicate significant milestones leading to the discovery and subsequent acquisition of the Côté Gold deposit by IAMGOLD, as discussed in the text.

Resource Delineation (2011-2012)

Key objectives of the 2011 and 2012 work programs on the Chester Property were to grow the Côté Gold resource by exploring the lateral and vertical limits of the deposit, increase confidence in grade and geological models to advance the classification of resources and commence preliminary activities ahead of a prefeasibility study. A total of 246 holes were completed for 134,547 metres during this period to cover a 1.4 kilometre strike length of the deposit on 50 metre spaced sections and to a vertical depth of 800 metres.

Updated NI 43-101 compliant mineral resource estimates for the Côté Gold deposit were announced on February 24, 2012, October 4, 2012 and January 22, 2013. Figure 6 summarises this work to illustrate the growth and upgrade of resources, and the progress of the resource delineation drilling program which was carried out using up to 13 rigs. The current resource update is based on all validated drill results available as at December 31, 2012 (293 diamond drillholes for 158,047 metres) and comprises an Indicated Resource of 269 Mt averaging 0.88 g/t Au (7.61 Moz) and an Inferred Resource of 44 Mt averaging 0.74 g/t Au (1.04 Moz; IAMGOLD, 2013). This resource estimate forms the basis of the ongoing prefeasibility study. However, a long term exploration strategy has also been implemented to maintain resource growth both at the Côté Gold deposit and on priority targets elsewhere within the 516 km^2 project landholdings.

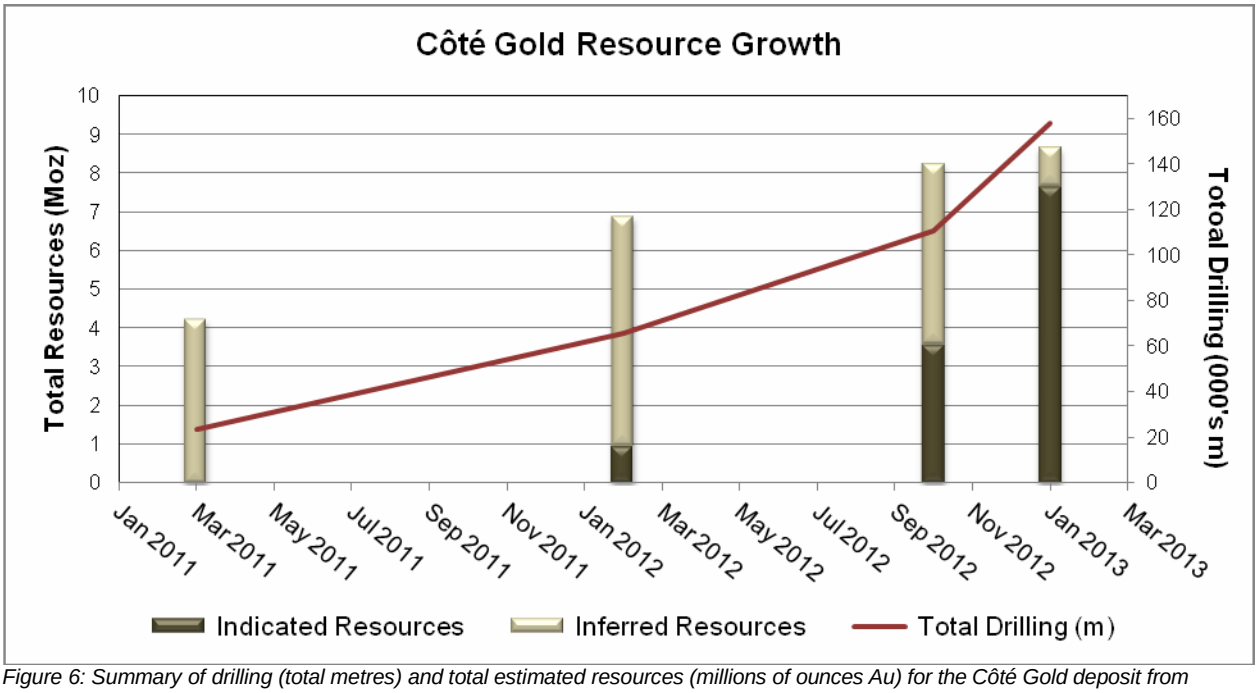

Figure 6: Summary of drilling (total metres) and total estimated resources (millions of ounces Au) for the Côté Gold deposit from December 2010 to December 2012. Notes: 1. CIM Definition Standards were followed for Mineral Resources. 2. Mineral Resources are reported on a 100% basis; IAMGOLD has a 92.5% average attributable ownership of this project. 3. Mineral Resources reported are constrained within a conceptual pit shell, generated using reasonable assumptions for economic and technical parameters (see associated press releases for details). 4. Mineral Resources are not Mineral Reserves and do not yet have demonstrated economic viability, but are deemed to have a reasonable prospect of economic extraction.

Two main domains of mineralisation have been modelled, referred to as the Southwest and Northeast domains, which are separated by an east-west striking, steeply north dipping fault zone and intruded by sub-vertical NNW-striking, post mineralisation dolerite dykes. Each domain includes one approximately tabular, NW-dipping, continuous and relatively thick zone that contains over 90% of the modelled gold mineralisation. These are referred to as the NE Main and SW Main Zones (Figs. 7 and 8). Smaller, sub- parallel gold mineralisation zones have also been modelled within each domain (NE200, NE300, NE400, SW200 and SW300 zones; Fig. 7). Additional solid modelling of host rock types will be attempted when the geological controls on gold distribution are better understood.

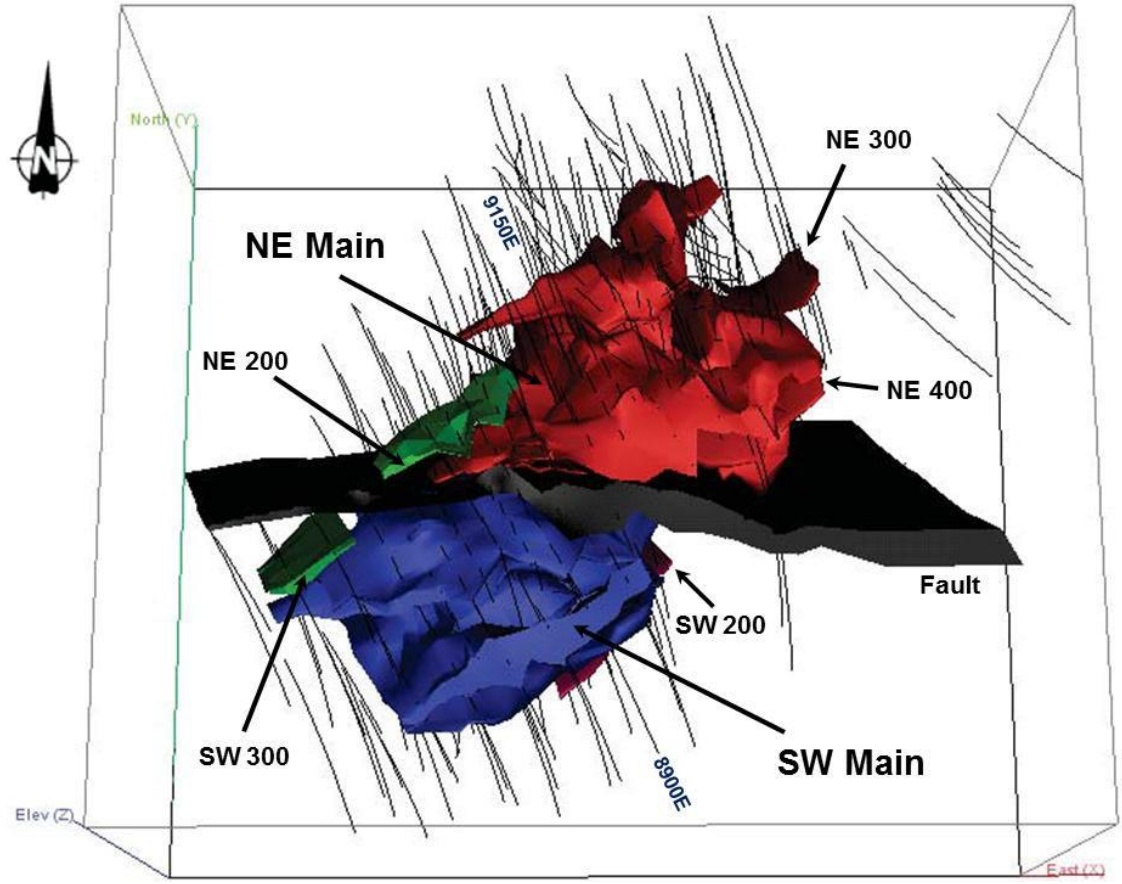

Figure 7: Geological model used for the October 4, 2012 Côté Gold mineral resource estimate, rotated slightly clockwise about an east-west axis (Lavigne and Roscoe, 2012). Scale can be determined by considering the average 100 metre spacing of drill sections. For clarity of presentation, the post-mineral dolerite dykes are not displayed.

Geology of the Côté Gold Deposit

Regional Geological Setting

The Côté Gold deposit is located in the Swayze greenstone belt (SGB) that is part of the much larger and gold rich (e.g., Timmins and Kirkland Lake camps) Abitibi Subprovince (ASP) of the Archean Superior Province of the Canadian Shield (Fig. 1). In its eastern part, the rocks of the SGB are inferred to be contiguous with the southwestern extension of the AGB (Ayer et al., 2002; van Breemen et al., 2006). These supracrustal rocks are surrounded by large composite granitoid complexes (i.e., Nat River, Kenogamissi, Ramsey-Algoma; Heather, 2001) to the north, east, and south, whereas to the west the SGB is bounded by the Kapukasing structural zone which consists of high-grade metamorphic rocks of mid-to lower crustal origin.

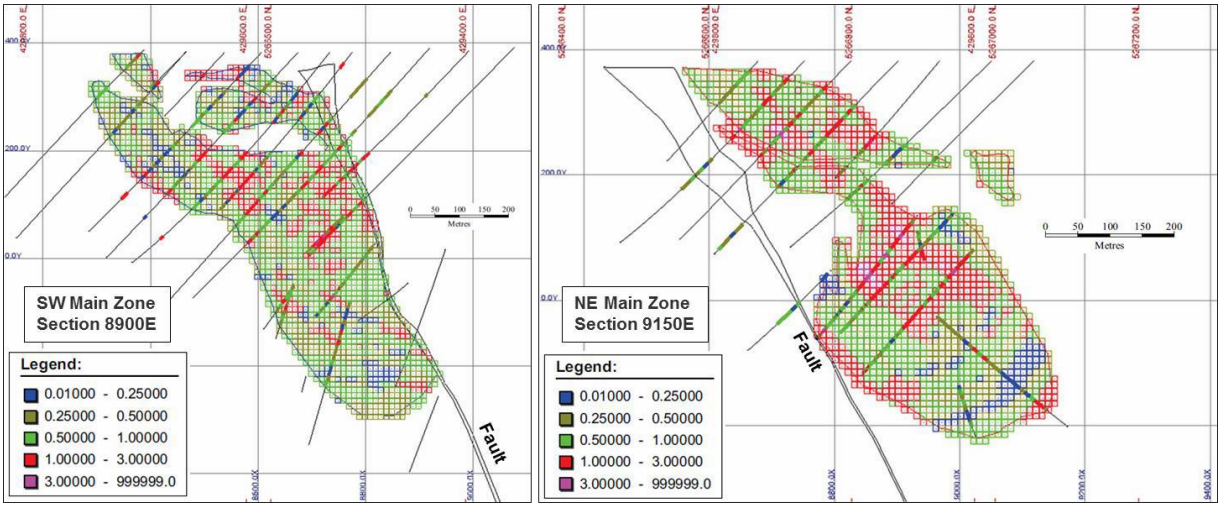

Figure 8: Comparison of estimated block model grades and downhole 10m composite grades for the SW Main Zone (Section 8900E) and NE Main Zone (Section 9150E) of the Côté Gold deposit (Lavigne and Roscoe, 2012). Location of drill sections are illustrated on Figure 7. View is towards the southwest for both sections.

The SGB consists of 6 supracrustal groups (the Chester, Marion, Biscotasing, Trailbreaker, Swayze and Ridout) with a total of 12 formations (Fig. 9; Heather, 2001). The lower part of this assemblage is dominated by mixed mafic and felsic volcanic rocks, the latter of which has massive rhyolite flows dated (U-Pb zircon) at ca. 2740 Ma (Heather, 2001). The upper part of the sequence is dominated by both clastic and chemical (i.e., iron formation) sedimentary rocks. The youngest rocks (i.e., Ridout Group) are similar to the Timiskaming assemblage of the ASP (Berger, 2012), and contain a detrital zircon population that provides a maximum (U-Pb) age of 2680 Ma for sedimentation (Berger and Lodge, 2012).

The plutonic rocks surrounding the SGB are subdivided into two compositional suites, one mafic to ultramafic and the other felsic to intermediate (Fig. 9; Heather, 2001). The latter suite is further subdivided into five categories based on their ages: (a) 2740 to 2696 Ma syn-volcanic diorite to tonalite intrusions, (b) 2685 to 2680 Ma syn-tectonic granodiorite intrusions, (c) a transitional suite of syn-volcanic diorite to tonalite and syn-tectonic granodiorite, which includes tonalite to quartz monzonite intrusions, that range in age from 2695to 2686 Ma, (d) post-tectonic granite of ca. 2665 Ma, and (e) a second transitional suite of syn-tectonic granodiorite to post-tectonic granite, including some diorite to monzonite intrusions, that range in age from 2680 to 2665 Ma. The majority of these granitoids, and the most important suite relevant to the nature of the Côté Gold deposit, correspond to the 2740 Ma syn-volcanic suite, which resemble large laccoliths, instead of circular- to elliptical-shaped stocks or batholiths (Heather, 2001). These intrusions typically display a sheet-like geometry, have
primary magmatic layering, and exhibit magma mixing and commingling textures (Heather et al., 1996; Berger 2012). The compositions of these syn-volcanic intrusions range from hornblende diorite, quartz diorite and monzodiorite through to hornblende (± biotite) tonalite and biotite tonalite to granodiorite (Heather, 2001). Geochemically, the felsic intrusions (e.g., tonalities) are similar to the felsic volcanic rocks of the SGB, indicating that they are possible correlatives (Heather et al., 1996; Berger 2012).

The SGB has undergone a complex structural history involving the development of multiple foliations, ductile high-strain zones and late brittle faulting (van Breemen et al., 2006). The oldest pervasive deformation (D1) consists of a penetrative foliation that is cryptically preserved in shear zones associated

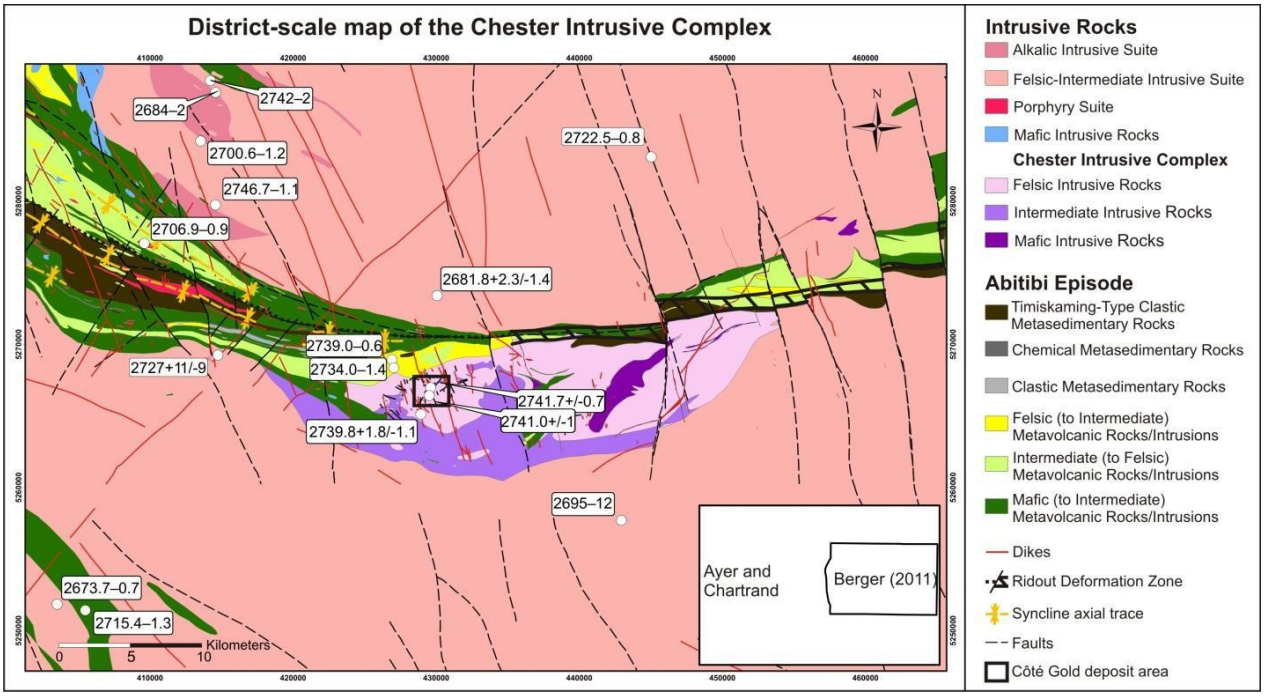

Figure 9: Simplified district-scale geological map of the Chester Intrusive Complex (CIC) and the southeastern arm of the Swayze greenstone belt, as compiled from Ayer and Chartrand (2011) and Berger (2011). The CIC intrudes the southeastern arm of the Swayze greenstone belt, is laccolithic in shape, and can be separated into two domains, a northern leucocratic, tonalite-dominated domain and a southern melanocratic, diorite-dominated domain. The 2741 Ma ages for the CIC in the deposit area represent new ages conducted as part of our ongoing studies; all other ages (U-Pb zircon) are compiled from previous workers.

with syn-volcanic intrusions and isoclinal folds (Heather, 2001; van Breemen et al., 2006). The map pattern is, however, dominated by regional F2 folding with an associated axial planar foliation (S2) that formed during orogen-wide shortening (Heather et al., 1995; van Breemen et al., 2006). Several, regionally extensive, D2 high-strain zones transect the SGB (e.g., Ridout deformation zone (RDZ)). The D2 event is inferred to have been synchronous with the generation of orogenic-style, quartz-carbonate veins carrying gold mineralisation, some of which occur in the vicinity of the Côté Gold deposit and were the original exploration targets in the area (see above). The RDZ, defining the northern contact of the SGB, is an anastomosing, but generally east-west trending high-strain zone up to two kilometres in width that extends the length of the SGB. The dominant D2 map pattern is locally modified by a crenulation cleavage in high strain zones and small-scale folds associated with both D3 and D4 deformation events.

Previous studies (Heather, 2001; van Breemen et al., 2006) have inferred the RDZ to be the western extension of the Cadillac-Larder-Lake deformation zone CLLDZ), which is an important structural element related to gold mineralisation in the ASB. However, Berger (2012), suggested that the two deformation zones are separate and unrelated structures, with the CLLDZ characterised by different kinematics along its length. In addition, he notes that the two deformation zones occur in different parts of the regional stratigraphy: the RDZ is located along the northern contact of the Timiskaming assemblage in the SGB, whereas the CLLDZ is at the southern contact of the Timiskaming assemblage (Berger, 2011).

Metamorphic grade within the southern part of the ASP ranges from subgreenschist to greenschist grade with higher grade conditions, up to amphibolite grade, locally attained next to large syn-volcanic and syn- tectonic intrusions. Peak metamorphism is estimated to have occurred from 2677 to 2643 Ma (Ayer et al., 2002).

Local Geological Setting

The Côté Gold deposit is located within the ca. 2742 Ma Chester Intrusive Complex (CIC; van Breemen et al., 2006; Kontak et al., 2013a, b; our unpubl. data). This multi-phase, syn-volcanic complex borders the southeastern margin of the SGB where it is bound by rocks of the Chester Group, the basal part of the SGB: to the west lie mafic volcanic rocks of the Arbutus Formation, with felsic to intermediate volcanic rocks of the Yeo Formation to the north. The RDZ, which forms the northern margin of the SGB, lies approximately three kilometres north of the deposit. The Arbutus Formation contains pillow-textured, mafic flows and massive, medium-grained amphibolite, interpreted to be either coarser-grained flows or intrusive sills. This formation is conformably overlain by the Yeo Formation (Heather, 2001), which consists of intercalated felsic and intermediate volcanic rocks, clastic sedimentary and volcaniclastic rocks, iron formation and iron-rich sedimentary rocks. This formation is considered to represent the eruptive equivalent of the tonalitic part of the CIC, which is supported by both geochronological (2739 ± 2 Ma U-Pb zircon age; Heather, 2001) and geochemical data (Heather et al., 1996; Berger, 2012). In detail, the felsic volcanic rocks range from poorly sorted to well-bedded, monolithic and heterolithic fragmental deposits, massive aphanitic flows and feldspar ± quartz phyric flows.

Heather (2001) describes the CIC as a composite intrusion of laccolithic geometry that can be subdivided into a northern, leucocratic tonalite-dominated phase and a southern, melanocratic diorite-dominated phase. The complex contains a number of screens and inclusions of mafic volcanic rocks of the Arbutus Formation (Heather, 2001; Berger, 2011). Several phases have been described: a biotite trondhjemite to tonalite, leucocratic quartz-rich trondhjemite and feldspar porphyritic trondhjemite (Heather et al., 1995; Heather, 2001; here the trondhjemite phases are included with tonalite). Based on core logging and petrography, the tonalite is texturally and compositionally homogeneous. The diorite consists of several phases: diorite, quartz diorite and hornblende-plagioclase pegmatite (Heather et al., 1995; Heather, 2001). Complex crosscutting relationships and textures in the CIC have been interpreted by various workers (e.g., Heather, 2001; Berger, 2011) to reflect magma mixing and commingling; these features include (1) diorite, quartz diorite and tonalite inclusions in tonalite with (frothy or pitted) dissolution textures; and (2) tonalite and rare diorite clasts with rounded, sub-rounded, cuspate and diffuse contacts in a dioritic matrix.

Two styles of gold mineralisation have been recognised in the CIC. The Côté Gold deposit is hosted by tonalitic and dioritic phases of the intrusive complex, with disseminated sulphide and gold mineralisation spatially associated with a series of “diorite” breccia bodies. The term “diorite” breccia is used for both magmatic and hydrothermal breccia, as the two are difficult to distinguish visually in drill core. The breccia is characterised by tonalite clasts in a black to dark-green chloritic matrix. The second mineralisation style occurs in the northern part of the CIC, where orogenic-style centimetre- to metre-wide, laminated quartz- carbonate-sulphide shear veins contain variable amounts of coarse gold and are locally associated with carbonate-sericite-tourmaline alteration haloes.

Deposit Geology

Host rocks: The principal host rocks of the Côté Gold deposit include tonalite, diorite and “diorite” breccia (Fig. 10), all of which are cut by a variety of mafic dykes, several phases of dacitic quartz-feldspar porphyry and a suite of post-mineral dolerite and lamprophyre dykes. Only the major phases are discussed below.

1) Tonalite is the most abundant rock type in the deposit area. It is typically medium-grained and homogeneous, and contains textural features such as miarolitic cavities, granophyre and autobreccia indicative of an upper crustal emplacement level. At least two tonalite phases are recognised (Fig. 10a); an early tonalite (I) that is intruded by the diorite and a younger tonalite (II) that contains enclaves of diorite (i.e., quenched mafic melt) and/or occurs as cross-cutting tonalite

dykes cutting both diorite and tonalite I. In addition, subordinate biotite- and hornblende-bearing varieties are observed locally.

2) Three phases of diorite occur within the mineralisation footprint; diorite, quartz diorite and hornblende- plagioclase pegmatite. Diorite and quartz diorite occur as discrete bodies ranging from five to over 100 metres in thickness and typically cross-cut the oldest tonalite phases. Diorite is the dominant mafic phase in the northern part of the deposit (Fig. 10b), whereas quartz diorite predominates in the south. Both are generally medium- to coarse-grained, dark- to medium-green in colour, and composed of plagioclase- hornblende ± quartz ± biotite, with minor magnetite and titanite. The subordinate pegmatite phase occurs as small (<1 m) dykes or as layers in diorite.

3) The "diorite" breccia phase is typically monolithic with clasts of leucotonalite in a black, dark- to light- green, fine-grained magmatic and/or hydrothermal groundmass (Fig. 10c and d). Heterolithic breccia occurs locally and is distinguished by the presence of diorite clasts or xenoliths. Tonalite clasts can be angular to rounded, coarse-grained to boulder-sized with sharp to diffuse boundaries, the latter being dependent upon the degree of alteration overprint. The magmatic breccia matrix consists of 30-40% plagioclase, 25-50% biotite/chlorite, 0-40% amphibole and 10-25% quartz, and is interpreted to represent an evolved, more volatile-rich fractionate of the diorite. The occurrence of coarse- to very coarse-grained amphibole grains in the matrix is considered diagnostic of this breccia type. By contrast, the hydrothermal breccia matrix is typically fine-grained and consists of 40-65% biotite, 30-45% quartz, <1-10% carbonate and <2% apatite, with trace amounts of rutile and fluorite.

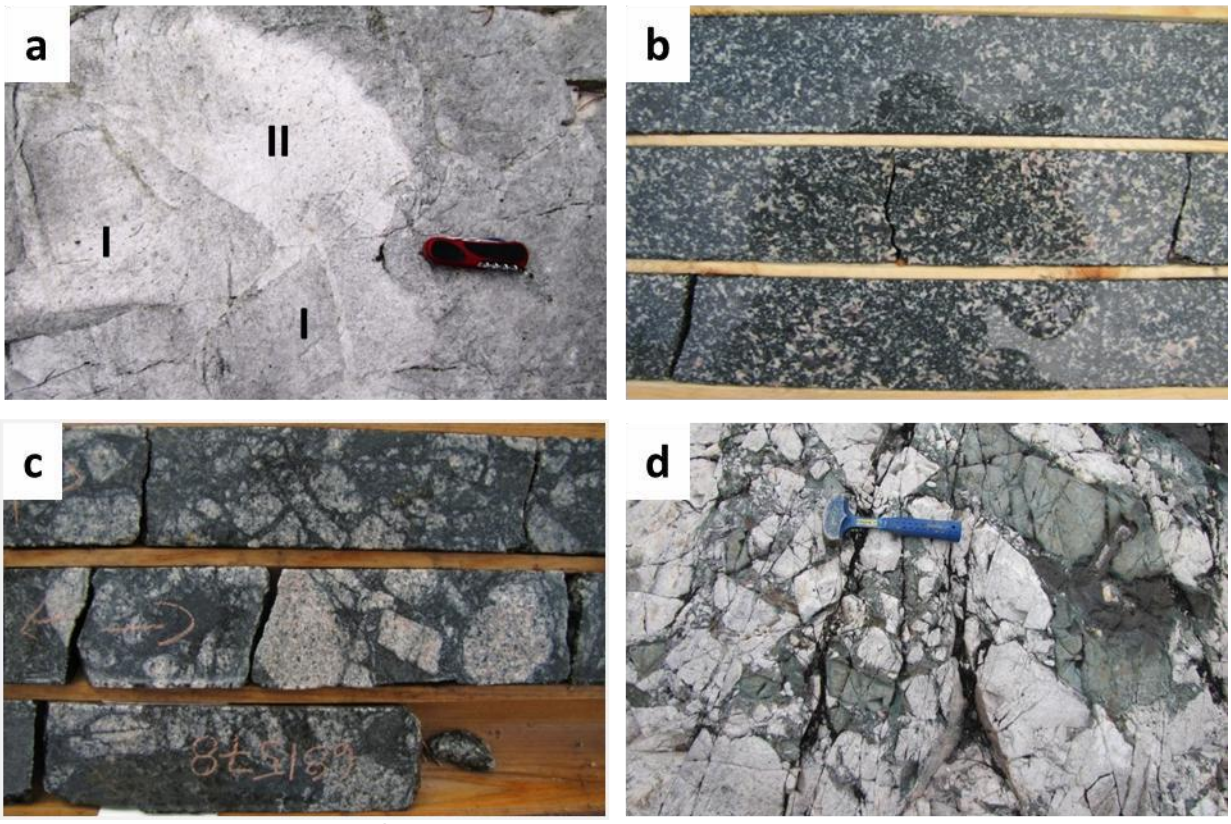

Figure 10: Examples of the principal Côté Gold host rocks. All drill core is NQ size. 10a: Tonalite (I) exposure in the deposit area with interpreted autobrecciation textures and infill by a younger leucocratic tonalite phase (II). 10b: Coarse-grained plagioclase-phyric diorite. 10c: Example of 'diorite' breccia in drill core. Note the dark biotite-rich matrix and variable sizes and shapes of tonalite clasts with disseminated biotite alteration. 10d: Typical 'diorite' breccia of magmatic origin outcropping within the deposit area.

Alteration and Mineralisation: Paragenetic studies of the Côté Gold deposit are in progress but at a very preliminary stage. The following narrative aims to provide an overview of the principal

alteration assemblages and mineralization styles documented to date. Advancing the understanding of the fundamental controls on gold distribution and the determination of a constrained mineral paragenesis are critical objectives of the ongoing geological research program.

Three main hydrothermal alteration assemblages are spatially associated with gold mineralisation, and are classified based on the dominant alteration mineral: biotite, silica-albite and sericite. Other alteration types include pervasive epidote and hematite, but these appear to be relatively late in the paragenetic sequence and are not associated with significant gold mineralisation.

1) Biotite alteration: This assemblage has the largest footprint, extending outside the gold mineralisation envelope, and is interpreted to represent the onset of hydrothermal alteration. It consists of biotite ± magnetite ± epidote ± sulphide, and typically occurs as infill in the matrix of 'diorite' breccia bodies (Fig. 10c and 11a) or as disseminated anhedral grains and aggregates in tonalite (Fig. 11b and c). Biotite may be intergrown with LREE-rich bastnaesite and allanite, in addition to euxenite, rutile and fluorite. Several generations of quartz-biotite ± chlorite ± carbonate ± epidote veining have also been documented. These are typically mineralised with pyrite, chalcopyrite, magnetite, hematite (after magnetite) and sphalerite, with minor molybdenite and gold.

2) Silica-albite alteration: This texturally-destructive, pervasive alteration assemblage overprints all of the major host rocks, the oldest quartz-feldspar porphyry phases and the biotite alteration assemblage. It occurs as discrete haloes around fractures or veins (Fig. 11d), but may coalesce into massive alteration zones exceeding 200 metres in thickness (Fig. 11e). In the latter case, the host rock protolith can be distinguished by the presence (diorite) or absence (tonalite) of resistate minerals such as leucoxene and titanite.

3) Sericite alteration: This dark-grey and grey-green alteration assemblage comprises sericite ± quartz ± carbonate ± pyrite, is texturally-destructive, overprints but appears to be co-spatial with the silica-albite alteration phase and may be associated with increased gold grades. Sericite alteration occurs as haloes (<1 to 10's cm) around individual quartz ± carbonate veins (<1 to 10 cm; Fig 11f) or can be pervasive in zones of high vein density. It is discontinuous throughout the deposit, most intense in the core and weakly developed distal to mineralisation. A post-mineralisation sericite-quartz-carbonate vein set is also recognised. This generation of sericite is medium-grained and white to silver in colour, and the host veins do not have visible alteration haloes.

Several styles of gold mineralisation can be discerned within the Côté Gold deposit. The most volumetrically significant is spatially associated with the "diorite" breccia, although disseminated, vein- hosted and fracture-controlled modes of occurrence are recognised in all host rocks.

1) Breccia-hosted gold: The NE Main and SW Main Zones of the deposit broadly coincide with an irregularly shaped, semi-continuous breccia body that extends for 1.4 kilometres along strike, reaches 600 metres in width and has been traced in drilling to a vertical depth of over one kilometre (Fig. 12). Gold mainly occurs in the breccia matrix, in association with pyrite ± chalcopyrite ± sphalerite ± molybdenite mineralisation.

2) Disseminated gold: This style of mineralisation occurs throughout the deposit in tonalite and dioritic host units and is typically associated with hydrothermal biotite and minor magnetite. Pyrite and chalcopyrite are the most abundant sulphides; chalcopyrite commonly occurs on fractures in pyrite and gold occurs as inclusions. Sulphides and molybdenite preferentially nucleate on biotite, chlorite and amphibole as anhedral to euhedral grains and cluster to form coarse aggregates.

3) Vein-hosted gold: Auriferous vein assemblages include quartz, quartz-carbonate, quartz-biotite, carbonate, chlorite ± carbonate and epidote ± quartz ± carbonate. These occur either as isolated veins or in stockwork arrays, with textures varying from massive to comb-like. Sulphide mineralisation can be semi-massive to locally massive on vein margins, but is more typically disseminated within veins.

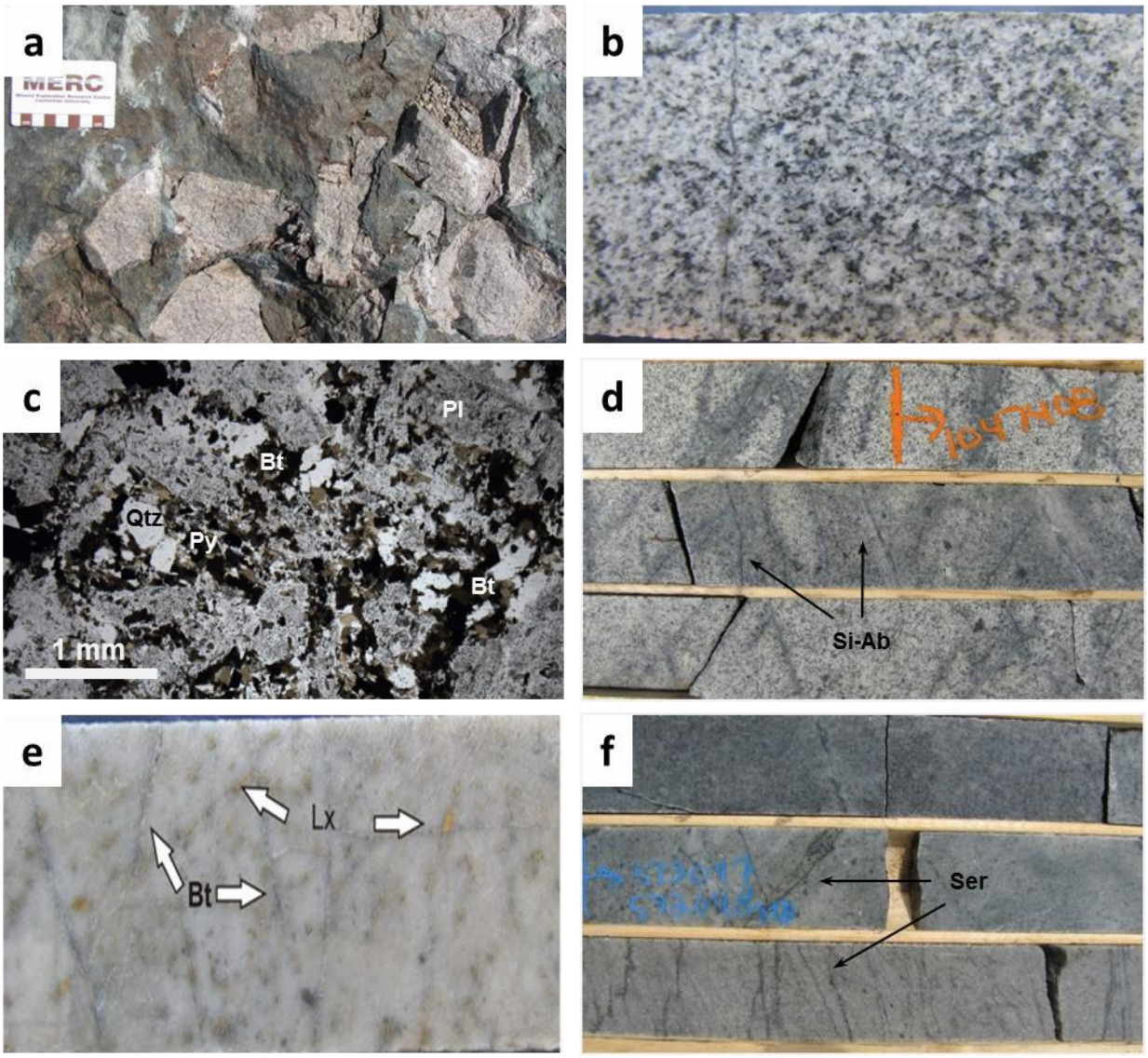

Figure 11: Examples of the main hydrothermal alteration assemblages recognised within the Côté Gold deposit. All drill core is NQ size. 11a: Surface exposure of chlorite altered, biotite-rich, matrix-supported hydrothermal breccia from the northern part of the deposit. 11b: Disseminated biotite alteration in tonalite. 11c: Photomicrograph of biotite altered tonalite in plane polarized light. Note that primary plagioclase has been replaced by secondary biotite. 11d: Fracture array in tonalite with associated silica-albite alteration (Si-Ab) overprinting pre-existing secondary biotite. 11e: Pervasive silica-albite alteration. Remnant fractures containing biotite/chlorite are preserved. The presence of orange leucoxene crystals indicates a mafic protolith. 11f: Fracture array in tonalite with quartz-pyrite infill and sericite alteration haloes (Ser)

Visible gold and molybdenite appear to be more prevalent in quartz, quartz-carbonate and quartz-biotite-chlorite ± carbonate vein types. The vein- and breccia-hosted gold mineralisation styles are interpreted to be cogenetic based on observed mutual cross-cutting relationships.

4) Fracture-controlled gold: This mineralisation style occurs in all host rocks, but is preferentially preserved within the relatively more brittle tonalite. Zones of sheeted fractures several metres in width and characterised by sericite or silica-albite alteration haloes can be developed locally. Gold mineralisation is associated with subhedral to euhedral pyrite and anhedral chalcopyrite coatings on fracture surfaces.

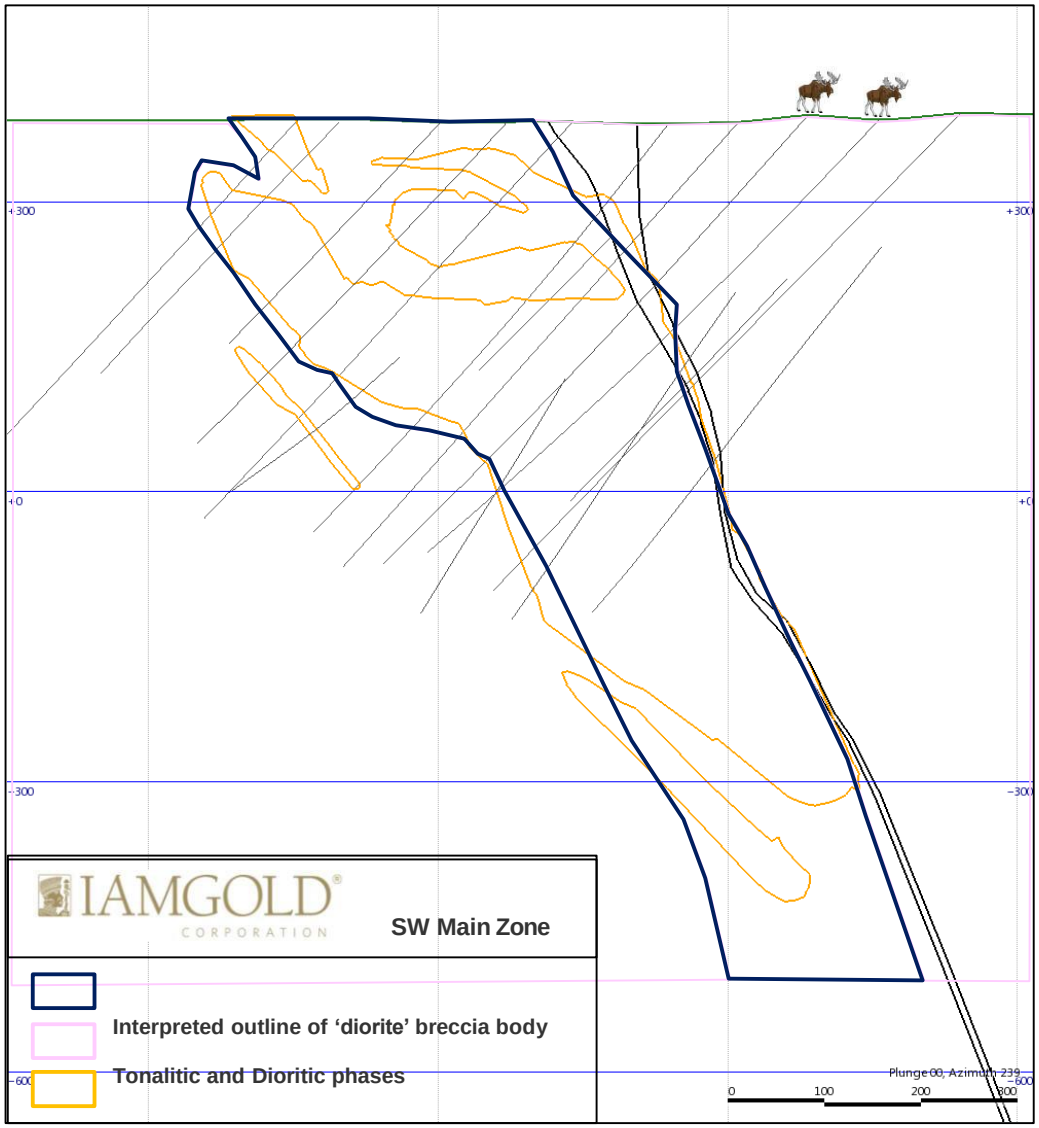

Figure 12: Comparison of 0.30 g/t gold mineralisation wireframes from the January 22, 2013 resource estimate and preliminary sectional interpretation of the 'diorite' breccia host unit in the Southwest domain of the Côté Gold deposit. Location of drill section is illustrated on Figure 7. View is towards the southwest. Moose are not to scale.

Geochronology: Kontak et al. (2013a, b) presented the results of two U-Pb zircon analysis for tonalite I (2741.1 ± 0.9 Ma) and magmatic breccia (2738.7 ± 0.8 Ma). In addition, these authors also presented results for two molybdenite separates analysed with the Re-Os method, one for massive molybdenite coating a fracture surface in tonalite I and the other from a silica altered tonalite where molybdenite was intergrown with chalcopyrite and coarse gold. These two samples yielded an average age of 2739 ± 8 Ma. Our additional unpublished data for several more samples, dated using the U-Pb zircon TIMS method, yielded 2741/2742 Ma for samples of diorite, diorite pegmatite and tonalite II, from a single outcrop area.

These data indicate that the host rocks to the Côté Gold deposit formed at ca. 2741 Ma and along with the Re-Os data provide a maximum age for mineralisation. The significance of the ca. 2739 Ma age noted above and whether the deposit represents several superimposed mineralising events will be addressed with future work.

Conclusions

As with the majority of exploration case histories, a number of contributing factors led to the discovery of the Côté Gold deposit. An important overriding dynamic has been the prevailing market conditions at the time when historical exploration results were received and/or reported. The Côté Gold mineralised system was intersected in drilling on three separate occasions between 1970 and 2005, with the last exploration company to do so going so far as to acknowledge the potential for an open pittable, multi-million ounce, low-grade resource. In all cases, however, the project was not advanced beyond the initial drill program due to the economic constraints of the day; the respective junior exploration companies could not maintain financial solvency and the corresponding exploration results were archived and largely forgotten.

In terms of the sequence of events leading to discovery, the first critical step occurred in the early 2000's when Condor Gold successfully consolidated a large group of claim blocks into a single contiguous landholding over the current deposit area. Prior to this point in time, exploration programs were typically restricted in scope, carried out in isolation and relatively short-lived due to the complex and fragmented ownership history of these claim blocks. Possession of a large consolidated land package allowed Trelawney to rapidly expand the Côté Gold resource and will enable IAMGOLD to optimise the design of mine and plant infrastructure should the project proceed to development.

The second crucial element in the Côté Gold discovery history was a fundamental change in the targeting philosophy of the Trelawney exploration team. Prior to 2009, most exploration companies operating in the Swayze greenstone belt considered the exploitation of high-grade vein-hosted gold mineralisation by narrow underground mining to be the only feasible end game. Indeed, Trelawney's initial objective in the district was to further explore the potential of the 'No. 3 Vein' on the historical Murgold-Chesbar claim block. However, three drillholes were added to the initial exploration campaign to test the historical low- tenor drill results that had been rediscovered in the archives during a regional data compilation and target generation exercise. The first of these drillholes, E09-01, can be considered as the genuine discovery hole, given that the corresponding assay result provided Trelawney with the encouragement to advance the Côté Gold project to what is now recognised as a multi-million ounce and, owing to improved economic constraints, potentially viable mineral resource.

Acknowledgements

The discovery and delineation of the Côté Gold deposit was made possible by the collective efforts of many individuals. The authors wish to acknowledge the contributions of past and present geological teams, support staff and corporate management, all of whom have helped to advance the project towards development.

Geological research on the Côté Gold deposit has been supported through several initiatives, with funding generously provided by Discover Abitibi of the Ontario Government, the Targeted Geoscience Initiative (TGI-4) of the Geological Survey of Canada, and graduate student support through IAMGOLD Corporation.

References

Ayer, J., Amelin, Y., Corfu, F., Kamo, S., Ketchum, J., Kwok, K., and Trowell, N., 2002. Evolution of the southern Abitibi greenstone belt based on U-Pb geochronology: autochthonous

volcanic construction followed by plutonism, regional deformation and sedimentation; Precambrian Research, v. 115, p. 63-95.

Ayer, J.A., and Chartrand, J.E., 2011. Geological compilation of the Abitibi greenstone belt; Ontario Geological Survey, Miscellaneous Release - Data 282.

Berger, B.R., 2011. Geological Investigations South of Gogama; *in* Summary of Field Work and Other Activities 2011, Ontario Geological Survey, Open File Report 6270, p. 3-1 to 3-7.

Berger, B.R., 2012. Interpretation of Geochemistry in the South of Gogama Area; *in* Summary of Field Work and Other Activities 2012, Ontario Geological Survey, Open File Report 6280, p. 3-1 to 3- 14.

Berger, B.R., and Lodge, R.W.D., 2012. Report on Geochronology for the South of Gogama Area; *in* Summary of Field Work and Other Activities 2012, Ontario Geological Survey, Open File Report 6280, p. 4-1 to 4-10.

Brown, P. A. R., 1992. Report on Diamond Drilling Program for Emerald Isle Resources Inc. Chester Twp. Ontario. Ontario Geological Survey, DD RPT 47 Chester Twp.

Condor Gold Corporation, 2003. Condor Gold Corp. Announces Jackrabbit Deposit Identified as Major Gold Depository. CGR press release, March 26, 2003.

Cook, R. B., 2010. Technical Report on the Chester Township Properties, Ontario, Canada. Prepared for Trelawney Mining and Exploration Inc., January 14, 2010.

Dubé, B., and Gosselin, P., 2007. Greenstone-hosted quartz-carbonate vein deposits; *in* Goodfellow, W.D., ed., Mineral Deposits of Canada: A Synthesis of Major Deposit-Types, District Metallogeny, the Evolution of Geological Provinces, and Exploration Methods: Geological Association of Canada, Mineral Deposits Division, Special Publication No. 5, p.49-73.

Heather, K.B., Shore, G.T. and van Breemen, O., 1995. The convoluted “layer-cake”, an old recipe with new ingredients for the Swayze greenstone belt, southern Superior Province, Ontario; *in* Current Research 1995-C, Geological Survey of Canada, p. 1-10.

Heather, K.B., Shore, G.T., and van Breemen, O., 1996. Geological investigations in the Swayze greenstone belt, southern Superior Province, Ontario: a final field update; *in* Current Research 1996-C; Geological Survey of Canada, p.125-136.

Heather, K.B., 2001. The geological evolution of the Archean Swayze Greenstone Belt, Superior Province, Canada; Ph.D thesis, Keele University, Keele, England, 370 p.

IAMGOLD Corporation, 2013. IAMGOLD provides mineral resource update for Côté Gold and reports strongest quarter for production in 2012 with confirmed production guidance for 2013. IMG press release, January 22, 2013.

Kontak, D.J., Creaser, R.A. and Hamilton, M.A., 2013a. Section 2: Geological and geochemical studies of the Côté Lake Au(-Cu) deposit area, Chester Township, Northern Ontario; report *in* Results

from the Shining Tree, Chester Township and Matachewan Gold Projects and the Northern Cobalt Embayment Polymetallic Vein Project, Ontario Geological Survey, Miscellaneous Release - Data 294.

Kontak, D.J., Katz, L., Creaser, R.A., Hamilton, M., 2013b. The Archean Côté gold Au(-Cu) deposit, northern Ontario, Canada: A large tonnage, low-grade Au deposit centred on a 2740 Ma magmatic-hydrothermal diorite complex (abstract): Geological Association of Canada - Mineralogical Association of Canada, Annual Meeting, 2013, Abstracts.

Laird, H. C., 1932. Geology of the Three Duck Lakes Area; Ann. Rept. Ont. Dept. Mines, v.41, pt. 3.

Lavigne, J., and Roscoe, W. E., 2012. Technical Report on the Côté Gold project, Chester Township, Ontario, Canada. Filed on SEDAR, October 24, 2012 by IAMGOLD Corp.

McBride, D. E., 2002. Qualifying Report on the Chester Township Property for Northville Gold Corporation. Filed on SEDAR, July 29, 2002 by Condor Gold Corp.

Poulsen, K.H., Robert, F., and Dubé, B., 2000. Geological Classification of Canadian Gold Deposits: Geological Survey of Canada, Bulletin 540, p. 106.

Roscoe, W. E., and Cook, R. B., 2011. Technical Report on the Côté Lake Deposit, Chester Property, Ontario, Canada. Filed on SEDAR, April 21, 2011 by Trelawney Mining & Exploration Inc.

Roscoe, W. E., and Cook, R. B., 2012. Technical Report on the Côté Lake Resource Update, Chester Property, Ontario, Canada. Filed on SEDAR, April 9, 2012 by Trelawney Mining & Exploration Inc.

Siragusa, G. M., 1993. Precambrian Geology, parts of Chester, Neville, Potier and Yeo Townships. Ontario Geological Survey, Open File Report 5844.

Trelawney Mining and Exploration Inc., 2010a. Trelawney Mining intersects 90.51 g/t Au over 1.00 metres within a larger zone of 1.16 g/t Au over 136.00 metres. TRR press release, January 18, 2010.

Trelawney Mining and Exploration Inc., 2010b. Trelawney intersects 139.00 metres of 1.62 g/t gold at the Côté Lake deposit. TRR press release, October 18, 2010.

Van Breemen, O., Heather, K.B., and Ayer, J.A., 2006. U-Pb geochronology of the Neoarchean Swayze sector of the southern Abitibi greenstone belt; in Current Research 2006-F1, Geological Survey of Canada, p. 1-32.

Appendix B

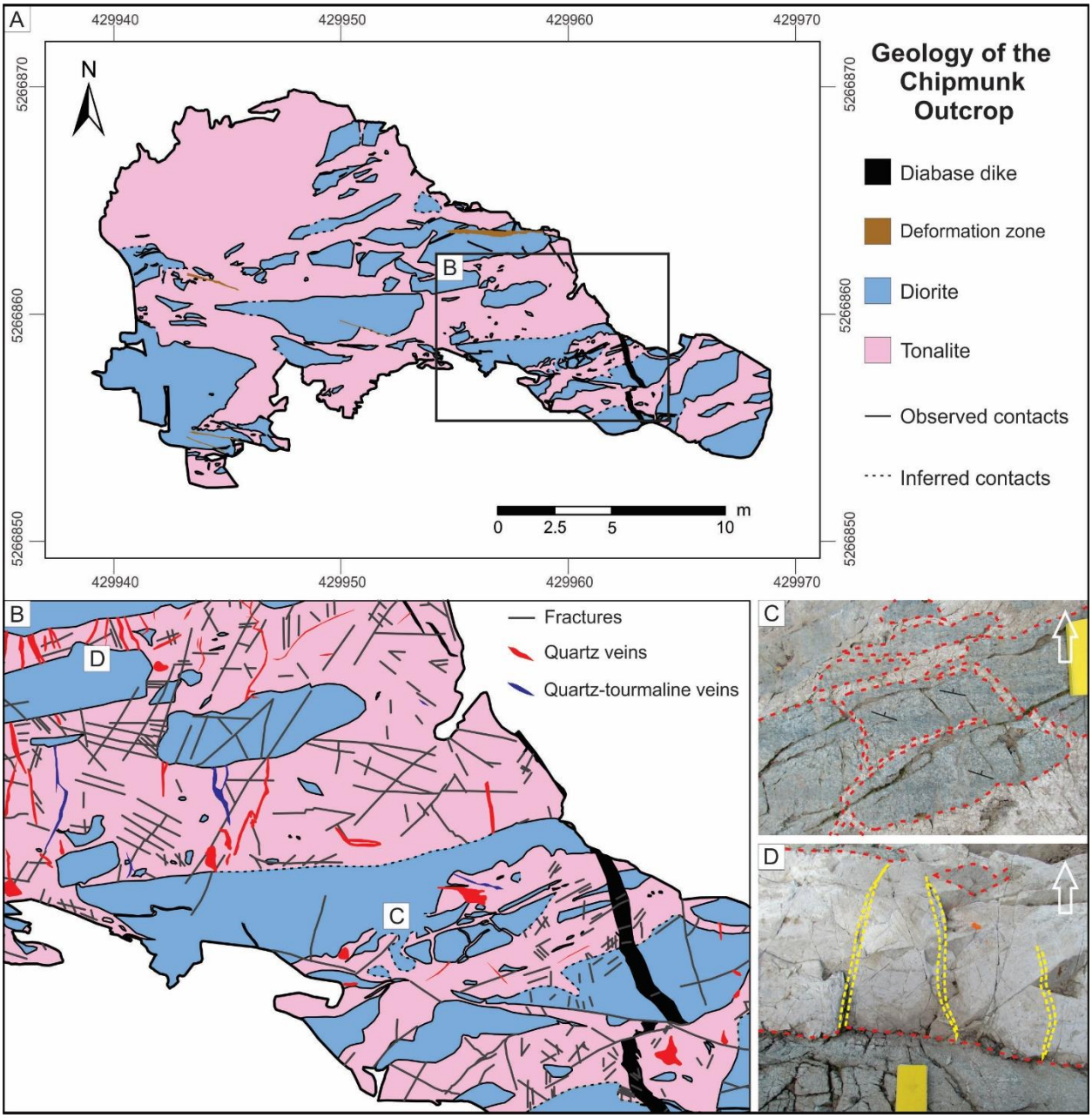

Figure B.1. Geological map of the Chipmunk Outcrop, along with outcrop photographs, that shows important crosscutting relationships. A) Geological map of a tonalite breccia with cm- to m-sized, angular to sub-rounded diorite fragments with sharp contacts. B) An enlarged area from A that shows an increase in the density of veins and fractures in tonalite compared to diorite. C) Outcrop photo from B that shows tonalite sharply intruding diorite. The contacts between tonalite and diorite are shown by red dashed lines. Note that diorite contains a foliation defined by amphibole. The yellow book for scale is 19 x 12 cm. D) Outcrop photo from B that shows quartz veins, outlined by yellow dashed lines, in tonalite that terminate at the contact with diorite, which is outlined in red dashed lines.

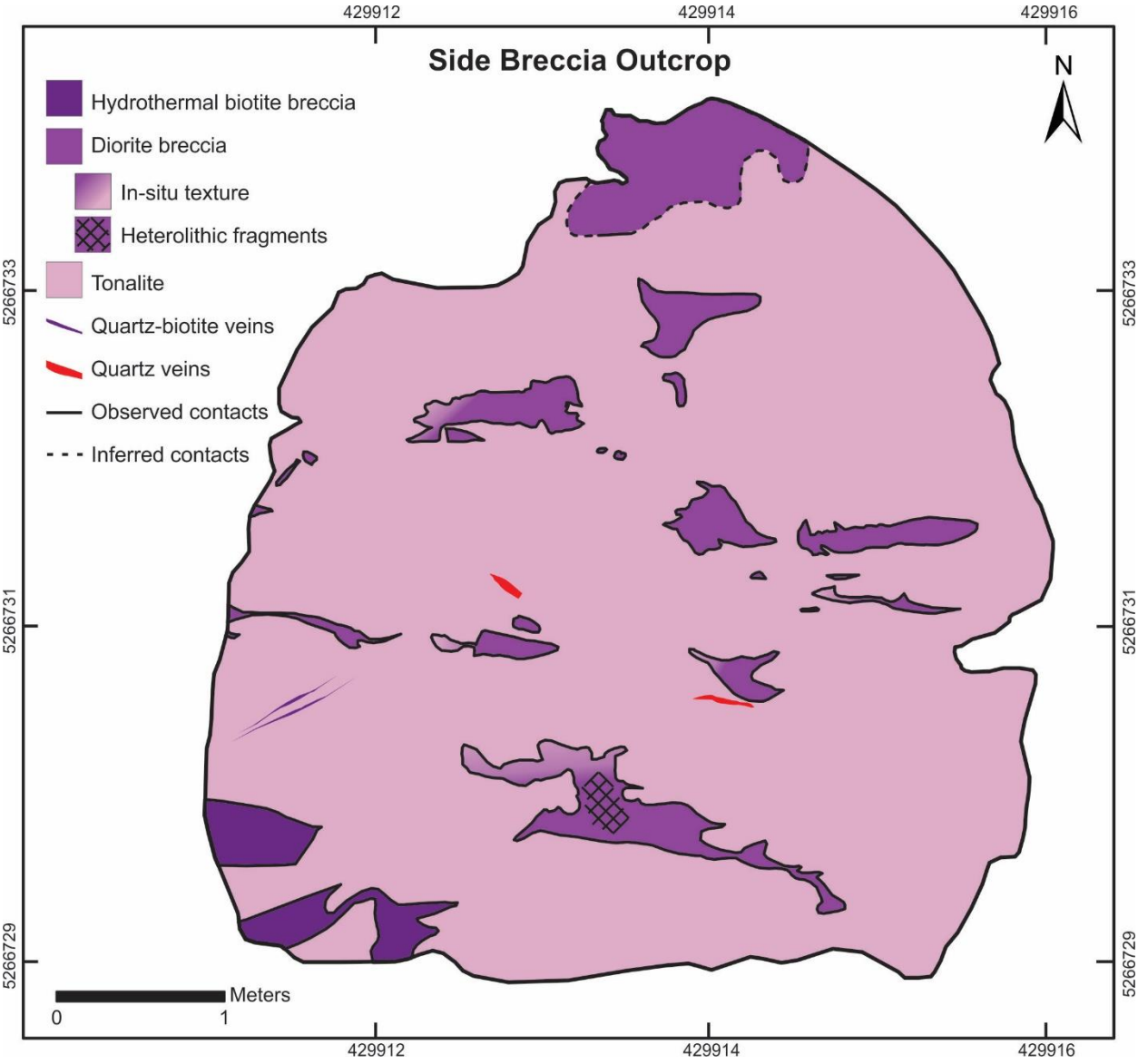

Figure B.2. Geological map of the Side Breccia Outcrop that shows the distribution and shape of small breccia bodies in tonalite. In-situ brecciation textures occur along the margins of the breccia units. In the largest breccia body the fragments are heterolithic (i.e., tonalite and diorite fragments), which suggests transport of tonalite and diorite.

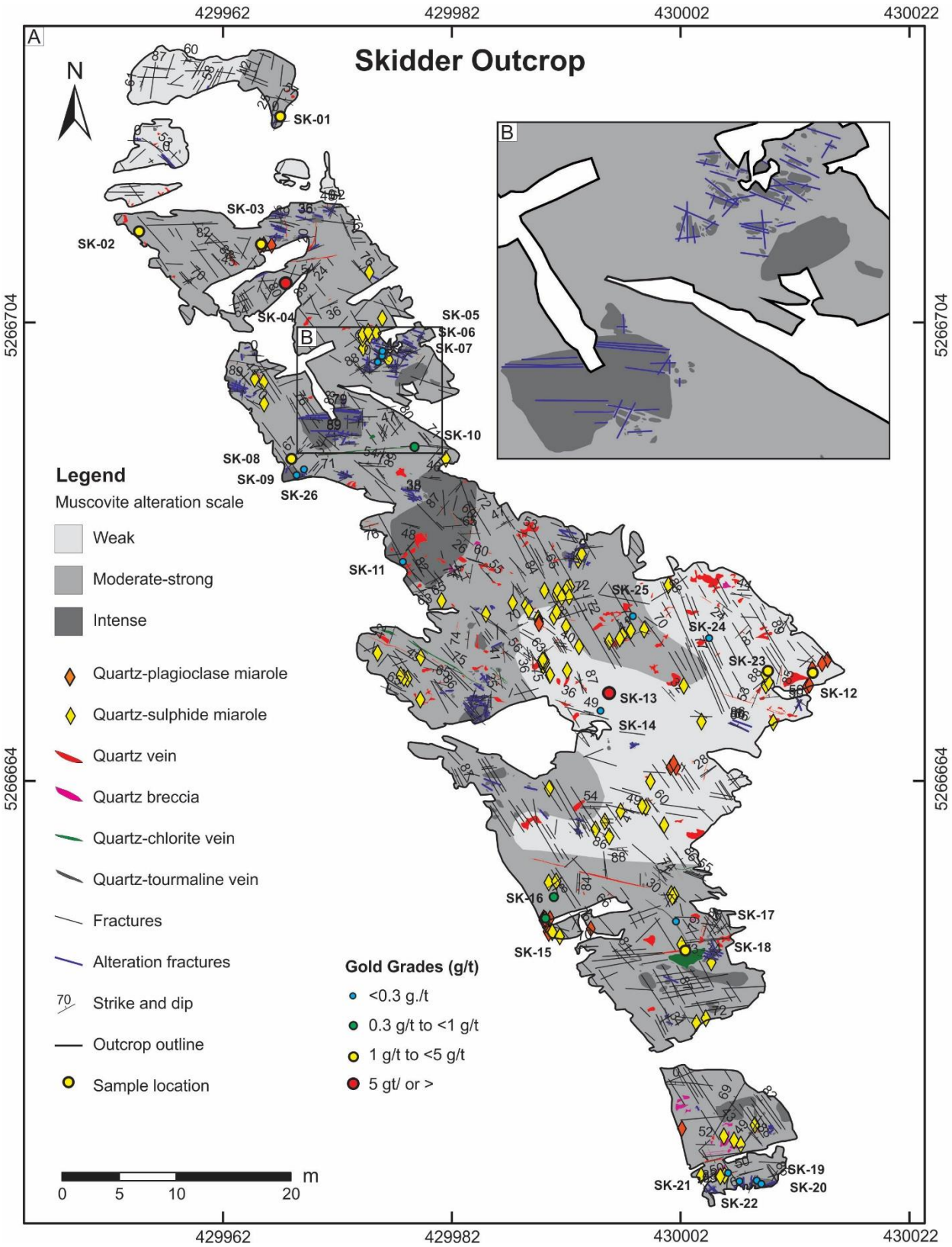
Skidder Outcrop
A
B
N
429962
429982
430002
430022
5266704
5266664
SK-01
SK-02
SK-03
SK-04
SK-05
SK-06
SK-07
SK-08
SK-09
SK-10
SK-11
SK-12
SK-13
SK-14
SK-15
SK-16
SK-17
SK-18
SK-19
SK-20
SK-21
SK-22
SK-23
SK-24
SK-25
SK-26
Legend
Muscovite alteration scale
Weak
Moderate-strong
Intense
Quartz-plagioclase miarole
Quartz-sulphide miarole
Quartz vein
Quartz breccia
Quartz-chlorite vein
Quartz-tourmaline vein
Fractures
Alteration fractures
Strike and dip
Outcrop outline
Sample location
Gold Grades (g/t)
<0.3 g./t
0.3 g/t to <1 g/t
1 g/t to <5 g/t
5 gt/ or >
0
5
10
20
m

Figure B.3. A) Alteration map of the Skidder Outcrop that shows the intensity and distribution of muscovite alteration. Areas of strong muscovite alteration correspond to weak areas of albite alteration (see Figure B.4). B) Close-up of fracture-controlled albite alteration, which overprints muscovite alteration, and follows three dominant orientations: 190-202º, 310-326º and 260-275º. The orientations of fracture-controlled albite alteration correspond to the orientations at the 53 Outcrop. Gold assays, along with samples numbers (i.e., SK-01) are included in the map. Gold assay results are presented in Table B.5 and selected samples for geochemical data are found in Table B.6. The outcrop was mapped by Laura Katz and Joycelyn Smith.

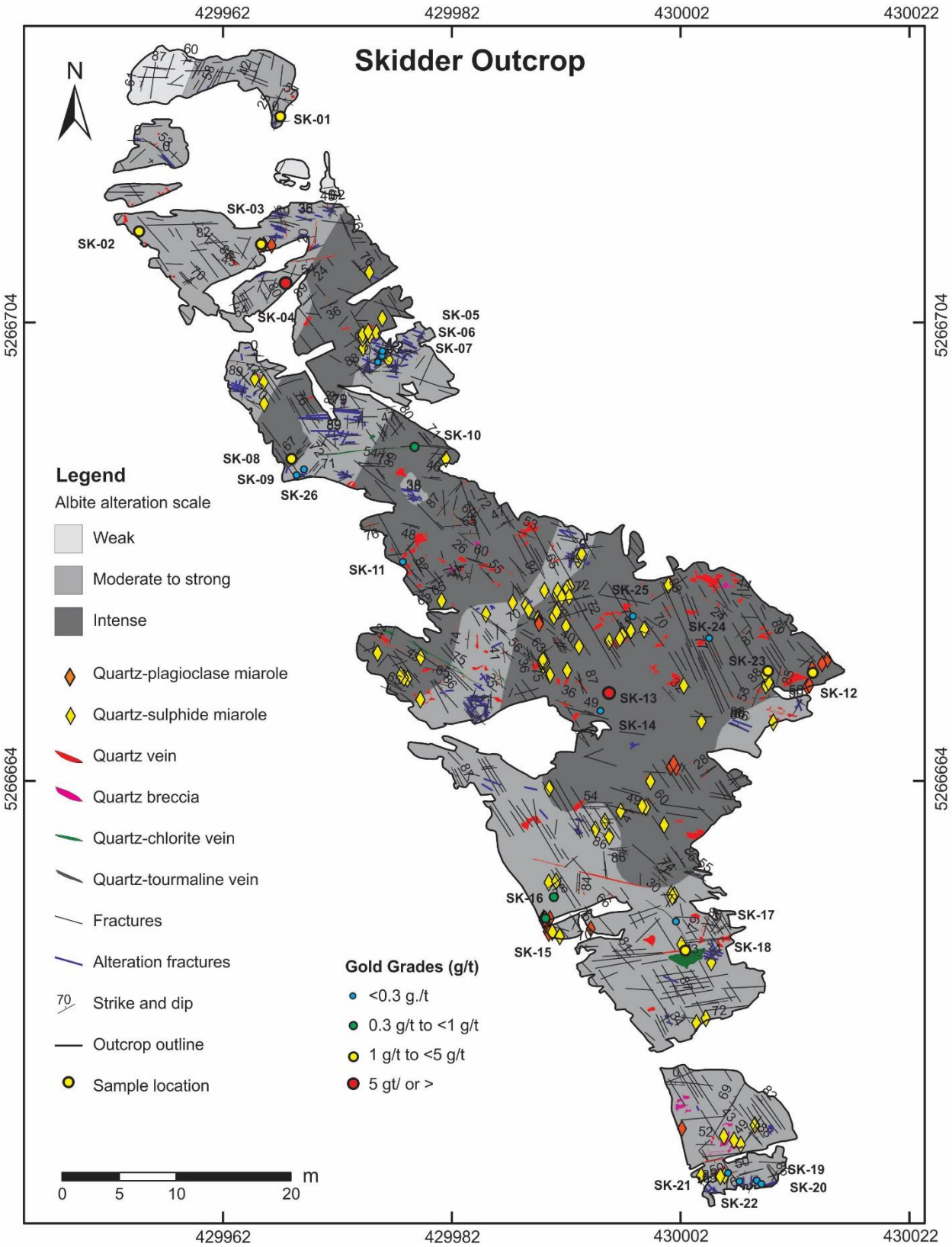
Skidder Outcrop
N
429962
429982
430002
430022
5266704
5266664
SK-01
SK-02
SK-03
SK-04
SK-05
SK-06
SK-07
SK-08
SK-09
SK-10
SK-11
SK-12
SK-13
SK-14
SK-15
SK-16
SK-17
SK-18
SK-19
SK-20
SK-21
SK-22
SK-23
SK-24
SK-25
SK-26
Legend
Albite alteration scale
Weak
Moderate to strong
Intense
Quartz-plagioclase miarole
Quartz-sulphide miarole
Quartz vein
Quartz breccia
Quartz-chlorite vein
Quartz-tourmaline vein
Fractures
Alteration fractures
Strike and dip
Outcrop outline
Sample location
Gold Grades (g/t)
<0.3 g./t
0.3 g/t to <1 g/t
1 g/t to <5 g/t
5 gt/ or >
0
5
10
20
m

Figure B.4. Alteration map of the Skidder Outcrop that shows the intensity and distribution of albite alteration. Gold assays, along with samples numbers (i.e., SK-01) are included in the map. Gold assay results are presented in Table B.5 and selected samples for geochemical data are found in Table B.6. The outcrop was mapped by Laura Katz and Joycelyn Smith.

Table B.1. Gold assay results with sample descriptions for the Skidder and 53 Outcrops

Field Name	Au (g/t)	Sample Description
53-01	1.63	E-W trending quartz-sulphide vein
53-02	4.076	Quartz-sulphide miarole
53-03	0.637	Pervasive muscovite altered tonalite
53-04	0.056	Pervasive albite altered tonalite
53-05	0.202	Pervasive muscovite altered tonalite
53-06	1.873	Pervasive albite altered tonalite
53-07	0.315	Pervasive muscovite altered tonalite
53-08	1.306	Pervasive albite altered tonalite
53-09	0.307	Pervasive muscovite altered tonalite
53-10	1.166	Diorite breccia
53-11	0.073	Tonalite breccia
53-12	0.133	Muscovite alteration halo around E-W quartz-sulphide vein
53-13	26.082	E-W trending quartz-sulphide vein
53-14	0.211	Quartz-tourmaline vein
53-15	27.865	Molybdenite sample in albite altered tonalite
53-16	2.017	Quartz-sulphide miarole
53-17	2.66	E-W trending quartz-sulphide vein
53-18	7.414	E-W trending quartz-sulphide vein
53-19	8.013	Pervasive albite altered tonalite
Sk-01	0.258	Diorite breccia
Sk-02	3.471	Pervasive albite altered diorite
Sk-03	2.517	Plagioclase-quartz miarole
Sk-04	24.382	Diorite breccia
Sk-05	0.136	Fracture-controlled albite alteration in tonalite
Sk-06	0.092	Pervasive muscovite altered tonalite
Sk-07	0.246	Pervasive albite altered tonalite
Sk-08	0.207	Fracture-controlled albite alteration in tonalite
Sk-09	0.007	Pervasive muscovite altered tonalite
Sk-10	0.311	E-W trending quartz-sulphide vein
Sk-11	0.191	Shallowly dipping, blobby quartz vein
Sk-12	2.685	Plagioclase-quartz miarole
Sk-13	12.644	Quartz-sulphide miarole
Sk-14	0.167	Sheared tonalite
Sk-15	0.795	Plagioclase-quartz miarole
Sk-16	0.544	Sheared tonalite
Sk-17	0.031	Quartz-tourmaline vein
Sk-18	2.777	E-W trending quartz-sulphide vein overprinted by shear
Sk-19	0.106	Fracture-controlled albite alteration in tonalite
Sk-20	0.006	Pervasive muscovite altered tonalite
Sk-21	0.009	E-W trending quartz-sulphide vein
Sk-22	0.015	Pervasive albite altered tonalite
Sk-23	2.299	Quartz-sulphide miarole
Sk-24	0.079	Shallowly dipping, blobby quartz vein
Sk-25	0.021	Pervasive albite altered tonalite
Sk-26	2.459	Pervasive albite altered tonalite

Table B.2. Major and trace element results from selected samples from the Skidder and 53 Outcrops

Sample Name	Au	Hg	S	Al	Fe	Mg	Mn	Ca	K	Ti	P	Sc	Be	V	Cr
53-03	0.637	<1	0.03	4.99	1.11	0.4	181	0.46	0.1	380	213	5	<2	11	722
53-04	0.056	<1	0.02	4.66	0.44	0.26	<100	0.52	0.26	433	<100	3	<2	7	55
53-15	27.865	<1	0.06	4.72	0.89	0.33	204	0.96	0.07	500	<100	3	<2	11	707
Sk-03	2.517	<1	0.03	6.06	0.53	0.24	135	1.04	0.03	153	<100	<1	2	4	482
Sk-05	0.136	<1	0.06	5.13	1.19	0.34	173	1.02	0.09	392	<100	3	2	11	461
Sk-06	0.092	<1	0.09	5.1	1.5	0.39	174	1.22	0.15	413	117	3	2	11	357
Sk-07	0.246	<1	0.03	4.89	0.38	0.21	<100	0.75	<0.01	272	<100	<1	2	4	31
Sk-10	0.311	<1	0.03	4.43	0.88	0.36	339	0.54	<0.01	520	<100	2	<2	9	249
Sk-15	0.795	<1	0.02	4.25	0.41	0.2	107	0.42	0.16	194	<100	<1	<2	3	308
Sk-17	0.031	<1	0.06	6.52	1.02	0.21	281	1.86	<0.01	4215	<100	1	3	12	431

Table B.2. Continued

Sample Name	Co	Ni	Cu	Ga	Ge	As	Rb	Sr	Y	Zr	Nb	Mo	Ag	In	Sn
53-03	6	340	307	15	<1	15	4	84	51.6	<1	7	21	<1	<1	<10
53-04	1	39	48	12	<1	10	12	71	19.8	<1	5	7	<1	1	<10
53-15	5	322	128	12	<1	21	1	71	14.8	9	5	403	4	<1	<10
Sk-03	3	235	28	16	<1	10	21	175	5.8	18	4	18	<1	<1	<10
Sk-05	5	227	99	14	<1	13	24	109	35.1	18	5	14	<1	<1	<10
Sk-06	5	181	116	14	<1	22	20	115	35.7	15	7	14	<1	<1	<10
Sk-07	<1	30	26	12	<1	17	33	98	14.4	<1	4	6	<1	<1	<10
Sk-10	3	136	42	10	<1	19	34	81	24.1	2	4	11	<1	<1	<10
Sk-15	2	160	25	10	<1	8	12	99	4.4	<1	3	13	<1	<1	<10
Sk-17	9	199	16	13	<1	13	47	263	75.3	46	7	14	<1	<1	<10

Table B.2. Continued

Sample Name	Sb	Ba	La	Ce	Nd	Pr	Sm	Eu	Gd	Tb	Dy	Ho	Er	Tm	Yb
53-03	<5	125	63.6	126.0	55.3	14.8	10.0	1.5	10.2	1.6	8.6	1.7	4.9	0.7	4.6
53-04	5	73	3.0	8.2	5.7	1.2	1.9	0.3	2.5	0.5	3.0	0.7	1.9	0.3	2.2
53-15	8	157	2.2	5.1	4.5	1.0	1.4	0.3	1.8	0.4	2.4	0.6	1.7	0.3	1.9
Sk-03	<5	88	1.0	2.0	1.4	0.3	0.4	0.1	0.5	0.1	0.7	0.2	0.6	0.1	0.9
Sk-05	5	133	21.3	44.7	20.6	5.0	4.9	0.6	5.4	1.0	6.1	1.3	3.7	0.6	3.9
Sk-06	6	171	32.0	67.2	29.9	7.8	6.4	0.7	6.5	1.1	6.2	1.3	3.8	0.6	4.0
Sk-07	<5	129	3.5	9.5	8.4	1.8	2.2	0.3	2.2	0.4	2.4	0.5	1.6	0.3	1.9
Sk-10	6	379	3.9	11.2	7.7	1.6	2.3	0.3	2.9	0.6	4.0	0.9	2.5	0.4	2.6
Sk-15	<5	69	1.3	3.1	2.2	0.5	0.7	0.1	0.7	0.1	0.8	0.2	0.4	0.1	0.5
Sk-17	8	84	8.4	35.4	33.5	6.4	10.3	1.1	10.8	1.9	12.0	2.7	8.6	1.3	9.9

Table B.2. Continued

Sample Name	Lu	Hf	Ta	W	Tl	Pb	Th	U	Te	Se	Bi	Cd	Li	Zn
53-03	0.7	<1	3	<10	<2	3	8.7	1	<1	24	3	<4	1	9
53-04	0.4	<1	<1	<10	<2	2	9.3	1	<1	22	4	<4	<1	<1
53-15	0.3	<1	<1	<10	<2	4	12.5	1	<1	24	3	<4	1	17
Sk-03	0.1	1	2	<10	<2	<1	0.5	<1	<1	26	4	<4	<1	7
Sk-05	0.6	<1	<1	<10	<2	5	11.3	2	<1	21	2	<4	2	33
Sk-06	0.6	1	<1	<10	<2	10	12.3	3	<1	20	4	<4	5	39
Sk-07	0.3	<1	<1	<10	<2	9	13.2	2	3	24	3	<4	<1	11
Sk-10	0.4	<1	1	<10	<2	7	5.9	1	1	17	5	<4	2	7
Sk-15	0.1	<1	<1	<10	<2	4	1.1	<1	<1	24	3	<4	<1	3
Sk-17	1.2	2	1	<10	<2	5	7.8	4	3	24	1	<4	6	7

Note: Au is in g/t, S, Al, Fe, Mg, Ca and K are in wt. % and the trace elements are in ppm

Appendix C

Table C.1 Microprobe analyses showing major elements (wt. %) and structural formula for calcic amphiboles

		Breccia											
	L.O.D	Bx1-1	Bx1-2	Bx1-3	Bx1-4	Bx1-5	Bx1-6	Bx2-1	Bx2-2	Bx2-3	Bx2-4	Bx2-5	Bx3-1
SiO_2	0.04	49.07	50.15	50.46	50.98	51.22	50.39	50.45	50.39	50.65	50.96	51.81	49.68
TiO_2	0.03	0.82	0.73	0.52	0.58	0.44	0.36	0.52	0.67	0.54	0.61	0.43	0.80
Al_2O_3	0.02	4.94	3.98	3.60	3.66	3.27	3.93	4.27	3.93	3.74	3.74	3.20	4.92
FeO	0.03	16.98	15.88	16.06	13.44	14.74	16.62	16.45	16.31	16.34	14.89	14.51	16.40
Cr_2O_3	0.03	b.d.l.	b.d.l.	b.d.l.	b.d.l.	0.01	b.d.l.	b.d.l.	b.d.l.	b.d.l.	b.d.l.	b.d.l.	b.d.l.
MnO	0.03	0.32	0.27	0.31	0.27	0.29	0.24	0.32	0.31	0.34	0.26	0.28	0.29
MgO	0.03	12.49	13.34	13.44	15.13	14.43	12.81	12.81	13.30	13.24	13.96	14.42	12.79
CaO	0.03	11.54	11.66	11.43	11.79	11.63	11.83	11.78	11.40	11.25	11.73	11.58	11.45
Na_2O	0.03	0.78	0.64	0.74	0.62	0.59	0.58	0.63	0.61	0.66	0.63	0.50	0.68
K_2O	0.02	0.54	0.40	0.34	0.35	0.34	0.34	0.40	0.42	0.37	0.36	0.32	0.52
F	0.10	0.21	0.27	0.49	0.47	0.40	0.17	0.19	0.22	0.18	0.27	0.34	0.21
Cl	0.01	0.21	0.15	0.12	0.13	0.12	0.15	0.21	0.19	0.14	0.14	0.11	0.18
Subtotal		97.90	97.47	97.50	97.43	97.46	97.43	98.02	97.73	97.44	97.53	97.49	97.90
O = Cl,F		0.13	0.15	0.23	0.23	0.19	0.11	0.13	0.13	0.11	0.15	0.17	0.13
Total		97.77	97.32	97.27	97.20	97.27	97.32	97.89	97.60	97.33	97.38	97.32	97.77
Cations calculated on the basis of 23 (O, F, Cl) p.f.u. and the average ferric iron constraint (values obtained from the average 15eNK and 13 eCNK)													
Si p.f.u.		7.25	7.38	7.44	7.43	7.49	7.44	7.41	7.40	7.45	7.46	7.56	7.30
Al		0.76	0.62	0.56	0.57	0.51	0.56	0.59	0.61	0.55	0.54	0.45	0.70
Fe^{3+}		0	0	0	0	0	0	0	0	0	0	0	0
Ti		0	0	0	0	0	0	0	0	0	0	0	0
T sites		8	8	8	8	8	8	8	8	8	8	8	8
Al		0.10	0.08	0.06	0.05	0.05	0.12	0.15	0.07	0.09	0.11	0.10	0.15
Cr		0	0	0	0	0	0	0	0	0	0	0	0
Fe^{3+}		0.33	0.29	0.32	0.32	0.32	0.27	0.24	0.35	0.35	0.24	0.28	0.31
Ti		0.09	0.08	0.06	0.06	0.05	0.04	0.06	0.07	0.06	0.07	0.05	0.09
Mg		2.75	2.93	2.95	3.29	3.14	2.82	2.81	2.91	2.90	3.05	3.13	2.80
Fe^{2+}		1.71	1.61	1.59	1.26	1.42	1.73	1.74	1.57	1.58	1.52	1.42	1.64
Mn		0.02	0.02	0.02	0.02	0.02	0.02	0.02	0.02	0.02	0.02	0.02	0.02
Ca		0	0	0	0	0	0	0	0	0	0	0	0
C sites		5	5	5	5	5	5	5	5	5	5	5	5
Mg		0	0	0	0	0	0	0	0	0	0	0	0
Fe^{2+}		0.06	0.06	0.07	0.06	0.07	0.05	0.05	0.08	0.09	0.06	0.07	0.07
Mn		0.02	0.02	0.02	0.02	0.02	0.02	0.02	0.02	0.02	0.02	0.02	0.02
Ca		1.83	1.84	1.80	1.84	1.82	1.87	1.85	1.79	1.77	1.84	1.81	1.80
Na		0.09	0.09	0.10	0.09	0.08	0.07	0.08	0.09	0.09	0.09	0.07	0.10
B sites		2	2	2	2	1.99	2	2	1.98	1.97	2	1.97	1.99
Ca		0	0	0	0	0	0	0	0	0	0	0	0
Na		0.13	0.10	0.11	0.09	0.08	0.10	0.10	0.09	0.10	0.09	0.07	0.10
K		0.10	0.08	0.06	0.07	0.06	0.06	0.08	0.08	0.07	0.07	0.06	0.10
A sites		0.23	0.17	0.17	0.16	0.15	0.16	0.18	0.17	0.16	0.16	0.13	0.20
cations		15.23	15.17	15.17	15.16	15.14	15.16	15.18	15.14	15.14	15.16	15.10	15.19
Cl		0.05	0.04	0.03	0.03	0.03	0.04	0.05	0.05	0.04	0.03	0.03	0.05
F		0.10	0.12	0.23	0.22	0.18	0.08	0.09	0.10	0.09	0.13	0.16	0.10
oxygen		23	23	23	23	23	23	23	23	23.01	23.01	23.02	23.01
Cl/(Cl + F)		0.35	0.23	0.12	0.13	0.14	0.31	0.38	0.32	0.29	0.21	0.15	0.31
Fe^{3+}/Fe^{2+}		0.19	0.18	0.20	0.26	0.22	0.16	0.14	0.22	0.22	0.16	0.20	0.19
Mg/(Mg+ΣFe)		0.57	0.60	0.60	0.67	0.64	0.58	0.58	0.59	0.59	0.63	0.64	0.58
$Mg/(Mg+Fe^{2+})$		0.61	0.64	0.64	0.71	0.68	0.61	0.61	0.64	0.64	0.66	0.68	0.62

Table C.1 Continued

	Breccia												
	Bx3-2	Bx3-3	Bx3-4	Bx3-5	Bx3-6	Bx3-7	Bxb1-1	Bxb1-2	Bxb2-1	Bxb2-2	Bxb3-1	Bxb3-2	Bxb4-1
SiO_2	50.43	51.18	51.48	51.72	48.87	50.58	39.36	40.11	40.06	39.68	40.07	40.76	42.05
TiO_2	0.73	0.65	0.57	0.32	0.49	0.23	0.25	0.24	0.29	0.27	0.24	0.28	0.35
Al_2O_3	3.96	3.99	3.57	3.96	4.71	3.98	16.32	15.81	16.10	16.34	15.71	15.01	13.83
FeO	15.84	14.38	14.28	12.33	19.95	17.38	22.82	21.71	21.97	22.38	22.51	21.64	21.61
Cr_2O_3	b.d.l.	b.d.l.	0.03	0.01	b.d.l.	b.d.l.	0.05	0.04	b.d.l.	b.d.l.	0.04	0.04	0.05
MnO	0.28	0.30	0.27	0.19	0.24	0.21	0.18	0.16	0.16	0.16	0.17	0.18	0.17
MgO	13.26	14.53	14.57	15.92	10.67	12.26	4.73	5.59	5.55	5.23	5.34	6.09	6.60
CaO	11.59	11.60	11.75	12.24	11.52	11.98	11.25	11.29	11.34	11.30	11.34	11.41	11.22
Na_2O	0.71	0.63	0.60	0.72	0.71	0.47	1.59	1.68	1.73	1.62	1.66	1.67	1.56
K_2O	0.40	0.36	0.32	0.30	0.43	0.26	0.47	0.40	0.45	0.54	0.48	0.41	0.34
F	0.31	0.32	0.33	0.41	0.07	0.17	0.19	0.20	0.20	0.24	0.24	0.28	0.15
Cl	0.16	0.14	0.12	0.09	0.22	0.14	0.15	0.11	0.13	0.14	0.11	0.09	0.08
Subtotal	97.67	98.07	97.85	98.20	97.86	97.66	97.30	97.29	97.97	97.88	97.87	97.82	97.95
O = Cl,F	0.16	0.17	0.16	0.19	0.08	0.10	0.11	0.11	0.11	0.13	0.13	0.14	0.08
Total	97.51	97.90	97.69	98.01	97.78	97.56	97.19	97.18	97.86	97.75	97.74	97.68	97.87
Cations calculated on the basis of 23 (O, F, Cl) p.f.u. and the average ferric iron constraint (values obtained from the average 15eNK and 13 eCNK)													
Si p.f.u.	7.42	7.42	7.48	7.43	7.30	7.46	6.05	6.13	6.09	6.05	6.11	6.19	6.35
Al	0.58	0.58	0.52	0.57	0.71	0.54	1.96	1.87	1.91	1.95	1.89	1.81	1.65
Fe^{3+}	0	0	0	0	0	0	0	0	0	0	0	0	0
Ti	0	0	0	0	0	0	0	0	0	0	0	0	0
T sites	8	8	8	8	8	8	8	8	8	8	8	8	8
Al	0.11	0.10	0.09	0.10	0.12	0.15	1.00	0.97	0.97	0.98	0.93	0.88	0.81
Cr	0	0	0	0	0	0	0.01	0	0	0	0	0.01	0.01
Fe^{3+}	0.25	0.31	0.27	0.27	0.35	0.26	0.49	0.43	0.44	0.49	0.47	0.44	0.44
Ti	0.08	0.07	0.06	0.04	0.06	0.03	0.03	0.03	0.03	0.03	0.03	0.03	0.04
Mg	2.91	3.14	3.16	3.41	2.37	2.70	1.08	1.27	1.26	1.19	1.21	1.38	1.48
Fe^{2+}	1.64	1.36	1.40	1.17	2.08	1.85	2.39	2.29	2.29	2.30	2.34	2.25	2.22
Mn	0.02	0.02	0.02	0.01	0.02	0.01	0.01	0.01	0.01	0.01	0.01	0.01	0.01
Ca	0	0	0	0	0	0	0	0	0	0	0	0	0
C sites	5	5	5	5	5	5	5	5	5	5	5	5	5
Mg	0	0	0	0	0	0	0	0	0	0	0	0	0
Fe^{2+}	0.06	0.07	0.06	0.04	0.06	0.04	0.06	0.06	0.06	0.06	0.06	0.06	0.08
Mn	0.02	0.02	0.02	0.01	0.02	0.01	0.01	0.01	0.01	0.01	0.01	0.01	0.01
Ca	1.83	1.80	1.83	1.88	1.84	1.89	1.85	1.85	1.85	1.85	1.85	1.86	1.81
Na	0.09	0.09	0.08	0.06	0.08	0.06	0.08	0.08	0.08	0.08	0.08	0.08	0.10
B sites	2	1.98	1.99	2	2	2	2	2	2	2	2	2	2
Ca	0	0	0	0	0	0	0	0	0	0	0	0	0
Na	0.11	0.09	0.09	0.14	0.12	0.08	0.39	0.42	0.43	0.40	0.41	0.42	0.36
K	0.08	0.07	0.06	0.06	0.08	0.05	0.09	0.08	0.09	0.10	0.09	0.08	0.07
A sites	0.19	0.16	0.14	0.19	0.20	0.13	0.49	0.49	0.52	0.50	0.50	0.50	0.42
cations	15.19	15.14	15.14	15.19	15.20	15.13	15.49	15.49	15.52	15.50	15.50	15.50	15.42
Cl	0.04	0.03	0.03	0.02	0.06	0.04	0.04	0.03	0.03	0.04	0.03	0.02	0.02
F	0.14	0.15	0.15	0.19	0.03	0.08	0.09	0.10	0.10	0.12	0.12	0.13	0.07
oxygen	23.02	23.01	23.01	23	23	23	23	23	23	23	23	23	23
Cl/(Cl + F)	0.22	0.18	0.16	0.11	0.64	0.31	0.29	0.24	0.25	0.23	0.20	0.14	0.22
Fe^{3+}/Fe^{2+}	0.15	0.23	0.19	0.23	0.17	0.14	0.20	0.19	0.19	0.21	0.20	0.20	0.20
Mg/(Mg+ΣFe)	0.60	0.64	0.65	0.70	0.49	0.56	0.27	0.31	0.31	0.29	0.30	0.33	0.35
$Mg/(Mg+Fe^{2+})$	0.63	0.69	0.68	0.74	0.53	0.59	0.31	0.35	0.35	0.33	0.34	0.37	0.39

Table C.1 Continued

	Breccia								Diorite			
	Bxb5-1	Bxb5-2	Bxb6-1	Bxb6-2	Bxb7-1	Bxb7-2	Bxb8-1	Bxb8-2	DR1-1	DR1-2	DR1-3	DR1-4
SiO_2	40.98	39.40	40.32	40.13	39.93	39.98	40.52	40.12	43.90	49.00	45.34	44.56
TiO_2	0.28	0.23	0.25	0.27	0.26	0.36	0.30	0.24	1.09	0.76	1.05	0.98
Al_2O_3	14.74	16.57	15.52	15.63	15.93	15.62	15.30	16.21	8.31	4.67	7.15	8.14
FeO	22.69	22.14	21.97	21.57	22.02	22.13	21.82	21.79	22.24	18.95	21.09	21.67
Cr_2O_3	b.d.l.	b.d.l.	0.04	b.d.l.	b.d.l.	b.d.l.	b.d.l.	b.d.l.	0.04	b.d.l.	0.04	0.05
MnO	0.17	0.16	0.15	0.18	0.16	0.16	0.15	0.15	0.22	0.30	0.21	0.24
MgO	5.54	5.13	5.63	5.96	5.42	5.58	5.90	5.77	8.20	11.42	9.24	8.74
CaO	11.07	11.29	11.21	11.13	11.15	11.04	11.08	11.20	11.48	11.26	11.67	11.28
Na_2O	1.61	1.65	1.69	1.68	1.68	1.71	1.65	1.71	1.11	0.81	0.99	1.09
K_2O	0.40	0.55	0.42	0.40	0.45	0.48	0.39	0.50	1.07	0.54	0.82	1.00
F	0.21	0.13	0.16	0.28	0.16	0.28	0.25	0.18	0.27	0.26	0.22	0.24
Cl	0.12	0.18	0.10	0.11	0.13	0.15	0.10	0.14	0.78	0.29	0.64	0.70
Subtotal	97.82	97.42	97.40	97.34	97.28	97.48	97.45	98.01	98.66	98.24	98.41	98.65
O = Cl,F	0.12	0.09	0.09	0.14	0.09	0.15	0.13	0.11	0.29	0.17	0.24	0.26
Total	97.70	97.33	97.31	97.20	97.19	97.33	97.32	97.90	98.37	98.07	98.17	98.39
Cations calculated on the basis of 23 (O, F, Cl) p.f.u. and the average ferric iron constraint (values obtained from the average 15eNK and 13 eCNK)												
Si p.f.u.	6.24	6.03	6.15	6.12	6.11	6.11	6.17	6.08	6.70	7.28	6.87	6.76
Al	1.76	1.97	1.85	1.88	1.89	1.89	1.83	1.92	1.30	0.72	1.13	1.25
Fe^{3+}	0	0	0	0	0	0	0	0	0	0	0	0
Ti	0	0	0	0	0	0	0	0	0	0	0	0
T sites	8	8	8	8	8	8	8	8	8	8	8	8
Al	0.89	1.02	0.94	0.92	0.98	0.93	0.92	0.97	0.20	0.09	0.14	0.21
Cr	0	0	0	0	0	0	0	0	0.01	0	0	0.01
Fe^{3+}	0.46	0.46	0.44	0.51	0.46	0.48	0.48	0.49	0.44	0.35	0.41	0.47
Ti	0.03	0.03	0.03	0.03	0.03	0.04	0.03	0.03	0.13	0.09	0.12	0.11
Mg	1.26	1.17	1.28	1.36	1.24	1.27	1.34	1.30	1.87	2.53	2.09	1.98
Fe^{2+}	2.35	2.31	2.29	2.16	2.29	2.27	2.22	2.20	2.36	1.93	2.22	2.21
Mn	0.01	0.01	0.01	0.01	0.01	0.01	0.01	0.01	0.01	0.02	0.01	0.02
Ca	0	0	0	0	0	0	0	0	0	0	0	0
C sites	5	5	5	5	5	5	5	5	5	5	5	5
Mg	0	0	0	0	0	0	0	0	0	0	0	0
Fe^{2+}	0.08	0.06	0.07	0.07	0.07	0.08	0.08	0.08	0.04	0.08	0.04	0.06
Mn	0.01	0.01	0.01	0.01	0.01	0.01	0.01	0.01	0.01	0.02	0.01	0.02
Ca	1.81	1.85	1.83	1.82	1.83	1.81	1.81	1.82	1.88	1.79	1.89	1.83
Na	0.10	0.08	0.09	0.10	0.09	0.10	0.10	0.10	0.07	0.11	0.06	0.09
B sites	2	2	2	2	2	2	2	2	2	2	2	2
Ca	0	0	0	0	0	0	0	0	0	0	0	0
Na	0.37	0.41	0.41	0.40	0.41	0.40	0.39	0.41	0.26	0.12	0.23	0.23
K	0.08	0.11	0.08	0.08	0.09	0.09	0.08	0.10	0.21	0.10	0.16	0.19
A sites	0.45	0.52	0.49	0.48	0.49	0.50	0.46	0.50	0.47	0.23	0.39	0.43
cations	15.45	15.52	15.49	15.48	15.49	15.50	15.46	15.50	15.47	15.23	15.39	15.43
Cl	0.03	0.05	0.03	0.03	0.03	0.04	0.03	0.04	0.20	0.07	0.17	0.18
F	0.10	0.06	0.08	0.14	0.08	0.14	0.12	0.09	0.13	0.12	0.11	0.12
oxygen	23	23	23	23	23	23	23	23	23	23	23	23
Cl/(Cl + F)	0.24	0.43	0.24	0.17	0.31	0.22	0.17	0.29	0.61	0.37	0.61	0.61
Fe^{3+}/Fe^{2+}	0.19	0.20	0.19	0.24	0.20	0.21	0.22	0.22	0.19	0.18	0.19	0.21
Mg/(Mg+ΣFe)	0.30	0.29	0.31	0.33	0.31	0.31	0.33	0.32	0.40	0.52	0.44	0.42
$Mg/(Mg+Fe^{2+})$	0.34	0.33	0.35	0.38	0.34	0.35	0.37	0.36	0.44	0.56	0.48	0.46

Table C.1 Continued

	Diorite											
	DR1-5	DR1-6	DR2-1	DR2-2	DR2-3	DR2-4	DR2-5	DR3-1	DR3-2	DR3-3	DR3-4	DR3-5
SiO_2	49.18	39.93	48.61	49.14	48.63	48.85	48.07	49.41	50.24	48.25	48.42	40.59
TiO_2	0.47	0.27	0.53	0.25	0.59	0.53	0.59	0.72	0.54	0.69	0.62	0.26
Al_2O_3	4.58	15.09	4.30	4.15	4.22	4.51	4.66	4.18	4.04	5.44	5.55	14.67
FeO	18.27	21.55	21.73	22.49	21.37	20.50	20.48	19.15	17.52	19.41	18.64	21.93
Cr_2O_3	0.08	0.06	b.d.l.	b.d.l.	0.03	0.03	0.04	0.03	b.d.l.	0.04	b.d.l.	0.06
MnO	0.27	0.24	0.23	0.28	0.27	0.26	0.30	0.31	0.24	0.26	0.24	0.22
MgO	11.48	6.16	9.59	9.13	9.75	10.32	10.17	11.57	12.21	10.78	11.01	6.49
CaO	11.52	11.23	11.37	11.40	11.31	11.12	11.22	10.96	11.75	11.52	11.77	11.39
Na_2O	0.70	1.65	0.66	0.60	0.62	0.80	0.77	0.73	0.59	0.80	0.76	1.68
K_2O	0.45	0.58	0.42	0.39	0.45	0.43	0.52	0.45	0.38	0.58	0.52	0.66
F	0.18	0.30	0.25	0.17	0.22	0.19	0.26	0.31	0.28	0.23	0.35	0.33
Cl	0.30	0.10	0.40	0.34	0.41	0.34	0.36	0.35	0.21	0.36	0.30	0.14
Subtotal	97.39	97.10	98.09	98.33	97.85	97.86	97.39	98.14	97.98	98.30	98.19	98.34
O = Cl,F	0.15	0.15	0.20	0.15	0.19	0.16	0.19	0.21	0.17	0.18	0.22	0.17
Total	97.24	96.95	97.89	98.18	97.66	97.70	97.20	97.93	97.81	98.12	97.97	98.17
Cations calculated on the basis of 23 (O, F, Cl) p.f.u. and the average ferric iron constraint (values obtained from the average 15eNK and 13 eCNK)												
Si p.f.u.	7.34	6.12	7.33	7.40	7.34	7.33	7.27	7.33	7.42	7.19	7.21	6.15
Al	0.66	1.88	0.67	0.61	0.66	0.67	0.73	0.66	0.58	0.81	0.79	1.85
Fe^{3+}	0	0	0	0	0	0	0	0.01	0	0	0	0
Ti	0	0	0	0	0	0	0	0	0	0	0	0
T sites	8	8	8	8	8	8	8	8	8	8	8	8
Al	0.14	0.84	0.09	0.13	0.09	0.12	0.10	0.07	0.12	0.15	0.19	0.76
Cr	0.01	0.01	0	0	0	0	0.01	0	0	0.01	0	0.01
Fe^{3+}	0.28	0.54	0.36	0.34	0.35	0.34	0.37	0.42	0.25	0.33	0.27	0.56
Ti	0.05	0.03	0.06	0.03	0.07	0.06	0.07	0.08	0.06	0.08	0.07	0.03
Mg	2.55	1.41	2.16	2.05	2.19	2.31	2.29	2.56	2.69	2.39	2.45	1.47
Fe^{2+}	1.94	2.16	2.32	2.44	2.28	2.15	2.16	1.85	1.87	2.03	2.01	2.16
Mn	0.02	0.02	0.01	0.02	0.02	0.02	0.02	0.02	0.02	0.02	0.02	0.01
Ca	0	0	0	0	0	0	0	0	0	0	0	0
C sites	5	5	5	5	5	5	5	5	5	5	5	5
Mg	0	0	0	0	0	0	0	0	0	0	0	0
Fe^{2+}	0.06	0.06	0.06	0.06	0.06	0.08	0.07	0.10	0.05	0.06	0.04	0.06
Mn	0.02	0.02	0.02	0.02	0.02	0.02	0.02	0.02	0.02	0.02	0.02	0.01
Ca	1.84	1.84	1.84	1.84	1.83	1.79	1.82	1.74	1.86	1.84	1.88	1.85
Na	0.08	0.08	0.09	0.09	0.09	0.11	0.10	0.10	0.08	0.09	0.07	0.08
B sites	2	2	2	2	2	2	2	1.97	2	2	2	2
Ca	0	0	0	0	0	0	0	0	0	0	0	0
Na	0.12	0.41	0.10	0.09	0.09	0.12	0.13	0.11	0.09	0.15	0.15	0.41
K	0.09	0.11	0.08	0.07	0.09	0.08	0.10	0.09	0.07	0.11	0.10	0.13
A sites	0.20	0.52	0.19	0.16	0.18	0.20	0.23	0.19	0.17	0.26	0.25	0.54
cations	15.20	15.52	15.19	15.16	15.18	15.20	15.23	15.16	15.17	15.26	15.25	15.54
Cl	0.08	0.03	0.10	0.09	0.11	0.09	0.09	0.09	0.05	0.09	0.08	0.04
F	0.09	0.15	0.12	0.08	0.11	0.09	0.12	0.15	0.13	0.11	0.17	0.16
oxygen	23	23	23	23	23	23.003	23	23	23	23	23	23
Cl/(Cl + F)	0.47	0.16	0.46	0.52	0.50	0.49	0.43	0.38	0.28	0.46	0.31	0.19
Fe^{3+}/Fe^{2+}	0.15	0.25	0.16	0.14	0.15	0.16	0.17	0.22	0.13	0.16	0.14	0.26
Mg/(Mg+ΣFe)	0.53	0.34	0.44	0.42	0.45	0.47	0.47	0.52	0.55	0.50	0.51	0.35
$Mg/(Mg+Fe^{2+})$	0.56	0.39	0.48	0.45	0.48	0.51	0.51	0.57	0.58	0.53	0.54	0.40

Table C.1 Continued

	Quartz diorite										Vein	
	QDR1-1	QDR1-3	QDR1-4	QDR1-5	QDR2-1	QDR2-2	QDR2-3	QDR3-1	QDR3-2	QDR3-3	Vn1-1	Vn1-2
SiO_2	47.72	48.59	49.42	40.72	41.38	46.83	45.84	47.01	46.91	40.11	47.71	50.15
TiO_2	1.26	0.97	0.65	0.19	0.27	1.48	0.87	1.46	1.35	0.44	0.45	0.33
Al_2O_3	5.73	4.86	4.22	16.01	14.15	6.19	8.78	6.04	6.63	15.56	6.01	4.29
FeO	17.85	18.97	18.12	20.96	20.52	19.36	18.98	19.70	17.95	21.31	19.38	17.75
Cr_2O_3	b.d.l.	b.d.l.	b.d.l.	b.d.l.	b.d.l.	b.d.l.	b.d.l.	b.d.l.	b.d.l.	b.d.l.	b.d.l.	b.d.l.
MnO	0.29	0.34	0.33	0.24	0.19	0.35	0.21	0.34	0.26	0.24	0.16	0.18
MgO	11.64	11.88	12.10	6.18	6.94	10.92	9.83	10.80	10.89	6.18	10.48	11.88
CaO	10.93	10.48	11.18	11.50	11.35	10.41	11.59	10.20	11.33	11.37	11.90	12.03
Na_2O	0.82	0.75	0.68	1.61	1.45	0.94	1.13	0.91	0.89	1.57	0.78	0.54
K_2O	0.61	0.56	0.44	0.67	0.69	0.40	0.50	0.37	0.48	0.70	0.51	0.32
F	0.23	0.32	0.28	0.22	0.19	0.17	0.25	0.17	0.23	0.25	0.19	0.22
Cl	0.28	0.37	0.31	0.20	0.27	0.23	0.18	0.25	0.26	0.21	0.28	0.15
Subtotal	97.35	98.10	97.73	98.49	97.40	97.29	98.15	97.24	97.18	97.94	97.85	97.83
O = Cl,F	0.16	0.22	0.19	0.14	0.14	0.13	0.15	0.13	0.16	0.15	0.15	0.13
Total	97.19	97.88	97.54	98.35	97.26	97.16	98.00	97.11	97.02	97.79	97.70	97.70
Cations calculated on the basis of 23 (O, F, Cl) p.f.u. and the average ferric iron constraint (values obtained from the average 15eNK and 13 eCNK)												
Si p.f.u.	7.12	7.19	7.33	6.14	6.29	7.00	6.84	7.03	7.04	6.10	7.15	7.42
Al	0.88	0.78	0.67	1.86	1.71	1.00	1.16	0.96	0.96	1.91	0.86	0.58
Fe^{3+}	0	0.03	0	0	0	0	0	0.01	0	0	0	0
Ti	0	0	0	0	0	0	0	0	0	0	0	0
T sites	8	8	8	8	8	8	8	8	8	8	8	8
Al	0.12	0.07	0.07	0.98	0.83	0.09	0.39	0.10	0.21	0.88	0.20	0.17
Cr	0	0	0	0	0	0	0	0	0	0	0	0
Fe^{3+}	0.40	0.56	0.42	0.39	0.41	0.58	0.31	0.59	0.29	0.48	0.32	0.22
Ti	0.14	0.11	0.07	0.02	0.03	0.17	0.10	0.16	0.15	0.05	0.05	0.04
Mg	2.59	2.62	2.68	1.39	1.58	2.43	2.19	2.41	2.44	1.40	2.34	2.62
Fe^{2+}	1.73	1.62	1.75	2.20	2.14	1.71	2.00	1.71	1.90	2.17	2.07	1.94
Mn	0.02	0.02	0.02	0.02	0.01	0.02	0.01	0.02	0.02	0.02	0.01	0.01
Ca	0	0	0	0	0	0	0	0	0	0	0	0
C sites	5	5	5	5	5	5	5	5	5	5	5	5
Mg	0	0	0	0	0	0	0	0	0	0	0	0
Fe^{2+}	0.10	0.14	0.08	0.05	0.06	0.13	0.06	0.15	0.07	0.05	0.03	0.03
Mn	0.02	0.02	0.02	0.02	0.01	0.02	0.01	0.02	0.02	0.02	0.01	0.01
Ca	1.75	1.66	1.78	1.86	1.85	1.67	1.85	1.63	1.82	1.85	1.91	1.91
Na	0.12	0.11	0.10	0.08	0.08	0.14	0.08	0.13	0.10	0.08	0.05	0.05
B sites	1.98	1.93	1.98	2	2	1.96	2	1.94	2	2	2	2
Ca	0	0	0	0	0	0	0	0	0	0	0	0
Na	0.12	0.11	0.10	0.39	0.35	0.14	0.25	0.13	0.16	0.38	0.18	0.10
K	0.12	0.11	0.08	0.13	0.13	0.08	0.10	0.07	0.09	0.14	0.10	0.06
A sites	0.24	0.22	0.18	0.52	0.48	0.22	0.34	0.20	0.26	0.52	0.28	0.17
cations	15.22	15.14	15.16	15.52	15.48	15.17	15.34	15.14	15.26	15.52	15.28	15.17
Cl	0.07	0.09	0.08	0.05	0.07	0.06	0.05	0.06	0.07	0.06	0.07	0.04
F	0.11	0.15	0.13	0.11	0.09	0.08	0.12	0.08	0.11	0.12	0.09	0.11
oxygen	23.01	23	23	23	23	23	23	23	23	23	23	23
Cl/(Cl + F)	0.40	0.38	0.37	0.33	0.43	0.42	0.28	0.44	0.38	0.31	0.44	0.26
Fe^{3+}/Fe^{2+}	0.23	0.35	0.24	0.18	0.19	0.34	0.16	0.35	0.15	0.22	0.16	0.12
Mg/(Mg+ΣFe)	0.54	0.53	0.54	0.34	0.38	0.50	0.48	0.49	0.52	0.34	0.49	0.54
$Mg/(Mg+Fe^{2+})$	0.59	0.60	0.59	0.38	0.42	0.57	0.52	0.56	0.55	0.39	0.53	0.57

Table C.1 Continued

	Vein											
	Vn1-3	Vn1-4	Vn1-5	Vn2-1	Vn2-2	Vn3-1	Vn3-2	Vn4-1	Vn4-2	Vn4-3	Vn4-4	Vn4-5
SiO_2	51.19	47.95	49.88	46.26	53.65	48.67	48.95	50.16	52.36	52.73	47.56	47.76
TiO_2	0.33	0.44	0.40	0.52	0.00	0.40	0.40	0.44	0.20	0.18	0.63	0.68
Al_2O_3	3.72	6.15	4.76	7.25	1.09	5.48	5.45	3.86	2.51	2.23	6.25	5.80
FeO	17.06	19.51	18.09	20.80	17.63	19.31	19.19	18.94	17.18	16.93	20.55	21.26
Cr_2O_3	b.d.l.	b.d.l.	b.d.l.	b.d.l.	b.d.l.	b.d.l.	b.d.l.	b.d.l.	b.d.l.	b.d.l.	b.d.l.	b.d.l.
MnO	0.21	0.21	0.22	0.18	0.25	0.17	0.18	0.23	0.21	0.23	0.26	0.29
MgO	12.39	10.30	11.74	9.58	12.59	10.76	11.00	11.37	12.80	13.04	9.23	9.24
CaO	12.03	11.86	11.95	11.79	12.48	11.99	11.88	11.95	12.18	12.06	11.86	11.70
Na_2O	0.43	0.75	0.56	0.94	0.06	0.76	0.75	0.48	0.31	0.28	0.65	0.73
K_2O	0.24	0.48	0.27	0.52	0.02	0.28	0.27	0.34	0.19	0.17	0.53	0.47
F	0.19	0.23	0.18	0.17	0.19	0.26	0.20	0.25	0.21	0.27	0.09	0.16
Cl	0.11	0.33	0.16	0.40	b.d.l.	0.21	0.21	0.14	0.12	0.08	0.30	0.20
Subtotal	97.88	98.20	98.21	98.43	97.95	98.30	98.47	98.14	98.28	98.18	97.90	98.28
O = Cl,F	0.10	0.17	0.11	0.16	0.08	0.16	0.13	0.14	0.12	0.13	0.11	0.11
Total	97.78	98.03	98.10	98.27	97.87	98.14	98.34	98.00	98.16	98.05	97.79	98.17
Cations calculated on the basis of 23 (O, F, Cl) p.f.u. and the average ferric iron constraint (values obtained from the average 15eNK and 13 eCNK)												
Si p.f.u.	7.53	7.16	7.35	6.94	7.88	7.23	7.24	7.44	7.66	7.71	7.17	7.17
Al	0.47	0.84	0.65	1.07	0.12	0.77	0.76	0.56	0.34	0.29	0.84	0.83
Fe^{3+}	0	0	0	0	0	0	0	0	0	0	0	0
Ti	0	0	0	0	0	0	0	0	0	0	0	0
T sites	8	8	8	8	8	8	8	8	8	8	8	8
Al	0.17	0.24	0.17	0.22	0.07	0.19	0.19	0.11	0.10	0.09	0.27	0.20
Cr	0	0	0	0	0	0	0	0	0	0	0	0
Fe^{3+}	0.17	0.30	0.30	0.47	0.07	0.31	0.34	0.26	0.17	0.18	0.22	0.30
Ti	0.04	0.05	0.04	0.06	0.00	0.04	0.04	0.05	0.02	0.02	0.07	0.08
Mg	2.72	2.29	2.58	2.14	2.76	2.38	2.42	2.51	2.79	2.84	2.07	2.07
Fe^{2+}	1.89	2.10	1.89	2.10	2.09	2.06	1.99	2.05	1.91	1.86	2.35	2.34
Mn	0.01	0.01	0.01	0.01	0.02	0.01	0.01	0.01	0.01	0.01	0.02	0.02
Ca	0	0	0	0	0	0	0	0	0	0	0	0
C sites	5	5	5	5	5	5	5	5	5	5	5	5
Mg	0	0	0	0	0	0	0	0	0	0	0	0
Fe^{2+}	0.04	0.04	0.04	0.04	0.00	0.03	0.04	0.03	0.03	0.04	0.02	0.04
Mn	0.01	0.01	0.01	0.01	0.02	0.01	0.01	0.01	0.01	0.01	0.02	0.02
Ca	1.89	1.90	1.89	1.89	1.96	1.91	1.88	1.90	1.91	1.89	1.91	1.88
Na	0.06	0.06	0.06	0.06	0.01	0.05	0.06	0.05	0.04	0.04	0.05	0.06
B sites	2	2	2	2	1.99	2	2	2	2.0	2	2	2
Ca	0	0	0	0	0	0	0	0	0	0	0	0
Na	0.07	0.16	0.10	0.22	0.01	0.17	0.15	0.08	0.04	0.04	0.15	0.15
K	0.05	0.09	0.05	0.10	0	0.05	0.05	0.06	0.04	0.03	0.10	0.09
A sites	0.11	0.25	0.15	0.32	0.01	0.23	0.20	0.15	0.08	0.07	0.25	0.24
cations	15.11	15.25	15.15	15.32	15.00	15.23	15.20	15.15	15.08	15.05	15.25	15.24
Cl	0.03	0.08	0.04	0.10	0	0.05	0.05	0.04	0.03	0.02	0.08	0.05
F	0.09	0.11	0.09	0.08	0.09	0.12	0.09	0.12	0.10	0.12	0.04	0.07
oxygen	23	23	23	23	23	23	23	23	23	23.003	23	23
Cl/(Cl + F)	0.24	0.44	0.32	0.56	0.01	0.31	0.36	0.23	0.24	0.13	0.63	0.41
Fe^{3+}/Fe^{2+}	0.09	0.14	0.16	0.22	0.04	0.15	0.17	0.13	0.09	0.09	0.09	0.13
Mg/(Mg+ΣFe)	0.56	0.48	0.54	0.45	0.56	0.50	0.51	0.52	0.57	0.58	0.44	0.44
$Mg/(Mg+Fe^{2+})$	0.59	0.52	0.57	0.50	0.57	0.53	0.54	0.55	0.59	0.60	0.47	0.47

L.O.D. = average limit of detection

Table C.2. Microprobe analyses showing major elements (wt. %) and structural formula of hydrothermal biotites from the Côté Gold deposit

		Disseminated														
		E11-95-268 (green-brown)						E11-105-133 (brown)						CL-58 (brown)		
	L.O.D	1-1	1-2	1-3	2-1	2-2	2-3	1-1	1-2	2-1	2-2	3-1	3-2	1-1	1-2	1-3
SiO_2	0.04	34.25	34.67	34.33	31.38	33.46	32.48	35.53	35.77	35.34	35.28	34.99	35.61	34.69	35.18	34.57
TiO_2	0.03	2.10	2.12	1.96	1.54	2.17	1.81	1.88	1.93	1.85	1.79	1.79	1.84	2.23	2.21	2.29
Al_2O_3	0.03	16.47	16.52	16.66	16.63	15.97	16.02	17.21	16.90	17.50	17.48	17.82	17.47	16.77	16.61	16.69
V_2O_3	0.03	b.d.l.	b.d.l.	b.d.l.	b.d.l.	b.d.l.	b.d.l.	0.05	0.05	0.04	0.03	b.d.l.	0.03	b.d.l.	b.d.l.	b.d.l.
Cr_2O_3	0.03	b.d.l.	b.d.l.	b.d.l.	b.d.l.	b.d.l.	b.d.l.	b.d.l.	b.d.l.	b.d.l.	b.d.l.	0.03	b.d.l.	b.d.l.	0.06	0.04
MgO	0.03	4.74	4.78	4.95	6.04	4.78	5.30	8.04	8.21	8.19	8.20	8.20	8.19	6.78	6.87	6.78
CaO	0.03	b.d.l.	b.d.l.	0.02	0.04	b.d.l.	b.d.l.	0.05	b.d.l.	0.04	0.03	b.d.l.	b.d.l.	b.d.l.	0.09	0.04
MnO	0.03	0.18	0.16	0.16	0.25	0.21	0.23	0.16	0.17	0.18	0.18	0.18	0.16	0.09	0.10	0.10
FeO	0.03	28.63	28.43	29.00	32.58	29.95	31.44	23.43	22.65	23.26	23.13	23.63	23.31	26.40	25.81	26.07
Na_2O	0.03	b.d.l.	b.d.l.	b.d.l.	b.d.l.	b.d.l.	b.d.l.	0.06	0.04	b.d.l.	b.d.l.	b.d.l.	b.d.l.	0.05	0.06	0.06
K_2O	0.02	9.47	9.65	9.29	5.80	8.85	7.49	9.51	9.67	9.60	9.63	9.40	9.67	9.27	9.11	9.27
F	0.10	0.26	0.26	0.24	0.14	0.17	0.12	0.32	0.35	0.40	0.28	0.22	0.33	0.51	0.62	0.54
Cl	0.01	0.24	0.24	0.21	0.15	0.21	0.17	0.19	0.17	0.17	0.21	0.16	0.14	0.37	0.37	0.36
Total		96.35	96.85	96.87	94.55	95.78	95.09	96.44	95.93	96.58	96.25	96.44	96.77	97.20	97.10	96.81
F = O		-0.11	-0.11	-0.10	-0.06	-0.07	-0.05	-0.13	-0.15	-0.17	-0.12	-0.09	-0.14	-0.21	-0.26	-0.23
Cl = O		-0.05	-0.06	-0.05	-0.03	-0.05	-0.04	-0.04	-0.04	-0.04	-0.05	-0.04	-0.03	-0.08	-0.08	-0.08
Total		96.19	96.69	96.72	94.46	95.66	94.99	96.26	95.74	96.37	96.09	96.31	96.60	96.91	96.76	96.50
Si		5.46	5.49	5.43	5.13	5.40	5.28	5.50	5.55	5.46	5.46	5.41	5.48	5.43	5.49	5.43
Al iv		2.54	2.51	2.57	2.87	2.60	2.72	2.50	2.45	2.54	2.54	2.59	2.52	2.57	2.51	2.57
Al vi		0.56	0.57	0.54	0.33	0.44	0.34	0.63	0.64	0.65	0.66	0.65	0.65	0.52	0.54	0.51
Ti		0.25	0.25	0.23	0.19	0.26	0.22	0.22	0.23	0.22	0.21	0.21	0.21	0.26	0.26	0.27
Cr		0	0	0	0	0	0	0	0	0	0	0	0	0	0.01	0.01
Fe		3.82	3.77	3.84	4.45	4.03	4.27	3.03	2.94	3.00	3.00	3.05	3.00	3.45	3.37	3.42
Mn		0.02	0.02	0.02	0.03	0.03	0.03	0.02	0.02	0.02	0.02	0.02	0.02	0.01	0.01	0.01
Mg		1.13	1.13	1.17	1.47	1.15	1.28	1.85	1.90	1.89	1.89	1.89	1.88	1.58	1.60	1.59
Ca		0	0	0.03	0.01	0	0.04	0.01	0	0.01	0	0	0	0	0.02	0.01
Na		0	0	0	0	0	0	0.02	0.01	0	0	0	0	0.01	0.02	0.02
K		1.93	1.95	1.88	1.21	1.82	1.55	1.88	1.91	1.89	1.90	1.85	1.90	1.85	1.81	1.86
OH*		3.81	3.81	3.82	3.89	3.86	3.89	3.79	3.78	3.76	3.81	3.85	3.80	3.65	3.60	3.64
F		0.13	0.13	0.12	0.07	0.09	0.06	0.16	0.17	0.20	0.13	0.11	0.16	0.25	0.30	0.27
Cl		0.06	0.07	0.06	0.04	0.06	0.05	0.05	0.04	0.04	0.05	0.04	0.04	0.10	0.10	0.10
Total		19.70	19.69	19.72	19.69	19.73	19.75	19.66	19.64	19.68	19.68	19.69	19.67	19.70	19.64	19.69
Y total		5.78	5.74	5.81	6.47	5.91	6.15	5.76	5.72	5.78	5.78	5.83	5.77	5.83	5.79	5.81
X total		1.93	1.95	1.91	1.22	1.82	1.59	1.90	1.92	1.90	1.91	1.85	1.90	1.87	1.85	1.88
Mg/Mg+Fe		0.23	0.23	0.23	0.25	0.22	0.23	0.38	0.39	0.39	0.39	0.38	0.39	0.31	0.32	0.32

Table C.2. Continued

	Disseminated															Vein	
	CL-58 (brown)			E11-60-172 (orange-brown)										E11-62-244 (orange-brown)			
	2-1	2-2	2-3	1-1	1-2	1-3	1-4	1-5	1-6	2-1	2-2	2-3	2-4	7-1	7-2	1-1	2-1
SiO_2	34.39	34.65	34.07	37.92	37.50	37.99	37.81	37.63	37.74	37.73	37.72	37.30	37.68	35.64	35.82	35.33	35.60
TiO_2	2.03	2.13	1.93	1.19	1.17	1.17	1.05	1.25	1.23	1.22	1.26	1.24	1.28	1.83	1.92	2.00	1.74
Al_2O_3	16.49	16.83	16.95	15.79	15.45	15.94	15.86	15.82	15.75	15.93	15.81	15.64	15.83	17.57	17.35	18.04	17.93
V_2O_3	b.d.l.	b.d.l.	b.d.l.	0.05	b.d.l.	0.03	0.04	0.04	0.04	b.d.l.	0.04	0.03	0.04	b.d.l.	b.d.l.	0.03	b.d.l.
Cr_2O_3	b.d.l.	b.d.l.	b.d.l.	0.04	0.03	0.05	0.07	b.d.l.	0.04	0.04	0.04	0.04	0.05	b.d.l.	b.d.l.	b.d.l.	b.d.l.
MgO	6.92	6.98	7.08	13.51	13.36	13.48	13.70	13.31	13.41	13.46	13.21	13.00	12.98	8.33	8.28	8.82	8.86
CaO	b.d.l.	b.d.l.	b.d.l.	b.d.l.	b.d.l.	0.03	b.d.l.	0.04	0.06	b.d.l.	b.d.l.	0.07	0.06	0.09	0.11	b.d.l.	b.d.l.
MnO	0.10	0.09	0.09	0.11	0.12	0.11	0.12	0.11	0.13	0.12	0.13	0.14	0.13	0.18	0.16	0.16	0.15
FeO	26.25	25.20	26.59	17.00	17.08	17.29	17.08	17.70	17.52	17.28	17.62	18.00	17.90	21.43	21.20	21.68	21.14
Na_2O	b.d.l.	0.05	b.d.l.	0.16	0.13	0.08	0.13	0.11	0.10	0.13	0.11	0.11	0.10	0.55	0.61	b.d.l.	0.08
K_2O	9.23	9.21	8.59	9.47	9.66	9.68	9.50	9.74	9.63	9.53	9.69	9.39	9.43	9.60	9.45	9.72	9.85
F	0.57	0.67	0.48	1.06	0.96	1.06	1.03	0.90	1.03	0.89	1.06	0.96	0.96	0.30	0.29	0.30	0.32
Cl	0.32	0.19	0.29	0.06	0.08	0.07	0.07	0.09	0.06	0.07	0.08	0.09	0.09	0.11	0.11	0.13	0.15
Total	96.31	96.03	96.11	96.37	95.56	96.99	96.44	96.75	96.73	96.42	96.78	96.01	96.51	95.62	95.29	96.22	95.84
F = O	-0.24	-0.28	-0.20	-0.45	-0.40	-0.45	-0.44	-0.38	-0.43	-0.38	-0.44	-0.41	-0.41	-0.13	-0.12	-0.13	-0.14
Cl = O	-0.07	-0.04	-0.06	-0.01	-0.02	-0.02	-0.01	-0.02	-0.01	-0.02	-0.02	-0.02	-0.02	-0.02	-0.02	-0.03	-0.03
Total	96.00	95.71	95.84	95.91	95.13	96.52	95.99	96.35	96.28	96.03	96.32	95.59	96.08	95.47	95.15	96.07	95.67
Si	5.43	5.46	5.38	5.70	5.70	5.67	5.69	5.66	5.68	5.67	5.68	5.66	5.68	5.51	5.54	5.43	1.49
Al iv	2.57	2.54	2.62	2.30	2.30	2.33	2.31	2.34	2.32	2.33	2.32	2.34	2.32	2.49	2.46	2.57	5.61
Al vi	0.51	0.58	0.53	0.50	0.47	0.47	0.50	0.47	0.47	0.50	0.48	0.46	0.49	0.71	0.71	0.70	0.00
Ti	0.24	0.25	0.23	0.13	0.13	0.13	0.12	0.14	0.14	0.14	0.14	0.14	0.15	0.21	0.22	0.23	0.35
Cr	0	0	0	0	0	0.01	0.01	0	0	0	0	0.01	0.01	0	0	0	0
Fe	3.47	3.32	3.51	2.14	2.17	2.24	2.15	2.23	2.20	2.17	2.22	2.29	2.26	2.77	2.74	2.79	4.69
Mn	0.01	0.01	0.01	0.01	0.02	0.01	0.01	0.01	0.02	0.02	0.02	0.02	0.02	0.02	0.02	0.02	0.03
Mg	1.63	1.64	1.67	3.03	3.03	3.00	3.07	2.98	3.01	3.02	2.96	2.94	2.92	1.92	1.91	2.02	3.51
Ca	0	0	0	0	0	0	0	0.01	0.01	0	0	0.01	0.01	0.02	0.02	0	0
Na	0	0.02	0	0.05	0.04	0.02	0.04	0.03	0.03	0.04	0.03	0.03	0.03	0.16	0.18	0	0.04
K	1.86	1.85	1.73	1.82	1.87	1.84	1.82	1.87	1.85	1.83	1.86	1.82	1.81	1.89	1.87	1.91	3.34
OH*	3.63	3.62	3.68	3.48	3.52	3.48	3.49	3.55	3.49	3.56	3.48	3.51	3.52	3.82	3.83	3.82	3.66
F	0.29	0.33	0.24	0.50	0.46	0.50	0.49	0.43	0.49	0.42	0.50	0.46	0.46	0.15	0.14	0.14	0.27
Cl	0.09	0.05	0.08	0.02	0.02	0.02	0.02	0.02	0.02	0.02	0.02	0.02	0.02	0.03	0.03	0.03	0.07
Total	19.72	19.66	19.68	19.69	19.73	19.73	19.72	19.74	19.72	19.71	19.72	19.72	19.69	19.71	19.67	19.66	23.05
Y total	5.86	5.80	5.95	5.83	5.82	5.86	5.86	5.84	5.84	5.84	5.83	5.85	5.83	5.63	5.61	5.75	8.58
X total	1.86	1.87	1.73	1.86	1.91	1.87	1.86	1.91	1.88	1.87	1.89	1.86	1.85	2.07	2.07	1.91	3.38
Mg/Mg+Fe	0.32	0.33	0.32	0.59	0.58	0.57	0.59	0.57	0.58	0.58	0.57	0.56	0.56	0.41	0.41	0.42	0.43

Table C.2. Continued

	Vein													Breccia			
	E11-62-244 (orange-brown)				E11-68-536.9 (orange-brown)							E11-68-536.9		CL-16 (green-brown)			
	3-1	4-1	5-1	6-1	1-1	2-1	2-2	3-1	4-1	5-1	6-1	7-1	7-2	1-1	1-2	1-3	1-4
SiO_2	35.42	35.35	35.73	34.97	36.58	36.54	36.33	36.36	36.72	36.57	36.95	36.64	37.00	34.67	35.37	34.82	34.03
TiO_2	1.84	2.19	2.09	1.82	1.32	1.40	1.28	1.38	1.35	1.54	1.33	1.24	1.30	1.51	1.46	1.36	1.33
Al_2O_3	18.36	17.79	17.83	17.39	16.31	16.69	16.20	16.57	16.49	16.63	16.66	16.93	16.82	16.57	16.36	16.57	16.62
V_2O_3	b.d.l.	b.d.l.	b.d.l.	b.d.l.	0.05	0.05	0.07	0.06	0.07	0.06	0.05	0.06	0.06	b.d.l.	0.06	0.07	0.05
Cr_2O_3	b.d.l.	b.d.l.	b.d.l.	b.d.l.	0.04	0.04	0.06	0.04	0.06	0.06	0.06	0.07	0.07	b.d.l.	b.d.l.	0.06	b.d.l.
MgO	8.90	8.57	8.77	8.94	11.31	11.31	11.18	11.38	11.35	11.21	11.30	11.44	11.47	8.28	8.71	8.39	8.71
CaO	b.d.l.	b.d.l.	b.d.l.	0.03	b.d.l.	b.d.l.	0.07	0.36	b.d.l.	b.d.l.	b.d.l.	b.d.l.	b.d.l.	b.d.l.	b.d.l.	0.18	b.d.l.
MnO	0.15	0.17	0.17	0.15	0.13	0.14	0.14	0.16	0.13	0.16	0.13	0.14	0.17	0.07	0.07	0.03	0.06
FeO	21.64	21.74	21.72	21.83	19.46	19.61	19.77	19.98	19.51	19.78	18.88	19.52	19.36	24.41	24.29	25.05	26.26
Na_2O	0.05	0.03	0.03	0.07	0.10	0.10	0.13	0.10	0.09	0.10	0.13	0.06	0.11	b.d.l.	0.03	b.d.l.	b.d.l.
K_2O	9.49	9.73	9.81	9.46	9.56	9.66	9.17	8.18	9.46	9.60	9.66	9.93	9.72	9.53	9.58	8.93	8.23
F	0.28	0.29	0.31	0.39	0.58	0.56	0.60	0.54	0.57	0.59	0.58	0.53	0.66	0.79	0.93	0.84	0.72
Cl	0.14	0.12	0.12	0.12	0.14	0.14	0.13	0.13	0.14	0.15	0.13	0.15	0.12	0.16	0.17	0.15	0.14
Total	96.32	96.01	96.63	95.22	95.59	96.25	95.12	95.25	95.95	96.43	95.86	96.70	96.86	96.05	97.06	96.48	96.17
F = O	-0.12	-0.12	-0.13	-0.17	-0.25	-0.23	-0.25	-0.23	-0.24	-0.25	-0.24	-0.22	-0.28	-0.33	-0.39	-0.36	-0.30
Cl = O	-0.03	-0.03	-0.03	-0.03	-0.03	-0.03	-0.03	-0.03	-0.03	-0.03	-0.03	-0.03	-0.03	-0.04	-0.04	-0.03	-0.03
Total	96.17	95.86	96.47	95.03	95.31	95.98	94.83	94.99	95.67	96.15	95.59	96.44	96.55	95.68	96.62	96.09	95.84
Si	5.42	5.45	5.47	5.45	5.61	5.57	5.60	5.57	5.60	5.57	5.63	5.56	5.59	5.46	5.50	5.46	5.36
Al iv	2.58	2.55	2.53	2.55	2.39	2.43	2.40	2.43	2.40	2.43	2.37	2.44	2.41	2.54	2.50	2.54	2.64
Al vi	0.74	0.68	0.68	0.64	0.56	0.57	0.55	0.56	0.57	0.55	0.62	0.58	0.59	0.53	0.51	0.52	0.44
Ti	0.21	0.25	0.24	0.21	0.15	0.16	0.15	0.16	0.15	0.18	0.15	0.14	0.15	0.18	0.17	0.16	0.16
Cr	0	0	0	0	0	0	0.01	0	0.01	0.01	0.01	0.01	0.01	0	0	0	0
Fe	2.77	2.80	2.78	2.84	2.50	2.50	2.55	2.56	2.49	2.52	2.40	2.48	2.45	3.21	3.16	3.28	3.46
Mn	0.02	0.02	0.02	0.02	0.02	0.02	0.02	0.02	0.02	0.02	0.02	0.02	0.02	0.01	0.01	0.00	0.01
Mg	2.03	1.97	2.00	2.08	2.59	2.57	2.57	2.60	2.58	2.54	2.57	2.59	2.59	1.94	2.02	1.96	2.05
Ca	0	0	0	0.00	0	0	0.01	0.06	0	0	0	0	0	0	0	0.03	0
Na	0.01	0.01	0.01	0.02	0.03	0.03	0.04	0.03	0.03	0.03	0.04	0.02	0.03	0	0.01	0	0
K	1.85	1.91	1.92	1.88	1.87	1.88	1.80	1.60	1.84	1.86	1.88	1.92	1.87	1.91	1.90	1.79	1.65
OH*	3.83	3.83	3.82	3.77	3.68	3.69	3.67	3.70	3.69	3.68	3.69	3.71	3.65	3.56	3.49	3.54	3.60
F	0.14	0.14	0.15	0.19	0.28	0.27	0.29	0.26	0.28	0.28	0.28	0.25	0.31	0.39	0.46	0.42	0.36
Cl	0.04	0.03	0.03	0.03	0.04	0.04	0.03	0.03	0.04	0.04	0.03	0.04	0.03	0.04	0.05	0.04	0.04
Total	19.64	19.64	19.65	19.70	19.71	19.72	19.69	19.59	19.69	19.71	19.68	19.75	19.71	19.78	19.78	19.74	19.77
Y total	5.77	5.72	5.72	5.79	5.81	5.82	5.84	5.90	5.82	5.81	5.76	5.81	5.80	5.87	5.87	5.93	6.11
X total	1.87	1.92	1.92	1.91	1.90	1.91	1.85	1.69	1.87	1.89	1.92	1.94	1.90	1.91	1.91	1.82	1.65
Mg/Mg+Fe	0.42	0.41	0.42	0.42	0.51	0.51	0.50	0.50	0.51	0.50	0.52	0.51	0.51	0.38	0.39	0.37	0.37

Table C.2. Continued

	Breccia																
	CL-16		E10-42-168.6B (brown)						E12-174-LK13-407 (brown)						E11-161-338 (brown)		
	1-5	1-6	1-1	1-2	1-3	1-4	2-1	2-2	1-1	1-2	1-3	1-4	1-5	1-6	1-1	1-2	1-3
SiO_2	35.02	34.94	37.14	36.54	36.83	36.79	36.60	36.58	36.99	36.93	37.05	36.85	38.09	38.43	36.16	34.62	33.70
TiO_2	1.40	1.61	1.45	1.34	1.43	1.65	1.63	1.52	1.65	1.62	1.53	1.58	1.59	1.58	1.70	1.61	1.59
Al_2O_3	16.47	16.41	15.32	15.46	15.49	15.50	15.89	15.63	16.24	16.68	16.38	16.56	16.03	15.53	16.18	16.87	16.36
V_2O_3	0.08	0.07	0.05	0.04	0.04	0.06	0.06	0.06	0.04	0.05	0.04	0.05	0.05	0.06	0.08	0.07	0.09
Cr_2O_3	b.d.l.	b.d.l.	b.d.l.	b.d.l.	b.d.l.	b.d.l.	b.d.l.	b.d.l.	0.03	b.d.l.	b.d.l.	b.d.l.	0.11	0.09	b.d.l.	b.d.l.	b.d.l.
MgO	8.56	8.25	10.15	9.95	10.14	10.02	9.77	9.78	13.05	13.46	13.51	13.36	13.64	14.01	8.07	7.41	7.11
CaO	b.d.l.	b.d.l.	b.d.l.	0.04	b.d.l.	0.23	b.d.l.	b.d.l.	b.d.l.	b.d.l.	b.d.l.	b.d.l.	b.d.l.	0.03	b.d.l.	b.d.l.	b.d.l.
MnO	0.07	0.04	0.07	0.05	0.05	0.06	0.05	0.07	0.10	0.13	0.10	0.09	0.11	0.09	0.05	0.04	0.07
FeO	25.00	25.07	22.02	22.98	22.53	23.00	22.35	22.62	16.92	16.99	17.19	17.00	16.25	16.21	24.75	25.49	27.89
Na_2O	b.d.l.	b.d.l.	0.05	0.03	0.05	0.12	0.07	0.04	0.06	0.08	0.05	0.07	0.04	0.08	0.03	0.03	b.d.l.
K_2O	9.52	9.48	9.78	9.55	9.63	6.27	9.74	9.82	9.95	9.80	9.60	9.60	9.94	9.80	9.75	9.54	8.73
F	0.77	0.88	1.03	0.99	0.89	1.11	0.89	1.00	0.43	0.35	0.49	0.45	0.56	0.56	0.96	0.73	0.55
Cl	0.17	0.17	0.18	0.17	0.18	0.19	0.18	0.20	0.09	0.08	0.07	0.08	0.07	0.06	0.22	0.20	0.18
Total	97.07	96.94	97.25	97.16	97.29	95.00	97.22	97.32	95.56	96.19	96.00	95.70	96.47	96.52	97.93	96.64	96.26
F = O	-0.32	-0.37	-0.43	-0.42	-0.37	-0.47	-0.37	-0.42	-0.18	-0.15	-0.20	-0.19	-0.23	-0.23	-0.02	-0.02	-0.03
Cl = O	-0.04	-0.04	-0.04	-0.04	-0.04	-0.04	-0.04	-0.04	-0.02	-0.02	-0.02	-0.02	-0.02	-0.01	-2.20	-2.15	-1.97
Total	96.71	96.53	96.78	96.70	96.87	94.49	96.81	96.85	95.36	96.03	95.78	95.50	96.22	96.27	95.71	94.47	94.27
Si	5.46	5.46	5.70	5.63	5.65	5.70	5.62	5.63	5.60	5.55	5.58	5.56	5.68	5.73	5.58	5.44	5.36
Al iv	2.54	2.54	2.30	2.37	2.35	2.30	2.38	2.37	2.40	2.45	2.42	2.44	2.32	2.27	2.42	2.56	2.64
Al vi	0.49	0.49	0.47	0.44	0.45	0.53	0.49	0.47	0.50	0.50	0.48	0.51	0.50	0.45	0.53	0.57	0.43
Ti	0.16	0.19	0.17	0.16	0.16	0.19	0.19	0.18	0.19	0.18	0.17	0.18	0.18	0.18	0.20	0.19	0.19
Cr	0	0	0	0	0	0	0	0	0	0	0	0	0.01	0.01	0	0	0
Fe	3.26	3.28	2.82	2.96	2.89	2.98	2.87	2.91	2.14	2.13	2.16	2.15	2.03	2.02	3.20	3.35	3.71
Mn	0.01	0.01	0.01	0.01	0.01	0.01	0.01	0.01	0.01	0.02	0.01	0.01	0.01	0.01	0.01	0.01	0.01
Mg	1.99	1.92	2.32	2.29	2.32	2.31	2.24	2.24	2.95	3.01	3.03	3.01	3.03	3.11	1.86	1.74	1.69
Ca	0	0	0	0.01	0	0.04	0	0	0	0	0	0	0	0	0	0	0
Na	0	0	0.01	0.01	0.01	0.04	0.02	0.01	0.02	0.02	0.02	0.02	0.01	0.02	0.01	0.01	0
K	1.89	1.89	1.91	1.88	1.89	1.24	1.91	1.93	1.92	1.88	1.84	1.85	1.89	1.86	1.92	1.91	1.77
OH*	3.58	3.52	3.45	3.47	3.52	3.41	3.52	3.46	3.77	3.81	3.75	3.77	3.72	3.72	3.47	3.58	3.68
F	0.38	0.44	0.50	0.48	0.43	0.54	0.43	0.49	0.21	0.17	0.23	0.21	0.26	0.26	0.47	0.36	0.28
Cl	0.05	0.04	0.05	0.05	0.05	0.05	0.05	0.05	0.02	0.02	0.02	0.02	0.02	0.02	0.06	0.05	0.05
Total	19.81	19.78	19.72	19.75	19.73	19.33	19.72	19.74	19.73	19.74	19.73	19.72	19.67	19.67	19.71	19.77	19.80
Y total	5.91	5.89	5.79	5.86	5.83	6.02	5.79	5.81	5.79	5.84	5.87	5.85	5.77	5.78	5.78	5.85	6.03
X total	1.89	1.89	1.93	1.89	1.90	1.31	1.93	1.94	1.94	1.90	1.86	1.87	1.90	1.89	1.93	1.92	1.77
Mg/Mg+Fe	0.38	0.37	0.45	0.44	0.45	0.44	0.44	0.44	0.58	0.59	0.58	0.58	0.60	0.61	0.37	0.34	0.31

Table C.2. Continued

	Breccia																	
	E11-161-338 (brown)					E11-116-LK13 (brown)			EL-161-340B (orange-brown)									
	1-4	1-5	1-6	1-7	1-8	1-1	2-1	3-1	1-1	1-2	1-3	1-4	2-1	2-2	3-1	3-2	3-3	
SiO_2	32.70	32.65	34.53	34.54	33.41	35.80	36.13	35.19	36.71	36.65	36.97	37.29	36.88	36.33	34.95	37.63	37.99	
TiO_2	1.15	1.37	1.65	1.79	1.64	1.53	1.71	1.50	1.54	1.51	1.48	1.48	1.43	1.51	1.41	1.46	1.54	
Al_2O_3	15.99	15.54	15.78	16.07	15.64	16.34	17.10	16.66	15.51	15.55	15.72	15.41	15.60	15.73	16.44	15.40	15.11	
V_2O_3	0.07	0.08	0.08	0.09	0.09	b.d.l.	b.d.l.	b.d.l.	0.06	0.08	0.09	0.10	0.08	0.07	0.10	0.09	0.08	
Cr_2O_3	b.d.l.	b.d.l.	b.d.l.	b.d.l.	b.d.l.	0.03	0.05	0.09	b.d.l.	b.d.l.	b.d.l.	b.d.l.	b.d.l.	b.d.l.	b.d.l.	b.d.l.	b.d.l.	
MgO	7.51	7.16	7.37	7.36	7.35	10.29	10.22	10.69	10.98	10.83	10.79	11.11	11.05	10.45	9.99	10.77	10.85	
CaO	b.d.l.	b.d.l.	b.d.l.	b.d.l.	b.d.l.	0.03	0.16	0.78	b.d.l.	b.d.l.	b.d.l.	0.04	0.03	0.05	0.15	0.14	0.08	
MnO	0.08	0.08	0.04	0.06	0.05	0.05	0.07	0.06	0.05	b.d.l.	0.05	b.d.l.	0.05	0.04	0.05	0.04	0.05	
FeO	30.54	30.11	26.70	26.44	28.97	21.13	20.70	21.54	21.55	21.76	20.99	20.79	20.49	21.89	23.50	21.36	21.01	
Na_2O	b.d.l.	b.d.l.	b.d.l.	b.d.l.	b.d.l.	0.07	0.29	0.37	0.07	0.04	0.07	0.06	0.07	0.03	b.d.l.	0.06	0.03	
K_2O	6.66	7.01	9.13	9.41	7.97	9.78	9.31	6.70	9.76	9.80	9.73	9.75	9.60	9.33	8.45	9.43	9.62	
F	0.59	0.64	0.81	0.85	0.78	0.63	0.62	0.61	1.21	1.36	1.15	1.29	1.33	1.22	0.87	1.34	1.40	
Cl	0.16	0.17	0.23	0.22	0.20	0.13	0.12	0.17	0.24	0.25	0.24	0.22	0.25	0.27	0.20	0.23	0.23	
Total	95.48	94.81	96.34	96.84	96.12	95.83	96.46	94.35	97.70	97.86	97.28	97.57	96.85	96.91	96.10	97.94	97.97	
F = O	-0.03	-0.03	-0.02	-0.02	-0.02	-0.27	-0.26	-0.25	-0.51	-0.57	-0.49	-0.54	-0.56	-0.51	-0.37	-0.57	-0.59	
Cl = O	-1.50	-1.58	-2.06	-2.12	-1.80	-0.03	-0.03	-0.04	-0.05	-0.06	-0.05	-0.05	-0.06	-0.06	-0.04	-0.05	-0.05	
Total	93.94	93.19	94.26	94.69	94.30	95.54	96.17	94.06	97.14	97.23	96.74	96.98	96.24	96.34	95.69	97.32	97.32	
Si	5.27	5.31	5.48	5.45	5.36	5.54	5.52	5.46	5.61	5.61	5.65	5.68	5.66	5.60	5.45	5.72	5.76	
Al iv	2.73	2.69	2.52	2.55	2.64	2.46	2.48	2.54	2.39	2.39	2.35	2.32	2.34	2.40	2.55	2.28	2.24	
Al vi	0.31	0.29	0.43	0.45	0.31	0.52	0.60	0.51	0.41	0.42	0.48	0.45	0.48	0.46	0.46	0.47	0.46	
Ti	0.14	0.17	0.20	0.21	0.20	0.18	0.20	0.18	0.18	0.17	0.17	0.17	0.16	0.18	0.17	0.17	0.18	
Cr	0	0	0	0	0	0	0.01	0.01	0	0	0	0	0	0	0	0	0	
Fe	4.12	4.10	3.54	3.49	3.88	2.73	2.64	2.80	2.76	2.79	2.68	2.65	2.63	2.82	3.06	2.71	2.67	
Mn	0.01	0.01	0.01	0.01	0.01	0.01	0.01	0.01	0.01	0	0.01	0	0.01	0	0.01	0.01	0.01	
Mg	1.81	1.74	1.74	1.73	1.76	2.37	2.33	2.47	2.50	2.47	2.46	2.52	2.53	2.40	2.32	2.44	2.45	
Ca	0	0	0	0	0	0	0	0.13	0	0	0	0.01	0	0.01	0.02	0.02	0.01	
Na	0	0	0	0	0	0.02	0.02	0.11	0.02	0.01	0.02	0.02	0.02	0.01	0	0.02	0.01	
K	1.37	1.45	1.85	1.89	1.63	1.93	1.90	1.33	1.90	1.91	1.90	1.90	1.88	1.83	1.68	1.83	1.86	
OH*	3.66	3.63	3.53	3.52	3.55	3.66	3.67	3.66	3.36	3.28	3.38	3.32	3.29	3.34	3.52	3.29	3.27	
F	0.30	0.33	0.41	0.42	0.39	0.31	0.30	0.30	0.58	0.66	0.56	0.62	0.65	0.59	0.43	0.65	0.67	
Cl	0.04	0.05	0.06	0.06	0.05	0.03	0.03	0.04	0.06	0.06	0.06	0.06	0.07	0.07	0.05	0.06	0.06	
Total	19.75	19.76	19.77	19.78	19.78	19.77	19.71	19.55	19.77	19.77	19.72	19.72	19.72	19.72	19.72	19.66	19.65	
Y total	6.38	6.30	5.92	5.89	6.15	5.81	5.78	5.98	5.85	5.85	5.80	5.80	5.81	5.86	6.02	5.80	5.76	
X total	1.37	1.45	1.85	1.89	1.63	1.95	1.93	1.57	1.92	1.92	1.92	1.92	1.91	1.85	1.70	1.87	1.88	
Mg/Mg+Fe	0.30	0.30	0.33	0.33	0.31	0.46	0.47	0.47	0.48	0.47	0.48	0.49	0.49	0.46	0.43	0.47	0.48	

L.O.D = limit of detection, b.d.l. = below detection limit

Appendix D

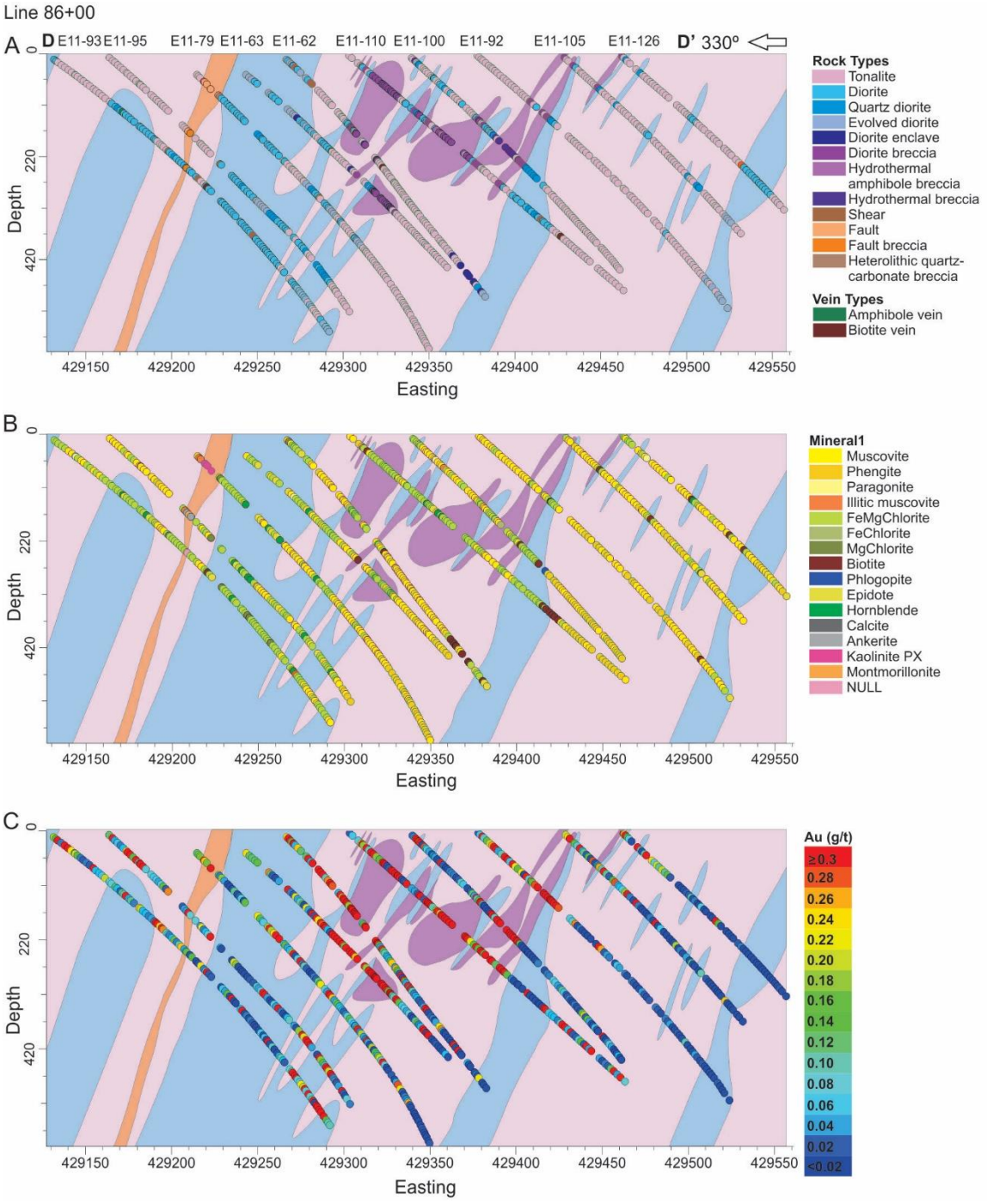

Figure D.1. Vertical cross sections of grid line 86+00 (D-D') from the Côté Gold deposit. A) Geological cross section showing major and minor rock types. B) Cross section showing the alteration mineral present, as inferred from TerraSpec measurements and discussed in the text. C) Cross section showing the distribution of Au (in g/t) which is spatially associated with the diorite breccia bodies.

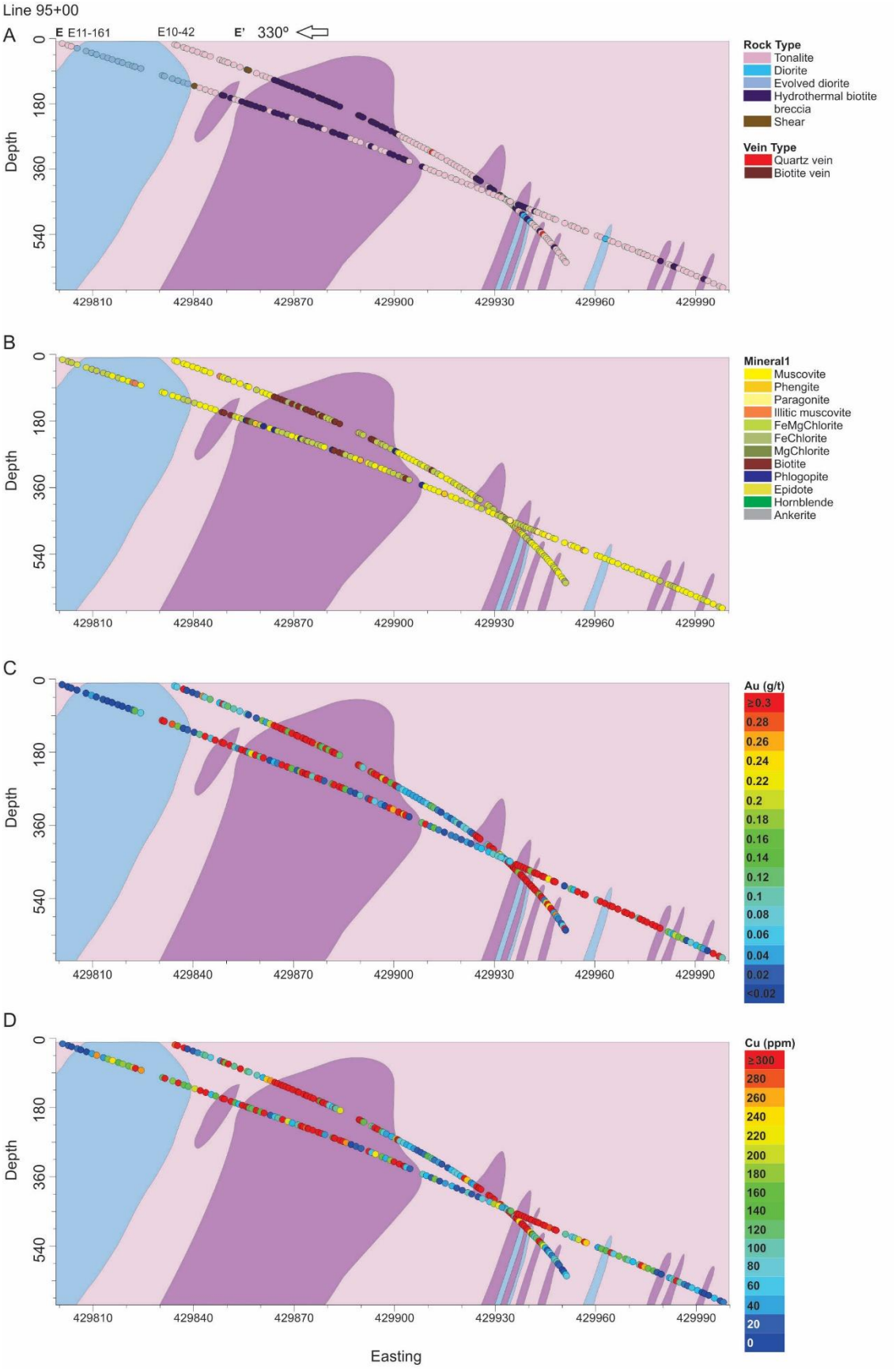
Line 95+00
A
E E11-161
E10-42
E'
330°
Depth
0
180
360
540
429810
429840
429870
429900
429930
429960
429990
Rock Type
Tonalite
Diorite
Evolved diorite
Hydrothermal biotite breccia
Shear
Vein Type
Quartz vein
Biotite vein
B
Mineral1
Muscovite
Phengite
Paragonite
Illitic muscovite
FeMgChlorite
FeChlorite
MgChlorite
Biotite
Phlogopite
Epidote
Hornblende
Ankerite
C
Au (g/t)
≥0.3
0.28
0.26
0.24
0.22
0.2
0.18
0.16
0.14
0.12
0.1
0.08
0.06
0.04
0.02
<0.02
D
Cu (ppm)
≥300
280
260
240
220
200
180
160
140
120
100
80
60
40
20
0
Easting

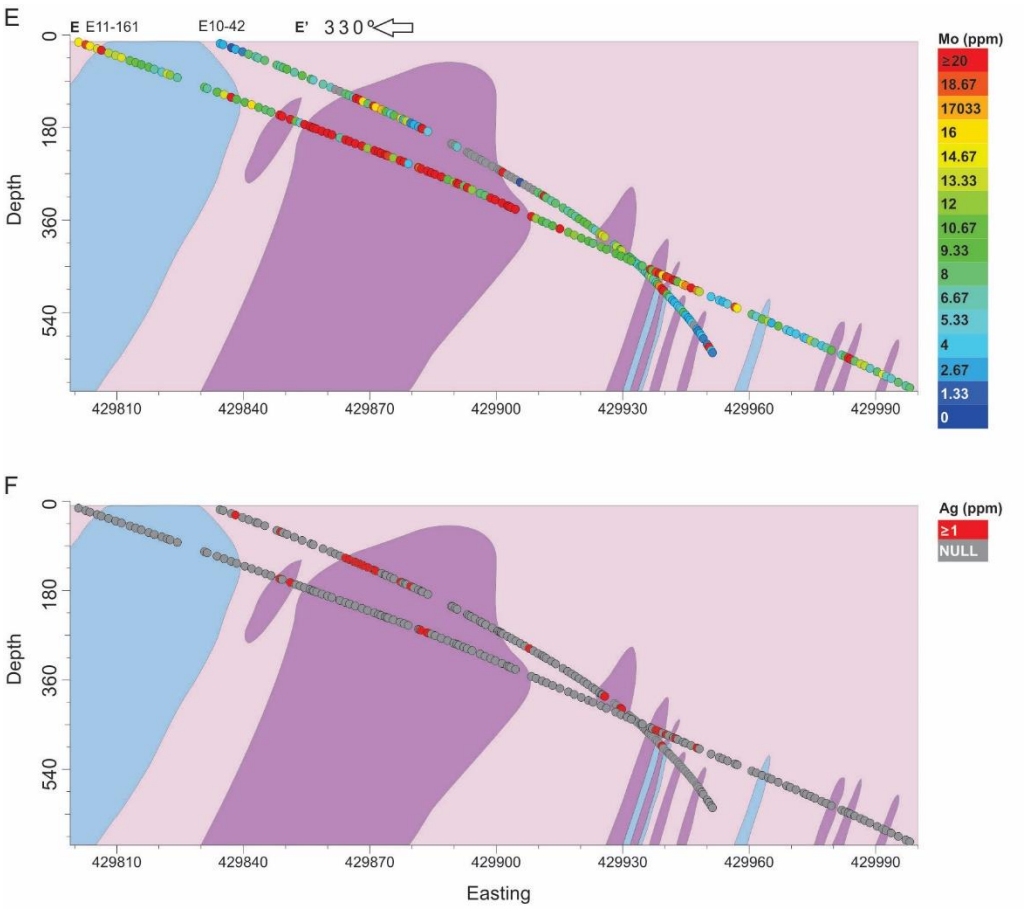

Figure D.2. Vertical cross sections of grid line 95+00 (E-E') from the Côté Gold deposit. A) Geological cross section showing major and minor rock types. B) Cross section showing the alteration mineral present, as inferred from TerraSpec measurements and discussed in the text. C) Cross section showing the distribution of Au. D) Cross section showing the distribution of Cu. E) Cross section showing the distribution of Mo. F) Cross section showing the distribution of Ag. Note the spatial association of Au, Cu, Mo and Ag with the hydrothermal biotite breccia bodies.

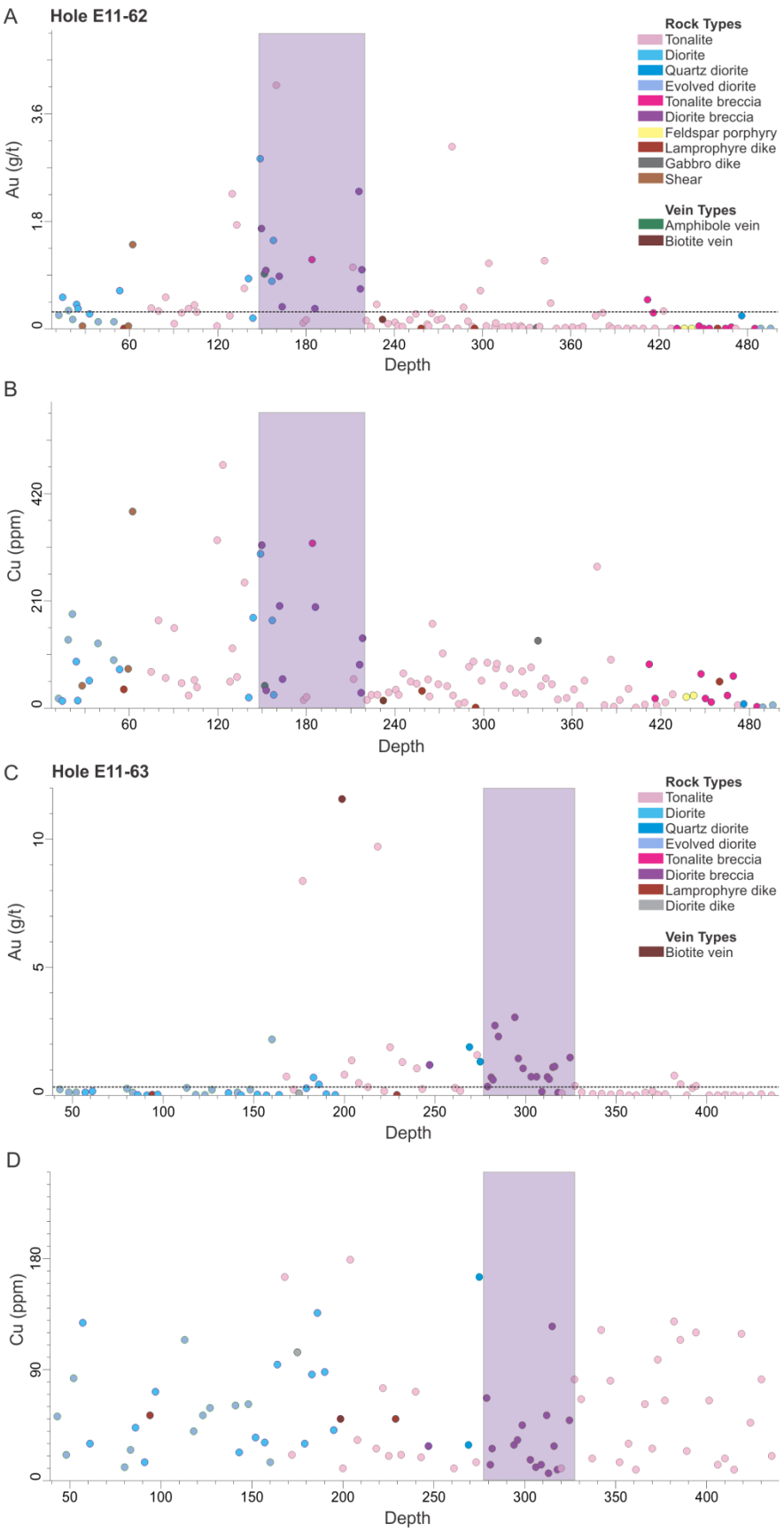
A
Hole E11-62
Rock Types
Tonalite
Diorite
Quartz diorite
Evolved diorite
Tonalite breccia
Diorite breccia
Feldspar porphyry
Lamprophyre dike
Gabbro dike
Shear
Vein Types
Amphibole vein
Biotite vein
Au (g/t)
0
1.8
3.6
60
120
180
240
300
360
420
480
Depth
B
Cu (ppm)
0
210
420
60
120
180
240
300
360
420
480
Depth
C
Hole E11-63
Rock Types
Tonalite
Diorite
Quartz diorite
Evolved diorite
Tonalite breccia
Diorite breccia
Lamprophyre dike
Diorite dike
Vein Types
Biotite vein
Au (g/t)
0
5
10
50
100
150
200
250
300
350
400
Depth
D
Cu (ppm)
0
90
180
50
100
150
200
250
300
350
400
Depth

Figure D.3. Metal versus depth plot of holes E11-62 and E11-63, located on line 86+00 (D-D'; see Fig. 3.3), showing the association of rock type with Au and Cu. A) Gold vs. depth plot of hole E11-62 that shows consistent increase in Au in the diorite breccia unit and in tonalite and diorite rocks in the hanging wall of the diorite breccia unit. The dashed black line is an approximation of the cut-off grade (0.3 g/t Au). B) Copper vs. depth plot of hole E11-62 that shows elevated Cu contents in the diorite breccia unit and in tonalite and diorite rocks in the hanging wall of the diorite breccia unit. C) Gold vs. depth plot of hole E11-63 that shows consistent increase in Au in the diorite breccia unit and in tonalite and diorite rocks in the hanging wall of the diorite breccia unit. D) Copper vs. depth plot of hole E11-63 that shows no elevated Cu content associated with the diorite breccia, unlike that of hole E11-62.